Transactions of the ASME®

Transactions of the ASME, Journal of Turbomachinery (ISSN 0889-504X) is published quarterly (Jan., Apr., July, Oct.) for $195.00 per year by The American Society of Mechanical Engineers, 345 East 47th Street, New York, NY 10017. Periodicals postage paid at New York, NY and additional mailing offices. POSTMASTER: Send address changes to Transactions of the ASME, Journal of Turbomachinery, c/o THE AMERICAN SOCIETY OF MECHANICAL ENGINEERS, 22 Law Drive, Box 2300. Fairfield, NJ 07007-2300.
CHANGES OF ADDRESS must be received at Society headquarters seven weeks before they are to be effective. Please send old label and new address.
PRICES: To members, $40.00, annually; to nonmembers, $195.00.
Add $24.00 for postage to countries outside the United States and Canada.
STATEMENT from By-Laws. The Society shall not be responsible for statements or opinions advanced in papers or . . . printed in its publications (B7.1, Par. 3).

INDEXED by Applied Mechanics Reviews and Engineering Information, Inc.
Canadian Goods & Services Tax Registration #126148048

Journal of Turbomachinery

Published Quarterly by The American Society of Mechanical Engineers

VOLUME 119 • NUMBER 4 • OCTOBER 1997

TECHNICAL PAPERS

ANNOUNCEMENTS

Structures and Dynamics Committee Best Paper of 1996 Award

Inlet Distortion Generated Forced Response of a Low-Aspect-Ratio Transonic Fan

S. R. Manwaring
GE Aircraft Engines,
Cincinnati, OH 44135

D. C. Rabe
Wright Laboratory,
Wright-Patterson AFB, OH 45433

C. B. Lorence

A. R. Wadia

GE Aircraft Engines,
Cincinnati, OH 44135

This paper describes a portion of an experimental and computational program (ADLARF), which incorporates, for the first time, measurements of all aspects of the forced response of an airfoil row, i.e., the flow defect, the unsteady pressure loadings, and the vibratory response. The purpose of this portion was to extend the knowledge of the unsteady aerodynamics associated with a low-aspect-ratio transonic fan where the flow defects were generated by inlet distortions. Measurements of screen distortion patterns were obtained with total pressure rakes and casing static pressures. The unsteady pressure loadings on the blade were determined from high response pressure transducers. The resulting blade vibrations were measured with strain gages. The steady flow was analyzed using a three-dimensional Navier–Stokes solver while the unsteady flow was determined with a quasi-three-dimensional linearized Euler solver. Experimental results showed that the distortions had strong vortical, moderate entropic, and weak acoustic parts. The three-dimensional Navier–Stokes analyses showed that the steady flow is predominantly two-dimensional, with radially outward flow existing only in the blade surface boundary layers downstream of shocks and in the aft part of the suction surface. At near resonance conditions, the strain gage data showed blade-to-blade motion variations and thus, linearized unsteady Euler solutions showed poorer agreement with the unsteady loading data than comparisons at off-resonance speeds. Data analysis showed that entropic waves generated unsteady loadings comparable to vortical waves in the blade regions where shocks existed.

Introduction

The development process for modern turbomachinery blading can be greatly improved with accurate predictions of blade unsteady aerodynamic loadings, which are in turn used to predict blade resonant amplitudes. In the design process, excitation frequencies and mode frequencies are adjusted to ensure that crossings do not occur in the higher speed ranges where vibrations may cause fatigue failures. However, with modern low-aspect-ratio (LAR) blading, modal compression occurs (mode frequencies are more closely packed) and thus, the designer is forced to accept crossings at higher speeds where significant vibrations may occur. Therefore, accurate predictions of blade unsteady loads and subsequent vibrational response are necessary to determine if resonance crossings can be tolerated.

In recent years a number of computational methods for unsteady flows have been developed. Several authors have calculated unsteady periodic flows by time-accurately marching the Euler (Whitfield et al., 1987; Giles, 1988) or Navier–Stokes (Huff, 1987; Rai, 1989) equations. Unfortunately, because of the significant computational expense associated with these analyses, they are best suited for occasional unsteady aerodynamic analysis, not for routine design.

To reduce this computational expense, linearized unsteady solution methods have been developed. In these schemes, the flow is assumed to be composed of a nonlinear steady flow plus a small harmonic unsteady flow. In general, these approaches require one to two orders of magnitude less computational time than their time-marching counterparts. Verdon and Caspar (1984) and Whitehead (1990) have developed linearized analyses for transonic flows using the potential equation. Potential methods, however, do not model strong shocks such as those found in LAR fans. A more suitable method, developed by Hall and Crawley (1989), is to use the linearized Euler equations. Recently, a number of linearized Euler analyses have been developed for two-dimensional and quasi-three-dimensional flows (some examples are Hall and Clark, 1993; Holmes and Chuang, 1993) as well as for fully three-dimensional flows (Hall and Lorence, 1993).

To understand the physical mechanisms and to determine the abilities and accuracies of these computational predictions, high-quality data are needed where the measurements are taken on a modern design while operating at realistic flow conditions. A complete data set defining the aeroelastic excitation and response of a fan must include measurements of the flow defect, the blade unsteady loading, and the resulting vibrational response.

However, prior experimental programs have incorporated only half of the full forced response problem, i.e., either gust response or oscillating airfoil response, and have been limited to two-dimensional, unsteady flow models. Fleeter and his colleagues (Fleeter et al., 1978, 1980; Capece and Fleeter, 1987; Manwaring and Fleeter, 1990, 1993; Henderson and Fleeter, 1993) have measured the midspan unsteady pressures on low-speed compressor blading where gusts were generated from distortions, wakes, and potential fields. In these experiments the airfoils are rigid and do not respond to the gusts. Gallus et al. (1980) performed rigid airfoil, gust response experiments on the midspan of an axial flow compressor. Manwaring and Wisler (1993) obtained gust response measurements for low-speed

Contributed by the International Gas Turbine Institute and presented at the 41st International Gas Turbine and Aeroengine Congress and Exhibition, Birmingham, United Kingdom, June 10–13, 1996. Manuscript received at ASME Headquarters February 1996. Paper No. 96-GT-376. Associated Technical Editor: J. N. Shinn.

compressor and turbine blading. For blade motion experiments, Bolcs and Fransson (1986) measured the midspan sections of compressor and turbine airfoils in an annular cascade where the airfoils were actuated. Buffum and Fleeter (1990) have obtained unsteady pressure measurements on the blade surfaces of a linear cascade of compressor blading, also using an actuation system to provide blade motion.

Thus, there is need for additional data and analysis in a three-dimensional, transonic unsteady flow environment. Therefore, a series of experiments were performed, where inlet distortions were generated and measurements of the unsteady pressure loadings and the resulting vibrations were made. The objective of this work is to understand further the physical mechanisms of the aeroelastic excitation and unsteady aerodynamic response in a three-dimensional transonic fan rotor. The unsteadiness is generated by both upstream disturbances and blade motions. Evaluation of current state-of-the-art design capabilities will be made.

The following analyses were performed to help meet this objective. Three-dimensional Navier–Stokes analyses were used to understand the steady flow environment more fully. Quasi-three-dimensional, linearized unsteady Euler predictions were obtained to assess their capabilities for LAR fans. This unsteady flow analysis was performed by specifying the gust and motion boundary conditions from measurements. Future work will be to perform the full forced response prediction wherein the unsteady stress is predicted and then compared to the measurements from the strain-gages.

Experimental Program

Facility and Test Article. The measurements were obtained in the Compressor Research Facility (CRF) at Wright-Patterson Air Force Base. The CRF is an open cycle tunnel with a 6.10 m (20 ft) diameter test section. An electric motor provides power to the fan, which for this test has a 0.7 m diameter rotor setting centered in the tunnel. Atmospheric filtered air is drawn through five inlet valves, which control inlet pressure. For this program near-atmospheric inlet conditions were maintained.

The machine tested was a two-stage fan with the first stage being a low aspect ratio (LAR) design. Table 1 shows the geometric and aerodynamic design parameters of this instrumented first-stage rotor. The compressor was designed for high axial flow, which gives transonic conditions in the outer half of the first-stage rotor. Data were acquired at two conditions, low operating line (LOL) and design or nominal operating line (NOL). The LOL was obtained at the full open throttle condition and the NOL was determined by the peak efficiency point of the speed line. Due to the risk of damaging sensor during a possible stall event, data were not acquired at a near-stall condition. Data and analysis at the NOL are presented in this paper.

Table 1 Rotor 1 design parameters

Number of Blades	16
Aspect Ratio, C_m/H_{SA}	1.0
Solidity, C_m/T	1.8
Tm/C at tip	0.028
Midspan Chord, cm	19.0
85% Span Chord, cm	20.4
Material	Ti 6–4
Tip Radius, cm	35.2
Tip Speed, m/s	490.4
Design Flow, Kg/s	71.95
Design Speed, RPM	13,288

Inlet screens of two, three, and eight periods per revolution were used to generate distorted flow. The screens were mounted on a circumferential rotator to allow for different angular positions to be obtained while the machine is in operation. The predicted Campbell diagram in Fig. 1 shows that the following four resonance crossings occur during the fan operation: 3/rev—first flex ($1F$) at 62 percent speed, 8/rev—second flex/first torsion ($2F/1T$) at 68 percent speed, 8/rev—two stripe ($2S$) at 98 percent speed, and 2/rev—$1F$ near 105 percent speed. During testing the anticipated 2/rev—$1F$ crossing at 105 percent was not obtainable. The predicted mode shapes for each of the crossings are also shown in Fig. 1.

Instrumentation

Steady Aerodynamic Performance. The overall steady performance was determined at several speeds from measurements of the overall flow and total temperature and pressure. The flow was obtained from a calibrated venturi at the exit of the test section. To determine the radial profiles of temperatures and

Nomenclature

b = semi-chord at 85 percent span = $C/2$
C = speed of sound, chord at 85 percent span
C_m = chord at midspan
$C'_{\Delta p}$ = unsteady pressure difference coefficient = $\Delta p'_s/(0.5\varrho W^2)/(w'/W)$
F_G = modal force per chordwise section
G = damping of blade
H_{SA} = blade height at stacking axis
LAR = low aspect ratio
LOL = low operating line
k = reduced frequency = $\omega b/W$
K = stiffness of blade
M = inertia of blade
Ma = steady absolute Mach number
NOL = nominal (design) operating line
p_s = first harmonic of unsteady static pressure
s = surface distance around blade surface
S = span
TE = trailing edge
T = blade tangential spacing at midspan
T_m = maximum thickness
U = blade speed
V = steady absolute velocity
v'_x = first harmonic of unsteady axial velocity
v'_y = first harmonic of unsteady tangential velocity
W = steady relative velocity
X = blade motion
δ = blade motion deflection
ϵ = blade vibratory strain
ζ = blade total system damping
λ = characteristic of first harmonic of unsteady flow
ϱ' = first harmonic of unsteady density
ω = frequency of flow defect excitation, rad/s
ω_n = natural frequency of blade mode, rad/s

Subscripts

FE = finite element solution
G = location of strain gage
MS = measurement
n = normal to blade surface

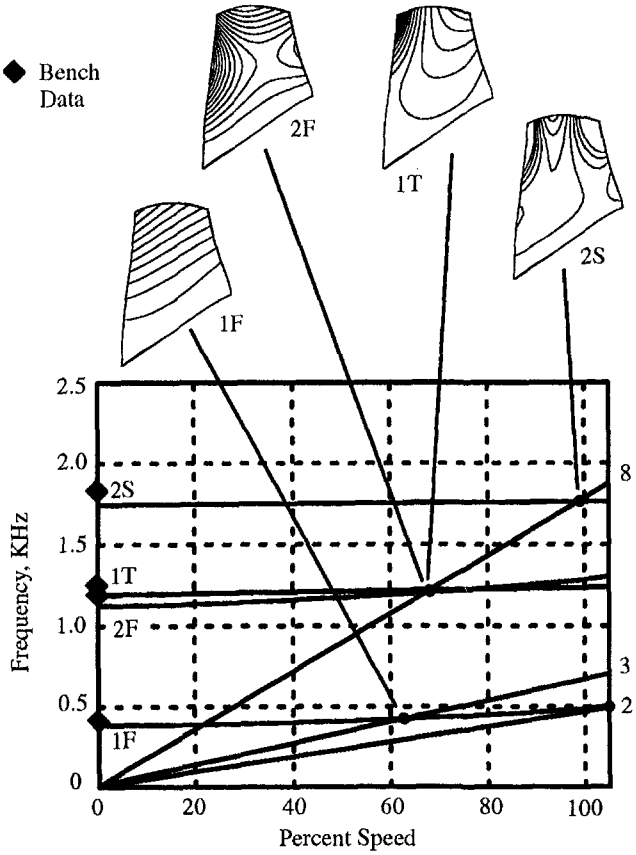

Fig. 1 Predicted Campbell diagram and measurements at zero speed

pressures, rakes were located at the inlet, inlet to stator 1 and 2 and stator 2 exit.

Flow Distortion. The measurements of the circumferential variation in total pressure due to the screens were obtained with eight five-element rakes located 37 cm (14.6 in.) upstream of the leading edge at the blade root as shown in Fig. 2. For each rake, a static pressure at the casing was measured using a tap located 10 deg from the rake. For the 3/rev distortion, measurements were taken at four screen rotations to give 32 points around the circumference or 10.67 points per period of the distortion. For the 8/rev distortion, ten screen rotations gave 10 points per period. For both the rake and casing static pressures, measurements were accurate to within ±0.002 atm, which is ±4.0 percent of the lowest dynamic pressure at the inlet encountered during the three crossings of interest.

Blade Unsteady Loading. The unsteady pressure difference across the blade was measured with Kulite model XCQ-093 dynamic pressure transducers with a 50 psid range. The transducers were located at 85 percent span on two adjacent blades, numbers 1 and 16 as shown in Fig. 3. Both of the blades had seven transducers located in identical chordwise positions. The accuracy of the transducers was ±0.031 atm., which is approximately 25 percent of the maximum measured periodic unsteadiness. During data acquisition the upstream rakes used for measuring distortions were removed to ensure blade unsteady loadings were only due to screen generated distortions.

Several transducer signals failed during testing, presumably due to the centrifugal loads encountered. At 62 percent speed 8 of the original 14 transducers were operational. At 68 percent speed, on a subsequent run, three of the sporadically failing transducers returned to give 11 measurements. At the high speeds only 5 of the original 14 had survived.

As a demonstration of the difficulty in measuring unsteady pressures on high-speed blading, the original instrumentation of the rotor did not survive the first minutes of operation and the blade was re-instrumented with pressure transducers. The first set of instrumentation failed due to the epoxy used in mounting the sensor diaphragms transmitting excessive blade strain into the sensor and causing failures. The second set of instrumentation used RTV to mount the diaphragms. The intent of this more flexible mounting was to prevent high strain from damaging the sensor. The failures for this testing were mostly attributed to lead wire breaks. For future testing, it is suspected that sputtering the leads directly to the blade surfaces will help retain on-blade measurements.

The transducers were embedded flush to one surface of the blade and pneumatically connected to the other surface with a vent hole in order to sense the differential unsteady pressures across the blade. The maximum vent hole length was 4.72 mm (0.120 in). The natural frequency of the installation system is 20 kHz. The highest excitation frequency encountered is 1.9 kHz for the 8/rev distortion at 98 percent speed, which is well within the flat response range of the transducer/installation system. Therefore, dynamic calibration of the measurement system was deemed unnecessary. The transducer sensitivities were determined from calibrations performed by the transducer manufacturer. Rabe et al. (1995) show in more detail the installation of the transducers and typical unsteady pressure measurements encountered during testing in this program.

Vibratory Response. Vibratory stresses were obtained by dynamic strain gages applied to the blade surfaces. Root strain gages were located on the pressure surfaces of the two Kulite

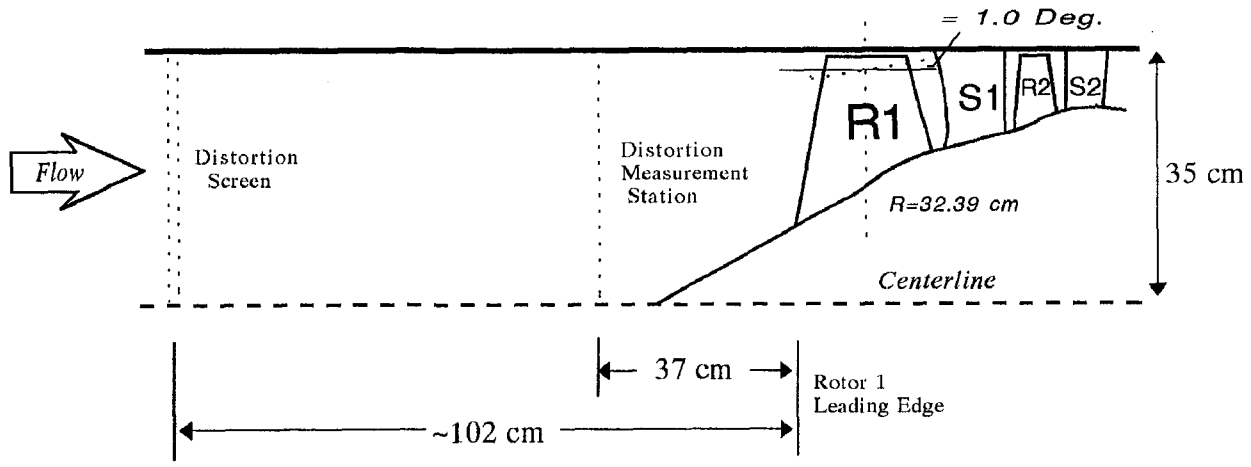

Fig. 2 Test fan and generation of distortion

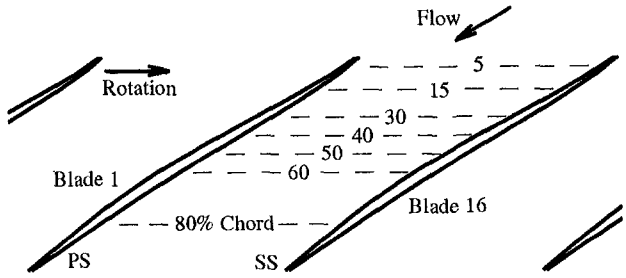

Fig. 3 Locations of blade-mounted pressure transducers at 85 percent span

instrumented blades and two other blades located roughly 120 deg around the circumference of the blade row. These gages were located to be sensitive to the $1F$, $2F$, and $1T$ modes. Trailing edge (TE) gages were located on the two Kulite instrumented blades to measure accurately the $2S$ chordwise-bending mode. However, during testing these TE gages failed almost immediately. Thus, the root gages have been used to determine amplitudes of the $2S$ deflections.

Data Reduction

Steady Aerodynamic Performance. To determine the detailed steady performance of the two-stage LAR fan, radial profiles of the circumferentially averaged total pressure and temperature were used to define the intrablade row conditions. These profiles and the speed and mass flow set the flow properties for a streamline-curvature, radial-equilibrium analysis. This throughflow analysis was then used to set the initial and boundary conditions of the computational analyses.

Flow Distortion. The "per rev" content of the excitation of the first-stage rotor was calculated from the Fourier decomposition of the circumferential distributions of measured total and casing static pressures. The variation in static pressure from its average value at the casing is normalized by the local value of the dynamic pressure obtained from the throughflow analysis. This normalized static pressure variation is assumed to remain constant across the span. Circumferential variation in total pressure at any span location is obtained by interpolating or extrapolating each harmonic and then reconstructing the distribution. The circumferential variation in velocities and densities at desired span locations can be calculated by using these pressure variations and the total temperature measurements. Fourier decomposition of these circumferential surveys at different spanwise locations give radial profiles of the first harmonic disturbance in terms of primitive variable perturbations, ϱ', v_x', v_y' and p_s'. The screens were designed to give pure tone disturbances, which were verified by second harmonic magnitudes being less than 5 percent of the first harmonics for both screens, 3/rev and 8/rev.

The primitive variable definition of the unsteadiness to the blade can be used to specify proper incoming boundary conditions for unsteady analyses. However, these definitions do not give a clear understanding of the physical mechanisms generating the unsteadiness. Giles (1988) and others have used an eigen-analysis of the two-dimensional Euler equations to determine the relationship between primitive variable perturbations and natural modes of the unsteady flowfield. There are four natural modes (characteristics) of the system: an entropy wave (λ_1), a vorticity wave (λ_2), one downstream moving pressure wave (λ_3), and one upstream moving pressure wave (λ_4). Because only incoming disturbances at the upstream boundary are of interest in this case, (λ_4) need not be calculated. A modified version of Giles' transformation may be used here, then, to compute the magnitudes and phases of the incoming characteristics. By describing the steady flow in the stationary versus rotating reference frame and setting the steady tangential velocity to zero, purely axial flow at the measurement plane (radial velocity is nearly zero), the following is obtained:

$$\begin{pmatrix} \rho' \\ v_x' \\ p_s' \end{pmatrix} = \begin{bmatrix} \dfrac{-M_a}{2} & 0 & \dfrac{U}{2VC^2}\dfrac{M_a}{\sqrt{M_a^2-1}} \\ 0 & \dfrac{-U}{2C} & \dfrac{-U}{4C}\dfrac{1}{\sqrt{M_a^2-1}} \\ 0 & 0 & \dfrac{U}{2V}\dfrac{M_a}{\sqrt{M_a^2-1}} \end{bmatrix} \begin{pmatrix} \lambda_1 \\ \lambda_2 \\ \lambda_3 \end{pmatrix} \quad (1a)$$

$$v_y' = \frac{\sqrt{M_a^2-1}}{2} p_s' \quad (1b)$$

The characteristics can be determined by inverse matrix manipulation. In this set of equations, the characteristics, λ_i, have been normalized by the dynamic pressure, $0.5\varrho V^2$, as well as the static pressure perturbation. The velocity perturbations have been normalized by the steady absolute velocity and the density perturbation by the steady density. The amplitudes and phases of the vortical and entropic waves are assumed to remain constant from the rake measurement axial location to the grid boundary of the computational analysis described below. The acoustic wave amplitude decays exponentially with axial distance.

Blade Unsteady Loads. The procedure used to obtain the unsteady pressure difference acting on the rotor measured by the transducers at 85 percent span is summarized below. Complete details may be found by referring to Woehr and Manwaring (1995). The signals were digitized from analog tape at sample rates that would give at least 50 points per period.

An "induced" pressure signal is obtained from two sources: the blade vibration transmitting strain into the transducer diaphragm, and the vibration of the diaphragm. To determine the relationship between transducer signal and vibratory strain for each of the modes that were encountered during testing, the instrumented blade was vibrated in a vacuum chamber. Then by using the measured strain during the tests, the "induced" signal was calculated and then subtracted from the measured value of unsteady pressure. In all cases this "induced" signal was small compared to the unsteadiness generated by unsteady aerodynamics from the gusts and blade motions. The largest relative value was for the $1T$ mode where the mechanically induced signal was 2 percent of the total signal. The use of flexible RTV for mounting the sensor diaphragm helps keep blade vibratory strain from being transmitted to the transducer sensor.

The unsteady pressure difference is presented as the unsteady pressure on the pressure surface minus the unsteady pressure on the suction surface. The unsteady pressure difference is normalized by the relative dynamic pressure and normalized velocity perturbation as shown below in the definition of the unsteady pressure difference coefficient:

$$C'_{\Delta p} = \frac{\Delta p_s'}{\frac{1}{2}\rho W^2\left(\frac{w'}{W}\right)} \quad (2)$$

The phases of the blade number 16 signals were adjusted by the interblade phase angle for comparisons with measurements from blade number 1. Since the flow defect is measured in the stationary reference frame, the phase of the pressures cannot be related to the forcing function in an absolute sense. Thus, comparisons between data and analyses can only be of chordwise trends and not absolute phase. For presentation purposes, the pressure data phase levels are adjusted for ease of comparison with the linearized Euler analyses.

Vibratory Response. The strain gage data were stored on analog tape simultaneously with the pressure transducer signals. The strain gage signals were digitized and Fourier analyzed to give amplitude and phase of the measured strain. During speed transients, near real time Fourier amplitudes are obtained at discrete frequencies versus time (speed), which are then plotted in Campbell diagram format.

Computational Program

This section describes the computational modeling of the blade mode shapes and the steady and linearized unsteady aerodynamics of the first-stage LAR rotor.

Blade Mode Shapes. Finite element modeling was used to determine the mode shapes for the stage 1 blade. Only the airfoil was included in the model due to the high relative stiffness of the rest of the structure. Twenty brick elements were used in the chordwise and spanwise directions. Four elements were used through the thickness. Good agreement of frequencies and mode shapes was found between bench tests and analytical results for zero speed, as can be seen in Fig. 1. Finite element analyses, including large deflection, stress stiffening, and spin softening options were used for the predictions. The mode shapes resulting from this analysis were used as surface boundary conditions for the blade unsteady loading calculations described below. In addition, the stress predictions were used to correlate the measured vibratory response from the strain gages to the modal amplitude.

Steady Aerodynamics. The prediction of the three-dimensional steady flow was obtained from a three-dimensional Navier–Stokes solver (Turner and Jennions, 1992). The grid used for these viscous calculations consisted of 260,000 nodes with 117 cells in the streamwise direction, 48 in the blade-to-blade direction, and 44 in the radial direction, 4 being in the tip gap region. $K-\epsilon$ turbulence modeling was used and wall functions were used for the boundary layer flow very close to the endwall and blade surfaces. Boundary and initial conditions were obtained from the streamline-curvature/data-match analysis described earlier. The blade untwist going from design speed to the part-speed conditions was assumed to have negligible effect on the steady and unsteady flow solutions so all computational analyses used the design speed geometry definitions.

Unsteady Aerodynamics. The unsteady aerodynamics is predicted with a quasi-three-dimensional linearized Euler solver where the steady flow is calculated with the full nonlinear Euler equations. The steady boundary conditions are obtained from the streamline-curvature/data-match analyses. The definition of the unsteady boundary conditions was described in the previous sections. The steady flow of the quasi-three-dimensional analysis was "tuned" to match the steady flow predicted by the three-dimensional Navier–Stokes solver described above. "Tuning" was achieved by adjusting the streamtube thickness distribution through the blade until the surface ideal Mach numbers nearly matched those of the viscous solution.

The linearized Euler analysis used in this paper (Holmes and Chuang, 1993) uses an unstructured, adaptive finite-volume scheme. The Euler equations are solved in conservation-law form with shock capturing used to model the shock impulse. Unlike subsonic flows, where solutions are weakly dependent on grid resolution, transonic flows are strongly dependent on the number of grid points used, as well as the artificial viscosity in the scheme. In principle, shocks may be increasingly refined until they have negligible width. While this may be useful from a code validation standpoint, such highly refined shocks are not representative of actual viscous flows. As a result, the quasi-three-dimensional grids used here were only moderately refined so as to simulate the three-dimensional viscous flow environment while maintaining sufficient resolution to predict the unsteady flowfield accurately. Numerical experiments have shown that additional grid refinement only produces more refined shocks, without significantly affecting the rest of the flowfield. In addition, the wavelengths of the unsteady disturbances have been computed analytically to ensure that the grids used appropriately resolve these waves. This approach is not without precedent. Lindquist and Giles (1994) and Hall et al. (1994) have shown that unsteady shock loads can be modeled accurately using linearized Euler analyses if the scheme is conservative and the shocks are sufficiently smeared.

The blade motion surface boundary conditions for the unsteady aerodynamic analyses are obtained from the finite element mode shape predictions and the root strain gage measurements. The amplitude of the deflections at any point on the blade is related to the strain at the root gage by the following equation.

$$\delta_i = \delta_{i,FE}\left(\frac{\epsilon_{G,MS}}{\epsilon_{G,FE}}\right) \tag{3}$$

where the *FE* subscripts denote finite element predicted strains and deflections and the *MS* subscript denotes measured strain.

Before the gust and blade motion unsteady solutions can be superimposed, the unsteady loadings must be properly phase related. The relationship between the gust and the blade motion is described with the following single-degree-of-freedom (SDOF) equation

$$M\ddot{X} + G\dot{X} + X = F_G \tag{4}$$

where X is the blade motion and F_G is the modal force of the gust. The modal force at the 85 percent span section is obtained by integrating the unsteady pressure times the modal deflections around the surface of the blade as the following equation shows:

$$F_G = \oint p'_s(s)\delta_n(s)ds \tag{5}$$

where p'_s and F_G are complex and δ_n is real and s is surface distance around the blade. Solving the differential equation shown above for SDOF motion, Eq. (4), the following relationship is obtained:

$$\frac{X}{F_G} = \frac{1}{\left[\left(\frac{i\omega}{\omega_n}\right)^2 + 2\zeta\left(\frac{i\omega}{\omega_n}\right) + 1\right]} \tag{6}$$

where ζ is the total system damping and is obtained by applying the half-power law to the resonance amplitude versus frequency (rpm) distribution measured with the root strain gages. For typical solutions of Eq. (6), the gust is assumed to be real (zero phase) and the phase of the motion is determined from Eq. (6). However, for these analyses, the blade motion, X is real (phase of zero) and Eq. (6) will quantify the amount that the gust leads the motion. The phase levels of the predicted gust generated unsteady pressures, p'_s, were re-referenced to ensure that the gust force, F_G, leads the motion by the correct amount.

Results

This section presents the results of the data and analysis of the steady and unsteady loading during the three crossings encountered during compressor operation with the two distortion screens. The details are presented starting with the lowest speed crossing and proceeding to the highest speed crossing, all at the design (nominal) operating line. For each crossing, analysis of the flow distortions is given followed by presentation of the strain gage measurements and mode shapes. Then the predictions of the steady flow through the rotor are discussed. Finally, unsteady loading data and analysis results are shown for off-resonance and near resonance.

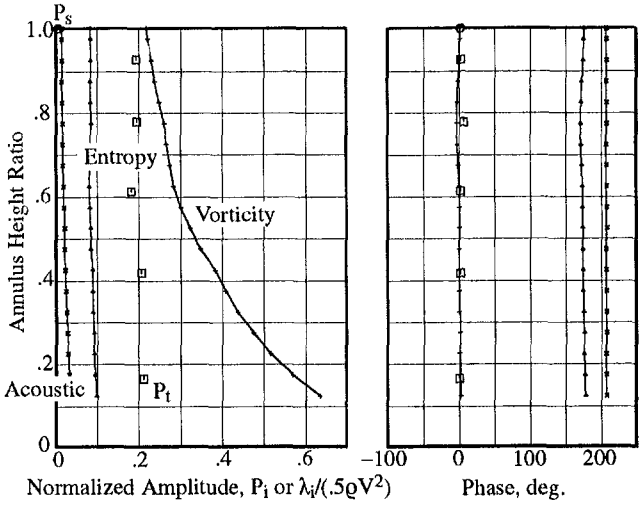

Fig. 4 First harmonic of pressures and flow defect characteristics from 3/rev distorted flow at 62 percent speed

3/Rev-1*F* Crossing at 62 Percent Speed. The Fourier decomposition of the circumferential distributions of total pressure and casing static pressure due to the distorted flow from the 3/rev screen is shown in Fig. 4. The spanwise profile of normalized amplitude and phase of the first harmonic of the total pressure is nearly uniform and approximately 20 percent of the dynamic pressure. The casing static pressure first harmonic is less than 1 percent of the dynamic pressure. The spanwise profiles of the entropy, vorticity, and acoustic characteristics calculated from the pressure and total temperature data are also shown in Fig. 4. The vortical wave is the strongest of the three, varying from 20 percent of the dynamic pressure at the casing to over 70 percent at the hub. The entropy wave is weaker, being only 8 to 9 percent of dynamic pressure. The acoustic wave is small, approximately 1 to 3 percent of dynamic pressure. Also, the acoustic wave is cut off and decays exponentially with axial distance and thus will be of negligible value at the leading edge of the rotor cascade. Thus, these vortical and entropic waves are used to set the linearized unsteady analysis. Harmonic incidence angles on the rotor help show the overall level of unsteadiness due to this distorted flow; incidence variations are roughly ±2 deg. The velocity perturbation is 3.0 percent of the steady relative velocity; we assume that the disturbances are modeled within the linear framework of the analysis.

The Campbell diagram, as obtained from the root strain gages on the two transducer-instrumented blades, is shown in Figs. 5(*a*) and 5(*b*). The measurements shown were taken at the low operating line (LOL). The test sequence is as follows. The compressor was slowly accelerated to 8800 rpm at the LOL then decelerated to 8100 rpm, the throttle set to the NOL, pressure transducer and strain gage data acquired, and then a slow acceleration to 8400 rpm, followed by another set of transient data being acquired. The speed was then dropped to 8100 rpm, the throttle set back to the LOL setting, and the machine shut down. Since the resonance occurs at approximately 8700 rpm, a full sweep through the resonance was not obtained at the NOL. Therefore, to obtain peak resonance frequencies and damping from the strain gage measurements, the LOL data were used and it is assumed that frequencies and total system damping is relatively unchanged between LOL and NOL. For both instrumented blades the difference between LOL and NOL vibrations was less than 5 percent at 8100 and 8400 rpm and thus, the above is assumed to be valid.

For blade No. 1, close examination of Fig. 5(*a*) shows the 1*F* resonance peak occurred at 8690 rpm (434.5 Hz) and damping (ζ) was calculated to be 0.008, while for blade No. 16, Fig. 5(*b*) shows the peak was at 8700 rpm (435.0 Hz) and damping was 0.010. The natural frequencies of blades 1 and 16 are nearly identical, 0.1 percent difference, while the damping differs by 20 to 25 percent.

At 8100 rpm for the NOL, the peak-to-peak stress determined from the root strain-gages was 5.2 KSI for blade No. 1 and 4.6 KSI for blade No. 16 (a 12 percent variation). The phase difference between measurements was 71.7 deg, which is 4.2 deg greater than what is determined from a three nodal diameter disturbance with 16 blades in the cascade. Calculations using the single-degree-of-freedom (SDOF) motion equation and the damping and peak resonances shown above, give that blade No. 1 should be 2 percent larger than blade 16 and that the phase difference from the interblade phase angle definition should be 0.8 deg. At 8400 rpm for NOL, the measured stress was 12.2 KSI for blade No. 1 and 9.4 KSI for blade No. 16 (a 26.0 percent variation). The difference in phase from what the interblade phase angle gives is still 4.2 deg. The SDOF calculations show the amplitude variations should be 4.0 percent and the phase difference from the interblade phase angle definition should be 2.3 deg. Thus slight blade mistuning variations in the damping and peak resonance account for some of the variability of the strain gage measurements.

The first-flex (1*F*) deflections predicted by the finite element model are shown in Fig. 1. The motion is mostly bending with a slight amount of twist. The strain gage was located in a region predicted to have a large unsteady stress gradient. Thus, accurate determination of deflections at other locations on the blade may be difficult.

The steady aerodynamics were predicted using the three-dimensional Navier–Stokes solver. Figure 6 shows the contours of ideal Mach number along the suction surface and the passage at a span roughly corresponding to the location of the chordwise array of pressure transducers, 85 percent span. A supersonic flow regime is seen just aft of the leading edge. The extent of the leading edge supersonic "bubble" decreases as span is decreased, going from approximately 10 percent chord at the tip to being nearly gone at 30 percent span. The flow is predominantly two dimensional; radially outward flow exists in the suction surface boundary layer just downstream of the shock and over the aft half from centrifuging of the boundary layer fluid.

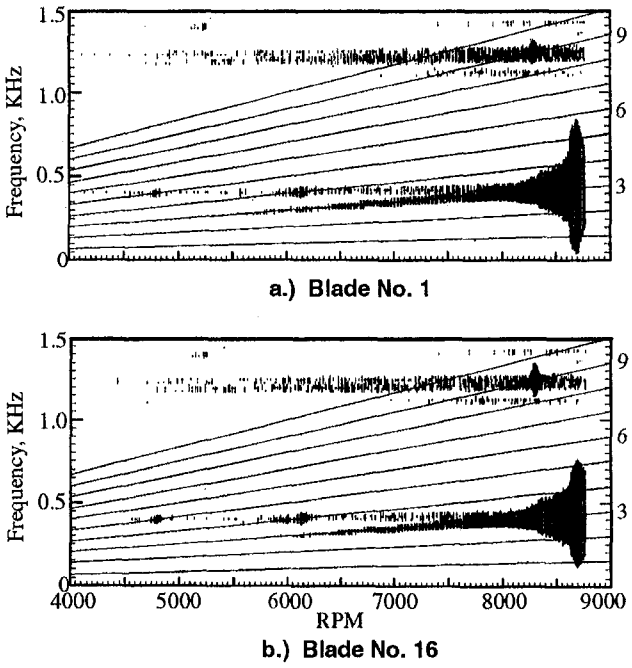

Fig. 5 Measured Campbell diagram for 3/rev distortion excitation near 62 percent speed

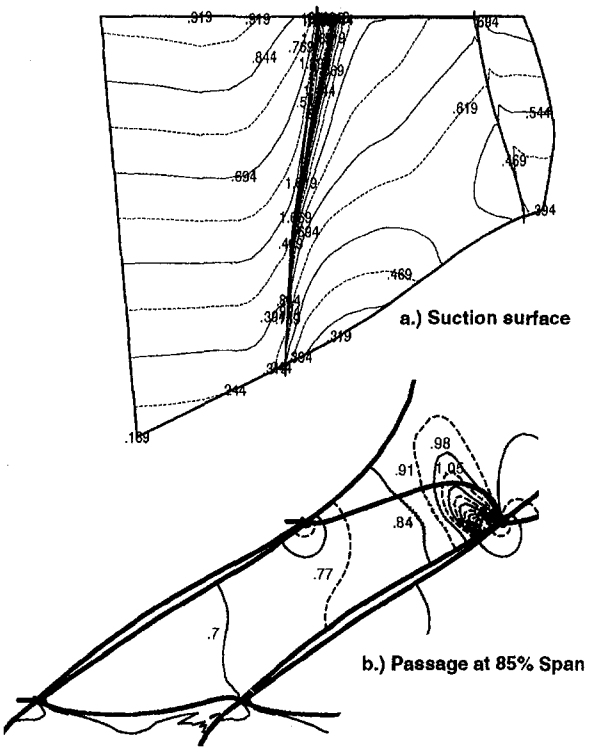

Fig. 6 Three-dimensional Navier–Stokes predicted contours of ideal Mach number

The measurements of unsteady loading were acquired at two speeds during the approach to resonance, 8100 and 8400. The reduced frequency, k, is 0.90 for both speeds. At 8100 rpm, the blade response was roughly 30 percent of scope limits (allowable values) while at 8400 rpm, the response was 60 percent of scope limits. Figure 7 shows the measured unsteady loading for both 8100 and 8400 rpm. The blade-to-blade variations are negligible with nearly identical chordwise trends occurring for both speeds. The amplitudes of the higher speed, closer to resonance, are approximately one-third higher than those of the lower speed due to the increase in unsteady pressures from the higher amplitude blade vibrations. Predictions from the linearized Euler analysis were not obtainable for this condition.

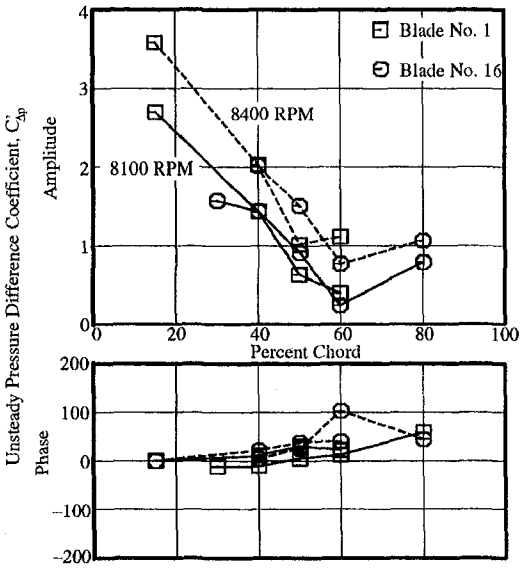

Fig. 7 Measured unsteady loading due to 3/rev excitation near 62 percent speed

8/Rev-2F/1T Crossing at 68 Percent Speed. The spanwise profiles of the first harmonics of the circumferential distributions of total and casing-static pressures, Fig. 8, show that the flow disturbance is radially nonuniform in amplitude with a peak value at 77.5 percent span. The phase is uniform across the span. The acoustic characteristic for this higher frequency distortion is nearly nonexistent, having a value of less than 1 percent of the dynamic pressure. The vortical and entropic characteristics have similar spanwise trends, which correspond to the total pressure profiles. The vortical wave is generally two to three times that of the entropic wave. The rotor incidence angle fluctuations vary across the span from ±1.5 deg at the hub to nearly ±4 deg at 82.5 percent span. The unsteady velocity perturbation is 7.0 percent of the steady relative velocity at 85 percent span.

The measured Campbell diagrams are shown in Figs. 9(a) and 9(b) for both transducer-instrumented blades at the NOL. Unlike the previous case, slow speed excursions were taken across the nearly full resonance response of the blades, going from 9100 to 10,400 rpm. The speed traverses were slow enough, 15 rpm/s, to allow for transducer and strain gage data to be acquired and analyzed during any part of the speed range. Therefore, transient data were analyzed at very near the resonance, 9388 rpm, and at a speed that the blade motion was negligible, 9950 rpm, during a slow acceleration. The resonance shows a two-peak response, which is possibly due to the 8/rev exciting both the 2F mode and the 1T mode, which are very close in frequency. For the linearized Euler analysis, two solutions were obtained, one with the motion assumed to be from the 1T mode only and the other with 2F mode only.

The amplitude of the unsteady stress obtained from the blade No. 1 gage is 28.4 KSI, while for blade No. 16 the measured unsteady stress is 32.2 KSI, showing a 12.7 percent variability between the blades. The phase difference between the blades is 121.5 deg, which is 58.5 deg from what is specified by the interblade phase angle, 180 deg. The peak resonance for blade No. 1 is 9348 rpm (1246 Hz) and the damping (ζ) is 0.0032 while for blade No. 16 the peak occurs at 9261 rpm (1235 Hz) and the damping is 0.0021. Blade No. 1 has a natural frequency of this combined mode that is 1.0 percent greater than that of blade No. 16 while the damping is 50 percent greater. The variation in amplitude as calculated from the SDOF equation is 34.0 percent and the difference in phase from what is prescribed by the interblade phase angle is 1.6 deg. These values

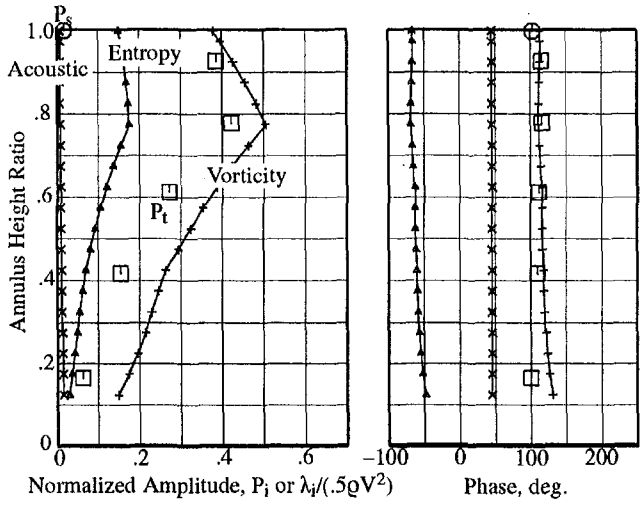

Fig. 8 First harmonic of pressures and flow defect characteristics from 8/rev distorted flow at 68 percent speed

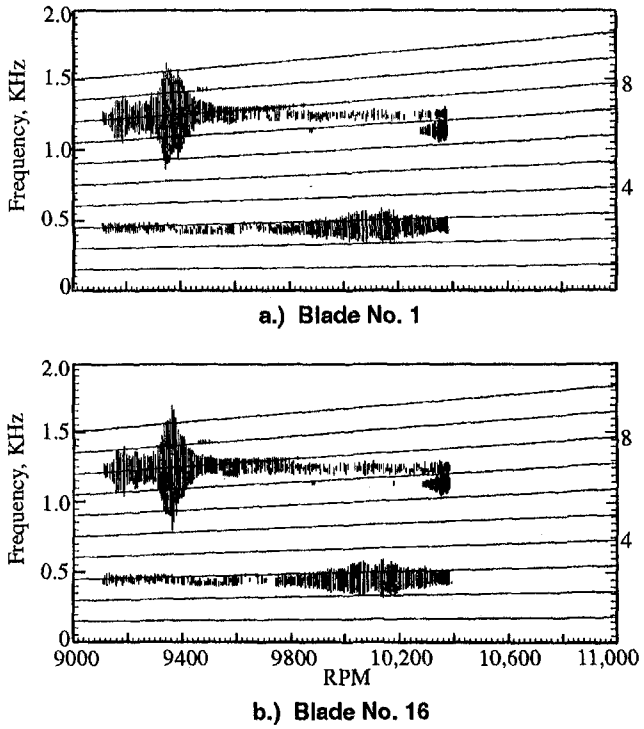

Fig. 9 Measured Campbell diagram for 8/rev distortion excitation near 68 percent speed

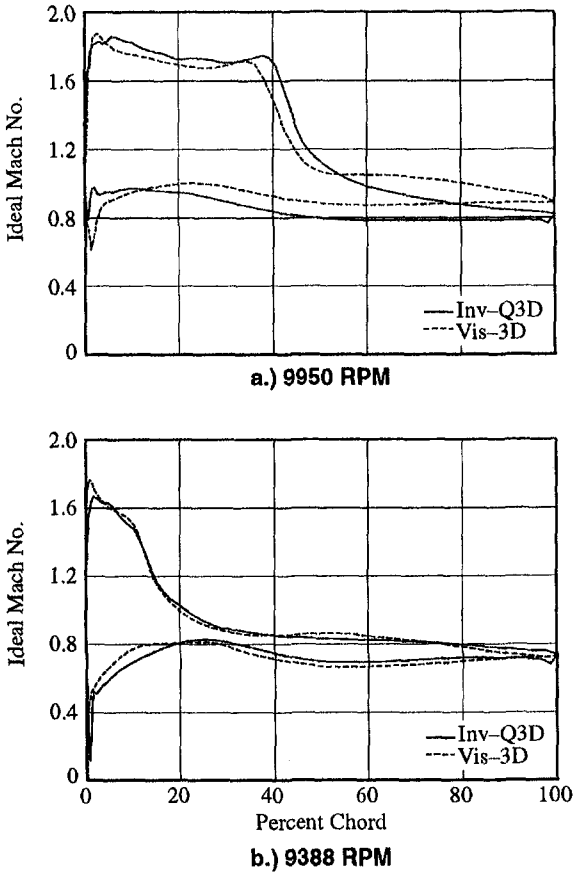

Fig. 10 Predicted steady loading on blade near 8/rev crossing at 68 percent speed

differ from what is measured, which further shows that the vibrations are a coupled $1T/2F$ mode since the SDOF equation only applies for single mode vibrations.

Steady flow predictions were obtained at three speeds, one for where the inlet distortion data were acquired, 9100 rpm, and the other two for where the unsteady pressure data were acquired, 9388 and 9950 rpm. At the two lower speeds the predicted flow is very similar to that shown for the 3/rev resonance at 62 percent speed, showing a supersonic flow "bubble" just aft of the leading edge on the suction side. At 9950 rpm the supersonic "bubble" is gone and is replaced by a nearly normal shock which extends from the leading edge to the suction surface. The steady flow is predominantly two dimensional along streamline descriptions with only outward radial flow beyond the streamlines being in the suction surface boundary layer.

The steady flow part of the Euler computation was tuned to have its predicted surface Mach numbers nearly match those of the three-dimensional Navier–Stokes analysis. Figures $10(a)$ and $10(b)$ show the chordwise distribution of Mach number predicted by the quasi-three-dimensional Euler analysis compared to that predicted by the three-dimensional, viscous analysis for both 9950 and 9938 rpm. For 9950 rpm, the tuned quasi-three-dimensional Euler matches well with the three-dimensional, viscous solution with both showing the shock centered at approximately 42 percent chord. At 9388 rpm, the tuned quasi-three-dimensional Euler analysis matched well with the viscous solution, with the peak Mach number being 1.6 for the Euler analysis and 1.8 for the viscous analysis. They both showed the shock to be centered at approximately 14 percent chord.

The predicted and measured unsteady loading response for the off-resonance speed, 9950 rpm ($k = 2.28$), is shown in Fig. 11. The blades have negligible motion and thus, both instrumented blades, Nos. 1 and 16, have nearly identical unsteady boundary conditions. Good repeatability of measurements is demonstrated by the small differences between blade 1 and 16 measurements. The predictions and measurements show good agreement. The chordwise trends in amplitude and phase are nearly identical. The only differences are that the calculations underpredict the increase in amplitude of unsteady loading in

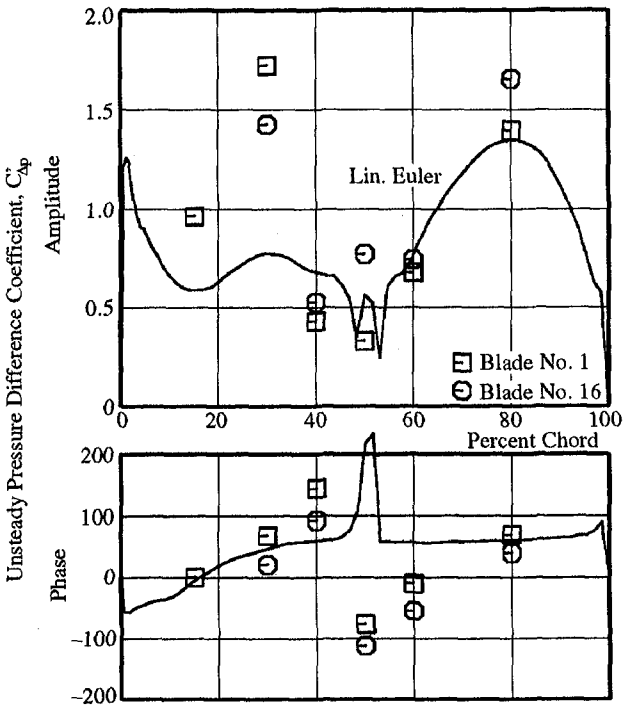

Fig. 11 Measured unsteady loading due to 8/rev excitation at 9950 rpm, off resonance

front of the shock, around 30 percent of chord, and over the aft half of the blade the phase predictions are constant while the data increase in value.

For the very near to resonance speed, 9388 rpm ($k = 2.38$), there is significant blade-to-blade variation between the blade No. 1 and blade No. 16 measurements, as can be seen in Fig. 12. The strain gage data showed large blade-to-blade variations, which would support the variations in unsteady loading measurements between the two blades. The motion of adjacent airfoils was not measured and thus, mistuning effects from blades 2 and 15 cannot be determined.

Predictions of the unsteady loading with both $1T$ only and $2F$ only motions were obtained from the linearized-unsteady analysis. The amplitude of the motions used in the analysis were determined from the averages of the blade 1 and blade 16 strain measurements. Significant differences in predicted unsteady loading occur between using $1T$ and $2F$ motions with neither solution showing a good comparison with the amplitude and phase data. The true mode is an unknown linear combination of these two modes and thus, the unsteady loading solutions would also be unknown linear combination of the two solutions shown in Fig. 12. For this linearized unsteady analysis, blade-to-blade variation in the cascade motions are not modeled and thus, predictions could not compare with both the blade 1 and blade 16 data. Also, three-dimensional unsteady flows can be generated from the blade motion due to the modeshapes, Fig. 1, having gradients in the radial direction. These effects are not accounted for in the two-dimensional modeling of the linearized-unsteady analysis.

8/Rev-2S Crossing at 98 Percent Speed. The spanwise profile of the first harmonic amplitude of the total pressure due to the 8/rev screen at 98 speed is shown in Fig. 13. By comparing to the 8/rev distortion data seen at lower speeds, Fig. 8, the effect of speed on the distortion is found to be minimal, with nearly identical profiles and a reduction of amplitude of approximately 10 percent. The speed does affect the characteristics of the disturbance as can be seen by comparing the spanwise

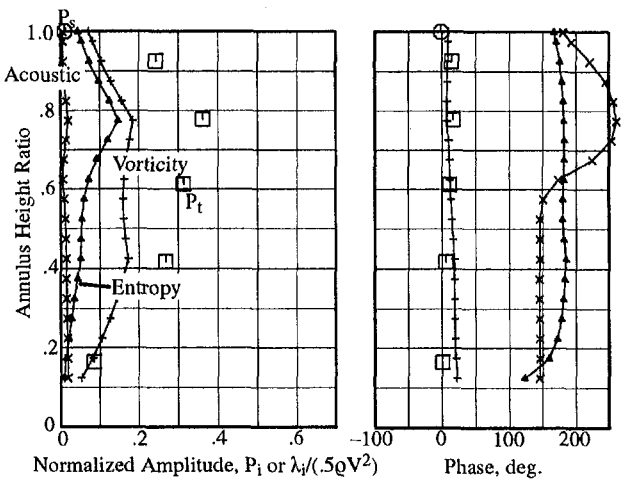

Fig. 13 First harmonic of pressures and flow defect characteristics from 8/rev distorted flow at 98 percent speed

profiles of entropy, vorticity, and acoustics for the high speed with those at the lower speed. The vorticity wave is decreased in magnitude and is comparable in strength to the entropy wave. The acoustic wave has grown but is still very small. The rotor incidence fluctuations are similar to those of the lower speed. The unsteady velocity harmonic is 3.2 percent of the steady relative velocity.

The root strain gages were used to measure the unsteady stresses and deflection due to this $2S$ mode since the trailing edge gages intended for measurement of the chordwise bending modes had failed early in the test. From the finite element model discussed below, the unsteady stress at the gage location is 12 percent of the highest unsteady stress on the blade, which implies that the gages will be marginally acceptable for accurate measurements of strains. The measured Campbell diagrams are shown in Fig. 14 for the LOL. Similar to the 62 percent speed case, the measurements at NOL did not traverse the full extent of the resonance and therefore LOL data will be used to deter-

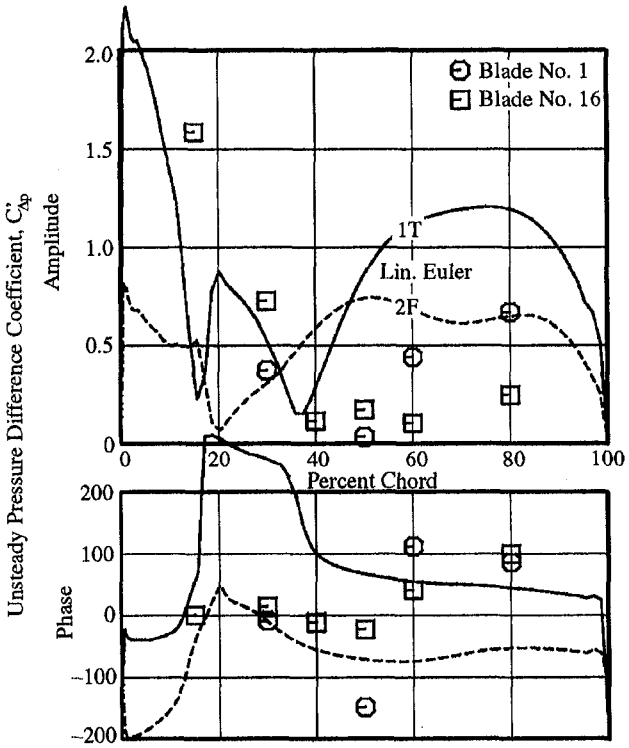

Fig. 12 Measured unsteady loading due to 8/rev excitation at 9388 rpm, very near resonance

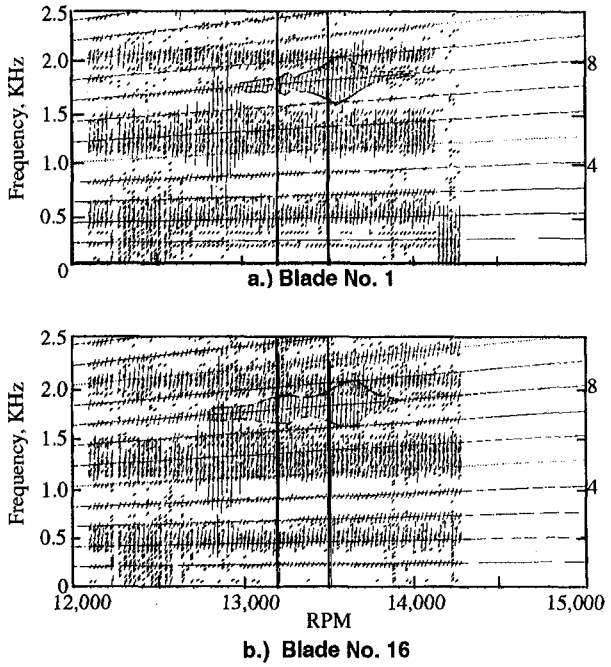

Fig. 14 Measured Campbell diagram for 8/rev distortion excitation near 98 percent speed

mine peak resonance and damping values. Blade No. 16 shows a double peak response while blade No. 1 shows only a slight "bump" in the response. The peak resonances were 13,550 rpm (1807 Hz) for blade No. 1 and 13,625 (1817 Hz) for blade No. 16 while the damping was 0.0061 for blade No. 1 and 0.0070 for blade No. 16. The natural frequency of blade No. 1 is 0.5 percent lower than that of blade No. 16 and the damping is 13.0 percent lower. Phase data for the strain gage measurements were not available for this crossing.

At NOL the transient data were acquired at 13,200 and 13,500 rpm. The reduced frequency for both speeds is 2.30. At the lower speed, the strain gages measured 1.5 KSI unsteady stress for blade No. 1 and 1.4 KSI for blade No. 16. At the higher speed, the measured unsteady stress was 3.0 KSI for blade No. 1 and 2.8 KSI for blade No. 16.

The steady flow is strongly supersonic for this high speed, with inlet Mach number of nearly 1.6 and a two shock system in the passage of the blade as seen by the ideal Mach number contours plotted in Fig. 15. An oblique shock extends from the leading edge to the suction surface at approximately 75 percent chord. An in-passage shock is located on the pressure surface at approximately 40 percent chord. The flow is two dimensional everywhere except very near the surfaces of the fan. The predicted velocity vectors very near the blade surfaces, shown in Fig. 16, demonstrate that the fluid is moving radially outward downstream of the shocks. These radial flows are confined to the boundary layers, within approximately 3.5 percent of the passage for the pressure surface and approximately 5 percent of the passage near the suction surface. The steady flow predicted by the Euler solutions was tuned to match the three-dimensional, viscous solutions. The surface Mach number distribution for the quasi-three-dimensional Euler analysis is shown compared to the previous analysis in Fig. 17.

For the 13,200 rpm speed, the amplitudes of the unsteady pressure chordwise distributions on the pressure and suction surfaces for an entropic wave, a vortical wave, and the proper blade motion are presented in Fig. 18 to show the relative importance of each to the total unsteadiness acting on the blade surfaces. The unsteady pressures due to the entropy wave are small everywhere except at the pressure surface shock location where the peak in the amplitude is comparable to that generated by the vorticity. The vorticity generates most of the unsteadiness at the trailing edge while at the leading edge both vortical and blade motion give equal levels of unsteady pressure.

Figure 19 shows these solutions combined and the unsteady pressure difference calculated and then compared to the measurements obtained from the differential pressure transducers. The predictions show relatively good comparison with the data. The increase in amplitude at the shock location is predicted; due to the sparsity of data points, the strength at the peak cannot be determined precisely. The increase in amplitude at the aft part of the blade due to the suction surface shock unsteadiness is shown by the data. However, the predictions miss the location of this increase significantly, 10 to 15 percent of chord. The phase chordwise distributions agree reasonably well, both showing similar increasing phase with chord trends. For current state-of-the-art linearized-unsteady analyses, this is a good comparison, but improvements are still needed. In determining a modal force for calculating the forcing functions, accurate solutions are needed at the blade leading and trailing edges for this 2*S* mode (deflections are largest at the blade ends). Therefore, inclusion of viscosity in the modeling is needed to determine accurately the unsteady loading in the trailing edge region.

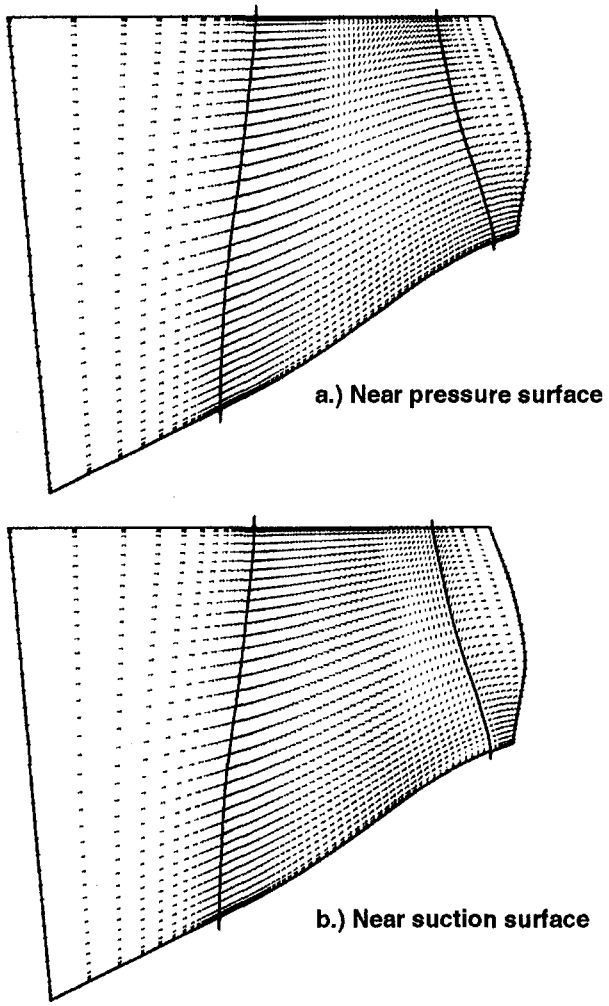

Fig. 16 Predicted velocity vectors near blade surfaces

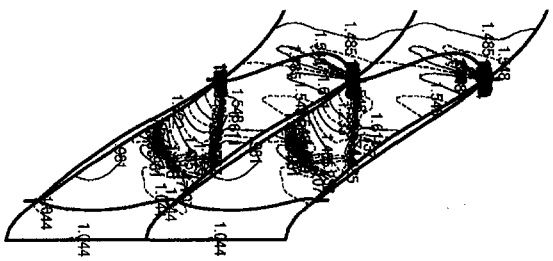

Fig. 15 Contours of ideal Mach number at 85 percent span for 98 percent speed

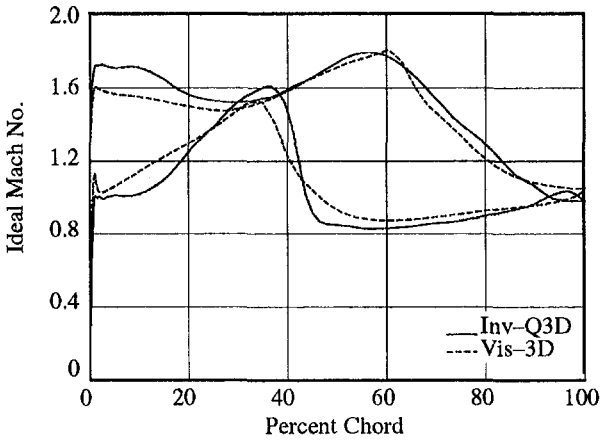

Fig. 17 Predicted steady loading on blade near 8/rev crossing at 98 percent speed

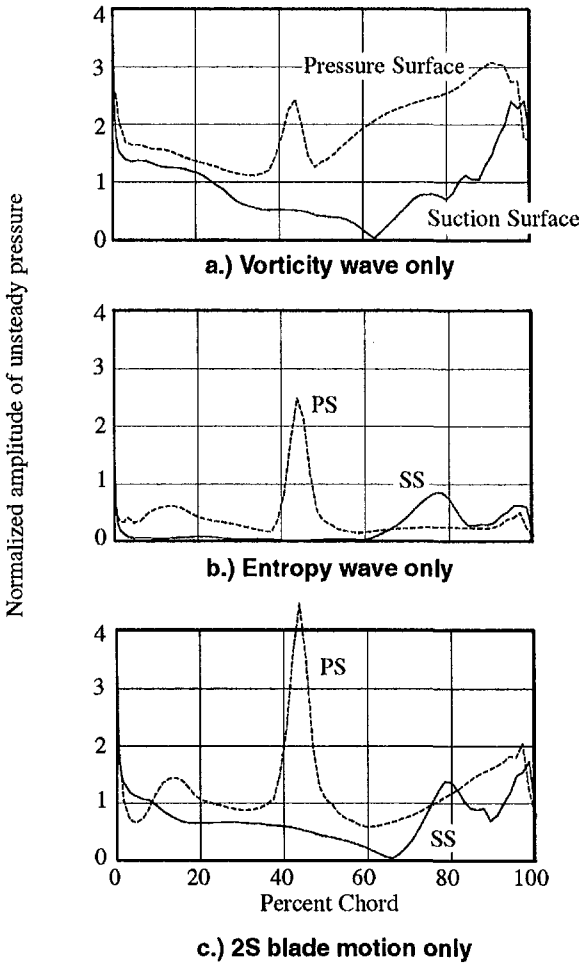

Fig. 18 Predicted unsteady pressures on each surface due to each type of unsteadiness

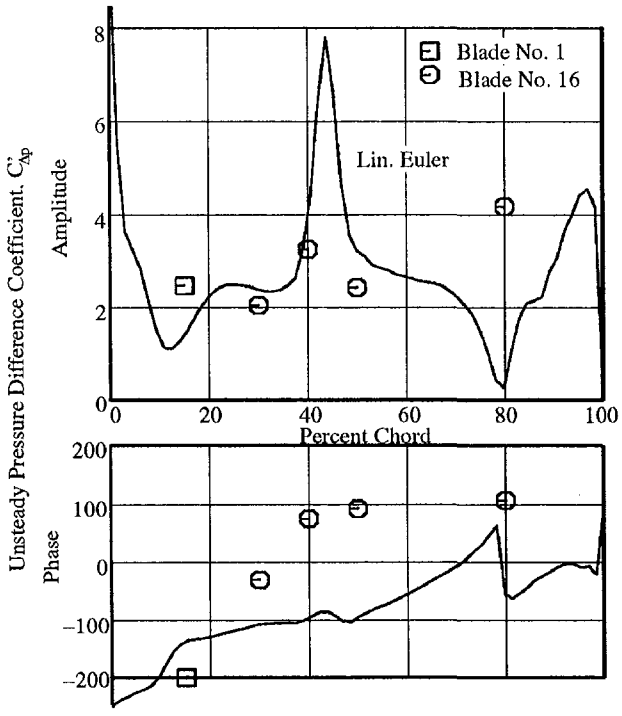

Fig. 19 Measured unsteady loading due to 8/rev excitation at 13,200 rpm

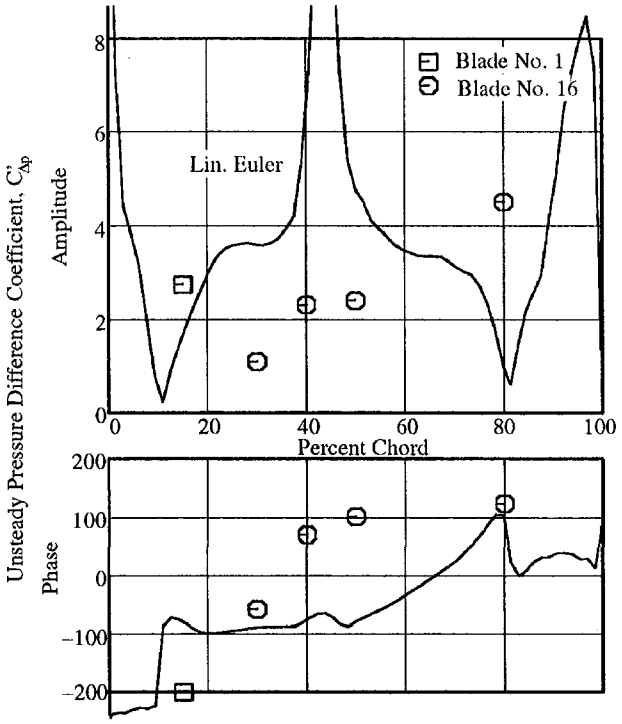

Fig. 20 Measured unsteady loading due to 8/rev excitation at 13,500 rpm

At the higher speed of 13,500 rpm, Fig. 20, the comparison between the prediction and the data becomes poorer. The analysis predicts that the unsteady loading due to the pressure surface shock should get larger while the data show the unsteady loading decreasing at the shock location. Also, the data show the overall levels of unsteady loading remaining relatively unchanged while the predictions show the unsteady loading increasing. Similar to the previous case, 8/rev at 68 percent speed, as blade deflections become a more significant part of the calculations, agreement with the data worsens. Unfortunately, phase information about the blade motions was not available and thus, the amount of blade-to-blade variation in phase seen for the lower speed crossing, is not known for this crossing.

Summary and Conclusions

A series of experiments were performed on the low-aspect-ratio, transonic, first-stage blade of a two-stage fan. Extensive detailed measurements of the forced response of an airfoil were made for the first time. Namely, the flow defect due to inlet distortions was measured; the resulting blade unsteady loading was obtained from on-blade pressure transducers, and the vibratory response to these unsteady loads was measured with blade mounted strain gages. Measurements were taken at three resonant crossings, i.e., 3/rev—1F at 62 percent of design speed, 8/rev—2F/1T at 68 percent speed, and 8/rev—2S at 98 percent speed.

The work presented in this paper is the first part of a series of papers that will describe the whole program. In this portion of the work, the measurements and two-dimensional analysis of the unsteady aerodynamics due to gusts and blade motions are presented.

The flow distortions were analyzed to determine the unsteady flow characteristics. Calculations were performed to obtain the vortical, acoustic and entropic parts of the distorted flow. This is the first time that flow defect measurements have been analyzed to give the entropy wave portion of the excitation.

Both the steady and unsteady flows were analyzed with computational models. The steady flow was predicted with a three-

dimensional Navier–Stokes solver while the unsteady flow prediction was obtained from a quasi-three-dimensional linearized unsteady Euler solution where the base steady flow is modeled with the quasi-three-dimensional, nonlinear Euler equations. A novel approach was used for setting the base steady flow solutions. The steady loading was tuned to match that of the three-dimensional, viscous solutions, which allowed the base steady flow to simulate three-dimensional and viscous effects.

The following is a summary of the important conclusions found from this work.

The distortions were shown to be strongly vortical and moderately entropic. The amplitudes of the downstream-going acoustic waves were nearly nonexistent.

The steady flow was predominantly two dimensional. Outward radial flows were confined to the boundary layers near the blade surfaces. In particular, the flow was centrifuged downstream of shocks and in the aft passage region near the suction surface.

Relatively good agreement was seen between the linearized unsteady Euler solutions and the unsteady pressure difference measurements at the "off" resonance speeds. Thus, the method of simulating viscous effects by tuning the base steady Euler solution to a Navier–Stokes steady solution demonstrated that adequate unsteady solutions can be obtained. At 98 percent speed, improvements in the solutions are still needed near the trailing edge of the blade. This is particularly important for modes where the trailing edge deflections are the dominant part of the motion, as is the case for this $2S$ mode.

As resonance was approached, the predicted unsteady loading showed poorer agreement with the measurements. In particular, for the crossing at 68 percent speed, which has a coupled $2F$ and $1T$ mode, significant blade-to-blade variations in the phase of the vibrations were measured.

Interrogation of the unsteady solution at the high speed showed that both vortical and entropic waves contribute significantly to the unsteady loading where the entropic contribution is mainly in the region of shocks.

Future work on this program will investigate the three dimensionality of the unsteady flow. As stated above, the steady flow was predominantly two-dimensional. However, the unsteady flow may be three dimensional and may be contributing to some of the poor comparisons between the two-dimensional analysis and the data. Three dimensionality due to radial gradients in modeshapes and other three-dimensional effects will be determined from in-passage measurements of three-dimensional velocity vectors and predictions from a three-dimensional, linearized unsteady Euler solver. Once a full understanding of the unsteady loading is achieved, a full forced response prediction of the unsteady stresses will be obtained and compared to the measurements. Also the effects of mistuned cascades on the unsteady aerodynamics will be investigated.

Acknowledgments

This program was a cooperative effort involving both GE Aircraft Engines and Wright Laboratory at Wright-Patterson Air Force Base. Many people were helpful in ensuring its success. We would like to thank the Wright Laboratory Compressor Research Facility staff for their many contributions to this effort. In particular, we would like to express our appreciation to Mr. Patrick Russler, Mr. Carl Williams and Dr. Ron Fost for their contribution to the data acquisition and reduction. At GE, the Aeromechanics Group was essential in the planning, design, test monitoring and data analysis. In particular, Dr. Robert Kielb provided guidance and insight throughout the program. We thank Mr. Dave Woehr for his long hours during testing and his help in the analysis of the strain gage data. Also, thanks to Mr. Josef Panovsky for the structural modeling and analysis of the rotor. The authors also wish to thank GE Aircraft Engines for permission to publish this paper.

References

Bolcs, A., and Fransson, T. H., 1986, "Aeroelasticity in Turbomachines: Comparison of Theoretical and Experimental Cascade Results," Air Force Office of Scientific Research, AFOSR-TR-87-0605.

Buffum, D. H., and Fleeter, S., 1990, "Aerodynamics of a Linear Oscillating Cascade," NASA TM-103250.

Capece, V. R., and Fleeter, S., 1987, "Unsteady Aerodynamic Interactions in a Multistage Compressor," ASME JOURNAL OF TURBOMACHINERY, Vol. 109, pp. 420–428.

Fleeter, S., Jay, R. L., and Bennett, W. A., 1978, "Rotor Wake Generated Unsteady Aerodynamic Response of a Compressor Stator," ASME *Journal of Engineering for Power,* Vol. 100, pp. 664–675.

Fleeter, S., Bennett, W. A., and Jay, R. L., 1980, "The Time-Variant Aerodynamic Response of a Stator Row Including the Effects of Airfoil Camber," ASME *Journal of Engineering for Power,* Vol. 102, pp. 334–343.

Gallus, H. E., Lambertz, J., and Wallman, T., 1980, "Blade-Row Interaction in an Axial-Flow Subsonic Compressor Stage," ASME *Journal of Engineering for Power,* Vol. 102, pp. 169–177.

Giles, M. B., 1988, "Calculation of Unsteady Wake/Rotor Interaction," *AIAA Journal of Propulsion,* Vol. 4, No. 4, pp. 356–362.

Hall, K. C., and Crawley, E. F., 1989, "Calculation of Unsteady Flows in Turbomachinery Using the Linearized Euler Equations," *AIAA Journal,* Vol. 27, No. 6, pp. 777–787.

Hall, K. C., and Clark, W. S., 1993, "Linearized Euler Predictions of Unsteady Aerodynamic Loads in Cascades," *AIAA Journal,* Vol. 31, No. 3, pp. 540–550.

Hall, K. C., and Lorence, C. B., 1989, "Calculation of Three-Dimensional Unsteady Flows in Turbomachinery Using the Linearized Harmonic Euler Equations," ASME JOURNAL OF TURBOMACHINERY, Vol. 115, pp. 800–809.

Hall, K. C., Clark, W. S., and Lorence, C. B., 1994, "A Linearized Euler Analysis of Unsteady Transonic Flows in Turbomachinery," ASME JOURNAL OF TURBOMACHINERY, Vol. 116, No. 3, pp. 477–488.

Henderson, G. H., and Fleeter, S., 1993, "Forcing Function Effects on Unsteady Aerodynamic Gust Response: Part 2—Low Solidity Airfoil Row Response," ASME JOURNAL OF TURBOMACHINERY, Vol. 115, pp. 751–761.

Holmes, D. G., and Chuang, H. A., 1993, "2D Linearized Harmonic Euler Flow Analysis for Flutter and Forced Response," in: *Unsteady Aerodynamics, Aeroacoustics, and Aeroelasticity of Turbomachines and Propellers,* H. M. Atassi, ed., Springer-Verlag, New York.

Huff, D. L., 1987, "Numerical Simulations of Unsteady, Viscous, Transonic Flow Over Isolated and Cascaded Sections by Using a Deforming Grid," AIAA Paper No. 89-2805.

Lindquist, D. R., and Giles, M. B., 1994, "Validity of Linearized Unsteady Euler Equations With Shock Capturing," *AIAA Journal,* Vol. 32, No. 1, pp. 46–53.

Manwaring, S. R., and Fleeter, S., 1990, "Inlet Distortion Generated Periodic Aerodynamic Rotor Response," ASME JOURNAL OF TURBOMACHINERY, Vol. 112, pp. 298–307.

Manwaring, S. R., and Fleeter, S., 1993, "Rotor Blade Unsteady Aerodynamic Gust Response to Inlet Guide Vane Wakes," ASME JOURNAL OF TURBOMACHINERY, Vol. 115, pp. 197–206.

Manwaring, S. R., and Wisler, D. C., 1993, "Unsteady Aerodynamic Gust Response in Compressors and Turbines," ASME JOURNAL OF TURBOMACHINERY, Vol. 115, pp. 724–740.

Rai, M. M., 1989, "Three-Dimensional Navier–Stokes Simulations of Turbine Rotor–Stator Interaction: Part I—Methodology, Part II—Results," *AIAA Journal of Propulsion,* Vol. 5, No. 3, pp. 307–319.

Rabe, D., Bolcs, A., and Russler, P., 1995, "Influence of Inlet Distortion on Transonic Compressor Blade Loading," AIAA Paper No. 95-2461.

Turner, M. G., and Jennions, I. K., 1992, "An Investigation of Turbulence Modeling in Transonic Fans Including a Novel Implementation of an Implicit k–ϵ Turbulence Model," ASME JOURNAL OF TURBOMACHINERY, Vol. 115, pp. 249–260.

Verdon, J. M., and Caspar, J. R., 1984, "A Linearized Unsteady Aerodynamic Analysis for Transonic Cascades," *Journal of Fluid Mechanics,* Vol. 149, pp. 403–429.

Whitehead, D. S., 1990, "A Finite Element Solution of Unsteady Two-Dimensional Flow in Cascades," *International Journal of Numerical Methods in Fluids,* Vol. 10, pp. 13–34.

Whitfield, D. L., Swafford, T. W., and Mulac, R. A., 1987, "Three-Dimensional Unsteady Euler Solutions for Propfans and Counter-rotating Propfans in Transonic Flow," AIAA Paper No. 87-1197.

Woehr, D. A., and Manwaring, S. R., 1994, *Augmented Damping of Low Aspect Ratio Fans (ADLARF),* WL-TR-95-2008.

Education Committee Best Paper of 1996 Award

Response of a Turbofan Engine Compression System to Disturbed Inlet Conditions

A. M. Abdel-Fattah
Aeronautical and Maritime Research Laboratory,
Defense Science and Technology Organisation,
Melbourne, Australia

A generic code DYNTECC has been adapted to perform a parametric study of the effect of inlet flow distortion on the stability of the Pratt and Whitney TF30 engine. This code was developed at Arnold Engineering Development Center, USA, for single and dual spool systems. It was modified at AMRL to accommodate the particular geometry of the TF30 engine. The stage characteristics needed to operate DYNTECC were derived from experimental data for the fan and low-pressure compressor. For the high-pressure compressor they were derived using the STGSTK code developed at NASA Lewis Research Center. This program was modified at AMRL to include real flow effects that were in turn derived using yet another adapted code, CASCAD. The code was primarily used at AMRL to predict the onset of system instability due to simulated full-face rapid inlet temperature ramps typical of those caused during armament firings. It was also run with sinusoidal total pressure oscillations of varying amplitudes and frequencies at the inlet. The code predictions were compared with available data whenever possible, and were found to be consistent with the observed experimental trends.

Introduction

Disturbances in the air intake flow at the engine face of a jet aircraft, in the form of ramps and transients in inlet total pressure or temperature, can produce adverse effects on the performance and stability of an aircraft's propulsion system. The most common form of this instability is axial compressor stall, which, depending on engine type and the aircraft flight envelope, can lead to surge with its serious and damaging effects. A discussion of inlet flow distortion, its sources, and expected trends in aerodynamic response of the compression systems, were presented by Hercock and Williams (1974).

The sources of information on the stability limits of a compression system and its response to inlet flow distortions were in the past mainly experimental. Tests with rapid inlet temperature transients rate in the range 2000–8000 K/s, which are typical of those experienced during gun or rocket wake ingestion, were carried out by Wallner et al. (1957), in an altitude test facility described by Gabriel et al. (1957). Tests with turbofan engines subjected to spatial and time-variant inlet temperature distortions in altitude test facilities for a representative range of inlet temperature transients are described by Rudey and Antl (1970) and Abdelwahab (1977, 1981). From the stability standpoint for a given engine, testing has shown that the response of the engine to the temperature transient is a function of altitude, the circumferential extent of distortion, rotor speed, the absolute level of temperature rise, and its rise rate at the engine face.

With the advent of fast computers in later years, together with increasing experimental cost, there has been a trend toward mathematical and computer modeling (Grashof, 1983). Some of the mathematical models proposed to simulate the response of a compression system to inlet flow distortion are discussed by Mokelke (1974). The modeling techniques ranged from dealing with the compressor as a component in conjunction with the engine thermodynamic model (Merrington, 1985, 1988), to dynamic simulations with details at stage level (Davis, 1982, 1991; Hale and Davis, 1992). The mathematical model reported by Das et al. (1983) was used to simulate the engine response to the ingestion of planar entropy waves resulting from rapid temperature ramps at the system inlet of a 15-stage axial flow compressor. Model predictions were validated with available experimental data of Wallner et al. (1957). This model complements the modeling technique reported by Das et al. (1982). The de-stabilizing influences of inlet distortion as predicted by the mathematical model reported by Baghdadi and Lueke (1982) and Baghdadi (1982), when applied to several simulations of inlet flow distortions, were experimentally verified. These simulations included inlet pressure and/or temperature distortion, planar inlet pressure pulsations, hot gas ingestion, sudden variable geometry reset, and compressor stalling behavior.

A one-dimensional stage-by-stage axial compression system mathematical model DYNTECC (DYNamic Turbine Engine Compressor Code), which is able to analyze a generic compression system, was developed by Sverdrup at the Arnold Engineering Development Center, USA. Full details of theory and capabilities are found from Hale and Davis (1992). In addition to the detailed geometry, a full set of individual stage characteristics of all the compression system components are required as input. This code has the capability to analyze the post-stall behavior, as well as predict the onset of system instability. Stability limit analysis can be conducted for single-spool and dual-spool compression systems. Spatial distortion and post-stall (surge or rotating stall) behavior can be analyzed for a single-spool compression system. This stage-by-stage modeling technique was successfully used to simulate different types of compression system. These included a 10-stage single-spool compressor by Davis (1991), and a 13-stage dual-spool compression system to the point of instability by Davis (1982). More recently the post-stall behavior of an axial/centrifugal compression system of a turboshaft engine was modeled by Owen and Davis (1994). The effect of casing treatment and distortion at the inlet of a two-stage axial flow fan has also been

Contributed by the International Gas Turbine Institute and presented at the 41st International Gas Turbine and Aeroengine Congress and Exhibition, Birmingham, United Kingdom, June 10–13, 1996. Manuscript received at ASME Headquarters February 1996. Paper No. 96-GT-206. Associate Technical Editor: J. N. Shinn.

simulated, by Gortell and Davis (1993), and by Shahrokhi and Davis (1995), respectively.

A current research program at AMRL is concerned with distortion-induced aerodynamic instabilities in engines. This was initiated to acquire and develop the capability to examine analytically the sensitivity of a jet engine performance to inlet distortion, and to predict the likelihood of the compression system encountering instability due to inlet transients. There are many sources for inlet flow distortion, but the emphasis in the present investigation is on those relevant to military aircraft power plant installations, in particular, those caused by rapid temperature ramps and transients and hot-gas ingestion experienced during rocket or armament firings. Model predictions for the system response when subjected to sinusoidal pulsations in total pressure of varying frequency and amplitude at the inlet were also determined. DYNTECC has been adapted in the present investigation to determine the effects of these on the stability and performance of the Pratt and Whitney TF30 engine in the F-111 aircraft. This code was originally developed for a single spool engine, and has been upgraded to accommodate a generic dual-spool engine. It was further modified at AMRL for triple-spool applications, and for the particular geometry of the TF30 compression system.

The process involved in the adaptation of DYNTECC for the particular geometry of the TF30 engine in terms of code inputs is described in this paper. Results in terms of code predictions for the effect of rapid temperature ramps and sinusoidal total pressure oscillations at the inlet are presented for two low-pressure compressor-corrected speeds $N1$ corresponding to 90 and 98 percent of normal rated military (NRM) corrected speeds. The sea-level static NRM for the LPC was 9525 rpm corrected to the fan inlet, and 10,360 rpm for the HPC corrected to the LPC exit conditions. All simulations in this study were carried out with the specification total pressure and temperature at the inlet, choked flow at the turbine inlet downstream of the compression system, and without activating any of the compression system bleeds.

DYNTECC is fully functional for a single-spool system, but for a multispool engine it is only capable of simulating full face inlet distortion. Further plans at AMRL are to extend its capabilities to study the effect of spatial and time-variant distortions at the engine face including the effect of system bleeds on the stability of a multispool compression system.

Code Input Development

The TF30-P-3 engine, shown in Fig. 1(a), is a two-spool axial flow turbofan with mixed flow after-burner. It utilizes a compression system of three components, namely, a three-stage fan, a six-stage low-pressure compressor (LPC) and a seven-stage high-pressure compressor (HPC). The fan and the LPC are in tandem on the low-pressure rotor spool.

The upgraded generic dual-spool version of DYNTECC is fully operational for dual-spool/two-compressor systems. Some of the options were activated, and the code was modified at AMRL for a generic triple-spool/three-compressor system. Accordingly, some changes in both the namelist and geometry input files were also necessary. The TF30 compression system was then accommodated by treating the fan and the LPC as two separate spools but with the same physical rotational speeds.

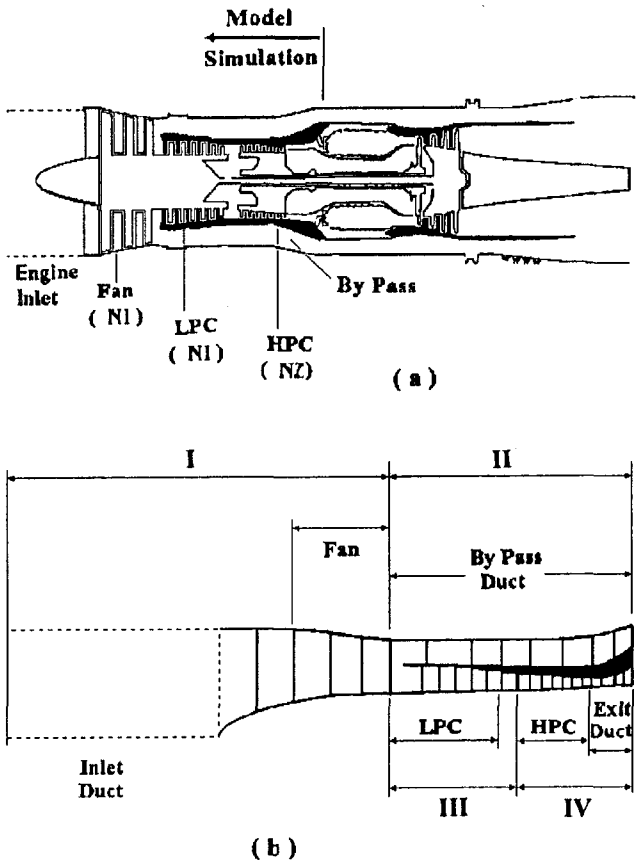

Fig. 1 The TF30-P-3 turbofan engine: (*a*) the uninstalled engine; (*b*) schematic of the compression system model

Geometry Inputs. The code geometry inputs were developed with the flow path shown in Fig. 1(b). This geometry covers the range from the intake lip to the start of the engine combustion chamber. The flow path was subdivided into four overall control volumes, I, II, III, and IV, and each of these was in turn subdivided into a set of elemental control volumes. The control volumes inside each of the three compressors each contain a rotor/stator combination. The bypass duct was modeled with seven control volumes, and the inlet duct from intake lip to the fan face with ten control volumes.

Stage Characteristics Inputs. As this is an axial compression system stage-by-stage mathematical model, it is essential that the stage characteristics for all stage are determined as they form a major part of the input to the model.

The individual prestall characteristics needed for the DYNTECC operation were derived from the acquired experimental data for the three-stage fan and the six-stage LPC of the TF30-P412 engine. From the initial agreement of the overall operating line of the LPC of the P412 with other test data and other validating sources, these were considered for the purpose of the present study to represent those of the TF30-P-3 compression system. The available data for the third stage of the fan were those measured in the core region of the stage, and were taken

Nomenclature

HPC = high-pressure compressor
LPC = low-pressure compressor
$N1$ = low rotor speed
$N2$ = high rotor speed
OL = nominal operating line
NRM = normal rated military speed
PHI = stage flow coefficient
PSI(P) = stage pressure coefficient
PSI(T) = stage temperature coefficient
SL = undistorted surge line

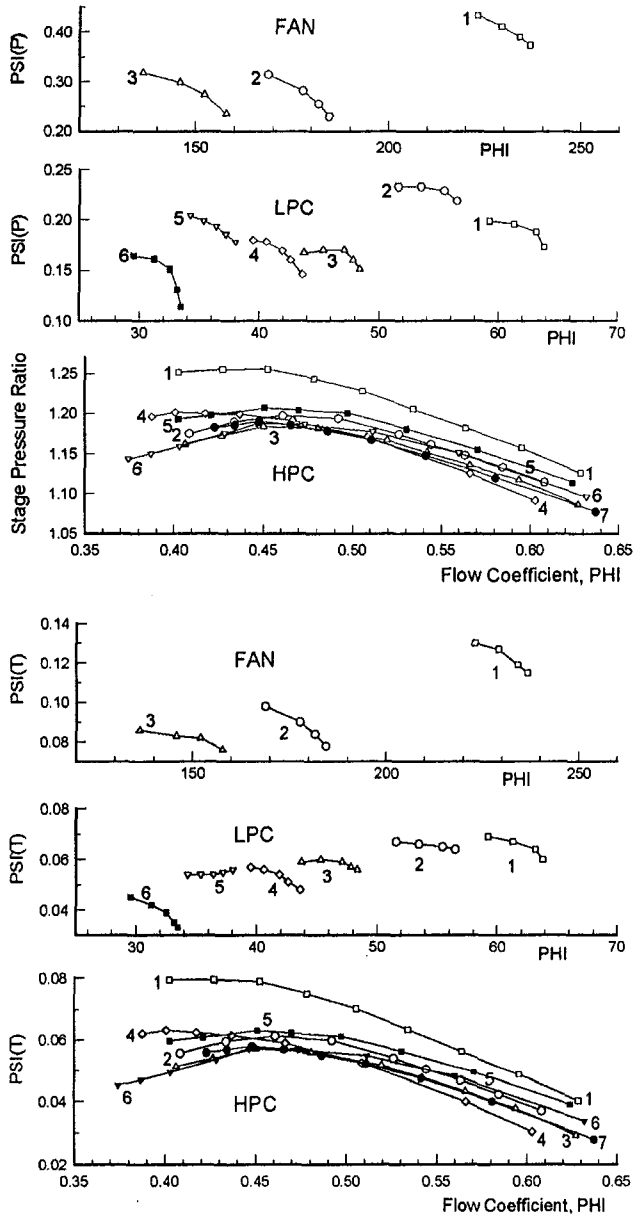

Fig. 2 Stage characteristics of the compression system at speed of N1 = 95 percent of NRM for the fan and LPC, and N2 = 98 percent of NRM for the HPC

in this study to represent the stage at mean radius. Steady-state, prestall characteristics were available for the low rotor corrected speeds of 95, 85, and 74 percent of NRM. They were converted into a format suitable for DYNTECC input, and are shown for the N1 = 95 percent of NRM in Fig. 2. The indicated numbers on the curves denote stage numbers.

No stage characteristics were available for the high-pressure compressor and therefore they were synthesized from overall map data using reverse engineering techniques. Details of the compressor geometry including blade/vane section profiles, along with the cascade data employed, are given by Abdel-Fattah and Frith (1995). The process involved the use of a one-dimensional inviscid compressible flow model STGSTK, which was developed at NASA Lewis Research Center for predicting the overall performance of multistage axial flow compressors using the stage-stacking technique with mean radius data (Steinke, 1982). The NASA program was modified to accommodate adjustments for losses and real-flow effects, which were estimated through the use of an adapted code CASCAD. This was presented as a subroutine in a major program developed by Davis (1970), which utilizes NACA and most known cascade correlations found in Jansen and Moffat (1967) and Johnsen and Bullock (1965).

A set of stage characteristics for the seven-stage high-pressure axial flow compressor was derived for a selected range of corrected speeds. These are presented in Fig. 2 for a fixed HPC corrected speed of $N2$ = 98 percent of the corresponding NRM. When these calculated individual characteristics were subsequently input to the program, the derived overall characteristics of the compressor were found to agree reasonably well with the original characteristics at the same corrected speeds.

Component Maps. Steady-state overall characteristic maps of the compression system components, over the entire compressor speed range, were initially extracted from the manufacturer's transient computer simulation of the TF30 engine. The nominal operating and surge lines, and the corresponding surge margins for the fan, LPC, and HPC for the design nozzle exit area (100 percent of rated) are shown in Fig. 4, for the low rotor speed range of $N1$ = (70–100 percent) of NRM. To eliminate confusion and interference with trajectories of other parameters under discussion, this speed range is indicated only on the fan map, and with only part of the speed lines shown in the vicinity of the operating line. These are presented in terms of component pressure ratio (overall exit over inlet) versus corrected air flow normalized with the values corresponding to the military operation. For the fan and LPC the air flow was normalized with total air flow, while for the HPC with that of the core air flow. The operating and surge lines of all components are compared with those obtained experimentally at NASA Lewis Research Center, which are found in Wasserbauser et al. (1985).

In the case of the fan, two operating lines are predicted by the manufacturer's thermodynamic model of the engine. The first corresponds to the hub region of the fan, with higher pressures than the second, which corresponds to the fan tip region. Initial validation runs with DYNTECC indicated that the overall fan operating point for a given low rotor speed was always located on or very close to the operating line corresponding to the fan hub. This is not surprising, and is thought to be due to the fact that the stage characteristic for the third fan stage, as was mentioned in the previous section, was that corresponding to the fan core. The fan core operating line was therefore used in the present analysis as the relevant fan nominal operating line. This appeared in Fig. 4 to be somewhat higher than that obtained experimentally at NASA. The manufacturer's thermodynamic model of the engine does not contain any surge data for the fan, and therefore the experimental one measured at NASA, which is also shown in Fig. 4, was used in the present investigation to determine the surge margin in the core region of the fan. For the LPC, the extracted surge and operating lines appear to agree fairly well with those obtained experimentally at NASA. Good agreement is also evident with the experimental operating line for the P412 engine low-pressure compressor.

As was the case with the fan core, the extracted operating line of the HPC appeared to be slightly higher than the experimental values. From comparisons carried out between several experimental data sets from different sources for the TF30 compression system, which are not shown here, this difference could very well be accommodated within the observed range of tolerance or engine-to-engine variation. For the surge line, on the other hand, the difference between the manufacturer's model and experimental results is relatively large, and cannot be explained in this way. For the purpose of the present investigation, this difference will not affect the results of the analysis and the conclusions drawn.

Results and Discussion

The model-predicted steady-state total pressure and temperature variations with axial distance from the duct inlet, which

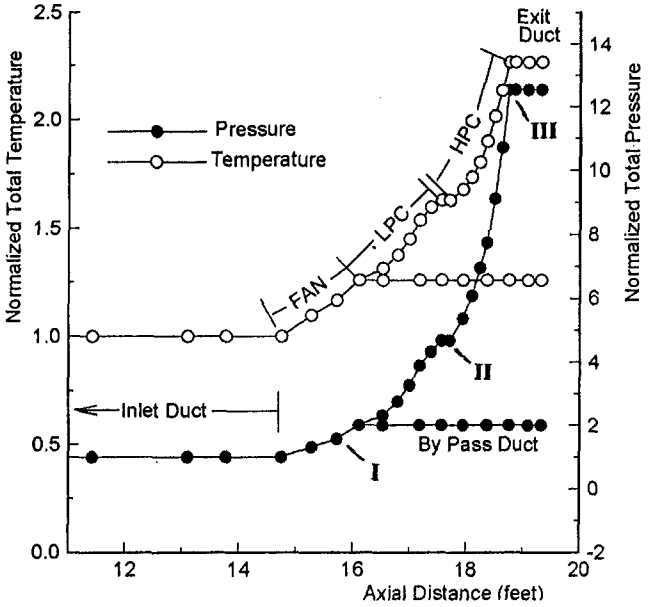

Fig. 3 Model-predicted variation of total pressure along the axial flow path for N1 = 90 percent of NRM

are shown in Fig. 3 as ratios to corresponding values at the intake lip, were used as one of the procedures applied for validating the model for the TF30 compression system. This figure shows, in relative terms, and in conjunction with the system geometry in Fig. 1, the stage-by-stage total pressure and temperature variations and their stack-up by the model to produce the overall values for each component and the compression system as a whole. These values, which are indicated by (I, II, and III) in Fig. 3, are comparable to the manufacturer's predicted data for the fan, LPC, and HPC, and overall compression system at the same corrected speed of $N1$ = 90 percent of NRM.

Inlet Temperature Ramps. In the study of the effects of temperature transients upon engine stability limits, the rate of temperature rise has been found by many researchers to be one of the most important parameters (Rudey and Antl, 1970; Rich, 1971; Das et al., 1983). Others indicated that both the temperature rise and rise rate at the engine inlet can contribute to compression system instability (Wallner et al., 1957; Mallet and Parcells, 1971). In Abdelwahab (1977, 1981) it was reported that the stability limits for the TF30 engine were a function of a critical inlet temperature rise, and were independent of the rise rate.

In the present study, the effect of different temperature ramps at the inlet of the TF30 intake duct has been simulated. The ramp rate was varied by changing the magnitude of temperature rise over a fixed time interval. The system responses to two different temperature changes of 85 K and 117 K corresponding to rise rates of 2832 K/s and 3883 K/s are shown in Fig. 4(a, b, c) for the fan, LPC, and HPC, respectively. These were simulated for $N1$ of 90 percent of NRM, and with compression system near the nominal operating point at sea level static, and standard day conditions. For a given duration and magnitude of temperature rise, the model simulates the transient by linearly increasing the temperature at the inlet to the limit or point corresponding to the onset of system instability. If the temperature level at the end of ramp duration is not high enough to cause instability, the system is brought back to operate at predisturbance conditions. Higher temperatures at the inlet result in reduction of the fan corrected mass flow and corrected speed. Starting from a point corresponding to the corrected speed on the nominal operating line, the resultant effect of hot gas ingestion is to drift the operating point away from its initial value along a trajectory toward the surge line. For a given engine and circumferential extent, the path followed by the compressor operating point is a function of the ramp rate. For low rise rates, the compressor at the end of the ramp would reach a new operating point located between the normal operating and surge lines before traversing back to predisturbance conditions. Typical behavior of the system is illustrated in Fig. 4(a) for the fan at the limiting condition with ramp A where the trajectory at the end of the ramp is nearly tangent to the surge line. In terms of magnitude and rate of fan inlet temperature change, this ramp amounted to 85 K and 2832 K/s, respectively. The response of the LPC to the same ramp is shown in Fig. 4(b), and is similar to that of the fan, in

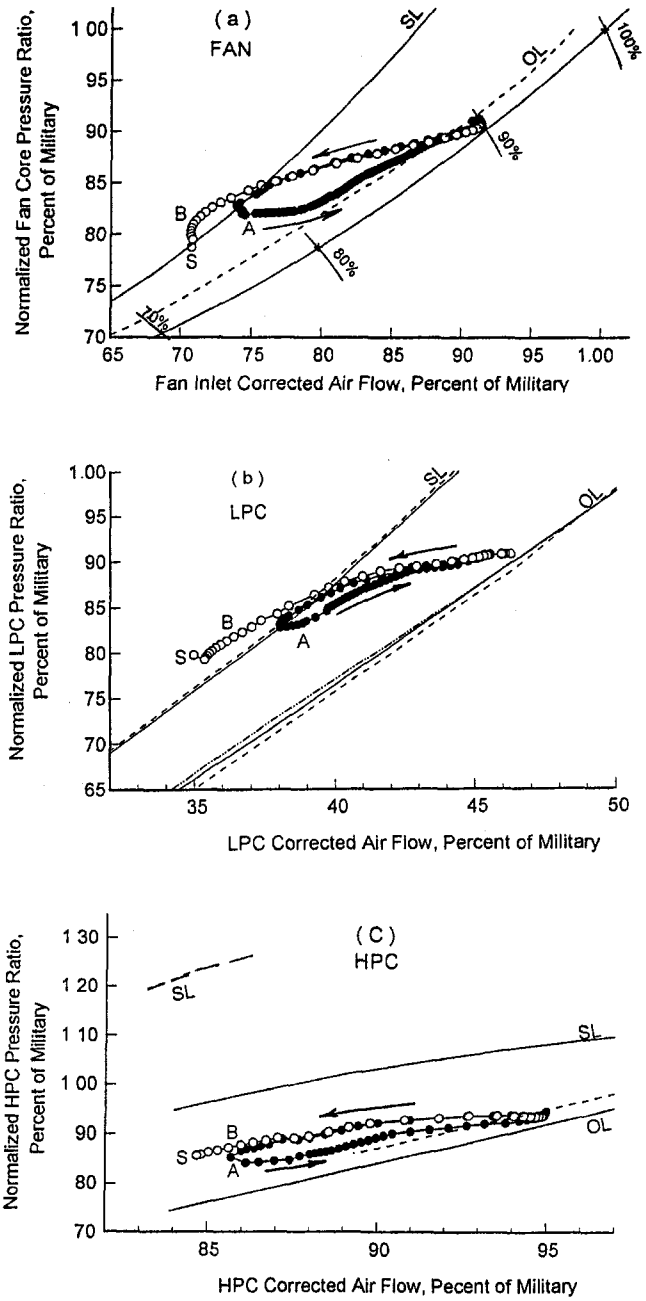

Fig. 4 Predicted response of the compression system to full face rapid temperature ramps for N1 = 90 percent of NRM; ----, manufacturer's model; ———, experimental, NASA. - · - · -, experimental, TF30-P412 engine. —●—, DYNTECC predictions for ramp A. —○—, DYNTECC predictions for ramp B.

that the trajectory is also nearly a tangent to the surge line. By contrast, the trajectory of the HPC response to the same ramp, as displayed in Fig. 4(*c*), appeared to be less affected by the rise in temperature, and continued to operate at more stable conditions relative to those of the fan and the LPC. This predicted limiting condition is lower than the one determined experimentally at NASA Lewis Research Center by Abdelwahab (1977). Abdelwahab generated temperature transients at the inlet of a TF30-P-3 engine for the same corrected rotor speed using a gaseous hydrogen burner system, and was able to show that a limiting condition for a full face temperature ramp involved values of 117 K and 3883 K/s for magnitude and rise rate, respectively. For this limiting condition, which was termed the critical temperature rise, and from data obtained during 180 deg-circumferential-extent tests, it was concluded that the stability limits for the TF30 engine were a function of the critical magnitude of the fan inlet temperature rise, and were independent of the temperature-rise rate. This was reinforced in a later report from experiments on the same engine with distortions of 90 deg-circumferential-extent (Abdelwahab, 1981).

When the inlet is subjected to greater temperature rises beyond the limiting rate corresponding to ramp A, the surge line would be traversed by the response trajectory, and system instability would be expected to take place (Wallner et al., 1957; Rudey and Antl, 1970; Das et al., 1982; Davis 1982; Merrington, 1988). This is illustrated in Fig. 4(*a*, *b*), where the surge lines of the fan and LPC, respectively, were traversed by their respective response trajectories to NASA's experimental ramp B of 117 K rise and of 3883 K/s rate, indicating that system instability has occurred. This was accompanied at this point in time, *S* in Fig. 4, by halting of model execution, indicating the existence of stalled stages. The model indicated that the third stage of the fan was responsible for initiating the system instability. This was confirmed from the model-predicted static pressure signatures obtained for the fan and LPC stages at the time of system instability, which are shown for the fan in Fig. 5. The increase in static pressure at the inlet of a stage indicates flow blockage or stagnation, while a decrease at the exit indicates recirculation due to flow separation from the aerofoil. This criterion has been used by many researchers (Abdelwahab, 1977; Das et al., 1983; Wallner et al., 1957; Davis, 1982) as an indication of the onset of stall and to infer the location of the stall initiation point along the air flow path.

The individual static pressure signatures shown in Fig. 5 were plotted separately to magnify the irregularity if any, in each, then stacked to indicate the effect in qualitative terms. The static pressure ordinate has not therefore been drawn to scale. Figure 5 indicates that at a time corresponding to 77.3 ms, an instability appeared to have started in the seventh stage of the compressor (fourth stage of the LPC). In this case a slight drop in static pressure downstream of stage 7 is accompanied by a sudden pressure rise in the stage upstream. Due to the hammer shock effect, the disturbance appeared to propagate to the up and downstream stages with similar rises and drops in static pressure, respectively. As the disturbance propagates at the local speed of sound, the static pressure behavior appeared progressive and occurred at different times for different stages. Obviously this disturbance did not appear to be strong enough to cause a noticeable effect on the compression system. It was only confined to the LPC stages, and is qualitatively similar to the momentary compressor instability noticed experimentally by Abdelwahab (1977). At a time of 79.8 ms, however, much larger changes in the static pressure signatures can be seen in the third stage of the fan. The obvious sudden increase and decrease in static pressure at the exit of the second and third stages, respectively, indicates clearly that the instability was initiated in the third stage of the fan, with effects propagating to all fan and LPC stages. In the application of

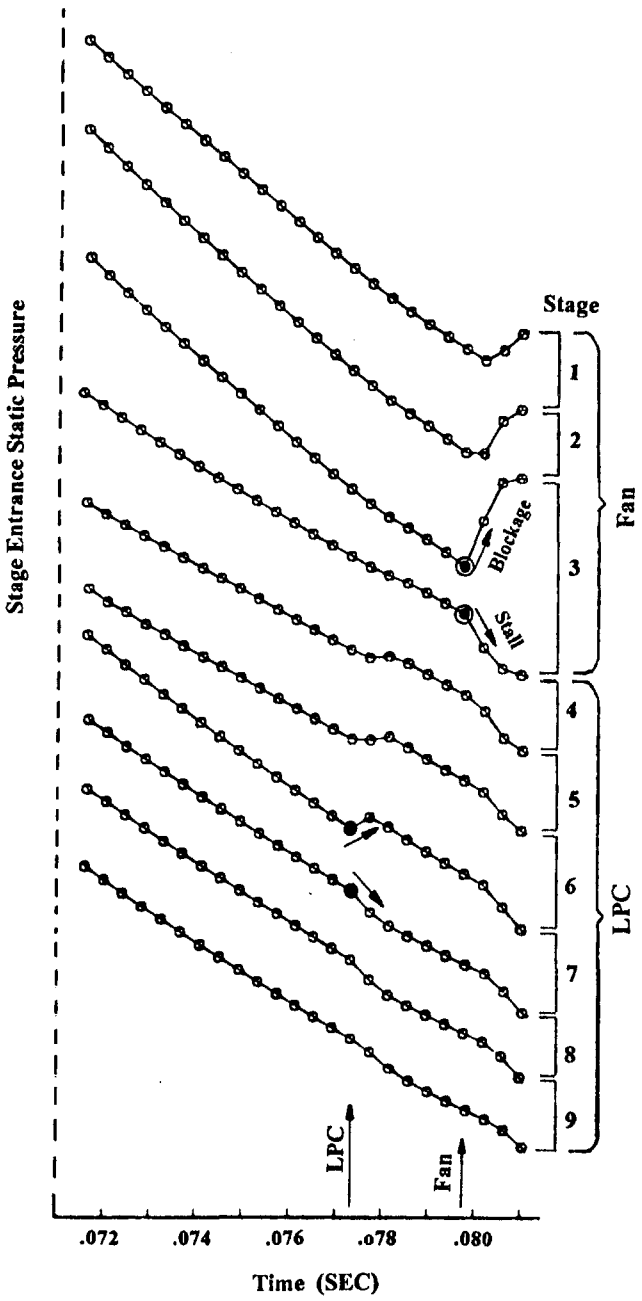

Fig. 5 Model predicted static pressure signatures at the time of compression system instability for N1 = 90 percent of NRM. The vertical static pressure ordinate was not drawn to scale.

the dual-spool version of DYNTECC (Davis, 1982), surge was found to be initiated in the first or second stages of the fan. The above irregularities were not noticeable in the static pressure signatures of the HPC stages, which are not included in Fig. 5. As was the case with the lower ramp rates, the HPC continued to operate within the stable range of its respective map, without appreciable erosion of its surge margin, as is shown in Fig. 4(*c*).

With a higher *N*1 of 98 percent of NRM, DYNTECC was again used to predict the response of the TF30 compression system to simulated full-face temperature ramps at the inlet. The fan, LPC, and HPC response trajectories for two ramps having different temperature magnitude and rise rates are depicted in Fig. 6. For both ramps, the available fan surge margin appeared to be eroded in advance of that for the LPC or the HPC. In terms of magnitude and temperature rise rate, the first

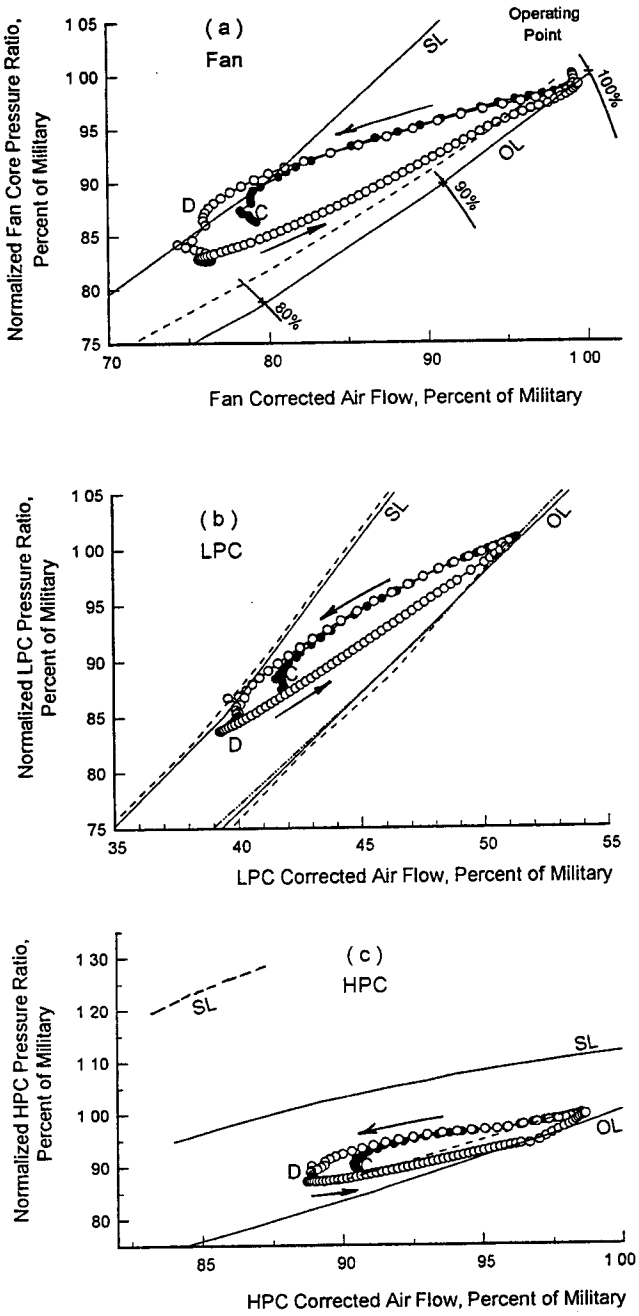

Fig. 6 Predicted response of the compression system to full face rapid temperature ramps for N1 = 98 percent of NRM; ----, manufacturer's model; ———, experimental, NASA; - · - · -, experimental, TF30-P412 engine. —●— DYNTECC predictions for ramp C. —○— DYNTECC predictions for ramp D.

simulated ramp C was 117 K and 3883 K/s, which is equivalent to ramp B in Fig. 4, and 144 K and 4800 K/s for the second ramp D. In terms of location of the predicted response trajectory relative to the component surge line, the ramp C appeared in Fig. 6(a) as the limiting stability condition for the fan, with ramp D as the limiting condition for the LPC. The response trajectories to ramp C for both the LPC and HPC as shown in Figs. 6(b) and 6(c), respectively, appear to be wholly within the stable range. In the case of the higher ramp D, although fan surge line appeared to have been traversed by the fan response trajectory, the model execution continued and the system was brought back to predisturbance conditions. Traversing the steady-state surge line as a limit to the occurrence of surge was examined by Gabriel et al. (1957). From their experimental results, they concluded that the use of the steady-state surge and operating lines, with a dynamic effect such as that resulting from rapid transient conditions, is not necessarily the only criterion for the onset of compressor surge.

Examination of model-predicted static pressure signatures obtained for the higher ramp revealed that sudden rises in static pressure existed at the exit of the first and second stages of the fan, but with slight reduction in static pressure at the exit of the third stage of the fan and the first stage of the LPC. This is similar to that noticed in the LPC static pressure signatures recorded with the $N1$ = 90 percent shown in Fig. 5, where it was possible for the compressor to readjust itself to the stage mismatch. Signatures recorded for the lower ramp C displayed similar static pressure behavior for the first and second fan stages, but this was not matched by a noticeable reduction in static pressure at any of the downstream stages.

This limit, ramp D, is higher than that predicted for the same $N1$ by Merrington (1987). In that work, using the manufacturer's thermodynamic model for the TF30-P-3 engine, the temperature transient was generated in the compressor map by keeping both fuel flow and mechanical speed constant, and with hot gas ingestion simulated by step changes in inlet temperature causing the operating point to move along a trajectory toward the surge line. The predicted temperature increments required to stall the compressor were also lower than those predicted experimentally by Abdelwahab (1977). With the absence of any fan stall data in the manufacturer's model, there was agreement that stall was more likely to be initiated in the low-pressure compressor.

The compression system stability limits in terms of magnitude of temperature rise, as being independent of the rise rate (Abdelwahab, 1977, 1981), was tentatively examined in the present investigation for the limiting temperature rise of 85 K of ramp A for $N1$ = 90 percent of NRM in Fig. 4. For a dual-spool compression system, ramps and distortions can be simulated by DYNTECC only at full face. The ramp rate in the model can be varied either by changing the time interval, the magnitude of temperature rise, or both. For a fixed temperature rise of 85 K, the ramp rate was varied by changing the time interval, and the predicted response trajectories for several rates in the range 2125–8500 K/s are shown in Fig. 7(a, b, c) for the fan, LPC, and HPC, respectively. It can be seen that the response trajectories for the fan, LPC, and HPC exhibited a very weak dependence on rise rates, with faster rates appearing to be associated with slightly higher pressures to a maximum of 1 percent, for the same mass flow, between the maximum and minimum in the range of rates tested. Nevertheless, the response trajectories, for each of the three compression system components, are very close and appear to collapse onto a narrow band. Shown in Fig. 7 also are the model-predicted response trajectories to ramp rates in the range of 2340–7800 K/s for the limiting temperature rise of 117 K of ramp C for $N1$ = 98 percent in Fig. 6. These also appeared to collapse onto a narrow band, and exhibit a weak dependence on the rise rate similar to that of the lower temperature limit of 85 K. From the definition of the limiting condition used in this paper as the tangency between the response trajectory and the surge line, Fig. 7 provides the evidence that for a given rotor speed, and at least in the range of rise rates tested, the limiting temperature rise is approximately independent of the ramp rate. This confirms and appears to be in agreement with that derived experimentally for the TF30 compression system by Abdelwahab (1977, 1981).

Repetitive Sinusoidal Pulsations. The system response to transient inlet conditions such as those caused by the presence of an unsteady shock system in the air intake duct was also examined. This was simulated with the flow cyclically disturbed

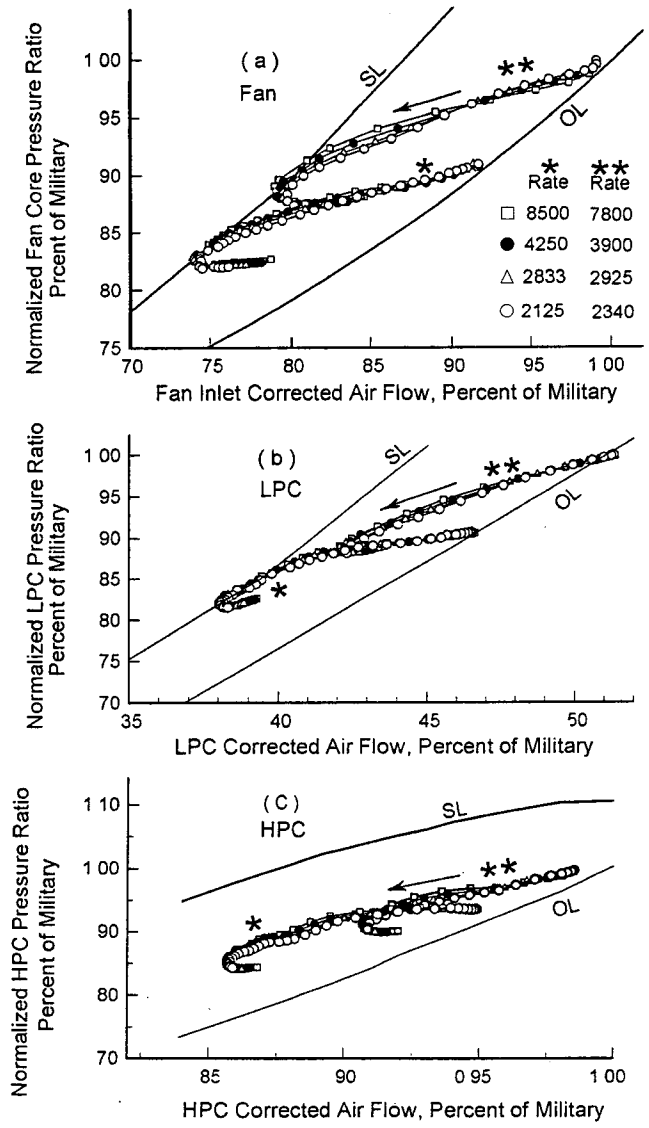

Fig. 7 Predicted response of the compression system to full face rapid temperature ramps for various rise rates but with fixed rotor speed and the limiting temperature rise. * N1 = 90 percent of NRM, T = 85 K. ** N1 = 98 percent of NRM, T = 117 K.

in the form of sinusoidal pulsations in inlet total pressure. A range of sinusoidal pulsations was applied to the system with varying frequency and amplitudes. For a given fixed frequency and amplitude, sinusoidal pulsations in inlet conditions cause the operating point to move along an orbital path around its initial location on the nominal operating line of the component map. This is illustrated in Fig. 8 with loops obtained for an oscillation frequency of 40 Hz, and $N1$ of 90 percent of NRM, superimposed on the corresponding fan, LPC, and HPC maps. Small pulsation amplitudes produce small orbital loops indicating stable operation. Increasing the pulse amplitude would result in larger loops at the expense of the surge margin of the component. Further amplitude increases beyond a limiting value would cause the surge line to be traversed by the orbital loops, and if the time at this condition is of sufficient duration, system instability would occur (Davis, 1982). Figure 8(a) shows the surge line of the fan being traversed by several of these loops, with the time above the surge line long enough to initiate stall in one or more of the fan stages. This was confirmed by the static pressure signatures, indicating that instability was initiated in the second stage of the fan. The surge lines of the other two system components, the LPC and the HPC, were not traversed by the orbital loops, but the HPC operation appeared in Fig. 8 to be more stable than the LPC.

The model predictions for the stability limit in terms of minimum amplitude for a given frequency to cause system instability for both speeds $N1$ of 90 and 98 percent of NRM, is shown normalized with ambient pressure in Fig. 9. This was obtained by increasing the amplitude for a given fixed frequency until stall of a stage or stage group was encountered. The stage or stages responsible for the initiation of system instability were also indicated by the model and were occasionally confirmed through examination of the corresponding static pressure signatures. In the very low-frequency range up to 5 Hz, for the $N1$ of 98 percent of NRM, instability was initiated in the first stage of the fan. In the higher frequency range up to 60 Hz, the critical stage was the second or third stage of the fan. For the rest of the higher frequency range, instability was initiated by the second or fourth stage of the LPC. Plots of results obtained in this high-frequency range, not shown here, indicate that only the surge line of the LPC was traversed by the corresponding orbital loops, while both the fan and the HPC remained in the stable range.

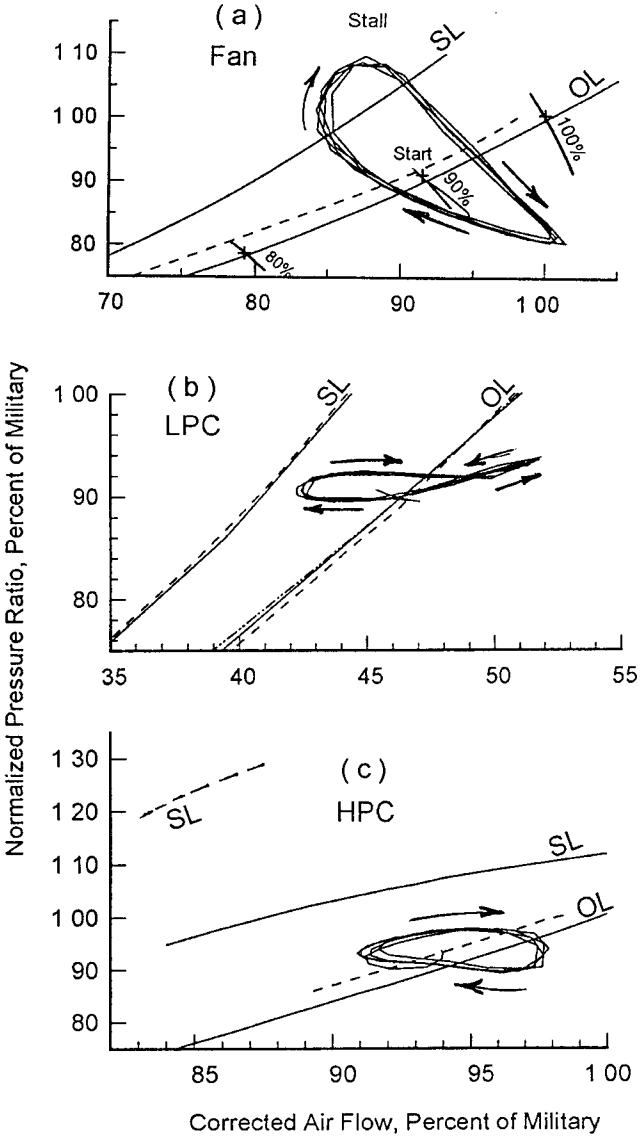

Fig. 8 Model predicted orbital loops resulting from planar oscillatory inflow and their effect on stability of the compression system; ----, manufacturer's model; ———, experimental, NASA

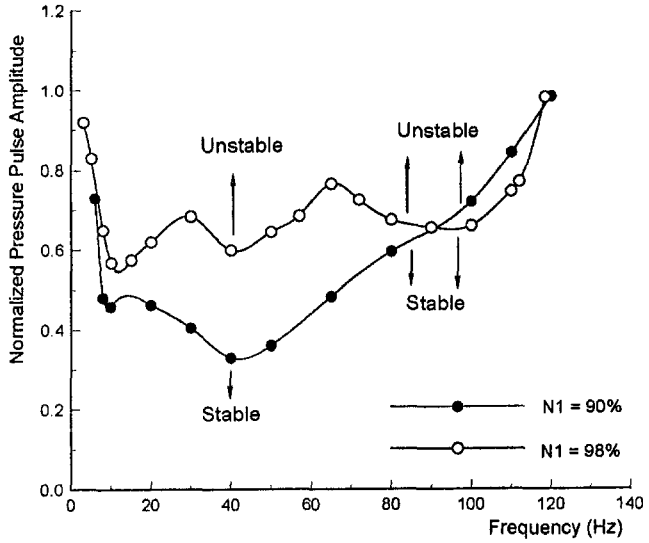

Fig. 9 Model predicted compression system stability limits to cyclic pulsations in inlet total pressure

Figure 9 indicates that the amplitude required to destabilize the compression system increased with corrected speed, and apart from the very low-frequency range, it also shows the trend of improved system stability with increased pulsation frequency. In other words, large disturbance amplitudes would be required in the high-frequency range to destabilize the compressor. This trend is similar to that obtained through the use of the actuator disk modeling technique for an axial flow compressor reported by Peacock and Eralp (1979). The upper limit on the frequency range shown in Fig. 9 is the maximum that can be predicted by the triple-spool DYNTECC for the present 16-stage compression system geometry shown in Fig. 1. With a 13-stage compression system, similar model frequency limitations in the higher frequency range beyond 300 Hz were reported by Davis (1982) for the dual-spool version of the model.

In the discussion of system stability limits and response to inlet transients in conjunction with Figs. 4, 6, and 8, the discontinuous changes in static pressure signatures at the inlet and exit of individual stages were always noticed whenever the temperature or oscillation amplitude was high enough to cause appreciable erosion in the surge margin indicating local compressor instability. This appeared to be distinct and to propagate in the upstream and downstream directions indicating global instability or surge, only whenever the system surge line has already been traversed by the system response trajectory. It appeared that the local or stage instability increased in strength, leading to the onset of global instability or surge, but from the available data at present this is not be conclusive. More detailed work is needed in this area.

Conclusions

The present study has shown that:

- The dual-spool TF30 compression system was successfully accommodated by the adapted three-spool DYNTECC.
- In terms of magnitude and rate of temperature ramp at the inlet, the predicted stability limit was lower than obtained experimentally at the same low rotor corrected speed.
- The stability limit of the system in response to inlet temperature ramps improved with increasing low rotor corrected speed.
- The stability limit in terms of temperature rise required to surge the compressor was found to be independent of the rise rate.
- At the time of instability as a response to inlet temperature ramp, the model predicted the possibility of the third stage of the fan as the critical stage responsible for compression system surge initiation.
- For the planar wave pulsations, the stability limit improved with low rotor corrected speed and with increasing pulse frequency, in the relatively high frequency range of operation.
- The location of the stage responsible for surge initiation was found to move downstream from the fan to the LPC stages with increasing oscillation frequency.

Acknowledgments

The author wishes to express his thanks to Dr. Milt Davis, Jr., of Sverdrup-AEDC, USA, for the acquisition of the single and the upgraded dual spool versions of DYNTECC. His prompt responses to some queries in relation to some aspects of code operation are very much appreciated.

References

Abdel-Fattah, A. M., and Frith, P. W., 1995, "Derivation of Axial Compressor Stage Characteristics From the Overall Performance Map," *Proc. 12th Australasian Fluid Mechanics Conference,* 8–15 Dec., Sydney, Australia.

Abdelwahab, M., 1977, "Effect of Temperature Transients at the Fan Inlet of a Turbofan Engine," NASA TP 1031.

Abdelwahab, M., 1981, "Effect of Fan Inlet Temperature Distortion on the Stability of a Turbofan Engine," NASA TM 82699.

Baghdadi, S., 1982, "Application of a Compression System Stability Model," AGARD CP-324, pp. 23, 1–15.

Baghdadi, S., and Lueke, J. J., 1982, "Compressor Stability Analysis," ASME *Journal of Fluids Engineering,* Vol. 104, pp. 242–249.

Das, D. K., Trippi, A., and Peacock, R. E., 1982, "Unsteady Response of an Axial Flow Compressor to Planar Temperature Transients," AIAA Paper No. 82-1266.

Das, D. K., Seyb, N. J., and Trippi, A., 1983, "A Study of the Response of a Turbojet Engine to the Inlet Temperature Transients," ISABE 83-7048.

Davis, M. W., Jr., 1982, "A Stage-by-Stage Dual Spool Compression System, Modelling Technique," ASME Paper No. 82-GT-189.

Davis, M. W., Jr., 1991, "Parametric Investigation Into the Combined Effects of Pressure and Temperature Distortion on Compression System Stability," AIAA Paper No. 91-1895.

Davis, W. R., 1970, "A Computer Program for the Analysis and Design of the Flow in Turbomachinery—Part B: Loss and Deviation Correlations," Carleton University, N71-12226.

Gabriel, D., Wallner, L., Lubick, R., and Vasu, G., 1957, "Some Effects of Inlet Pressure and Temperature Transients on Turbojet Engines," *Aeronautical Engineering Review,* Vol. 16, No. 9, pp. 54–68.

Gorrell, S. E., and Davis, M. W., Jr., 1993, "Application of a Dynamic Compression System Model to a Low Aspect Ratio Fan: Casing Treatment and Distortion," AIAA Paper No. 93-1871.

Grashof, J., 1983, "Numerical Investigation of Three Dimensional Transonic Flow Through Air Intakes Disturbed by Missile Plume," AIAA Paper No. 83-1854.

Hale, A. A., and Davis, M. W., Jr., 1992, "Dynamic Turbine Engine Compressor Code DYNTECC—Theory and Capabilities," AIAA Paper No. 92-3190.

Hercock, R. G., and Williams, D. D., 1974, "Aerodynamic Response," AGARD-LS-72, pp. 3, 1–38.

Jansen, W., and Moffat, W. C., 1967, "The Off-Design Analysis of Axial-Flow Compressors," ASME *Journal of Engineering for Power,* Vol. 89, pp. 453–462.

Johnsen, I. A., and Bullock, R. O., eds., 1965, "Aerodynamic Design of Axial-Flow Compressors," NASA SP-36, Chaps. VI and X.

Mallet, W. E., and Parcells, R. F., 1971, "Catapult Steam Ingestion Test of Three Turbofan Engines in the A-7 Aircraft," presented at the 10th National Conference on Environmental Effects on Aircraft and Propulsion Systems, Trenton, NJ, May 1971.

Merrington, G. L., 1985, "ATAR-09C-Missile Gas Ingestion and Inlet Temperature Tolerance to Stall," Defence Science and Technology Organisation, Aeronautical Research Laboratories, ARL-AERO-PROP-TM-431.

Merrington, G. L., 1988, "Missile Plume Gas Ingestion in the TF30 Engine," Defence Science and Technology Organisation, Aeronautical Research Laboratories, ARL-AERO-PROP-TM-447.

Mokelke, H., 1974, "Prediction Techniques," AGARD-LS-72, pp. 5, 1–32.

Owen, K. A., and Davis, M. W., Jr., 1994, "Modeling the Dynamic Behaviour of an Axial Centrifugal Compression System," AIAA Paper No. 94-2802.

Peacock, R. E., and Eralp, O. C., 1979, "Compressor Response to Spatially Repetitive and Non-Repetitive Transients," ASME Paper No. 79-GT-Isr.-14.

Rich, W. A., 1971, "The Simulation of the Ingestion of Missile Exhaust by Turbojets," presented at the 10th National Conference on Environmental Effects on Aircraft and Propulsion Systems, Trenton, NJ, May.

Rudey, R. A., and Antl, R. J., 1970, "The Effect of Inlet Temperature Distortion on the Performance of a Turbo-fan Engine Compressor System," NASA TM X-52788.

Shahrokhi, K. A., and Davis, M. W., 1995, "Application of a Modified Dynamic Compression System Model to a Low Aspect Ratio Fan: Effects of Inlet Distortion," AIAA Paper No. 95-0301.

Steinke, R. J., 1982, "STGSTK—A Computer Code for Predicting Multistage Axial Flow Compressor Performance by a Meanline Stage-Stacking Method," NASA Technical Paper No. 2020.35.

Wallner, L. E., Useller, J. W., and Sari, M. J., 1957, "A Study of Temperature Transients at the Inlet of a Turbojet Engine," NACA RM E57C22.

Wasserbauser, J. F., Neumann, H. E., and Shaw, R. J., 1985, "Performance and Surge Limits of a TF30-P-3 Turbofan Engine/Axisymmetric Mixed-Compression Inlet Propulsion System at Mach 2.5," NASA TP 2461.

A Linearized Unsteady Aerodynamic Analysis for Real Blade Supersonic Cascades

M. D. Montgomery

J. M. Verdon

United Technologies Research Center,
Theoretical & Computational
Fluid Dynamics,
East Hartford, CT 06108

S. Fleeter

Purdue University,
School of Mechanical Engineering,
West Lafayette, IN 47907

The prediction capabilities of a linearized unsteady potential analysis have been extended to include supersonic cascades with subsonic axial flow. The numerical analysis of this type of flow presents several difficulties. First, complex oblique shock patterns exist within the cascade passage. Second, the acoustic response is discontinuous and propagates upstream and downstream of the blade row. Finally, a numerical scheme based on the domain of dependence is required for numerical stability. These difficulties are addressed by developing a discontinuity capturing scheme and matching the numerical near-field solution to an analytical far-field solution. Comparisons with semi-analytic results for flat plate cascades show that reasonable predictions of the unsteady aerodynamic response at the airfoil surfaces are possible, but aeroacoustic response calculations are difficult. Comparisons between flat plate and real blade cascade results show that one effect of real blades is the impulsive loads due to motion of finite strength shocks.

Introduction

Flow-induced blade vibrations continue to be a problem in the operation of turbomachinery. When vibrational motions of the blades extract energy from the passing fluid, the blades will flutter. The stresses induced by this vibration can result in fatigue failure, and so limit the high-speed operation of the machine. One type of flutter occurring in the fans of axial flow turbomachines is unstalled supersonic flutter (Snyder and Commerford, 1974), which occurs when the outer span of the blades operates at supersonic relative speed, but with subsonic axial velocity. This condition is known as supersonic flow with subsonic leading edge locus. The blades typically vibrate in the torsional mode at approximately unit reduced frequency and constant interblade phase angle.

The prediction of unstalled supersonic flutter has been a concern for some time. Previous investigators (Verdon, 1977; Adamczyk and Goldstein, 1978; Nagashima and Whitehead, 1977) have solved the subsonic leading edge locus problem for flat plate cascades with no mean loading (see Fig. 1). The plates of the cascade are assumed to undergo identical, infinitesimal, harmonic motions with a constant phase angle between the motions of adjacent blades, so that the flow field is composed of a uniform mean flow with a small harmonic unsteady perturbation. The uniform mean flow assumption leads to a linear constant-coefficient partial differential equation describing the unsteady perturbation, which can be solved using analytic or semi-analytic methods. This classical linear theory approach neglects the effect of mean blade loading on the unsteady aerodynamic response.

A nonuniform mean flow affects the aerodynamics of self-induced motion since the unsteady aerodynamic response is changed and the airfoil is oscillating in a nonuniform mean pressure field. Complete nonlinear unsteady analyses (Huff et al., 1991; Gerolymos et al., 1990) require more computational time and resources than are typically available for design purposes, and are likely to remain this way for some time. To reduce the computational requirements, especially the required computational time, a linearized unsteady model incorporating mean loading effects can be derived using perturbation techniques. The development of such a model for supersonic flow conditions is described herein, and involves an extension of the LINFLO analysis developed by Verdon et al. (Caspar and Verdon, 1981; Verdon and Caspar, 1984; Usab and Verdon, 1991). The FINSUP analysis (Whitehead, 1990) has been applied to this problem, but the results show highly smeared shocks.

In the linearized unsteady model, the full nonlinear governing equations are first solved to determine the steady, or mean, flow through the cascade. The mean flow solution includes the effects of flow incidence and real airfoil geometry, such as thickness and camber. The mean solution is required for the linearized model since the linearized governing equations contain coefficients based on the underlying mean flow. Solving the linearized equations yields the linearized unsteady aerodynamic response, and thus determines the flutter stability of a cascade undergoing prescribed airfoil motions or the linearized response of a cascade subjected to an incident aerodynamic disturbance, or gust.

The numerical prediction of the unsteady aerodynamic responses of supersonic cascades with subsonic axial flow presents several difficulties. First, complex oblique shock or Mach wave patterns exist within each cascade passage because shocks are reflected by adjacent airfoils. The numerical resolution of multiple intersecting discontinuities is a challenging problem. Second, the acoustic response far upstream and downstream of the cascade is discontinuous, due to the presence of leading- and/or trailing-edge Mach waves and their reflections. These discontinuities imply an infinite acoustic spectrum, which must be adequately represented on a finite computational grid. Finally, due to the supersonic nature of the flow, a differencing scheme based on the domain of dependence must be developed to ensure the stability of the numerical scheme.

To investigate how well numerical methods can overcome these difficulties, the unsteady aerodynamic response of a flat plate cascade was computed and compared with a semi-analytic solution (Montgomery et al., 1995). As a result of this earlier study, the linearized unsteady potential analysis has been verified for flat plate cascades. In the present study, it has been applied to a cascade of realistic airfoils and the results are compared with those of a nonlinear Euler analysis, NPHASE (Swafford et al., 1994).

Contributed by the International Gas Turbine Institute and presented at the 41st International Gas Turbine and Aeroengine Congress and Exhibition, Birmingham, United Kingdom, June 10–13, 1996. Manuscript received at ASME Headquarters February 1996. Paper No. 96-GT-124. Associate Technical Editor: J. N. Shinn.

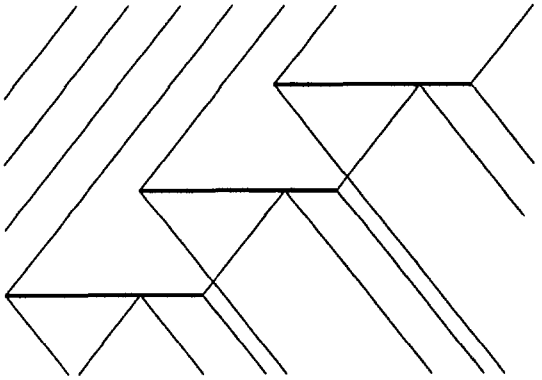

Fig. 1 Supersonic flat plate cascade with subsonic axial flow

Governing Equations

The governing equations are expressed in dimensionless form, with length normalized by the airfoil chord and velocity normalized by the upstream free-stream speed. Density is normalized by the upstream free-stream density. Pressure is thus normalized by the product of the upstream free-stream density and the square of the upstream free-stream speed.

The cascade is assumed to be an infinite array of identical, uniformly spaced airfoils. The gap vector between adjacent airfoil leading edges is denoted by G, as shown in Fig. 2. The axial and circumferential coordinates are ξ and η, respectively, and x measures distance along the airfoil chord. The cascade stagger angle is Θ, and the far field flow angles are $\Omega_{-\infty}$ upstream and $\Omega_{+\infty}$ downstream. The computational domain is truncated at finite axial distances from the cascade, with the location of the inlet and exit boundaries denoted by $\xi = \xi_{-\infty}$ and $\xi = \xi_{+\infty}$, respectively.

The mean flow far upstream is assumed to be isentropic and irrotational. In addition, any shocks that occur in the flow are assumed to be weak and to have negligible curvature, and thus to generate negligible entropy and vorticity. These assumptions imply that the mean flow is isentropic and irrotational, so that the mean flow velocity is derivable from a potential.

Unsteady disturbances are assumed to be periodic in time and in the cascade circumferential direction and small compared to the corresponding mean flow quantities. As a result, the equations governing the unsteady disturbances can be linearized about the mean flow and solved in the frequency domain. Unsteady excitations that are periodic in time and space can be decomposed into excitations that are harmonic and exhibit phase-lagged passage to passage periodicity. Since the unsteady equations are linearized, a harmonic and spatially periodic excitation produces a harmonic and spatially periodic response. These assumptions thus allow the entire unsteady flow field to be determined from the solution over a single cascade passage. The linearized unsteady response to arbitrary disturbances can then be determined by superposing Fourier modes.

The flow field is assumed to consist of a steady, or mean, component that is taken to be $\mathcal{O}(1)$, and an unsteady perturbation that is taken to be $\mathcal{O}(\epsilon) \ll 1$. The terms in the linearized unsteady equations are first order in ϵ. The notation adopted here is that upper case terms are zeroth-order or mean quantities and lower case terms are first-order unsteady perturbation quantities. For example, pressure is expressed as $P(\mathbf{x}) + \mathrm{Re}\{p(\mathbf{x}) \times \exp(i\omega t)\} + \mathcal{O}(\epsilon^2)$, where P is the mean pressure and p is the complex amplitude of the first-order unsteady perturbation pressure. The only exception to this case dependent notation is the mean density, denoted by $\bar{\rho}$.

Steady Background Flow. The steady potential equation expressed in conservation form is

$$\nabla \cdot (\bar{\rho} \nabla \Phi) = 0, \tag{1}$$

where, assuming $\bar{\rho}_{-\infty} = V_{-\infty} = 1$, it follows from the Bernoulli and thermodynamic relations that

$$\bar{\rho} = \left[1 + \frac{\gamma - 1}{2} M_{-\infty}^2 (1 - |\nabla \Phi|^2) \right]^{1/(\gamma-1)}. \tag{2}$$

The flow tangency condition on the airfoil surfaces is $\nabla \Phi \cdot \mathbf{n} = 0$, and the far-field boundary conditions are described below.

The steady potential flow analysis used in the present effort is the SFLOW analysis (Hoyniak and Verdon, 1995), which was modified for supersonic applications and is still under development. SFLOW employs a Newton iteration scheme to solve Eq. (1), which is based on a linearization of the steady potential equation expressed as

$$(A^2 - \Phi_\xi^2)\Phi_{\xi\xi} - 2\Phi_\xi \Phi_\eta \Phi_{\xi\eta} + (A^2 - \Phi_\eta^2)\Phi_{\eta\eta} = 0, \tag{3}$$

where the sound speed is determined by

$$A^2 = \frac{1}{M_{-\infty}^2} + \frac{\gamma - 1}{2}(1 - |\nabla \Phi|^2), \tag{4}$$

assuming $V_{-\infty} = 1$. The derivatives in Eq. (3) are approximated using upwind differencing to introduce the numerical dissipation required for numerical stability.

At the far-field boundaries, the steady flow is assumed to be a uniform stream plus a small perturbation. Two flow variables, such as Mach number and flow angle, define the uniform component of the steady flow. For subsonic flow, the two variables can be specified upstream and either the Kutta condition can be imposed or one flow variable can be prescribed downstream, with the second downstream flow variable determined from global mass conservation.

For supersonic flow with subsonic axial velocity, one upstream flow variable may be specified, either the flow direction, tangential velocity, or Mach number. The other upstream variable must be determined from the unique incidence condition (Lawaczeck, 1972), which links the inlet Mach number and flow angle. The inlet Mach number and flow angle must be such that the flow is tangent to the airfoil surfaces when the flow is turned by the compression or expansion waves emanating from the leading edge. The relationship between inlet Mach number and flow angle is thus determined by the cascade and airfoil geometry. At the downstream boundary either the flow

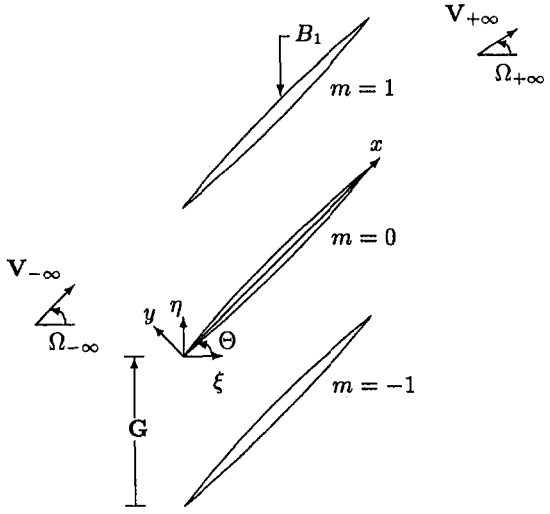

Fig. 2 Two-dimensional cascade and nomenclature

direction or Mach number must be specified, with the second downstream variable determined from global mass conservation. The far field boundary conditions are nonreflecting, i.e., they account for steady perturbations to a uniform flow that in supersonic flow can persist far from the cascade. These boundary conditions are based on Fourier series solutions that are similar to the solutions used in the unsteady far field boundary conditions.

Linearized Unsteady Flow. The linearized unsteady potential equation can be expressed in nonconservative form as a convected wave equation for the complex amplitude of the disturbance potential, i.e.,

$$\bar{\rho}\frac{\bar{D}}{Dt}\left(\frac{1}{A^2}\frac{\bar{D}\phi}{Dt}\right) - \nabla\cdot(\bar{\rho}\nabla\phi) = 0, \tag{5}$$

where $\bar{D}(\ )/Dt = i\omega(\ ) + \nabla\Phi\cdot\nabla(\ )$ is the material derivative based on the mean flow velocity.

The prescribed blade motion is given by

$$\mathcal{R}(\mathbf{x} + mG, t) = \mathrm{Re}\{\mathbf{r}(\mathbf{x})\exp[i(\omega t + m\sigma)]\}, \tag{6}$$

where Re{ } denotes the real part of a complex quantity, $\mathbf{x}$ is a point on the mean position of the airfoil surface, $\mathbf{r}$ is the airfoil displacement vector, ω is the reduced frequency based on airfoil chord and free-stream speed, $m = 0, \pm1, \pm2, \ldots$ is the integer index of airfoils in the cascade, and σ is the interblade phase angle. In design calculations, the quantities $\mathbf{r}$, ω, and σ are determined from the vibrational modes of the blade-row structure and are prescribed in an unsteady aerodynamic calculation.

The flow tangency condition, which is imposed at the mean airfoil surfaces, is

$$\nabla\phi\cdot\mathbf{n} = \{i\omega\mathbf{r} + (\nabla\Phi\cdot\boldsymbol{\tau})(\boldsymbol{\tau}\cdot\nabla)\mathbf{r} - (\mathbf{r}\cdot\nabla)\nabla\Phi\}\mathbf{n}, \tag{7}$$

where $\mathbf{n}$ and $\boldsymbol{\tau}$ are unit normal and tangent vectors, respectively. The phase-lagged periodicity condition is $\phi(\mathbf{x} + \mathbf{G}) = \phi(\mathbf{x}) \times \exp(i\sigma)$. The pressure, $p = -\bar{\rho}\bar{D}\phi/Dt$, and normal velocity are continuous across airfoil wakes, and therefore

$$\left[\!\left[\frac{\bar{D}\phi}{Dt}\right]\!\right] = 0 \quad \text{and} \quad [\![\nabla\phi]\!]\cdot\mathbf{n} = 0, \tag{8}$$

where $[\![\cdot]\!]$ denotes the jump in a quantity across a mean wake surface.

The far field boundary conditions are nonreflecting, and are based on matching analytic solutions for the unsteady perturbation to a uniform mean flow to a numerical near-field solution. The analytic solutions for the potential due to the acoustic response are based on a Fourier series solution (Verdon, 1989) of the form

$$\phi_{\pm\infty} = \sum_{n=-\infty}^{\infty} a_{n\pm\infty}\exp[i\mathbf{k}_{n\pm\infty}\cdot\mathbf{x}]\exp[\beta_{n\pm\infty}\xi]. \tag{9}$$

The axial attenuation coefficient, β_n, of the nth acoustic mode is determined by the mean flow conditions, i.e., M and Ω, and the nature of the unsteady disturbance, i.e., ω and σ. For subsonic flows β_n is zero for, at most, a handful of modes. In contrast, for supersonic flows β_n is zero for all or almost all n, and so an infinite number of modes propagate, which can lead to numerical difficulties. An analytic expression of the form

$$\phi_R = \begin{cases} 0 & \xi < \xi_{-\infty} \\ F(n_W)\exp(-i\omega\tau_W/V_{+\infty}) & \xi > \xi_{+\infty} \end{cases} \tag{10}$$

is used to account for the potential due to the unsteady vorticity shed along the blade wakes.

Numerical Method

The LINFLO analysis uses the weighted least-squares discretization (Caspar and Verdon, 1981; Verdon and Caspar, 1984), in which interpolants that are low-order polynomials are used to match the first few terms in a Taylor series. Discretization methods based on polynomials do a poor job of representing discontinuous functions. To overcome this shortcoming, discontinuities can either be fit by changing the nature of the discretization around the discontinuity, or captured by explicitly adding terms to the discretized equation that smear discontinuities into smooth functions. Both discontinuity fitting and capturing approaches were developed (Montgomery et al., 1995). Because the capturing approach was found to be more robust, it has been used for all results presented herein.

In the discontinuity capturing approach the added smoothing terms reduce the solution gradients in the region of the discontinuity and so suppress oscillations that would otherwise result on either side of the discontinuity. Because the addition of smoothing is motivated by shortcomings in the numerical approximation, the goal is to minimize the amount of smoothing required to obtain physically meaningful (i.e., nonoscillatory) solutions. To meet this goal, a numerical scheme based on upwinded interpolants was devised that allows control over the amount of numerical smoothing. For the linearized unsteady problem, the locations of the discontinuities emanating from the airfoil leading and trailing edges can be determined from the mean flow solution. By tracking these discontinuities through the flow, computational cells that contain a discontinuity can be flagged. A high level of smoothing is added around captured discontinuities, while a low level of smoothing is used in continuous regions of the flow. Both levels of smoothing are controllable, as is the width of the regions of high smoothing around discontinuities.

To examine the effect of smoothing on the numerical resolution of discontinuities, a simple model problem was studied (Williams, 1991; Montgomery, 1994) to determine the order of accuracy of the scheme, i.e., the rate at which truncation error decreases as the mesh spacing, h, approaches zero. The results of this study revealed that even though the discretization error in continuous regions of the flow may be of $\mathcal{O}(h^2)$, the error associated with a smeared discontinuity is $\mathcal{O}(h^{1/2})$, which corresponds to a considerably slower asymptotic rate of mesh convergence for the solution in the vicinity of discontinuities. This was verified by numerical experiments.

Discontinuity fitting could be used in formulating the far-field boundary condition by representing the acoustic response as a combination of continuous and discontinuous functions. However, a discontinuity fitting representation is not necessarily beneficial since the near-field discretization is incapable of propagating discontinuities without smearing. Thus, when the acoustic response reaches the far-field boundary it is effectively smooth. This implies that the far-field Fourier spectrum is truncated, and the high wave-number content resulting from the discontinuity will be lost. The severity of the truncation of the Fourier spectrum is dependent on the amount of smoothing used in the near-field discretization and the distance of the far-field boundaries from the origin of the discontinuities, i.e., the airfoil leading and/or trailing edges. As the smoothing and the distance from the far-field boundaries to the cascade decrease, the truncation of the Fourier spectrum will decrease. However, lower bounds are placed on the amount of smoothing by the stability of the near field discretization. Lower bounds are also placed on the distance to the far-field boundary since the mean flow must be uniform, to within $\mathcal{O}(\epsilon)$, for the assumed Fourier series solution of Eq. (9) to be valid.

Results

The unsteady aerodynamic response of a flat plate cascade undergoing torsional motions about midchord was computed

based on linearized potential semi-analytic (Verdon, 1977) and numeric (LINFLO) analyses. The cascade considered is Cascade A (Verdon, 1977), which is also one of the Eighth Standard Cascade Configurations (Fransson and Verdon, 1993). Cascade A is defined by mean flow and cascade stagger angles of 59.53 degrees, a gap to chord ratio of 0.7889, and an inlet Mach number of 1.345. In this cascade the downward traveling leading edge Mach wave passes just downstream of the trailing edge of the lower adjacent plate, as shown in Fig. 1. Thus there is only one discontinuity in the surface pressure, which occurs on the lower surface (at $x = 0.68$ for the reference blade) due to the impingement and reflection of the upward traveling trailing edge Mach wave from the adjacent plate below.

Real blade and blade loading effects were investigated by comparing the unsteady aerodynamic response of a cascade of double circular arc airfoils with the response of Cascade A. This cascade geometry was chosen to produce a flow with a finite strength shock, namely an oblique shock at the trailing edge. The cascade has a geometry similar to that of Cascade A, and operates under supersonic inflow conditions as a lightly loaded compressor.

Flat Plates: Comparison With a Semi-Analytic Analysis. The imaginary (out-of-phase with respect to blade displacement) pressure fields as predicted by the semi-analytic and numeric potential analyses are shown in Fig. 3. The numerical pressure field was calculated using a uniform 300×100 mesh that extends one axial chord upstream and downstream of the cascade. The upstream and downstream traveling leading edge Mach waves are clearly visible in both solutions. Because of the contouring levels chosen, the upstream traveling trailing edge Mach waves and their reflections are not as visible, but they are evident by the kink in the pressure that can be seen above the trailing edge. The downstream region has been omitted from the semi-analytic solution because pressure waves not affecting the plate surfaces were not included in the analysis. The two solutions agree well in the cascade passage, and on the plate surfaces, but differ in the far field due to the smearing of discontinuities. The smearing of leading edge Mach waves by the numerical analysis can be seen by comparing the semi-analytic solution, where the pressure changes abruptly across a Mach wave, with the numerical solution, where the pressure change occurs across a region of finite width.

The smearing of discontinuities by the discontinuity capturing scheme causes the loss of the high wave-number content of the acoustic response because the higher spatial gradients are preferentially damped. This loss is illustrated in Fig. 4, which shows the semi-analytic and numerical Fourier spectra at one axial chord upstream of the cascade. The semi-analytic spectrum displays the $1/n$ behavior characteristic of a discontinuous function, whereas the numerical spectrum decays rapidly with increasing wave number to round-off error levels. If the far-field boundary was placed further from the cascade, or a coarser mesh was used, the numerical Fourier spectrum would be even more distorted.

Since the far-field boundary conditions presume that the mean flow is uniform, the far-field boundaries must be sufficiently far from the cascade that the mean potential field decays. This minimum distance results in numerical smearing of the acoustic response at the far-field boundary due to dissipative error in the near field, which reduces the high wave-number content of the acoustic response. The loss of the high wave-number content implies that the radiated noise levels will be underpredicted and that only a finite number of Fourier modes are required to match the analytic far-field and numerical near-field solutions. For example, for the numerical spectrum in Fig. 4, the Fourier modes for $|n| < 10$ would be adequate to match the numerically predicted acoustic response. This loss of the high wave-number content will be common to all numerical shock capturing analyses because it is due to the dissipative error inherent in the near-field discretization.

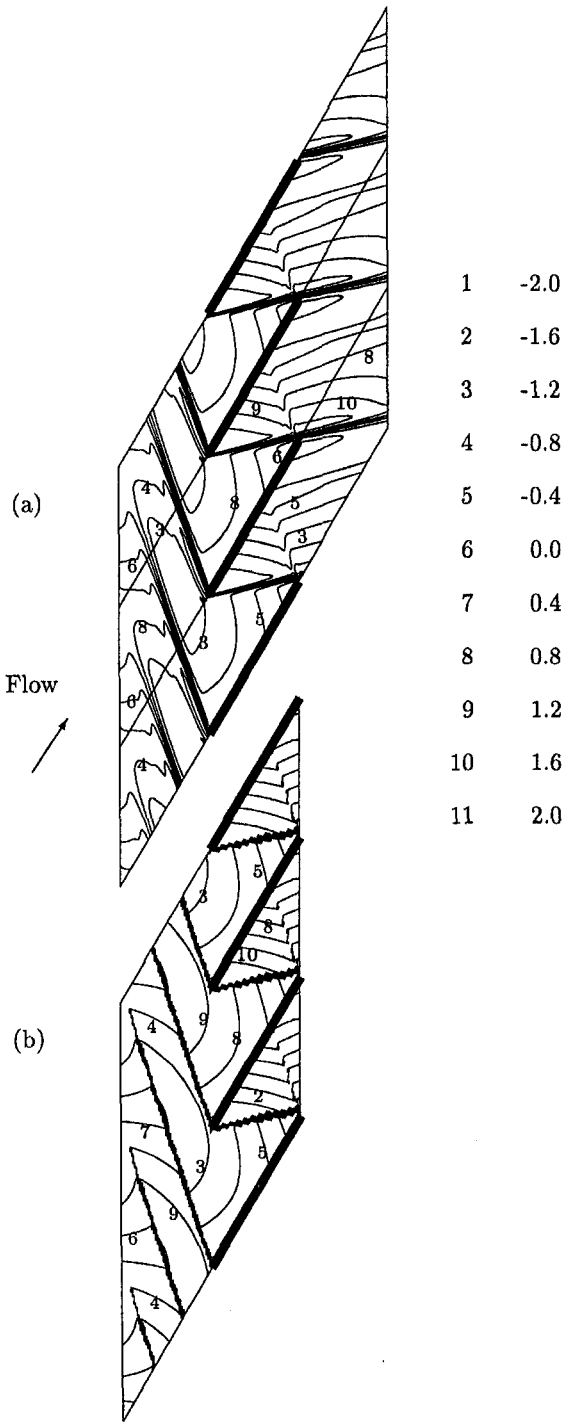

Fig. 3 Out-of-phase pressure field of Cascade A undergoing a torsional motion about midchord with $\omega = 1.0$ and $\sigma = 180$ deg: (*a*) numeric, (*b*) semi-analytic. Three passages are shown in the cascade frame.

Based on the rate of smearing of discontinuities an effective Reynold's number ($\mathrm{Re}_{\mathrm{eff}}$) can be defined that characterizes the dissipative error in the near-field discretization. $\mathrm{Re}_{\mathrm{eff}}$ was estimated by modeling the leading-edge Mach waves with the convection-diffusion equation, i.e., $f_y + cf_x = \mathrm{Re}_{\mathrm{eff}}^{-1} f_{xx}$, where $c = \sqrt{M^2 - 1}$ and the diffusion is due to dissipative error. This equation has an error function solution of the form $\mathrm{erf}\,[(x - cy)\sqrt{\mathrm{Re}_{\mathrm{eff}}/y}]$. By fitting the numerical solution in the vicinity of a discontinuity to the error function solution at various dis-

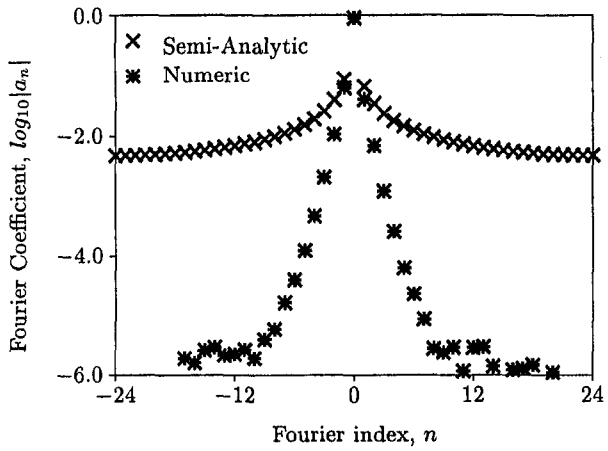

Fig. 4 Semi-analytic and numeric Fourier spectra for the pressure response one axial chord upstream of Cascade A undergoing torsional motion about midchord with $\omega = 1.0$ and $\sigma = 0$ deg

tances from the leading edge, i.e., x and y in Fig. 2, Re_{eff} was estimated as approximately 200 on the 300 × 100 mesh. This low value of Re_{eff} on a relatively fine mesh implies that it is impractical to mesh resolve discontinuities, and mesh extrapolation schemes should be employed.

The work per cycle as a function of interblade phase angle, i.e., $W_C(\sigma)$, was computed by the semi-analytic and numerical potential analyses, with excellent agreement (Montgomery et al., 1995). Because of the slow rate of mesh convergence, mesh extrapolation of W_C as predicted on 75 × 25, 150 × 50, and 300 × 100 meshes was applied to obtain the W_C predictions and mesh convergence rates. The solution converges slowly in the vicinity of a discontinuity, with approximately the predicted $\mathcal{O}(h^{1/2})$ mesh convergence rate. However, mesh convergence rates for global unsteady aerodynamic quantities, such as W_C, were closer to the $\mathcal{O}(h^2)$ behavior found in continuous regions, which implies that the smearing of the discontinuity is not a dominant source of error. This may be because the smearing of the step function discontinuities that exist for supersonic flat plates tends to be an odd function, and so the integrated effect of the smearing tends to be small.

The unsteady aerodynamic response of a flat plate cascade in which multiple discontinuities intersect the plate surfaces was also investigated, again with excellent agreement for $W_C(\sigma)$ as predicted by the semi-analytic and numerical analyses (Montgomery, 1994). The flat plate cascade considered here is Cascade B (Verdon, 1977), in which the downward traveling leading edge Mach wave impinges on and is reflected from the adjacent plate below, and this reflected wave is then reflected from the originating plate's lower surface. As with the Cascade A results, the agreement between the semi-analytic and numerical solutions was found to be good in continuous regions of the flow, with errors in the vicinity of the smeared discontinuity that decrease slowly as the mesh is refined. The rate of mesh convergence for global unsteady aerodynamic quantities is slower for Cascade B than for Cascade A, presumably because of the increased number of discontinuities intersecting the plate surfaces, but is still closer to $\mathcal{O}(h^2)$ than $\mathcal{O}(h^{1/2})$.

Real Blades. To investigate the effects of real blade geometry on the unsteady aerodynamic behavior of a vibrating cascade, the aerodynamic response of a cascade of flat bottom double circular arc (DCA) airfoils to prescribed airfoil motion was compared with the response of an analogous flat plate cascade. The cascade geometry and inlet Mach number were taken from the Eighth Standard Cascade Configuration, namely Verdon's Cascade A. The airfoil geometry was taken from the Ninth Standard Cascade Configuration, which defines circular arc airfoils. The lower airfoil surface is flat ($y = 0$) and the upper airfoil surface is defined by $y = T - R + \sqrt{R^2 - (x - 0.5)^2}$, $0 < x < 1$, where $R = (T^2 + 0.5^2)/2T$ is the radius and T is the airfoil thickness at midchord. Both 2 percent ($T = 0.02$) and 4 percent ($T = 0.04$) thick airfoils were considered. This blade geometry was chosen to be generic and to introduce mean loading effects and a finite strength discontinuity into the flow field, namely a trailing edge oblique shock. Real blade results were obtained with the linearized potential analysis and a nonlinear Euler analysis, NPHASE (Swafford et al., 1994), and compared with each other and with flat plate cascade results from the semi-analytic analysis.

Steady Flow. The ratio of downstream static pressure to upstream stagnation pressure ($P_2/P_{01} \equiv 0.40$) was chosen so that the cascade is choked, with a trailing edge oblique shock reflecting from each airfoil lower surface. For both airfoil thicknesses, the downward traveling leading edge Mach waves reflect off the adjacent lower airfoil just upstream of the trailing edge, and seem to coalesce with the trailing edge oblique shocks. Thus there is a single discontinuity on the airfoil surfaces, namely the upward traveling trailing-edge oblique shock reflection (near $x = 0.7$ on the reference blade) on the lower surfaces.

For the 2 percent thick airfoils with an inlet Mach number of 1.345 the unique incidence condition results in an incidence angle of 3.0 deg ($\Omega_{-\infty} = 62.5$ deg). The Euler analysis predicts a downstream Mach number of 1.20, flow angle of 63.2 deg, and a static pressure rise of 18 percent across the cascade, which corresponds to a total pressure loss, due to the oblique shock, of 3.0 percent. To match the strength of the trailing edge shock predicted by the Euler analysis, a downstream Mach number of 1.25 was specified in the steady potential analysis, which results in a downstream flow angle of 63.5 deg and a static pressure rise of 14 percent across the cascade. The potential analysis assumes isentropic flow, so there is no total pressure loss in the potential results. Figure 5(a) shows the mean pressure on the airfoil surfaces for the 2 percent thick airfoil cascade as predicted by the potential and Euler analyses. The meshes used for the steady analyses are the same as those used for the unsteady analyses, which are described below. For both analyses, the oblique shock reflected from the lower surface of each blade has a finite width since it is smeared by numerical diffusion as it crosses the cascade passage. The width of the shock is larger for the potential analyses, presumably because for this calculation the potential solution used more upwinding in the field approximation than the Euler analysis. The location of the shock predicted by the potential analysis is downstream of the location predicted by the Euler analysis, which is consistent with other potential analyses (Westland and Hounjet, 1993).

For the 4 percent thick airfoils with an inlet Mach number of 1.345 the unique incidence condition results in an incidence angle of 5.8 deg ($\Omega_{-\infty} = 65.3$ deg). The Euler analysis predicts a downstream Mach number of 1.16, flow angle of 64.7 deg, and a static pressure rise of 15 percent across the cascade, which corresponds to a total pressure loss of 7.8 percent. To match the strength of the trailing edge shock predicted by the Euler analysis, a downstream Mach number of 1.24 was specified in the steady potential analysis, which results in a downstream flow angle of 66.3 deg and a static pressure rise of 15 percent across the cascade. Figure 5(b) shows the mean pressure on the airfoil surfaces for the 4 percent thick airfoil cascade as predicted by the potential and Euler analyses.

Unsteady Flow. The finest meshes used have 300 axial grid lines, with 100 lines intersecting the airfoil surfaces, and 100 circumferential grid lines. The mesh used for the linearized potential solutions is nearly uniform and extends one half axial chord upstream and one and one-half axial chords downstream of the cascade, e.g., see Fig. 6. The greater axial extent downstream was chosen so that the downstream traveling reflection

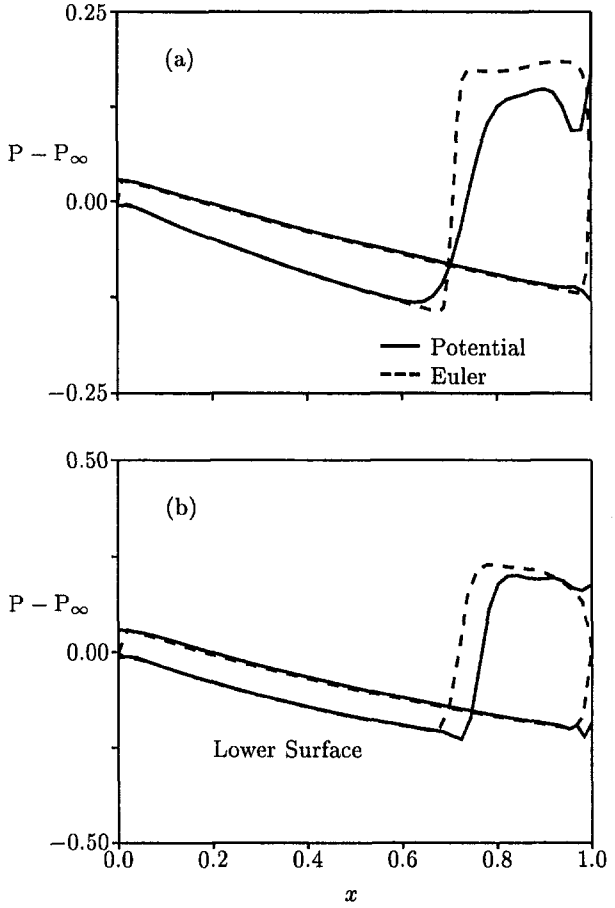

Fig. 5 Mean pressure distribution on the airfoil surfaces for the double circular arc cascades as predicted by the potential and Euler analyses: (*a*) 2 percent thick blades, (*b*) 4 percent thick blades

of the trailing edge shock is smeared by the near-field dissipative error before reaching the far-field boundary. The mesh used for the Euler solutions is nearly uniform in the circumferential direction away from the airfoil and clustered to the airfoil surface. The Euler mesh axial distribution is nearly uniform on the airfoil surface, but the mesh both upstream and downstream of the cascade is stretched in the axial direction to dissipate outgoing waves (Huff, 1992). A stretched mesh is required for the nonlinear Euler analysis because the far-field boundary conditions are currently based on one-dimensional characteristic theory, which leads to reflection of the acoustic response at the far field boundaries. Mesh stretching was applied with a hyperbolic tangent method using the IGB grid generator (Beach, 1990). Stretching the mesh so that cells at the far-field boundary were 1.0 axial chord in length and 15 airfoil chords away from the cascade was found to be insufficient to dissipate the acoustic response, however, stretching so that cells at the far-field boundary were 2.0 axial chords in length and 25 airfoil chords away from the cascade was found to be sufficient.

The nonlinear Euler analysis was executed for five cycles of motion with a torsional amplitude of 2 deg, using 400 time steps per cycle of motion with 1 Newton iteration and 2 Gauss–Seidel sub-iterations per time step. This was found to be the minimum time resolution necessary to obtain good agreement with the semi-analytic results for the flat plate cascade test case. The semi-analytic calculation requires less than 1 second of CPU time, the linearized potential calculation requires approximately 7 minutes, and the nonlinear Euler calculation requires approximately 20 hours per cascade passage. The linearized potential calculation thus reduces the required computing time by two orders of magnitude as compared with the nonlinear Euler calculation. All timings were determined on a SGI INDIGO workstation with a series R4000 CPU operating at 100 MHz.

The imaginary (out-of-phase with respect to blade motion) component of the first harmonic unsteady pressure on the reference airfoil surfaces for interblade phase angles of 0 and 180 deg is shown in Fig. 7 for the 2 percent thick airfoils and in Fig. 8 for the 4 percent thick airfoils. The corresponding flat plate results are also shown for comparison. The pressure on the lower surface has an impulse near $x = 0.7$ due to the motion of the finite strength trailing edge oblique shock. This impulse is a delta function for infinitesimal blade motions (Hall et al., 1994), but is smeared in the numerical solution into an impulse of finite width. This impulsive loading for real blades differs from that for flat plates, which have a step function behavior due to the trailing edge Mach wave. In addition to the numerical smearing of the shock profile, there is another source of smearing of the shock impulse in the time-accurate nonlinear analysis. The shock at each instant of time may be sharp, e.g., see Fig. 5, but because of shock motion during the time integration used to determine the first harmonic of the unsteady pressure, the shock impulse is smeared.

The agreement between the semi-analytic flat plate solutions, given by the dots, and the real blade solutions, given by the solid and dashed lines, is good on the upper surface of the airfoil, where flow properties are continuous. The agreement is better for the 2 percent thick airfoils than the four percent thick airfoils because of the smaller mean loading. The flat plate and

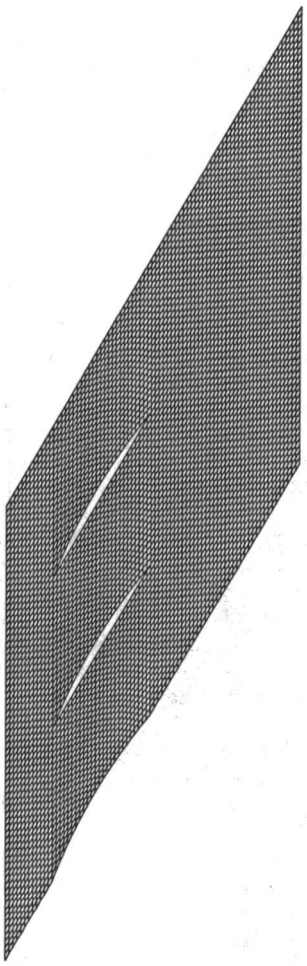

Fig. 6 Uniform mesh for the 4 percent thick airfoil used for the linearized potential analysis. For clarity, three passages of a 75 × 25 mesh are shown.

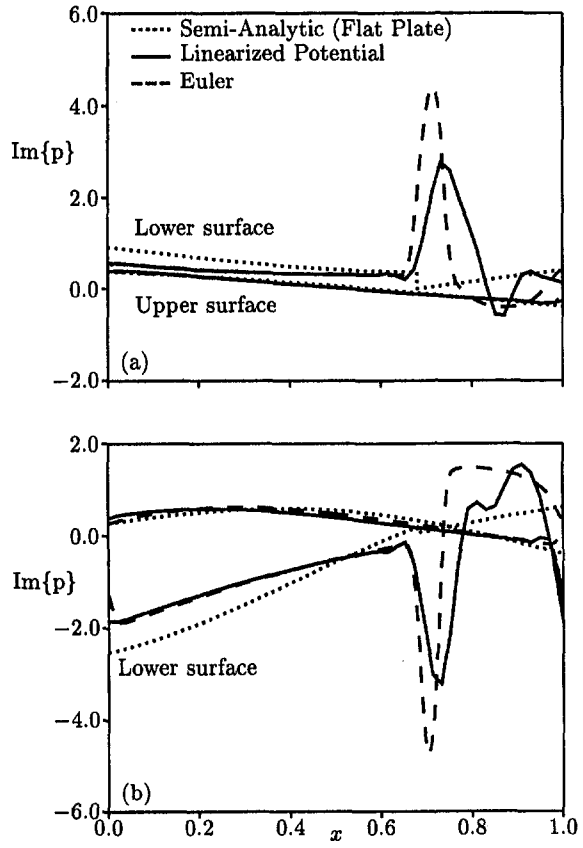

Fig. 7 Out-of-phase first harmonic pressure distribution on the airfoil surfaces for the flat plate and 2 percent thick airfoil cascades undergoing torsional motions about midchord at $\omega = 1.0$: (*a*) $\sigma = 0$ deg, (*b*) $\sigma = 180$ deg

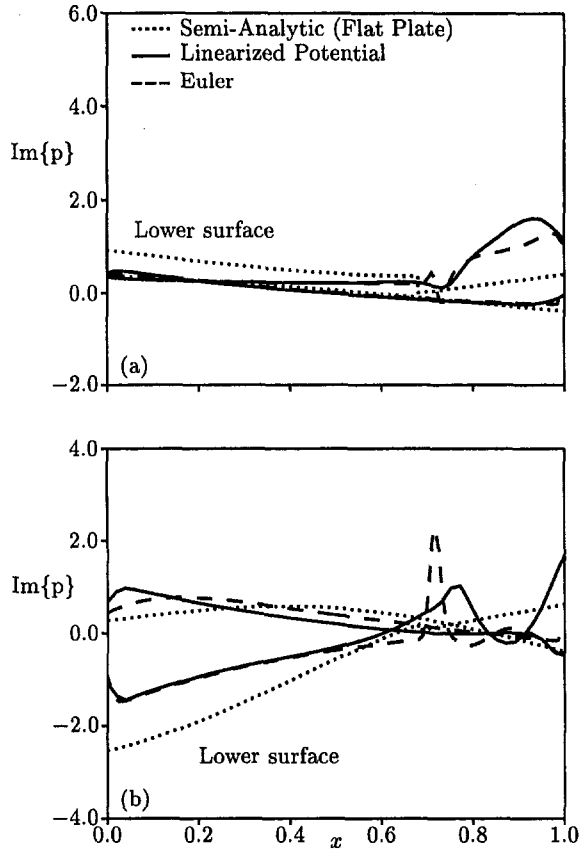

Fig. 8 Out-of-phase first harmonic pressure distribution on the airfoil surfaces for the flat plate and 4 percent thick airfoil cascades undergoing torsional motions about midchord at $\omega = 1.0$: (*a*) $\sigma = 0$ deg, (*b*) $\sigma = 180$ deg

real blade solutions disagree on the lower surface due to mean loading and the shock impulse, which is associated with the trailing-edge oblique shock present in the real blade flows. The real blade and flat plate pressures also differ downstream of the reflected oblique shock where there is significant mean loading.

The upwinding coefficient used for the numerical potential analysis was 0.05 for the 2 percent thick airfoils and 2.0 for the 4 percent thick airfoils. The large variation in these two coefficients illustrates the fact that the smoothing required to suppress oscillations is problem dependent. The rather high value for the 4 percent thick airfoils was required to suppress oscillations, but resulted in more smearing of the shock impulse than is exhibited by the Euler analysis. While the smoothing level affects the shape of the shock impulse, we concluded that the mesh extrapolated work per cycle results were relatively insensitive to the smoothing level. The location of the shock impulse predicted by the unsteady potential analysis is downstream of the location predicted by the Euler analysis, which is attributed to error in the mean shock location in the steady potential solution.

The agreement between the linearized potential and nonlinear Euler solutions is good in continuous regions of the flow field, but there are differences near the reflected oblique shock on the lower surface and near the trailing edge. These differences illustrate the difficulties in comparing discontinuity capturing schemes, since the shape of the shock impulse depends on both the analysis and the grid. For the linearized analysis, the prediction of the shock impulse is also limited by the accuracy of the mean shock location and profile determined by the steady potential flow analysis. Overall, the agreement between the linearized potential and nonlinear Euler analyses is reasonable, considering the differences in the steady solutions. Improvements in the shock capturing capability of the steady potential analysis should enable more accurate prediction of the shock impulse by the unsteady potential analysis.

Grid extrapolation was applied to work per cycle predictions on 150×50, 225×75, and 300×100 meshes, with the results given in Fig. 9. Results obtained for the flat plate cascade by extrapolating the numerical potential predictions on these meshes are indistinguishable from the semi-analytic results (Montgomery et al., 1995). The numerical linearized potential results are for interblade phase angles at multiples of 15 deg, which may not be fine enough to resolve acoustic resonances. The nonlinear Euler results are only given for interblade phase angles corresponding to four or fewer passages. The agreement between the two analyses is reasonable, except for $\sigma = 90$ deg. The reason for disagreement at this particular phase angle is currently unknown. Any fault does not necessarily lie with the potential solution, since the Euler results may contain errors due to the axial mesh stretching, which distorts the acoustic response.

The work per cycle predictions and computed mesh convergence rates for two interblade phase angles ($\sigma = 240$ and 270 deg) are given in Tables 1 and 2. The differences between the flat plate and real blade results at these phase angles (see Fig. 9) indicate that the impulsive shock loading is contributing significantly to the works per cycle. The convergence rates are approximately second order, even with the impulsive shock loading contribution. The convergence rates are not integers, presumably because the coarser meshes are not in the asymptotic mesh convergence regime.

The linearized potential and nonlinear Euler results differ on similar meshes, but mesh extrapolated values are in reasonable agreement. For example, for the 2 percent thick cascade at σ

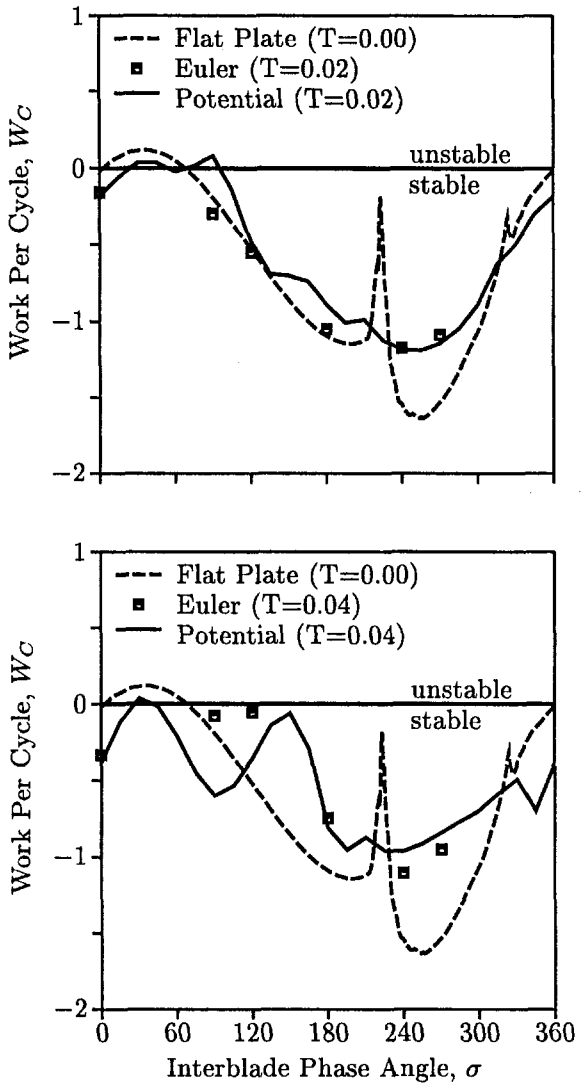

Fig. 9 Work per cycle as a function of interblade phase angle for flat plates and 2 and 4 percent thick flat bottomed DCA airfoils in the Cascade A configuration

$= 0$, the potential versus Euler results are -0.265 versus -0.166 on a 150×50 mesh, -0.186 versus -0.156 on a 300×100 mesh, and -0.160 versus -0.153 when extrapolated.

The flat plate and real blade predictions differ, as they should, but are in qualitative agreement, except near the acoustic resonance conditions for the flat plate cascade. As expected, the differences increase with blade thickness. One major cause of this difference is believed to be the shock impulse that exists for real blades due to the motion of the finite strength trailing-edge oblique shock. This can be seen by examining the surface pressures given in Figs. 7 and 8, where the real blade and flat plate pressures agree fairly well except near the reflected oblique shock. Another possible source of difference is the change in the acoustic propagation conditions due to the turning of the mean flow by the real blade cascades. The potential and Euler solutions are in reasonable agreement, which indicates the potential analysis is representing the shock impulse in a reasonable manner.

Table 1 Work per cycle predictions of the numerical linearized potential analysis for the 2 percent thick airfoil

	$\sigma = 240$	$\sigma = 270$
150x50 Mesh	-1.160	-1.132
300x100 Mesh	-1.222	-1.195
Mesh Extrapolated	-1.243	-1.216

Conclusions

A linearized unsteady potential numerical analysis for supersonic cascades with subsonic axial flow was developed and verified against a semi-analytic analysis for flat plate cascades. This analysis has been shown to yield good aeroelastic response information. For example, mesh extrapolated work per cycle predictions for flat plate cascades are in excellent agreement with the semi-analytic values.

However, since a shock capturing method was used, the high wave-number content of the far-field acoustic response is lost. Therefore, it would seem that for supersonic cascades numerical flutter predictions are possible (if mesh extrapolation is employed and care is taken to achieve accurate shock resolution) but numerical aeroacoustic response calculations are very difficult. If the high wave-number content of the acoustic response is of interest, then shock capturing methods should be used with care. As expected, the width of numerically smeared discontinuities decreases slowly as the mesh is refined. However, the global unsteady aerodynamic quantities of interest converge at a faster rate.

Comparing the response of flat plate and real blade cascades shows that one effect of real blade geometry and blade loading on the unsteady aerodynamic response in supersonic flow is the shock impulse due to the unsteady motion of a finite strength shock. This shock impulse can be stabilizing or destabilizing depending on the phase of the shock motion with respect to the blade motion. An accurate prediction of the shock impulse by a linearized unsteady analysis is limited by the accuracy of the shock determined by the mean flow analysis.

Comparisons between the time-linearized unsteady potential analysis and a time-accurate nonlinear Euler analysis show that the potential analysis can give reasonably accurate predictions for the unsteady aerodynamic response while using orders of magnitude less computing time. The linearized potential analysis attempts to resolve the acoustic response by matching to an analytic solution in the far field, while the nonlinear Euler analysis uses mesh stretching to dissipate the acoustic response. Besides being unable to resolve the acoustic response or define acoustic excitations, the mesh stretching approach may require many mesh cells away from the region of interest, i.e., the cascade. Also, the stretching required to dissipate the acoustic response sufficiently is problem dependent.

The steady potential analysis places the oblique shock downstream of its true location and also smears the shock due to numerical smoothing. One possible improvement to the steady potential analysis is to implement a Clebsch formulation (Westland and Hounjet, 1993), which would include entropy generation effects and should improve the prediction of the mean shock location. Improvements in the shock capturing capability of the steady potential solver should enable a more accurate prediction of the shock impulse by the unsteady potential analysis.

Table 2 Work per cycle predictions and mesh convergence rates of the nonlinear Euler analysis for the 2 percent thick airfoil

	$\sigma = 240$	$\sigma = 270$
150x50 Mesh	-1.102	-1.016
225x75 Mesh	-1.151	-1.055
300x100 Mesh	-1.162	-1.069
Mesh Extrapolated	-1.173	-1.087
Convergence Rate	2.6	1.9

References

Adamczyk, J. J., and Goldstein, M. E., 1978, "Unsteady Flow in a Supersonic Cascade With Subsonic Leading-Edge Locus," *AIAA Journal,* Vol. 16, No. 12, pp. 1248–1254.

Beach, T. A., 1990, "An Interactive Grid Generation Procedure for Axial and Radial Flow Turbomachinery," AIAA Paper No. 90-0344.

Caspar, J. R., and Verdon, J. M., 1981, "Numerical Treatment of Unsteady Subsonic Flow Past an Oscillating Cascade," *AIAA Journal,* Vol. 19, No. 12, pp. 1531–1539.

Fransson, T. H., and Verdon, J. M., 1993, "Standard Configurations for Unsteady Flow Through Vibrating Axial-Flow Turbomachine Cascades," *Unsteady Aerodynamics, Aeroacoustics and Aeroelasticity of Turbomachines and Propellers,* H. M. Atassi, ed., Springer-Verlag, New York, pp. 859–889.

Gerolymos, G. A., Blin, E., and Quiniou, H., 1990, "Comparison of Inviscid Computations With Theory and Experiment in Vibrating Transonic Compressor Cascades," ASME Paper No. 90-GT-373.

Hall, K. C., Clark, W. S., and Lorence, C. B., 1994, "A Linearized Euler Analysis of Unsteady Transonic Flows in Turbomachinery," ASME JOURNAL OF TURBOMACHINERY, Vol. 116, pp. 477–488.

Hoyniak, D., and Verdon, J. M., 1995, "Steady and Linearized Unsteady Transonic Analyses of Turbomachinery Blade Rows," *Proc. Seventh International Symposium on Unsteady Aerodynamics and Aeroelasticity of Turbomachines,* Elsevier Science, Y. Tanida and M. Namba, eds., Amsterdam, pp. 109–124.

Huff, D. L., Swafford, T. W., and Reddy, T. S. R., 1991, "Euler Flow Predictions for an Oscillating Cascade Using a High Resolution Wave-Split Scheme," ASME Paper No. 91-GT-198.

Huff, D. L., 1992, "Pressure Wave Propagation Studies for Oscillating Cascades," AIAA Paper No. 92-0145.

Lawaczeck, O. K., 1972, "Calculation of the Flow Properties Up- and Downstream of and Within a Supersonic Turbine Cascade," ASME Paper No. 72-GT-74.

Montgomery, M. D., 1994, "Linearized Unsteady Aerodynamic Analysis of Supersonic Cascades With Subsonic Axial Velocity," Ph.D. Thesis, Purdue University School of Mechanical Engineering, West Lafayette, IN.

Montgomery, M. D., Verdon, J. M., and Fleeter, S., 1995, "A Linearized Unsteady Aerodynamic Analysis for Supersonic Cascades," *Proc. Seventh International Symposium on Unsteady Aerodynamics and Aeroelasticity of Turbomachines,* Elsevier Science, Y. Tanida and M. Namba, eds., Amsterdam, pp. 125–142.

Nagashima, T., and Whitehead, D. S., 1978, "Linearized Supersonic Unsteady Flow in Cascades," R&M 3811, British Aeronautical Research Council, London, UK.

Snyder, L. E., and Commerford, G. L., 1974, "Supersonic Unstalled Flutter in Fan Rotors; Analytical and Experimental Results," ASME *Journal of Engineering for Power,* Vol. 96, pp. 379–386.

Swafford, T. W., Loe, D. H., Huff, D. L., Huddleston, D. H., and Reddy, T. S. R., 1994, "The Evolution of NPHASE: Euler/Navier–Stokes Computations of Unsteady Two-Dimensional Cascade Flow Fields," AIAA Paper No. 94-1834.

Usab, W. J., Jr., and Verdon, J. M., 1991, "Advances in the Numerical Analysis of Linearized Unsteady Cascade Flows," ASME JOURNAL OF TURBOMACHINERY, Vol. 113, pp. 633–643.

Verdon, J. M., 1977, "Further Developments in the Aerodynamic Analysis of Unsteady Supersonic Cascades; Part 1—The Unsteady Pressure Field; Part 2—Aerodynamic Response Predictions," ASME *Journal of Engineering for Power,* Vol. 99, pp. 509–525.

Verdon, J. M., and Caspar, J. R., 1984, "A Linearized Unsteady Aerodynamic Analysis for Transonic Cascades," *Journal of Fluid Mechanics,* Vol. 149, pp. 403–429.

Verdon, J. M., 1989, "The Unsteady Flow in the Far Field of an Isolated Blade Row," *Journal of Fluids and Structures,* Vol. 3, No. 2, pp. 123–149.

Westland, J., and Hounjet, M. H. L., 1993, "Clebsch Variable Model for Unsteady, Inviscid, Transonic Flow With Strong Shock Waves," AIAA Paper No. 93-3025.

Whitehead, D. S., 1990, "A Finite Element Solution of Unsteady Two-Dimensional Flow in Cascades," *International Journal for Numerical Methods in Fluids,* Vol. 10, No. 1, pp. 13–34.

Williams, M. H., 1991, private communication.

Rotordynamic Forces Due to Turbine Tip Leakage: Part I—Blade Scale Effects

S. J. Song
Department of Aerospace Engineering,
Inha University,
Namgu, Inchon, Korea

M. Martinez-Sanchez
Department of Aeronautics/
Astronautics,
MIT,
Cambridge, MA 02139

An experimental and theoretical investigation has been conducted on rotordynamic forces due to nonaxisymmetric turbine tip leakage effects. This paper presents an actuator disk model that describes the flow response to a finite clearance at the rotor tip. The model simplifies the flow field by assuming that the radially uniform flow splits into two streams as it goes through the rotor. The stream associated with the tip clearance, or the underturned stream, induces radially uniform unloading of the rest of the flow, called the bladed stream. Thus, a shear layer forms between the two streams. The fraction of each stream and the strength of shear layer between the two are found as functions of the turbine loading and flow parameters without resorting to empirical correlations. The results show that this model's efficiency predictions compare favorably with the experimental data and predictions from various correlations. A companion paper builds on this analysis to yield a model of the three-dimensional disturbances around an offset turbine and to predict the subsequent cross forces.

1 Introduction

One of the major problems that has always limited the development of high-performance turbomachinery is the vibration of its structure. Ehrich and Childs (1984) have reviewed the various types of self-excited vibrations encountered in practice. Self-excited vibrations that occur in rotor systems are referred to as *rotordynamic instability*. The most publicized rotordynamic instability occurred during the development of the cryogenic turbopumps for the Space Shuttle Main Engine (SSME). One of the major causes was attributed to a phenomenon referred to in the US as the "Alford force." This phenomenon occurs due to fluid excitation forces caused by an asymmetric tip clearance distribution, feeding energy into the whirling motion of the shaft.

Thomas (1958) first identified the problem in high power steam turbines, and Alford (1965) identified the same problem in jet engines. They independently proposed an identical mechanism to explain the observed aerodynamic instability. Essentially, the local efficiency is higher in the smaller tip gap region, and the local torque and the tangential force exerted on the turbine by the fluid increase with the local efficiency. This assumption is based on empirical evidence that the efficiency of a turbine stage varies linearly with the tip clearance gap (Kofskey and Nusbaum, 1968). When integrated around the circumference, the net result is a force acting orthogonal to the displacement which adds energy to the forward whirling motion. Figure 1, from Ehrich and Childs, illustrates the mechanism.

Although other rotordynamic instabilities (e.g., destabilizing forces in labyrinth seals) have been extensively studied, relatively little effort has been expended on the tip clearance excitation force. Urlichs (1983) and Vance and Laudadio (1984) established the existence and linearity of the Alford force in an unshrouded turbine and an axial fan, respectively. However, a basic physical understanding of the influence of various geometric and flow-related parameters in the generation and scaling of the tip clearance excitation force was still lacking.

Therefore, the objective of this investigation was to gain physical understanding of the force generation mechanism via experimental and theoretical methods. The current investigation's experimental methods and results were previously reported by Martinez-Sanchez et al. (1995). This paper presents the first part of a model developed during the theoretical phase of the investigation.

2 Model Description

The flow response to an eccentric turbine involves the three scales of the tip gap, t, the blade span, H_b, and the turbine radius, R. They are typically in ratios of the order $t/H_b \sim 0.01$ and $H_b/R \sim 0.1-0.3$ (Fig. 2). Therefore, the gap-scale effects such as the leakage flow velocity, which is driven by local tip conditions, can be decoupled from the other two larger length scales. The larger length scale effects such as the tip blade loading become boundary conditions. The blade scale effects include the radial migration of throughflow toward the tip gap and the underturning of flow in the outer region of the blade span due to the gap leakage flow. These effects are influenced not only by the tip gap effects, which determine the leakage rate, but also by the radius scale effects, which determine the local turbine inlet and outlet conditions. In reality, the inlet and outlet conditions would vary azimuthally for an eccentric turbine. However, at the blade scale, these boundary conditions can be assumed to be axisymmetric at the local value. Thus, the blade scale effects link the effects of the tip gap and the turbine radius. Finally, at the turbine radius scale, the turbine eccentricity causes azimuthal variations of flow variables (e.g., the flow coefficient). The effects of two smaller scales are seen mainly as connecting conditions between the upstream and downstream flows.

The differences in the relative importance of unsteady effects are also pronounced at different scales. A rotor simultaneously spinning at angular frequency, ω, and whirling at angular frequency, Ω, can have a radius scale reduced frequency, $\Omega R/c_x$, close to the order of unity. However, at the two smaller scales, the reduced frequencies, $\Omega H_b/c_x$ and $\Omega t/c_x$, are orders of magnitude smaller than unity. Therefore, the unsteady effects need to be considered only at the radius

Contributed by the International Gas Turbine Institute and presented at the 41st International Gas Turbine and Aeroengine Congress and Exhibition, Birmingham, United Kingdom, June 10–13, 1996. Manuscript received at ASME Headquarters February 1996. Paper No. 96-GT-364. Associate Technical Editor: J. N. Shinn.

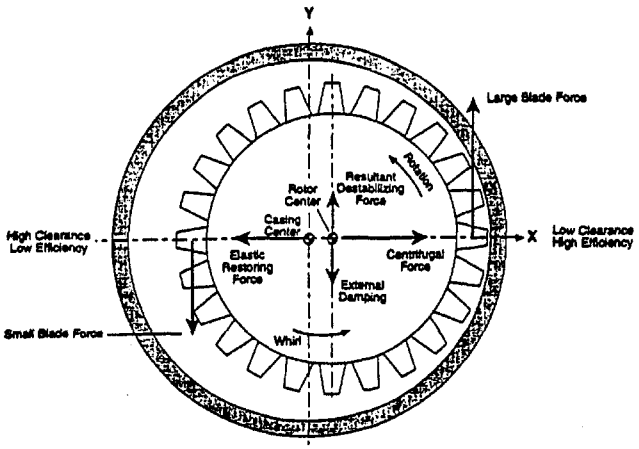

Fig. 1 Thomas–Alford destabilizing mechanism

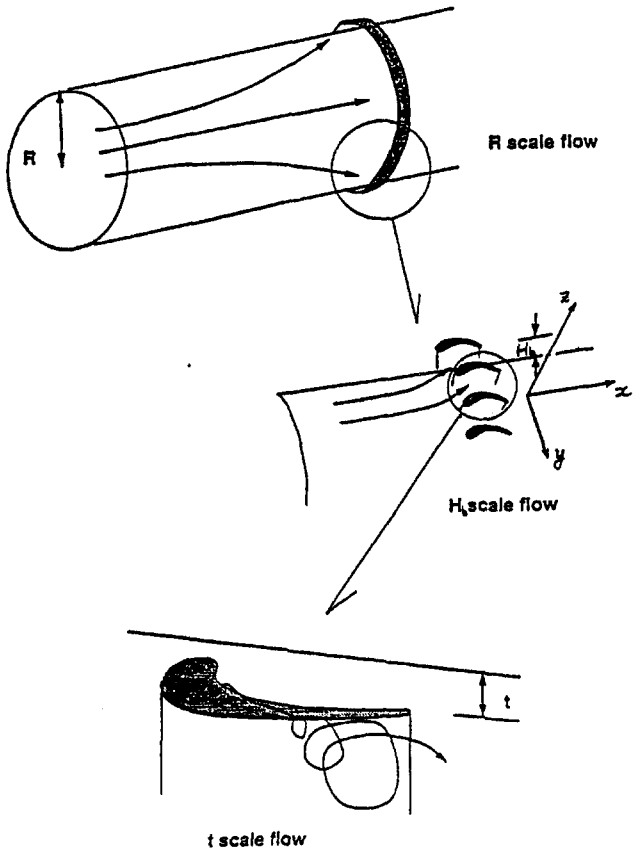

Fig. 2 Flow features at different length scales in a turbine with an eccentric rotor

scale, and the flow can be assumed to be quasi-steady at the other two smaller scales.

For the case of a turbine with a whirling rotor, both the stator row and the rotor blade rows are unwrapped and collapsed into a single actuator disk (Fig. 3). In this coordinate system, x is the direction of the throughflow, y is the tangential (azimuthal) direction, and z is the radial direction.

The analysis proceeds at two levels, as shown in Fig. 3. The first is a quasi-steady blade scale analysis in the meridional (xz) plane. This analysis focuses on the radial flow redistribution effects due to the existence of rotor tip gap and does not consider the tangential flow redistribution that occurs upstream and downstream of the disk. The second is an unsteady radius scale analysis in the radial (xy) plane, which focuses on the tangential flow redistribution effects due to a whirling turbine. This more global, radius scale (xy) analysis, presented in a companion paper, utilizes the results from the blade scale (xz) analysis as connecting conditions across the actuator disk. Such a framework can accommodate a flexible, modular approach in which various submodels at different length scales can be separately incorporated into the analysis.

This paper exclusively presents the blade scale (xz) model. It is capable of analytically predicting the effects of turbine rotor tip clearance on the losses and the turbine performance. The blade scale model builds on previous efforts by Gauthier (1990) and Martinez-Sanchez and Gauthier (1990).

Nomenclature

$B_\perp$ = total enthalpy of meridional flow
c = absolute flow velocity; axial blade chord
c_l = lift coefficient
$D = 2R$ = turbine mean diameter
G = factor defined in Eq. (40a)
H = annulus height
H_b = blade span
Q, q = shear layer strength
P, p = pressure
R_D = radius of rolled-up vortex
s = blade pitch
t = radial tip clearance
$U = \omega R$ = turbine rotational speed at mean radius
w = relative velocity; work defect factor
W^+, W^- = work done per unit mass by underturned and main flow
ZW = Zweifel coefficient
α = pitch angle; absolute flow angle
$\beta = -\partial\eta/\partial(t/H)$ = efficiency loss factor
β = yaw angle; relative flow angle
β_m = mean rotor blade angle
δ_{jet} = clearance jet thickness
Δ = thickness of underturned layer downstream of the actuator disk
Γ = circulation of clearance vortex
η = turbine efficiency
θ = azimuthal angle measured in direction of rotation from minimum gap location; underturning relative to mean flow angle
λ = nondimensional underturned flow rate
ξ = rolled-up vorticity
π = turbine pressure ratio; pi
ρ = density
$\phi = c_x/U$ = turbine flow coefficient
ψ = meridional stream function
$\Psi = (h_{01} - h_{03})/U^2$ = (turbine stage loading factor, or work coefficient
ω = angular velocity of rotor shaft rotation
ω_y = vorticity of meridional flow
Ω = angular velocity of rotor shaft whirl

Subscripts

0 = far upstream of actuator disk in blade scale analysis
1 = stator inlet in blade scale analysis
$2r$ = rotor inlet in blade scale analysis
$2s$ = stator exit in blade scale analysis
3 = rotor exit in blade scale analysis
4 = far downstream of actuator disk in blade scale analysis, axially at the same location as 0+ of the radius scale analysis
r = rotor
s = stator, static; length along clearance vortex
$\perp$ = azimuthal component; perpendicular to rolled-up vortex

Superscripts

$^-$ = part of flow downstream that has crossed bladed part of turbine flow
$^+$ = part of flow downstream that was underturned due to rotor tip gap

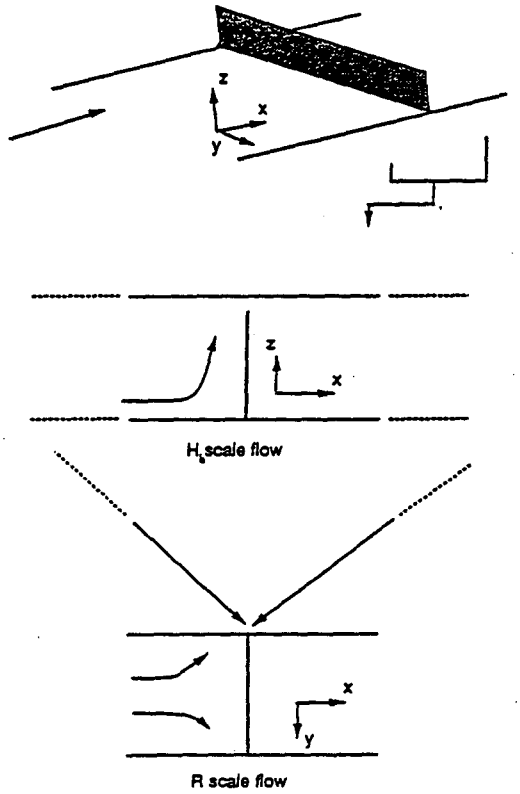

Fig. 3 Modeling the flow field at blade and radius scales

The following is assumed in deriving the governing equations:

1 Incompressible, inviscid flow.
2 Turbine stage collapsed in the axial direction to $x = 0$.
3 The blades guide the flow perfectly (except for the leakage flow) so that the relative flow exit angle is same as the blade exit angle.
4 The flow is axisymmetric ($\partial/\partial y = 0$).
5 Except for the rotor tip gap, the blade geometry is assumed to be radially uniform ($\partial/\partial z = 0$) and to be equivalent to that at the mean radius.
6 Flow conditions are radially uniform at the stator exit.

The blade actuator disk consists of a full-span stator row and a partial-span rotor row as shown in Fig. 4. Far upstream the stator row is referred to as 0. The inlet to the stator row is referred to as Station 1 and the stator exit is called $2s$. The inlet to the rotor is referred to as $2r$ and rotor exit is referred to as 3. Far downstream of the rotor row on the blade scale is Station 4.

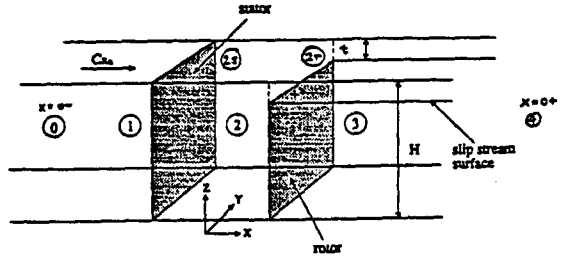

Fig. 4 A blade scale view of the actuator disk, showing various axial stations

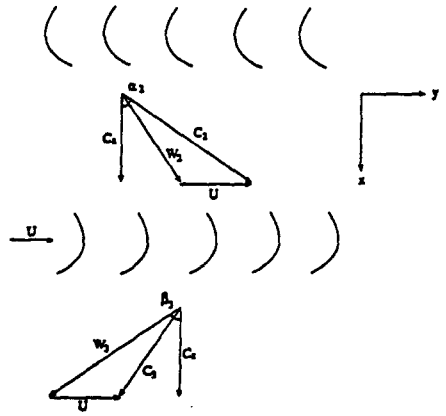

Fig. 5 Turbine velocity triangles

Figure 5 shows the turbine blading geometry with the velocity triangles. U is the turbine rotational speed; c is the absolute flow velocity; and w is the relative flow velocity. The angles α and β refer, respectively, to the absolute and the relative flow angles.

3 Tip Scale Analysis

Martinez-Sanchez and Gauthier (1990) showed that, because of the leakage flow roll-up, an *underturned layer* can be identified downstream of the rotor, containing equal amounts of leakage and blade-region flow. The fluid in this region has undergone less turning than the main bladed flow, but not zero turning, and has therefore done a finite amount of work. This underturned fluid is dealt with in this section.

The blade tip region has been analyzed using a variety of approaches. The simple model of Rains (1954), which is most appropriate for thin, lightly loaded blades, uses ideal, pressure-driven flow concepts to derive the velocity of the gap "jet." Even for the case of the thicker turbine blading, ideal flow is a fairly good approximation. For example, Rains gave a criterion for viscous forces to be negligible, and many turbines satisfy this condition. On the other hand, although the effects of chordwise pressure gradients on thick blade tip flows, as well as that of relative wall motion are still potentially significant, they have not been modeled.

The gap jet is known to interact strongly with the passage flow and to roll up into a concentrated vortex-like structure. Rains derived a semi-empirical expression for its trajectory. Lakshminarayana (1970) also used empirical information on the tip vortex location and strength to predict details of the blade pressure distribution. In fact, the strength of the vortex was explicitly related to a "partial blade tip loading parameter," K, varying from 0 to 1, and inferred from extrapolation of surface pressure measurements near the tip to the end wall.

This section introduces an analytical approach that leads to simple, but accurate expressions for the location and size of the leakage vortex. This can then be used in calculating the flow leaving angle of, and hence the work done by, the leakage flow.

Figure 6 shows schematically the essential features of the leakage flow. The fluid approaches a blade (here represented as a flat plate) with a relative velocity, $\vec{w}_2$, which evolves into the passage flow velocity, $\vec{w}_{\text{pass}}$, at locations away from the tip gap. Under the action of the pressure differential across the blade, a jet of leakage flow at velocity $\vec{w}_{\text{jet}}$ escapes under the blade. This jet penetrates a certain distance into the passage, but is eventually stopped by the main flow, which separates the jet from the wall, turns it backwards, and leads to the formation of a rolled-up structure containing both leakage and passage fluid. This "collision" of the two streams is again shown in Fig. 7 in plan form, and Fig. 8 shows a schematic of the flow

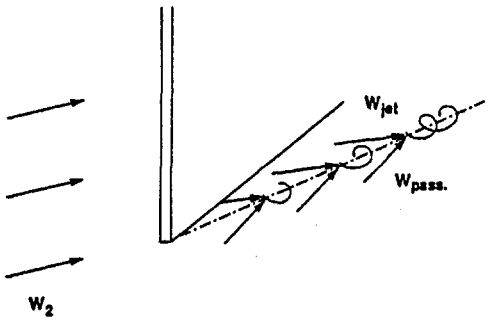

Fig. 6 Schematic of the colliding leakage jet and passage flows

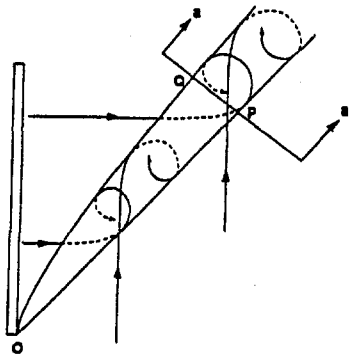

Fig. 7 Planform view of Fig. 6

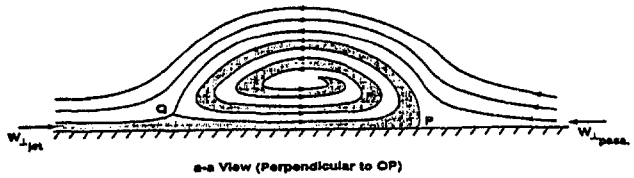

Fig. 8 Flow pattern in plane *a-a* of Fig. 7

structure seen in a cut such as *a-a* in Fig. 7 with leakage fluid shown dashed.

Consider the situation at points along the jet separation line, such as *P* in Figs. 7 and 8. Ignoring frictional effects, the two streams that meet there (jet and passage flows) can both be traced back, along different paths, to the inlet flow, and hence have equal total pressures and temperatures. Since they also have equal static pressures along their contact line (and generally similar static pressures throughout the region), these two streams must have equal velocity magnitudes. If the section *a-a* is perpendicular to *OP*, we can think of point *P* (Fig. 8) as the common stagnation point of the two "colliding" flows, approaching each other with equal velocities, which are each the component of $\vec{w}_{\text{jet}}$ and $\vec{w}_{\text{pass}}$ perpendicular to line *OP*. It follows that line *OP* must bisect the angle made by $\vec{w}_{\text{jet}}$ and $\vec{w}_{\text{pass}}$. This gives a first and important piece of information about the location of the rolled-up structure, but, since this structure has a finite and increasing transverse dimension, it does not yet locate its center.

Notice that the transverse momentum balance of a fluid element near point *P* requires that both transverse colliding flows must bring equal and opposite momentum fluxes to the rolled-up structure. Since the two velocities are equal, we find that equal mass flows must be entering the rolled-up structure from both fluids. In other words, the clear and dashed areas in Fig. 8 must occupy equal fractions of the total "vortex" cross section. Let δ_{jet} be the jet thickness, and $w_{\parallel}$, $w_{\perp}$ the common components along and across *OP* of the colliding streams. The rate of increase of the cross section $A_{\perp}$ of the rolled structure along *OP* is then given by

$$w_{\parallel} \frac{dA_{\perp}}{ds} = 2w_{\perp}\delta_{\text{jet}} \tag{1}$$

or, calling $\theta = \tan^{-1}(w_{\perp}/w_{\parallel})$, i.e., the angle made by the separation line *OP* and the blade itself,

$$\frac{dA_{\perp}}{ds} = 2\delta_{\text{jet}} \tan\theta \tag{2}$$

where *s* is measured along the vortex trajectory.

The precise shape of the rolled-up structure is more difficult to establish, but it seems reasonable to model it as a (half) cylindrical ideal vortex in a cross flow. Following Batchelor (1967), such a vortex is described by the stream function

$$\Psi = 1.298 w_{\perp} R_D J_1\left(3.83 \frac{r}{R_D}\right) \sin\theta_1 \tag{3}$$

where R_D is the radius of the dividing streamline, $J_1(x)$ is the Bessel's function of the first order (with a zero at $x = 3.83$), and (r, θ_1) are polar coordinates. The vorticity in this flow is distributed inside the semi-circle of radius R_D in proportion to Ψ:

$$\xi = \left(\frac{3.83}{R_D}\right)^2 \Psi \tag{4}$$

and is zero outside. Integration of ξ gives an overall circulation $\Gamma = 6.83 w_{\perp} R_D$, whereas integration of $r \sin\vartheta$, gives a center of vorticity height of $z_C = 0.460 R_D$. We thus make $A_{\perp} = (1/2)\pi R_D^2$, and measuring distance along the blade ($x_{bl} = s\cos\vartheta$), we can integrate Eq. (2) to obtain

$$R_D = \sqrt{\frac{4}{\pi}\left(\frac{\tan\theta}{\cos\theta}\right)\delta_{\text{jet}} x_{bl}} \tag{5}$$

The trajectory of the vortex center then follows (Fig. 9) as

$$y_c = x_{bl}\tan\theta - \frac{R_D}{\cos\theta} \tag{6}$$

To complete the analysis, the angle θ must now be determined. From our discussion of the separation line *OP*, this angle was shown to be half of the angle β between the blade and the jet flow, i.e., $\theta = \beta/2$ (Fig. 9). This angle β follows from the simple local analysis first proposed by Rains (1954), which applies to thin blades when viscous effects can be neglected. In Fig. 10, w_p and w_s are the flow velocities on the pressure and suction sides of the blade, respectively. Application of Bernoulli's equation relates these velocities to the corresponding pressures:

$$w_p = \sqrt{w_2^2 - 2\frac{p_p - p_2}{\rho}} \tag{7}$$

$$w_s = \sqrt{w_2^2 + 2\frac{p_p - p_2}{\rho}} \tag{8}$$

where p_2, w_2 correspond to inlet conditions. On the other hand, the leakage jet emerges from the gap with a velocity component perpendicular to the blade of

$$w_G = \sqrt{2\frac{p_p - p_s}{\rho}} \tag{9}$$

and its component parallel to the blade is simply w_p, since no momentum is added or lost in that direction during passage

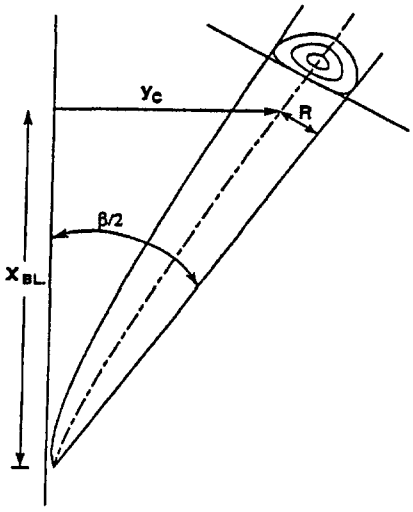

Fig. 9 Position and width of rolled-up leakage vortex

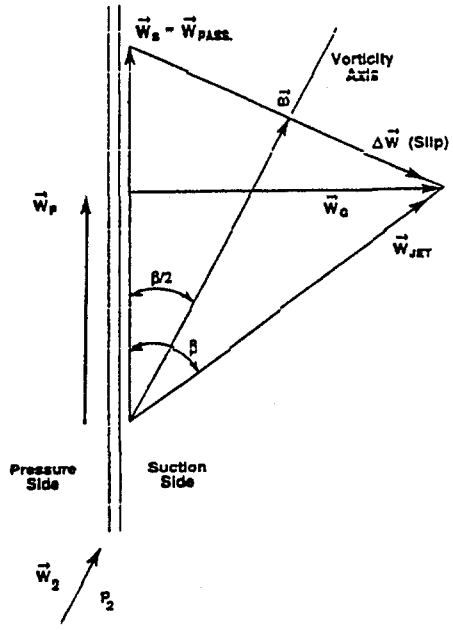

Fig. 10 Velocities and angles associated with roll-up

through the gap. It can be verified that the net magnitude w_{jet} of the jet velocity is then equal to w_s, as indicated previously. We then obtain (Fig. 10)

$$\tan \beta = \frac{w_G}{w_p} = \sqrt{\frac{(c_p)_p - (c_p)_s}{1 - (c_p)_p}} \tag{10}$$

where $c_p = 2(p - p_2)/\rho w_2^2$ in each case. Note that $(c_p)_p - (c_p)_s$ is the local lift coefficient, c_l, referred to the relative turbine inlet velocity. Using the half-angle trigonometric formulae,

$$\tan \theta = \frac{\sqrt{(c_p)_p - (c_p)_s}}{\sqrt{1 - (c_p)_s} + \sqrt{1 - (c_p)_p}} \tag{11}$$

Notice that, as shown in Fig. 9, the vorticity vector corresponding to the shear between the jet and the adjacent passage flow is inclined at ϑ with respect to the blade, i.e., it is parallel to the outer edge OP (Fig. 7) of the rolled-up structure. This is also the direction of the mean flow between the two sides of the shear layer, which means that the shear vorticity is not convected at all toward the line OP. The only reasons the vorticity Γ rolled up into the structure increases with downstream distance is that the growth of R_D gradually overlaps more and more of the shear vorticity. In this sense, the commonly invoked view of the rolled-up vortex growing by the convection of shed vortices must be used with caution.

Equations (5), (6), and (11) can now be used to calculate the vortex geometry if the suction and pressure side c_p distributions are prescribed. A simple approximation can be obtained using the theory of lightly loaded thin wing profiles. In this approximation, $(w_p + w_s)/2 \cong w_2$, which when used in Eqs. (7), (8) reduces both $(c_p)_p$ and $(c_p)_s$ to functions of $c_l = (c_p)_p - (c_p)_s$ alone. Using this in Eq. (11) gives finally

$$\vartheta = \tan^{-1}\left(\sqrt{\frac{c_l}{4}}\right) \tag{12}$$

where c_l is the lift coefficient per unit blade span and is related to the Zweifel coefficient, a blade loading parameter. Zweifel coefficient, ZW, and the lift coefficient, c_l, are determined as follows:

$$ZW = 2 * \frac{s}{c} \cos^2 \beta_3 (\tan \beta_2 + \tan \beta_3) \tag{13}$$

where s/c is the blade pitch normalized by the axial blade chord, and

$$c_l = ZW * \frac{\cos^2 \beta_2}{\cos^2 \beta_3} \cos \gamma \cos \beta_m \tag{14}$$

where γ is the rotor blade stagger angle.

4 Comparison to Vorticity Dynamics Model and to Data

Chen's similarity analysis (1991) has provided a means of correlating a variety of rolled-up vortex data. Transverse distances are normalized by gap width, t, and axial distance (or time-of-flight) are characterized by a parameter

$$t^* = \frac{x}{c_x t}\sqrt{\frac{\Delta P}{\rho}} \tag{15}$$

where x and c_x are the axial distance and velocity and $\Delta P = p_p - p_s$. The data from many experiments (mainly from compressor cascades) correlate well with t^*. In addition, a calculational method was developed by Chen to track a series of shed tip vortices from an impulsively started plate, which represents the situation seen from a convective frame as the flow passes over a blade. The calculated results were shown to also correlate well with t^* and with the data.

We use the correspondences $c_x/w_2 = \cos \beta_2$, $x/x_{bl} = \cos \beta_m$ where β_2 and β_m represent the inlet and average relative flow angles at the rotor, respectively, to derive

$$\frac{x_{bl}}{\delta_{\text{jet}}} = \frac{\sqrt{2}}{c_D}\frac{w_2}{w_G}\frac{\cos \beta_2}{\cos \beta_m} t^* \tag{16}$$

where $c_D = \delta_{\text{jet}}/t$ is the gap discharge coefficient. Note also that $w_2/w_G = 1/\sqrt{c_l}$.

For an approximate comparison, Rains' (1954) values $c_D = 0.785$, $c_l = 1.35$, and $\cos \beta_m/\cos \beta_2 = 1.1$ are used to relate t^* to x_{bl}, and then calculate the vortex trajectory using Eqs. (5), (6), (11), and (12). The results are compared in Fig. 11 to those reported in Chen. The agreement with the data is satisfactory. Additional verification against the theory of Chen is provided by comparing the predictions of both theories regarding the "center of vorticity" location in a cross-plane similar to that shown in Fig. 8. In order to be consistent with Chen's calculations, we have included here both the rolled-up vorticity $\Gamma = 6.83 w_\perp R_D$ and a vorticity $2w_\perp$ per unit length (perpendicular

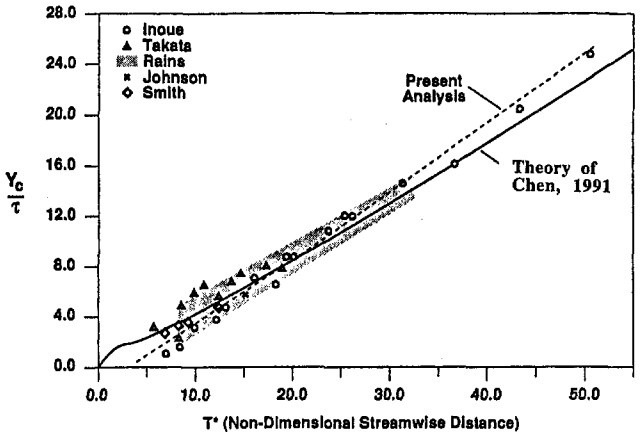

Fig. 11 Trajectory of vortex centroid compared to data and theory of Chen (1991)

to $\vec{\xi}$) of the not-yet-rolled shear layer. In calculating the distance z_c between the center of vorticity and the wall, we took this latter contribution to be at a distance δ_{jet}, and that of the rolled-up vortex to be at $\delta_{\text{jet}} + 0.46R_D$. The results are shown in Fig. 12, which again shows good agreement between our method and that of Chen.

5 Blade Scale Analysis

This section focuses on the rest of the flow, which goes through the blades as designed. The azimuthal momentum equation for the flow is

$$\vec{c}_\perp \cdot \nabla c_y = 0 \tag{17}$$

where $\vec{c}_\perp$ is the meridional velocity defined as $\vec{c}_\perp = \vec{i}c_x + \vec{k}c_z$. The vorticity equation also reduces to

$$\vec{c}_\perp \cdot \nabla \omega_y = 0 \quad \left(\omega_y = \frac{\partial c_x}{\partial z} - \frac{\partial c_z}{\partial x}\right) \tag{18}$$

Also, the Bernoulli equation reduces to

$$\vec{c}_\perp \cdot \nabla B_\perp = 0$$

$$B_\perp = \frac{p}{\rho} + \frac{1}{2}\vec{c}_\perp^{\,2} = \frac{p}{\rho} + \left(\frac{1}{2}c_x^2 + \frac{1}{2}c_z^2\right) \tag{19}$$

Continuity is ensured by introducing the stream function $\psi(x, z)$ for the meridional flow where $c_x = \partial\psi/\partial z$, $c_z = -(\partial\psi/\partial x)$, so that

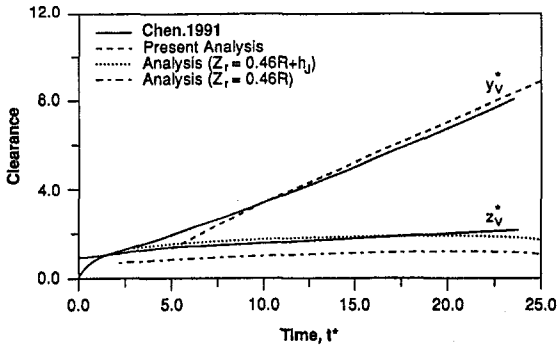

Fig. 12 Coordinates of vorticity centroid for tip clearance vortex

$$\omega_y(\psi) = \nabla_\perp^2 \psi \quad \left(\nabla_\perp^2 = \frac{\partial^2}{\partial x^2} + \frac{\partial^2}{\partial z^2}\right) \tag{20}$$

Thus, the meridional flow (c_x, c_z) is decoupled from c_y, and, therefore, can be solved for first.

Upstream of the stage ($x < 0$), the flow is assumed to be irrotational ($\omega_y = 0$). Thus, ψ obeys Laplace's equation.

Gauthier (1990) showed that it is a good approximation to assume that the axial velocity at the rotor is *piecewise constant*, with a discontinuity at the blade tip. This implies constant work extraction in each of the two regions (blade and gap), and so the ω_y vorticity source is concentrated on a surface at their common boundary.

Downstream ($x > 0$), the flow is radially nonuniform, and may show a contact discontinuity on the tip streamline, thus dividing the flow into two streams, the underturned flow due to the rotor gap (marked by a superscript +) and the main passage flow (marked by a superscript −). The presence of the rotor tip clearance induces a radially nonuniform work extraction, which, in turn, gives rise to a radially nonuniform Bernoulli constant downstream of the rotor. Because of the relationship

$$\omega_y = \frac{dB_\perp}{d\psi} \tag{21}$$

this creates ω_y vorticity, which is then convected along each streamline. Then by Eq. (20), ψ obeys Poisson's equation for $x > 0$.

From the definition of $B_\perp$, with the continuity constraint and the assumption of spanwise uniform blading,

$$B_{\perp 1} - B_{\perp 3} = \frac{p_1 - p_3}{\rho} \tag{22}$$

Since $dB_{\perp 1}/d\psi = 0$ by the assumption of irrotationality, Eq. (21) can be rewritten as

$$\omega_{y3} = -\frac{d(B_{\perp 1} - B_{\perp 3})}{d\psi} = -\frac{d}{d\psi}\left(\frac{p_1 - p_3}{\rho}\right) \tag{23}$$

Thus, the radial distribution of static pressure drop can be used to determine the downstream vorticity.

For the bladed stream, $(p_1 - p_3)/\rho$ is equivalent to the stagnation enthalpy drop, given by Euler's turbine equation, minus the kinetic energy gain. According to Euler's equation, the stagnation enthalpy drop, $-\Delta h_t$, is given as

$$-\Delta h_t = U[c_{y2r} - \bar{c_{y3}}] \tag{24}$$

where U is the turbine's rotational speed. The additional subscript r in c_{y2r} denotes the rotor end of the axial space between stator and rotor. The stator exit end would, in general, have a different tangential velocity, c_{y2s}.[1] The kinetic energy gain, ΔK.E., is ΔK.E. $= (1/2)(\bar{c_{y3}})^2$. At the rotor exit (3), the flow has split into two streams. For the bladed stream,

$$\bar{c_{y3}} = U - \bar{c_{x3}} \tan \beta_3 \tag{25}$$

Thus,

$$\left(\frac{p_1 - p_3}{\rho}\right)^- = Uc_{x0} \tan \alpha_2 - \frac{1}{2}[U^2 - (\bar{c_{x3}})^2 \tan^2 \beta_3] \tag{26}$$

For the underturned stream, c_{y2r} is the same as that for the bladed stream because the flow is assumed to be radially uniform upstream of the rotor. Thus,

[1] This interblade gap effect is modeled and explained in Section 3.4 of the companion paper.

$$\left(\frac{p_1 - p_3}{\rho}\right)^+ = U[c_{x0}\tan\alpha_2 - (U - c_{y3}^+)]$$

$$+ \frac{1}{2}(c_{y3}^+)^2 + \frac{1}{2}\left(c_{x3}^+\frac{\sin\theta}{\cos\beta_m}\right)^2 \quad (27)$$

The last term in Eq. (27) is included to account for the kinetic energy dissipated when the flow, which leaked through the rotor gap collides with an equal amount of the passage flow before rolling up into vortices.

$d/d\psi$ in Eq. (23) can be expressed as

$$\frac{d}{d\psi} = \left(\frac{1}{c_x}\frac{\partial c_x}{\partial z}\right)_{x=0+}\frac{\partial}{\partial c_x} \quad (28)$$

Then from Eqs. (23), (26), (27), (28), the equation for ψ becomes

Upstream ($x < 0$):

$$\nabla_\perp^2\psi = 0 \quad (29)$$

Downstream ($x > 0$):

$$\nabla_\perp^2\psi = Q\delta(\psi - \psi_{tip}) \quad (30)$$

where $Q = \int_-^+ \omega_y d\psi = B_{\perp 3}^+ - B_{\perp 3}^-$. δ is Dirac's delta function, and Q is the strength of the y component of the shear layer between the underturned and bladed streams. From Eqs. (22), (26), and (27) and the fact that $B_{\perp 1}$ is continuous,

$$Q = U(c_{y2r} - c_{y3}^-) - U(c_{y2r} - c_{y3}^+) + \frac{1}{2}\left[(c_{y3}^-)^2 - (c_{y3}^+)^2 - \left(c_{x3}^+\frac{\sin\theta}{\cos\beta_m}\right)^2\right] \quad (31)$$

can be obtained. The boundary conditions are

$$\psi(x, 0) = 0$$
$$\psi(x, H) = c_{x0}H$$
$$\psi(x = 0-, z) = c_{x0}z$$
$$\frac{\partial\psi}{\partial x}(x = 0+, z) = 0$$
$$\psi_1(z) = \psi_3(z)$$
$$\frac{\partial\psi_1(z)}{\partial z} = \frac{\partial\psi_3(z)}{\partial z} \quad (32)$$

The axial velocities for each stream are related to the shear parameter, Q, using overall continuity, as

$$c_{x3}^+ = c_{x2r}\left(1 + \frac{q}{2}(1 - \lambda)\right) \quad (33)$$

$$c_{x3}^- = c_{x2r}\left(1 - \lambda\frac{q}{2}\right) \quad (34)$$

where $q = Q/c_{x2r}^2$ and λ is the amount of underturned flow normalized by the total through flow.

The tangential velocity for the underturned layer is given by

$$c_{y3}^+ = U - c_{x3}^+\frac{\cos\theta\sin(\beta_m - \theta)}{\cos\beta_m} \quad (35)$$

and that for the bladed stream is given by

$$c_{y3}^- = U - c_{x3}^-\tan\beta_3 \quad (36)$$

One feature of the actuator disk approximation is that only half of the total change visible far downstream of the disk occurs at the disk with the other half occurring in the flow downstream from the disk (Horlock, 1978). Therefore, far downstream on the blade scale (at 4 or $x = 0+$), the axial velocities are as follows:

$$c_{x4}^+ = c_{x2r}(1 + q(1 - \lambda)) \quad (37)$$

$$c_{x4}^- = c_{x2r}(1 - \lambda q) \quad (38)$$

Since the shear between the two layers is simply convected downstream, the tangential velocities far downstream remain the same as those at the disk given by Eqs. (35) and (36).

The underturned flow consists of the flow that leaked through the rotor gap and an equal amount of the bladed flow entrained by the tip vortex (Fig. 8). Therefore, the amount of flow leaked through the gap is $\lambda/2$, which is shown (Gauthier, 1990) to be a function of the tip gap height, t/H, and q,

$$\frac{t}{H} = \frac{\lambda}{2}\left[1 - \left(1 - \frac{\lambda}{2}\right)\frac{q}{2}\right] \quad (39)$$

In turn, q is a function of λ and the geometry of the turbine blading. Substituting Eqs. (33)–(36) into Eq. (31) results in a quadratic equation for q:

$$[G(1 - \lambda)^2 - (\lambda\tan\beta_3)^2]\left(\frac{q}{2}\right)^2 + 2[2.0 + G(1 - \lambda) + \lambda\tan^2\beta_3]\left(\frac{q}{2}\right) + [G - \tan^2\beta_3] = 0 \quad (40)$$

where

$$G = \left(\frac{\cos\theta\sin(\beta_m - \theta)}{\cos\beta_m}\right)^2 + \left(\frac{\sin\theta}{\cos\beta_m}\right)^2 \quad (40a)$$

Thus, for a given t/H, the values of λ and q that satisfy the system of two Eqs. (39) and (40) can be found. Once λ and q are determined, all of the velocities can be determined from Eqs. (33)–(36).

Furthermore, other far downstream (4) conditions such as the thickness of the underturned layer (Δ) and the pressure are needed as connecting conditions at the radius scale. From continuity relations between Stations 3 and 4, the following expression for Δ/H is obtained:

$$\frac{\Delta}{H} = \lambda\left(1 - \left(1 - \frac{\lambda}{2}\right)\frac{q}{2}\right)\frac{1 + \frac{q}{2}(1 - \lambda)}{1 + q(1 - \lambda)} \quad (41)$$

Also, keeping in mind the assumption of lack of radial redistribution of flow in the stator and the assumption of quasi-steady flow on the blade scale which permits the use of Bernoulli equation, the expression for pressure drop between stations 0 and 4 (or $x = 0-$ and $x = 0+$) can be obtained as follows:

$$\frac{p_0 - p_4}{\rho U^2} = \frac{c_{x2r}}{U}\tan\alpha_2 - \frac{1}{2} + \frac{1}{2}\left(\tan\beta_3\frac{c_{x3}^-}{U}\right)^2 - \frac{1}{2}\left(\frac{c_{x3}^-}{U}\right)^2 + \frac{1}{2}\left(\frac{c_{x4}^-}{U}\right)^2 \quad (42)$$

5.1 Work Defect and Efficiency Loss Determination. Application of the Euler equation to both fluids gives the work done per unit mass by each stream:

$$W^+ = U(c_{x2s} \tan \alpha_2 - c_{y3}^+) \tag{43}$$

$$W^- = U(c_{x2s} \tan \alpha_2 - c_{y3}^-) \tag{44}$$

Then, the total turbine work per unit mass is

$$W = \lambda W^+ + (1 - \lambda) W^- \tag{45}$$

In coefficient form, the power extracted by the turbine, and, hence, the tip loss coefficient can also be calculated easily,

$$\Psi \equiv \frac{1}{\dot{m}U^2}\left[\int_0^{\psi_{\text{tip}}} (h_{t1} - h_{t3}^-)\rho d\psi + \int_{\psi_{\text{tip}}}^1 (h_{t1} - h_{t3}^+)\rho d\psi\right] \tag{46}$$

The total pressure drop in the mixed-out region is given by

$$\frac{p_{t0} - p_{t4}}{\rho} = \frac{p_0 - p_4}{\rho} - \frac{1}{2} c_{y4}^2 \tag{47}$$

where p_4 is at far downstream of the disk (on the blade scale), and we have taken advantage of axial and radial velocities being zero at this location. The static pressure drop between Stations 0 and 4 is given by Eq. (42). Then, the efficiency is

$$\eta = \frac{\Psi}{\left(\frac{p_{t0} - p_{t4}}{\rho U^2}\right)} \tag{48}$$

where Ψ is as given by Eq. (46). The efficiency loss factor follows as

$$\beta = \frac{1 - \eta}{t/H} \tag{49}$$

The work defect factor (different from β) is defined as

$$w = \frac{\frac{\Psi_0 - \Psi}{\Psi_0}}{t/H} \tag{50}$$

where Ψ_0 is the work coefficient for for zero leakage ($\lambda = 0$).

5.2 Model Predictions. We can now compare the calculated losses to those reported in the experimental literature. We rely for this on the compilation by Waterman (1986), which gives data for ten cases (nine different turbines) over a wide range of parameters. Waterman reports for each case the tip values of the work coefficient, Ψ, degree of reaction, R, flow coefficient, ϕ and individual blade loading, Zweifel coefficient.

One potential difficulty in application is that only tip parameters are given, whereas from the nature of our theory we suspect that mean parameters might be more appropriate.

Scanning Table 1, we first notice a large disagreement for Case 1 (Kofskey turbine). This is an impulse rocket turbopump stage with an extremely large tip loading ($\psi = 7.0$). Case 4, with very high reaction, is also substantially underpredicted, which may point out an insufficient predicted underturning angle ϑ for these conditions. The rest of the cases are well predicted. Excluding Case 1, the mean squared error is $\epsilon^2 = 0.1162$ and the mean error is $\bar{\epsilon} = -0.1408$. If Case 4 is removed, the two quantities would be, respectively, 0.0363 and 0.0498. Perhaps more effort should be devoted to an understanding of the leakage and underturning for high reaction rotors.

6 Summary and Conclusions

A model has been developed to illuminate the effects of spanwise flow redistribution caused by the presence of a small rotor blade-tip gap. To this end, the blade-to-blade details are ignored by using an incomplete actuator disk formulation, which collapses both stator and rotor to a plane, across which connecting conditions are imposed.

The model assumes that near the gap region, the underturned layer originates partly from the gap flow and partly from the passage flow, both leaving the passage in the form of rolled-up tip vortex. The trajectory and other details of this vortex are calculated using a simple model involving the collision of the ideal pressure-driven leakage jet with the passage fluid. This model was calibrated against both data and theory of Chen (1991). The new theory allows prediction of the vortex strength and trajectory.

The model predictions were then compared to a set of data involving nine different turbines. With the exception of one anomalous case, the calculated efficiency loss factors are reasonably close to the data, showing less deviation than the loss correlations of Ainley, Soderberg, Roelke, Kofskey, and Lakshminarayana.

Table 1 Efficiency loss and work defect factors (calculated from the blade scale analysis) compared to data. The last line is computed with modified work coefficient chosen for near-exit flow.

Case	Author	ZW	ϕ	Ψ_0	R	t/Hb	βdata	βcalc	wcalc	Kcalc
1	Kofskey	55	0.79	7.00	0.02	0.05	1.02	2.90	4.096	1.025
2A	Marshall-Rogo	1.02	0.50	1.48	0.32	0.035	1.51	1.44	2.563	0.346
2B	Marshall-Rogo	1.09	0.44	1.25	0.35	0.035	1.23	1.42	2.757	0.290
3	Szanca-Behning-Schum	1.59	0.57	1.46	0.47	0.033	1.90	1.68	3.066	0.369
4	Holeski-Futral	0.35	0.26	0.69	0.69	0.031	2.53	1.66	4.880	0.365
5	Ewen-Huber-Mitchell	0.70	0.25	1.05	0.45	0.02	1.50	1.46	3.914	0.411
6	Lart	0.92	0.51	1.41	0.51	0.02	1.80	1.92	3.500	0.375
7	Yamamoto	0.79	0.42	1.52	0.47	0.03	1.63	1.80	3.558	0.452
8	Patel	0.70	0.28	1.15	0.61	0.01	1.81	1.42	4.813	0.683
9	Haas-Kofskey	0.80	0.35	1.37	0.47	0.03	1.80	1.64	4.714	0.468
1M	Kofskey (if Ψ_0=2)	0.55	0.79	2.0	0.02	0.05	1.02	0.93	1.614	0.473

These results suggest that upstream flow redistributions, which have been largely ignored so far, may be of importance in understanding the basic physics of tip leakage effects.

Acknowledgments

This work was performed under NASA Contract NAS 8-35018. Glenn E. Wilmer, Jr., is the Technical Monitor.

References

Alford, J. S., 1965, "Protecting Turbomachinery From Self-Excited Rotor Whirl," *Journal of Engineering for Power,* Vol. 87, pp. 333–344.

Batchelor, G. K., 1967, *An Introduction to Fluid Dynamics,* Cambridge University Press.

Chen, G. T., 1991, "Vortical Structures in Turbomachinery Tip Clearance Flows," Ph.D. Thesis, Department of Aeronautics and Astronautics, MIT.

Ehrich, F. F., and Childs, D. W., 1984, "Self-Excited Vibration in High Performance Turbomachinery," *Mechanical Engineering,* May, pp. 66–79.

Gauthier, R. P., 1990, "An Investigation of Flow Field Perturbation Caused by Constant Blade Tip Clearance in a Turbine," S. M. Thesis, Department of Aeronautics and Astronautics, MIT.

Horlock, J. H., 1978, *Actuator Disc Theory,* McGraw-Hill.

Kofskey, M. G., and Nusbaum, W. J., 1968, "Performance Evaluation of a Two Stage Axial Flow Turbine for Two Values of Tip Clearance," NASA TN D4388.

Lakshminarayana, B., 1970, "Methods of Predicting the Tip Clearance Effects in Axial Flow Turbomachinery," ASME *Journal of Basic Engineering,* Vol. 104, pp. 467–481.

Martinez-Sanchez, M., and Gauthier, R. P., 1990, "Blade Scale Effects of Tip Leakage," Gas Turbine Laboratory Report #202, MIT.

Martinez-Sanchez, M., Jaroux, B., Song, S. J., and Yoo, S., 1995, "Measurement of Turbine Blade-Tip Rotordynamic Excitation Forces," ASME JOURNAL OF TURBOMACHINERY, Vol. 117, pp. 384–393.

Rains, D. A., 1954, "Tip Clearance Flow in Axial Flow Compressors and Pumps," Hydrodynamics and Mechanical Engineering Laboratories Report No. 5, California Institute of Technology.

Thomas, H. J., 1958, "Instabile Eigenschwingungen von Turbinenlaeufern Angefacht durch die Spaltstroemung in Stopfubuchsen und Bechauchflug (Unstable Natural Vibrations of Turbine Rotors Induced by the Clearance Flows in Glands and Blading)," *Bull. de L.A.I.M.,* 71 No. 11/12, pp. 1039–1063.

Urlichs, K., 1983, "Durch Spaltstroemungen hervorgerufene Querkraefte an den Laufern Thermischer Turbomaschinen (Clearance Flow-Generated Transverse Forces at the Rotors of Thermal Turbomachines)," NASA TM-77292.

Vance, J. M., and Laudadio, F. J., 1984, "Experimental Measurement of Alford's Force in Axial Flow Turbomachinery," ASME *Journal of Engineering for Gas Turbines and Power,* Vol. 106, pp. 585–590.

Waterman, W. F., 1986, "Turbine Loss Correlations and Analysis," in: *Proc. Tip Clearance Effects in Axial Turbomachines,* Apr. 14–18. The Pennsylvania State University, University Park, PA.

Rotordynamic Forces Due to Turbine Tip Leakage: Part II—Radius Scale Effects and Experimental Verification

S. J. Song
Department of Aerospace Engineering,
Inha University,
Namgu, Inchon, Korea

M. Martinez-Sanchez
Department of Aeronautics/
Astronautics,
MIT,
Cambridge, MA 02139

This paper presents a radius scale actuator disk model, which describes the flow response to a whirling/spinning rotor in an unshrouded turbine. At each azimuth, the upstream–downstream flow variables are matched by the results from a steady blade scale analysis presented in a companion paper, with allowance for mass storage in the stator–rotor region. The new model can accurately predict the magnitude of both direct and cross excitation forces as well as their breakdown into work extraction and pressure effects. The trends versus the mean flow coefficient and interblade distance are predicted. While underpredicted, a trend versus mean rotor tip clearance height is also indicated. Thus, the new model captures the dominant physical effects caused by a whirling/spinning rotor in an unshrouded turbine.

1 Introduction

The problem of self-excited vibration in rotor systems, or rotordynamic instability, has plagued development of various turbomachines. The rotordynamic instability caused by asymmetric tip clearance in turbines has been the focus of this investigation. The experimental results were presented by Martinez-Sanchez et al. (1995) and an analytical model for the blade scale effects of a finite rotor tip clearance is presented in a companion paper.

In a turbine with an eccentric rotor, the efficiency is higher in the region with the smaller tip clearance, resulting in a higher local torque. Upon azimuthal integration, the torque asymmetry leads to a force perpendicular to the rotor eccentricity, which feeds energy into the forward whirling mode (Fig. 1 in the companion paper). The implicit assumption was that the flow remains perfectly uniform upstream of the eccentric turbine, as well as downstream of it. In reality, the presence of an eccentric rotor would induce an azimuthal flow redistribution, causing a force variation even without the efficiency variation.

Qiu (1985) developed an actuator disk analysis to examine the azimuthal distribution effect on the lateral forces in a turbine with a whirling rotor. This was an adaptation of an analysis for a compressor by Horlock and Greitzer (1983). A radially averaged (2-D), inviscid, incompressible flow was assumed. The connecting conditions at the disk were provided by the equations of continuity, momentum, and an empirical correlation for turbine efficiency. The flow redistribution was shown to increase the magnitude of the lateral forces above what would be predicted on the basis of efficiency variation alone. However, the assumption of perfect flow guidance by the blades ignored the effects of the tip gap flow, and, therefore, the predictions were unsatisfactory.

This paper presents a new radius-scale analysis, which uses the results from the blade scale analysis as its coupling conditions. Thus, this model does not resort to empiricism in accounting for the localized effects (e.g., losses) associated with the tip clearance flow. A comparison of the model predictions with the experimental data is also given.

Contributed by the International Gas Turbine Institute and presented at the 41st International Gas Turbine and Aeroengine Congress and Exhibition, Birmingham, United Kingdom, June 10–13, 1996. Manuscript received at ASME Headquarters February 1996. Paper No. 96-GT-365. Associate Technical Editor: J. N. Shinn.

2 Analytical Model

As in the blade scale analysis, the stage is collapsed into an actuator disk (Fig. 1). x is the throughflow direction, y is the azimuthal direction, and z is the radial direction. The axial locations of stations referred to in the analysis are as follows. The "actuator disk" consists of a turbine stage collapsed into a plane at $x = 0$. The axial stations far upstream and far downstream of the actuator disk, on the radius scale, are referred to as $-\infty$ and ∞, respectively. The stations near upstream and near downstream of the actuator disk, on the radius scale, are referred to as $0-$ and $0+$, respectively (Fig. 4 in the companion paper). Although the actuator disk is assumed to have zero axial thickness on the radius scale, it actually consists of a full-span stator row and a partial-span rotor row as shown in the figure.

To model a turbine whirling at some amplitude, e, much smaller than the blade span, H_b, a linear perturbation approximation is used. Thus, the flow variables are assumed to contain a small perturbation about the mean, which in this case is the centered turbine case. The solution procedure is based on previous efforts by Leung (1991) and Yoo (1993).

The assumptions of this model are equivalent to those found in the blade scale model, with the obvious exception of the relaxation of the axisymmetric flow assumption to facilitate the analysis of a whirling turbine. Other newly incorporated effects include the following: First, a nonaxisymmetric, mass storage effect of the axial gap between the stator and the rotor was incorporated. Second, the nonaxisymmetric pressure pattern in the rotor region was identified as another source of lateral excitation forces and, therefore, was added to the analysis.

Figure 2 illustrates a turbine rotor, with a mean radius R, simultaneously spinning at angular frequency ω and executing a circular whirl of amplitude e at angular frequency Ω. XY is the inertial frame of reference, and $X'Y'$ is the whirling frame. Whirling in the direction of spin is considered positive. The azimuthal location of the maximum tip gap is $\Omega t + \pi$ radians from the inertial X axis. y' is the distance from the maximum tip gap in the azimuthal direction defined as $y' = y - R\Omega t$. The flow is steady in the whirling frame $X'Y'$. However, in the inertial frame,

$$\left(\frac{\partial}{\partial t}\right) = -\Omega R \frac{\partial}{\partial y} \tag{1}$$

where the rotor's whirling motion introduces unsteadiness. For

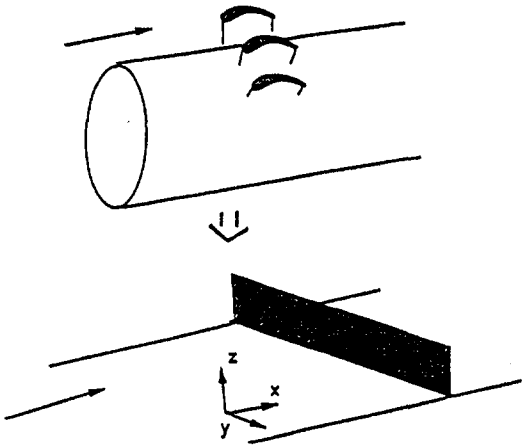

Fig. 1 A radius scale view of the actuator disk (Yoo, 1993)

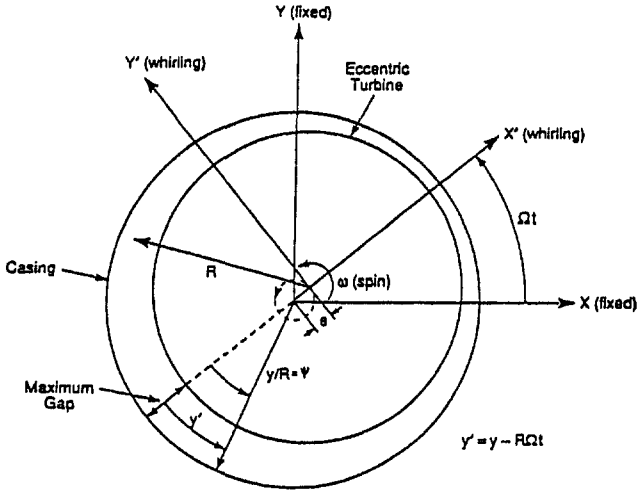

Fig. 2 Coordinate system used in the unsteady actuator disk analysis (Yoo, 1993)

small tip gaps ($t/R \ll 1$) with an offset rotor, due to linear perturbation approximation, the azimuthal distribution of the rotor tip gap is given as

$$t = \bar{t} + \mathrm{Re}[\hat{e}e^{i(y/R-\Omega t)}] \tag{2}$$

where $\bar{t}$ is the mean rotor tip gap, and the fixed frame distance y is from the X axis. Note that $\hat{e}$ is real due to the choice of y origin.

2.1 Upstream Flow. At $x = -\infty$, the flow is uniform, steady, and axial. Then, for $x < 0-$, the velocity vector can be described as the gradient of a potential ϕ, which obeys Laplace's equation:

$$(c_x, c_y) = \nabla\phi; \quad \nabla^2\phi = 0 \tag{3}$$

with periodic boundary conditions in y, $c_x(-\infty) = \bar{c}_{x0}$ being a given constant, and downstream conditions which match the turbine flow. At $x = 0-$, where the xy redistribution is likely to have occurred, the assumed axial velocity is

$$c_x(0-, y, t) = \mathrm{Re}[\bar{c}_{x0} + \hat{K}_0 e^{i((y/R)-\Omega t)}] \tag{4}$$

where $\hat{K}_0$ is the complex amplitude of axial velocity perturbation as the flow approaches the disk. Therefore, at $x < 0-$,

$$c_x(x, y, t) = \bar{c}_{x0} + \mathrm{Re}[\hat{K}_0 e^{x/R+i(y/R-\Omega t)}] \tag{5}$$

$$c_y(x, y, t) = \mathrm{Re}[i\hat{K}_0 e^{x/R+i(y/R-\Omega t)}] \tag{6}$$

$$p(x, y, t) = p(-\infty) - \mathrm{Re}[\rho(\bar{c}_{x0} - i\Omega R)\hat{K}_0 e^{x/R+i(y/R-\Omega t)}] \tag{7}$$

From now on, the Re [ ] notation will be dropped for convenience.

Nomenclature

a = constant between 0 and 1 (Eq. (18))
A_y = interblade area for azimuthal flow
c = absolute flow velocity; axial blade chord
d = axial distance between stator trailing edge and rotor leading edge
e = magnitude of rotor offset
E_i = eigenvector for downstream perturbations
F_x = lateral force in the direction of the offset
F_y = lateral force perpendicular to the direction of the offset
$\hat{K}_j$ = complex amplitude of flow perturbations
L = rotor thickness
Q = turbine torque
q = dynamic head; mass flow per unit circumference of turbine
R = mean turbine radius; gas constant; correlation coefficient; turbine reaction
s = blade pitch
t = radial tip clearance; time
w = relative velocity
X = direction of minimum gap in fixed coordinate system
Y = direction perpendicular to X
x, y, z = axial flow direction
α = pitch angle; absolute flow angle; eigenvalue for downstream perturbations
$\alpha_X = 2F_X/[(Q/R)(e/H_b)]$ = direct excitation force coefficient
$\alpha_Y = 2F_Y/[(Q/R)(e/H_b)]$ = cross excitation force coefficient
γ = ratio of specific heats ($\gamma = 1.12$ for R-12); blade stagger angle
θ = azimuthal angle measured in the direction of rotation from the minimum gap location
ϕ = upstream velocity potential
$\phi = c_x/U$ = turbine flow coefficient
$\psi = (h_{01} - h_{03})/U^2$ = turbine stage loading factor, or work coefficient
ω = angular velocity of rotor shaft rotation
Ω = angular velocity of rotor shaft whirl

Subscripts

0− = near upstream of actuator disk in radius scale analysis
0+ = near downstream of actuator disk in radius scale analysis
1−9 = casing instrument stations at $x/c = -3.56, -2.38, -2.08, -0.21, 0.06, 0.029, 0.53, 1.42$, and 2.84, respectively
D = design value
p = indicates force due to action of nonuniform pressures
wd = indicates force due to tangential variation of work extraction

Superscripts

′ = nonaxisymmetric perturbation
− = azimuthal mean, or axisymmetric value
^ = complex amplitude

Note: Symbols common with Part I are omitted from this list.

2.2 Downstream Flow. For $x > 0+$, after the completion of radial redistribution, the flow consists of two distinct regions. The first region contains the main passage flow, which has traversed the bladed part of the rotor (denoted by a ($^-$) superscript) and the second region contains the underturned flow (denoted by a ($^+$) superscript) due to the rotor tip gap. This splitting of streams is described in greater detail in the companion paper.

The equations of conservation of mass, x-momentum, and y-momentum can be written for each region, assuming radially averaged properties in each. The mass conservation equations can be written as

$$\frac{\partial \Delta}{\partial t} + \frac{\partial (c_x^+ \Delta)}{\partial x} + \frac{\partial (c_y^+ \Delta)}{\partial y} = 0 \tag{8}$$

$$\frac{\partial (H - \Delta)}{\partial t} + \frac{\partial (c_x^- (H - \Delta))}{\partial x} + \frac{\partial (c_y^- (H - \Delta))}{\partial y} = 0 \tag{9}$$

where H is annulus height and Δ is the thickness of the underturned layer. The momentum equations can be written as

$$\frac{\partial \bar{c}^{\pm}}{\partial t} + (\bar{c}^{\pm} \cdot \nabla)\bar{c}^{\pm} + \frac{1}{\rho} \nabla p = 0 \tag{10}$$

where all vectors are two-dimensional (x, y).

Assuming $e \ll H$, Δ, c_x^+, c_y^+, c_x^-, c_y^-, and p can each be expressed as a mean value plus a small perturbation, e.g.,

$$\Delta = \bar{\Delta} + \Delta' \tag{11}$$

The perturbation part is assumed to be the first harmonic of the whirling angle $(y/R - \Omega t)$ with an exponentially decaying amplitude, associated with potential effects. For example,

$$\Delta' = \mathrm{Re}[\hat{\Delta} e^{\alpha x + i(y/R - \Omega t)}] \tag{12}$$

After substitution of equations such as Eq. (12) into the Eqs. (8) $\sim$ (10) and linearization of the resulting equations, a homogeneous set of equations for the eigenvalues α can be obtained:

$$\begin{bmatrix} \alpha\Delta & i\bar{\Delta}/R & 0 & 0 & A_{15} & 0 \\ 0 & 0 & \alpha(H-\bar{\Delta}) & i(H-\bar{\Delta})/R & A_{25} & 0 \\ A_{31} & 0 & 0 & 0 & 0 & \alpha \\ 0 & A_{42} & 0 & 0 & 0 & i/R \\ 0 & 0 & A_{53} & 0 & 0 & \alpha \\ 0 & 0 & 0 & A_{64} & 0 & i/R \end{bmatrix} \begin{bmatrix} \hat{c}_x^+ \\ \hat{c}_y^+ \\ \hat{c}_x^- \\ \hat{c}_y^- \\ \hat{\Delta} \\ \hat{p}/\rho \end{bmatrix} = 0 \tag{13}$$

where

$$A_{15} = A_{31} = A_{42} = \alpha \overline{c_x^+} + i\left(\overline{\frac{c_y^+}{R}} - \Omega\right)$$

$$A_{53} = A_{64} = \alpha \overline{c_x^-} + i\left(\overline{\frac{c_y^-}{R}} - \Omega\right)$$

$$A_{25} = -\alpha \overline{c_x^-} - i\left(\overline{\frac{c_y^-}{R}} - \Omega\right)$$

Upon determination of eigenvalues, α_i, and eigenvectors, E_i, the nontrivial homogeneous solution to the system of equations above can be written as

$$\left(\hat{c}_x^+, \hat{c}_y^+, \hat{c}_x^-, \hat{c}_y^-, \hat{\Delta}, \frac{\hat{p}}{\rho}\right) = \sum_{i=1}^{5} \hat{K}_i E_i \tag{14}$$

where the complex constants $\hat{K}_i$'s have to be determined.

2.3 The Upstream–Downstream Coupling. The blade scale analysis relates the flow variables at $x = 0-$ to those at $x = 0+$. $x = 0-$ and $x = 0+$ are equivalent to far upstream and far downstream stations, respectively, on the blade scale. Thus, the far upstream and far downstream values of flow variables determined from the blade scale analysis are equivalent to the same flow variables at $x = 0-$ and $x = 0+$, respectively, on the radius scale.

The blade scale analysis shows that the nondimensional flow variables depend on three parameters, t/H, ϕ, and $c_y(0-, y)$. For example, noting that $x = 0+$ is Station 4,

$$\frac{c_{x4}^+}{U} = \frac{c_{x4}^+}{U}\left(\frac{t}{H}, \phi, \frac{c_y(0-, y)}{U}\right) \tag{15}$$

where a local flow coefficient is introduced as

$$\phi = \frac{c_x(0-, y)}{U} \tag{16}$$

The value of t/H is the "local" value corresponding to the azimuthal location, y. ϕ and $c_y(0-, y)/U$ are functions of y to be determined from matching. Then the perturbation quantities on the radius scale at $x = 0+$ are related to those on the blade scale at Station 4 as shown below:

$$\begin{bmatrix} \hat{c}_x^+ \\ \hat{c}_y^+ \\ \hat{c}_x^- \\ \hat{c}_y^- \\ \hat{\Delta} \\ \hat{p}/\rho \end{bmatrix}_{x=0+} = \left[\frac{\hat{c}_x(0-)}{U}\frac{\partial}{\partial \phi} + \frac{\hat{c}_y(0-)}{U}\frac{\partial}{\partial \frac{c_{y0}}{U}} + \left(\frac{e}{H}\right)\frac{\partial}{\partial \frac{t}{H}}\right] \times \begin{bmatrix} c_{x4}^+ \\ c_{y4}^+ \\ c_{x4}^- \\ c_{y4}^- \\ \Delta \\ (p_0 - (p_0 - p_4)/\rho) \end{bmatrix} \tag{17}$$

where the partial derivatives are to be calculated from the blade-scale analysis. Moreover, $\hat{c}_x(0-)/U = \hat{K}_0/U$ and $\hat{c}_y(0-)/U = i\hat{K}_0/U$, and the partial derivatives with respect to c_{y0} are all zero, even though $\hat{c}_{y0}$ is not zero.

Now, Eqs. (14) and (17) can be set equal to each other. Then, the terms due to (e/H) act as forcing terms which determine the particular complex amplitudes $\hat{K}_i$'s.[1] Subsequently, the six perturbation quantities at Station 4, or $x = 0+$, can be determined.

2.4 Formulation for Interblade Gap Effect. This section presents an extension of the analysis to incorporate the effects of interblade distance, d, on the lateral forces.

In the companion paper, where blade-scale effects were analyzed, the perturbations in flow variables such as local mass flow rate and velocity at the rotor inlet $(2r)$ were assumed to be equivalent to those at the stator exit $(2s)$. However, in an eccentric turbine, the azimuthal flow area, A_y (Fig. 3), varies azimuthally. The strongly swirling flow in the axial gap can accommodate this change in the flow area by either changes in the tangential velocity, c_y, or local imbalances between the local flow rates entering from the stator $(2s)$ and exiting to the rotor $(2r)$. If the latter dominates, the azimuthal pressure nonuniformity required for such an imbalance generates a cross force. This effect is similar to that suggested by Millsaps (1992) for whirling labyrinth seals. Consequently, the perturbations at the rotor inlet are different from those at the stator exit in magnitude and phase.

[1] p_0 in the last equation in Eq. (17) is time dependent and is given by Eq. (7).

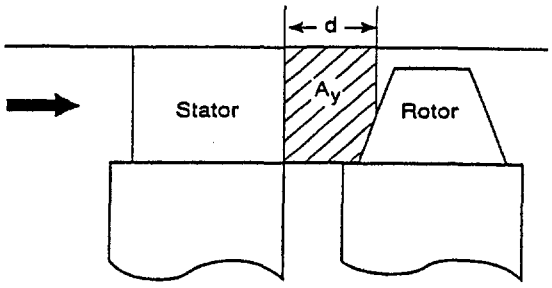

Fig. 3 Tangential cross-sectional flow area, *Ay*, between the stator and the rotor

As the tip gap increases from $\bar{t}$ to $\bar{t} + t'$, A_y is also increased. Thus,

$$A_y' = adt' \tag{18}$$

where d is the interblade distance between the stator and the rotor, and a is a constant whose value ranges from 0 to 1 because only parts of the rotor and stator hubs are involved. The exact value of a would depend the stator hub geometry downstream of the stator trailing edge and the rotor hub geometry upstream of the rotor leading edge. If most of the axial gap d is taken up by the rotor hub, the value of a would be closer to 1, maximizing this effect. On the other hand, if d is mostly covered by the (fixed) stator hub, then the value of a would be closer to 0.

For a differential volume with the cross-sectional area A_y and unit depth in the y direction (Fig. 4), the continuity and the momentum equations in the y direction can be written as:

$$\frac{\partial}{\partial t}[\rho d(H + at')] + \frac{\partial}{\partial y}[\rho d(H + at')(\bar{c}_{y2r} + c'_{y2r})] = q_{2s} - q_{2r} \tag{19}$$

$$\frac{\partial}{\partial t}[\rho d(H + at')(\bar{c}_{y2r} + c'_{y2r})] + \frac{\partial}{\partial y}[\rho d(H + at')(\bar{c}_{y2r} + c'_{y2r})^2] + q_{2r}(\bar{c}_{y2r} + c'_{y2r}) - q_{2s}c_{y2s} + d(H + at')\frac{\partial p_{2r}}{\partial y} = 0 \tag{20}$$

where q_{2s} is the mass flux per unit depth into the control volume from the stator and q_{2r} is the mass flux out of the control volume to the rotor. Linearizing and expressing each variable as $(\ )' = (\hat{\ })e^{i(y/R - \Omega t)}$, Eqs. (19) and (20) become

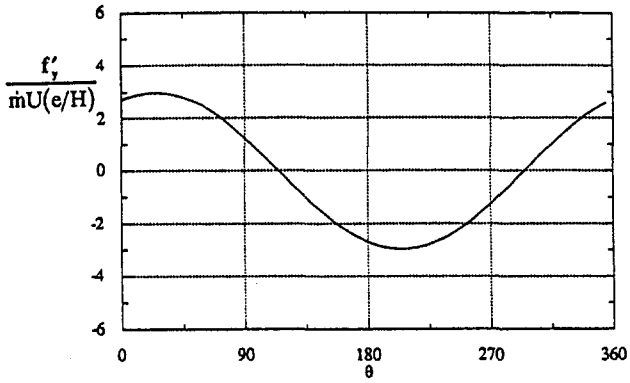

Fig. 4 Predicted nondimensional tangential force perturbation versus azimuthal angle (maximum gap at 180 deg)

$$\frac{i}{R}\rho da(\bar{c}_{y2r} - \Omega R)\hat{e} + \frac{i}{R}\rho dH\hat{c}_{y2r} = \hat{q}_{2s} - \hat{q}_{2r} \tag{21}$$

$$\frac{i}{R}\left(\bar{c}_{y2r} - \Omega R - i\frac{\bar{q}_2 R}{\rho dH}\right)\hat{c}_{y2r} - \frac{\bar{q}_2}{\rho dH}\hat{c}_{y2s} + \frac{i}{R}\frac{\hat{p}_2}{\rho} = 0 \tag{22}$$

Here $\hat{q}_{2s} = \rho H\hat{c}_{x1}$ is related to the axial velocity perturbation at $x = 0-$ on the radius scale. We have written $\hat{p}_2$ for $\hat{p}_{2r}$, since we assume $\hat{p}_{2r} = \hat{p}_{2s}$, both varying with y. Note also that, if the stator trailing edge angle is α_2, we have $\hat{c}_{y2s} = \hat{c}_{x1}\tan\alpha_2$. Thus, Eqs. (21) and (22) relate $\hat{c}_{y2r}$, $\hat{c}_{x1}$, $\hat{q}_{2r}$, and $\hat{p}_2$ to gap variations, $\hat{e}$. An additional equation can be obtained as follows. From Eqs. (5) and (7), the total pressure perturbations upstream of the stator are related to those of the axial flow by

$$\frac{\hat{p}_{t1}}{\rho} = i\Omega R\hat{c}_{x1} \tag{23}$$

and across the (quasi-steady, ideal) stator, $\hat{p}_{t2s} = \hat{p}_{t1}$, i.e.,

$$i\Omega R\hat{c}_{x1} = \frac{\hat{p}_2}{\rho} + \bar{c}_{x2s}\hat{c}_{x1} + \bar{c}_{y2s}\hat{c}_{y2s} = \frac{\hat{p}_2}{\rho} + \bar{c}_{x0}(1 + \tan^2\alpha_2)\hat{c}_{x1}$$

or

$$\frac{\hat{p}_2}{\rho} = -\bar{c}_{x0}\left(1 + \tan^2\alpha_2 - i\frac{\Omega R}{\bar{c}_{x0}}\right)\hat{c}_{x1} \tag{24}$$

Using Eqs. (21), (22), and (24), the flow quantities can be solved for in terms of $\hat{e}/H$ and one of the unknowns. Since $\hat{q}_{2r} = \rho H\hat{c}_{2r}$ connects directly with the x–z analysis of a centered rotor, $\hat{q}_{2r}$ is chosen as this remaining parameter. The results are:

$$\frac{\hat{c}_{x1}}{\bar{c}_{x0}} = \frac{(1 + f_2)\left(af_2\dfrac{\hat{e}}{H} + \dfrac{\hat{q}_{2r}}{\bar{q}}\right)}{1 - i\left(\dfrac{d}{R}\right)W + \left(\dfrac{d}{R}\right)^2 f_1} \tag{25}$$

$$\frac{\hat{p}_2}{\rho\bar{c}_{x0}^2} = -f_1\frac{\hat{c}_{x1}}{\bar{c}_{x0}} \tag{26}$$

$$\frac{\hat{c}_{y2r}}{\bar{c}_{x0}} = \frac{i\dfrac{d}{R}f_1 + \tan\alpha_2}{1 + f_2}\frac{\hat{c}_{x1}}{\bar{c}_{x0}} \tag{27}$$

where

$$f_1 = 1 + \tan^2\alpha_2 - iW$$

$$f_2 = i\frac{d}{R}(\tan\alpha_2 - W)$$

$$W = \frac{\Omega R}{\bar{c}_{x0}}$$

Notice that in the limit $d/R \to 0$, $\hat{c}_{x1}/\bar{c}_{x0} \to \hat{q}_{2r}/\bar{q}$ and $\hat{c}_{y2r} \to \hat{c}_{x1}\tan\alpha_2 = \hat{c}_{y2s}$. For finite stator–rotor axial gap, d, this formulation introduces differences between stator exit and rotor inlet velocity components.

2.5 Calculation of Rotordynamic Coefficients. The excitation force coefficients can be obtained from the perturbation quantities. Defining the tangential force exerted on the turbine per azimuthal length, f_y, as the sum of forces by the underturned flow and the bladed flow,

$$f_y = \lambda q_{2r}(c_{y2r} - c_{y3}^{+}) + (1 - \lambda)q_{2r}(c_{y2r} - c_{y3}^{-}) \tag{28}$$

Then the azimuthal mean and the perturbation of f_y are, respectively,

$$\bar{f}_y = \bar{\lambda}\bar{q}_{2r}(\bar{c}_{y2r} - \bar{c}^{+}_{y3}) + (1 - \bar{\lambda})\bar{q}_{2r}(\bar{c}_{y2r} - \bar{c}^{-}_{y3}) \quad (29)$$

$$f'_y = \bar{\lambda}\bar{q}_{2r}(\bar{c}_{y2r} - \bar{c}^{+}_{y3})\left[\frac{\lambda'}{\bar{\lambda}} + \frac{q'_{2r}}{q_{2r}} + \frac{c'_{y2r} - c'^{+}_{y3}}{\bar{c}_{y2r} - \bar{c}^{+}_{y3}}\right]$$

$$+ (1 - \bar{\lambda})\bar{q}_{2r}(\bar{c}_{y2r} - \bar{c}^{-}_{y3})\left[\frac{-\lambda'}{1 - \bar{\lambda}} + \frac{q'_{2r}}{q_{2r}} + \frac{c'_{y2r} - c'^{-}_{y3}}{\bar{c}_{y2r} - \bar{c}^{-}_{y3}}\right] \quad (30)$$

The perturbation in f_y contains the combined effects of flow redistribution on the radius scale and nonuniform flow turning, both of which are caused by an eccentric rotor. Both Thomas (1958) and Alford (1965) assumed that the former did not occur and considered only the latter in their formulation. Thus, from the fluid mechanics perspective, the expression above provides a more complete solution to the problem of nonuniform tangential force in an eccentric turbine. As in the experimental data section, these lateral forces, caused by the tangential force variation, are denoted by $(\ )_{wd}$ subscript (for "work defect").

Another contribution to flow forces is the direct effect on the turbine hub of the nonaxisymmetric pressure, which causes the tangential flow redistribution. Note that the redistribution leading to these variations is on a scale much larger than blade length, and, hence, p' is nearly the same at the hub as at the casing. Here, the pressure acting on the rotor hub is approximated as the average of pressures at stations $2r$ and 3 on the blade scale (inlet and exit of the rotor), $\langle p \rangle$.

$$\langle p \rangle = \frac{p_2 + p_3}{2} = p_2 - \frac{(p_2 - p_3)}{2}$$

$$= p_2 - \frac{1}{2}\frac{\rho}{2}[(c_{x3})^2 \tan^2 \beta_3 - (c_{y2r} - U)^2] \quad (31)$$

The perturbation in $\langle p \rangle$ is

$$\langle p \rangle' = p'_2 - \frac{\rho}{2}[\tan^2 \beta_3 \bar{c}_{x3} c'_{x3} - (\bar{c}_{y2r} - U)c'_{y2r}] \quad (32)$$

where p'_2 is given by Eq. (24). Upon projection of the pressure forces on to the X', Y' axes (Fig. 2), the total excitation force coefficients, or the rotordynamic coefficients, are

$$(\alpha_{Y'} + \alpha_{X'})_{\text{total}} = \frac{-\hat{f}_y + iL\langle \hat{p} \rangle}{\hat{f}_y(e/H)} \quad (33)$$

Equation (33) summarizes the results of the theory, and its linear nature makes it straightforward in application. Also, for static offsets, $\alpha_{X'}$ and $\alpha_{Y'}$ are equivalent to α_X and α_Y, respectively. Parametric variations and specific comparisons to experimental data (including the net forces and flow perturbations) will be presented in the next section.

3 Model Predictions

This part presents predictions from the model. First, the predicted values for a baseline case are discussed. Second, the sensitivity of the model's predicted excitation force coefficients, α_X and α_Y, to various parameters is examined for the steady condition of a statically offset rotor. The parameters can be categorized into those of the turbine design, the turbine operating conditions, and the turbine geometry. Third, the influence of the unsteady whirling effects ($\Omega R/U \neq 0$) on the predicted coefficients is examined. Finally, predictions from the current model are compared with the experimental data from Martinez-Sanchez et al. (1995).

Table 1 The turbine parameter values selected for the baseline case calculation

Parameter	Value
ϕ_D	0.580
R_D	0.208
ψ_D	1.508
$\bar{\phi}$	0.580
$\bar{\psi}$	1.508
$\Omega R/U$	0.000
d/R	0.050
$\bar{t}/R$	0.020
s/c	0.547
γ	-26°

The turbine design parameters include the design flow coefficient, ϕ_D; the design reaction, R_D, and the design work coefficient, ψ_D. The turbine operating parameters include the mean flow coefficient, $\bar{\phi}$, and the mean work coefficient, $\bar{\psi}$. The turbine geometry parameters are the interblade distance, d/R, and the mean rotor tip gap, $\bar{t}/H$. Due to the linear nature of the model, the predicted excitation force coefficients are proportional to the whirling eccentricity of the rotor, $\hat{e}$, and, therefore, this dependence is not otherwise examined.

The baseline set of parameter values are close to one of the configurations tested in the MIT Alford Force Test Facility (AFTF) (Martinez-Sanchez et al., 1995). When the turbine design parameters are varied, the mean turbine operating parameters are assumed to be at the design value. Thus, off-design effects are examined only for the selected baseline turbine. For the sensitivity analysis, one parameter is varied while the remaining parameters are held constant at their baseline values.

The excitation force coefficients, α_X and α_Y, are computed from Eq. (33). They are split here between the work defect contributions (α_{wd}) and nonuniform pressure contributions (α_p).

For the baseline case, the predicted excitation force coefficients are as shown in Table 2. The cross force is positive, and, therefore, destabilizing to forward whirl. The direct force is negative, and, therefore, stabilizing. Also, the magnitudes of the direct and cross forces are comparable.

For both direct and cross forces, α_{wd} and α_p have the same sign and, thus, add to each other. Moreover, roughly 70 percent of the direct force and 40 percent of the cross force are due to the pressure nonaxisymmetry with the remainder coming from the tangential force variation. The tangential force perturbation is plotted versus azimuthal angle θ, measured from the minimum gap, in Fig. 4.

The forces due to the pressure nonuniformity in Table 2 result from a perturbation in the rotor inlet axial velocity, which, in turn, is a result of azimuthal flow redistribution caused by the rotor offset. This redistribution actually begins far upstream of the stator row, and, without it, the pressure forces would vanish. $\langle p \rangle'/\rho U^2(e/H)$ and $\phi'/(e/H)$ are plotted versus θ in Fig. 5.

Table 2 Predicted excitation force coefficients due to nonaxisymmetric tangential force and nonaxisymmetric pressure for the baseline case. The entries are $\alpha_{x_{wd}}$, α_{x_p}, $\alpha_{y_{wd}}$, α_{y_p}, etc.

Direction	α_{wd}	α_p	α_{total}
X	-0.9	-1.8	-2.7
Y	+1.8	+1.4	+3.2

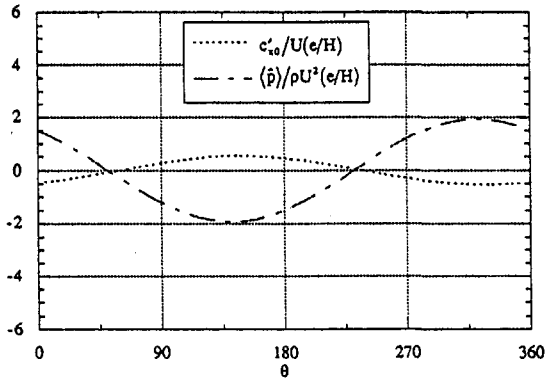

Fig. 5 Predicted perturbations in the upstream axial velocity (station 1 on the blade scale) and the rotor region pressure (average of inlet and exit) versus azimuthal angle (maximum gap at 180 deg)

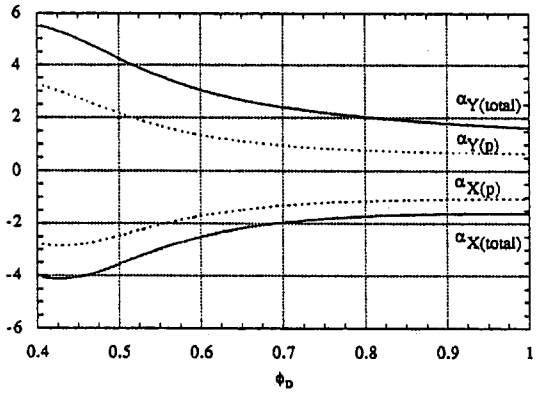

Fig. 6 Predicted total and pressure excitation force coefficients versus design flow coefficient

The cross force due to nonuniform pressure pattern results from an interaction between the nonuniform rotor tip gap distribution and the stator blade row. As the upstream flow senses the rotor eccentricity, the flow preferentially migrates toward the maximum gap region. Thus, locally, the axial velocity increases while that near the minimum gap region decreases. This preferential migration by itself would result in a pressure distribution with a minimum at $\theta = 180$ deg. However, since the stator introduces swirl into the flow, $c_{y2s} = c_{x1} \tan \alpha_2$, increased axial velocity means more tangential momentum entering the interblade region (Fig. 3) near the maximum gap. Per unit depth in y, the tangential momentum equation for the flow through the rotor can be written as

$$q_3(c_x \tan \alpha_3) - q_{2r}(c_{x2r} \tan \alpha_2) = -L(H_b + t)\frac{\partial p}{\partial y} - f_{\text{rotor}} \tag{34}$$

If it is assumed, for now, that the perturbations in $q_3(c_x \tan \alpha_3)$ and f_{rotor} are small compared to that in $q_{2r}(c_{x2r} \tan \alpha_2)$, Eq. (34) can be approximated as

$$(q_{2r}c_{x2r} \tan \alpha_2)' \approx L(H_b + t)\frac{\partial p'}{\partial y} \tag{35}$$

Essentially, the axial velocity perturbation at the rotor inlet introduces more tangential momentum to the maximum gap region than to the minimum gap region. This nonaxisymmetric tangential momentum influx is accommodated (in part) by a nonaxisymmetric pressure, with its minimum at $\theta = 90$ deg, generating the destabilizing cross force. Thus, the competing effects of the preferential flow migration toward the maximum gap and the asymmetric tangential momentum influx at the rotor result in a pressure asymmetry with its minimum around $\theta = 150$ deg.

The sensitivity of the model's predictions to various parameters under steady conditions is discussed next. To examine the effects of ϕ_D, the absolute velocity at the rotor exit is assumed to be axial, which is often the case for single-stage turbines or the last stage of multistage turbines. The axial exit flow condition is also a good approximation for the MIT turbine, which has a design absolute rotor exit flow angle of -3 deg. For a fixed value of R_D, an increasing ϕ_D reduces flow turning in both stator and rotor. Figure 6 illustrates the excitation force coefficients versus the design flow coefficient, ϕ_D. The solid lines are the total excitation force coefficients ($\alpha_{X_{\text{total}}}$ and $\alpha_{Y_{\text{total}}}$), and the dotted lines are the parts due to pressure (α_{X_p} and α_{Y_p}). All of the coefficients decrease in magnitude as ϕ_D increases. Moreover, the differences between the total and pressure coefficients, or the effects of tangential force variation ($\alpha_{X_{wd}}$ and $\alpha_{Y_{wd}}$), also decrease as ϕ_D increases. Such sensitivity of cross forces to the incoming swirl has been well documented, experimentally and theoretically, for labyrinth seals (Millsaps, 1992). Thus, even though the mechanisms are different, the overall trend of decreasing cross forces with decreasing swirl coming into the rotor is similar in both turbines and labyrinth seals.

Figure 7 shows the effects of off-design operation (i.e., fixed geometry with varying operating point) on the excitation force coefficients. Their magnitudes also decrease with increasing mean flow coefficient, $\bar{\phi}$, except for α_{X_p}, which is practically insensitive to $\bar{\phi}$.

The turbine operating point can be alternatively represented by the mean work coefficient, $\bar{\psi}$, given by

$$\bar{\psi} = \bar{f}_y/\dot{m}U \propto \bar{\phi} \tag{36}$$

The dependence of the excitation force coefficients on $\bar{\psi}$ is shown in Fig. 8.

Figure 9 shows the influence of the distance between the stator and rotor blades, d/R, on the excitation force coefficients. For these calculations, the value of a in Eq. (18) is assumed to be 1. Therefore, Fig. 9 shows the maximum sensitivity of excitation coefficients to the interblade distance, d/R. Figure 9 shows that this azimuthal flow redistribution within the interblade gap, d, increases the lateral forces due to tangential force variation; it also rotates the lateral forces due to nonaxisymmetric pressure, decreasing the direct force while increasing the cross force.[2]

[2] This "mass storage" effect was originally described by Millsaps (1992) in relation to the lateral forces that arise due to whirling motion of labyrinth seals.

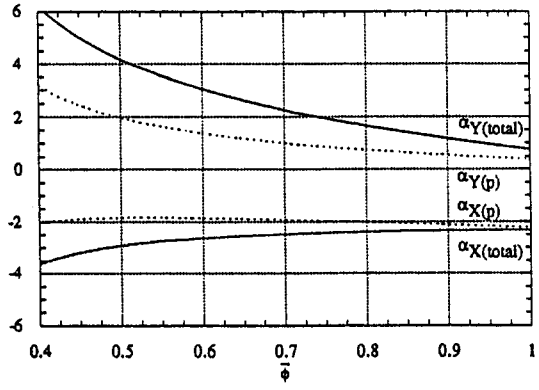

Fig. 7 Predicted total and pressure excitation force coefficients versus mean flow coefficient

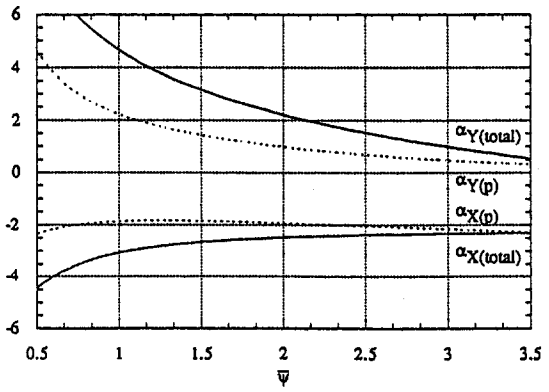

Fig. 8 Predicted total and pressure excitation force coefficients versus mean work coefficient

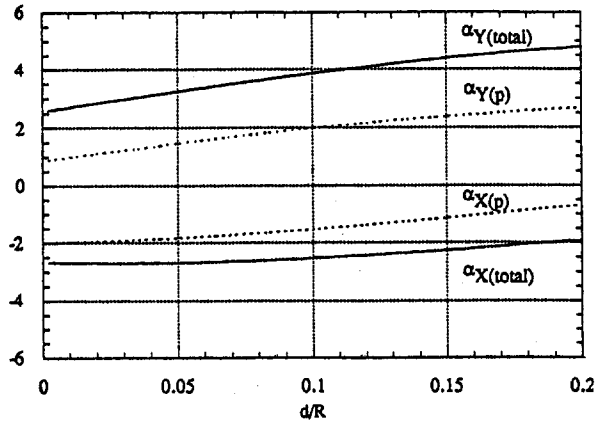

Fig. 9 Predicted total and pressure excitation force coefficients versus interblade distance

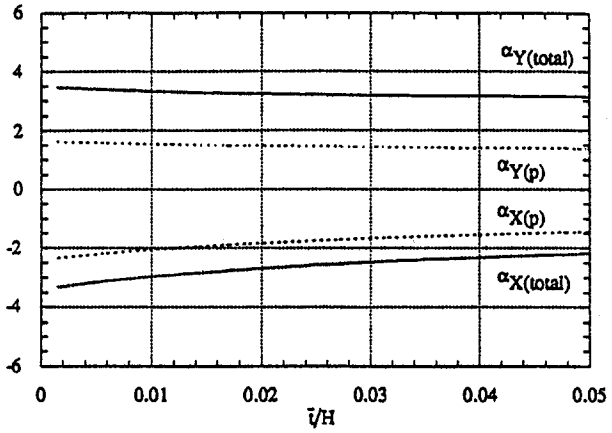

Fig. 10 Predicted total and pressure excitation force coefficients versus mean radial tip gap

The predicted influence of the mean height of the rotor tip gap, $\bar{t}/H$, on the excitation force coefficients is illustrated in Fig. 10. All of the coefficients decrease as $\bar{t}/H$ is increased; however, the direct force coefficients are more sensitive to $\bar{t}/H$ than the cross force coefficients, and, as will be shown, both trends are weaker than those seen in the data.

Figure 11 shows the calculated effects of unsteady whirling motion on the total excitation force coefficients. The $\Omega R/U$ range of -1.0 to 1.0 spans the frequency ratios from backward synchronous whirl to the forward synchronous whirl. The restoring nature of the direct force and forward whirling nature of the cross force are not affected by the whirling motion. The slopes of the curves of $\alpha_{X'}$, $\alpha_{Y'}$ can be interpreted as damping coefficients. In particular, the negative slope of $\alpha_{Y'}$ indicates positive damping of the forward whirling forces.

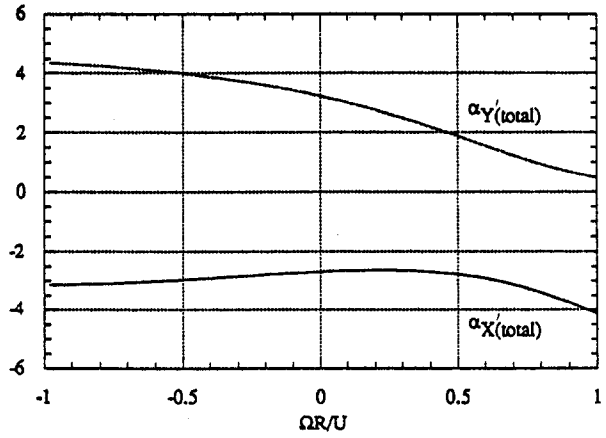

Fig. 11 Predicted total excitation force coefficients versus whirling frequency

Figure 12 shows graphs of excitation force coefficients due to the pressure (α_p's) and work extraction variations (α_{wd}'s) versus $\Omega R/U$. Again, the restoring nature of direct forces and the forward whirling nature of the cross forces remain unaltered. The $|\alpha_{Y'_{wd}}|$ shows an inertia-like parabolic dependence on $\Omega R/U$. $|\alpha_{X'_{wd}}|$ increases throughout most of the frequency range. $|\alpha_{Y'_p}|$ decreases almost linearly throughout the frequency range, vanishing near the forward synchronous whirl frequency. $|\alpha_{X'_p}|$ is insensitive to backward whirl and increases with whirl frequency. The tangential momentum balance, which was used to explain the cross force due to nonaxisymmetric pressure in a turbine with a statically offset rotor (Eqs. (34)–(35)) can again be invoked here. In the frame $X'Y'$ whirling with the rotor, Eq. (35) becomes

$$(q_{2r}c_{x2r}\tan\alpha_2 - q_{2r}\,\Omega R)' = L(H_b + t)\frac{\partial p'}{\partial y} \qquad (37)$$

With increasing ΩR, $c_{x2r}\tan\alpha_2 - \Omega R$ decreases almost linearly. Consequently, the azimuthal pressure gradient $\partial p'/\partial y$ is reduced, and $|\alpha_{Y'_p}|$ is decreased. Thus, the damping effect is seen to be due to the kinematics of the rotor whirling motion.

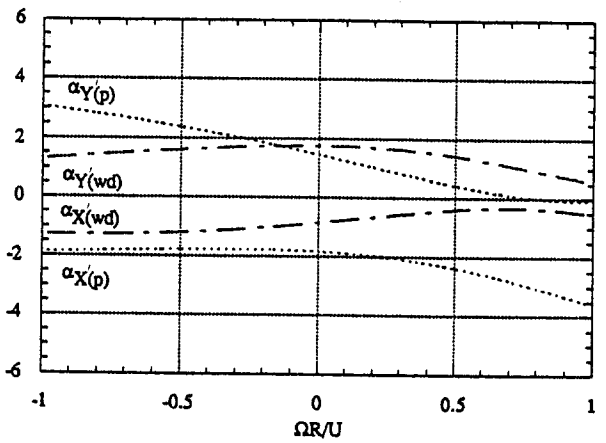

Fig. 12 Predicted pressure and tangential excitation force coefficients versus whirling frequency

Table 3 Comparison of cross force predictions from existing correlations and the data from Configuration 4 (Song, 1995) at $\bar{\phi} = 0.58$

Author	α_Y (model)	$\alpha_{Y_{wd}}$ (measured)	$\alpha_{Y_{TOTAL}}$ (measured)
Alford (range recommended)	+1.0~+1.5	+1.9	+3.5
Experimental $\partial\eta/\partial(\bar{t}/H)$	+2.5	+1.9	+3.5
Traupel	+0.8~+0.9	+1.9	+3.5
Farokhi	+1.0	+1.9	+3.5
Dunham & Came	+1.7	+1.9	+3.5

Table 4 Comparison of direct force predictions from existing correlations and the data from Configuration 4 (Song, 1995) at $\bar{\phi} = 0.58$

Author	$\alpha_{X(\text{model})}$	$\alpha_{X_{wd}(\text{measured})}$	$\alpha_{X_{TOTAL}(\text{measured})}$
Alford	0.0	-0.6	-3.4
Traupel	0.0	-0.6	-3.4
Farokhi	0.0	-0.6	-3.4
Dunham & Came	0.0	-0.6	-3.4

Table 5 Comparison of the predicted and the measured total excitation force coefficients from Configuration 4 (Song, 1995) at $\bar{\phi} = 0.58$

Direction	α_{total}(model)	α_{total}(measured)
X	-2.7	-3.4
Y	+3.2	+3.5

The slope of cross excitation force coefficient is an indication of direct damping, which along with cross stiffness, determines the stability of the rotor system. Figures 11 and 12 make clear that the damping effect is provided primarily by the pressure force. The work extraction forces actually show negative damping for $\Omega R/U$ less than +0.3, but the cross force due to work extraction variation remains a destabilizing force for forward whirl.

4 Comparison of Model Predictions and Experimental Data

This section presents a comparison of the experimental data and the analytical predictions. First, the experimental data are compared against predictions from the pre-existing models. Then, the newly predicted and measured magnitudes and the composition of forces are compared. It is to be noted that no data exist for dynamic (whirling) conditions. In view of the significant predicted damping, this should be a priority for further testing.

The experimental data are compared against predictions from a few widely used correlations and models for efficiency loss due to clearance effects, which were available before the development of the current model. The implied assumption is that the *work loss* and the *efficiency loss* are equal. This is not accurate because, as shown by the new model, the pressure drop (a factor in the efficiency definition) is also strongly affected by clearance changes. The correlations of Alford (1965), Traupel (1958), Farokhi (1988), and Dunham and Came[3] (1970) were selected. The equations for the correlations are listed in Song (1995). Table 3 presents a comparison of the cross excitation force coefficient. While the prediction of Dunham and Came's correlation is better than others, it misses the pressure contribution, and because of this, the experimental value is still twice the predicted value. Thus, Table 3 shows the poor state of existing predictive capability.

Table 4 shows the comparison of direct forces. The azimuthal redistribution of flow due to a rotor offset was previously neither recognized nor modeled, and the work defect mechanism was assumed to occur 180 deg out of phase with the clearance distribution. Thus, zero direct force was predicted.

Next, the same experimental data are compared to the predictions from the new model. Table 5 shows a comparison of the predictions and the dynamometer measurements. α_{total} represents the sum of the pressure and blade force contributions. While the model still underpredicts excitation coefficients, the predictions of both cross and direct excitation force coefficients are within 20 percent of the measured values.

The new model's prediction of the total force in each direction consists of those due to nonaxisymmetric pressure and work extraction. To verify each effect's relative contribution, the model predictions are compared to the data from the pressure taps and the multihole probes (Martinez-Sanchez et al., 1993). Table 6 lists the excitation coefficients from the aerodynamic measurements and the model predictions. Though still underpredicted, the contributions of different effects are well captured. Tables 5 and 6 show that the current model's cross force prediction is more accurate than the direct force prediction in both the total magnitude and the separation of effects. The theoretical pressure force excitation coefficient is determined from the average of pressures at the rotor inlet and exit. The experimental pressure force excitation coefficient is determined from only the rotor inlet pressure due to lack of rotor exit pressure data. Figure 14 shows the predicted and measured pressure perturbations at the rotor inlet.

Figures 13 and 14 display, respectively, the graphs of predicted and measured perturbations in tangential force and rotor inlet pressure versus azimuthal angle for the baseline case. The agreement between theory and experiment is good in both cases. The magnitudes of the perturbations, which are determined by the prescribed eccentricity, are accurately predicted. More importantly, the phases of the perturbations are also well predicted. The phases are important for the following reasons: First, the component of tangential force perturbation 90 deg out of phase with eccentricity contributes one third of the total direct force; second, the pressure perturbation component 90 deg out of phase with eccentricity contributes about 40 percent of the cross force. Overall, the model captures the dominant physical effects in flows through a turbine with an eccentric rotor.

Figure 15 shows a comparison of the variation of the measured and predicted total excitation force coefficients, α_{total}'s, with the mean flow coefficient, $\bar{\phi}$. Qualitatively, the model pre-

[3] This correlation is an adaptation of the correlation originally developed by Ainley and Mathieson (1951). As noted by Denton (1993), this correlation has been widely used by the engine manufacturers.

Table 6 Comparison of the predicted and the measured rotordynamic coefficients (from the aerodynamic data) from Configuration 4 (Song, 1995) at $\bar{\phi} = 0.58$

Direction	αp(model)	αwd(model)	αt(model)	αp(data)	αwd(data)	αt(data)
X	-1.8	-0.9	-2.7	-2.6	-0.6	-3.2
Y	+1.4	+1.8	+3.2	+1.6	+1.9	+3.5

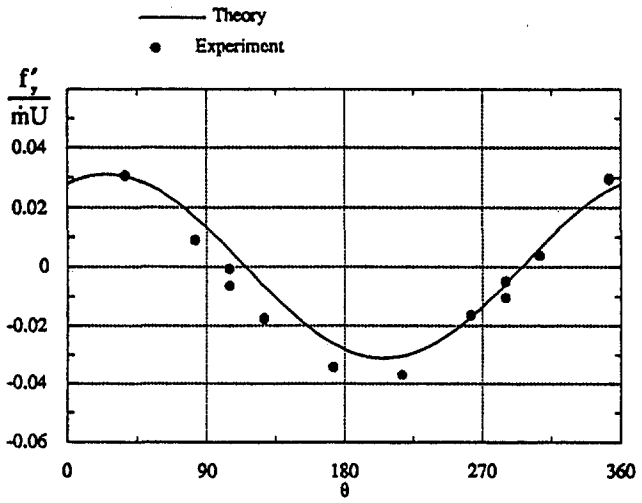

Fig. 13 Measured and predicted tangential force perturbation versus azimuthal angle for Configuration 4 at $\bar{\phi} = 0.58$ and $e/H_b = 0.011$ (maximum gap at 180 deg)

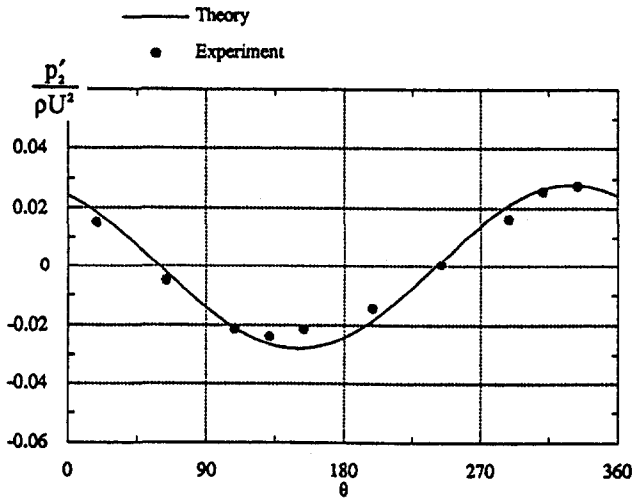

Fig. 14 Measured and predicted rotor inlet pressure perturbation versus azimuthal angle for Configuration 4 at $\bar{\phi} = 0.58$ & $e/H_b = 0.011$ (maximum gap at 180 deg)

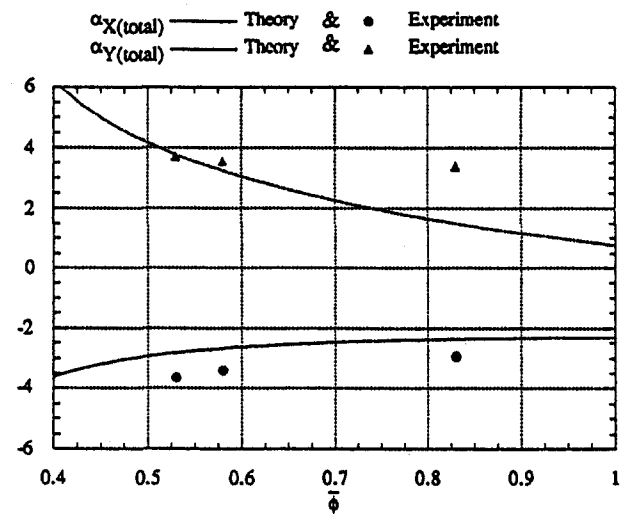

Fig. 15 Measured and predicted total force excitation coefficients versus mean flow coefficient for Configuration 4

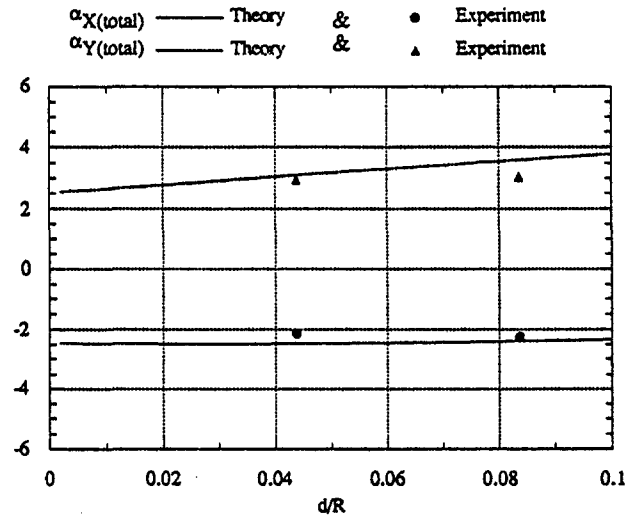

Fig. 16 Measured and predicted total force excitation coefficients versus interblade distance (Configurations 1 and 2 at $\bar{\phi} = 0.58$)

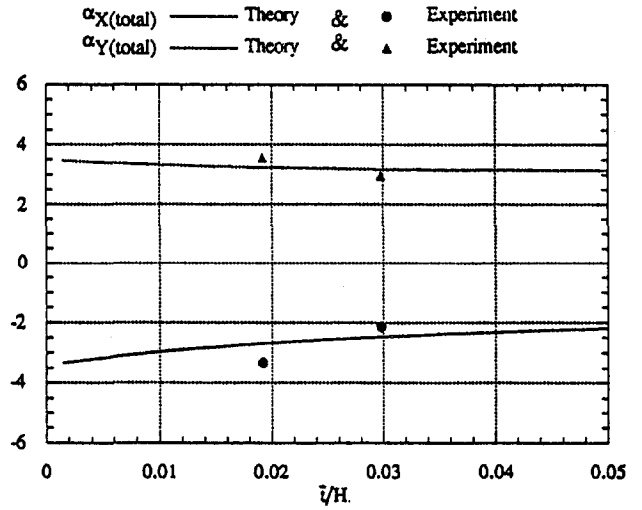

Fig. 17 Measured and predicted total force excitation coefficients versus mean radial tip gap (Configurations 2 and 4 at $\bar{\phi} = 0.58$)

dicts the correct trends of direct and cross force coefficients versus $\bar{\phi}$. However, the predicted α_Y is more sensitive to $\bar{\phi}$ than the actual data. This is probably because, in real machines, increased losses occur at the off-design points. Thus, the actual torque extracted by the machine is less than the ideal value assumed in the model. Since the forces are normalized by the actual torque, the measured data are likely to be larger in magnitude than the predicted ones. Therefore, this discrepancy is worse at $\bar{\phi} = 0.83$ where the off-design effects are likely the largest.

Figure 16 shows the predicted and measured dependence of the α_{total}'s on the interblade distance, d/R. Though the sensitivity is weak, the prediction and the measured data show similar trends. The predicted results show the maximum possible sensitivity to d/R, and the actual sensitivity is likely to be weaker. Urlichs (1983) also found a similar trend, though with higher sensitivity.

Figure 17 shows plots of the measured and predicted α_{total}'s versus the mean rotor tip clearance, $\bar{t}/H$. The model predicts the correct trend of decreasing magnitude of α_{total}'s with increasing $\bar{t}/H$; however, the predicted sensitivity is much weaker than that of the actual data. One reason is the linearized nature of

the model, which neglects the nonlinear effects. The physically more important reasons are most likely due to the unmodeled effects of viscosity and endwall motion that affect the tip clearance flow, especially in turbines, where the inviscid gap flow concepts used in the theory may be invalid (Chen, 1991; Heyes and Hodson, 1993; Graham, 1985; Yaras and Sjolander, 1992).

5 Conclusions

The comparison of predictions and experimental data shows that the new model can accurately predict both direct and cross excitation force coefficients as well as their breakdown into work extraction and pressure effects. Also, the trends versus mean flow coefficient and interblade distance are predicted. However, the model underpredicts the effects of the mean rotor tip clearance height.

Thus, the main conclusions from this investigation include the following:

1 An actuator disk based approach can predict the radius scale flow response to an eccentric turbine rotor.
2 In addition to the Thomas–Alford mechanism, a significant contribution to the cross forces comes from a nonuniform pressure pattern, which develops over the rotor.
3 This pressure pattern is responsible for almost all of the restoring force, which is much larger in magnitude than previously expected.
4 This pressure pattern extends over axial lengths on the order of the turbine radius, which indicates that this effect is due to tangential flow redistribution caused by the rotor offset.
5 Both the direct and cross force coefficients increase as the flow coefficient is decreased.
6 The excitation forces increase with separation between stator and rotor.
7 The theory predicts significant damping effects. No experimental data on this effect exist.

Acknowledgments

This work was performed under NASA Grant NAS 8-35018. Glenn E. Wilmer, Jr., is the Technical Monitor.

References

Ainley, D. G., and Mathieson, G. C. R., 1991, "A Method of Performance Estimation for Axial Flow Turbines," British ARC, R & M 2974.

Alford, J. S., 1965, "Protecting Turbomachinery From Self-Excited Rotor Whirl," ASME *Journal of Engineering for Power,* Vol. 87, pp. 333–344.

Chen, G. T., 1991, "Vortical Structures in Turbomachinery Tip Clearance Flows," Ph.D. Thesis, Department of Aeronautics and Astronautics, M.I.T.

Denton, J. D., 1993, "Loss Mechanisms in Turbomachines," ASME JOURNAL OF TURBOMACHINERY, Vol. 115, pp. 621–656.

Dunham, J., and Came, P. M., 1970, "Improvements to the Ainley-Mathieson Method of Turbine Performance Prediction," ASME Paper No. 70-GT-2.

Farokhi, S., 1988, "Analysis of Rotor Tip Clearance Loss in Axial-Flow Turbines," *AIAA Journal of Propulsion,* Vol. 4, No. 5, pp. 452–457.

Graham, J. A. H., 1985, "Investigation of a Tip Clearance Cascade in a Water Analogy Rig," ASME Paper No. 85-IGT-65.

Heyes, F. J. G., and Hodson, H. P., 1993, "The Measurement and Prediction of the Tip Clearance Flow in Linear Turbine Cascades," ASME JOURNAL OF TURBOMACHINERY, Vol. 115, pp. 376–382.

Horlock, J. H., and Greitzer, E. M., 1983, "Nonuniform Flows in Axial Compressors Due to Tip Clearance Variation," *Proc. Inst. Mech. Engrs.,* Vol. 197C, pp. 173–178.

Leung, E. K. Y., 1991, "3D Turbine Tip Clearance Flow Redistribution due to Gap Variation," S.M. Thesis, Department of Aeronautics and Astronautics, M.I.T.

Martinez-Sanchez, M., Jaroux, B., Song, S. J., and Yoo, S., 1995, "Measurement of Turbine Blade-Tip Rotordynamic Excitation Forces," ASME JOURNAL OF TURBOMACHINERY, Vol. 117, pp. 384–393.

Millsaps, K. T., 1992, "The Impact of Unsteady Swirling Flow in a Single Gland Labyrinth Seal on Rotordynamic Stability: Theory and Experiment," Ph.D. Thesis, Department of Aeronautics and Astronautics, M.I.T.

Qiu, Y. J., 1985, "An Investigation of Destabilizing Blade Tip Forces for Shrouded and Unshrouded Turbines," S.M. Thesis, Department of Aeronautics and Astronautics, M.I.T.

Song, S. J., 1995, "An Investigation of Tip Clearance Flow Excitation Forces in a Single-Stage Unshrouded Turbine," Sc.D. Thesis, Department of Aeronautics and Astronautics, M.I.T.

Traupel, W., 1958, *Thermische Turbomaschinen,* Vol. 1, Springer-Verlag, Berlin.

Urlichs, K., 1983, "Durch Spaltstromungen hervorgerufene Querkrafte an den Laufern Thermischer Turbomaschinen (Clearance Flow-Generated Transverse Forces at the Rotors of Thermal Turbomachines)," NASA TM-77292.

Yaras, M. I., and Sjolander, S. A., 1992, "Effects of Simulated Rotation on Tip Leakage in a Planar Cascade of Turbine Blades: Part I—Tip Gap Flow," ASME JOURNAL OF TURBOMACHINERY, Vol. 114, pp. 652–659.

Yoo, S., 1993, "Modeling of Alford Force and Tip Clearance Flow for Turbine Blades," S.M. Thesis, Department of Aeronautics and Astronautics, M.I.T.

Analysis of Instability Inception in High-Speed Multistage Axial-Flow Compressors

G. J. Hendricks

J. S. Sabnis

M. R. Feulner

United Technologies Research Center,
411 Silver Lane,
East Hartford, CT 06108

A nonlinear, two-dimensional, compressible dynamic model has been developed to study rotating stall/surge inception and development in high-speed, multistage, axial flow compressors. The flow dynamics are represented by the unsteady Euler equations, solved in each interblade row gap and inlet and exit ducts as two-dimensional domains, and in each blade passage as a one-dimensional domain. The resulting equations are solved on a computational grid. The boundary conditions between domains are represented by ideal turning coupled with empirical loss and deviation correlations. Results are presented comparing model simulations to instability inception data of an eleven stage, high-pressure-ratio compressor operating at both part and full power, and the results analyzed in the context of a linear modal analysis.

Introduction

The operability of gas turbine engines is adversely affected by instabilities in the compression system. These instabilities in axial flow compressors manifest themselves as rotating stall and/or surge, where rotating stall is associated with large-amplitude nonaxisymmetric flow variations rotating around the compressor annulus, and surge is associated with large-amplitude axisymmetric flow variations interacting with a downstream volume. These instabilities, when fully developed, result in a loss in compressor performance and an increase in structural loads. Due to this detrimental effect on engine operability and structural integrity, there is a strong incentive to understand, avoid, and/or control surge and rotating stall in high-pressure-ratio axial flow compressors.

Early efforts to understand and analyze these instabilities started with Emmons et al. (1955), where the approach was to extend the unsteady aerodynamics of a cascade to that of a stage and subsequently to the compressor. This approach attempts to analyze the compression system behavior based upon that of a single blade row embedded in the system. The enormous complexity of the system limits the usefulness of this approach in analyzing the dynamic behavior of the compression system. An alternate approach directly models the system dynamics. This approach was proposed by Greitzer (1976), Day et al. (1978), Day and Cumpsty (1978), and Koff and Greitzer (1984). The analysis of Moore and Greitzer (1986) showed that surge and rotating stall appear as mature forms of natural oscillatory modes of the compression system. This model characterizes surge as the lowest (zero) order mode and rotating stall as higher order modes of the compression system, having one mode for each circumferential spatial harmonic. Greitzer and Moore (1986) exercised this theory to demonstrate its ability to simulate system transients into surge or rotating stall, depending upon the relevant system parameters. Longley (1994) provides an excellent review of compressor stability models.

As the experimental analysis and control of rotating stall and surge are performed on compressors with higher speeds and more blade rows (Eveker et al., 1997; Feulner et al., 1996; Tryfonidis et al., 1995; Day and Freeman, 1994; Gallops et al., 1993; Hoying, 1993), the compressor dynamic modeling needed to be extended beyond that of Moore and Greitzer. The first effort along this path was a linear compressible model of rotating stall and surge (Bonnaure, 1991). This model is applicable to the study of small-amplitude perturbations in the compressor, and the instability prediction for high-speed compressors, where compressibility is important. This model was extended by Hendricks et al. (1993) and reformulated for control design by Feulner et al. (1996). This model was the first to predict higher frequency rotating stall modes (i.e., nonaxisymmetric compressor resonances beyond that of the incompressible rotating stall models) as well as axial acoustic modes. While the linear model is important for the study of compressor modes up to the stability boundary, it provides little information on the instability inception process and the coupling of rotating stall and surge. Early efforts in two-dimensional nonlinear compressor dynamic modeling included Ishii and Kashiwabara (1992), who developed a nonlinear model using a modal formulation and matched speedlines and stall points in various compressors. Alexandrov et al. (1995) also developed a quasi-three-dimensional nonlinear model, but only applied it to a single rotor. The present effort is aimed at developing a two-dimensional nonlinear, compressible, dynamic model for axial flow compressors that can be used in the study of prestall dynamic behavior, the instability inception process, the fully developed surge and rotating stall phenomena, and the analysis of nonlinear control strategies.

Model Formulation

The approach used in the formulation of the dynamic model was to describe the unsteady dynamics (essentially inertia and compressible wave propagation effects) by the unsteady Euler equations. Real fluid viscous effects were incorporated into the analysis in the form of phenomenological models. This approach has been used successfully in previous compressor stability studies (Haynes et al., 1994; Bonnaure, 1991; Hendricks et al., 1993). The flow field through the compressor was broken down into computational domains corresponding to the inlet duct, blade passages, interblade spaces, exit duct, plenum (or combustor), and the exit throttle (or turbine). Interstage compressor bleeds, which are found in most gas turbine engines, were also modeled. As in the flow path, the dynamics of the flow fields within the bleed plenums were modeled by the Euler equations.

A schematic of the model structure is shown in Fig. 1. The flow is represented by the two-dimensional (axial and circumferential) unsteady Euler equations in the inlet duct, inter-

Contributed by the International Gas Turbine Institute and presented at the 41st International Gas Turbine and Aeroengine Congress and Exhibition, Birmingham, United Kingdom, June 10–13, 1996. Manuscript received at ASME Headquarters February 1996. Paper No. 96-GT-360. Associate Technical Editor: J. N. Shinn.

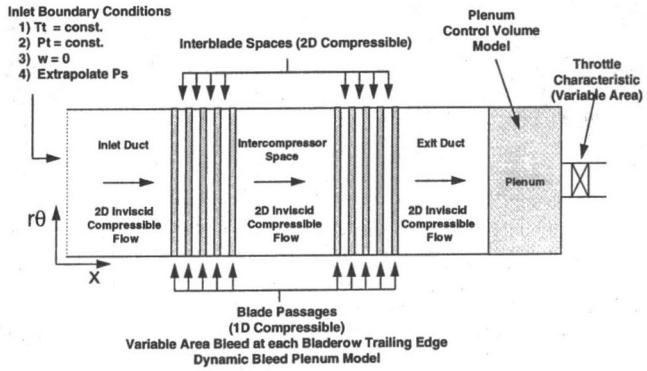

Fig. 1 Model structure

bladerow spaces, and the exit duct and by the one-dimensional unsteady Euler equations in the blade passages.

The two-dimensional flow fields are coupled to the one-dimensional flow fields in the bladed regions by appropriate matching conditions. At the leading edges of the bladed regions the following matching conditions are applied:

1 Continuity.
2 Relative total temperature change to account for mean radius change through the rotors (constant rothalpy); constant T_t (stators).
3 A loss in relative total pressure to account for viscous losses within each blade passage.

At the trailing edges of the bladed regions the following matching conditions are applied:

1 Continuity.
2 Constant relative total temperature.
3 Constant relative total pressure.
4 Flow exit angle (blade metal angle + deviation angle).

Losses and deviations are computed from a model based on both theoretical analysis and experimental correlations obtained from blade row cascade and compressor rig tests. This model was extracted from a meanline performance prediction code currently being used in the aircraft gas turbine engine industry. This loss and deviation model was incorporated into the dynamic analysis as a subroutine in the computer code. At each time step in the solution procedure, the flow conditions at the inlet and exit of each blade passage are used to compute the quasi-steady blade row total pressure loss and exit deviation angle. The ideal pressure rise corresponding to the blade row geometry and speed, together with the loss and deviation characteristics computed from the meanline model, determine the pressure rise characteristic of a blade passage. When the flow through the blade passages is unsteady, however, losses and deviations do not respond instantaneously to changes in inlet and exit conditions (Mazzawy, 1977; Nagano et al., 1971) because they result from viscous flow effects, which evolve over a finite time. A phenomenological model similar to the one used by Haynes et al. (1994) is applied in the analysis to account for both the loss and deviation evolution. The loss and deviation evolution are described by the first-order rate equation:

$$\tau \frac{df}{dt} = f_{ss} - f$$

where f represents either the loss or deviation in the blade passage, f_{ss} the quasi-steady quantity computed from the meanline model, and τ the time constant for the evolution of the computed quantity, which, for the present study, was set equal to one and a half times the blade passage flow through time.

Even when a compressor operates in a stable manner, the flow is unsteady due to physical effects that are not captured by the current analysis. Phenomena like rotor–stator wake interaction and turbulence ingestion result in unsteady pressure and velocity fluctuations, which can be considered as a forcing function for the dynamics that we are interested in. To capture this effect, a noise model was incorporated into the analysis in the following way: at each time step a random fluctuation was added to the quasi-steady loss in each blade passage. The level of the random loss fluctuation was adjusted so that the pressure fluctuations in the model at various axial stations matched experimental data.

The inlet boundary conditions shown in Fig. 1 represent clean undistorted inlet flow. These boundary conditions can be modified appropriately to represent both total pressure and total temperature distortions. The exit duct is coupled to a lumped parameter model of a plenum (combustion chamber) which is coupled to a model of a throttle valve.

Because of its complexity, the capability to model reverse flows during a surge cycle has, at this stage, not been included in the computational procedure. For the current study this is not a limitation since the focus in on the instability inception process rather than the large-amplitude limit cycle instability behavior of compressors. The compressor pressure rise characteristic was suitably modified to prevent the flow in the compressor from reversing during a surge cycle. The capability to model reverse flows will be incorporated into the code in the future.

The formulation of the model as described above allows the following:

1 Compressor behavior can be analyzed during throttle transients from the design point to instability.
2 Blade row speeds can be set independently, which enables one to analyze multispool compressors.
3 The effects of compressor speed transients on stability can be analyzed.
4 Vane stagger angles can be scheduled transiently to model real compressor transient behavior.
5 The inclusion of interstage bleeds and bleed plenums allows one to analyze the effect of bleed opening and closing transients.
6 Clearance can be specified as a function of circumferential location, which allows for the analysis of both stationary and rotating asymmetric clearance effects.
7 Clearance can be specified as a function of time, which allows for the analysis of the effect of clearance variations due to thermal effects on stability.

The computer code was implemented with an option to perform the analysis in a one-dimensional (axial) mode so that the one-dimensional dynamics could be studied independently.

The Euler equations describing the unsteady flow were solved using the Flux Corrected Transport (FCT) method developed by Boris and Book (1976) and Boris et al. (1987). Details of the numerical procedure can be found in the publications cited. The computational grid used in the simulations that will be presented had a total of 110 grid points in the axial direction and 24 points circumferentially. Computational times were approximately 12 hours on an IBM RS/6000 390 workstation for a 100 revolution transient simulation.

Results

Results of the analysis of an eleven-stage variable geometry compressor, which is representative of current high-pressure compressor design in aircraft gas turbine engines, are presented and compared with experimental data taken in a compressor test rig. Simulation and experimental results will be presented at both design speed and a part-speed condition (80 percent of design speed). Results for the part-speed condition will be presented first.

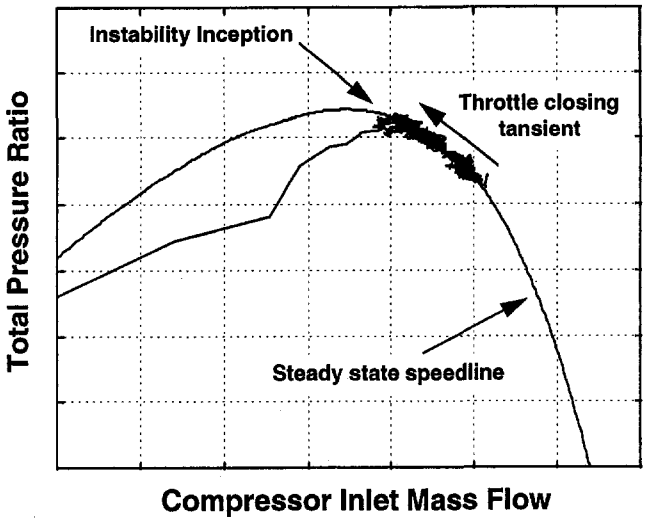

Fig. 2 Throttle closing transient (part speed)

In the rig test, the compressor was brought to a steady-state condition at an operating point close to instability. An exit throttle valve was then slowly closed, reducing the mass flow until the compressor became unstable. This scenario was simulated with the dynamic model. Figure 2 shows the annulus-averaged speedline for the compressor with the result of the unsteady simulation superposed on it. The plot shows a period of stable operation where the result of the unsteady simulation overlays the steady-state, annulus-averaged speedline, followed by instability inception where the unsteady trace starts to deviate from the steady-state speedline. Figure 3(a) shows pressure traces at four circumferential locations around the compressor inlet. Figure 4(a) shows the experimental data for the same condition. The similarity of the modeled results and the experimental data indicates that the model captures the instability inception and development reasonably well.

Both the experimental data and the model results indicate that the instability event involves participation of both one-dimensional (surge and planar compressible wave or "acoustic" oscillations) and two-dimensional rotating disturbances. The traces were processed to separate the one and two-dimensional disturbances in order to investigate the role of each in the instability inception and development process. The processing was done as follows. At each time step a discrete spatial Fourier transform was performed on eight pressure measurements around the compressor annulus. This analysis yields the amplitude and phase of the first three spatial harmonics of the pressure field; the zeroth harmonic represents planar disturbances, and the first and second harmonics represent one and two-lobed disturbances around the compressor annulus. The frequency content of each spatial harmonic was then obtained by performing a Fast Fourier Transform (FFT) on the signals obtained from this analysis.

An analysis of the large-amplitude instability development at part speed will be presented first, followed by a more detailed discussion of the prestall perturbation development. Figures 3(b) and 4(b) show the planar components of both the experimental data and simulation results. The planar disturbance shows an initial spike, which results from the deceleration of the fluid in the inlet duct during the initial part of the surge cycle. This spike has been referred to as the "hammer shock" in some previous studies. The oscillation that follows the initial spike corresponds to an acoustic oscillation of the fluid in the compressor duct. The one-dimensional component of the pressure disturbance was subtracted from each pressure trace to determine the participation of two-dimensional rotating disturbances in the instability development process. Figures 3(c) and 4(c) show the presence of a significant degree of rotating stall with a rotational frequency approximately half of the rotor frequency during instability development, both in the experimental data and in the simulation results. The pressure signature at the inlet appears to indicate that both surge and rotating stall develop simultaneously, but the static pressure signature at a location within the compressor shown in Fig. 5(a, b) clearly shows the development of rotating stall prior to the compressor's losing stability. This indicates that rotating stall is the stability limiting phenomenon for this operating condition. Figure 5 shows the rotating stall developing at a lower rotational speed in the computation than in the experiment. A possible reason for this is that the rotating stall developing in the experimental rig might have three-dimensional (radial) structure associated with it, even if it predominantly two-dimensional (i.e., circumferential–axial). It is well known that the rotational speed of a rotating stall perturbation is determined by the inertia of the fluid involved in the stall inception process. If a smaller amount

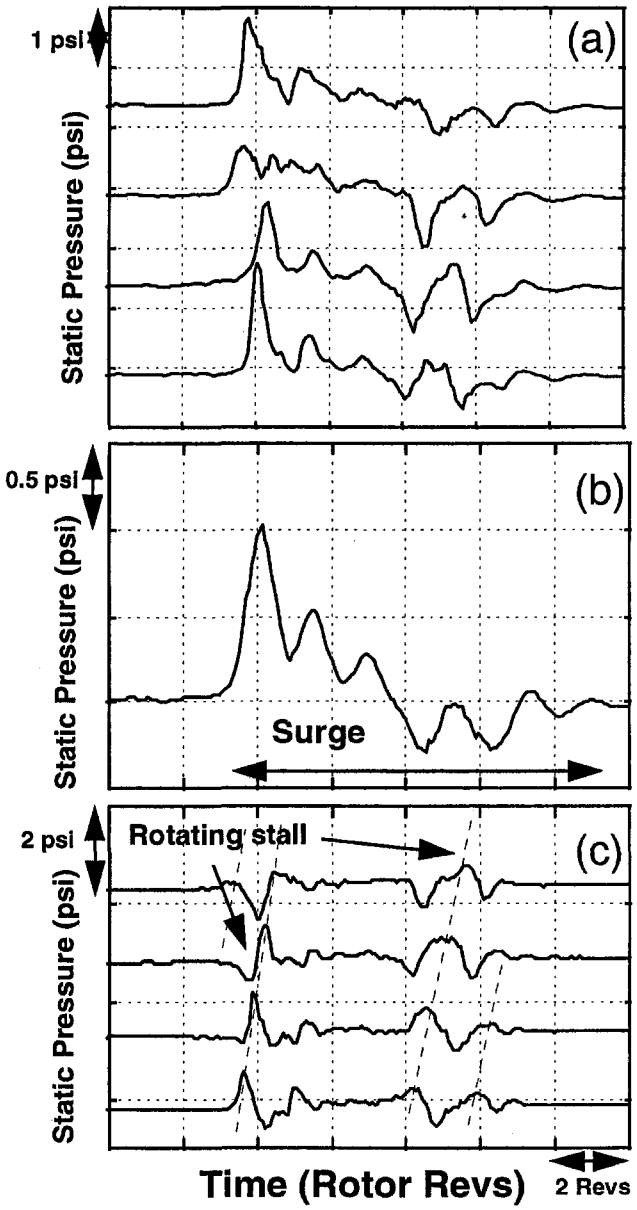

Fig. 3 Simulation results (part speed): (a) four static pressure traces equally spaced circumferentially around the compressor inlet (offset represents circumferential spacing); (b) planar component of inlet static pressure; (c) rotating component of inlet static pressure

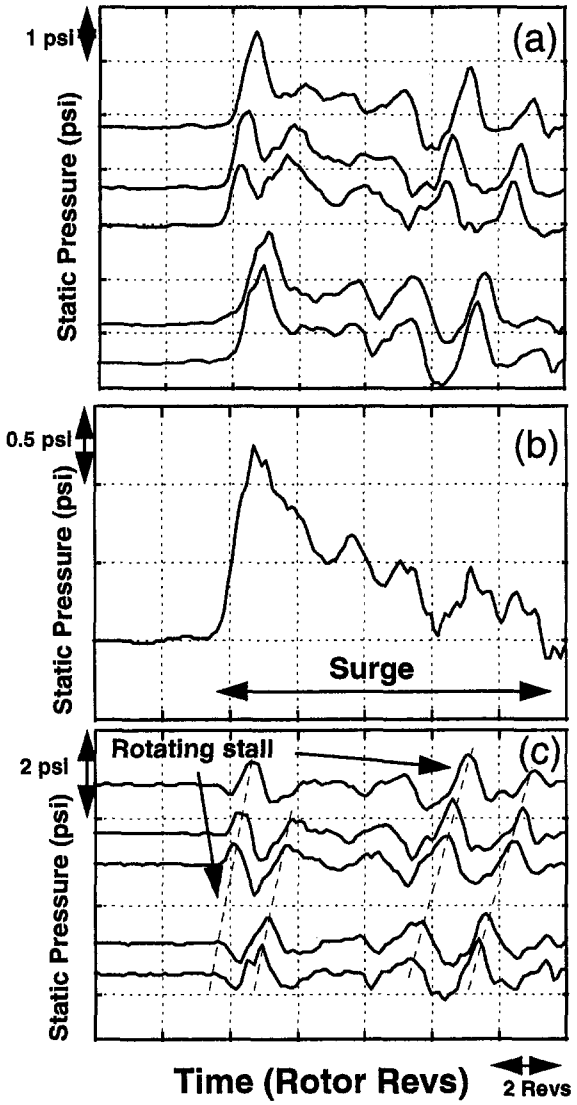

Fig. 4 Experimental data (part speed): (*a*) five static pressure traces spaced circumferentially around the compressor inlet (offset represents circumferential spacing); (*b*) planar component of inlet static pressure; (*c*) rotating component of inlet static pressure

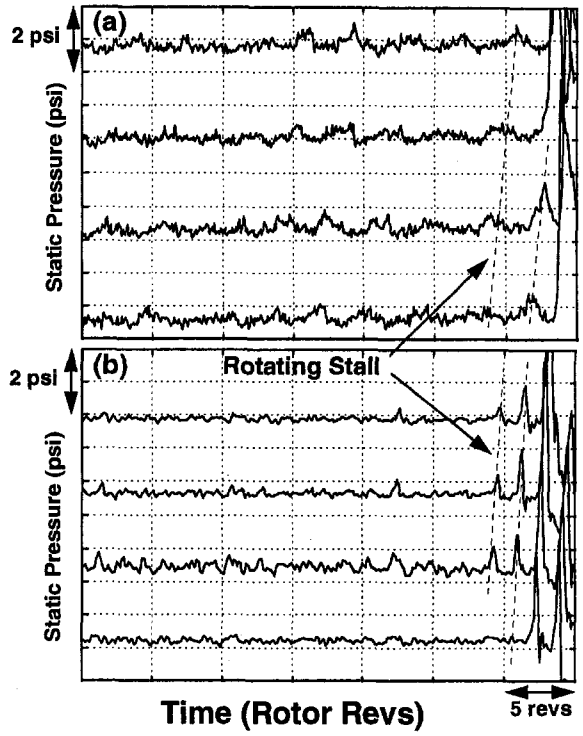

Fig. 5 Static pressure traces at the fourth stage of the compressor showing the evolution of rotating stall before the surge event at the part speed operating: (*a*) simulation, (*b*) experiment

of fluid is involved, which would be the case if the perturbation had a three-dimensional structure, the perturbations would tend to travel at higher circumferential speeds. Figure 6 shows that rotating stall is detectable at the exit of the compressor prior to surge, which implies that the rotating stall is not a part-span event localized to the front of the compressor, but has a significant axial length scale.

The discussion above focused on the large-amplitude instability development. Careful analysis of the period before the large-amplitude instability event provides useful insight into the instability inception process, in particular, the development of the various instability modes prior to the instability inception event. As with the large-amplitude analysis, the pressure traces were decomposed into planar one-dimensional and circumferential, two-dimensional components.

The planar component of the inlet pressure signal is shown in Figs. 7(*a*) (simulation) and 8(*a*) (experiment). The time traces for both the simulation and experimental data show clear oscillations at approximately 60 percent of rotor frequency, corresponding to an acoustic or "organ pipe" oscillation of the fluid in the compressor duct. This oscillation seems to be modulated at a much lower frequency, approximately one cycle in thirty rotor revolutions. FFTs corresponding to three segments (each corresponding to a 20 revolution duration) of the time trace are plotted below the time trace. These show the frequency content of the time trace as the compressor is throttled toward stall. Both the simulation result and the experimen-

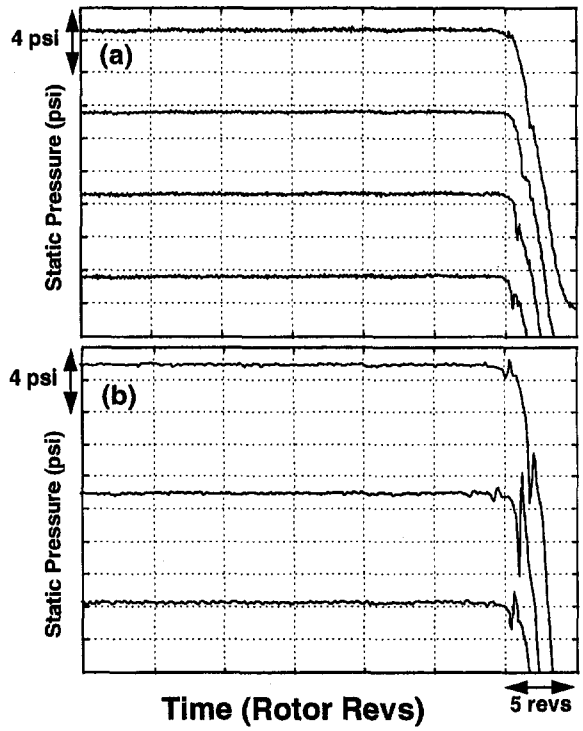

Fig. 6 Static pressure traces at the exit of the compressor showing the surge event at the part-speed operating condition: (*a*) simulation, (*b*) experiment

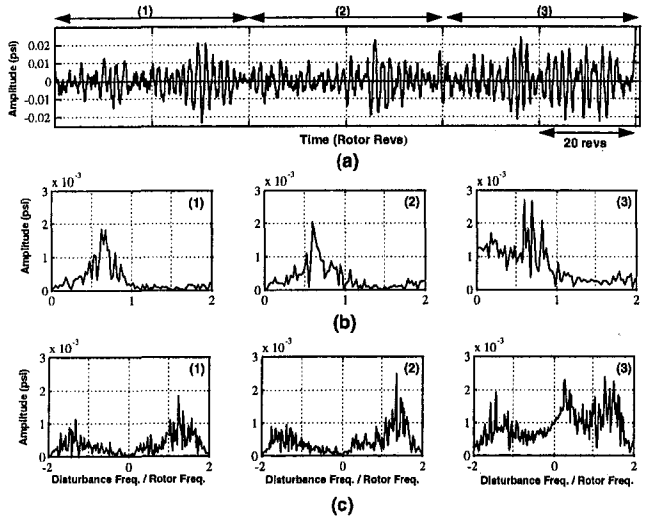

Fig. 7 Simulation results (part speed): (*a*) planar disturbances at the compressor inlet; (*b*) frequency content of planar disturbances; (*c*) frequency content of rotating disturbances

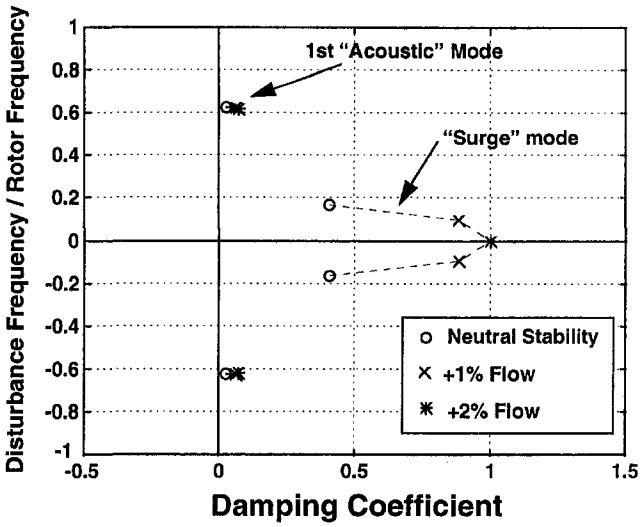

Fig. 9 Linear analysis of the zeroth spatial harmonic (planar modes) showing eigenvalue trajectories as the compressor is throttled toward instability at the part-speed operating condition

tal data show a well-defined peak at around 60 percent of rotor frequency, which grows in amplitude as the compressor approaches instability.

Figure 7(*c*) shows the amplitude and frequency content of the first circumferential spatial harmonic of the pressure at the inlet to the compressor for the same three time segments as the compressor is throttled toward stall. Peaks can be seen in the FFTs at approximately −120, 35 percent, and 130 percent of rotor frequency. The presence of these peaks indicates the possibility of system resonances at these frequencies. The amplitude of the −120 percent peak remains approximately constant as the compressor is throttled toward stall, the 130 percent peak grows gradually, but the 30 percent peak grows rapidly as the compressor approaches the instability condition. The FFT of the experimental data shown in Fig. 8(*c*) has similar features. A peak in the FFT can clearly be seen at 130 percent of rotor frequency, though the peak at the negative frequency is much less pronounced. Close to instability a growth in rotational energy can be seen between 20 and 60 percent of rotor frequency though a peak in the FFT is not as well defined as in the simulation result.

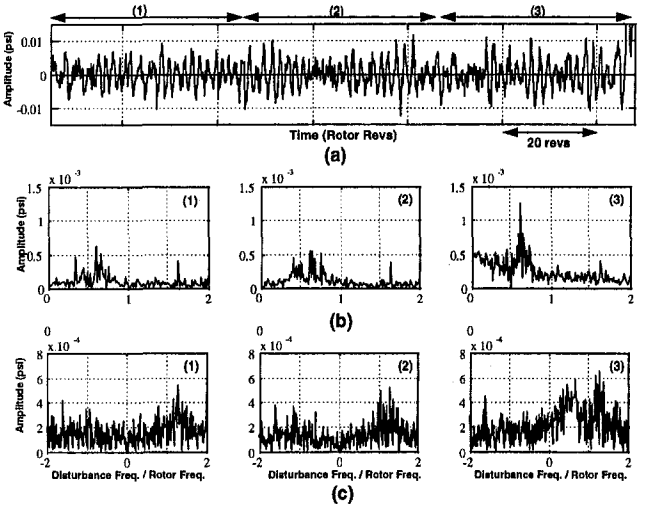

Fig. 8 Experimental results (part speed): (*a*) planar disturbances at the compressor inlet; (*b*) frequency content of planar disturbances; (*c*) frequency content of rotating disturbances

A two-dimensional, compressible, linear stability model that had previously been developed (Bonnaure, 1991; Hendricks et al., 1993) was used to gain insight into the significance of the observed peaks in the inlet pressure perturbations. The model computes eigenvalues, which provide information about the damping and frequencies of the compression system modes. A mode with a positive damping value will decay with time if perturbed and will have no adverse effect on compressor stability. When the damping of a mode becomes negative, its amplitude will grow exponentially in time, which will cause the compression system to lose stability.

Figure 9 shows an eigenvalue plot for the planar modes (zeroth spatial harmonic) of the system as the mass flow through the compressor is reduced. The lowest frequency eigenvalue corresponds to the surge or Helmholtz mode of the system and the higher frequency mode to the first acoustic mode of the fluid in the compressor duct. The mass flow range that was covered corresponds to that in the throttle closing transient that was modeled with the nonlinear simulation. The plot indicates that the acoustic mode with a frequency of approximately 60 percent of rotor frequency is lightly damped over the mass flow range modeled. This is consistent with the pressure signatures observed at the inlet of the compressor both in the nonlinear simulation and the experimental data. The eigenvalue associated with the Helmholtz mode is well damped over the modeled flow range, indicating that it does not play an important role in the instability inception process for this operating condition.

Figure 10 shows the eigenvalue plot for the first circumferential spatial harmonic. Eigenvalues are present at approximately the same frequencies as the peaks shown in the FFT of the dynamic simulation output. As the mass flow through the compressor is reduced, the eigenvalues at the higher frequencies (−180, −120, and 140 percent of rotor frequency) move very little, whereas the eigenvalue at 50 percent of rotor frequency moves rapidly toward the neutral stability axis. The analysis shows that even though the higher frequency modes are more lightly damped than the lower frequency mode at high mass flows, the damping of the lower frequency mode changes rapidly as the compressor mass flow is reduced. This explains why the peaks at the high frequencies observed in the FFTs of the simulation result are present over the entire mass flow range covered in the simulation, whereas the low-frequency peak (approx. 40 percent of rotor speed) becomes visible only very close to the instability point. From the eigenvalue plot it is apparent that the lower frequency eigenvalue becomes negatively

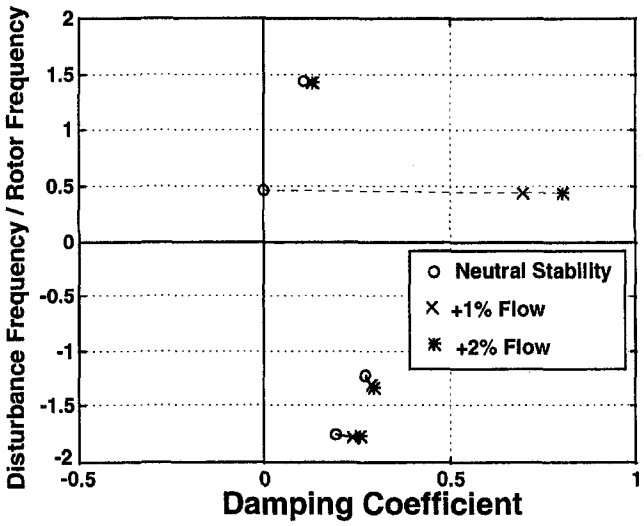

Fig. 10 Linear analysis of the first circumferential spatial harmonic showing eigenvalue trajectories as the compressor is throttled toward instability at the part-speed operating condition

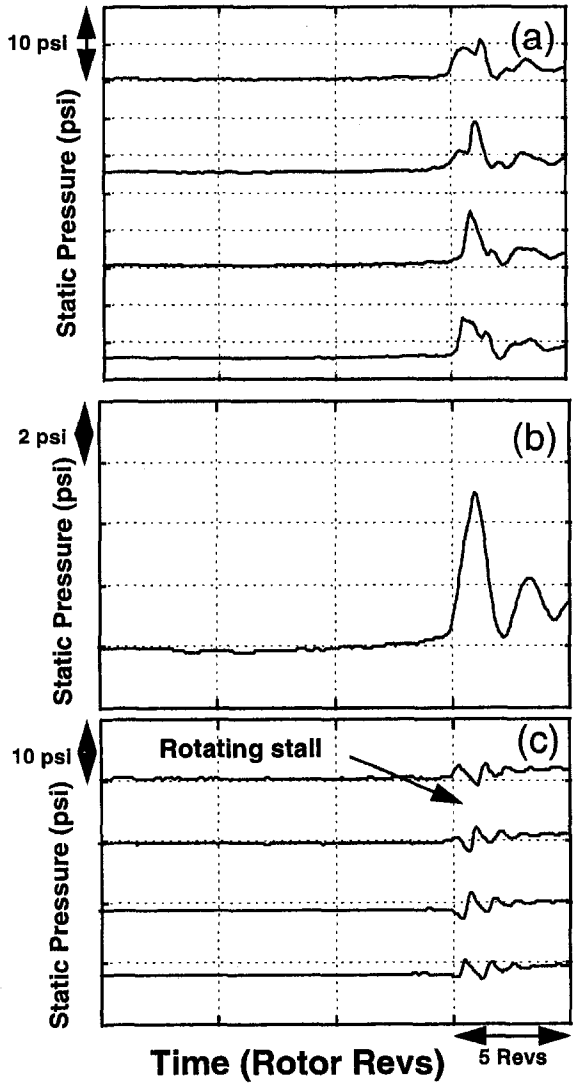

Fig. 11 Simulation results (design speed): (*a*) four static pressure traces equally spaced circumferentially around the compressor inlet (offset represents circumferential spacing); (*b*) planar component of inlet static pressure; (c) rotating component of inlet static pressure

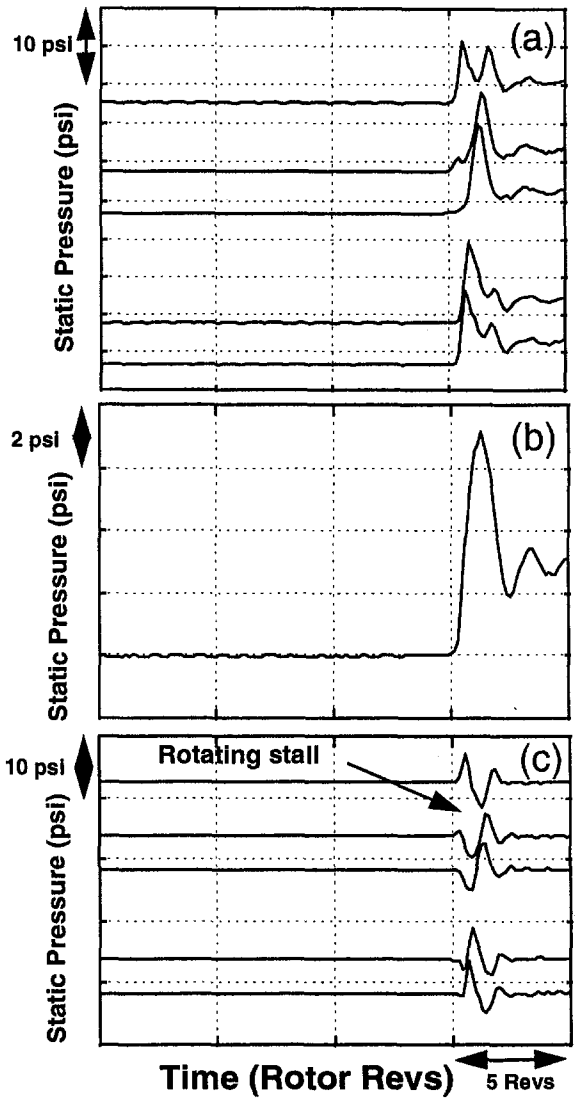

Fig. 12 Experimental data (design speed): (*a*) five static pressure traces spaced circumferentially around the compressor inlet (offset represents circumferential spacing); (*b*) planar component of inlet static pressure; (*c*) rotating component of inlet static pressure

damped first, and is therefore responsible for the system becoming unstable. This is consistent with the result of the nonlinear dynamic simulation, which shows a rapid growth of a rotating disturbance at a fraction of the rotor speed as the compressor approaches the instability condition.

The compressor stability behavior at the design speed will now be discussed. The results are presented in a way similar to those at part speed. The pressure traces showing the large-amplitude instability at the compressor inlet are presented for the simulation in Fig. 11(*a*) and for the experiment in Fig. 12(*a*). The planar and rotating components of the inlet disturbances are shown in subplots (*b*) and (*c*) for each figure. As in the part-speed case, both planar and rotating disturbances are present during the instability inception process and both appear to originate simultaneously. The signature of the planar disturbance is similar to the part-speed case, except that the initial spike in this case is much larger in amplitude. The spike is again followed by an acoustic oscillation of the fluid in the compressor duct. The rotating disturbance exists for a very short time coincident with the initial part of the surge cycle. The pressure traces at the fourth stage (Fig. 13) again show the existence of rotating stall prior to the final surge event both in the simulation and in the experiment as was the case at the part-

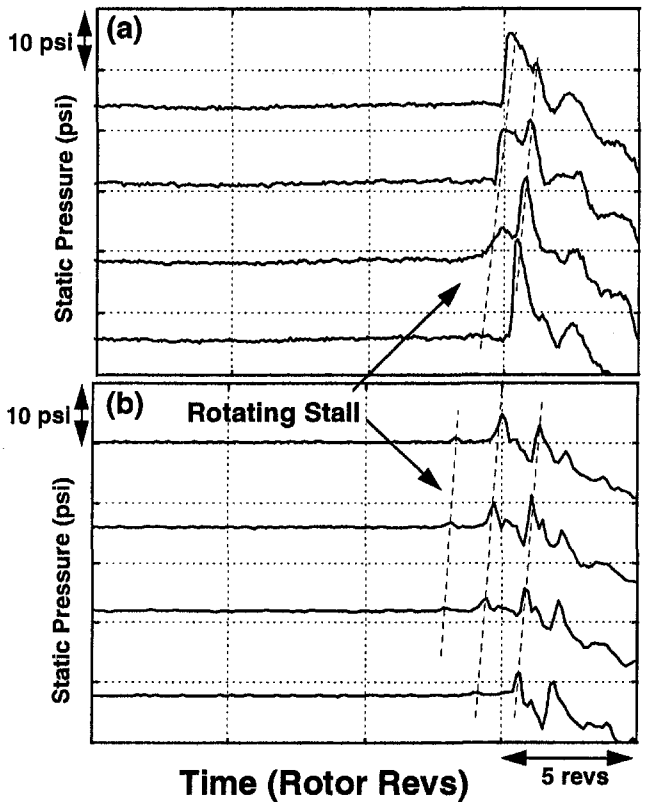

Fig. 13 Static pressure traces at the fourth stage of the compressor showing the evolution of rotating stall before the surge event at the design speed of the compressor: (*a*) simulation, (*b*) experiment

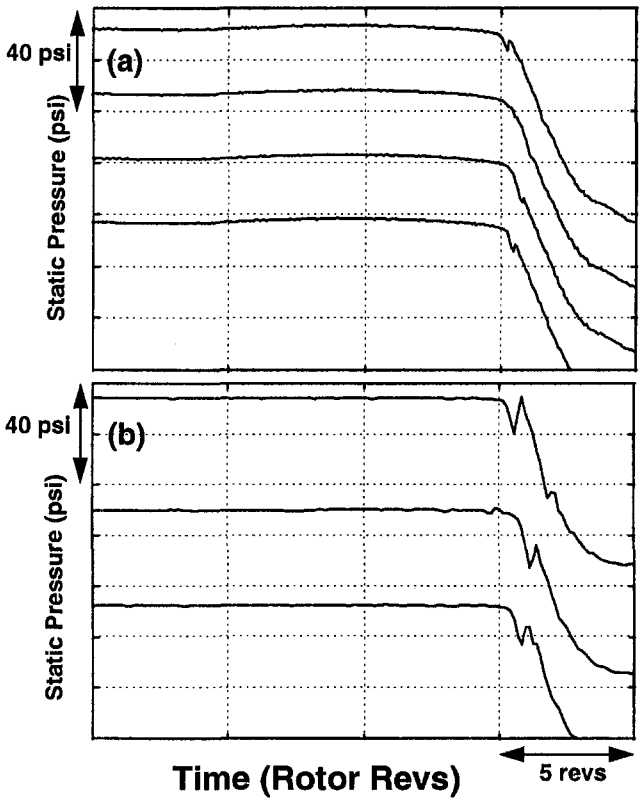

Fig. 14 Static pressure traces at the exit of the compressor showing the surge event at design speed: (*a*) simulation, (*b*) experiment

speed operating condition. The pressure traces at the exit of the compressor (Fig. 14) also show the development of rotating stall prior to surge.

It is evident from the results that have been presented thus far that the instability events at part and design speeds are qualitatively similar, even though at part speed, rotating stall is predicted to be the limiting instability, while at design speed, surge is predicted to be the limiting instability. This implies that it is difficult from experimental data alone to determine whether surge or rotating stall is the limiting instability. The axial blade loading distribution seems to be an important factor in determining the limiting instability since it changes with speed and with geometry, and is currently under investigation.

The FFTs of the simulation results, which show the development of small amplitude planar disturbances (Figs. 15(*a*, *b*)) prior to instability, indicate a strong oscillation at around 10 percent of rotor frequency. This oscillation corresponds to the Helmholtz mode of the compression system. This oscillation is not as well defined in the experimental data (Figs. 16(*a*, *b*)). The FFT of the rotating disturbance for the simulation (Fig. 15(*c*)) shows peaks around −100, 50, and 100 percent of rotor frequency. The peak at −100 percent of rotor frequency is not very well defined but the peaks at 50 and 100 percent grow significantly as the compressor approaches the instability condition. The FFT for the rotating component of the experimental data (Fig. 16(*c*)) is less clear. A strong peak can be seen developing at around 120 percent of rotor frequency, and a peak can be seen growing at 50 percent of rotor frequency as the compressor approaches instability.

The results of the linear analysis for this are shown in Figs. 17 and 18. The analysis of the zeroth spatial harmonic shows the "surge" or "Helmholtz" mode of the compression system becoming unstable first. This result corresponds with the nonlinear simulation, which shows a low-frequency planar oscillation growing as the instability condition is approached. The surge oscillation is not clearly present in the experimental data. A possible reason for this discrepancy is that the mean flow compressor performance on which the analytical models are dependent might not represent the true axial blade loading distribution. The two-dimensional linear analysis shows eigenvalues approximately at the frequencies corresponding to the peaks of the FFTs of the nonlinear simulation.

While these results are representative of the compressor behavior at the conditions that were presented, it should be noted that the compressor instability behavior can be dependent on

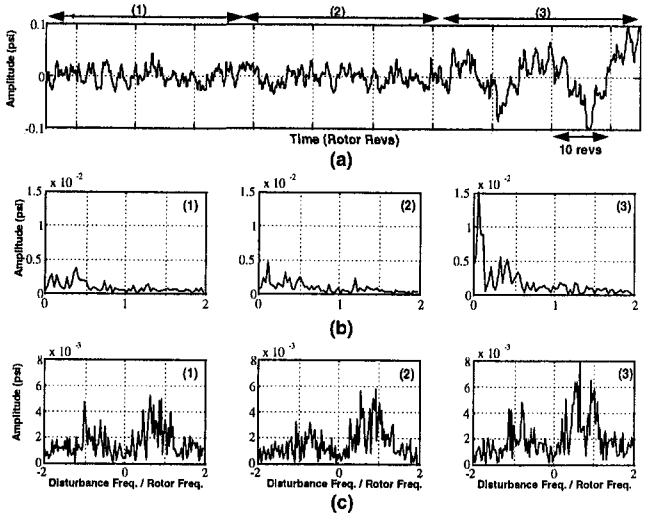

Fig. 15 Simulation results (design speed): (*a*) planar disturbances at the compressor inlet; (*b*) frequency content of planar disturbances; (*c*) frequency content of rotating disturbances

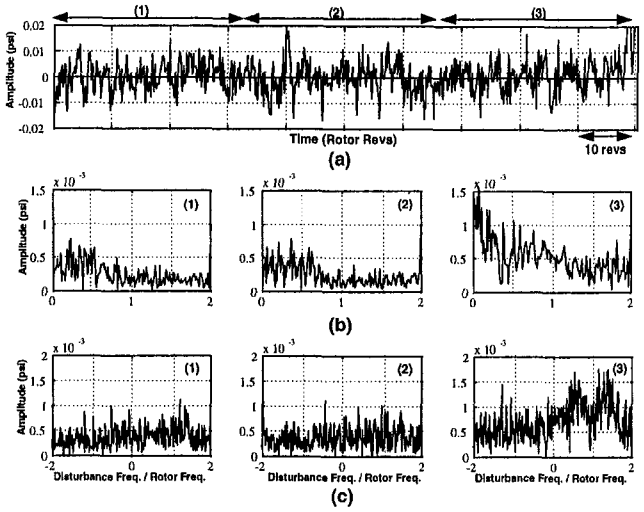

Fig. 16 Experimental results (design speed): (*a*) planar disturbances at the compressor inlet; (*b*) frequency content of planar disturbances; (*c*) frequency content of rotating disturbances

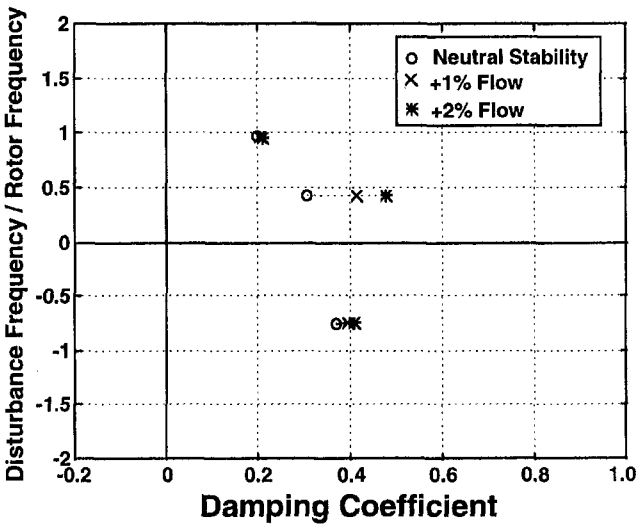

Fig. 18 Linear analysis of the first circumferential spatial harmonic showing eigenvalue trajectories as the compressor is throttled toward instability at the design speed of the compressor

compressor speed, geometry, and stage loading distribution through the compressor. The pressure signatures at various axial locations change, for example, when variable vane schedules are changed even at a fixed speed. This is due to the fact that the damping of the various modes of the compression system is dependent on the loading distribution through the compressor.

Conclusions

A nonlinear two-dimensional compressible simulation technique has been developed to study instability inception in high-speed multistage axial-flow compressors. The assumptions used in the nonlinear analysis are essentially the same as those in the linear compressible model developed previously, except that nonlinear effects are no longer ignored. The solution method employed has an advantage in that it allows simulations to be performed at any spatial resolution desired by increasing the computational grid density without code modification. The compressor blade rows are modeled as semi-actuator disks with the flowfields within the blade passages described by the one-dimensional unsteady Euler equations. The inlet duct, inter-blade-row spaces, and exit duct are described by the two-dimensional unsteady Euler equations. Real flow effects such as viscous losses and blade row exit deviation angles are described by an empirically based model currently used in the aircraft engine industry. The dynamic simulation model has been shown to capture the essential features of instability inception for a high-speed eleven-stage compressor.

The analysis of instability inception indicates the presence of both rotating stall and surge at the compressor inlet. The rotating disturbance at inception has a frequency at around 40 percent of the rotor frequency. The pressure signature within the compressor indicates that the cause of the instability is rotating stall since it can be observed well before surge is induced. A detailed analysis of the period before instability inception indicates the presence of both planar and rotating disturbances, which grow in amplitude as the compressor is throttled toward the instability condition. The simulation results and experimental data show similar behavior, and the pressure signature observed can be explained with the aid of results from a linear model of the compression system.

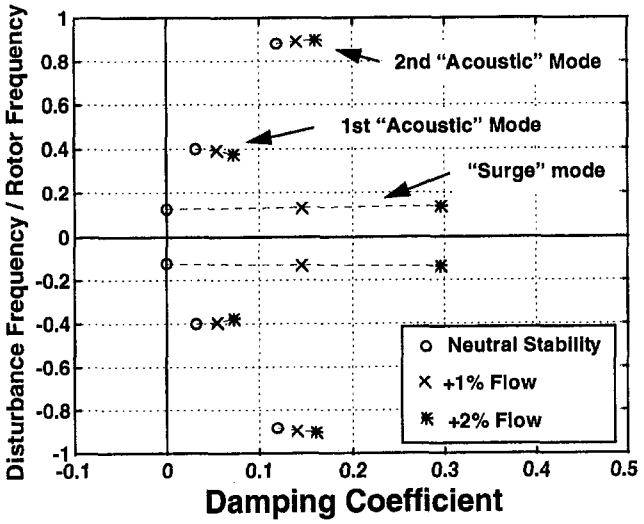

Fig. 17 Linear analysis of the zeroth spatial harmonic (planar modes) showing eigenvalue trajectories as the compressor is throttled toward instability at the design speed of the compressor

References

Alexandrov, V. G., Grin, V. T., and Shironosov, V. A., 1995, "Simulation and Active Control of Unstable Regimes in Air-Breathing Engine Elements," AIAA Paper No. 95-2364.

Bonnaure, L. P., 1991, "Modelling High Speed Multistage Compressor Stability," M.S. Thesis, Department of Aeronautics and Astronautics, MIT.

Boris, J. P., and Book, D. L., 1976, "Solution of the Continuity Equation by the Method of Flux-Corrected Transport," *Methods in Computational Physics,* Vol. 16, pp. 85–129.

Boris, J. P., Gardner, J. H., Oran, E. S., Guirguis, R. H., and Patnaik, G., 1987, "LCPFCT—Flux-Corrected Transport for Generalized Continuity Equations," NRL Memorandum Report, Naval Research Laboratory.

Day, I. J., and Cumpsty, N. A., 1978, "The Measurement and Interpretation of Flow Within Rotating Stall Cells in Axial Compressors," *Journal of Mechanical Engineering Sciences,* Vol. 20, pp. 101–114.

Day, I. J., Greitzer, E. M., and Cumpsty, N. A., 1978, "Prediction of Compressor Performance in Rotating Stall," ASME *Journal of Engineering for Power,* Vol. 100, pp. 1–14.

Day, I. J., and Freeman, C., 1994, "The Unstable Behavior of Low and High-Speed Compressors," ASME JOURNAL OF TURBOMACHINERY, Vol. 116, pp. 194–201.

Emmons, H. W., Pearson, C. E., and Grant, H. P., 1955, "Compressor Surge and Stall Propagation," *ASME Transactions,* Vol. 79, pp. 455–469.

Eveker, K. M., Gysling, D. L., Nett, C. N., and Sharma, O. P., "Integrated Control of Rotating Stall and Surge in High-Speed Multi-Stage Compression Systems," ASME Paper No. 97-GT-352.

Feulner, M. R., Hendricks, G. J., and Paduano, J. D., 1996, "Modeling for Control of Rotating Stall in High-Speed Multistage Axial Compressors," ASME JOURNAL OF TURBOMACHINERY, Vol. 118, pp. 1–10.

Gallops, G. W., Roadinger, T. J., and French, J. V., 1993, "Stall Testing and Analysis of Two Mixed Flow Turbofans," ASME Paper No. 93-GT-62.

Greitzer, E. M., 1976, "Surge and Rotating Stall in Axial Flow Compressors: Part I—Theoretical Compressor System Model," ASME *Journal of Engineering for Power*, Vol. 98, pp. 190–198; "Part II—Experimental Results and Comparison With Theory," *ibid.*, pp. 199–217.

Greitzer, E. M., and Moore, F. K., 1986, "A Theory of Post-Stall Transients in Axial Compression Systems: Part II—Application," ASME *Journal of Engineering for Gas Turbines and Power*, Vol. 108, pp. 231–239.

Haynes, J. M., Hendricks, G. J., and Epstein, A. M., 1994, "Active Stabilization of Rotating Stall in a Three-Stage Axial Compressor," ASME JOURNAL OF TURBOMACHINERY, Vol. 116, pp. 226–239.

Hendricks, G. J., Bonnaure, L. P., Longley, J. P., Greitzer, E. M. and Epstein, A. M., 1993, "Analysis of Rotating Stall Onset in High Speed Axial Flow Compressors," AIAA Paper No. 93-2233.

Hoying, D. A., 1993, "Stall Inception in a Multistage High Speed Axial Compressors," AIAA Paper No. 93-2386.

Ishii, H., and Kashiwabara, Y., "A Numerical Study of Surge and Rotating Stall in Multistage Axial Compressors," AIAA Paper No. 92-3193.

Koff, S. G., and Greitzer, E. M., 1984, "Stalled Flow Performance for Axial Compressors—I: Axisymmetric Characteristics," ASME Paper No. 84-GT-93.

Longley, J. P., 1994, "A Review of Nonsteady Flow Models for Compressor Stability," ASME JOURNAL OF TURBOMACHINERY, Vol. 116, pp. 202–215.

Mazzawy, R. S., 1977, "Multiple Segment Parallel Compressor Model for Circumferential Flow Distortion," ASME *Journal of Engineering for Power*, Vol. 99, No. 2.

Moore, F. K., and Greitzer, E. M., 1986, "A Theory of Post-stall Transients in Axial Compressors: Part 1—Development of the Equations," ASME *Journal of Engineering for Gas Turbines and Power*, Vol. 108, pp. 68–76.

Nagano, S., Machida, Y., and Takata, H., 1971, "Dynamic Performance of Stalled Blade Rows," Japan Society of Mechanical Engineering Paper JSME 11, presented at the Tokyo Joint International Gas Turbine Conference, Tokyo, Japan.

Oran, E. S., and Boris, J. P., 1987, *Numerical Simulation of Reactive Flow*, Elsevier.

Tryfonidis, H., Etchevers, O., Paduano, J. D., Epstein, A. H., and Hendricks, G. J., 1995, "Prestall Behavior of Several High-Speed Compressors," ASME JOURNAL OF TURBOMACHINERY, Vol. 117, pp. 62–80.

The Simulation of Turbomachinery Blade Rows in Asymmetric Flow Using Actuator Disks

W. G. Joo[1]

T. P. Hynes

Whittle Laboratory,
University of Cambridge,
Cambridge, United Kingdom

This paper describes the development of actuator disk models to simulate the asymmetric flow through high-speed low hub-to-tip ratio blade rows. The actuator disks represent boundaries between regions of the flow in which the flow field is solved by numerical computation. The appropriate boundary conditions and their numerical implementation are described, and particular attention is paid to the problem of simulating the effect of blade row blockage near choking conditions. Guidelines on choice of axial position of the disk are reported. In addition, semi-actuator disk models are briefly described and the limitations in the application of the model to supersonic flow are discussed.

1 Introduction

An installed civil turbofan engine is often subjected to a nonuniform inlet flow. This may be due to asymmetry in the design of the intake, present at all flight conditions, or it may be due to partial separation of the flow in the vicinity of the intake lip at high incidence. In addition, further asymmetric flow is introduced by the substantial blockage of the bypass exit ducting by the pylon and other core engine support struts. The effect of this nonuniform flow on engine performance and stability is a matter of some concern to manufacturers. The set of experiments performed by Hodder (1981) indicate that the intake and engine flow fields are often strongly coupled and cannot be considered to be independent. Despite this, there are, as yet, few reported theoretical methods of prediction, or experimental procedures for correlation, to resolve the engine and intake flow field coupling issue. As a result, the design of the intake and installation and that of the engine still take place to a large extent separately.

Any model for use in this context must comprise two parts: a method for calculating the intake flow field, and a reliable way of estimating fan performance in asymmetric flow. Flow field calculation methods for intakes, although not without need for improvement, are reasonably well developed, and it is the estimation of fan performance that is the more pressing issue.

A characteristic feature of the flow field asymmetry associated with intakes and pylons is that the circumferential length scales of interest are long when compared with a blade pitch. Most of the models applicable to low hub-to-tip ratio blade rows developed to date exploit this feature and use an actuator disk or a semi-actuator disk blade row model. The essential idea is that the local blade performance at each radius and at each circumferential location can be related to the performance that the blade would exhibit in clean flow when subjected to the same inlet conditions. Simple corrections to try and account for the effects of unsteady flow in the case of rotors can also be incorporated.

The earliest low hub-to-tip actuator disk model, in which the presence of a blade row is simulated by a discontinuity in the flow field, was developed by Dunham (1965). This applied to incompressible, free vortex flow through blade rows installed in constant radius ducts, and, in addition, was restricted to small (linearized) levels of flow asymmetry. Under these conditions it is possible to solve the flow field equations in terms of a series of Bessel functions. This theory was later extended by Hawthorne et al. (1978). Mitchell (1979) compared predictions of the results predicted by this model with the test results of Rizvi (1977) for the case of a free vortex rotor with a distorted inflow. He obtained good agreement when the rotor was operating close to its design flow coefficient, but the agreement became poor as the flow coefficient was reduced (and the flow behind the rotor ceased to approximate a free vortex).

Semi-actuator disk models simulate rotor passages as one-dimensional channels. The flow within each passage is usually solved for using one-dimensional, unsteady, linearized equations of motion. These models account for the effects of inertia of the fluid within the blade passage, which are associated with inviscid unsteady effects. Semi-actuator disks were first developed for use in predicting the passage of sound waves through high hub-to-tip ratio blade rows (Kaji and Okazaki, 1970). An extension of this type of model to three dimensions was made by Billet et al. (1988). They solved the Euler equations in regions external to blade rows by a flux-splitting (McCormack) method and modeled blade rows by a simple form of semi-actuator disk. Within each blade row, the flow was assumed to follow a series of one-dimensional channels. These are formed by the blade profile and by the clean flow meridional stream surfaces (obtained from a throughflow calculation). The flow is further assumed to follow this direction even in distorted flow. The local blade performance and corrections for unsteady flow are applied in exactly the same way as for the two-dimensional actuator disk models described above.

Joubert (1990) has compared the results of calculations using the method developed by Billet et al. with the results of experiment. The test case was a relatively high hub-to-tip ratio three stage compressor, tested with inlet total pressure distortion. Excellent agreement was demonstrated between the experimental and calculated results. This approach does, however, need more empirical input than is sometimes available. Because the flow within blades is modeled in a one-dimensional manner, it is difficult to frame sufficient boundary conditions at blade exits to match to the three-dimensional flow downstream. In particular, it is not easy to pose a boundary condition for the radial

[1] Current address: Department of Mechanical Engineering, Yonsei University, Seoul 120-749, Korea.

Contributed by the Turbomachinery Committee for publication in the JOURNAL OF TURBOMACHINERY. Manuscript received by the Turbomachinery Committee May 15, 1995. Associate Technical Editor: R. A. Delaney.

velocity. Joubert proceeded by using measured values of static pressure at the compressor exit to calculate radial velocities there. It is hard to gage how this expedient affected the agreement between calculation and experiment. For high hub-to-tip ratio blade rows, one might circumvent the need for it by neglecting radial variations, but it is not obvious that the model could be applied with any degree of confidence to calculations through low hub-to-tip ratio blade rows.

When operating with a nonuniform inlet flow, rotor blades experience an unsteady flow field and this unsteadiness affects the local pressure rise. Moore (1984) argued that most of the physics of asymmetric, unsteady flow is retained if the *unsteady* aspects of the flow are treated as inviscid, even if viscous effects are important in the flow as a whole. When semi-actuator disk models are applied to low-speed flows (and the only inviscid unsteady effects are those due to inertia), a single parameter, λ, a measure of the inertia of the flow in rotor passages, emerges. Hynes and Greitzer (1987) applied such models to the problem of loss of compressor stability margin due to inlet total pressure distortion. Their predictions successfully reproduced correlation techniques that have been shown to be successful (Hercock and Williams, 1974) for a wide variety of compressors. Longley (1988) performed a series of experiments that verified that a model of the λ type is adequate to predict the unsteady performance of low-speed, high hub-to-tip ratio rotors in circumferentially distorted flow.

Using this model, Joo (1994) showed that the unsteady effects on the compressor performance for a single low hub-to-tip ratio rotor operating in low-speed flow at the design operating condition were small. For most of the results of the present study, unsteady effects are neglected. Some evidence will be provided in a companion paper (Joo and Hynes, 1997) that the inclusion of unsteady effects using a λ type approach makes little difference to the results presented in these papers.

The success of Billet et al. (1988) and Joubert (1990) determined that it is the difficulty of finding analytic solutions to the *flow field* equations that limited the applicability of this type of model to the few special cases studied by the early workers. In particular, if one is willing to solve the flow field equations numerically, then the restrictions to parallel annuli, free vortex, incompressible, and small distortion levels no longer need apply. This paper describes a method for calculating fan and intake flow field interaction in civil turbofan engines, in which the flow field equations are solved numerically in regions outside blade rows and the blade rows are replaced by actuator disks. An application to a complete engine installation and comparison with the results of other models is the subject of the companion paper (Joo and Hynes, 1997).

2 Typical Problem

The method we are discussing is a general one, but in order to proceed further with its description and to explore the various issues involved with its implementation, it is necessary to have a specific problem in mind. Figure 1 shows a cross section of an under-wing mounted, modern high-bypass-ratio turbofan, operating behind an inlet simulator. This inlet simulator consists of essentially three parts. The part immediately upstream of the fan has the same shape as a proposed inlet design. In order to take account of the upstream potential effect that the aircraft wing has on the flow ahead of the engine intake, the centerline of the inlet is drooped relative to the engine centerline. In addition, the inlet is nonaxisymmetric, being thicker at the bottom to allow for the effect of flow incidence onto the inlet.

Upstream of the part of the simulator that models the inlet, a section is inserted to model part of the streamtube, which is estimated to be captured by the inlet at cruise conditions. The final, furthest upstream section of the simulator is chosen to try and ensure a smooth nonseparating flow from ambient conditions.

The use of such a simulator enables the effect of the inlet at cruise to be tested using static conditions. Accurate simulation of cruise conditions using such an arrangement as sketched in Fig. 1 is a difficult thing to get right without some degree of trial and error. Subsequent experience indicated, however, that this example was reasonably successful, producing a potential flow ahead of the engine position, which was similar in *pattern* to that in the true intake, but with a nonuniformity that was a little larger in *magnitude.*

The measured total pressure downstream of the fan is shown in Fig. 2. Our major interest is the circumferential asymmetry in the flow and, to display this in a simple manner, the values shown are percentage variations about a mean, the mean representing the average value at that particular radius. The asymmetry in the pattern is caused by the nonaxisymmetric inlet geometry and by the upstream effect of the pylon, which blocks a significant portion of the top part of the bypass ducting. Of note is the large size of the circumferential variation and the fact that there is significant asymmetric flow even in the hub region downstream of the fan.

3 Actuator Disk Boundary Conditions

Figure 2 showed that the length scales that are likely to characterize the flow interaction of fans and intakes are much larger than a blade pitch. In addition, it will emerge that some of the compatibility issues do not directly involve the flow within the blade rows themselves. In these circumstances an actuator disk model for a blade row would seem a useful first approximation.

We will consider, for simplicity of the description of an actuator disk model, an intake and rotor flow field alone, shown schematically in Fig. 3. The fan is contracted to a plane actuator disk, located at some convenient axial position, for example, at the trailing edge of the blades, or at the midchord plane. The flow fields upstream and downstream of the blade row are coupled by boundary conditions imposed across the actuator disk to represent the fan performance. One major feature of this model is that the fan is replaced by an actuator disk within the *true annulus.* As a result, the radial redistribution of the flow that would have occurred within the blade row in a real fan takes place outside the blade. This introduces an error with length scale of the order of an axial blade chord and one might expect that errors of this length scale hold only secondary interest in the study of intake/engine flow field coupling. We will address this issue in a later section.

Five matching conditions are required across an actuator disk, corresponding to the five independent flow variables in the equations of motion. The boundary conditions used in the present model, which are applied at each radial location and at each circumferential position, are:

(i) conservation of mass,
(ii) conservation of radial momentum,
(iii) conservation of rothalpy,
(iv) relative exit flow angle specified,
(v) entropy rise (or stagnation pressure change) specified.

The first and third conditions are obvious consequences of neglecting the capacity of the blade row to store mass and energy. The second condition results from neglecting the radial force exerted by the blades on the flow. If a model of the radial force on the flow due to the blades is available, then this can easily be incorporated into this condition. The last two conditions are associated with flow variables, which are discontinuous across the actuator disk. Blade performance characteristics (loss and deviation) are used to provide the data necessary for those conditions, and these can be considered as functions of local incidence and local Mach number.

The flow angle at exit to the actuator disk could be taken directly from the values of the measured or calculated flow

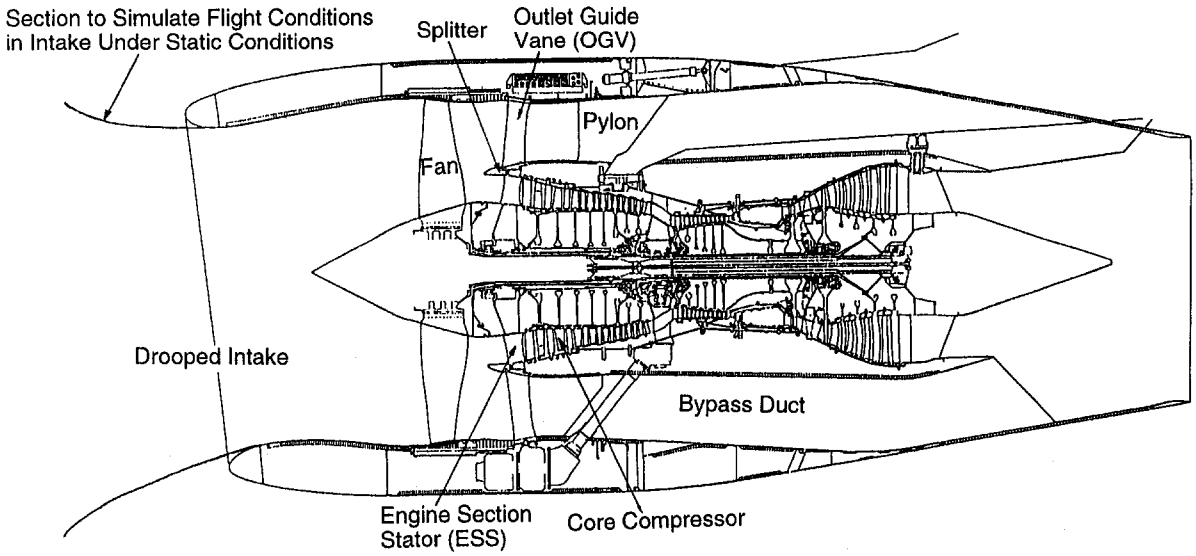

Fig. 1 Schematic of turbofan engine with inlet simulator

angle at the fan trailing edge. If the radius of the annulus varies significantly through the blade row, as in the fan of turbofan engines, the work done by the disk is influenced somewhat by the disk location when the true blade exit flow angles are used. In order to reproduce the correct work distribution, the true flow angle must be corrected slightly. One approximate method for making this correction is presented in the appendix.

There are a number of issues associated with the integration of these actuator disk boundary conditions into a numerical model. These include the fact that the primary flow variables used in most numerical calculation methods are not the same as those that appear naturally in the actuator disk conditions and, indeed, there is a nonunique relationship between them. The problems that this causes are, we believe, common to all numerical implementations but, in order to discuss them, it is necessary to give some of the details of the numerical scheme we used.

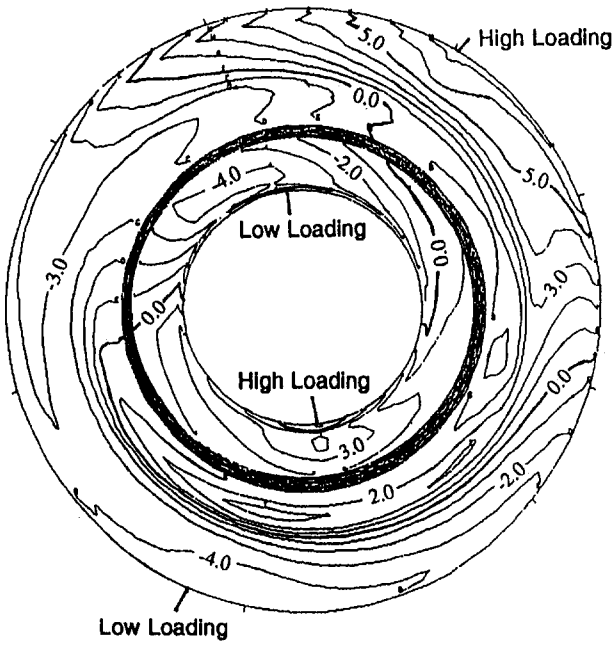

Fig. 2 Measured circumferential variations in total pressure behind fan operating with inlet simulator

4 Computational Method for Flow Field Regions

A method for calculating the flow fields upstream and downstream of the fan shown in Fig. 3 are based on the three-dimensional Navier–Stokes solver developed by Dawes (1986, 1988). As this code was written for the calculation of the flow in one blade passage of a single blade row, simple modifications and extensions were made. The basic numerical algorithm is relatively well known so only a brief description is given here.

Equations of Motion and Solution Algorithm. The equations to be solved are the three-dimensional Reynolds-averaged Navier–Stokes equations in conservation form. These equations are written in the *absolute* frame using a cylindrical coordinate system, because the distorted flow field is assumed to be steady in this frame. The equations are discretized on a set of control volumes, formed by a simple, structured **H**-grid construction. Flow variables are stored at cell centers and these are considered as *average* values of the flow variables over the control volume rather than values at a point at the center of a cell. Values on cell faces for flux evaluation are thus found by a simple average of the cell variables on either side of the face with second-order accuracy on smoothly varying grids.

There are potential problems raised by the singular points at zero radius in a cylindrical coordinate system, but these singular points pose few problems for cell centered finite volume meth-

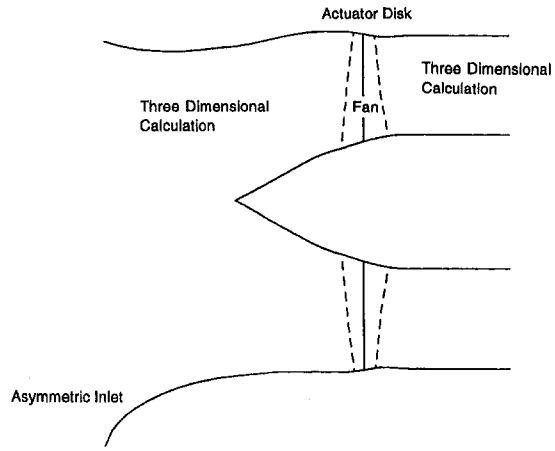

Fig. 3 Actuator disk model of a rotor for asymmetric flow

ods, since flow variables need not be defined there. Only the evaluation of fluxes through the face located at zero radius is required to solve the discretised equations of motion. These fluxes are set to zero because the face area is zero.

The size of grids near boundaries used for the calculation is too large in comparison with a boundary layer thickness to resolve annulus boundary layers. Therefore, although the equations solved are the Navier–Stokes equations, the calculation becomes effectively an inviscid one.

The discretized set of equations of motion is solved by time marching. The basic solution algorithm consists of a two-step explicit and one-step implicit scheme derived as a preprocessed simplification of the Beam–Warming algorithm; detailed discussions can be found in Dawes (1986, 1988).

Inlet and Outlet Boundary Conditions. The upstream end of the flow domain is some distance upstream of the first row where the influence of the presence of the engine is assumed to be neglected. Values of stagnation pressure, stagnation temperature, meridional pitch angle (i.e., $\tan^{-1}(V_r/V_x)$) and swirl angle (i.e., $\tan^{-1}(V_\theta/\sqrt{V_r^2 + V_x^2})$) are specified over this inlet plane. Static pressure is extrapolated from the interior domain with zero gradient to complete the inlet boundary condition.

The specification of the downstream boundary conditions requires a little care. A single boundary condition involving some prescription for the static pressure at the downstream end of the calculation domain is usually applied. This is usually a good approximation for the flow through single blade passages. The single blade passage flow is almost invariably considered as circumferentially uniform at the exit to the calculation domain and, in addition, for swirling flow it is also assumed to be in radial equilibrium. The only circumferential static pressure variation present has a length scale of at most *one blade pitch* and variations, which are made up of high order circumferential harmonics that decay axially in a short distance. Any interaction of these static pressure variations with the downstream boundary usually has a negligible effect on the flow in the blade row.

If the farthest downstream blade row in the present type of calculation (the flow field interaction of fans, stators, and their installation) is a stator with a more or less axial exit flow, then uniform static pressure is a reasonable exit condition. If the farthest downstream component is a rotor, the static pressure variations have considerable *low order* circumferential harmonics present, which persist a long way downstream. Radial equilibrium is thus not appropriate as an outlet boundary condition, and its imposition, even at some far distant downstream location, caused considerable problems with numerical convergence to a steady solution. A simple, new approach was made to handle such a complicated boundary condition in the present study.

When the furthest downstream blade row is a rotor, the calculation domain is imagined to be terminated at the downstream end by a gauze-honeycomb. This was chosen since a gauze-honeycomb is an almost realizable device, which will turn the flow at each radial and circumferential position to the axial direction. The static pressure downstream of the honeycomb will thus be uniform. The gauze-honeycomb also has throttlelike pressure drop characteristics and this might be expected to have a benign effect on the transient aspect of the convergence process. The presence of such a device will, of course, affect the flow upstream of the outlet boundary, so that the outlet boundary should still extend to a sufficient length downstream of the fan to ensure that the flow through the rotor itself is not affected.

The pressure drop through a gauze-honeycomb can be expressed in the form

$$P_{01} - p_2 = \kappa \rho V_x^2 \tag{1}$$

where κ is the loss coefficient and the subscripts 1 and 2 refer to the upstream and downstream sides, respectively. There is no advantage to be gained in modeling the flow particularly accurately here and Eq. (1) can be treated in an incompressible manner. The equation for the axial velocity in each grid cell at the outlet boundary, $j = JM - 1$, is written,

$$(V_x)_{JM-1} = \alpha\sqrt{(P_0)_{JM-1} - p_2} \tag{2}$$

where j is used to number cells in the axial direction. The static pressure, p_2, downstream of the gauze-honeycomb can be arbitrarily set to atmospheric pressure. The value of the "throttle" coefficient, α, is specified and effectively determines the operating point of the fan.

This throttlelike outlet boundary condition is appropriate to the outlet boundary condition of an isolated rotor. A real turbofan engine has components such as a pylon or core engine downstream of the outlet boundary, which can influence the inlet and engine flow field interaction. The outlet boundary conditions for simulating those downstream components are described in a separate paper on the application of this method (Joo and Hynes, 1997).

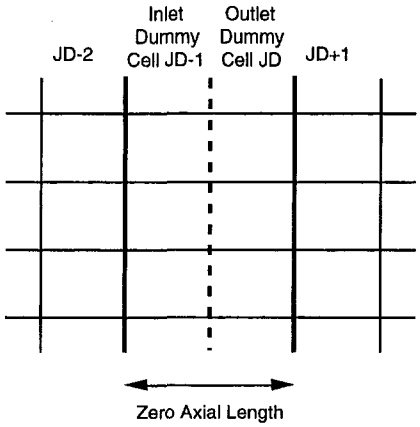

Fig. 4 Two sets of dummy cells representing an actuator disk

5 Numerical Implementation of the Actuator Disk Boundary Conditions

The actuator disks used for the calculations presented in this paper and the companion paper are often inclined to the axial direction. This causes a complication of detail, rather than of principle, and the description for noninclined disks is presented here. To facilitate the application of the actuator disk boundary conditions, two sets of *dummy cells* are introduced upstream and downstream of the plane of the actuator disk. These dummy cells, which have zero axial length, are shown in Fig. 4. The cells with j less than or equal to $JD - 2$ and J greater than $JD + 1$ are treated as interior points of the upstream and downstream flow fields.

Natural Boundary Conditions. Various ways of implementing the actuator disk boundary conditions are possible, but two strategies proved of value (Joo, 1994). The first of these is to apply what might be termed "numerically natural" boundary conditions. The $JD - 1$ cell is treated as the farthest downstream cell of one flow field and the JD cell as the farthest upstream cell of the other. If the flow is subsonic in the direction normal to the actuator disk plane, there are four outgoing characteristics and one incoming characteristic at the actuator disk inlet ($JD - 1$ cell) and, on the other hand, one outgoing characteristic and four incoming characteristics at the disk outlet (JD cell). One variable, therefore, propagates upstream across the actuator disk and four variables downstream; these variables are to be found from the other flow fields using the actuator disk boundary conditions.

Static pressure is usually used as the variable propagating upstream, but an alternative is mass flux as long as the axial flow at the boundary is subsonic. Since one of the actuator disk boundary conditions involves local axial mass flux, ρV_x, directly it is more convenient to use mass flux as the one variable to pass to the upstream side of the disk. We shall see later that this also makes the handling of a choking blade section particularly easy. The remaining variables in each of the dummy cells are extrapolated from the interior domain to complete the boundary conditions at the actuator disk.

The nonchoking boundary conditions are, then, in detail:

(a) Inlet Dummy Cell

(*i*) Since cell face areas are equal,

$$(\rho V_x)_{JD-1} = (\rho V_x)_{JD+1} \tag{3a}$$

(*ii*) $$(V_r)_{JD-1} = 2(V_r)_{JD-2} - (V_r)_{JD-3} \tag{4a}$$

(*iii*) $(I)_{JD-1} = 2(I)_{JD-2} - (I)_{JD-3}$ where

$$I = c_p T + \frac{W^2}{2} - \frac{r^2\omega^2}{2} \tag{5a}$$

(*iv*) $$(rV_\theta)_{JD-1} = 2(rV_\theta)_{JD-2} - (rV_\theta)_{JD-3} \tag{6a}$$

(*v*) $s_{JD-1} = 2s_{JD-2} - s_{JD-3}$ where $s = \dfrac{p}{\rho^\gamma}$ (7*a*)

(b) Outlet Dummy Cell

(*i*) $$(\rho V_x)_{JD} = 2(\rho V_x)_{JD+1} - (\rho V_x)_{JD+2} \tag{3b}$$

(*ii*) $$(V_r)_{JD} = (V_r)_{JD-2} \tag{4b}$$

(*iii*) $$(I)_{JD} = (I)_{JD-2} \tag{5b}$$

(*iv*) The relative exit flow angle is assumed known. The circumferential velocity is defined from this angle

$$(V_\theta)_{JD} = (V_x)_{JD} \tan \beta_{JD} + r_{JD}\omega \tag{6b}$$

(*v*) The increase in entropy across the actuator disk is specified, so

$$s_{JD} = s_{JD-2} + s_{loss} \tag{7b}$$

Swapped Boundary Conditions. The idea of a "swapped" way of implementing the boundary conditions is to recast the first three boundary conditions equations, Eqs. (3), (4), and (5), in terms of fluxes of properties through the cell faces, represented by bold lines in Fig. 4. The boundary condition implying equal axial mass fluxes across these cell faces is, remembering that cell face areas are equal,

$$\frac{(\rho V_x)_{JD-2} + (\rho V_x)_{JD-1}}{2} = \frac{(\rho V_x)_{JD} + (\rho V_x)_{JD+1}}{2}$$

This will be satisfied *automatically,* at each time step, if we take as boundary conditions

$$(\rho V_x)_{JD-1} = (\rho V_x)_{JD+1} \quad \text{and} \quad (\rho V_x)_{JD} = (\rho V_x)_{JD-2} \tag{3c}$$

A similar treatment of the other flow variables, V_r and I, gives

$$(V_r)_{JD-1} = (V_r)_{JD+1} \quad \text{and} \quad (V_r)_{JD} = (V_r)_{JD-2} \tag{4c}$$

$$I_{JD-1} = I_{JD+1} \quad \text{and} \quad I_{JD} = I_{JD-2} \tag{5c}$$

This swapped boundary conditions proves to be a particularly convenient form for building in a correction to account for the effect of unsteadiness, as described in the companion paper (Joo and Hynes, 1997).

6 Calculation of Primary Variables for Dummy Cells

Equations (3)–(7) determine ρV_x, ρV_θ, V_r, I, and s for the two sets of dummy cells. These are the natural variables imposed by the actuator disk boundary conditions, but there is still the issue of how to recover the primary flow variables (ρ, ρV_x, $r\rho V_\theta$, ρV_r, ρE). The relationship between the two sets of variables follows from the definition of rothalpy:

$$I = \frac{\gamma}{\gamma - 1} s\rho^{\gamma-1} + \frac{1}{2}\{V_x^2 + (V_\theta - r\omega)^2 + V_r^2\} - \frac{r^2\omega^2}{2}$$

$$\text{where} \quad s = \frac{p}{\rho^\gamma}$$

This equation can be rearranged as

$$\frac{\gamma}{\gamma - 1} s\rho^{\gamma+1} + \frac{1}{2}(V_r^2 - 2r\omega V_\theta - 2I)\rho^2 + \frac{1}{2}\{(\rho V_x)^2 + (\rho V_\theta)^2\} = 0 \tag{8}$$

This is essentially *an equation for* ρ, as everything else in this equation is known from the five matching conditions.

Equation (8) usually has *two* positive solutions for density ρ, one corresponding to supersonic relative flow and one to subsonic. In addition, it is possible that, with the actuator disk variables determined in the manner outlined above (i.e., by mixing values from either side of the disk), there is *no* solution for ρ. This is especially true during the large initial numerical transient, when flow conditions upstream and downstream of the disk are greatly different to those pertaining to the final steady state. This problem is particularly acute for dummy cells on the downstream side of rotor tips, where the flow is expected to be close to sonic. During the initial transient, until the solution begins to settle down, the flow here is likely to be at times subsonic and at times supersonic.

The solution procedure just outlined attempts to satisfy all of the actuator disk boundary conditions exactly at each time step. The problem of which solution to choose and what to do when there is no solution can be bypassed if these boundary conditions are satisfied only approximately at each intermediate time step, provided they are satisfied exactly in the converged solution. Instead of using Eq. (8), then, an extrapolation from upstream is used as the first guess for the density in the inlet dummy cell and one from downstream for the outlet dummy cell. These first guesses are then refined once using Eq. (8). The errors that these approximations make for the density are monitored to ensure that they become zero as the solution converges. Having found the density in the dummy cells, the rest of the primary variables there follow in a straightforward manner.

7 A Choking Model

A high-speed blade row is choked at high mass flow conditions, but the simple actuator disk described in the previous section, which does not include an allowance for blade blockage, cannot predict this choked flow.

The choking of a particular blade section is usually associated with a local rapid rise in loss with small changes in mass flow. If the loss characteristics specified in the actuator disk boundary conditions exhibit a sufficiently steep rise in loss with incidence, the level of mass flow through any blade section can be controlled and thus solutions can be obtained that appear to have "choked" sections. However, these are very sensitive to the precise form chosen for this loss and an unacceptable amount of trial and error is necessary to simulate the true blade performance. Directly specifying the choking mass flow for any section is a much more feasible way of controlling the flow field.

A simple model for choking was incorporated into the actuator disk boundary conditions based upon two-dimensional flow into a choked blade section. A sketch of the flow through a

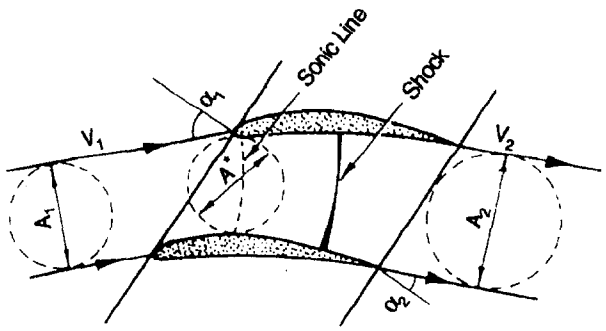

Fig. 5 Schematic of choked flow in a blade passage

two-dimensional choked blade passage is shown in Fig. 5. If the flow conditions are assumed uniform across the passage, the sonic line is straight and the effective throat area is simply calculated.

Neglecting any loss upstream of the sonic line, the maximum value of axial mass flux that this blade section will pass is given by

$$\rho_1 V_{x1}|_{\max} = \frac{F^* P_{01}^{\text{rel}}}{\sqrt{C_p T_{01}^{\text{rel}}}} \frac{A^*}{A_{x1}} \tag{9}$$

where A_{x1} and A^* are the streamtube axial cross-sectional area at actuator disk inlet and throat cross-sectional area, respectively, and where F^* is the appropriate compressible flow function.

For an actuator disk placed at the blade leading edge, Eq. (9) is directly applicable. If an actuator disk is placed at any other position, allowance must be made for the streamtube contraction and radial shift that takes place in that part of the actuator disk flow field that is downstream of the true blade leading edge. A first approximation would be to assume that the stream surfaces of the flow within this region follow grid lines. Under these assumptions the maximum mass flow through actuator disk is corrected by multiplying the ratio of the cell face area at actuator disk inlet to one at true blade inlet.

The actuator disk boundary conditions given by Eqs. (3*a*)–(7*a*) are modified by the inclusion of this simple blade choking model by, at each time step, comparing the disk inlet mass flux with the maximum that can be passed through this blade section as given by Eq. (9). If the mass flux is smaller than the choked flow, the inlet boundary conditions of the disk are applied exactly as described above. If not, the mass flow for the inlet dummy cell is fixed to the choked value and then flow variables in the exit dummy cell are calculated using this choked mass flow. In these circumstances, the static pressure there is extrapolated from the downstream flow field and the specified loss coefficient for this section is *not* applied.

8 Sensitivity of Actuator Disk Solutions

There are a number of other issues that must be addressed before a given blade row is simulated by an actuator disk. The first of these is the precise disk position. In order to explore this, a realistic fan geometry (typical of a modern high bypass engine) was chosen. Calculations were performed for clean inlet flow using a fully three-dimensional viscous calculation (BTOB3D—see Dawes, 1988). The purpose of the three-dimensional calculation was not to explore the accuracy of the calculation method but to generate comparison data against which to test the actuator disk model. Accordingly, no account was taken of the tip clearance and the flow on the hub and tip outside of the blade row was treated as inviscid. This three-dimensional calculation provides the loss and deviation at each blade section over a range of mass flows, which are used, when appropriate, as the "empirical" inputs to the actuator disk model.

A series of calculations was performed to obtain stagnation pressure rise characteristics for the fan in clean inlet flow using actuator disks located at the leading edge, the midchord, and the trailing edge. A throttle-like boundary condition is imposed at the outlet boundary and operating points throughout the fan operating range are obtained by setting various values of the throttle coefficient α, as given by Eq. (2). Relative flow angles specified at the disk exit are taken from the three-dimensional calculation of the fan operating *at design.* These flow angles are adjusted slightly for the three positions, by the process described in the appendix, to ensure equal work input at the design flow for each disk position.

Figure 6 shows the stagnation pressure rise characteristics calculated for the leading edge and midchord disk positions neglecting any changes in loss and deviation. The three-dimensional prediction is also shown in the figure and it is this that is assumed to represent the "true" fan performance.

The trailing edge disk (not shown) produced poor quality solutions over part of the span. When the annulus is contracting quite strongly in the region ahead of the disk, the upstream flow has as its "throat" the inlet to the actuator disk and a maximum mass flow can be set by choking of the *annulus.* If the maximum flow due to choking of the annulus is less than one due to choking of the blade estimated by Eq. (9), as the trailing edge disk case, axially supersonic flow appears over part of the span at the disk inlet. Then, the actuator disk boundary conditions, which are set up assuming subsonic axial flow, are not consistent with the flow field solution method and a solution of poor quality, exhibiting a considerable amount of odd and even decoupling of cell centered values or no solution is obtained.

Maximum mass flows predicted by the leading edge and midchord actuator disks are similar to that computed using the fully three-dimensional calculation. For closer investigation of the solutions, Fig. 7 shows the radial distribution of axial velocity at the trailing edge of the fan at the operating point marked with a "C" in Fig. 6. Calculation results using the leading edge actuator disk model are in good agreement with three-dimensional predictions, while the agreement of the midchord actuator disk prediction is not that good. This suggests that local maximum flow estimated approximately by Eq. (9) is not

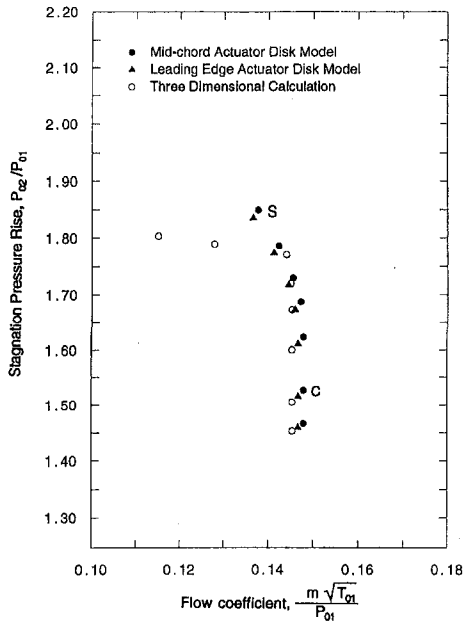

Fig. 6 Characteristics for disks at different positions with simple choking model

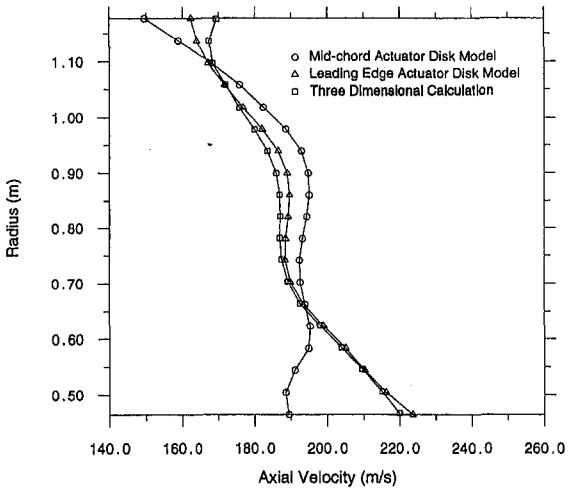

Fig. 7 Radial distribution of axial velocity near maximum flow for disks at different positions using simple choking model

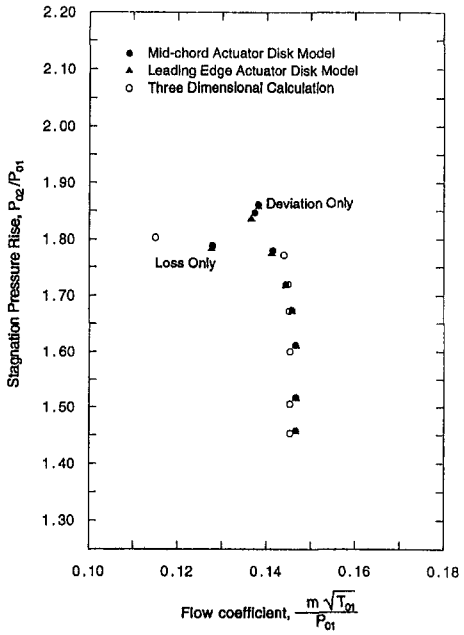

Fig. 9 With loss and deviation actuator disk simulates correct overall performance through flow range

accurate for actuator disks placed at any position other than leading edge. Guided by the radial distribution of mass flux taken from the three-dimensional solution for operating point C, it is relatively easy to define an "effective" throat area that ensures the "correct" radial distribution of flow properties for an actuator disk in any position. Results are shown in Fig. 8 for the case of actuator disks at leading edge and at midchord, and similar agreement is possible with care for the trailing edge case (not shown).

It appears that provided one is prepared to carry out a careful calculation of the flow field, it is possible to simulate a blade row accurately with an actuator disk in any position. There is, however, another aspect to this. The calculations presented in this section are for *axisymmetric* flow and the results indicate that the further rearward of the leading edge the disk is positioned, the higher the levels of actuator disk inlet axial Mach number and the more sensitive the solution becomes to the precise level of the radial distribution of blockage. When actuator disks are applied to calculations of the flow through fans operating with *nonaxisymmetric* inlets, when flow conditions are varying around the annulus, it is not obvious that the "effective" blockage would remain unchanged. For that case, there is no three-dimensional calculation to provide guidance, and the message of the results presented here is that the leading edge is the safest place to place the disk. This, unfortunately, is where the correlation of the blade exit flow angle, in the manner outline in the appendix, is largest.

Finally, the actuator disk model neglecting any change in loss and deviation predicts a higher pressure rise than three-dimensional prediction at the low mass flow conditions. This difference is principally attributed to loss and deviation produced at high blade incidence. Figures 9 and 10 show the effect of the loss and deviation on the flow through the actuator disk. The values of loss and deviation were taken from the three-dimensional calculation for the fan operating at point S close to stall in Fig. 6. (These also can be obtained by employing empirical loss and deviation models in the actuator disk model.) For this fan design, the deviation appears to make very little difference and the addition of loss ensures correct simulation of the flow through the fan with a disk in any position (the choking model is irrelevant in this flow range).

9 A Semi-actuator Disk Blade Row Model and Its Limitation

When a blade row is subjected to the asymmetric flow in which the length scale of flow variations is much longer than

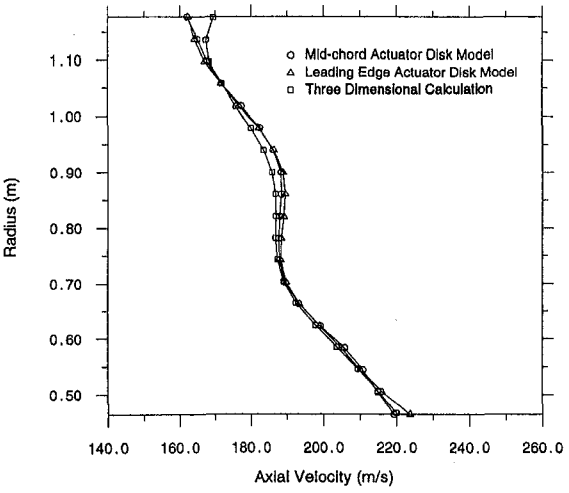

Fig. 8 Radial distribution of axial velocity near maximum flow for disks at different positions using effective area choking model

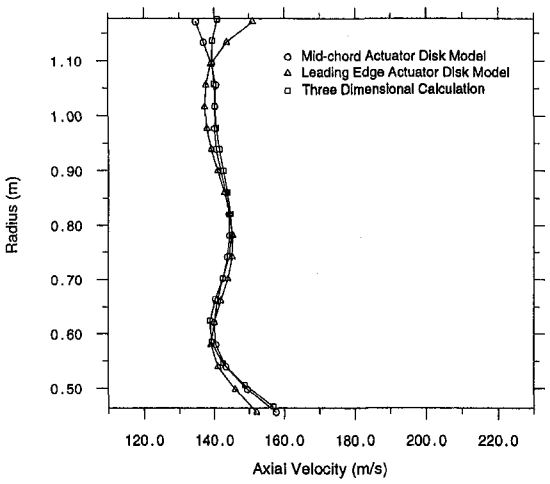

Fig. 10 Radial distribution of axial velocity near stall for disks at different positions

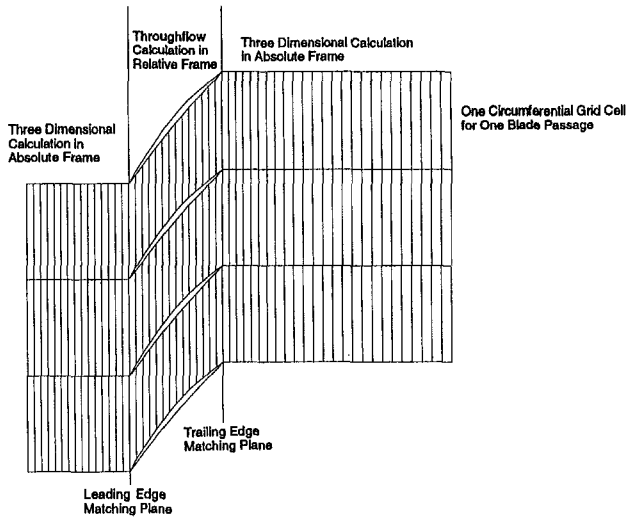

Fig. 11 Typical blade to blade grid used in semi-actuator disk blade row model

a blade pitch, the flow through blade passage could be approximated using semi-actuator disks as well as actuator disks. The semi-actuator disks model the flow field within blade passages and thus may resolve the problems that the actuator disk models inherently have by the contraction of the internal fan flow field to a disk of zero thickness, such as positioning of disks and choking relevant to a blade geometry. It was found, however, that the semi-actuator disk model has severe limitations in its capability to handle supersonic flow resulting in shock within blade rows and it is worth discussing these limitations to complete the description of an actuator disk model.

Figure 11 shows a typical finite volume grid on a streamwise surface constructed for the calculation using a semi-actuator disk model. The calculation domain is divided into flow fields outside the blade row and a flow field within blade passages by matching planes placed at the leading edge and trailing edge. The flow outside the blade row is solved in the *absolute* frame using the three-dimensional numerical method described in Section 4.

The flow within the blade passages is solved in the *relative* frame using a time-marching throughflow method. Since the variations over a pitch are neglected, a separate throughflow calculation can be performed for each blade passage of the row. Therefore, successive passages have slightly different inlet and exit conditions, compatible with the three-dimensional flow fields in the regions upstream and downstream of the blade row.

A throughflow calculation method using a time marching numerical technique was developed by some authors, for example, Spurr (1980), Dawes (1990), etc. In the present work, the throughflow model developed for simulating axisymmetric blade rows in a multistage environment by Dawes (1990) is adapted. This throughflow model represents an extension of a semi-actuator disk model that was used by Billet et al. (1988) in that the model not only allows the radial redistribution of the flow through a blade row but also models the presence of the blade.

The throughflow model assumes that the relative flow angle in the blade-to-blade plane is known and the flow is constrained to flow in this prescribed direction. This flow angle is usually chosen with the blade camber line direction and the body force, which represents the blade force necessary for turning the flow to this prescribed circumferential direction is determined from the angular momentum equation. Then circumferentially averaged passage equations including this body force are being solved and the detailed description is found in Dawes (1990).

The two flow fields are coupled by matching conditions imposed at the leading edge and trailing edge matching planes. The boundary conditions at the blade leading edge are that the fluxes of mass, rothalpy, radial momentum, and entropy are conserved. On the upstream side of the leading edge, tangential velocity is simply extrapolated, while the need for a boundary condition on flow angle downstream of the edge (i.e., inside the row) is removed using the assumption that the flow there lines up with the blades. This provides the requisite number of conditions for the two flow fields: five conditions on the flow outside of the row and four on the flow inside. At the blade trailing edge again conservation of the flux of mass, rothalpy, radial momentum, and entropy provide the four boundary conditions necessary for the flow within the passage, while the fifth condition for the downstream flow is provided by specifying the relative flow angle. The boundary conditions at the leading and trailing edges of the blades are implemented using dummy rows of cells in a similar way to that used for an actuator disk (see Section 5).

When the flow ahead of the rotor is nonuniform in the circumferential direction, the conditions at entry will appear unsteady when viewed from the rotating frame. The flow within the blade passages will, therefore, necessarily be unsteady. This unsteadiness is neglected here, and the flow in the rotating frame is assumed to adjust in a quasi-steady manner to the changes in inlet conditions.

A calculation was performed for the transonic fan considered in the previous section, which is operating at a mass flow close to design with uniform inlet flow. Great difficulty is experienced in getting the flow to settle down. Figure 12 shows contours of Mach number when the solution is closest to settling down during this transient phase. The two strong shocks that appear in the blade passage are not really physical. This is caused by the assumption used in the throughflow model that the flow is constrained to the blade camberline direction. When a shock is

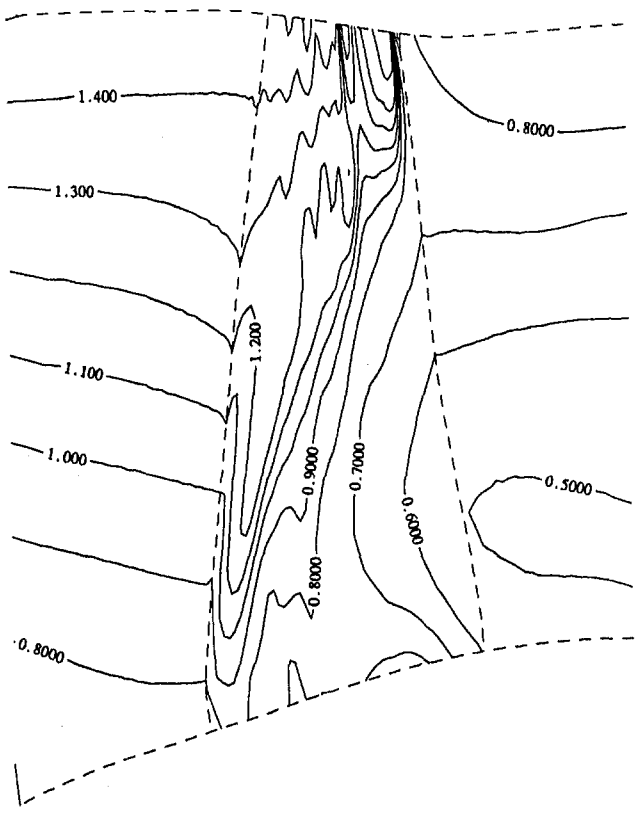

Fig. 12 Relative Mach number contours just before failure of calculation

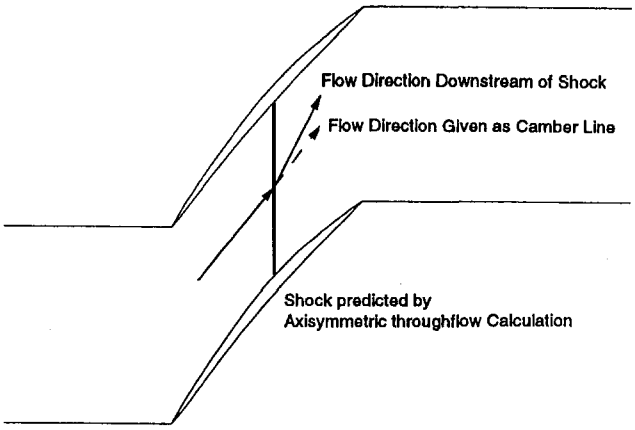

Fig. 13 Illustration of incompatibility between given flow angle and true one across shock

present within a blade passage the flow angle must change discontinuously across it, as illustrated in Fig. 13.

There are immense difficulties reconciling this with the continuous flow angle implied by the blade direction. To avoid this problem, Ginder (1984) used rW_θ rather than flow angle as an input for the throughflow calculation. The chordwise distribution of rW_θ was given as that expected from typical blade to blade flows and thus did not correspond to any particular blading. Such a remedy, in effect, requires related blade-to-blade calculations and is not really practical for use here. The amount of computational effort would be better employed attempting three-dimensional calculations within individual blade passages, as discussed in the companion paper (Joo and Hynes, 1997).

This semi-actuator disk model, however, can produce good solutions for subsonic flow where a shock does not appear in blade passages (Joo, 1994) and even for supersonic flow that inlet relative Mach number is not too high (1.15 at tip in Dawes, 1990) and thus the shock is not too strong.

In summary, the uses and advantages of this type of semi-actuator disk model rest upon the fact that it should certainly be more accurate than an actuator disk representation, but restricted to high subsonic or just supersonic flow relative to the blades in its application. The Mach numbers experienced in inlet guide vane and stator rows are usually such that these considerations pose no restriction in the use of semi-actuator disk models for stationary rows.

10 Summary/Conclusions

A new three-dimensional numerical method has been developed to predict the highly coupled intake and engine flow fields associated with modern turbofan installations. Compressor blade rows are modeled by using actuator disks that provide boundary conditions to numerical calculation domains. A number of numerical implementations of the actuator disk boundary conditions are possible.

The relationship between the variables in which it is natural to pose the actuator disk conditions and the primary variables used in the numerical calculation of the flow field is a nonunique one. This paper has presented a strategy for overcoming this difficulty.

We have shown that it is possible to represent the performance of a high-speed rotor faithfully throughout the flow range at a given speed provided suitable loss and deviation rules and, most importantly, a suitable model to simulate the effect of the choking of a blade row are used. This can be done with an actuator disk in any axial position between the leading and trailing edges of the blade row, provided sufficient care is taken with the specification of the choking model. The flow through the disk is, however, sensitive to the precise details of the choking model when the disk is anywhere other than the leading edge.

The relative insensitivity of the performance of a blade row, as simulated by an actuator disk positioned at the leading edge, to the details of the choking model enables the use of a simple choking model derived from the blade geometry alone.

A outlet boundary condition suitable for calculations in which the flow at exit to the flow domain is highly swirling and varies circumferentially over a long length scale (as is typical of the flow downstream of a rotor operating behind a nonsymmetric inlet) has been developed.

A semi-actuator disk model has far fewer inherent approximations than an actuator disk model, but it has severe limitations in their capability to handle supersonic flow within blade rows. Thus their application is restricted to high subsonic or just supersonic flow relative to the blades.

Acknowledgments

The authors gratefully acknowledge the financial support of Rolls Royce plc and D.T.I. for funding the work described in this paper. They are also grateful for the intellectual and logistic support provided by Dr. Nigel Birch and his colleagues at Rolls Royce.

References

Billet, G., Huard, J., Chevalier, P., and Laval, P., 1988, "Experimental and Numerical Study of the Response of an Axial Compressor to Distorted Inlet Flow," ASME *Journal of Fluids Engineering,* Vol. 110, pp. 355–360.

Dawes, W. N., 1986, "Numerical Techniques for Viscous Flow Calculations in Turbomachinery Blading," *Application of Full Navier–Stokes Solvers to Turbomachinery Flow Problems,* Von Karman Institute Lecture Series 1986–02.

Dawes, W. N., 1988, "Development of a 3D Navier–Stokes Solver for Application to All Types of Turbomachinery," ASME Paper No. 88-GT-70.

Dawes, W. N., 1990, "Towards Improved Throughflow Capability: The Use of 3D Viscous Flow Solvers in a Multistage Environment," ASME JOURNAL OF TURBOMACHINERY, Vol. 109, pp. 83–90.

Dunham, J., 1965, "Non-axisymmetric Flows in Axial Flow Compressors," Mech. Eng. Sci. Monograph No. 3, pp. 1–32.

Ginder, R. B., 1984, "A Streamline Curvature Throughflow Calculation for Transonic Axial-Flow Compressors, Including Stations Within the Blade Row," *Computational Methods in Turbomachinery,* IMechE 1984-3, C65/84.

Hawthorne, W. R., Mitchell, N. A., McCune, J. E., and Tan, C. S., 1978, "Non-axisymmetric Flow Through Annular Actuator Discs: Inlet Distortion Problem," ASME *Journal of Engineering for Power,* Vol. 100, pp. 604–617.

Hercock, R. G., and Williams, D. D., 1974, "Aerodynamic Response," AGARD Lecture Series 72.

Hodder, B. K., 1981, "An Investigation of Engine Influence on Inlet Performance," NASA CR 166136.

Hynes, T. P., and Greitzer, E. M., 1987, "A Method for Assessing Effects of Circumferential Flow Distortion on Compressor Stability," ASME JOURNAL OF TURBOMACHINERY, Vol. 109, pp. 371–379.

Joo, W. G., 1994, "Intake/Engine Flowfield Coupling in Turbofan Engines," Ph.D. Thesis, Cambridge University Engineering Department, United Kingdom.

Joo, W. G., and Hynes, T. P., 1997, "The Application of Actuator Disks to Calculations of the Flow in Turbofan Installations," ASME JOURNAL OF TURBOMACHINERY, Vol. 119, this issue, pp. 733–741.

Joubert, H., 1990, "Flowfield Calculation in Compressor Operating With Distorted Inlet Flow," ASME Paper No. 90-GT-212.

Kaji, S., and Okazaki, T., 1970, "Propagation of Sound Waves Through a Blade Row—Part I: Analysis Based on the Semi-actuator Disk Theory," *Journal of Sound and Vibration,* Vol. 11, pp. 339–353.

Longley, J. P., 1988, "Inlet Distortion and Compressor Stability," Ph.D. Thesis, Cambridge University Engineering Department, United Kingdom.

Mitchell, N. A., 1979, "Non-axisymmetric Flow Through Axial Turbomachines," Ph.D. Thesis, Cambridge University Engineering Department, United Kingdom.

Moore, F. K., 1984, "A Theory of Rotating Stall of Multistage Compressors: Part I—Small Disturbances," ASME *Journal of Engineering for Gas Turbines and Power,* Vol. 106, pp. 313–320.

Rizvi, S. A. H., 1977, "Inlet Maldistibution Effects in Axial Compressor Rotors," Ph.D. Thesis, Cambridge University Engineering Department, United Kingdom.

Spurr, A., 1980, "A Computational and Experimental Study of Fully Three Dimensional Transonic Flow in Turbomachinery," Ph.D. Thesis, University of Southampton, United Kingdom.

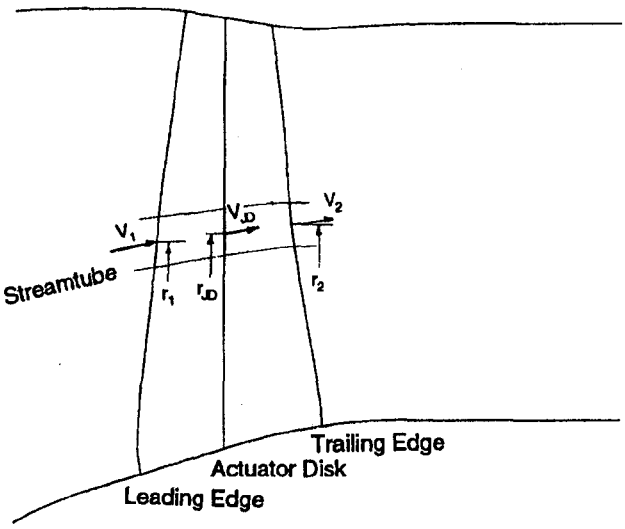

Fig. A1 Schematic of a fan in highly contracting annulus

APPENDIX

Correction Made to Exit Flow Angle

The relative flow angle specified at the actuator disk exit is usually taken from experimental measurements, empirical data, or three-dimensional predictions obtained at the trailing edge. If, as shown in Fig. A1, the annulus contracts highly through blade rows, the work input into the disk depends upon the position of disk if the true blade exit flow angles are used. When the actuator disk is not at the trailing edge, it is possible to improve the agreement between predicted and true performance by modifying these flow angles slightly.

The work input per unit mass through the fan and the actuator disk for a given streamtube is given by (on the assumption that swirl at inlet is negligible)

$$W_{\text{fan}} = \omega r_2 V_{\theta 2} \quad W_{\text{disk}} = \omega r_{JD} V_{\theta JD}$$

where the subscript 2 indicates blade exit, and the subscript JD represents disk exit. In terms of the relative flow angle, β, these equations can be rewritten as

$$W_{\text{fan}} = r_2\omega(V_{x2} \tan \beta_2 + r_2\omega)$$

$$W_{\text{disk}} = r_{JD}\omega(V_{xJD} \tan \beta_{JD} + r_{JD}\omega)$$

The disk exit flow angle for producing the same work as the real fan is thus given by

$$\tan \beta_{JD} = \frac{r_2}{r_{JD}} \frac{V_{x2}}{V_{xJD}} \tan \beta_2 + \frac{r_{JD}\omega}{V_{xJD}} \left(\frac{r_2^2}{r_{JD}^2} - 1 \right)$$

In the present calculation, for this purpose, streamwise grid surfaces are further assumed to be stream surfaces. The axial velocity at the disk exit, V_{xJD}, is estimated by

$$V_{xJD} = V_{x2} \frac{A_{x2}}{A_{xJD}}$$

where A_x is the axial area of quasi-orthogonal faces of cells at the specified location.

The Application of Actuator Disks to Calculations of the Flow in Turbofan Installations

W. G. Joo[1]

T. P. Hynes

Whittle Laboratory,
University of Cambridge,
Cambridge, United Kingdom

This paper discusses the application of an actuator disk model to the problem of calculating the asymmetric performance of a turbofan operating behind a nonaxisymmetric intake and due to the presence of the engine pylon. Good agreement between predictions and experimental results is demonstrated. Further validation of the model is obtained by comparison with the results of a three-dimensional calculation of an isolated fan operating with a nonaxisymmetric inlet. Some justification of the neglect of unsteady aspects of the flow in the fan is presented. The quantitative features of the interaction of the pylon and fan flow fields are discussed.

1 Introduction

The design of the intake for modern turbofan engine installations traditionally, and to a large extent still, takes place independently of that of the engine. The acceptability of the intake design is usually determined by experiments performed on the intake alone. However, when the engine is installed in its intake, the performance characteristics of the intake and the fan can be very different from those measured in isolation. This is largely caused by the coupling between the flow field delivered by the intake and that of the engine.

The intake of a civil high bypass ratio turbofan engine is usually drooped relative to the engine centerline, at typically six or so degrees, to align the intake more fully with the oncoming flow, which has a positive vertical component induced ahead of the wing. In addition, the intake is usually asymmetric with a thicker lower lip to allow for the fact that, during take-off and climb, the inlet will be subjected to positive incidence. Even though the flow delivered to a fan is a uniform stagnation pressure flow, a nonuniform static pressure field is produced at the fan face by the asymmetric nature of such a drooped nonaxisymmetric intake.

In addition, there is usually a large pylon that supports the weight (and carries various engine services) and at least one other strut that provides some rigidity for the engine structure. These support structures for the core and rotating assemblies of a modern turbofan engine present a considerable blockage for the bypass section and subject the fan to a nonuniform back pressure.

This nonuniform static pressure field upstream and downstream of the fan affects performance and stability of the fan and it is a matter of some concern to manufacturers. Despite the importance of the problem, however, few prediction methods or empirical correlations have been reported for the flow through a fan that takes account of the interaction with the inlet and with the pylon. It was argued in a companion paper (Joo and Hynes, 1997) that, since the nonuniformities of static pressure due to the droop and due to the presence of the pylon have a length scale of the order of the circumference, actuator disk models of blade rows are an appropriate approximation. This paper presents the results of a series of calculations performed for a typical modern high bypass turbofan engine using the actuator disk model described in the companion paper.

Since general details of actuator disk models of blade rows have been discussed in the companion paper, Section 2 describes the extra details relevant to the current application and compares the calculation results with measurements taken on a full-scale engine, providing partial validation of the approach. More detailed validation is provided in Sections 3 and 4, which first attempt to justify the use of a coarse grid for calculating the flow in a rotor passage. A simple model to account for the effect of unsteady flow in a rotor is described in Section 5 and used to indicate that neglecting unsteadiness is a reasonable first approximation. In Section 6, the nature of the interaction of the flow fields of the pylon and rotor flow fields is discussed.

2 An Actuator Disk Model for a Turbofan Engine and Its Installation

Figure 1 shows a cross section of the calculation domain used to model the flow through the engine and its installation. The engine has a droop simulator designed for taking account of the effect of a drooped intake at cruise, as described in the companion paper (Joo and Hynes, 1997). The fan and the bypass outlet guide vane row (OGV) are replaced by actuator disks. The fan actuator disk is positioned at midchord and the locations of the OGV actuator disk and the splitter are moved slightly toward the fan to maintain the actual distances between them and the fan. The relative flow angles specified at the exit to the fan actuator disk are taken from a three-dimensional viscous calculation of the flow through the fan operating near design in uniform inlet flow (using BTOB3D; see Dawes, 1988). The OGV is assumed to turn the flow to the axial direction without deviation. The actuator disk boundary conditions are applied neglecting the fact that the flow through the rotor is unsteady to a certain extent.

The flow at the inlet boundary to the calculation domain is assumed to be nonswirling, to have uniform stagnation pressure and stagnation temperature and to be roughly aligned with the streamwise surfaces of the calculation grid. This boundary is thought to be far enough away to neglect the effect of any uncertainty in meridional angle on the fan.

It is necessary to simulate all components of the engine downstream of the fan that are thought to affect the response of the fan. The flow field downstream is split into core and bypass streams. The calculation domain in the core section is extended to just upstream of the engine section stator (ESS) where a boundary condition simulates the presence of the core engine. The pressure rise characteristics of the core engine are very steep when compared with that of the fan root and thus the core compressor will not accept much in the way of a circumferen-

[1] Current address: Department of Mechanical Engineering, Yonsei University, Seoul 120-749, Korea.

Contributed by the Turbomachinery Committee for publication in the JOURNAL OF TURBOMACHINERY. Manuscript received by the Turbomachinery Committee May 15, 1995. Associate Technical Editor: R. A. Delaney.

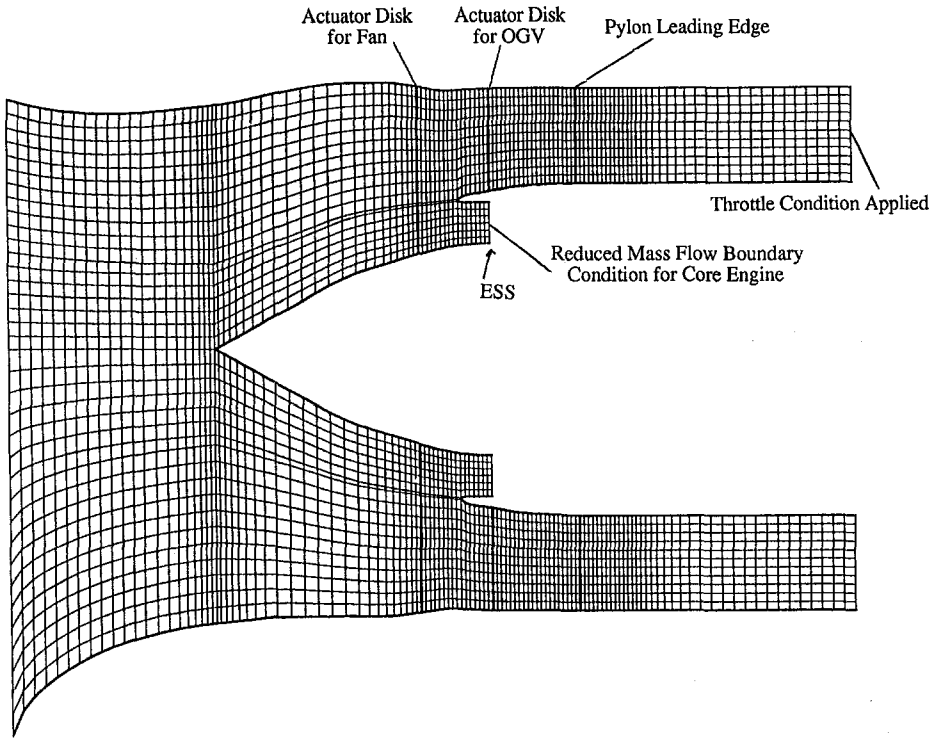

Fig. 1 Cross section of flow field model to simulate engine and installation

tially nonuniform reduced mass flow. A constant mass flow coefficient is, therefore, specified at each radius and circumferential position as the core boundary. A detailed description of this boundary condition is found in Appendix A1.

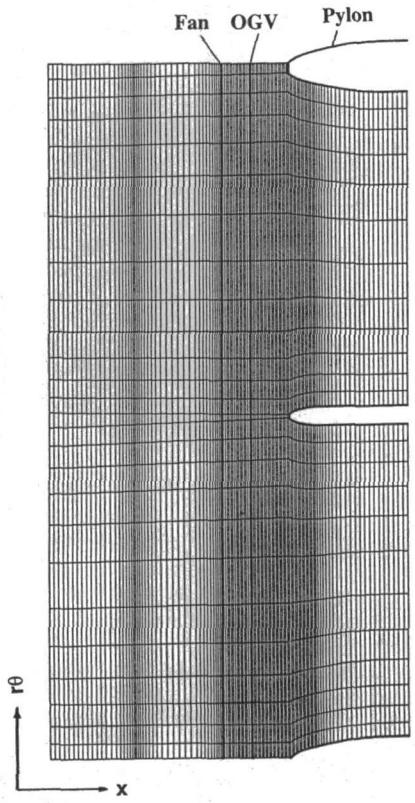

Fig. 2 "Unwrapped" annulus near casing showing pylon and true length scales

The calculation domain in the bypass stream is continued around the pylon and the corresponding strut at bottom dead center to a section well past the pylon leading edge. The pylon represents a considerable blockage to the bypass stream and generates large static pressure disturbances associated with low harmonics of long length scale. Its effect can be felt a long way upstream and will still be significant at the fan exit. A view of the grid in an axial-circumferential sense in the vicinity of the casing is shown in Fig. 2. The grid is drawn with equal scales for axial and circumferential distances to show just how close (in aerodynamic terms) are the fan, OGV blade rows, and struts.

Total pressures measured using a number of rakes mounted near the leading edge of the OGV and ESS, for an engine operating at 95 percent of design fan speed, are shown in Fig. 3 alongside the calculation results. The variation of total pressure is presented in the form of a percentage of the circumferentially averaged value at that radius as

$$\frac{P_0(r,\theta) - \bar{P}_0(r)}{\bar{P}_0(r)} \times 100 \text{ (percent)}$$

The figure shows that the calculation results are in good agreement with the experimental data for both the level and pattern of the variation. The major difference between the two results is in the angular position; the predicted flow field is shifted by about 30 deg in the opposite direction to fan rotation relative to the measurements. Both sets of results show that the delivered fan total pressure has an 11 percent variation about the mean value around the annulus at the tip and 8 percent at the hub. The size of the variation in the hub region is perhaps surprising because the effect of the pylon and the largest effects of the droop are given in the bypass section. This variation emphasizes that the interaction of the pylon, intake, and rotor flow fields is strong and fully three dimensional. Asymmetric exit conditions to the rotor result in asymmetric flow fan pressure rise, which in turn results in a circumferential pressure variation ahead of the fan. This drives radial flow and affects the flow in the core region.

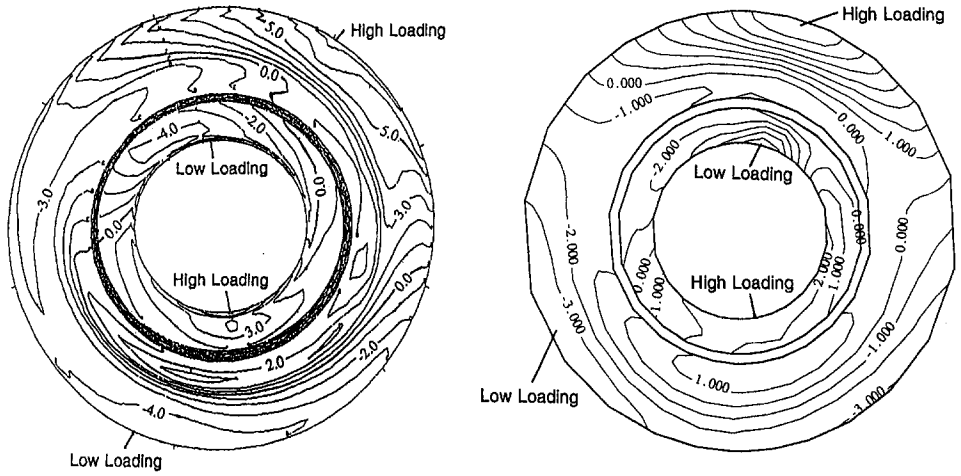

Fig. 3 Comparison of measured and predicted circumferential variations in total pressure behind fan operating with inlet simulator

The quality and quantity of the data available from engine instrumentation are somewhat limited and it is difficult to draw conclusions as to the cause of the discrepancy between the two sets of results. Neglecting unsteadiness, which causes the time lag response of the fan, in framing the rotor actuator disk boundary conditions is a possibility, as is the modeling of the entire core section of the engine by a boundary condition. In addition, there is another possible reason, which will be discussed in Section 6.

The agreement between the calculated and the measured results is more than good enough for many engineering purposes. The flow field immediately downstream of the fan and, by inference, the flow field immediately upstream is probably accurate enough, for example, to enable realistic estimates of the circumferential variation in loading on rotor blades to be made for the purposes of fan vibration and noise level assessments. Modern turbofans often use a nonaxisymmetric set of OGV's to ameliorate the upstream effect of the pylon blockage. The agreement between the two sets of results is probably good enough to indicate that the method can be applied to the design of optimum OGV's.

3 Coarse Grid Three-Dimensional Calculations in a Blade Row

To provide further validity to an actuator disk model, a separate three-dimensional calculation within each passage of a rotor operating behind the drooped intake simulator has been performed. To keep memory and CPU time requirements within the capabilities of existing computers, relatively coarse grids in each passage must, of necessity, be used. The first issue to be addressed for this type of calculation is that of how coarse grids can still provide a reasonable representation of the flow within transonic fan blades where one or more shocks and a strong shock-boundary layer interaction occur, with local separation.

Freeman and Cumpsty (1992) showed that the fan performance and the efficiency of transonic fan tip sections can be predicted remarkably well by applying control volume analysis for the conservation of mass, energy, and momentum to a cascade of flat plates, which is modeled using two control volumes. Their analysis confirmed their view that the flow is determined by overall conservation constraints. It is likely that any numerical method that satisfies the conservation equations should be able to predict the flow reasonably well even though the mesh is not fine enough to resolve boundary layers and shocks.

In contemplating a coupled calculation of the flow in each passage of a rotor row operating in a circumferentially nonuniform flow, the requirement for circumferential grid resolution places the biggest demands on computational resources. It is envisaged that existing resources would limit the grids within individual blade passages to about five or so cells circumferentially across each passage. In order to examine the effect that such a coarse grid would have on the computed solutions, a series of clean flow calculations were performed for a single passage using the grids that are systematically coarsened. Figure 4 shows the different size grids used. The first of these is a typical "viscous" grid, consisting of 32 cells across the passage, which are relatively widely spaced in the center of the passage and become finer in the vicinity of the blade surfaces in order to resolve the blade boundary layers. The other grids represent three different levels of "inviscid" grid sizes (grid points equally spaced in the circumferential direction): coarse (five mesh cells in one blade passage), medium (ten mesh cells), and fine (21 mesh cells = same midpassage spacing as the "viscous" grid). The fan described in Section 2 is used as a test case and the BTOB3D code with the Baldwin–Lomax mixing length turbulence model (Dawes, 1988) is used for viscous grid calculations.

The predictions for overall (mass-averaged) pressure ratio are shown in Fig. 5. The inviscid grids predict very similar levels of fan performance regardless of the size of grid and, for the purposes of this study, indicate satisfactory agreement with the results of the calculation using the viscous grid. A similar level of agreement is obtained in the details of the flow fields predicted using the various grids. Figure 6 shows radial distributions of mass-averaged total pressure and temperature downstream of the rotor at an operating point close to design. There is little to choose between the various inviscid grids, each showing a similar level of agreement with the viscous grid. The major discrepancies are in the endwall regions where viscous and clearance effects dominate.

It appears that, unless the grid is configured to resolve the boundary layers on the blades, there is no reason to use anything other than comparatively coarse circumferential grid spacings. Realistic estimates of fan performance, radial distribution of flow, and choked mass flow should result from the use of the coarsest of the inviscid grids to the problem of the flow through a fan operating behind an asymmetric intake.

4 Coarse Grid Drooped Intake Calculations

Calculations have been performed for an isolated fan operating behind the drooped inlet simulator. Each blade passage

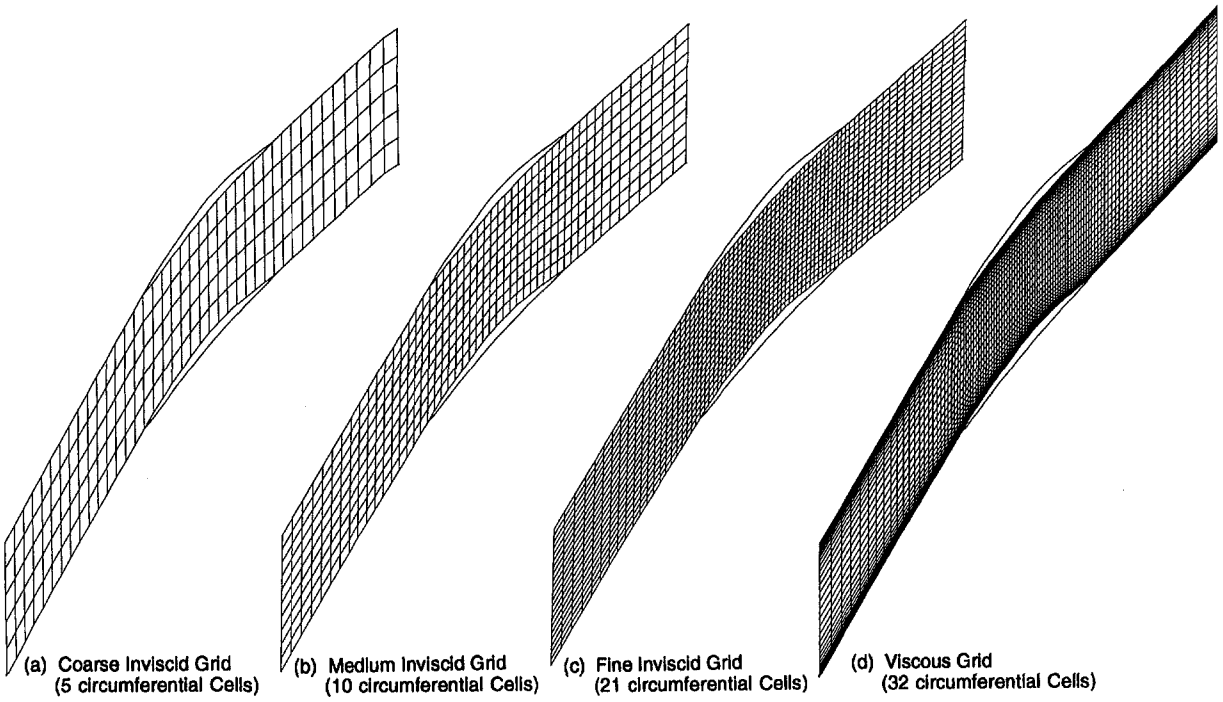

Fig. 4 Circumferential choices of grid spacing for clean flow coarse grid study

was modeled using a coarse grid consisting of five cells in the circumferential direction, as shown in Fig. 7. As, for the purposes of this study, no attempt was made to model any downstream component, the flow downstream of the rotor is a highly swirling three-dimensional flow. Accordingly, a "throttle-like" boundary condition was applied at the downstream end as described in the companion paper.

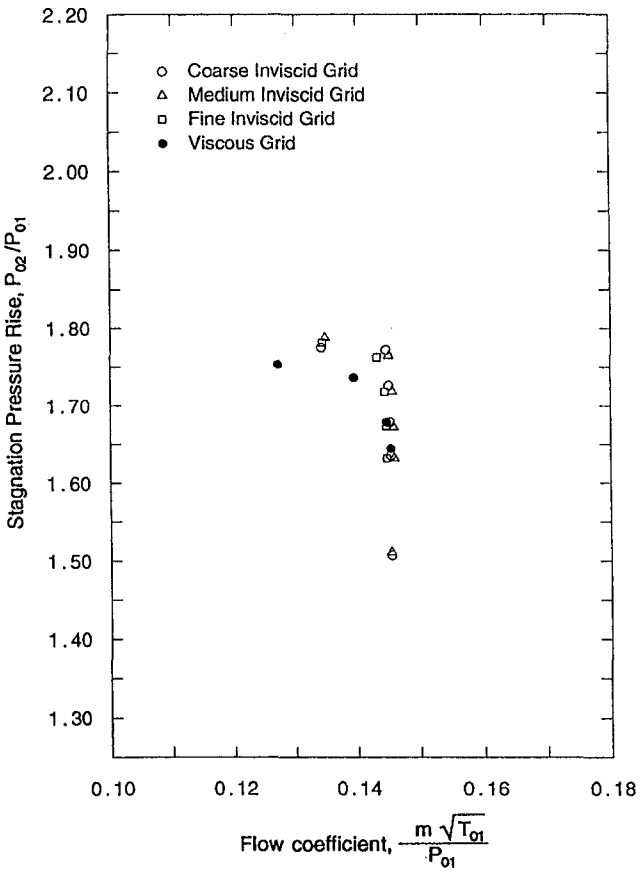

Fig. 5 Predicted characteristics for various choices of circumferential grid spacing

The unsteadiness of the flow through the rotor is neglected. This means that the flow up to the leading edge is calculated in the *absolute* frame and considered steady, whereupon the frame is changed to the *rotating* frame for the calculation in the blade row itself, which is again considered steady, and the calculation downstream of the blade row is also performed in the *absolute* frame in a steady manner. Conceptually, the grid in each rotor passage is rotating relative to the absolute frame and a slightly different result is obtained for each relative alignment of the grid in the rotor passage. In addition there is a slight ambiguity as to whether or not the grid within the rotor passage is considered to rotate when deciding at which circumferential locations to match the rotor passage grid to those of the upstream and downstream flow fields. Both of these effects contribute a potential phase shift less than one blade pitch, which is not very significant for the comparison presented here. We shall not pursue this point in this paper, but a full discussion can be found in Joo (1994).

Figure 8 shows predicted stagnation pressure contours at the fan exit obtained from this coarse grid calculation (again presented as a variation about a mean at the that radius). An almost periodic pattern is observed, showing clearly both the variation associated with individual blade passages and the longer length scale variations from passage to passage caused by the nonuniform inlet flow. In order to compare this result with the predictions of that using an actuator disk representation of the blade row, the passage length scale variations are filtered out by taking, at each radius, a running average over one blade pitch. The resulting percentage variation of averaged absolute stagnation pressure at the trailing edge is shown in Fig. 9 where it is compared with results at disk exit obtained using a midchord actuator disk model. The agreement is excellent in both pattern and distortion level.

There are a number of points apparent from these results that are worth discussing further. The first is the issue of the size of error made in neglecting the fact that the flow within the

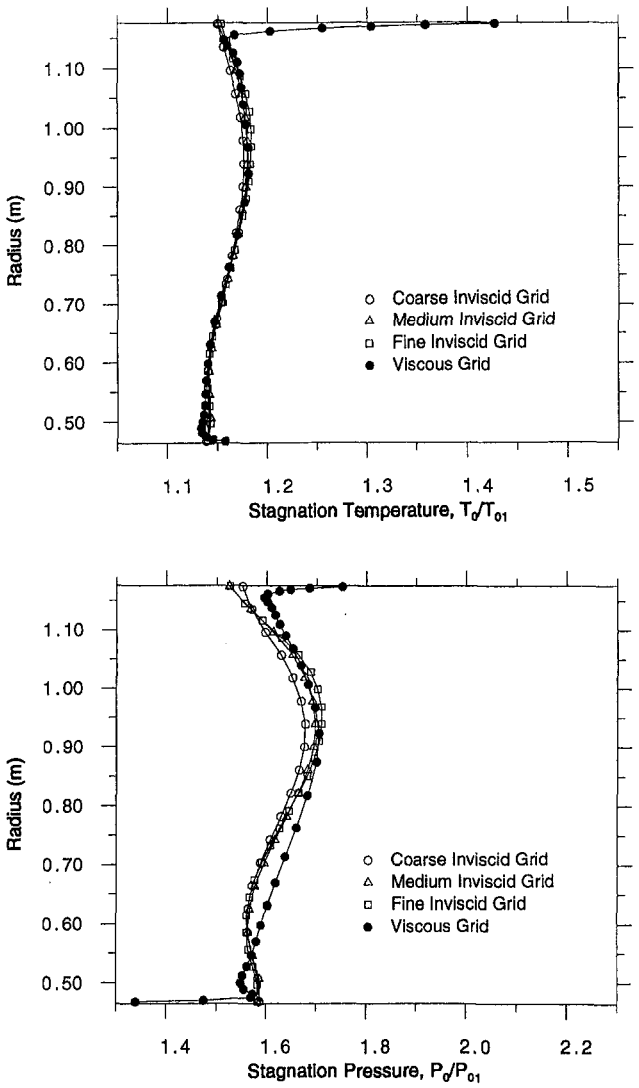

Fig. 6 Predicted radial distribution of total pressure at fan exit for various choices of circumferential grid spacing

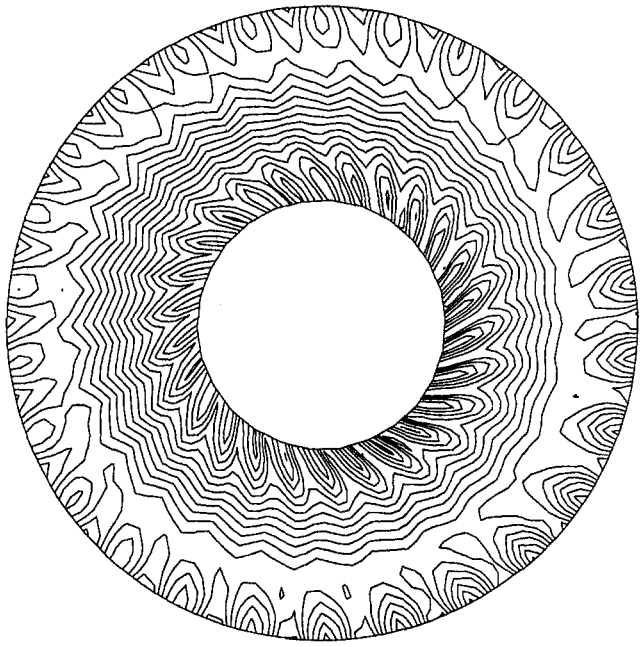

Fig. 8 Predicted circumferential variation in total pressure downstream of isolated rotor operating behind inlet simulator using coarse grid rotor model

rotor is unsteady. Both the coarse grid and the actuator disk models neglect the effect of unsteadiness in an essentially similar manner. The agreement between the two sets of results shown in Fig. 9 does not shed any light on the size or nature of this approximation.

The agreement shown in Fig. 9 does, however, provide some evidence for the fundamental idea of an actuator disk: that each blade element in a circumferentially nonuniform flow can be considered to operate in response to the local inlet flow conditions (and to local values of back pressure for sections effectively choked). The actuator disk model assumes this, the coarse grid model does not.

Coarse grids cannot *accurately* reproduce viscous effects, but one might expect inviscid features of the flow to be accurately modeled. In particular, a coarse grid should give a reasonable representation of blade row blockage, which is important when parts of the span are operating close to their choking mass flows. It should also give a good first estimate of the position and the

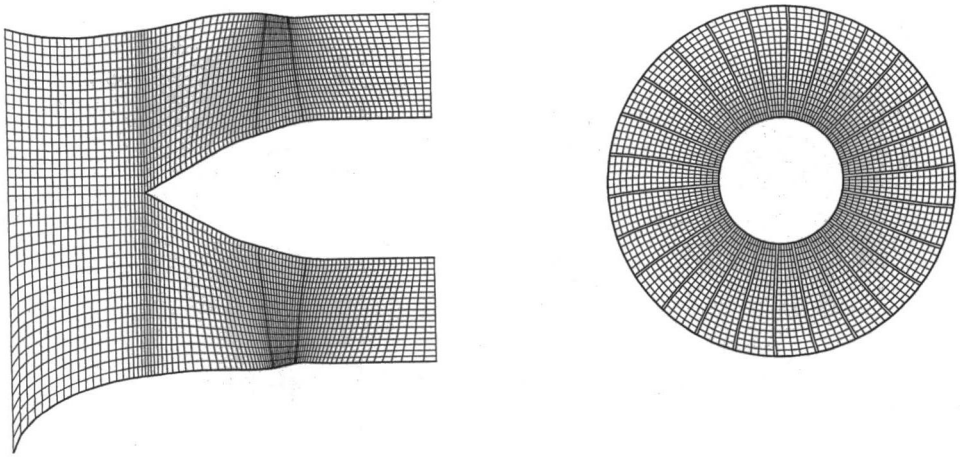

(a) Meridional Plane (Top to Bottom) (b) Quasi-Orthogonal Plane (Mid-Chord)

Fig. 7 Calculation grid for coupled three-dimensional intake and rotor calculation

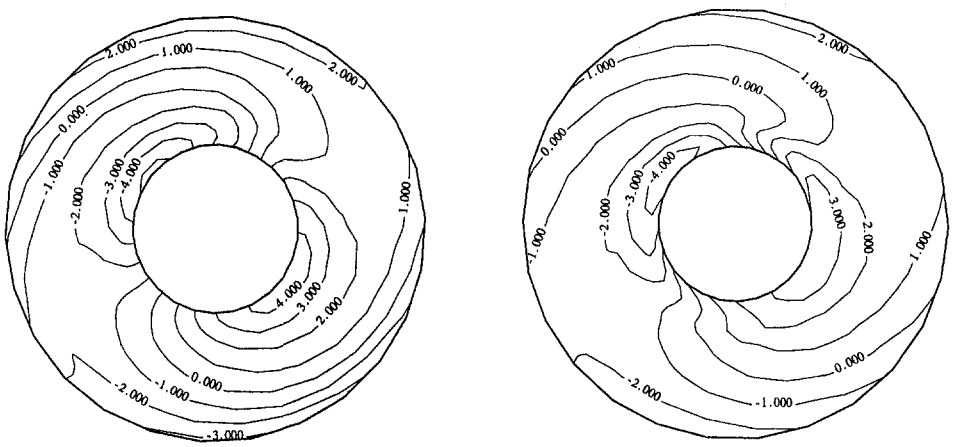

(a) Three Dimensional Coarse Grid Model (Trailing Edge)

(b) Actuator Disk Model (Disk Exit)

Fig. 9 Comparison of predicted circumferential variation in total pressure downstream of isolated rotor operating behind inlet simulator using coarse grid rotor model and actuator disk model

strength of any shocks within the blade passages and of the deviation that results from inviscid considerations of the flow.

The final conclusion worth commenting upon from this study is the relative importance of the pylon and the intake asymmetry upon the rotor performance. The variation of fan performance shown in Fig. 9 is induced by the asymmetric intake alone. It was shown in Joo (1994) that the presence of the OGV's and core section of the engine has little effect on the actuator disk predictions shown in Fig. 9 in the bypass section. From the comparison with the results shown in Fig. 3, this suggests that the pylon presence is responsible for most of the asymmetry in the bypass section.

5 An Estimate of the Effect of Unsteadiness

In all the calculations to date, the effect of unsteadiness of the flow in the rotor has been neglected. The companion paper (Joo and Hynes, 1997) discussed in the introduction that, following Moore (1984), it is the *inviscid* aspects of unsteady flow that are the most important to model, and further, that a linearized treatment is a reasonable first approximation. Following this line of approach, we attempt to model the flow within the rotor passages as the linearized unsteady flow within one-dimensional straight channels. The unsteadiness assessed from the model is incorporated into the actuator disk boundary conditions to allow for some aspects of unsteadiness.

In a linearized treatment, circumferential harmonics can be considered separately and it can also be shown that the general solution is a sum of three modes. Two of these correspond to acoustic disturbances propagating upstream and downstream, while the other one corresponds to a variation in entropy, which is simply convected with the unsteady flow. Three boundary conditions at leading and trailing edges couple these perturbations to the flow upstream and downstream of the rotor. These boundary conditions are the natural ones: conservation of mass flux, conservation of rothalpy (energy) flux, and matching of the local value of entropy. For the application considered here, the flow in the asymmetric intake to the engine is nonuniform but has a *uniform* entropy. It is clear then that a boundary condition of conservation of entropy flux at the leading edge will imply that there is no unsteady entropy variation in the passage. In this type of model, entropy generated within the passage is added at the trailing edge.

The solution for the linearized unsteady flow in the rotor passage thus consists of a combination of sums of two modes.

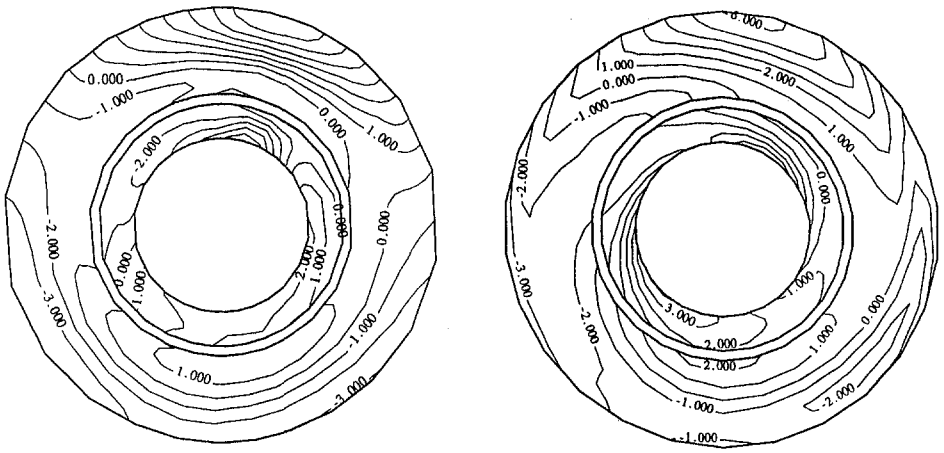

(a) Unsteadiness neglected

(b) Simple Unsteadiness Correction Applied

Fig. 10 Effect of including simple unsteadiness correction into turbofan model

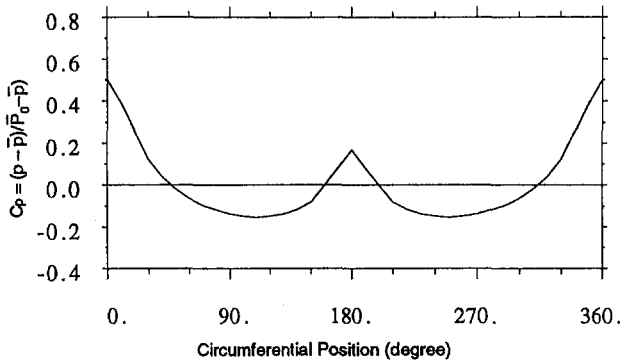

Fig. 11 Predicted static pressure variation ahead of pylon using actuator disk mode

These affect two of the actuator disk boundary conditions. It is the *swapped* version of the boundary conditions described in the companion paper that is most easily adapted to allow for this unsteady modification. It is relatively easy to modify the mass flux and rothalpy variables to account for unsteadiness before passing them to the opposite side of the disk. At convergence, the unsteady boundary conditions are satisfied. The details of how upstream variables are corrected before passing to the downstream flow field are:

(*i*) At each radial location, ρV_x and rothalpy, I, are taken from the upstream flow field and decomposed into a sum of circumferential harmonics

$$\rho V_x = \sum_{n=-N}^{N} A_n e^{in\theta} \quad I = \sum_{n=-N}^{N} B_n e^{in\theta} \qquad (1)$$

where $2N + 1$ is the number of circumferential grid points.

(*ii*) In the relative frame the nth harmonic is unsteady with radian frequency $n\omega$ (ω = the rotor rotational speed)

$$\rho V_x = \sum_{n=-N}^{N} A_n e^{in\omega t + in\theta'} \quad I = \sum_{n=-N}^{N} B_n e^{in\omega t + in\theta'} \qquad (2)$$

and θ' is a circumferential angle relative to *rotor* coordinates.

(*iii*) Within the rotor passage just downstream of the leading edge, the linearized flow variations in mass flux and rothalpy can be written in terms of upstream and downstream propagating modes as

$$\rho V_x = \sum C_n^{up} e^{in\omega t + in\theta' + i\alpha x/r} + \sum C_n^{dn} e^{in\omega t + in\theta' + i\beta x/r} \qquad (3)$$

$$I = \sum FC_n^{up} e^{in\omega t + in\theta' + i\alpha x/r} + \sum GC_n^{dn} e^{in\omega t + in\theta' + i\beta x/r} \qquad (4)$$

where α and β are found from the frequency and the convection speeds of the two modes (based upon circumferentially averaged properties), and F and G also depend simply on the local average value of Mach number.

Conservation of mass flux and rothalpy applied at the leading edge ($x = 0$) determines the coefficients C_n^{up} and C_n^{dn}. Mass flux and rothalpy just upstream of the trailing edge are given by Eqs. (3) and (4) with x = chord. These are then passed to the downstream flow field.

(*iv*) The variables passed to the upstream flow field across the disk are treated in an exactly similar manner.

It should be emphasized that this modification to the actuator disk boundary conditions does not represent a linearization. If the blade chord is shrunk to zero then the application of Eqs. (1) to (4) has *no effect* on the variables being passed and the actuator disk boundary conditions become exactly those described in the companion paper. The process is that variables to be passed are modified to account for unsteadiness, and this *unsteady modification* is calculated assuming linearized, unsteady flow within a one-dimensional blade passage.

Figure 10 shows the effects of including unsteadiness into the flow calculation through the complete engine model described in Section 2. It is concluded that the effects of the flow unsteadiness estimated in the one-dimensional linearized manner on the phase shift are small. It can be seen, however, that compared with the experimental results (Fig. 3(*a*)), the unsteady effects improve the details of distortion pattern.

The unsteady flow through the transonic fan is very complicated and two or three-dimensional unsteady effects may be more important. These effects could be investigated using the full three-dimensional unsteady numerical method.

6 Pylon Fan Flow Field Interaction

In this section we return to discuss some of the features of the flow field interaction of the fan and pylon flow fields. An understanding of the nature of this interaction is a great help in

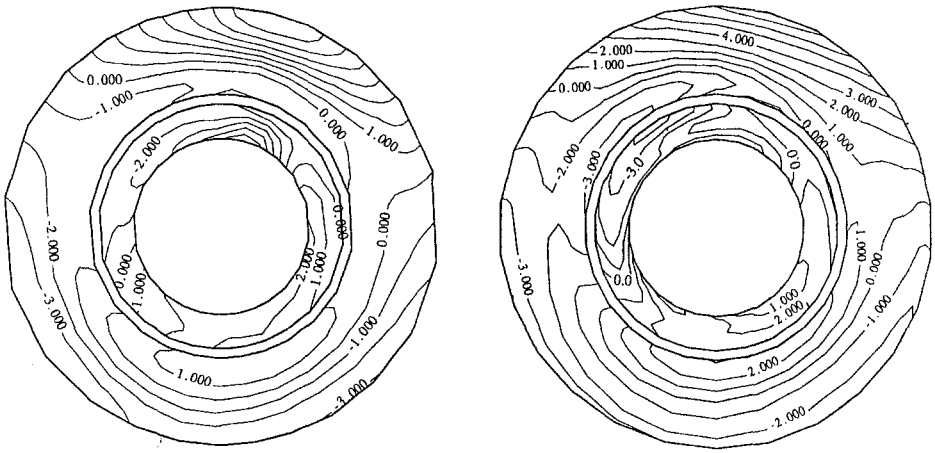

(a) Pylon Present (b) Pylon Simulated by C_p Boundary Condition

Fig. 12 Comparison of predicted circumferential variation in total pressure downstream of fan with pylon modeled and with pylon simulated using C_p boundary condition

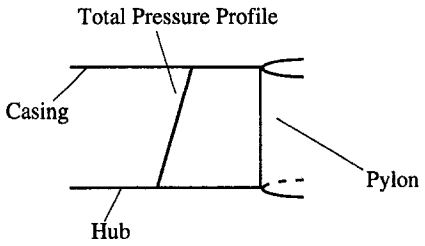

Fig. 13 Radial profile of total pressure approaching pylon

the problems such as how to model it and how accurately the details of the pylon must be simulated, etc.

The key feature is that the static pressure field induced ahead of the pylon is a potential one. It thus decays in exponential fashion with upstream distance, and the longer length scale component decays more slowly. In addition, since pressure variations in the radial direction decay faster than circumferential variations with longer wavelength, the most important part of the nonuniform pressure field due to the pylon, as far as the interaction with the rotor flow field is concerned, is independent of radius.

Figure 11 shows the static pressure variation ahead of the pylon predicted by the calculation including the pylon described in Section 2. In practice, it is not very different from that which would be obtained from a calculation of uniform (potential) flow around an *isolated* pylon. The static pressure variation is nearly two dimensional and it is likely to become more so with upstream distance. As pointed out by Ham and Williams (1983), then, the presence of the pylon is likely to be simulated by an equivalent boundary condition. This would be a pressure coefficient, C_p, specified at a convenient plane just upstream of the pylon leading edge and it can be adequately estimated from a calculation around an isolated pylon. Figure 12 shows the variation in rotor performance predicted using this procedure and compared with that obtained by the calculation including the pylon. The details of the implementation of the boundary condition simulating the pylon using a pressure coefficient are described in Appendix A2.

There is, however, another aspect in the fan and pylon interaction. The presentation of the fan performance in terms of the circumferential variation hides a somewhat more subtle effect. At operating points close to design (in clean flow, and with no pylon present) there is a more or less radially uniform total pressure profile at the fan exit. When the drooped intake and pylon are present, the results shown in Fig. 12 indicate that there is a strong radial profile of total pressure in the top portion of the bypass stream. The radial distribution is high in the tip region and low in the vicinity of the bypass hub, as shown in Fig. 13.

When such a shear flow approaches the pylon, it will induce a flow radially inward in the vicinity of the pylon leading edge. In extreme cases it is likely to result in a "horseshoe" vortex ahead of the pylon. The calculation described in Section 2 shows evidence of such a flow feature (Fig. 14) though the grid resolution used was not sufficient to fully resolve the flow in this region.

The flow in the vicinity of the pylon is complicated, but the details do not effect the long circumferential length scales in the upstream static pressure field significantly. The conclusion that the effect of the pylon on the flow through the rotor can be modelled using a pressure coefficient, C_p, would appear to remain true.

It is worth returning to Fig. 2 at this point, to remind oneself of the length scale of the pylon interaction. If something akin to a horseshoe vortex appears ahead of the pylon, then its intensity and the distance that it "stands off" ahead of the pylon are determined by the pylon width. This is comparable to the distance between the pylon leading edge and the OGV trailing edge. The blades in this portion of the annulus are thus likely to be driven severely off design by this disturbance. It is unlikely that the loss and deviation rules applied in the calculations, which were framed with flows in the vicinity of design, can

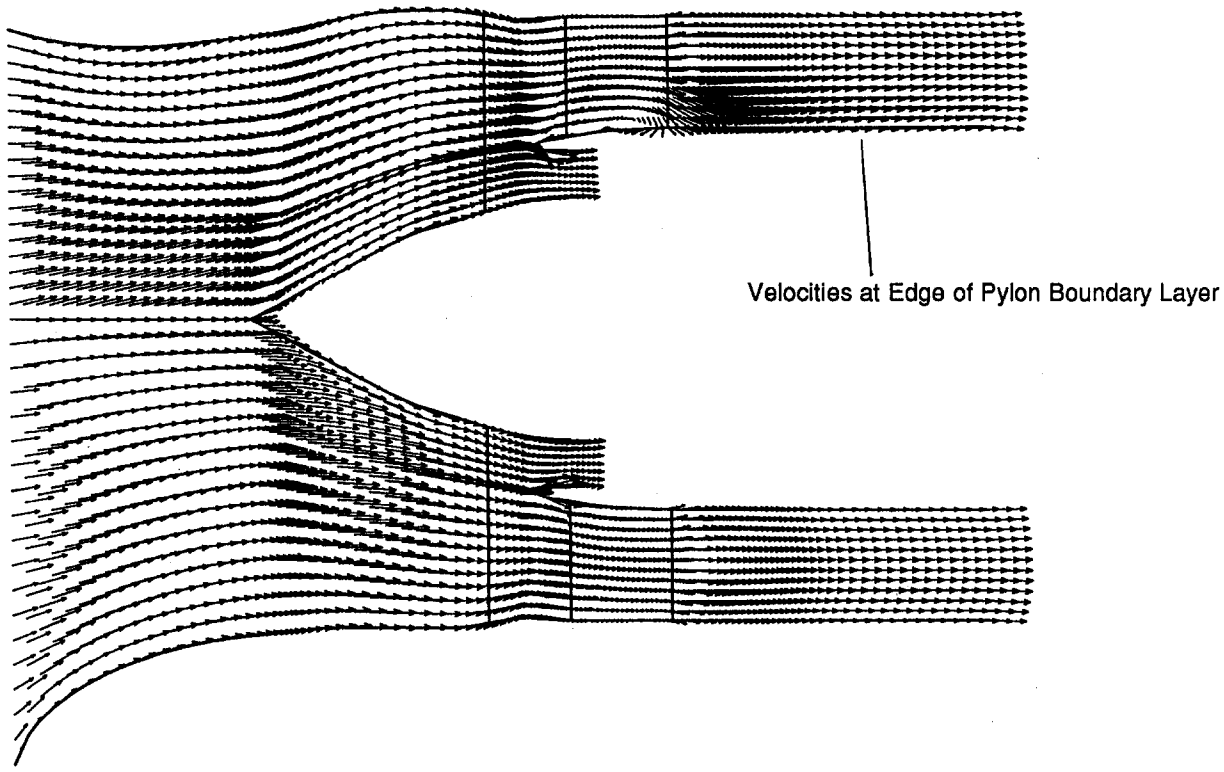

Fig. 14 Predicted velocities for turbofan arrangement with pylon and intake simulator

adequately cope with disturbances of the magnitude and form shown in Fig. 14. It is the authors' opinion that this inadequacy in the modeling of the flow through the vanes in this portion of the annulus would be partly responsible for the phase difference between predicted and measured flows shown in Fig. 3.

In many real designs, nonaxisymmetric sets of OGV's are used to minimize the effect of the pressure disturbance induced by a pylon on fan performance. The developed method can apply to this study by simply specifying the nonuniform OGV exit flow angles in actuator disk boundary conditions.

6 Conclusions

An actuator disk model has been applied to the calculation of the flow through a high bypass ratio turbofan geometry including the effects of the presence of the core support pylon and a nonaxisymmetric inlet. Comparison with experimental results indicates that the actuator disk model gives a good prediction of the major flow field coupling effects of the fan with its environment, giving levels and patterns of asymmetric performance to acceptable accuracy.

A three-dimensional coarse grid model has been used to provide further validation of an actuator disk as a model for a transonic rotor. Predictions for nonuniform fan performance due to the drooped intake obtained using the two models demonstrate excellent agreement.

An estimate of the effect of neglecting unsteady aspects of the flow through a rotor has been made using a simple unsteadiness correction. This estimate indicates that the effects of unsteadiness are relatively small.

Estimates of the size of the asymmetry in the flow through a modern turbofan geometry indicate that the effect of the blockage due to the pylon has a significantly more pronounced effect on the flow through the rotor than does the presence of an asymmetric inlet over most of the span except near hub. Estimates of the asymmetric flow entering the core section of the engine indicate that the levels of asymmetry there are likely to be almost as high as in the bypass section of the engine.

It has been demonstrated that, as far as calculating the effect of asymmetric flow on the fan in a turbofan arrangement, it is not necessary to simulate the details of the flow around the pylon. The pylon can be simulated by the presence of a boundary condition alone. The flow in the vicinity of the pylon, on the other hand, cannot be simulated in this way.

Acknowledgments

The authors gratefully acknowledge the financial support of Rolls Royce plc and D. T. I. for funding the work described in this paper. They are also grateful for the intellectual and logistic support provided by Dr. Nigel Birch and his colleagues at Rolls Royce.

References

Dawes, W. N., 1988, "Development of a 3D Navier–Stokes Solver for Application to All Types of Turbomachinery," ASME Paper No. 88-GT-70.

Freeman, C., and Cumpsty, N. A., 1992, "Method for the Prediction of Supersonic Compressor Blade Performance," AIAA *Journal of Propulsion,* Vol. 8, pp. 199–208.

Ham, X. X., and Williams, Y. Y., 1983, "Flow Field Coupling Between Compression System Components," presented at the IGTC Tokyo Conference.

Joo, W. G., 1994, "Intake/Engine Flow Field Coupling in Turbofan Engines," Ph.D. Thesis, Cambridge University Engineering Department, United Kingdom.

Joo, W. G., and Hynes, T. P., 1997, "The Simulation of Turbomachinery Blade Rows in Asymmetric Flow Using Actuator Disks," ASME JOURNAL OF TURBOMACHINERY, Vol. 119, this issue, pp. 723–732.

Moore, F. K., 1984, "A Theory of Rotating Stall of Multistage Compressors: Part I—Small Disturbances," ASME *Journal of Engineering for Gas Turbines and Power,* Vol. 106, pp. 313–320.

APPENDIX

Outlet Boundary Conditions for Simulating Downstream Components

A1 Simulating Core Engine. Core compressors usually have steep pressure rise characteristics and will tolerate only small variations in flow coefficient, ϕ, defined as,

$$\phi = \frac{m\sqrt{C_p T_0}}{AP_0} \tag{A1}$$

A first approximation for simulating such a component, therefore, is to take ϕ constant at the entry to the first core compressor, i.e., at the outlet boundary of the core section in the numerical calculation domain.

In practice, ρV_x is imposed for the outlet boundary cell of the core section, $j = JC - 1$, at each radial and circumferential position, which is calculated as

$$(\rho V_x)_{JC-1} = \frac{\phi^*(P_0)_{JC-1}}{\sqrt{(T_0)_{JC-1}}} \tag{A2}$$

where total pressure, P_0 and total temperature, T_0, are extrapolated from the interior domain. The fixed constant, ϕ^*, ultimately determines the bypass ratio.

A2 Simulating Pylon. The pylon downstream of the fan in the bypass duct produces a strong static pressure distortion upstream of itself. This static pressure variation could be simulated using the pressure coefficient, C_p, which is obtained from experiments or calculations performed for isolated struts, defined as

$$C_p = \frac{p - \bar{p}}{\bar{P}_0 - \bar{p}} \tag{A3}$$

where $\bar{p}$ and $\bar{P}_0$ are the static pressure and the total pressure averaged over an annulus, respectively, and C_p varies radially and circumferentially.

This pressure coefficient distribution and the averaged static pressure are specified at the outlet boundary of the bypass duct, $j = JB - 1$, which is positioned at a convenient plane just upstream of the pylon leading edge.

The value of static pressure imposed for an outlet boundary cell in bypass section at each radial and circumferential position is found from

$$p_{JB-1} = \bar{p} + C_p(\bar{P}_0 - \bar{p}) \tag{A4}$$

where the averaged total pressure, $\bar{P}_0$, is calculated using the values extrapolated from the interior domain.

R. D'Andrea
Sibley School of Mechanical and Aerospace Engineering,
Cornell University,
Ithaca, NY 14853
rd28@cornell.edu

R. L. Behnken
WL/MNAG,
101 W. Eglin Pkwy., STE 334,
Eglin AFB, FL 32542

R. M. Murray
Division of Engineering and Applied Science,
California Institute of Technology,
Pasadena, CA 91125
murray@indra.caltech.edu

Rotating Stall Control of an Axial Flow Compressor Using Pulsed Air Injection

This paper presents the use of pulsed air injection to control rotating stall in a low-speed, axial flow compressor. In the first part of the paper, the injection of air is modeled as an unsteady shift of the compressor characteristic, and incorporated into a low dimensional model of the compressor. By observing the change in the bifurcation behavior of this model subject to nonlinear feedback, the viability of various air injection orientations is established. An orientation consistent with this analysis is then used for feedback control. By measuring the unsteady pressures near the rotor face, a control algorithm determines the magnitude and phase of the first mode of rotating stall and controls the injection of air in the front of the rotor face. Experimental results show that this technique eliminates the hysteresis loop normally associated with rotating stall. A parametric study is used to determine the optimal control parameters for suppression of stall. The resulting control strategy is also shown to suppress surge when a plenum is present. Using a high-fidelity model, the main features of the experimental results are duplicated via simulations.

1 Introduction

As gas turbine engines have become better understood and better designed, substantial performance increases in engine designs have become harder to achieve, especially with passive control methods. The presence of full authority digital engine controllers (FADECs) on modern gas turbines has enabled the use of active control to achieve additional performance enhancement. Virtually all modern aircraft engines rely on the use of FADECs for controlling engine operation, although the use of dynamic feedback to modify engine operation is relatively rudimentary.

One example of the use of active control to improve engine performance is the Performance Seeking Control (PSC) program at NASA Dryden Flight Research Center. The basic idea behind performance seeking control is to modulate the engine parameters to achieve optimal performance based on the current operating conditions. In simulation studies, a 3 percent decrease in fuel consumption and a 15 percent increase in thrust with the use of a controller that scheduled engine parameters have been reported (Smith et al., 1991). Subsonic flight tests at NASA Dryden Flight Research center validated the technique and showed a 1–2 percent decrease in fuel consumption during minimum fuel mode operation and measured thrust increase of up to 15 percent during maximum thrust mode (Gilyard and Orme, 1992).

Future applications of active control to jet engines will increasingly rely on the use of feedback to modify the dynamics of the engine and provide enhanced stability, which is currently unachievable with passive methods. The development of so-called smart engines (Paduano et al., 1993b) is an area of intense research activity, both in academia and in industry. A major goal is the use of feedback controllers to reduce the effects of performance limiting instabilities that currently constrain the available power and efficiency of jet engines. In addition to technological advances, success in this area requires new techniques for modeling of jet engine dynamics for the purposes of control, as well as development and application of advanced control techniques capable of taking into account the high noise levels and nonlinear operating characteristics of aeroengines.

An initial step in the development of active control techniques for gas turbine engines is active control of the compressor core of the engine. Two of the main limiting factors in the performance of compression systems are rotating stall and surge. Rotating stall refers to a dynamic instability that occurs when a nonaxisymmetric flow pattern develops in the blade passages of a compressor stage and forces a drastic reduction in the performance of the compressor. This degradation in performance is usually unacceptable and must be avoided. Surge is a large-amplitude, axisymmetric oscillation in the engine, which results from exciting unstable dynamics in the overall pumping system. While surge and stall are separate phenomena, the presence of stall is a precursor to the onset of surge in many compressor systems. A more detailed description of these phenomena and their effects on overall performance can be found in the survey paper by Greitzer (1981).

The goal of active control of stall and surge is to improve *operability* of the engine by allowing operation closer to the stall line of the compressor. This could substantially reduce overdesign currently performed to ensure reliable operation. In particular, one of the significant features of high-performance axial-flow compressors is hysteresis in the performance of the compressor. As a consequence, if the operating point of a compressor momentarily crosses over the stall line due to a transient effect, the operating point of the compressor does not return to its original value, but rather to a much lower pressure/flow point. Thus to be insensitive to transient effects, the compressor needs to be operated a significant distance away from the compressor stall line (see Greitzer, 1981, for an in-depth treatment of the effects of hysteresis on a compression system). Using active control methods, it is possible to modify the dynamics of the system such that hysteresis effects are either delayed or eliminated (depending on the approach used), allowing closer operation to the stall line.

Previous Work. Early work on rotating stall and surge concentrated on developing theoretical models that captured the main features of the two effects. Greitzer (1976) presented a one-dimensional (axial) model that predicted the onset of surge using a single parameter, B. For large values of B, the pumping system exhibits surge, while for small values it oper-

Contributed by the Turbomachinery Committee for publication in the JOURNAL OF TURBOMACHINERY. Manuscript received by the Turbomachinery Committee January 5, 1996. Associate Technical Editor: R. A. Delaney.

ates in rotating stall. Moore and Greitzer (1986) presented a refined model of rotating stall and surge that uses three coupled, nonlinear, ordinary differential equations to model the pressure and flow in a compressor system. The original work of Moore and Greitzer is the starting point for many of the current models used for rotating stall. In addition to fundamental modeling issues, there has also been work in studying the details of how stall occurs in experimental systems (see Day, 1993b, for a recent survey). The detailed dynamics of stall and surge are not yet understood, but the basic mechanisms of stall and surge are fairly well classified and models that capture the main features of these instabilities are currently available in the literature.

There have been some recent papers that give a good overview of the basic analysis techniques that can be brought to bear (Abed et al., 1993; McCaughan, 1989, 1990). These papers analyze the global bifurcation behavior of the uncontrolled system and illuminate the nonlinear characteristics of the system that lead to instability as well as hysteresis. These techniques are particularly important in understanding the difference between improving operability of the engine and stabilization of the unstable dynamics.

Despite the complexity of the dynamics of the system, experimental work has demonstrated that active control can be used to extend the operating point of the compressor past the normal stall limit. Paduano et al. (1993a), for example, reported a 20 percent decrease in mass flow for stall inception, using actuated inlet guide vanes to generate an upstream distortion. They used circumferential modes to model the compressor, actuators, and sensors and assumed a decoupled, linear model for the evolution of the modal coefficients. Day (1993a) used a similar technique with air injection as the actuation scheme, and achieved approximately a 5 percent extension in the stall point. Day also explored the use of air injection for destabilizing finite stall cells by injecting air in the jet nearest the stall cell. The control design was ad hoc, but gave good performance and did not rely on modal behavior. Active stabilization using aeromechanical feedback has been reported by Gysling (1993) and Gysling and Greitzer (1995), where an array of 24 small reed valves upstream of the rotor were used to inject air based on the unsteady pressure exerted on the reed valve during rotating stall. By properly tuning the mechanical properties of the reed valve mechanism, rotating stall was stabilized past the normal stall point of the compressor. A modal analysis (in the circumferential variable) of the controller was used to validate the experimental results on an analytical model.

A somewhat different approach is the use of one-dimensional actuation via bleed valves for control of rotating stall and surge. The controllers are based on a low-order, nonlinear model of the compressor, which captures the hysteresis and global dynamics of the system. The controllers change the nonlinear characteristics of the system so that surge does not occur and the change in operating point due to rotating stall is minimized. The approach used by Badmus et al. (1995) used axisymmetric actuation (an outlet bleed valve) to eliminate the hysteresis effects of stall and also prevent surge without eliminating the stall cells per se. A theoretical description of this approach has been given by Liaw and Abed (1996). More recent experimental and numerical investigations of this technique can be found from Eveker et al. (1995).

Overview of Paper. In this paper, we present a control strategy aimed at eliminating the hysteresis region normally associated with rotating stall. As previously mentioned, this objective is a worthwhile pursuit in that it would allow operation closer to the stall line of the compressor. From a practical point of view, the elimination of the hysteresis region is a more realistic design objective than stabilizing the unstable branch of the compressor characteristic. This latter objective is typically only viable for systems with well-defined stall precursors; for many high-speed systems these precursors do not exist.

We depart from previous studies in the sense that we make use of a small number of pulsed air injectors (three) as our means of actuation, and that the orientation of the injected air relative to the rotor face is not restricted to be in the axial direction. The motivation for this control method is that pulsed air injection is a potentially practical technology for implementation on real engines. For similar reasons, we have concentrated on the use of wall-mounted static pressure sensors for detecting stall rather than using hot-wire anemometers. Indeed, one of the goals of our work is to indicate to what extent air injection is a viable actuation technology for controlling rotating stall. A preliminary version of our experimental results appeared in D'Andrea et al. (1995) and extends the earlier work of Khalak and Murray (1995).

This paper is organized as follows. We begin with a description of the experimental setup in Section 2. The relevant characteristics of the compressor system are described, including the steady-state performance characteristic of the compressor and the effects of continuous air injection on the steady-state performance characteristic. In Section 3, a three-state model for a compression system based on a single mode Galerkin projection, proposed by Moore and Greitzer (1986), is used to explore qualitatively the effects of air injection as a stabilizing mechanism. In Section 4, experimental results are presented for a control law that slightly extends the stable operating region of the compressor and eliminates the rotating stall hysteresis loop. A detailed parametric study is presented that gives the optimal settings for various control parameters. We conclude with simulation studies in Section 5 using the distributed model of Mansoux et al. (1994), which duplicate the main experimental results and confirm the legitimacy of modeling the air injection as a local shift of the compressor characteristic. Section 6 summarizes the main conclusions and indicates several possible avenues of future research.

2 Experimental Setup

In order to test the effects of air injection for stabilization of rotating stall, we have built a low-speed, axial flow compressor facility. The entire experimental setup is shown in Fig. 1 and was designed and constructed in accordance with standards for measurement and calibration of compressors of this type [AMCA/ASHRAE, 1985]. The compressor is a 17-cm-dia, single-stage, axial flow compressor with 14 blades, a hub-to-tip ratio of 0.7, and a blade chord length of 3.75 cm. In addition to the compressor unit, the system consists of an inlet nozzle, adjustable downstream throttle, and an optional plenum. Sensors include a pair of static pressure rings on the inlet and outlet ducting, a pitot measuring plane near the outlet, and an array of six static pressure transducers located near the front of the compressor face. Actuation is achieved with a low-speed, electrically driven throttle at the outlet, a high-speed bleed valve that can be located either before or after the optional plenum, and a set of three air injectors at the compressor face (described in more detail below).

For the experiments presented in this paper, the compressor was run at 6000 rpm, giving a peak head coefficient of 0.38 at a flow coefficient of 0.37, as shown in Fig. 3. In physical units,

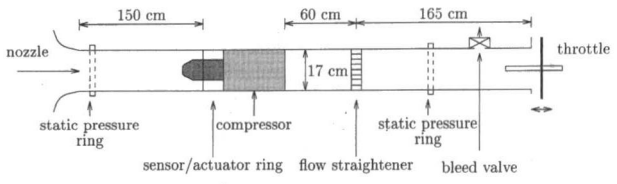

Fig. 1 Caltech compressor rig

this corresponds to 940 Pa at 0.19 m^3/s. The high-speed bleed valve was only used to generate disturbances, and the optional plenum was only used in the experiments of Section 4.3. All sensors and actuators are interfaced to a PC-based real-time control computer running at a servo rate of 2000 iterations per second.

The sensor ring shown in Fig. 2 is located at the compressor inlet and used to measure the unsteady pressures upstream of the rotor. The ring has six pressure transducers equally spaced around the compressor circumference, approximately 5 cm (0.7 mean rotor radii) upstream of the rotor. The transducers have a resolution of approximately 1.2 Pa, a bandwidth of 1 kHz, and are low pass filtered at 500 Hz prior to sampling by a 12 bit A/D converter. The inlet and outlet static pressure rings shown in Fig. 1 are instrumented with similar transducers, but are not filtered prior to sampling.

Three air injection actuators are also located on the sensor ring shown in Fig. 2. The injectors are controlled by on/off solenoid valves, which can be placed at a variety of (static) locations and orientations. The valves are actuated via custom overdriving circuitry interfaced directly to the computer, and are capable of a 50 percent duty cycle at up to 200 Hz. Hot-wire measurements were performed to determine the velocity profile of the air injection at the compressor face for the active control experiments outlined in Section 4. The injected air was found to disperse from 3 mm at the exit of the injector to approximately 20 mm at the compressor face; this dispersion occurred over a distance of 9 cm (the distance between the exit of the air injector and the rotor face).

Three measures of control authority were calculated to characterize the air injectors: the mass flux, the momentum flux, and the energy flux. As a percentage of the mean values for the compressor operating at the peak of the compressor characteristic, continuous flow through each air injector contributed 1.7 percent of the mass flux, 2.4 percent of the momentum flux, and 1.3 percent of the energy flux. Each of the control authority measures is thus small compared to the corresponding values for the compressor.

The effects of the air injectors can be roughly characterized by their effect on the static compressor map. D'Andrea et al. (1995) investigated the effect of continuous air injection into the rotor face at different incident angles. The experimental results indicated that the compressor characteristic could be altered by air injection. In Fig. 4, the shifted compressor characteristics are plotted for various incident angles. Note that for positive angles (air injected into the blade rotation), the shifting of the characteristic is approximately the same, with the only difference being the stall inception point (as marked by circles).

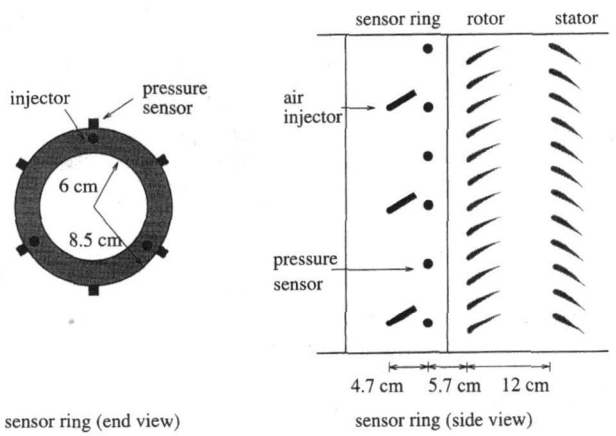

Fig. 2 Sensor ring

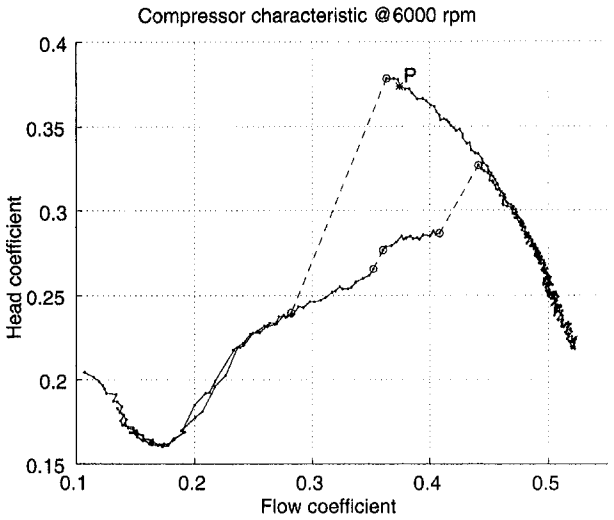

Fig. 3 Compressor characteristic for the Caltech rig at 6000 rpm. The flow coefficient is is defined to be $\dot{m}/(\rho A_s U_r)$, where $\dot{m}$ is the mass flow rate through the compressor, ρ is the density of air, A_s is the cross-sectional area of the annulus, and U_r is the rotor blade speed at midspan. The head coefficient is defined to be $\Delta P/(\rho U_r^2)$, where ΔP is the pressure rise across the compressor. Dark lines indicate continuous changes in the operating point while lighter lines represent discontinuous changes. The circles mark the points of discontinuity. 'P' is the operating point for the parametric studies outlined in Section 4.

3 Compressor Dynamics and Characteristic Shifting

In this section, a three-state model for a compression system, proposed by Moore and Greitzer (1986), is used to explore qualitatively the effects of air injection as a stabilizing mechanism. This model is too simple to be able to reproduce in detail the operation of a compressor. This model does, however, capture the essential dynamics of the compressor. By analyzing this low-dimensional model and modeling the injection of air as a shift of the compressor characteristic, the viability of various control configurations is established by observing the change in the bifurcation behavior of the system under nonlinear feedback.

3.1 Moore–Greitzer Three-State Model. We begin with Eqs. (44), (54), and (55) from Moore and Greitzer (1986), which are reproduced here for clarity (where the parameter W has been set to one):

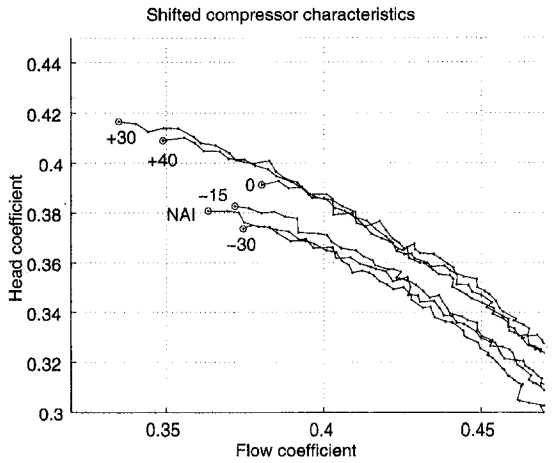

Fig. 4 Compressor characteristics for various air injection angles. The flow coefficient calculation is based on the total flow through the compressor (i.e., it includes the contribution from the air injectors). NAI corresponds to the unactuated case (no air injection). The circles mark the peak operating point for each compressor characteristic.

$$\frac{d\Psi(\xi)}{d\xi} = \frac{1}{4l_cB^2}\left(\Phi(\xi) - \gamma\sqrt{\Psi(\xi)}\right), \quad (1)$$

$$\Psi(\xi) + l_c\frac{d\Phi(\xi)}{d\xi} = \frac{1}{2\pi}\int_0^{2\pi} \Psi_c(\Phi(\xi) + A(\xi)\sin\zeta), d\zeta \quad (2)$$

$$\left(m + \frac{1}{a}\right)\frac{dA(\xi)}{d\xi} = \frac{1}{\pi}\int_0^{2\pi} \Psi_c(\Phi(\xi) + A(\xi)\sin\zeta)\sin\zeta d\zeta. \quad (3)$$

In the equations, Ψ is the pressure rise coefficient, Φ is the annulus-averaged flow coefficient, A is the amplitude of the sinusoidal flow coefficient perturbation, ξ is dimensionless time, Ψ_c is the steady-state compressor characteristic, and the quantities l_c, B, a, and m are parameters that depend on the compression system.

Based on the open-loop results shown in Fig. 4, we attempt to model the air injectors as direct actuators of the steady-state compressor characteristic, and then analyze the dynamics of the closed-loop system when the feedback is proportional to the size of the first mode of the stall cell squared. It should be stressed that this cannot be duplicated experimentally since the air injectors can only be either on or off. The benefits of this simplified analysis will, however, become apparent shortly. The controlled compressor characteristic is taken to be

$$\Psi_c = \Psi_{cnom} + KJ\Psi_{cu}, \quad (4)$$

where

$$\Psi_{cnom}(\Phi) = a_0 + a_1\Phi + a_2\Phi^2 + a_3\Phi^3,$$
$$\Psi_{cu}(\Phi) = c_0 + c_1\Phi. \quad (5)$$

By performing the integrals indicated above and substituting $J = A^2$, we obtain the following set of ODEs, which describe the dynamics of the compression system:

$$\dot{\Psi} = \frac{1}{4l_cB^2}\left(\Phi - \gamma\sqrt{\Psi}\right),$$
$$\dot{\Phi} = \frac{1}{l_c}\left(\Psi_c(\Phi) - \Psi + \frac{J}{4}\frac{\partial^2\Psi_c(\Phi)}{\partial\Phi^2}\right),$$
$$\dot{J} = \frac{2a}{1+ma}J\left(\frac{\partial\Psi_c(\Phi)}{\partial\Phi} + \frac{J}{8}\frac{\partial^3\Psi_c(\Phi)}{\partial\Phi^3}\right). \quad (6)$$

3.2 Bifurcation Analysis. The bifurcation properties of the open-loop three-state compression system model were initially studied by McCaughan (1989, 1990), where the bifurcations for the pure rotating stall case, the pure surge case, and combination stall/surge case were thoroughly investigated. A throttle-based closed-loop system for the pure rotating stall case was developed and analyzed by Liaw and Abed (1996).

In this paper we are interested only in the pure rotating stall case for the closed-loop compression system with the control based on shifting of the steady-state compressor characteristic. For the open-loop case, the bifurcation diagram for a representative compressor characteristic is known to have a transcritical bifurcation (for the choice of coordinates used in this paper) at the point that corresponds to operating at the peak of the steady-state compressor characteristic (see Fig. 5). This throttle setting, which corresponds to the peak of the characteristic $(\partial\Psi_c(\Phi)/\partial\Phi = 0)$, will be denoted by γ^*. This operating point corresponds to where the stalled branch intersects the horizontal axis in the bifurcation diagram shown in Fig. 5. This diagram suggests a hysteresis region since as the throttle is closed (γ is decreased) $J = 0$ is a stable solution until γ^* is reached, at which point the stable solution for J is nonzero (which corresponds to a jump to rotating stall). As γ continues to decrease, the stable solution for J continues to be nonzero. If the throttle is then opened, beginning at $\gamma < \gamma^*$, the system continues to evolve along the stalled branch until γ is increased to a value substantially greater than γ^* before returning to the $J = 0$ branch. The system has substantially different solutions depending on the path that γ follows.

We next analyze how the closed-loop system based on a shifting of the steady-state compressor characteristic affects this bifurcation diagram, and in particular, the hysteresis region. On the stalled branch of the bifurcation diagram, the following algebraic equations must hold:

$$\Phi^2 = \gamma^2\Psi, \quad (7)$$

$$\Psi_c(\Phi) = \Psi - \frac{J}{4}\frac{\partial^2\Psi_c(\Phi)}{\partial\Phi^2}, \quad (8)$$

$$\frac{\partial\Psi_c(\Phi)}{\partial\Phi} = -\frac{J}{8}\frac{\partial^3\Psi_c(\Phi)}{\partial\Phi^3}. \quad (9)$$

Since Φ, Ψ, and γ may be determined from J for each equilibrium solution on the stalled branch of the bifurcation diagram, we may differentiate Eq. (7) with respect to J to obtain

$$2\Phi\frac{d\Phi}{dJ} = 2\gamma\frac{d\gamma}{dJ}\Psi + \gamma^2\frac{d\Psi}{dJ}. \quad (10)$$

Differentiating Eq. (8) with respect to J and evaluating $(d\Psi/dJ)$ at the peak of the compressor characteristic yields

$$\left.\frac{d\Psi}{dJ}\right|_{\gamma=\gamma^*} = K\Psi_{cu}(\Phi) + \frac{1}{4}\frac{\partial^2\Psi_{cnom}(\Phi)}{\partial\Phi^2}. \quad (11)$$

Similarly, differentiating Eq. (9) with respect to J yields

$$\left.\frac{d\Phi}{dJ}\right|_{\gamma=\gamma^*} = \frac{K\dfrac{\partial\Psi_{cu}(\Phi)}{\partial\Phi} + \dfrac{1}{8}\dfrac{\partial^3\Psi_{cnom}(\Phi)}{\partial\Phi^3}}{-\dfrac{\partial^2\Psi_{cnom}(\Phi)}{\partial\Phi^2}}. \quad (12)$$

Substituting Eqs. (11) and (12) into Eq. (10) and solving for $(dJ/d\gamma)$, the slope of the bifurcation diagram at the equilibrium point associated with γ^* is:

$$\left.\frac{dJ}{d\gamma}\right|_{\gamma=\gamma^*} = \frac{\sqrt{\Psi}}{\dfrac{K\dfrac{\partial\Psi_{cu}(\Phi)}{\partial\Phi} + \dfrac{1}{8}\dfrac{\partial^3\Psi_{cnom}(\Phi)}{\partial\Phi^3}}{-\dfrac{\partial^2\Psi_{cnom}(\Phi)}{\partial\Phi^2}} - \dfrac{\Phi}{2\Psi}\left(K\Psi_{cu}(\Phi) + \dfrac{1}{4}\dfrac{\partial^2\Psi_{cnom}(\Phi)}{\partial\Phi^2}\right)}, \quad (13)$$

where all expressions in the right-hand side of Eq. (13) are evaluated at the equilibrium point at the peak of the compressor characteristic.

Without feedback ($K = 0$), the denominator in Eq. (13) must be positive and greater than 0 to yield the hysteresis region in Fig. 5. In order to eliminate this hysteresis region, the denominator must be made 0 or negative. The term associated with $-K$ is as follows:

$$\frac{\dfrac{\partial\Psi_{cu}(\Phi)}{\partial\Phi}}{\dfrac{\partial^2\Psi_{cnom}(\Phi)}{\partial\Phi^2}} + \frac{\Phi\Psi_{cu}(\Phi)}{2\Psi} \quad (14)$$

Thus, in order to make the denominator as negative as possible for a fixed K, this quantity needs to be made as large as possible. Since the second partial derivative of $\Psi_{cnom}(\Phi)$ with respect to Φ is negative at the stall inception point, this suggests

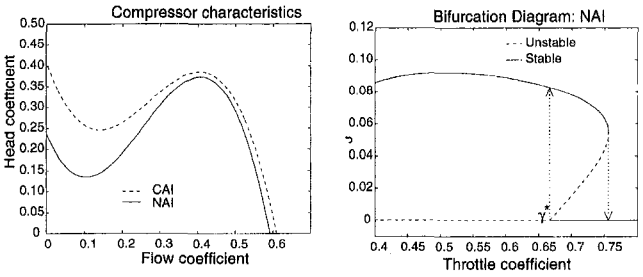

Fig. 5 Bifurcation diagram showing jumps associated with the hysteresis loop for the open-loop compression system corresponding to the no air injection (NAI) characteristic Ψ_{cnom} shown at the left. Also shown in the left diagram is the continuous air injection (CAI) shifted characteristic. The linear approximation of the difference between these two characteristics at the stall inception point is Ψ_{cu}. The numerical values were determined by fitting the various model parameters in Eq. (6) to the Caltech rig.

that the most beneficial shift is one that has the largest positive offset and the largest negative slope. Referring back to the steady state shifts of Fig. 4, this analysis suggests that the +30 and +40 characteristics are good candidates for feedback control.

4 Experimental Results Using Pulsed Air Injection

In this section, we present the experimental results on the use of air injection to control rotating stall. The effects of this control strategy on the surge dynamics are also explored. In Fig. 6, the altered characteristic is plotted for an incident angle of 40 deg, along with the unactuated characteristic for comparison purposes. This orientation was used for all the active control experiments in this section.

4.1 Description of Control Algorithm. The basic strategy of the control algorithm is to sense the location and magnitude of the peak of the first-mode component of a circumferential pressure disturbance and apply pulses of air based on the size and location of this first mode relative to the air injectors, essentially the same strategy employed by Day (1993a).

The plots in Fig. 7 show the spatial, Fourier modal components of the pressure disturbance when a transition from unstalled to stalled behavior occurs. Since six equally spaced pressure transducers were used to measure the pressure disturbance, only the first two modes could be determined. As can be seen, the dominant mode is the first one. From the slope of the phase plots, one can conclude that the first and second mode disturbances are rotating at a rate of approximately 65 Hz. To ascertain that no significant aliasing was taking place due to the use of only six pressure transducers, time domain measurements were analyzed for each pressure transducer and the power spectrum determined. It was found that most of the signal power was contained in two bands centered around 65 and 130 Hz. Assuming that the pressure disturbance is a traveling wave about the circumference of the compressor, this would indicate that the third mode component is also negligible spatially about the circumference of the compressor.

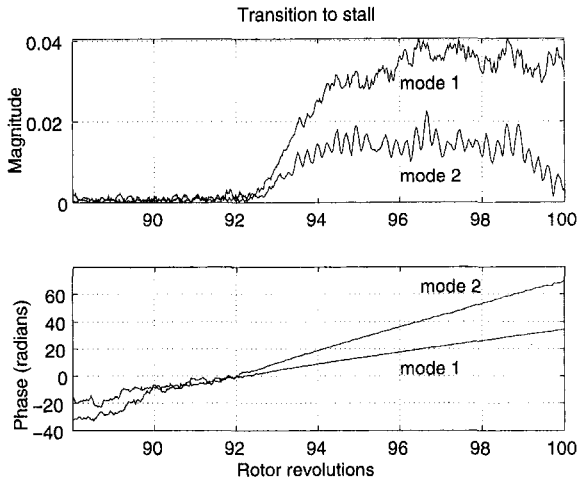

Fig. 7 Transition to stall

The parameters used in the control algorithm are:

jeton	injector pulse width
threshold	threshold for stall detection
window	angle window for stall detection
angle1	threshold angle for injector 1
angle2	threshold angle for injector 2
angle3	threshold angle for injector 3

The algorithm is shown in Fig. 8, and behaves as follows. Each air injector is activated when the magnitude of the first mode is greater than threshold and the location of the peak of the first mode is within a prespecified window (as determined by **angle** and **window**); once an air injector is activated, it remains activated for **jeton** number of servo-loops, irrespective of the magnitude **mag** and location **phase** of the first mode. Note that **phase** and **mag** refer to the phase and magnitude of the first Fourier coefficient, not the physical location and value of the peak pressure disturbance at the compressor face. In the

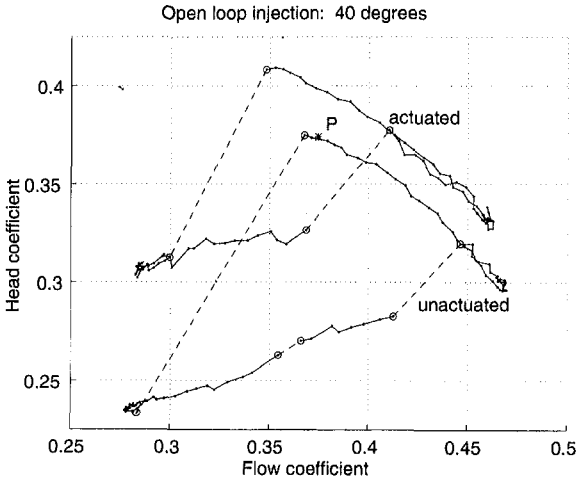

Fig. 6 Compressor characteristic at air injection angle of 40 deg

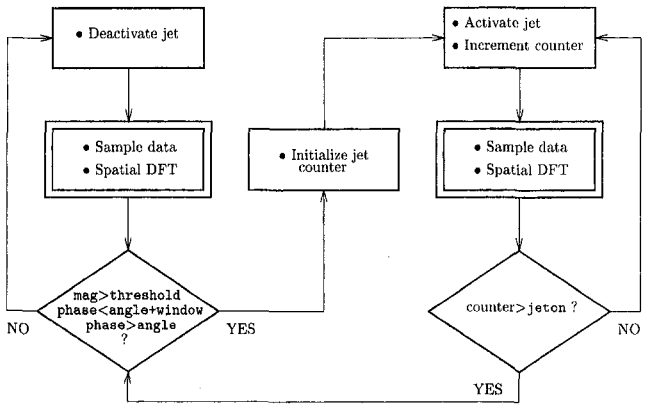

Fig. 8 Control algorithm. The same logic is repeated for each air injector. The double rectangle corresponds to the beginning of a servo loop, which occurs at a rate of 2000 iterations per second.

case that the pressure disturbance is sinusoidal (which is a good approximation when fully stalled), **phase** and the physical location of the peak pressure disturbance differ by a constant. This is due to delays in the data acquisition stage; this delay was calculated to be 1.5 ms.

4.2 Parametric Study. The controller parameters were varied in order to determine the optimal operating conditions for the controller, and to determine the effects on the closed-loop behavior. The parameters varied were **jeton** and **angle1, angle2** and **angle3.** For this parametric study, the value of **threshold** was set to correspond to a head coefficient of 0.004 (10 Pa), and **window** was set to correspond to 25 deg. The chosen value of **threshold** was slightly above that of the noise level, and thus allowed the control algorithm to sense a stall cell forming as quickly as possible. Assuming that the first mode rotates at a constant rate of 65 Hz, one servo period corresponds to a rotation of 12 deg. By setting **window** larger than this value, we ensure that the peak of the stall cell disturbance will not be missed. On the other hand, the window should not be too large, to ensure that we do not have double activations (this is guaranteed by setting **window** $< 12*$**jeton**), and to ensure that an air injector activates at the same time relative to the stall location (this might be a problem if the magnitude of the stall cell becomes greater than threshold near the end of an air injector's window). It was found experimentally that the value of **window** could be set in the range of 15 to 90 deg without changing the performance of the controller.

Effect of Activation Angles. For a fixed value of **jeton,** a search was performed over the activation angle for each air injector to determine the optimal strategy. The compressor was operated at point P in Figs. 3 and 6. Parameters **angle1, angle2,** and **angle3** were each varied in 30 deg increments, from 0 to 330 deg. Thus a total of 1728 different controllers were tested for each value of **jeton.** For each of these parameter choices,

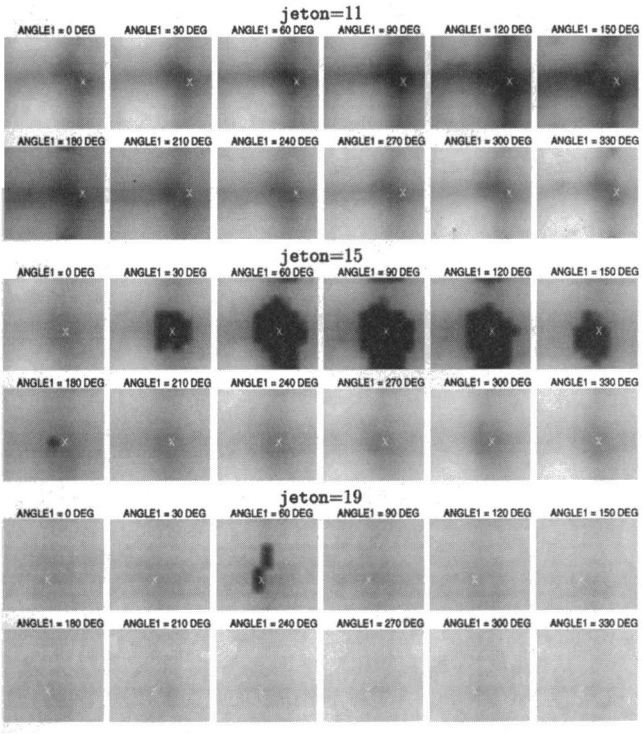

Fig. 9 Parametric study, jeton = **11, 15, and 19. Dark areas correspond to low average values for the first-mode disturbance, light areas correspond to large average values. The horizontal axis for each plot corresponds to** angle2, **0–360 deg; the vertical axis corresponds to** angle3, **180–540 deg, shifted to center the dark areas. The white 'X' corresponds to the optimal setting for** angle2 **and** angle3.

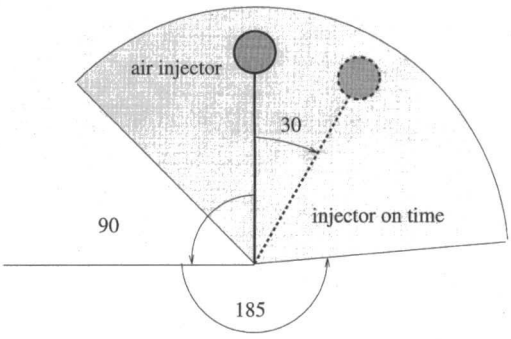

Fig. 10 On-time for air injector 1, jeton = **15. The shaded region corresponds to the location of the peak of the first-mode disturbance for which an air injector is on, assuming a constant rotational rate of 65 Hz: the 90 deg rotation corresponds to the experimentally determined optimal lag; the 185 deg lag corresponds to the delay from sensing to actuation; the −30 deg rotation corresponds to the measured physical location where the injected air strikes the rotor face (recall that the air injectors were angled into the blade rotation).**

the control algorithm was operated for 16 seconds, and the average size of the stall cell and amount of time each air injector was on was recorded. A 0.1 second disturbance was generated every second via the high-speed bleed valve to ensure that the compressor would stall.

The criterion used to determine the optimal setting for **angle1, angle2,** and **angle3** for a fixed **jeton** was the setting that yielded the lowest value for the average magnitude of the first mode (other criteria were also investigated, such as the total time that air injectors were on and the average pressure rise across the compressor, and produced roughly the same results).

The results of this parametric study for **jeton** = 11, 15 and 19 may be found in Fig. 9. Referring to Fig. 9, for each value of **jeton** there are twelve separate plots, one for each setting of **angle1.** From these plots, one may conclude that the optimal setting for **angle1, angle2,** and **angle3** is roughly (90, 210, 330) for **jeton** = 15, and that the performance of the control algorithm is insensitive to simultaneous parameter deviations of up to 30 deg from this optimal setting. A similar observation for **jeton** = 11 and 19 yields (120, 270, 0) and (60, 180, 300), respectively, for the optimal setting. By taking into account the activation, de-activation, and transport delays, and assuming a constant rotational speed for the pressure disturbance of 65 Hz, these optimal parameter settings correspond to each injector being on when the peak of the first mode component of the disturbance is within a window (whose width is determined by **jeton**) centered around the injector position. This is depicted in Fig. 10. A typical operation of the controller may be found in Fig. 11.

Effect of Pulse Width. It was found that for values of **jeton** less than or equal to 9, and greater than or equal to 22, the compressor remained stalled all the time. Taking the activation and deactivation delays into account, a value of 9 corresponds to approximately 2.5 ms of on-time for each injector, or about 60 deg when the disturbance rotates at 65 Hz. This amount of time apparently was not enough to bring the compressor out of stall.

A value of 22 for **jeton** corresponds to approximately 9 ms of on-time for each injector, or about 210 deg at a rotation rate of 65 Hz. Thus for this value, an air injector remains active even when the local flow is above the spatially averaged value through the compressor.

One can understand why there should exist an upper and a lower bound for values of **jeton** that eliminate stall through limiting arguments. Clearly for **jeton** = 0 (no control), the compressor will transition into stall. To understand what happens when **jeton** = ∞, one need only look at the plot of Fig.

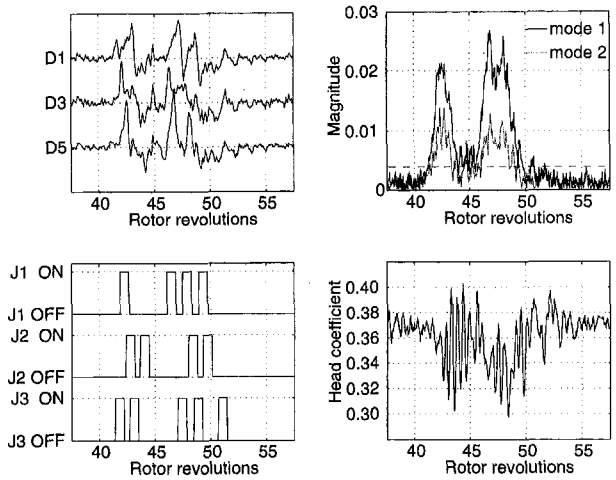

Fig. 11 Closed-loop operation. The upper left plot consists of the pressure data for transducers 1, 3, and 5. The lower left plot consists of the control signals applied to the air injectors. The upper right plot consists of the calculated first and second-mode magnitudes; the dashed line corresponds to the setting for threshold. **The lower right plot consists of the variation in the head coefficient.**

6; when operating near the stall point of the compressor, there are two possible operating points the compressor may reach when all the air injectors are turned on. One is the unstalled branch, while the other is the stalled branch. If the compressor is unstalled when the air injectors are activated, the operating point will shift to the upper branch; if the compressor is stalled, the operating point will shift to the lower branch (this was verified experimentally). Furthermore, phase information is lost when activating the air injectors for long periods of time. Thus one cannot eliminate the rotating stall condition by simply turning all the air injectors on.

Closed Loop Performance. The closed-loop compressor performance curve is shown in Fig. 12 for the optimal choice of injector phasing for **jeton** = 15. It was determined that operating points to the left of the peak were not dependent on the initial conditions of the system, i.e., the hysteresis region usually associated with stall was eliminated.

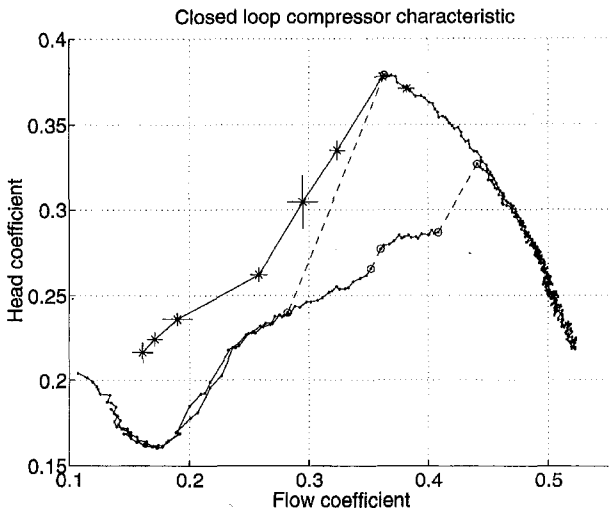

Fig. 12 Closed-loop compressor characteristic for jeton = **15, optimal controller. The asterisks correspond to time-averaged data, while the solid lines interpolate these points. The pressure and flow variance are included for each data point as error bars. The open-loop compressor characteristic is included for comparison purposes.**

4.3 Effects of Control Algorithm on Surge Dynamics. Several experiments were performed to determine the effect of the control algorithm when the optional plenum was attached to the compressor. The results may be found in Fig. 13. At operating point P (see Fig. 3), a disturbance lasting 20 rotor revolutions (0.2 seconds) was generated via the high-speed bleed valve (the time for which the bleed valve was closed is represented by a horizontal line in the upper left plots in Fig. 13).

Referring to the uncontrolled data, the system promptly went into surge. As can be seen from the plots, there were two different surge modes, one at 1.4 Hz and the other at 1.8 Hz. The compressor was stalled during the low-flow intervals, and unstalled during the high-flow intervals. The head coefficient versus flow coefficient plot clearly illustrates the surge limit cycle; starting at point P (the asterisk), the graph is traversed in a counterclockwise direction. The two different surge modes ap-

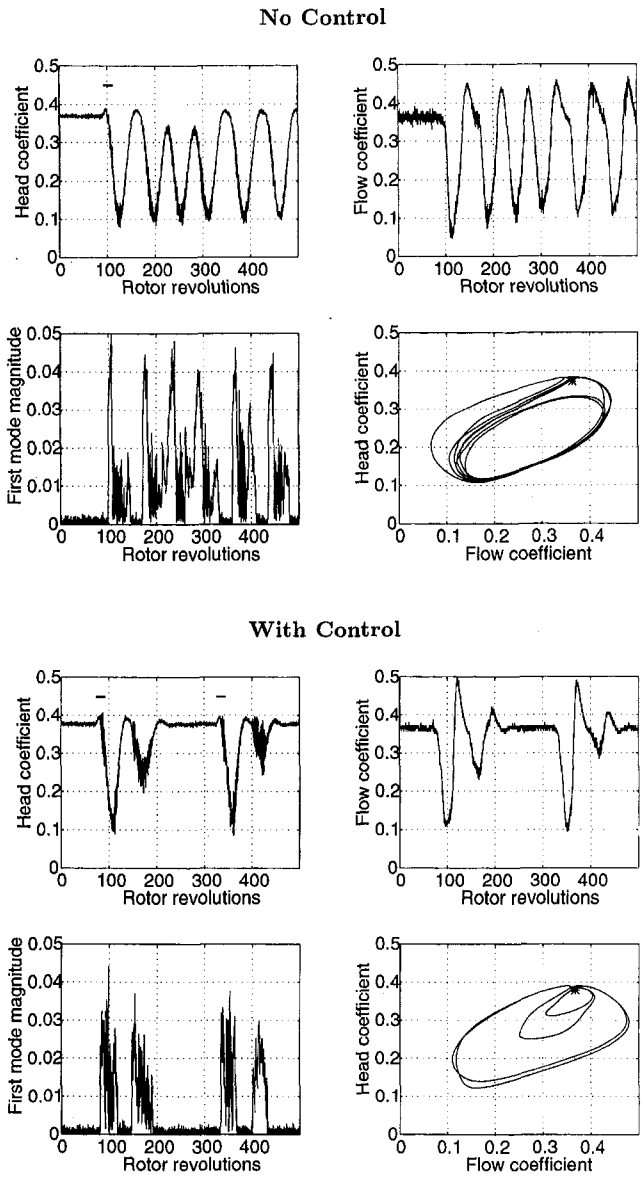

Fig. 13 Compressor dynamics with plenum: the top set of plots correspond to data taken without the controller, the bottom set of plots with the controller. In each of the Head coefficient versus Rotor revolutions plots, a solid line is used to indicate the length of time for which the high-speed bleed valve was activated. All data were low-pass filtered at 150 Hz, except for the Head coefficient versus Flow coefficient plots, where the data was filtered at 10 Hz; the asterisk in these plots corresponds to operating point P, as per Fig. 3.

pear as two different closed circuits in this plot, which share a substantial part of the trajectory. Note that there exists a hysteresis region associated with the surge dynamics; the system did not exit surge when the disturbance was removed. This is due to the strong coupling between stall and surge. Also note that the duration of the disturbance corresponded approximately to the time it took for the pressure and flow to reach their minimum value; this observation is important in the analysis of the closed-loop behavior given below.

Two throttle disturbances were generated approximately 2.5 seconds apart with the controller activated. As before, each throttle disturbance destabilized the system. Note that the controller had virtually no effect on the surge trajectory during the time the disturbance was present (in this 20 revolution time period, the trajectory is virtually the same as the one in the previous experiment). On the subsequent cycle, however, the pressure and flow variations were substantially decreased, and were completely eliminated by the end of the third cycle. It was determined that by shortening the time duration of the throttle disturbance (while still keeping it large enough to cause the open-loop system to go into surge), the pressure and flow variations during the first cycle were reduced, with the limiting behavior approaching the trajectories commencing from the second cycle in the plots. Thus, if the duration of the throttle disturbance was short enough, the magnitude of the pressure and flow disturbances could be kept to within 30 percent of the operating pressure and flow.

A possible explanation of why the control algorithm is successful at eliminating stall and surge is the strong coupling between the surge and stall dynamics; the compressor is stalled when the flow coefficient is decreasing. The control algorithm at this point activates, and tries to eliminate the stalled condition. This has the effect of increasing the net flow across the compressor during the periods of decreasing flow coefficient. Thus, the control algorithm is in effect providing positive damping to the surge dynamics. This is a topic for future research.

Note that this control strategy does not displace the steady-state surge line. What it does do is make the system less susceptible to disturbances by taking advantage of the strong coupling between stall and surge. This is further explored by Behnken (1996), where the bleed valve is used to control the surge instability directly, and the air injectors are used to control rotating stall.

5 Simulations

In this section, simulations using a high-fidelity model are presented. The main motivation for performing the simulations was to demonstrate the validity of modeling the air injection actuation as a local shift of the compressor characteristic. This relatively simple approach to modeling the aggregate effects of injecting air into the rotor blades is very attractive from a computational (and thus control) perspective; the eventual goal is to provide a low-order mechanism that captures the essential features of air injection, analogous to capturing the dominant dynamics of a compression system via the Moore–Greitzer equations, and thus facilitate subsequent analyses and control designs that make use of air injectors. Another function of the simulations is to corroborate the experimental results and thus to give confidence in the control strategy of Section 4.

The model used here is the distributed model of Mansoux et al. (1994), which is a system of equations describing the dynamics of the flow coefficient Φ at discrete points around the compressor annulus. The simulations presented here also include additional effects such time lags associated with change in the pressure rise delivered ($\Psi_c(\Phi)$ has dynamics associated with it) and the mass/momentum addition effects associated with air injection. The distributed model was used to perform a simulation based parametric study similarly to what was performed on the experiment and to model the hysteresis region of the compressor running with and without the air injection. We first present the equations of the basic distributed model and then describe simulation results.

5.1 Distributed Model. The full details of the distributed model presented by Mansoux et al. (1994) should be obtained from that reference; only the details required to explain how the compressor characteristic shifting was included in the model will be presented here. The final equations (Eq. (20)) from Mansoux et al. (1994), which make up the distributed model for a compression system, are given by:

$$\dot{\Psi} = \frac{1}{4l_c B^2}\left(S\Phi - \gamma\sqrt{\Psi}\right) \tag{15}$$

and

$$G^{-1}D_E G\dot{\Phi} = -G^{-1}D_A G\Phi + \Psi_c(\Phi) - T\Psi, \tag{16}$$

where Ψ is the annulus-averaged pressure rise coefficient, Φ is the vector of flow coefficients at discrete points around the compressor annulus, γ is the throttle position, and D_A, D_E, T, S, B and l_c are constants, which depend on the compressor rig (see Mansoux et al., 1994). G is the discrete Fourier transform matrix, i.e.,

$$\Phi = \begin{bmatrix} \Phi_1 \\ \Phi_2 \\ \vdots \\ \Phi_{2n+1} \end{bmatrix} \quad G{:}\Phi \mapsto \begin{bmatrix} \tilde{\Phi}_0 \\ \mathrm{Re}\,\tilde{\Phi}_1 \\ \mathrm{Im}\,\tilde{\Phi}_1 \\ \vdots \\ \mathrm{Re}\,\tilde{\Phi}_n \\ \mathrm{Im}\,\tilde{\Phi}_n \end{bmatrix},$$

where $\tilde{\Phi}_i$ is the Fourier coefficient associated with mode i, and n is the number of modes included in the model. Seven modes were used for the results presented here. Two additional effects not included in these equations but included in the simulations are the effects of unsteady flow on the pressure rise delivered by the compressor and the mass/momentum addition terms associated with air injection. The unsteady flow effects on the delivered pressure rise have been studied by Haynes et al. (1994), and it is straightforward to append the linear model presented there to the dynamics reproduced here (this is suggested in the distributed model presentation by Mansoux et al., 1994). The mass/momentum addition terms associated with the air injection were derived for the linear case by Hendricks and Gysling (1994). The results presented there have been extended to include the nonlinear terms for the simulations presented here. A complete description of our modeling efforts is beyond the scope of this paper; for additional details see Behnken (1996).

The Caltech compressor rig has three air injectors placed 120 deg apart around the compressor annulus (as in Fig. 2), and each injector has an effect on a small region of the compressor rotor. In the distributed model, the vector of pressure rise coefficients around the compressor annulus is given by $\Psi_c(\Phi)$. In order to include the compressor characteristic shifting as a local effect, the shift is included as

$$\Psi_c(\Phi_i) = \Psi_{cnom}(\Phi_i) + (\Psi_{shf}(\Phi_i) - \Psi_{cnom}(\Phi_i))\mathbf{L}(u_i) \tag{17}$$

at the three points around the annulus that have injectors associated with them and as

$$\Psi_c(\Phi_i) = \Psi_{cnom}(\Phi_i) \tag{18}$$

for the remaining positions. Here Ψ_{cnom} is the nominal compressor characteristic, while Ψ_{shf} is the locally shifted characteristic. The control variables are the u_i, which take the values of 0 or 1 if the air injector is off or on, respectively. The transient effect of the air injection on the compressor characteristic shift is modeled as a delay followed by a first order lag; this is captured

by operator **L**. The values for the delay and lag were chosen to correspond to the values observed in the experiment.

The geometric parameters associated with the distributed model were first calculated from physical measurements of the Caltech rig, and initial guesses were taken for those that remained. The simulation parameters were then adjusted (specifically the compressor characteristics) to match the rotation and growth rate of the transition to rotating stall and to match the pressure rise delivered during fully developed rotating stall. Compressor characteristics were determined for both the no air injection (NAI) and continuous air injection (CAI) cases, as per the experimental data shown in Fig. 6. Figure 14 shows the compressor characteristics used in simulation for both cases, as well as the experimental data for comparison purposes.

Since the simulation parametric study will compare how controllers respond to a disturbance from the peak of the unstalled compressor characteristic (as was done for the experimental setup), the compressor characteristics for the two cases were selected so that stall occurred at the same point as determined experimentally (there is a slight discrepancy to account for the noise in the experimental setup). In addition, the characteristics were adjusted so that the open-loop simulations corresponded to the behavior observed experimentally at the transition to stall and at recovery from rotating stall. For this reason, the simulated open-loop characteristics do not match up perfectly with those observed experimentally over the entire hysteresis region. In order to correct these errors, the details of fully developed rotating stall would have to be modeled over the entire range of the throttle settings, and a substantially more complicated model would be required.

The next step was to simulate the open-loop air injection case with a nonuniform compressor characteristic. From the characteristics shown in Fig. 14, the equivalent local compressor characteristic for the stations where air injectors are located, Ψ_{shf}, can be determined. This was done by requiring that the average characteristic obtained when using the characteristic shown on the right of Fig. 14 have the same value as that obtained when using the locally shifted characteristic Ψ_{shf} at three stations, and the average nominal compressor characteristic Ψ_{cnom} (shown on the left in Fig. 14) at the remaining stations. The plot on the left of Fig. 15 shows the characteristics used in the simulation study, and the plot on the right shows the resulting hysteresis loop obtained via simulation using the local nonuniform characteristic.

5.2 Parametric Study. The goal of the simulation-based parametric study was to determine the optimal control strategy based on a model for the compressor. In particular, a search for the optimal phasing for the activation of each air injector relative to the measured position of the peak of the first mode stall disturbance was performed.

The control algorithm was essentially the same as the one described in Fig. 8 in Section 4. The major difference was in the implementation of what corresponded to activating the air injectors for **jeton** number of servo iterations in the experimental study. This was accomplished by activating each air injector when the magnitude of the first mode disturbance became

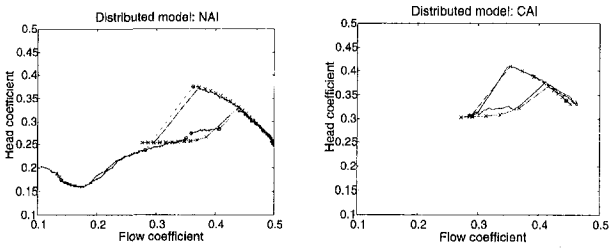

Fig. 14 Hysteresis loops for simulation compressor characteristics. Simulation data points are denoted with an *x*.

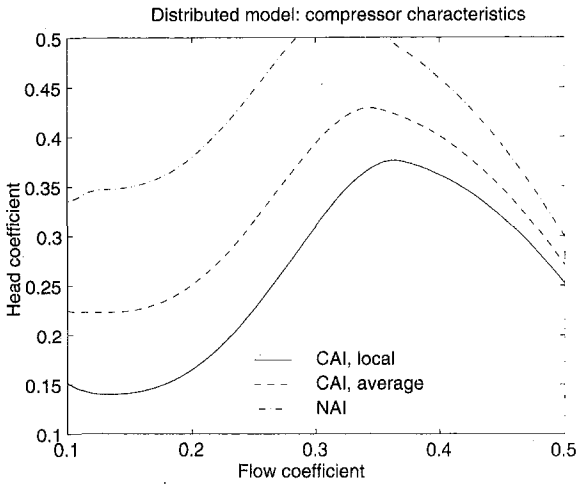

Fig. 15 Shifted compressor characteristics

greater than some threshold magnitude and the phase of the first mode disturbance was within a prespecified window. The threshold magnitude was based on the noise level in the experimental determination of the magnitude of the first mode.

In terms of the logic of Fig. 8, this corresponds to setting **jeton** to 0 and **window** to 120 deg, and running the servo loop at an infinitely high rate. This is roughly how the control algorithm behaved in the experimental studies. This algorithm was used to simplify the simulation code and vastly decrease its running time.

As in the experimental study, the phasing of each air injector was independently varied in 30 deg increments. For each controller tested, the average amplitude of the first mode stall cell was recorded. In all the simulations, the same initial stall cell disturbance (both in magnitude and phase) was used. Figure 16 shows the results of the simulation parametric study in the same format that the experimental results were presented in Fig. 9. The simulation study predicts the same periodic trends for the optimal phasing as were seen in the experimental data.

The optimal phase setting for the simulation parametric study is approximately (150, 270, 30). The activation, de-activation, and transport delays were implemented by a Pade approximation (operator **L** in Eq. (17)). In the experimental setup, the air injectors were not symmetric with respect to the turn on and turn off times; it was found that the air injectors would take approximately 2 ms longer to turn on than to turn off (this was taken into account in the analysis of Fig. 10), which corresponds to roughly 50 deg of stall rotation. This asymmetry was not implemented in the simulation. When this 50 deg lead is subtracted from the optimal setting, a value consistent with the optimal setting obtained experimentally is obtained.

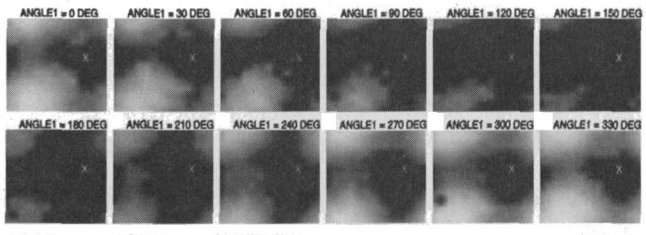

Fig. 16 Simulation parametric study. Dark areas correspond to low average values for the first-mode disturbance, light areas correspond to large average values. The horizontal axis for each plot corresponds to angle2, 0–360 deg; the vertical axis corresponds to angle3, 180–540 deg, shifted to center the dark areas. The white 'X' corresponds to the optimal setting for angle2 and angle3.

5.3 Closed-Loop Simulations. The closed-loop characteristic for the optimal controller obtained via simulation is shown in Fig. 17. The hysteresis region has essentially been eliminated, as was determined experimentally. The transition to rotating stall is also gradual, i.e., there is no jump from zero stall to fully developed stall. These two results, along with the matching of the trends between the experimental and simulation parametric studies strongly support the air injection model presented here. Further work on refining the model will focus on using numerical techniques to determine the bifurcation characteristics, and coupling surge controllers with the pulsed air injection controller for rotating stall.

6 Conclusions and Future Work

The active control techniques presented in this paper proved to be simple, easy to implement, and yet at the same time extremely effective in eliminating the hysteresis region normally associated with rotating stall. The following procedure is suggested by the results in this paper:

1 Experimentally determine the air injector orientation that results in a shifted compressor characteristic Ψ_{cu} maximizing the quantity

$$\frac{\dfrac{\partial \Psi_{cu}(\Phi)}{\partial \Phi}}{\dfrac{\partial^2 \Psi_{cnom}(\Phi)}{\partial \Phi^2}} + \frac{\Phi \Psi_{cu}(\Phi)}{2\Psi}, \tag{19}$$

evaluated at the peak of the compressor characteristic. This is suggested by the bifurcation analysis of Section 3; maximizing this quantity tends to bend back the unstable bifurcation branch by the largest amount for a fixed amount of proportional feedback.

2 Pulse air onto the rotor face based on the strategy outlined in the flow chart of Fig. 8; center each pulse about the peak of the first mode disturbance, and activate each air injector for the amount of time that yields the best performance.

The simulation studies performed with a high-fidelity model were in agreement with the experimental results; furthermore, they justified the modeling of air injection as a localized shift in the compressor characteristic.

It should be emphasized that this strategy for controlling rotating stall is not based on precursors; for our system, the time scale associated with the growth of the stall disturbance is comparable to the bandwidth of our actuators (see Fig. 7), rendering control strategies based on small signal behavior ineffective. Our control scheme beats down stall after it starts to develop, but before it grows to full size. In addition, this control scheme can eliminate rotating stall starting from a fully stalled condition.

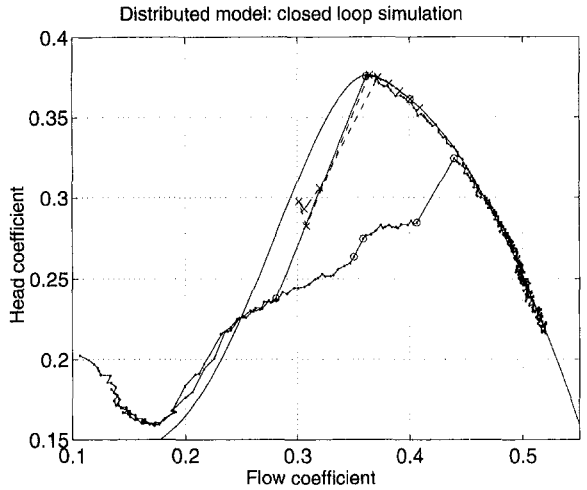

Fig. 17 Simulated closed-loop compressor characteristic. Simulation data points are denoted with an *x*. The open-loop compressor characteristic is included for comparison purposes.

The main physical phenomenon utilized in the experimental work and the ensuing analysis was that the steady-state compressor characteristic could be shifted by injecting air at the face of the compressor. While it has been previously shown that by introducing preswirl at the inlet and using of inlet guide vanes, the compressor characteristic can be altered for many compressors (Longley, 1994), the extent to which this effect can be achieved using air injection is an open research topic. The impact of the results presented thus hinge on demonstrating the genericness of shifting the compressor characteristic using localized air injection.

The experiments were performed with three air injectors at a fixed flow rate and distance from the compressor face. It is important to characterize how the performance of the control design varies by varying these parameters. For example, given an upper limit on the total flow that can be introduced by the air injectors, what is the optimal number of air injectors that should be used for feedback control? How should they be oriented relative to the compressor face? What is the tradeoff between the velocity of injected air and the performance of the compressor? These same questions can be asked for a fixed power limit on the actuation, or velocity limit, or combinations thereof. In order to answer these questions, more parametric studies need to be performed, and a more detailed model that captures the fluid dynamic interactions needs to be developed and studied.

While it is important to determine how the closed-loop performance varies as a function of these parameters, it is equally important to determine the regions of implementability for these parameters. For example, injecting air at a velocity much greater than the mean velocity through the compressor would not be feasible for high-speed systems. It is also desirable to use recirculation as the means to provide the needed flow for air injection (Gysling and Greitzer, 1995), which will restrict the velocity at which air can be injected. Another issue is the effect of pulsing high-momentum flow onto the rotor blades; this should be studied to determine what the detrimental effects are, and see if they are offset by the resulting benefits.

The control effort required to eliminate the hysteresis region is approximately 1.3 percent in terms of power and 1.7 percent in terms of flow of the compressor operating near the peak of the compressor characteristic. For a jet engine, however, these figures are large in an absolute sense. Subsequent to the experimental results presented in this paper, these figures were drastically reduced by moving the air injectors closer to the rotor face. In particular, the power figure was reduced to approximately 0.15 percent and the flow figure to 0.35 percent. Furthermore, the time each air injector was on (as determined by **jeton**) was reduced to approximately 45 deg of a stall disturbance revolution; this is consistent with hot-wire measurements near the rotor face, which show that the stall disturbance is localized to roughly two rotor blades, or approximately 50 deg.

Even though controlling rotating stall was the main purpose of the work presented in this paper, the elimination of surge is also an important aspect of extending the operability of a compressor. We have demonstrated that the controller designed to eliminate the hysteresis region can also have positive effects on the surge dynamics. This is due to the strong coupling between surge and stall, although a more detailed analysis needs to be performed to explain this interaction fully.

Acknowledgments

The authors would like to thank Simon Yeung, Wayne Hurwitz, Jim Paduano, Carl Nett, Kevin Eveker, Dan Gysling, Allan

Acosta, and John Doyle for their many helpful suggestions and comments. Funding for this research was provided in part by AFOSR grant No. F49620-95-1-0409. RD was partially supported by NSERC. RLB was partially supported by an NSF Graduate Research Fellowship.

References

Abed, E. H., Houpt, P. K., and Hosny, W. M., 1993, "Bifurcation Analysis of Surge and Rotating Stall in Axial Flow Compressors," ASME JOURNAL OF TURBOMACHINERY, Vol. 115, pp. 817–824.

AMCA/ASHRAE, 1985, "Laboratory Methods of Testing Fans for Rating," Technical Report ANSI/AMCA Standard 210-85, Air Movement and Control Association.

Badmus, O. O., Chowdhury, S., Eveker, K. M., and Nett, C. N., 1995. "Control-Oriented High-Frequency Turbomachinery Modeling—Single-Stage Compression System One-Dimensional Model," ASME JOURNAL OF TURBOMACHINERY, Vol. 117, pp. 47–61.

Behnken, R. L., 1996, "Nonlinear Control of an Axial Flow Compressor," PhD thesis, Department of Mechanical Engineering, California Institute of Technology.

D'Andrea, R., Behnken, R. L., and Murray, R. M., 1995, "Active Control of Rotating Stall Using Pulsed Air Injection: A Parametric Study on a Low-Speed, Axial Flow Compressor," in *Sensing, Actuation, and Control in Aeropropulsion,* SPIE International Symposium on Aerospace/Defense Sensing and Dual-Use Photonics, pp. 152–165.

Day, I. J., 1993a, "Active Suppression of Rotating Stall and Surge in Axial Compressors," ASME JOURNAL OF TURBOMACHINERY, Vol. 115, pp. 40–47.

Day, I. J., 1993b, "Stall Inception in Axial Flow Compressors," ASME JOURNAL OF TURBOMACHINERY, Vol. 115, pp. 1–9.

Eveker, K. M., Gysling, D. L., Nett, C. N., and Sharma, O. P., 1995, "Integrated Control of Rotating Stall and Surge in Aeroengines," in: *Sensing, Actuation, and Control in Aeropropulsion,* SPIE 1995 International Symposium on Aerospace/Defense Sensing and Dual-Use Photonics, pp. 21–35.

Gilyard, G. B., and Orme, J. S., 1992, "Subsonic Flight Test Evaluation of a Performance Seeking Control Algorithm on an F-15 Airplane," in: *Joint Propulsion Conference and Exhibit,* AIAA Paper No. 92-3743.

Greitzer, E. M., 1976, "Surge and Rotating Stall in Axial Flow Compressors: Part I—Theoretical Compression System Model," ASME *Journal of Engineering for Power,* Vol. 98, pp. 190–198.

Greitzer, E. M., 1981, "The Stability of Pumping Systems—The 1980 Freeman Scholar Lecture," ASME *Journal of Fluids Engineering,* Vol. 103, pp. 193–242.

Gysling, D. L., 1993, "Dynamic Control of Rotating Stall in Axial Flow Compressors Using Aeromechanical Feedback," PhD thesis, Department of Aeronautics and Astronautics, Massachusetts Institute of Technology, Cambridge, MA.

Gysling, D. L., and Greitzer, E. M., 1995, "Dynamic Control of Rotating Stall in Axial-Flow Compressors Using Aeromechanical Feedback," ASME JOURNAL OF TURBOMACHINERY, Vol. 117(3), pp. 307–319.

Haynes, J. M., Hendricks, G. J., and Epstein, A. H., 1994, "Active Stabilization of Rotating Stall in a Three-Stage Axial Compressor," ASME JOURNAL OF TURBOMACHINERY, Vol. 116, pp. 226–239.

Hendricks, G. J., and Gysling, D. L., 1994, "Theoretical Study of Sensor-Actuator Schemes for Rotating Stall Control," *Journal of Propulsion and Power,* Vol. 10(1), pp. 101–109.

Khalak, A., and Murray, R. M., 1995, "Experimental Evaluation of Air Injection for Actuation of Rotating Stall in a Low Speed, Axial Fan," ASME Paper No. 95-GT-???.

Liaw, D. C., and Abed, E. H., 1996, "Control of Compressor Stall Inception—a Bifurcation-Theoretic Approach," *Automatica,* Vol. 32(1), pp. 109–115.

Longley, J. P., 1994, "A Review of Nonsteady Flow Models for Compressor Stability," ASME JOURNAL OF TURBOMACHINERY, Vol. 116, pp. 202–215.

Mansoux, C. A., Gysling, D. L., Setiawan, J. D., and Paduano, J. D., 1994, "Distributed Nonlinear Modeling and Stability Analysis of Axial Compressor Stall and Surge," in: *Proc. American Control Conference,* pp. 2305–2316.

McCaughan, F. E., 1989, "Application of Bifurcation Theory to Axial Flow Compressor Instability," ASME JOURNAL OF TURBOMACHINERY, Vol. 111, pp. 426–433.

McCaughan, F. E., 1990, "Bifurcation Analysis of Axial Flow Compressor Stability," *SIAM Journal of Applied Mathematics,* Vol. 20(5), pp. 1232–1253.

Moore, F. K., and Greitzer, E. M., 1986, "A Theory of Post-stall Transients in Axial Compression Systems—Part I: Development of Equations," ASME JOURNAL OF TURBOMACHINERY, Vol. 108, pp. 68–76.

Paduano, J. D., Epstein, A. H., Valavani, L., Longley, J. P., Greitzer, E. M., and Guenette, G. R., 1993a, "Active Control of Rotating Stall in a Low-Speed Axial Compressor," ASME JOURNAL OF TURBOMACHINERY, Vol. 115, pp. 48–56.

Paduano, J. D., Greitzer, E. M., Epstein, A. H., Guenette, G. R., Gysling, D. L., Haynes, J., Hendricks, G. J., Simon, J. S., and Valavani, L., 1993b, "Smart Engines: Concept and Application," *Integrated Computer-Aided Engineering,* Vol. 1(1), pp. 3–28.

Smith, R. H., Chisholm, J. D., and Stewart, J. F., 1991, "Optimizing Aircraft Performance With Adaptive, Integrated Flight/Propulsion Control," ASME *Journal of Engineering for Gas Turbines and Power,* Vol. 113, pp. 87–94.

Investigation of the Heat-Island Effect for Heat-Flux Measurements in Short-Duration Facilities

M. G. Dunn
Gas Turbine Laboratory,
The Ohio State University,
Columbus, OH 43235

J. Kim
Dept. of Engineering,
University of Denver,
Denver, CO 80208

W. J. Rae
Dept. of Mechanical and Aerospace Engineering,
State University of New York at Buffalo,
Buffalo, NY 14260

This paper presents the results of an experimental investigation designed to determine the possible influence of a surface-temperature discontinuity on the heat-flux history inferred from the temperature history of a miniature thin-film heat-flux gage (painted on an insulator) embedded in the surface of a metallic component. The resulting surface material discontinuity has the potential of causing a heat-island effect. Simultaneous measurements of the heat-flux history at selected locations along the midspan of a representative turbine airfoil (metal) were performed using continuous strip-type contoured inserts (without temperature discontinuity) and button-type inserts (with temperature discontinuity). Measurements are reported for two Reynolds number conditions. The experimental results suggest that for the experimental conditions of interest to gas turbine research in short-duration facilities, the influence of a potential heat-island on the measured heat flux is insignificant.

Introduction

Thin-film heat-flux gages have been used for about forty years in short-duration facilities (test times typically on the order of one to ten milliseconds) to measure surface distributions of heat flux for a wide variety of high-energy flow situations (Vidal, 1956; Jones and Schultz 1970; Schultz and Jones, 1973). These gages consist of a thin platinum strip (typically 1×10^{-8} m thick) bonded to the surface of a material of low thermal diffusivity (typically quartz, Pyrex glass, or Macor ceramic). The thermal characteristics of quartz and Pyrex are well known, having been measured as a function of temperature (e.g., Skinner, 1961, and Hartunian and Varwig, 1962), and these materials are produced with excellent quality control by their manufacturer.

Thin-film gage types vary among research institutions primarily because the test times and the flow environments associated with the individual facilities differ. For the short-duration facility used for the measurements reported here, the single-sided platinum gage bonded to an insulating substrate is used. Construction of the thin-film heat-flux gage is documented by Vidal (1956) and Bogdan and Garberoglio (1967). The gage is operated in a constant-current circuit (typically 1 mA) from which the film temperature history during the experiment is deduced using a temperature coefficient of resistance calibration for that particular gage. The heat transfer rate that must have produced the inferred temperature history of the substrate is then calculated using a one-dimensional, time-dependent heat conduction approximation.

Two types of gage are used in this study, both constructed from the substrate material Pyrex 7740. The button gage ($\approx$1 mm diameter) is cut from a flat sheet, the surface is polished, notches are cut on the sides of the cylinder, a platinum strip is painted on the polished side, silver is bonded to the ends of the strip, lead wires (housed in the notches just noted) are soldered to the silver, and a coating of magnesium fluoride is placed over the gage. Strip (or leading-edge) gages are constructed from strips of material that are polished and contoured over the wetted length of the surface. Both leading-edge and strip inserts were used here. The surface finish of the polished substrate is on the order of 3×10^{-7} m. The particular inserts used in this study were approximately 7 mm wide and had a thickness ranging from 3 to 16 mm. Platinum gages are painted on the surface in the same manner as described for the buttons. Both types of gages are held in place using epoxy, and photographs of the installation are given later in the paper. The gages are installed in the turbine hardware under a microscope (using a magnification of 50 or more) and the substrate is measured to be flush with the surface to within less than 2.5×10^{-5} m (0.001 in.).

This technology has undergone many levels of refinement during the past several decades; most recent have been its extension to millimeter-scale miniaturization and the ability to infer time-resolved heat-flux values with microsecond time resolution (Dunn, 1986; Dunn et al., 1986; George et al., 1987). Though time-resolved heat-flux data have been obtained with these devices, the discussion presented here is confined to time-averaged data. The surface with the button gages installed has been shown to be hydraulically smooth (see Dunn et al., 1992) even for a blade surface much rougher than the one used for these experiments.

Techniques other than that described herein to measure heat-flux distributions on gas turbine components are in use at several other laboratories, e.g., Consigny and Richards (1982), Doorly and Oldfield (1986), Epstein et al. (1986), and Hager et al. (1991). The choice of which technique to use depends upon many things, among them the particular facility in which the measurements are to be performed and the familiarity of the individual researcher with a particular technique.

The problem that is the subject of this paper can be stated as follows: The basic reason for using a low thermal-diffusivity material as the gage substrate is to "hold the heat at the surface," i.e., the gage is usually embedded in a metal component whose thermal diffusivity is so high that the surface temperature increases by a relatively small amount during the short duration (on the order of 40 milliseconds) of the experiment. In order to amplify the signal, it is desirable to achieve a higher surface-temperature increase; materials like Pyrex or quartz have thermal diffusivities that can be as much as 25 times smaller than that of the surrounding metal, and can lead to increases that are typically on the order of 5 degrees Kelvin or larger. The re-

Contributed by the International Gas Turbine Institute for publication in the JOURNAL OF TURBOMACHINERY. Manuscript received at ASME Headquarters July 1997. Associate Technical Editor: T. H. Okiishi.

sulting improvement in signal-to-noise ratio is an important factor in the success of these devices.

The temperature increase of the insulating substrate above that of the surrounding metal mentioned in the previous paragraph causes a localized "heat-island," which has the potential to complicate the interpretation of the data. The driving temperature difference (i.e., the free-stream temperature minus the gas temperature at the wall) does not have the same value at points above a gage as it does at adjacent points above the metal. Thus one might argue that the heat transfer to the gage could differ from that to the adjacent metal due to the local gradients in surface temperature. This mechanism is similar to the "heat island" observed in atmospheric phenomena near large cities.

For small variations in surface temperature (gages warmer than the surrounding metal by, say 10 K) and for free-stream temperatures of 1000 K and more, the error in heat transfer rate (i.e., the difference between the heat transfer rates to gage and metal) is only a few percent, and one would expect an even smaller difference in Stanton number, depending on how quickly this parameter adjusts to surface-temperature gradients. Dunn et al. (1984) measured the surface distribution of heat flux over a wide range of free-stream total temperatures, but for the same initial wall temperature. Though the values of local heat flux were very different for each experimental condition, when the Stanton number results were compared the distributions collapsed to within 10 percent over the range of conditions utilized, a level of uncertainty that is quite acceptable for such a difficult measurement.

In more recent years, with experimental facilities having much longer test times, a considerable body of experimental data in which the results from the button-type gages embedded in a larger metal component have been compared to predictions (e.g., Wittliff, 1977) and to flight data (e.g., Wittliff, 1983).

Kim et al. (1996) performed a series of numerical simulations of a two-dimensional insulator strip embedded within a metal flat plate. A dimensional analysis was also performed that indicated that there are three parameters that affect the magnitude of the heat island effect: (1) The rate at which heat is diffused in the fluid. This affects how fast the boundary layer is able to react to changes in wall boundary condition. (2) The magnitude of the temperature increase of the insulator (Pyrex in this case). The larger the temperature increase, of course, the larger the heat island effect. (3) The rate at which heat diffuses in the insulator and metal laterally. The lateral heating gives the boundary layer a chance to adjust to the change in the wall temperature variation before the flow actually reaches the gage. Preliminary calculations indicate that the magnitudes of the errors to be expected are within 10 percent for the idealized case to two-dimensional gages. It was also shown that the semi-infinite solid approximation was not violated, and that the temperature profiles in the button can be considered to be one-dimensional for the times of interest. Further work is being performed to look at three-dimensional and unsteadiness effects on gage performance.

The primary objective of the work described here was to conduct a controlled series of experiments in which heat-flux measurements were made using button-type, contoured leading-edge type and continuous-strip-type gages, which were simultaneously exposed to identical flow conditions. In the case of the contoured leading-edge insert there is no temperature discontinuity. For the case of the strip insert, there is a significant portion of insulator ahead of the initial gage so that even the initial sensing element should not experience a temperature discontinuity. Clearly, those elements after the initial one would not experience a temperature discontinuity. The gages were placed at locations where spanwise components of the flow were expected to be small, so that the wall material upstream of each gage would be essentially all-metal or all-Pyrex. The premise of the experiments was that a heat-island effect, if present, would produce a systematic difference in the heat-flux values over the surface of the component inferred from the different types of gage installation. A numerical treatment of this three-dimensional problem, including time-dependent axial conduction, has been lacking. Studies are presently being conducted on a representative two-dimensional problem, however.

Description of the Experiment

The experimental apparatus used here consists of a shock-tunnel facility, a turbine stage, and the heat-flux gages. Brief descriptions of each of these components are given in the following paragraphs.

Shock-Tunnel Facility. The experimental facility is a large reflected-shock tunnel device for which a detailed description is provided in the document referenced in the footnote. It consists of a 0.46-m (18.5-in.) i.d. helium/air driven shock tube with a 12.2-m (40-ft) long driver tube, an 18.3-m (60-ft) long driven tube, a primary nozzle, and a 2.75-m (9-ft) diameter by 10.4-m (34-ft) long dump tank. The driver tube is sufficiently long that the wave system reflected from the closed end does not terminate the test time prematurely. This facility has a long running time for a shock-tunnel facility, being on the order of 40 ms or more.

A full-stage (rotating) high-pressure turbine consisting of a vane row and a 0.73-m (29-in) diameter rotor was used for these measurements. The turbine design values of flow function, stage pressure ratio, wall to total temperature ratio, and corrected speed were all duplicated. To do so required a facility[1] that could accommodate the physical size and weight-flow requirements of such a large turbine stage. Though the rotor portion of the stage was fully instrumented with both button-type and contoured insert-type thin-film gages (and the on-blade data comparison between the two types of instrumentation was consistent with what is shown later in this paper for different turbines), this discussion will be confined to data taken on the vane. The experimental sequence is that the driver and driven tubes are pressurized to the appropriate pressure levels so as to create the desired reflected-shock conditions. The desired reflected-shock temperature and pressure are predetermined values and the load conditions required to obtain these values are experimentally verified. The test section containing the turbine

[1] A detailed description of the facility and its operation is beyond the scope of this paper. For a complete description of the facility construction, operation, and calibration the reader is referred to Final Report WRDC-TR-89-2027, "Operating Point Verification Data for a Large Shock Tunnel Test Facility," 1989.

Nomenclature

A = reference cross-sectional area at vane inlet
c = substrate specific heat
$H_0(T_0)$ = enthalpy of the external flow evaluated at the total temperature, T_0
$H_w(T)$ = enthalpy of the substrate evaluated at temperature T
k = substrate thermal conductivity
$\dot{q}_c(T)$ = heat flux evaluated at the gage temperature T occurring during the test interval
Re = Reynolds number
St = Stanton number = $(\dot{q}_c(T)/\{\dot{W}/A)[H_0(T_0) - H_w(T)]\}$
T = gage temperature at the time $\dot{q}_c(T)$ is evaluated
$\dot{W}$ = weight flow of gas through the turbine stage
α = thermal diffusivity = $k/\rho c$
ρ = density (of substrate)

stage is initially in a vacuum, being separated from the shock tube by a fast acting mechanical valve, which opens and closes upon demand. Just prior to initiating the experiment (by rupturing the diaphragms separating the driver gas from the driven gas), an impulse air motor is used to accelerate the rotor from rest to the desired speed. The air input to the rotor is terminated immediately prior to initiation of the experiment. The moment of inertia of the rotating system is measured prior to installing the turbine in the facility and the time rate of change of speed during the experiment is recorded. Knowing the moment of inertia and the speed change, the torque can be calculated.

Heat-Flux Gage Instrumentation. It was noted in the introduction that the question being investigated centered around whether or not a tiny button gage (containing an even smaller thin platinum film) located flush with the surface of a turbine component (vane or blade) represents a heat island because of the surface temperature discontinuity between the insulator and the surrounding metal. A strip of the substrate material extending in the chordwise direction from the leading edge to the trailing edge of the vane would not represent a chordwise temperature discontinuity. The experiment was thus designed so that separate vanes in the same vane row would be instrumented with button-type heat-flux gages containing thin-film elements, with a contoured leading-edge insert containing gages both on the pressure and suction side of the geometric stagnation point, and with the same type of thin-film elements painted on a contoured-strip extending from near the leading edge to near the trailing edge on both the pressure and suction surfaces. The measurements were to be performed with the instrumentation located nominally at 50 percent span and both buttons and inserts were to be used for a given experiment. Flow field calculations performed for the turbine stage of interest suggested that three-dimensional flow effects should be small for this particular vane.

Figure 1 is a photograph of the Pyrex 7740 button-type gages installed on the vane pressure surface. The button has a diameter of 1.01×10^{-3} m (0.040 in.) and a thickness of 8.06×10^{-4} m (0.032 in.). The thickness was selected so that the error in the deduced heat flux caused by assuming the Pyrex substrate to be a one-dimensional semi-infinite solid would be 1 percent for a test time of 350 ms. As noted earlier, the test time for these experiments is on the order of 35 to 40 ms so the error in the heat flux caused by using the one-dimensional approximation would be predicted to be significantly less than 1 percent. The leading-edge region of this particular vane was sufficiently blunt that a button-type gage could be placed very near the geometric stagnation point without disturbing the contour of the leading edge.

The thin-film heat flux gage that is painted on the button substrate is approximately 1.007×10^{-4} m (0.004 in.) wide, by about 5.04×10^{-4} m (0.020 in.) long, by 1×10^{-8} m thick. By comparison, the vane span is on the order of 0.09 m (3.5 in.). The resistance of the gage is on the order of 100 ohms. The gages are installed in the vane surface using a microscope and, as noted earlier, they are flush with the surface to within less than 2.5×10^{-5} m (0.001 in.). The button is held in the vane by an Epoxy adhesive placed around the diameter and at the bottom of the hole. After installation of the buttons, the location of the gage along the wetted surface of the vane in the chordwise and spanwise directions is measured. This measurement is performed by wrapping a piece of masking tape around the vane from trailing edge to trailing edge immediately adjacent to the row of gages. The gage locations are marked on the tape, which is then unwrapped and positions are measured under a microscope. The vanes and blades are engine hardware and one does encounter some part-to-part variations.

It was noted above that a leading-edge insert as well as contoured inserts on the pressure and suction surface of the vane were used in this experiment. The leading-edge insert is void of a temperature discontinuity, the contoured inserts have a leading portion of insulator but it is possible that the initial gage may see a temperature discontinuity, and all of the button gages will see the temperature discontinuity. Figures 2 and 3 are photographs of the contoured leading-edge insert and the contoured pressure surface insert, respectively. In addition to showing the pressure surface insert, Fig. 3 also illustrates a small portion of

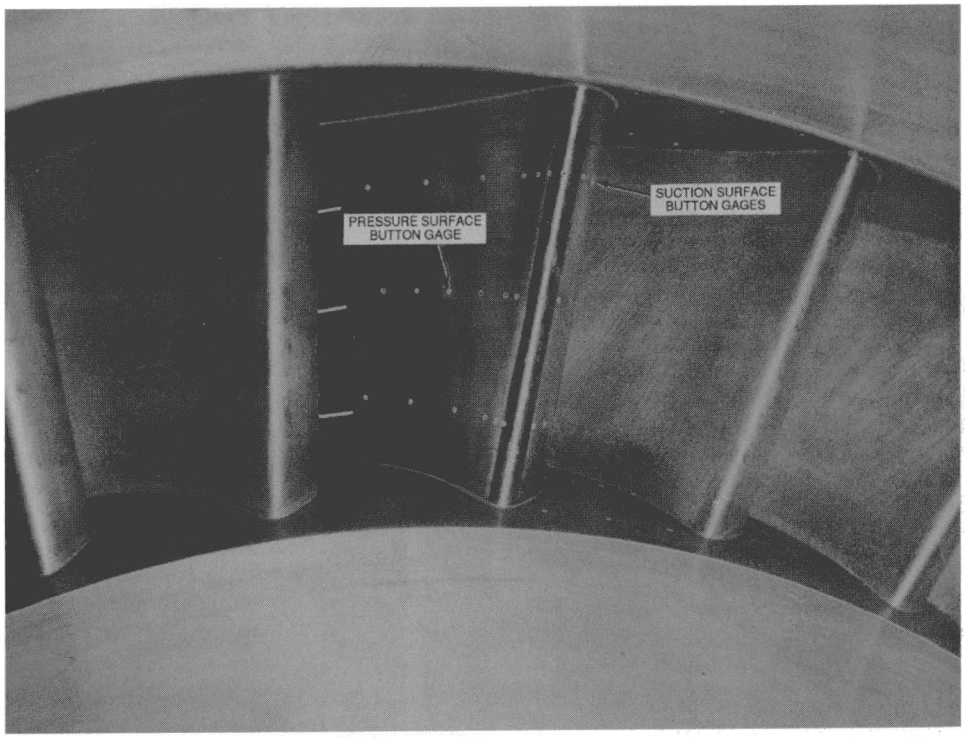

Fig. 1 Photograph of button-type gages on vane pressure surface

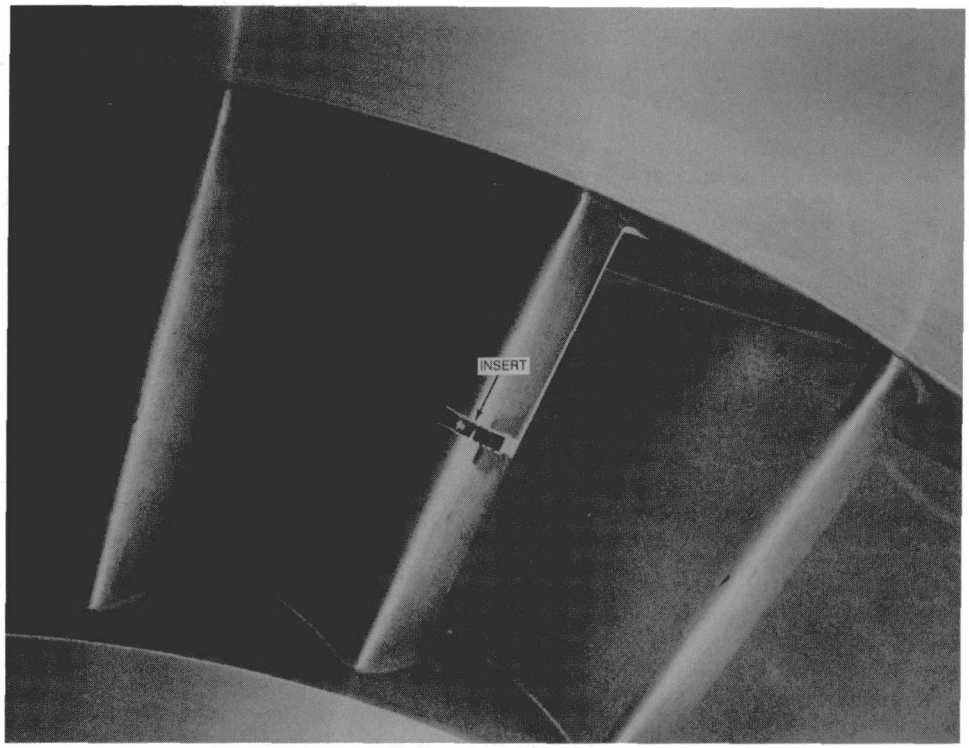

Fig. 2 Photograph of vane contoured leading-edge insert

the suction surface contoured. All three of the inserts were located at the local 50 percent span location.

The leading edge insert contained 10 thin-film gages, 5 on the pressure surface and 5 on the suction surface. The nearest gage to the geometric stagnation point was at 7.05×10^{-4} m (0.028 in.) on the suction surface side. The gages of this insert were spaced about 1.51×10^{-3} m (0.060 in.) apart. The pressure surface contoured strip insert contained 13 gages. The gage-to-gage spacing varied from 1.007×10^{-3} (0.040 in.) to 7.55×10^{-3} m (0.30 in.) depending upon the particular wetted distance location. The suction surface contoured strip insert also contained 13 gages. The spacing on the suction surface insert was

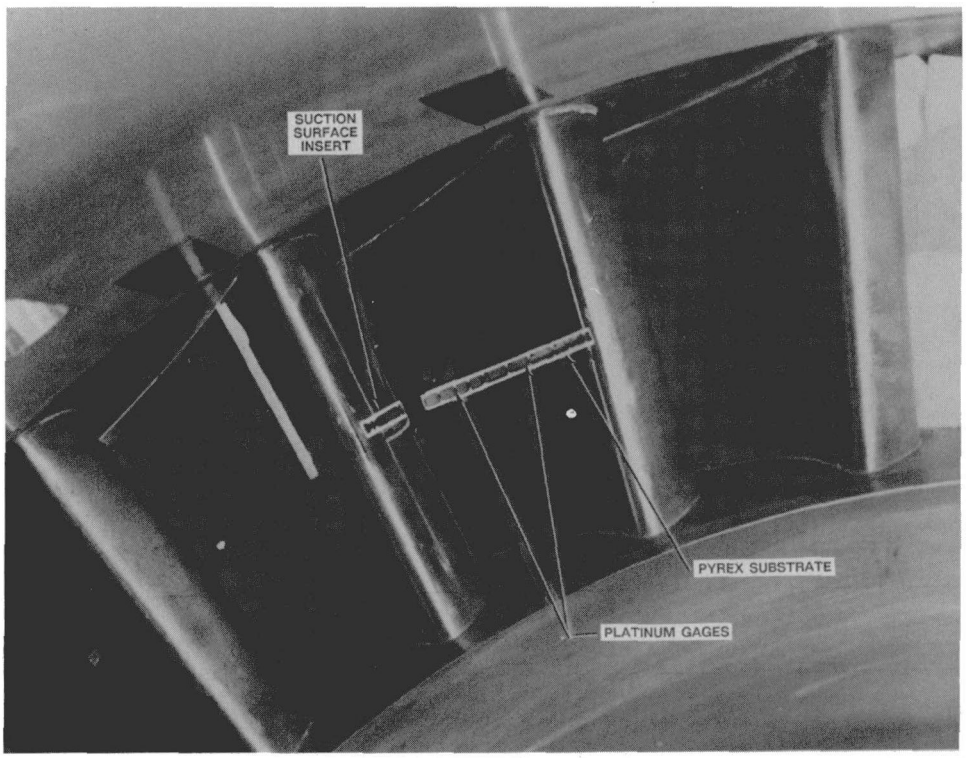

Fig. 3 Photograph of gages on vane pressure surface insert

approximately the same as just described for the pressure surface insert. These inserts were contoured to the vane surface and installed under a microscope to be flush within less than 2.5×10^{-5} m (0.001 in.). The leading-edge and strip insert substrates are much thicker than the button substrate material. The thickest portion of the leading-edge insert was on the order of 1.57×10^{-2} m (0.625 in.). The two strip inserts are 3.14×10^{-3} m (0.125 in.) thick at the thinnest substrate locations.

Experimental Conditions. The measurements were performed using a full-stage turbine operating at the design flow function and with the rotor speed being equal to the design corrected speed. Heat-flux measurements were performed for two experimental conditions: (1) a vane inlet total temperature of 585 K (1054 R) and a total pressure of 434 kPa (63 psia), and (2) a vane inlet total temperature of 600 K (1081 R) and a total pressure of 627 kPa (91 psia). The axial chord of the vane is on the order of 0.061 m (2.4 in.) and the span is on the order of 0.086 m (3.4 in.). The corresponding vane inlet Reynolds numbers based on vane chord for the two test conditions were about 3.6×10^5 and 5.2×10^5, respectively.

Discussion of Experimental Results

Data Reduction Technique. The thin-film gage is a resistance thermometer used to infer the surface temperature of the material upon which it is bonded. Regardless of the materials used to construct the gage or how the sensing element is attached to the substrate, the unit must be capable of being calibrated. There are two parts to the calibration process for the thin-film gages used here: (*a*) determining the temperature versus resistance characteristic of each gage and (*b*) determining the variable thermal properties of the substrate to which the gage is bonded. This calibration information allows the deduced temperature versus time data to be converted to a heat-flux history.

The gage coefficient of resistance is measured over the temperature range anticipated. The temperature versus resistance characteristic of each gage is determined, using the same electrical circuit that will be used during the experiment, by submerging the gages in a precision oil bath and measuring the gage resistance with a precision meter at discrete values of oil temperature. For temperatures up to about 370 K above room temperature, the resistance varies linearly with temperature. As noted in (*b*), the other part of the calibration process involves determining the variable thermal properties of the substrate to which the thin film is bonded. Over the years, we have experimented with quartz, Pyrex, and Macor as substrate materials. Each of these materials has advantages and disadvantages, but based on our experience Pyrex 7740 has been selected as the material of choice. Over the past forty years, the $\sqrt{\rho c k}$ versus

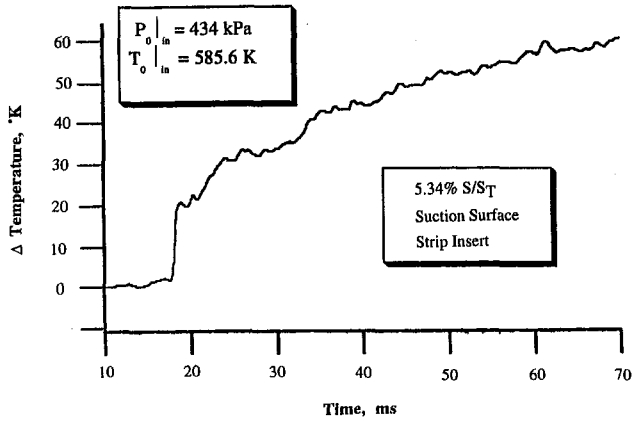

Fig. 4 Temperature history of thin-film gage on insert

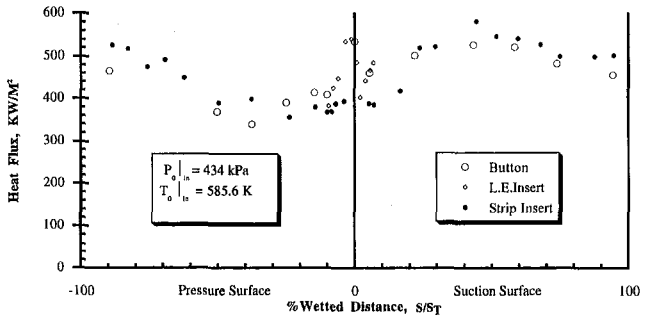

Fig. 5 Comparison of button-type with insert-type heat-flux results for vane (low-Reynolds-number case)

temperature characteristics of this material and of quartz have been measured and the results of these measurements have been presented, e.g., Vidal (1956), Skinner (1961, 1962), Hartunian and Varwig (1962), and Bogdan and Garberoglio (1967). The thermal properties of Pyrex 7740 have been found to be very consistent over the course of years.

The raw data obtained during an experiment is a time history of voltage across a gage when a small known current is passed through the gage, which, by using the previously described calibration data for each gage, can be converted to gage temperature history. The button and insert gage measurements are obtained at the same instant in time. Each gage has an A/D channel assigned to it, and data are sampled at a fixed frequency. A typical temperature history is shown in Fig. 4. Using this temperature versus time history, a numerical solution (Seymour, 1987) to the one-dimensional heat conduction equation is used to produce the time history of surface heat flux corrected for variable thermal properties of the substrate. Having converted the voltage data to gage temperature and the temperature history data to heat flux, one has a time history of $\dot{q}_c$ (T) and the substrate surface temperature (T). For the purposes of the time-averaged results presented here, $\dot{q}_c$ (T) is averaged over a portion of the test duration.

For the purposes of the comparison between button-type and insert-type heat-flux gages, only heat-flux data are presented. Later in the paper, previous data obtained for the blade of other turbines are presented and those data are presented in the form of a Stanton number. That Stanton number is based on conditions at the first vane inlet. The relationship used to evaluate the Stanton number was

$$\mathrm{St} = \frac{\dot{q}(T)}{(\dot{W}/A[H_0(T_0) - H_w(T)])}$$

The parameter W/A corresponds to the turbine weight flow divided by the value of the annular area immediately upstream of the first stage vane inlet. In this formulation, the heat flux and the wall enthalpy are both evaluated at the same temperature, T.

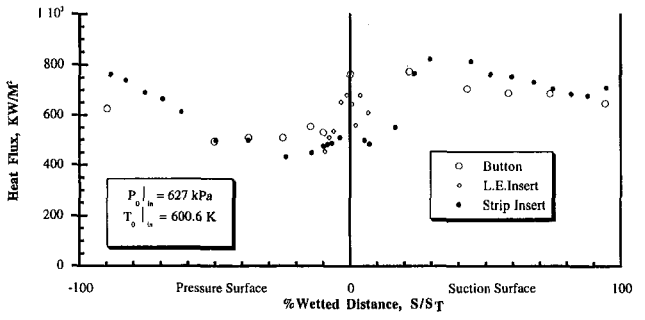

Fig. 6 Comparison of button-type with insert-type heat-flux results for vane (high-Reynolds-number case)

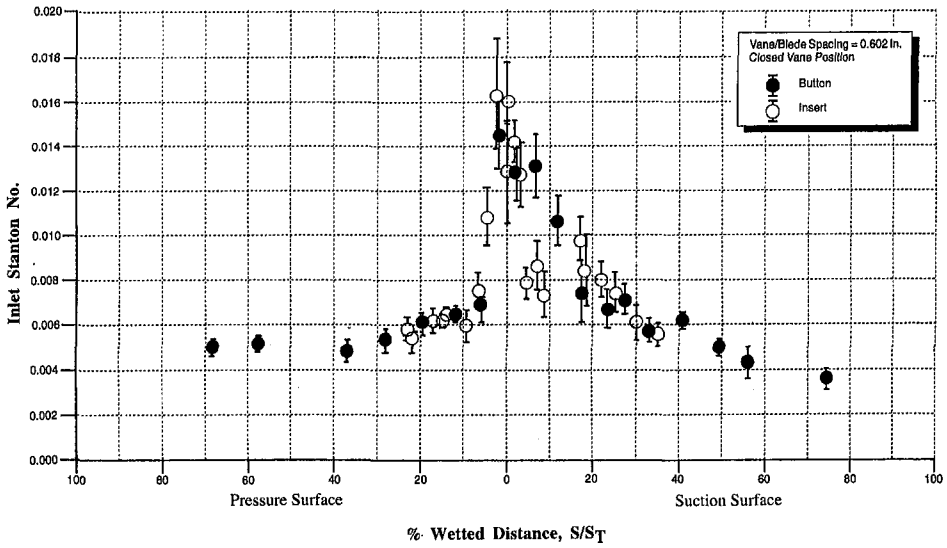

Fig. 7 Comparison of button-type with insert-type Stanton number results for blade of Allison VBI turbine

If the cold-wall heat flux, $\dot{q}(T_w)$, is desired, then it can be obtained by multiplying the given Stanton number by $(\dot{W}/A)[H_0(T_0) - H_w(T_w)]$.

Heat-Flux Results for Vane. As previously noted, measurements were performed at two Reynolds number conditions. Figure 5 presents the heat-flux results for the low-Reynolds-number condition. As can be seen, there were more thin-film gages painted on the three inserts than there were button gages installed in the vane. The data from the leading-edge insert, the pressure and suction surface contoured strip inserts, and the button gages are delineated by separate symbols. There is a single button gage near the geometric stagnation point and one at about 5 percent wetted distance on the suction surface. At the stagnation point and at 5 percent wetted distance, the agreement between the heat-flux results obtained with the button-type and the contoured insert-type gages is seen to be within 5 percent. The most significant disagreement occurs on the suction surface between the contoured insert data and the initial two gages on the contoured strip. Comparison at this particular region on the suction surface is very sensitive to precise location of the thin-film gage. The gage location is determined after installation by wrapping a piece of masking tape around the component from trailing edge to trailing edge immediately adjacent to the gages and marking both the center of the thin-film element and the trailing edges. The distances are then measured under the microscope. One might have an uncertainty in this measurement on the order of 0.001 in. but not much more. The larger uncertainty comes from the casting to casting variation of the vanes, which can be on the order of tens of thousands of an inch. The buttons, the leading-edge insert, and the contoured inserts are all on different vanes. The difference in vane-to-vane wetted distance is especially critical near the suction surface leading edge where gradients in surface pressure or heat flux are large. No attempt was made to correct for manufacturing tolerance in this work.

As mentioned earlier, a temperature discontinuity in the streamline direction is not present for the leading-edge insert, but the initial one or two gages on the strip inserts may see a temperature discontinuity, and the button gages should see a temperature discontinuity. However, the button data are in excellent agreement with the contoured insert data

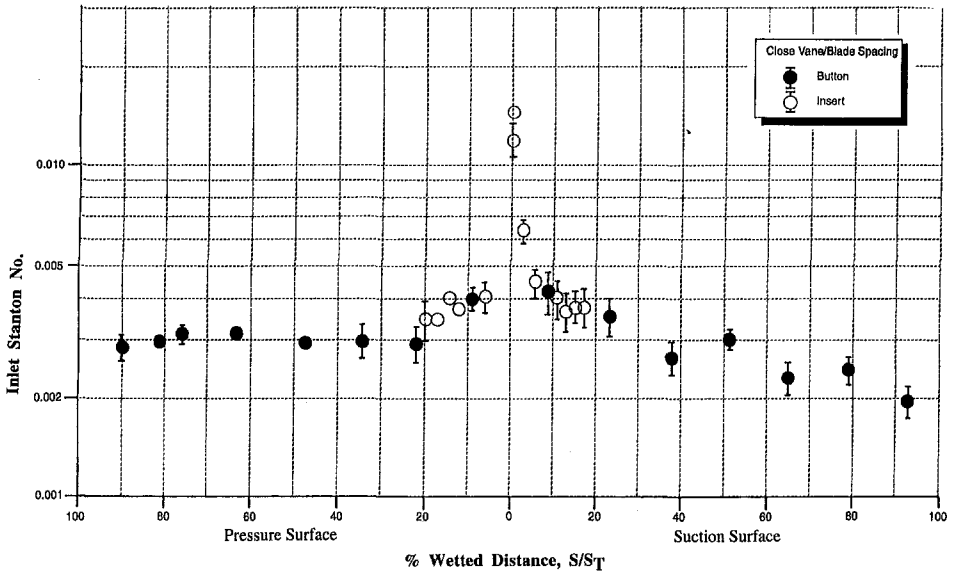

Fig. 8 Comparison of button-type with insert-type Stanton number results for Teledyne 702 blade

for which there is no temperature discontinuity. The experimental results show that if there is a surface temperature discontinuity effect on the button-type gage data, then it is small for the given experimental conditions. The data also suggest that the initial two gages on the contoured insert may be improperly located.

Figure 6 presents similar vane heat-flux distributions for the higher Reynolds number case. With the exception of the button gage data point at 90 percent wetted distance on the pressure surface and the data point at 42 percent wetted distance on the suction surface, the agreement between the results obtained with the buttons versus inserts is again within 5 percent. At this high-Reynolds-number condition, the button gage in the vicinity of 5 percent wetted distance on the suction surface was broken and thus this data point was not available for comparison. However, for the low-Reynolds-number experiment, that gage was operational and the data point obtained is shown to be in good agreement with the contoured insert data. At the low Reynolds number for which the data are described in the previous paragraph, the agreement between button and insert data is very good. For the high-Reynolds-number case, there are two button gage data points that disagree with the insert data by more than 5 percent, one at 42 percent on the suction surface and the other at 90 percent on the pressure surface. Post-test inspection of the gage installation didn't indicate anything physically unusual that would explain these two data points. It is felt that insufficient data are available to attach any significance to either of them.

Results From Previous Measurement Programs. Numerous full-stage turbine measurement programs have been performed in the past for which both button-type substrates and leading-edge insert substrates were used on the blade of a full-stage turbine. It was previously noted that there is no temperature discontinuity for the contoured leading-edge insert configuration. In all of these cases, the comparison between the data obtained with the different substrate configurations has been in excellent agreement. The following two figures present examples of this comparison for the blade of two very different turbine configurations. Figure 7 presents a comparison of the blade Stanton numbers deduced using the relationship outlined earlier for the button heat-flux data with those deduced using the contoured insert heat-flux data for the Allison vane/blade interaction (VBI) turbine (Rao et al., 1994). The closed symbols are the button data and the open symbols are the insert data. The experimental configuration for which these data were obtained is the closed vane setting (vane exit Mach number of about 1.1) and the close vane/blade spacing. For these experiments, two different blades contained contoured leading-edge inserts, and the inserts extended to about 25 percent wetted distance on the pressure surface and to about 35 percent wetted distance on the suction surface. The blades also contained numerous button-type gages, but these were not placed on the same blades containing the inserts. The buttons were placed at wetted distances so that there was some overlap in the data as can be seen from Fig. 7. The agreement between the Stanton numbers deduced with the two types of gage installation is demonstrated to be very good.

Figure 8 shows a similar comparison for the blade of the Teledyne 702 high-pressure turbine (Dunn and Chupp, 1988). This particular blade (a photograph of which is shown in the reference cited) has a significantly smaller chord and span than the Allison VBI blade, it has significant twist, and it has significant bow. For this particular blade, the contoured leading-edge inserts extended to about 20 percent wetted distance on both the pressure and suction surfaces. For these measurements, the vane exit Mach number was subsonic and the vane/blade position was in the close spacing. Similar to the data described in the previous paragraph for the Allison turbine, the button gages were not installed on the same blade as the contoured insert. Though the duplication of locations is not as much as was demonstrated for the Allison turbine, the agreement between the Stanton numbers deduced from the heat-flux data obtained from the buttons versus the leading-edge inserts is shown to be very good.

Conclusions

The main conclusion drawn from this study is that the experimental data demonstrate the validity of using the gage-measured Stanton number as a basis for inferring heat transfer to the adjacent metal. The experiments were conducted under controlled conditions, where effects of substrate geometry should have been apparent if a heat-island effect were present.

References

Bogdan, L., and Garberoglio, J. E., 1967, "Transient Heat Transfer Measurements With Thin-Film Resistance Thermometers—Data Reduction Techniques," AFAPL-TR-67-141.

Bogdan, L., and Garberoglio, J. E., 1967, "Transient Heat Transfer Measurements With Thin-Film Resistance Thermometers—Fabrication and Application Technology," AFAPL-TR-67-72.

Consigny, H., and Richards, B. E., 1982, "Short-Duration Measurements of Heat-Transfer Rate to a Gas Turbine Rotor Blade," ASME *Journal of Engineering for Power,* Vol. 104, pp. 542–551.

Doorley, J. E., and Oldfield, M. L. G., 1986, "New Heat Transfer Gages for Use on Multilayered Substrates," ASME JOURNAL OF TURBOMACHINERY, Vol. 108, pp. 153–160.

Dunn, M. G., Rae, W. J., and Holt, J. L., 1984, "Measurement and Analysis of Heat-Flux Data in a Turbine Stage: Part I: Description of Experimental Apparatus and Data Analysis and Part II: Discussion of Results and Comparison With Predictions," ASME *Journal of Engineering for Gas Turbines and Power,* Vol. 106, No. 1, pp. 229–240.

Dunn, M. G., 1986, "Heat-Flux Measurements for the Rotor of a Full-Stage Turbine: Part I—Time-Averaged Results," ASME JOURNAL OF TURBOMACHINERY, Vol. 108, pp. 90–97.

Dunn, M. G., George, W. K., Rae, W. J., Woodward, S. H., Moller, J. C., and Seymour, P. J., 1986, "Heat-Flux Measurements for the Rotor of a Full-Stage Turbine: Part II—Description of Analysis Technique and Typical Time-Resolved Measurements," ASME JOURNAL OF TURBOMACHINERY, Vol. 108, pp. 98–107.

Dunn, M. G., and Chupp, R. E., 1988, "Time-Averaged Heat-Flux Distributions and Comparison With Prediction for the Teledyne 702 HP Turbine Stage," ASME JOURNAL OF TURBOMACHINERY, Vol. 110, pp. 51–56.

Dunn, M. G., Kim, J., Civinskas, K. C., and Boyle, R. J., 1994, "Time-Averaged Heat Transfer and Pressure Measurements and Comparison With Prediction for a Two-Stage Turbine," ASME JOURNAL OF TURBOMACHINERY, Vol. 116, pp. 14–22.

Epstein, A. H., Guenette, G. R., Norton, R. J. G., and Yazhang, C., 1986, "High-Frequency Response Heat-Flux Gage," *Rev. Sci. Instruments,* Vol. 57(4), pp. 639–649.

George, W. K., Rae, W. J., Seymour, P. J., and Sonnenmeir, J. K., 1987, "An Evaluation of Analog and Numerical Techniques for Unsteady Heat Transfer Measurements With Thin-Film Gages in Transient Facilities," *Proc. of the 1987 ASME–JSME Thermal Engineering Joint Conf.,* pp. 611–617.

Hager, J. M., Langley, L. W., Onishi, S., and Diller, T. E., 1991, "High-Temperature Heat Flux Measurements," AIAA Paper No. 91-0165.

Hartunian, R. A., and Varwig, R. L., 1962, "On Thin-Film Heat-Transfer Measurements in Shock Tubes and Shock Tunnels," *The Physics of Fluids,* Vol. 5, No. 2, pp. 169–174.

Jones, T. V., and Schultz, D. L., 1970, "A Study of Film Cooling Related to Gas Turbines Using Transient Techniques," Univ. of Oxford Report No. 1121/70.

Kim, J., Ross, R. A., and Dunn, M. G., 1996, "Numerical Investigation of the Heat-Island Effect for Button-Type, Transient, Heat-Flux Gauge Measurements," *ASME Proc. 31st National Heat Transfer Conference,* Vol. 5, pp. 33–39.

Miller, C. G., 1981, "Comparison of Thin-Film Resistance Heat-Transfer Gages With Thin-Skin Transient Calorimeter Gages in Conventional Hypersonic Wind Tunnels," NASA Technical Memorandum 83197.

Rao, K. V., Delaney, R. A., and Dunn, M. G., 1994, "Vane-Blade Interaction in a Transonic Turbine, Part II: Heat Transfer," *J. of Propulsion and Power,* Vol. 10, No. 3, pp. 312–317.

Schultz, D. L., and Jones, T. V., 1973, "Heat-Transfer Measurements in Short-Duration Hypersonic Facilities," AGARDograph No. 165.

Seymour, P. J., 1987, "Techniques for Numerical Evaluation of Unsteady Heat Flux From Thin Film Gages," MS Thesis, State University of New York at Buffalo.

Skinner, G. T., 1961, "Calibration of Thin-Film Backing Materials," *J. of the American Rocket Society,* Vol., 31, No. 5, pp. 671–672.

Skinner, G. T., 1962, "A New Method of Calibrating Thin Film Gauge Backing Materials," Cornell Aeronautical Laboratory Report No. 105.

Vidal, R. J., 1956, "Model Instrumentation Techniques for Heat Transfer and Force Measurements in a Hypersonic Shock Tunnel," Calspan Report No. AD-917-A-1.

Wittliff, C. E., 1977, "Space Shuttle Leading Edge Heat Transfer Investigation in the Calspan 96-in. Hypersonic Shock Tunnel," *International Congress on Instrumentation in Aerospace Simulation Facilities '77 Record,* IEEE Publication 77 CH 1251-8 AES, pp. 101–112.

Wittliff, C. E., 1983, "Hypersonic Shock Tunnel Heat Transfer Tests of the Space Shuttle SILTS Pod Configuration," AIAA Paper No. AIAA-83-1535.

Effect of Plenum Crossflow on Heat (Mass) Transfer Near and Within the Entrance of Film Cooling Holes

R. J. Goldstein
Department of Mechanical Engineering,
University of Minnesota,
Minneapolis, MN 55455

H. H. Cho
Department of Mechanical Engineering,
Yonsei University,
Seoul, Korea 120-749

M. Y. Jabbari
Department of Mechanical Engineering,
Saginaw Valley State University,
University Center, MI 48710

Convective heat/mass transfer near and within the entrance region of film cooling holes supplied with air from an internal duct (plenum) behind the cooling holes has been measured using a naphthalene sublimation technique. The experiments are conducted for duct Reynolds number, based on the duct inlet flow condition, of 1800 to 13,500, which results in a range of hole Reynolds numbers of 8000 to 30,000, close to actual engine operating conditions. The flow entering the hole can be considered a combination of flow along a 90 deg tube bend and a sudden contraction duct flow. The flow separates at the inner corner and a secondary flow is induced by the centrifugal force associated with the streamline curvature. The mass transfer coefficient for the duct wall (surface of film-cooled plate) with a cooling hole is three to five times higher than for a fully developed duct flow. With a smaller duct, the overall transfer coefficient on the hole entrance surface increases due to the higher duct Reynolds numbers, but the flow has less secondary flow effects within the smaller space. Generally, transfer coefficients on the hole entrance surface are largely unaffected by the duct end presence, but the transfer coefficient is larger downstream for a short distance from the center of the last hole to the duct end. In tests with multiple film cooling holes, the flow at the first hole is more of a curved duct flow (strong secondary flow) and the flow at the last hole is more of a sink-like flow. At the middle hole, the flow is a combination of both flows. The mass transfer rates on the inner hole surfaces are found to be the same for holes with corresponding positions relative to the duct end, although the total number of open holes is different.

Introduction

The thermal efficiency and specific power of gas turbine systems depend strongly on turbine inlet temperature. The inlet temperature has in past decades been raised to values that make intensive cooling of the hot components necessary. Film cooling has been a standard method of turbine blade/vane and combustor wall cooling in combination with additional convective cooling methods (e.g., internal cooling of blades). With film cooling, the coolant flow is supplied to the injection holes through internal passages of the gas turbine blades. This pattern is similar to that found in flow passages of laminate plates and in manifolds of heat exchangers. The crossflow entering a hole from the plenum induces a secondary flow due to the curvature of streamlines and a separation at the inner corner of the hole entrance. These flow patterns affect heat transfer, causing significant increases and nonuniformity around the hole entrance.

A complete analysis of heat transfer with film cooling requires heat transfer coefficient distributions at the internal (plenum) wall and inside hole surfaces as well as adiabatic wall temperatures (film cooling effectiveness) and heat transfer coefficient distributions on the exposed surfaces. The objective of the present experiments is to determine the local heat transfer coefficient distribution on the cooling hole inner surfaces and the blade wall of the plenum that provides the flow to the cooling holes.

It is difficult to measure the local heat transfer rate near the hole and inside the hole surface in heat transfer experiments. Such an experiment would include large conduction effects resulting from spatial variation in the heat transfer rates and resulting temperature gradients around the hole entrance. Therefore, a mass transfer technique is used to measure transfer rates on the inside hole surface and on the plate around the hole entrance. The mass transfer experiment excludes conduction in the solid wall and gives finer spatial resolution of transfer coefficients. Detailed knowledge of the heat/mass transfer near and inside the film cooling holes is important because turbine component life is strongly influenced by thermal stress. This detailed information is also required for computational methods of flow and heat/mass transfer around film cooling holes. Note that the mass transfer results can be converted to the heat transfer results using the heat/mass transfer analogy.

In the present experiments, local mass transfer rates are obtained from the test plate cast with naphthalene around the hole and inside the hole. The surface boundary condition corresponds to an isothermal surface in an analogous heat transfer system. Concentration gradients and the mass flux are analogous to temperature gradients and the heat flux. The time-averaged local mass transfer rates are obtained from measurement of the sublimation depths. While the heat/mass transfer coefficient is obtained with an isothermal condition, it can be useful for other boundary conditions because the heat/mass transfer coefficient is usually a weak function of the wall temperature distribution in turbulent flows.

Previous Work. The crossflow entering holes has been investigated for dividing flows at tee junctions, for flows in a manifold into multiple branch tubes of heat exchangers, and for both combined (Fried and Indelchik, 1989; Miller, 1990). These studies reported the flow distribution and pressure loss (head loss), which depend on the area ratio, the angle between branch

Contributed by the Heat Transfer Committee for publication in the JOURNAL OF TURBOMACHINERY. Manuscript received by the Heat Transfer Committee October 1, 1996. Associate Technical Editor: M. G. Dunn.

and duct, and the chamfers or radii at the junction of branch. They did not consider the heat transfer.

Wesley and Sparrow (1976) measured heat transfer rates in a tube downstream of a tee for Re = 18,700 to 47,900. Sparrow and Kermink (1979) studied heat transfer downstream of a fluid withdrawal branch in a tube with different flow splittings for Re = 5000 to 20,000. They showed that the heat transfer rates in the thermal entrance region were much higher than those for parallel flow entering (axisymmetric tube flows) and the thermal entrance length was much longer. The heat transfer rates had significant circumferential variations (20 ~ 30 percent from average values).

Metzger and Cordaro (1979) investigated the average heat transfer rate in a short branch tube with crossflow entering. They had a range of length-to-diameter ratios of 5 to 10 and variable crossflow-to-tube velocity ratios for Re_h = 10,000 to 100,000 (based on tube mean velocity and hole diameter). They noted that the heat transfer was enhanced with increasing crossflow-to-tube velocity ratio.

Byerley et al. (1988) studied the heat transfer near and within the entrance of a branch hole with a crossflow stream using a liquid crystal technique. The experiments were conducted at ratios of tube-to-crossflow velocity of 0 to 8 and a duct crossflow Reynolds number, Re_{duct} = 25,000. They found that local heat transfer rates on the duct wall downstream of the branch hole are up to six times that of fully developed flow.

Cho and Goldstein (1995) showed that transfer coefficients in a film cooling hole are weakly influenced by the crossflow at the hole exit and the affected zone is confined close to the hole exit (about 0.15 hole diameter in depth). They also found that transfer coefficients on hole entrance (backside) surfaces are essentially the same as those with no crossflow at the hole exit. Thus, heat transfer in a film cooling hole and on the plenum walls of actual turbine components can be closely approximated from experiments without crossflow at the hole exit.

Operating Conditions. Most previous investigators studied a single branch tube from duct or tee junctions in heat transfer problems. In the present study, the mass transfer coefficients are measured on the plenum wall in the near region of the entrance hole and inside hole surfaces for one to three branch holes to simulate the internal passage flows in turbine blades. Also, the effects of the hole-to-hole spacing of 3D and 6D, and duct height (duct cross section) are investigated for duct Reynolds number, based on the duct inlet flow condition, of 1800 to 13,500, which results in a range of Re_h = 8000 to 30,000, close to actual engine operating conditions.

Experimental Apparatus and Procedure

1 Duct. Two different duct cross sections are tested, one 76.2 mm (3D) high by 101.6 mm (4D) wide while the second is 38.1 mm (1.5D) high by 101.6 mm (4D) wide. As shown in Fig. 1, the duct has three holes that are perpendicular to the duct flow direction. One, two, or three open holes are used to determine the effects of neighboring holes, hole spacing, distance to end of duct, and duct height. The top wall and location of the closed end of the duct are adjustable. The tunnel has a square-edged inlet, which accepts flow from a large plenum. The large plenum/baffle device prior to the duct inlet is used to reduce large eddy motions from the room air. The air flow is sucked through the duct, the test holes, and a large plenum chamber behind the holes by a vacuum pump, and then is ejected outside the building. The approach flow conditions, with a duct length of about 15 times the hydraulic diameter of the duct cross section (25 times for the 1.5D duct height), are expected to be almost fully developed in the axial flow velocities but probably not for secondary flow patterns in the noncircular duct. The pressure drop across the orifice plate for flow rate measurements is maintained to within ±1 percent of the desired pressure difference during a run.

For the two or three open holes, each hole may have a slightly different flow rate. The maximum deviation between the hole flows is expected to be less than 2.6 percent from a correlation of flow distribution in a manifold (Acrivos et al., 1959). This small difference is due to the large pressure drop through the holes compared to that in the duct because of the large area ratio between the hole and the duct. Therefore, flow rates in each hole can be assumed to be equal in the present experiments.

2 Test Plate and Naphthalene Casting Procedure. The apparatus is designed to enable measurement of the local naphthalene sublimation rate on the duct wall near the holes and the inside surface of cooling (branch) holes. The test surface areas are coated with a thin naphthalene layer for sublimation prior to being exposed to the air stream. The mass transfer active area starts 2D upstream of the first hole center. Therefore, the present experiment is analogous to a system in which heating starts at a line $X = -2D$ on the duct wall in heat transfer.

The naphthalene surface employed in the experiments is made by a casting process. This is achieved by pouring molten naphthalene into a mold, allowing the naphthalene to solidify, and separating the mold from the test plate. The mold consists of the test plate, a highly polished aluminum flat plate, and a circular cylinder. The smoothness of the exposed naphthalene

Nomenclature

D = cooling (branch) hole diameter = 25.4 mm
D_{naph} = mass diffusion coefficient for naphthalene vapor in air
H = duct height
h_m = local mass transfer coefficient, Eq. (1)
$\dot{m}$ = local naphthalene mass transfer rate per unit area
Nu_0 = reference Nusselt number of a fully developed circular tube flow
Pr = Prandtl number
Re_{duct} = Reynolds number based on the duct hydraulic diameter and the average velocity in the duct
Re_h = Reynolds number based on the hole diameter and the average velocity in a hole
S = hole-to-hole spacing
Sh = Sherwood number based on the hole diameter, Eq. (2)
Sh_0 = reference Sherwood number of a fully developed circular tube flow; based on the duct hydraulic diameter and the average velocity in the duct
$\overline{Sh}$ = lateral/circumferential average of Sherwood number
t = plate thickness
T_w = local wall temperature
X = streamwise (duct flow) distance from the center of the first hole
X_c = position of the center of each hole
XL = distance from the center of the last hole to the duct (closed) end
Y = axial distance from the inlet of cooling holes
Z = lateral distance across span measured from center of holes
$\delta\tau$ = test duration
δz = local sublimation depth of naphthalene
ρ_s = density of solid naphthalene
$\rho_{v,w}$ = naphthalene vapor density on the surface
$\rho_{v,\infty}$ = naphthalene vapor density of the approaching flow ($\rho_{v,\infty}$ = 0 in the present study)
σ = standard deviation

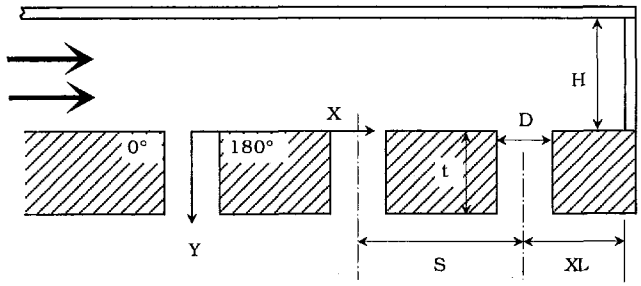

Fig. 1 Experimental apparatus and coordinate system

surface is comparable to that of the polished aluminum adjacent to it.

3 Data Acquisition System. An automated surface measurement system is used to scan the profile of the naphthalene surface. This system satisfies many requirements to obtain useful local sublimation depths of a naphthalene surface; these include precise positioning of the plates, accurate depth measuring, and rapid data acquisition to minimize the natural convection losses. Two different computer-controlled measurement systems, an *XY*-Table and a Four-Axis Table, are used for the flat plate measurement and the inside hole measurement, respectively.

The measurement systems consist of a depth gage, a linear signal conditioner, a digital multimeter, stepper-motor driven positioners, a motor controller, and a microcomputer (cf. Goldstein and Cho, 1995). This automated system typically obtains about 2000 data points in one hour.

The depth gage (a linear variable differential transformer; LVDT) has 0.5 mm linear range and 25.4 nm (1.0 μin.) resolution. The nominal sublimation depth in a test is around 50 μm (2 mil), about three orders of magnitude larger than the resolution. The linearity of the LVDT is within 0.1 percent of the measuring range. The measurement errors of the LVDT are about 0.15 μm (6 μin.; 2σ) for the flat plate measurement and about 0.45 μm (18 μin.) for the inside hole measurement at a 95 percent confidence level.

4 Measurements. To measure inside hole mass transfer rates, an extended stylus is used to reach deep inside the hole. The profile of the naphthalene surface elevation is determined on the measurement tables before and after each test run. The difference between the two sets of surface elevations (with respect to reference positions on the nonsubliming metal surface) is a measure of the sublimation depth. Each test run time is selected so that the average sublimation depth of the naphthalene surface will be about 0.05 mm. The maximum sublimation depth, about 0.2 mm, is about 0.8 percent of the nominal hole diameter of 25.4 mm. Because the vapor pressure of naphthalene is quite sensitive to temperature (about 10 percent change per °C), the naphthalene surface temperature is measured using *T*-type (copper-constantan) thermocouples installed within the naphthalene, as close as possible to the surface. During the run, the temperature variation of the naphthalene surface is within about 0.2°C.

The local mass transfer coefficient is defined as:

$$h_m = \frac{\dot{m}}{\rho_{v,w} - \rho_{v,\infty}} = \frac{\rho_s(\delta z/\delta \tau)}{\rho_{v,w}} \tag{1}$$

where $\rho_{v,\infty} = 0$ as would occur in a boundary layer flow. This is similar in the duct flow as the bulk (mean) flow density is close to 0. The Sherwood number can be expressed as:

$$\mathrm{Sh} = \frac{h_m D}{D_{\mathrm{naph}}} \tag{2}$$

The naphthalene vapor pressure is obtained from a correlation (vapor pressure–temperature relation) of Ambrose et al. (1975). Then, the naphthalene vapor density, $\rho_{v,w}$, is calculated from the perfect gas law. D_{naph} is determined from a correlation recommended by Goldstein and Cho (1995). During the experiment, extraneous sublimation losses by natural convection are corrected from the total sublimation rate based on a natural convection rate and the measurement duration (Cho, 1992).

Uncertainty of the Reynolds numbers using Kline and McClintock's (1953) method for single sample experiments, considering the nonuniform flow distribution and flow fluctuation, is within 2.8 percent for three open holes (but much less for single holes) in the entire operating range of the measurement based on a 95 percent confidence interval. Uncertainty of the Sherwood numbers, considering the measured temperature, depth, position and correlation equations, is within 7.1 percent in the entire operating range of the measurement. This uncertainty is mainly attributed to the uncertainty of the properties of naphthalene, such as the naphthalene saturated vapor pressure (3.77 percent) and diffusion coefficient of naphthalene vapor in air (5.1 percent). In contrast, the error due to the depth measurement is only 0.9 percent.

Results and Discussion

The flow entering a hole can be thought of as the combination of flow along a 90 deg tube bend and a sink flow (sudden contraction). When the flow stream changes direction near the perpendicular hole, the flow pattern will be similar to the flow in a right-angle tube bend or a sharp bend. The flow is separated at the inner corner and the secondary flow will be induced by the centrifugal force associated with the streamline curvature. The secondary flow will be weakened by the separation near the entrance. Since the cross-sectional area of the main duct is much larger than the hole area (15.3 times and 7.64 times for the 3.0D and 1.5D plenums, respectively), the entering flow in the hole from the duct will act like a sink flow (sudden contraction). In general, the flow entering the first cooling (branch) hole is more similar to the flow pattern of a 90 deg tube bend. However, the flow pattern for the other cooling holes is closer to the sinklike flow when hole-to-hole spacing is small.

The flow pattern, based on flow visualization and local transfer rates, is shown schematically in Fig. 2. Surface flow visualization was conducted on the duct wall around the hole entrance using an ink-dot method (Cho, 1992). The results for one, two, or three open holes and for Re_h = 15,000 and Re_h = 30,000 showed curved-ink traces, which were anticipated from the secondary flow pattern. For the two open holes, a separation zone behind the first hole was expected as shown by scattered-ink traces. The streaks of the ink around the perimeter of the second hole were straighter than for the first hole. This suggested that the flow around the second hole was more akin to a sink flow.

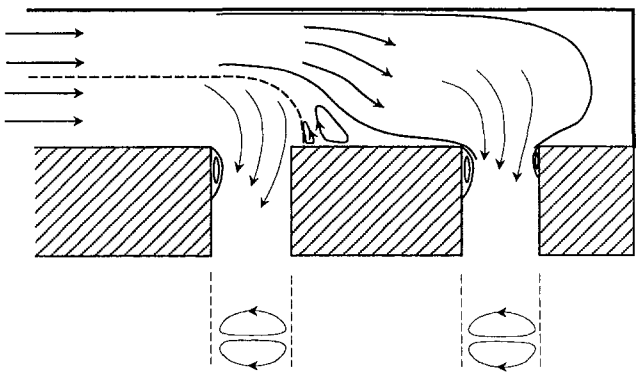

Fig. 2 Schematic pattern of cross entering flows

For the three open holes, the separation zones were also expected behind the first hole and the second hole. Around the second hole (middle hole), the flow pattern in the upstream and side regions was similar to that of the last hole, while the flow in the downstream region was similar to that of the first hole.

1 Duct Wall Near the Entrance of the Cooling Holes. The origin of the X coordinate (streamwise direction in the main duct flow) is at the center of the first hole, as shown in Fig. 1. The active (sublimating) area starts at $X/D = -2$. Figure 3 shows the normalized Sh, an enhancement factor, on the duct wall near the hole entrance for a single hole with H = 3D for Re_h = 7800 to 30,000. The reference Sherwood number, Sh_0, is taken from a fully developed circular tube flow correlation ($Nu_0 = 0.0397\ Re_{duct}^{0.73}\ Pr^{0.33}$; Mills (1962); based on the hydraulic diameter of the duct cross section).

The maximum enhancement, Sh/Sh_0, is approximately 5 on the sides and downstream of the hole and decreases with increasing Reynolds number. The mass transfer rate on the surface upstream of the hole entrance shows an increase due to the acceleration of the duct flow (thinning of the boundary layer in duct flow). Downstream of this hole, the mass transfer rate also increases due to the disturbance in the duct flow (sudden enlargement). It is also enhanced by the duct core flow, high velocity, and low concentration, which touches the surface; the wall boundary layer flow is removed by suction from the cooling (branch) hole. On the side region of the hole, the mass transfer increases due to an acceleration of the flow to the hole (a sink-like flow) and a swirling of flow induced by the secondary flow pattern of the effusion stream as shown in Fig. 2. Thus, the transfer rate around the film cooling hole is much higher than that for simple duct flow. The normalized Sherwood numbers show the difference between a simple duct and a duct with a cooling hole (the value is approximately 1 at $X/D = -1.5$, an inlet condition). However, the normalized values are somewhat arbitrary because the reference Sherwood number, Sh_0, has been taken from a circular tube correlation. Thus, from this point the mass transfer results will be presented as actual values, instead of in normalized form, with Sh based on the hole diameter.

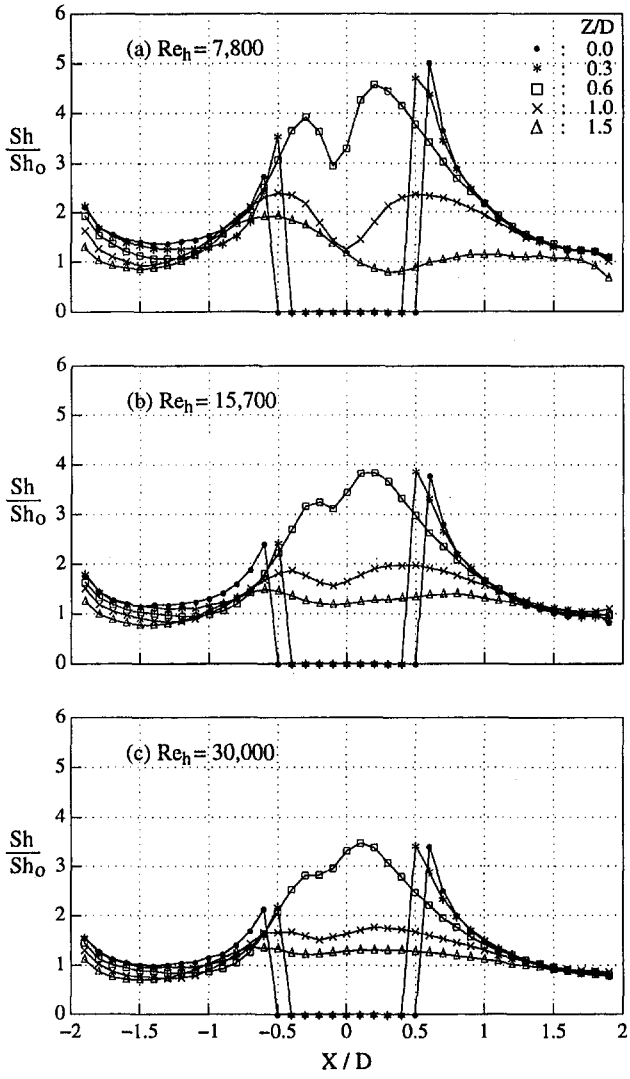

Fig. 3 Normalized Sh on plenum wall with one open hole for H = 3D and XL = 2D

1.1 One Open Hole With XL = 2D and H = 3D. Axial and lateral distributions of the local Sh for Re_h = 15,700 are given in Fig. 4. The area ratio of the duct cross section to the hole is 15.3 indicating considerable acceleration of the flow as the duct flow enters the hole. The Sh decreases slightly, as the mass boundary layer thickness increases, from $X/D = -2$ where the mass active surface starts, and reaches a minimum value. The lateral distribution at the upstream region is fairly flat, as shown in Fig. 4(*b*). At $X/D = -1$ (near front region of the hole), Sh starts to increase due to acceleration of flow into the hole and thinning of the boundary layer. Near X/D = 0 (side region of the hole), Sh at Z/D = 0.6 is about four times the value at $X/D = -1.5$ and wavy, with a minimum near X/D = 0. The wavy pattern of Sh reduces with increasing Reynolds number. The high and wavy Sh is caused by the secondary flow pattern on the surface induced by the secondary flow of the effused stream into the hole. Sh decreases rapidly away from the hole in the lateral direction (Fig. 4(*b*)). The flow is similar to a simple sink flow as discussed by Cho (1992). Downstream of the hole (Fig. 4(*a*)), Sh is high because the duct flow is highly disturbed and the duct core flow of high velocity and low concentration of naphthalene touches on this region. Sh decreases rapidly with X/D due to the presence of the duct (closed) end at X/D = 2, and is distributed uniformly in the lateral direction (Fig. 4(*b*)). There is reverse flow in this region near the surface. Sh near X/D = 2 has the same level as the inlet flow even though it is very close to the duct end.

Auxiliary runs, in which the hole is 5 percent off from the center of the duct width, have shown asymmetric streaklines with high swirling from the surface flow visualization (Cho, 1992). This pattern is also observed from local measurement of the mass transfer (in contour plot). It suggests that the flow pattern around an off-center hole, even with minor asymmetry, can be very different from that for a centered hole.

1.2 Effect of Duct Cross-Sectional Area (One Open Hole). With the smaller duct cross-sectional area (duct height H = 1.5D), the area ratio of the duct to the hole is 7.64, and Fig. 5 shows results for Re_h = 15,600. In maintaining the hole Reynolds number, the mean velocity in the duct is twice that in the previous case (H = 3D). Thus, Sh at the upstream region on the hole entrance is higher than that in the previous case (Fig. 4). However, Sh increases less near the hole and has a similar value at the leading edge of the hole. This suggests that Sh near the hole depends on the sink flow to the hole rather than the duct flow. Around X/D = 0 (side region of the hole), Sh has only one peak value at X/D = 0 and the level of Sh is similar to that with H = 3D. The flow is expected to produce less swirling motion due to the short height of the duct (small spacing). Downstream of the hole, Sh is much higher than with H = 3D for $-0.5 \le Z/D \le +0.5$. Sh decreases rapidly as one proceeds downstream but increases again near the end of the duct; this is different from the previous case. This result could be caused by a redeveloping boundary layer in the reverse direction after the duct core flow touches near the end of the duct.

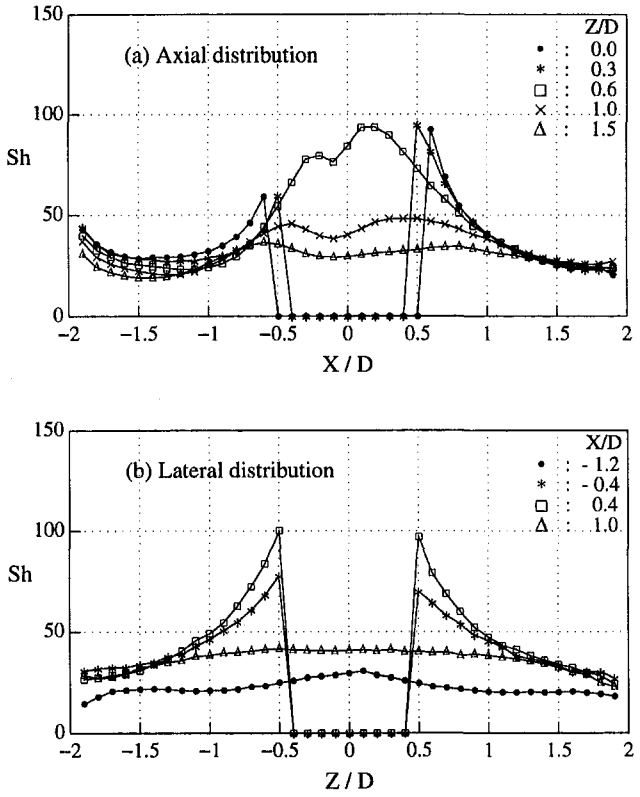

Fig. 4 Local Sh on plenum wall with one open hole for H = 3D and XL = 2D at Re_h = 15,700

In the lateral distribution, Sh is higher at the center part (around $Z/D = 0$) while it is flat in the case of H = 3D.

Laterally averaged values Sh are compared in Fig. 6(a). As expected, the average Sh for H = 1.5D is higher some distance upstream and downstream region, especially close to the duct end (around $X/D = 1.7$), than that for H = 3D. A big difference is also found around $X/D = 0$, due probably to the different strengths of secondary flows. However, the results for the different heights are similar at the leading edge (at $X/D = -0.5$) and the trailing edge (at $X/D = 0.5$) of the hole. As shown in Fig. 6(b), the local Sh near the hole is two times higher than the laterally averaged value.

1.3 Two Open Holes With XL = 2D, H = 3D, and Spacing S = 3D. Two cooling (branch) holes are opened with hole-to-hole spacing S = 3D. Pressure drop occurs mostly through the holes rather than the duct flow due to a large duct-to-hole area ratio (15.3 times). Thus, approximately equal flow rates through each hole can be assumed (maximum deviation is less than 2.6 percent as discussed in the previous section). The local Sh around the first and second holes is presented in Fig. 7 at Re_h = 15,700. When the duct flow approaches the cooling holes, the lower half of the duct stream tends to enter the first hole (Fig. 2). Consequently, the upper half of the duct flow suddenly expands, due to the increasing flow area. This sudden expansion of the flow will produce greater turbulence and a small separation bubble downstream of the first cooling hole. The duct flow velocity is reduced as approximately half the flow enters the first hole. At the first hole, the duct flow (lower half) entering the hole is expected to have a pattern similar to the flow for a single hole with duct height H = 1.5D. In fact, the local Sh distribution at the first hole is similar to that of one hole with H = 1.5D except in the downstream region (cf. Fig. 5). In the downstream region, Sh is higher due to the upper half core stream touching on the surface. The high Sh upstream of the second hole is caused by a high turbulence level of the suddenly expanding flow. It is also enhanced by the core duct flow of high velocity and low concentration of naphthalene touching the surface because the near-wall portion of the duct flow has been removed through the first hole. In the side region and downstream of the second hole, the flow pattern is expected to be similar to the simple sink flow because the main duct flow loses axial stream momentum (X direction) in the sudden expansion. Sh at the second hole follows circular contour lines like a sink flow. The laterally averaged Sh at the

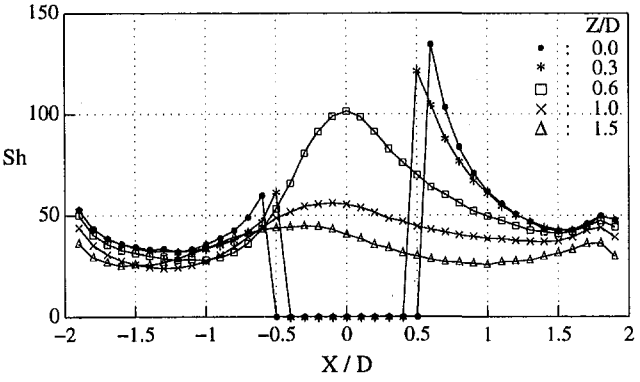

Fig. 5 Local Sh on plenum wall with one open hole for H = 1.5D and XL = 2D at Re_h = 15,600

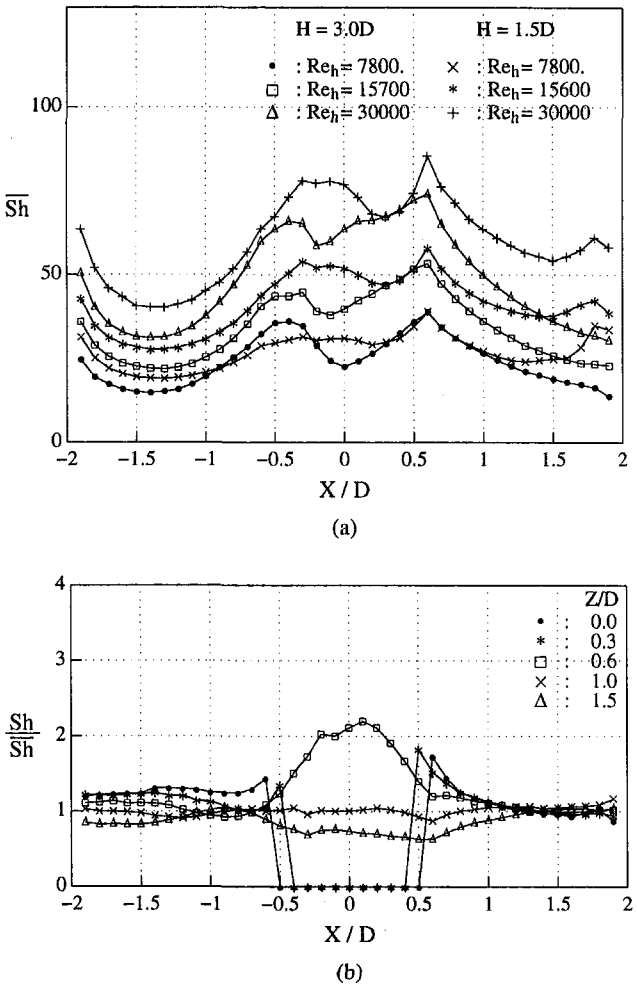

Fig. 6 Sh on plenum wall for one hole open with XL = 2D: (a) averaged Sh for different duct heights; (b) normalized Sh at Re_h = 15,700 and H = 3D

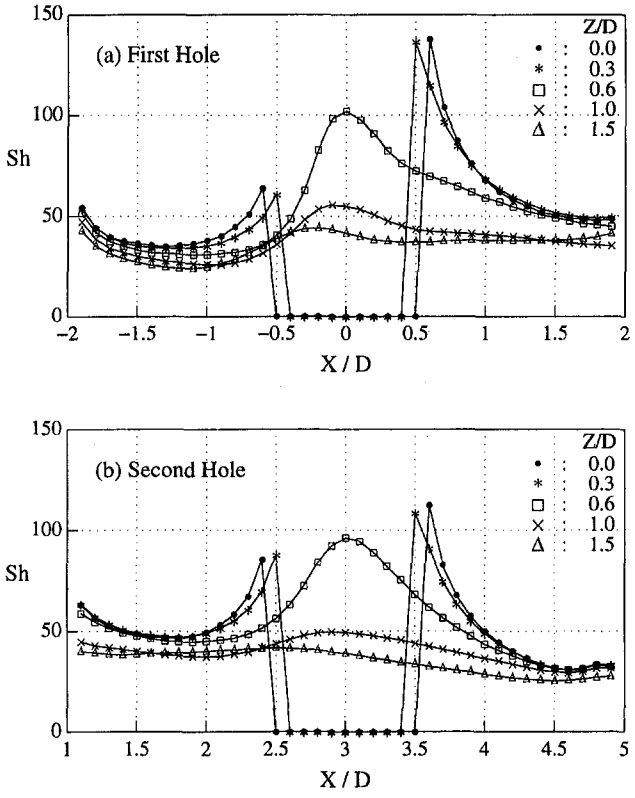

Fig. 7 Local Sh for two open holes with H = 3D, XL = 2D, S = 3D, and Re_h = 15,700

first hole is similar to that for one open hole with H = 1.5D except in the downstream region.

1.4 Effect of Hole-to-Hole Spacing for Two Open Holes. An experiment with two open holes was conducted with Re_h = 15,700 and hole-to-hole spacing S = 6D to compare with S = 3D. The results show differences of local Sh only in the region upstream of the second hole. At the large spacing S = 6D, the upper half of the duct stream will have more time to develop after the sudden expansion at the first hole. A lower mass transfer rate on the upstream region is found for this greater duct flow development. The laterally averaged Sh near the first holes show little difference for these cases.

1.5 Three Open Holes With XL = 2D, H = 3D, and S = 3D. Experiments with three open holes were performed at Re_h = 15,500 and the results are presented in Fig. 8. At the first hole, the flow pattern is expected to be the same as that around the first hole of the two-hole case. However, Sh on the duct wall before the first hole is higher than for two open holes due to the higher inlet duct flow rate (maintaining the same hole Reynolds number). Approximately the lower one-third of the duct flow stream will enter the first hole and the remaining two thirds of the stream will expand suddenly downstream. The higher flow rate (compared with that for two open holes) increases the Sh downstream of the first hole (the upstream region of the second hole). When the disturbed flow enters the next hole with close hole-to-hole spacing, there is little opportunity for the flow to develop again and the flow pattern is close to that for sink flow. This is shown by the streamlines of the flow approaching the hole more directly rather than in a crossflow manner. This pattern continues for the following holes with small hole-to-hole spacing. The sink flow pattern becomes more dominant for the hole near the end of the duct. High mass transfer rates are obtained in both the upstream and downstream regions of the second (middle) hole. The contour plot (Fig. 8)

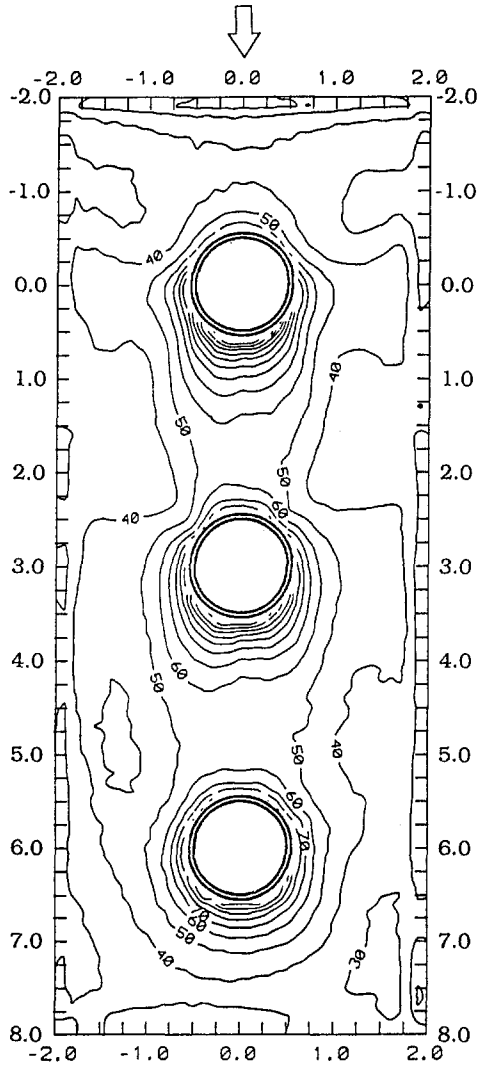

Fig. 8 Sh contour plot of plenum wall for crossflow entering holes at Re_h = 15,500 (three open holes, S = 3D and H = 3D)

shows that the flow near this center hole combines effects from the first hole (more like a swirling flow) and the last hole (more like a sink flow). At the third (last) hole, Sh distribution is similar to that around the second (last) hole with two open holes. The laterally averaged Sh are similar for two open holes and three open holes (Fig. 9). The average Sh near the third (last) hole with three open holes is very close to that for the second (last) hole for two open holes. This suggests that Sh

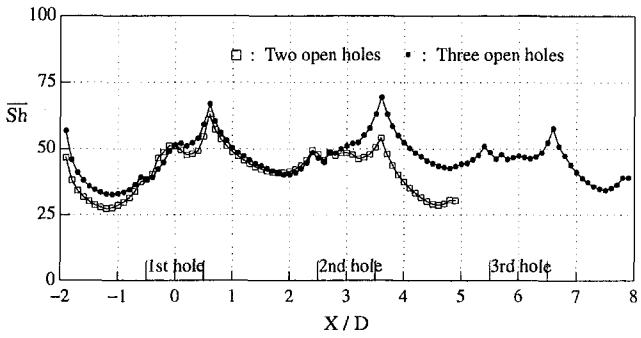

Fig. 9 Laterally averaged Sh for the three open holes with H = 3D, XL = 2D, S = 3D, and Re_h = 15,500 (compared with the two open holes)

around the last hole is largely unaffected by the number of upstream holes and has a sink flow pattern.

1.6 Comparison With a Sink Flow at Open Area (No Crossflow). The duct crossflow entering into the single hole is compared with a sink flow in an open area (Cho, 1992). The comparison indicates that Sh in the crossflow case is approximately 30 percent higher than that for the open sink flow at Re_h = 15,600, Fig. 10. The higher value is due to the turbulent duct flow, while the open sink flow is expected to have a laminar approaching flow. Sh for the duct flow case is also enhanced by swirling/secondary flow induced by the stream curvature as the flow enters the hole.

2 Inside the Hole(s). On the inside hole surface, the heat transfer rate is enhanced by the secondary flow motion, which is created by the crossflow at the hole entrance, but is reduced by a large separation bubble at the leading edge corner. The heat transfer is expected to increase near the trailing edge (180 deg) of the hole due to flow impingement. The heat transfer at the leading edge (0 deg) is less than that for an ordinary sink flow due to enhanced flow separation.

2.1 One Open Hole With *XL* = 2D and *H* = 3D. When the duct flow enters the perpendicular hole, a secondary motion of hole flow is induced by the curvature of the flow stream and separation is expected at the entrance region of the hole inlet especially along the leading edge side (0 deg). Note that 0 deg is at the leading edge of the hole and 180 deg is at the trailing edge as shown in Fig. 2.

The local Sh for a single hole with H = 3D and XL = 2D is shown in Fig. 11 for Re_h = 15,700. Separation flow exists all around the entrance of the hole with a larger length of separation at the leading edge side (0 deg) based on peak Sh. The trend indicates that the flow near the entrance is more like a sink flow than a flow in a 90 deg bend tube. However, peak Sh is very high at the trailing edge side (180 deg) and decreases rapidly circumferentially to the leading edge side (0 deg). This is caused not only by the secondary motion of the curved streamline but also by the impingement effect of the stream. This impingement will help the secondary motion due to the high pressure produced on the trailing edge side. However, it is expected that the secondary motion loses strength rapidly when it includes a separation flow. Downstream in the hole (beyond Y/D = 0.9) Sh is fairly uniform around the perimeter of the hole.

2.2 Two Open Holes With *XL* = 2D, *H* = 3D, and *S* = 3D. When the duct flow approaches the first hole, much of the lower half of the duct stream will enter the first hole. Thus, the flow inside the first hole is expected to have a pattern similar to the flow inside a single hole with duct height H = 1.5D. The local Sh distribution inside the first hole is similar to that of

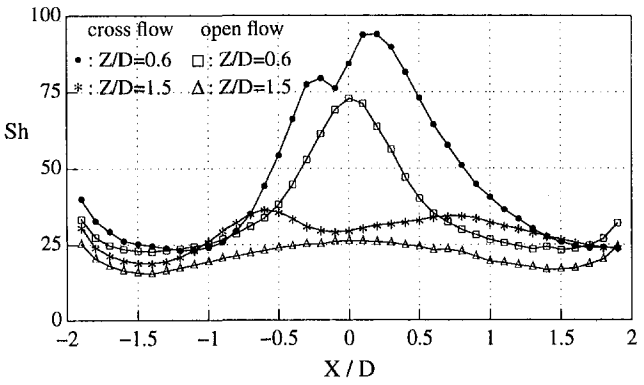

Fig. 10 Comparison of local Sh near a single hole for crossflow entering and open suction flow (Cho, 1992) at Re_h = 15,600

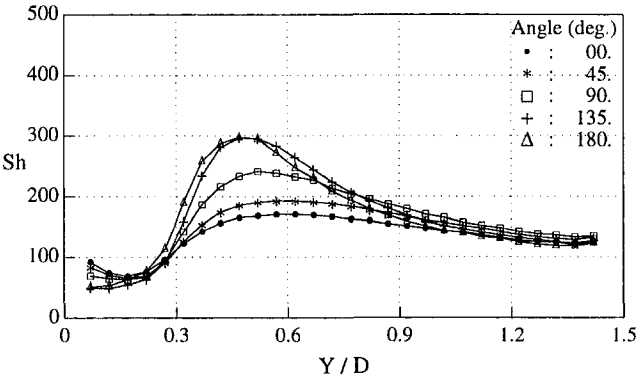

Fig. 11 Local Sh inside hole for one open hole with H = 3D and XL = 2D at Re_h = 15,700

one hole with H = 1.5D, but has higher values at the trailing edge side. Inside the second hole, the local Sh distribution is close to that for one open hole with H = 3D but with a shorter separation at the entrance of the hole. The shorter separation is expected due to the higher turbulence levels of the inlet flow following the sudden expansion after the first hole effusion.

When the results are compared with the local Sh with one open hole of two different duct heights along the leading edge line (0 deg) and the trailing edge line (180 deg), Sh at

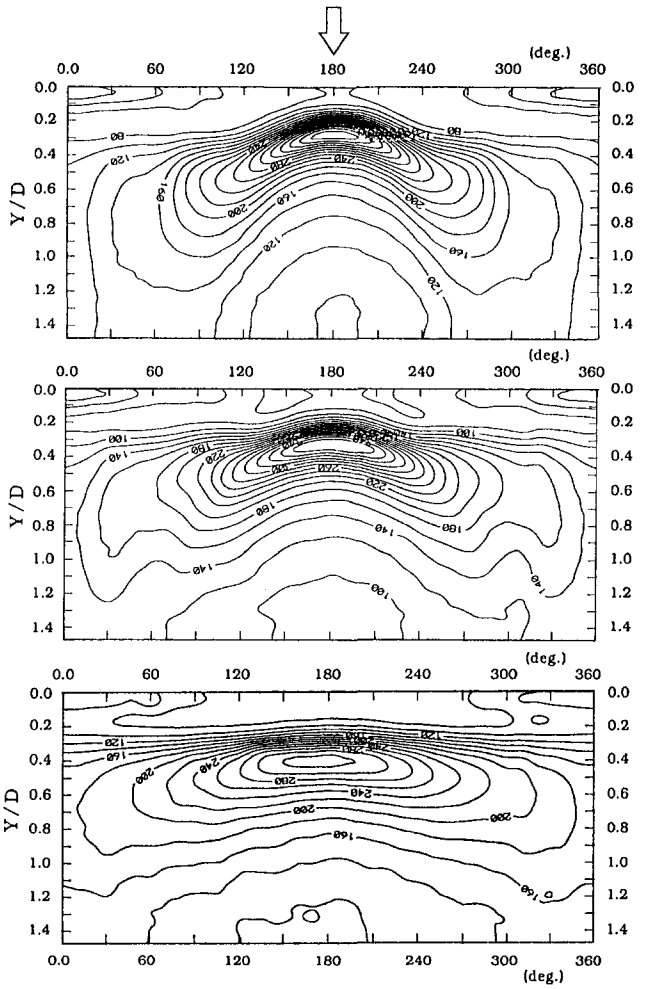

Fig. 12 Contour plots on the inside hole surfaces for three open holes at Re_h = 15,700: (*a*) first hole; (*b*) second hole; (*c*) third hole

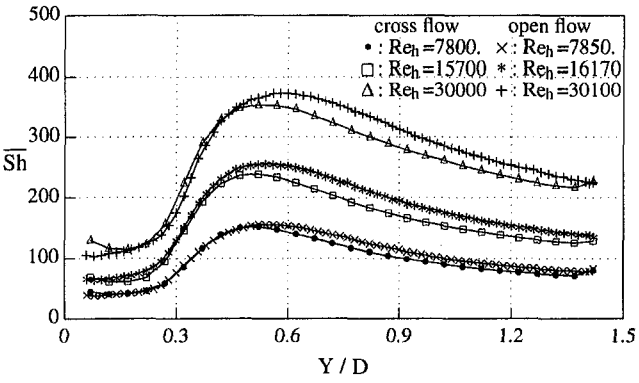

Fig. 13 Comparison of crossflow entering and open suction flow (Cho, 1992) for average Sh inside single hole

the first hole matches well with that for one open hole with H = 1.5D along the leading edge line. Along the trailing edge line, Sh at both holes is different from that with one open hole at the entrance region but all are similar in the downstream region. The circumferential average Sh for the first hole also compares well with that for one open hole with H = 1.5D. Inside the second hole, the circumferential average Sh is slightly higher than that with one open hole for H = 3D at the entrance region but the two are nearly the same in the downstream region. The overall-average Sh shows that the difference from one open hole is about 3 percent when the first hole is compared with H = 1.5D and the second hole with H = 3D. It may be said that the transfer rate on the inside hole surface of multiple open holes can be simulated well with a single open hole.

2.3 Three Open Holes With XL = 2D, H = 3D, and S = 3D. Contour plots of the local Sh are presented in Fig. 12 for Re_h = 15,700. In the first hole, the separation region, judged by the peak Sh, is very short at the trailing edge side (180 deg) and increases toward the leading edge side (0 deg). Sh inside the first hole is expected to be influenced by the stronger secondary flow of the curved stream because the crossflow turns from a smaller space (one-third of the duct height). The crossflow with this small curvature of the flow produces a long separation at the leading edge side. The Sh distribution in circumferential direction is flatter for the third (last) hole. The separation zone at the entrance is quite uniform along the perimeter of the last hole, as in a sink flow.

When these values are compared with those for two open holes, Sh in the second hole with three open holes is close to that in the first hole of a two open holes and the third (last) hole is similar to the second (last) hole of a two open holes. Thus, even though the number of open holes is different, the mass transfer rates are expected to be the same counting holes from the duct end. This pattern is somewhat different from the Sh values for the duct wall (refer to previous section).

2.4 Comparison With a Sink Flow in an Open Area (No Crossflow). The duct flow entering into the single hole can be compared with a sink flow from an open area (Cho, 1992). As shown in Fig. 13, the circumferentially averaged Sh for the crossflow is slightly lower than that for the open sink flow for Re_h = 7800 to Re_h = 30,000, but both values are very close at the entrance region (inside separation zone). The overall-average Sh are different by about 6 percent. This suggests that the mass transfer rate for a sink flow can be used for the duct flow case to get the circumferential average rate even though the local Sh is quite different around the circumference of the hole.

Conclusions

Duct Wall

(*i*) Sh on the duct (plenum) wall with a cooling (branch) hole is enhanced by the secondary flow induced by the flow stream curvature and by the thinning of the boundary layer due to the local acceleration of the sink flow. Local Sh near the hole are three to five times higher than for fully developed duct flow and these local values are also two times higher than laterally averaged values under the same conditions and 30 percent higher than the local values in an open sink flow.

(*ii*) When the duct cross-sectional area is reduced by half, the overall Sh on the hole entrance surface increases due to the higher duct flow velocity, but the flow has less swirling motion due to the smaller aspect ratio.

(*iii*) With two open holes, Sh for the first hole are similar to those for a single hole with a half duct height because the lower half duct flow can be considered to enter the first hole. At the second hole, the flow is similar to a sink flow because the duct flow loses axial momentum in the sudden expansion. Sh is little affected by the hole-to-hole spacing.

(*iv*) With three open holes, the flow at the first hole is similar to a curved duct flow (strong secondary flow) and the flow at the last hole is more like a sink flow. At the middle hole, the flow is a combination of these flows.

Inside the Hole

(*i*) The flow into a hole (for one open hole) can be thought of as the combination of flow along a 90 deg tube bend and a sink flow (sudden contraction). Sh around the circumference of the inside hole surface vary considerably due to the secondary/impingement flows. Sh near the trailing edge side of the hole entrance is about two times that on the leading edge side. However, Sh is quite uniform near the exit of the hole.

(*ii*) With three open holes, the average Sh inside the hole increases for downstream holes due to the smaller separation zones in the holes. In a comparison with two open holes, the mass transfer rates on the inner hole surfaces are expected to be the same, counting holes from the duct end, although the total number of open holes is different.

(*iii*) Although the local Sh is very nonuniform around the circumference of the hole, the circumferential average Sh inside the hole is only about 6 percent lower than that for open sink flow. This suggests that the average mass transfer rate in the hole for a sink flow can be used to approximate that for duct flow.

Acknowledgments

Support from the Air Force Office of Scientific Research and the Department of Energy AGTS program greatly aided the conduct of this study.

References

Acrivos, A., Babcock, B. D., and Pigford, R. L., 1959, "Flow Distributions in Manifolds," *Chemical Engineering Science*, Vol. 10, pp. 112–124.

Ambrose, D., Lawrenson, I. J., and Sparke, C. H. S., 1975, "The Vapor Pressure of Naphthalene," *J. Chem. Thermodynam.*, Vol. 7, pp. 1173–1176.

Byerley, A. R., Ireland, P. T., Jones, T. V., and Ashton, S. A., 1988, "Detailed Heat Transfer Measurements Near and Within the Entrance of a Film Cooling Hole," ASME Paper No. 88-GT-155.

Cho, H. H., 1992, "Heat/Mass Transfer Flow Through an Array of Holes and Slits," Ph.D. Thesis, University of Minnesota.

Cho, H. H., and Goldstein, R. J., 1995, "Heat (Mass) Transfer and Film Cooling Effectiveness With Injection Through Discrete Holes: Part I—Within Holes and on the Back Surface," ASME JOURNAL OF TURBOMACHINERY, Vol. 117, pp. 440–450.

Fried, E., and Idelchik, I. E., 1989, *Flow Resistance: A Design Guide for Engineers,* 2nd ed., Hemisphere Publishing Corp., pp. 248–251.

Goldstein, R. J., and Cho, H. H., 1995, "A Review of Mass Transfer Measurements Using Naphthalene Sublimation," *Experimental Thermal and Fluid Science,* Vol. 10, pp. 416–434.

Kline, S. J., and McClintock, F. A., 1953, "Describing Uncertainty in Single-Sample Experiments," *Mech. Engineering,* Vol. 75, Jan., pp. 3–8.

Metzger, D. E., and Cordaro, J. V., 1979, "Heat Transfer in Short Tubes Supplies From a Cross-Flowing Stream," ASME Paper No. 79-WA/HT-16.

Miller, D. S., 1990, *Internal Flow Systems: Design and Performance Prediction,* 2nd ed., Gulf Publishing Company, pp. 71–87; pp. 303–361.

Mills, A. F., 1962, "Experimental Investigation of Turbulent Heat Transfer in the Entrance Region of a Circular Conduit," *J. Mech. Eng. Sci.,* Vol. 4, pp. 63–77.

Sparrow, E. M., and Kermink, R. G., 1979, "Heat Transfer Downstream of a Fluid Withdrawal Branch in a Tube," ASME *Journal of Heat Transfer,* Vol. 101, pp. 23–28.

Wesley, D. A., and Sparrow, E. M., 1976, "Circumferentially Local and Average Turbulent Heat-Transfer Coefficients in a Tube Downstream of a Tee," *Int. J. Heat Mass Transfer,* Vol. 19, pp. 1205–1213.

Film Cooling From a Single Row of Holes Oriented in Spanwise/Normal Planes

P. M. Ligrani
Professor,
Department of Mechanical Engineering,
University of Utah,
Salt Lake City, UT 84112
Mem. ASME

A. E. Ramsey
Graduate Student,
Department of Mechanical Engineering,
Naval Postgraduate School,
Monterey, CA 93943

Experimental results are presented that describe the development and structure of flow downstream of a single row of film-cooling holes inclined at 30 deg from the test surface in spanwise/normal planes. With this configuration, holes are spaced 6d apart in the spanwise direction in a single row. Results are presented for a ratio of injectant density to free-stream density near 1.0, and injection blowing ratios from 0.5 to 1.5. Compared to results measured downstream of simple angle (streamwise) oriented holes, spanwise-averaged adiabatic effectiveness values are significantly higher for the same spanwise hole spacing, normalized streamwise location x/d, and blowing ratio m when m = 1.0 and 1.5 for x/d < 80. The injectant from the spanwise/normal holes is also less likely to lift off of the test surface than injectant from simple angle holes. This is because lateral components of momentum keep higher concentrations of injectant in closer proximity to the surface. As a result, local adiabatic effectiveness values show significantly greater spanwise variations and higher local maxima at locations immediately downstream of the holes. Spanwise-averaged iso-energetic Stanton number ratios range between 1.07 and 1.26, which are significantly higher than values measured downstream of two other injection configurations (one of which is simple angle, streamwise holes) when compared at the same x/d and blowing ratio.

Introduction

The present study is conducted as part of a larger comprehensive experimental test program (Ligrani et al., 1994a, b; Ligrani and Ramsey, 1997) to investigate the effects of different hole angle arrangements on film cooling performance. The influences of injection hole geometry are important since changes have direct effects on the most important factors that affect the protection provided by a cooling film. These are: (*i*) the locations of the film, particularly distributions of injectant concentrations in the boundary layer and coverage over the surface, and (*ii*) the ability to absorb and store thermal energy as indicated by temperature and/or enthalpy relative to the surface and surrounding hot gas.

Here, we focus on laterally injected film cooling from a single row of holes placed in *spanwise*/normal planes. A large spanwise hole spacing of $6d$ is employed, an arrangement important from several perspectives. First, the data obtained downstream of these holes provide important test cases for the development of prediction codes. Second, film cooling holes with $6d$ spacing allow understanding of film cooling phenomena, which are not apparent from configurations with more closely spaced holes. The relatively large hole spacing reduces coalescence and interactions between injectant fluid from adjacent holes, particularly at small x/d. Consequently, trajectories and diffusion of injectant from individual holes can be observed that provide insight into the behavior of injectant from individual holes.

Other investigations of film cooling from holes with compound angle orientations are described by Mayle and Camarata (1975), Gauntner (1977), Kim et al. (1978), Mehendale and Han (1992), Sen et al. (1996), and Schmidt et al. (1996). Of these, the last two are of particular interest to the present investigation because results are presented for the same $6d$ spanwise hole spacing. Sen et al. (1996) and Schmidt et al. (1996) compare adiabatic effectiveness and iso-energetic heat transfer coefficient ratio from three different hole arrangements, one simple angle, one compound angle, and one compound angle with diffusing expanded exit.

Work conducted with lateral injection from holes in *spanwise*/normal planes is described by Goldstein et al. (1970), Honami and Fukagawa (1987), Sathyamurthy and Patankar (1990), and Honami et al. (1994). Compared to streamwise injection from simple angle holes, measurements from Goldstein et al. (1970) indicate that lateral injection produces more effective cooling because the film is located closer to the wall. Honami and Fukagawa (1987) describe temperature profiles, velocity profiles, and turbulence intensity profiles produced by streamwise and lateral injection over flat and concave curved surfaces. Sathyamurthy and Patankar (1990) predict lateral film cooling from single rows of holes spaced $3d$, $4d$, and $5d$ apart. According to these investigators, laterally injected films show almost no change in tendency to lift-off as blowing changes from 0.1 to 1.0. Honami et al. (1994) present surface temperature distributions, and surveys of time-averaged velocity and temperature over flow cross sections downstream of a row of lateral holes with $5d$ spanwise spacing. A large-scale asymmetric vortex is described on one side of the film distribution, which becomes more asymmetric as the blowing ratio increases.

The present study provides a more comprehensive look at lateral injection. This is accomplished by comparing results from the lateral configuration to data from a different compound angle arrangement and to data from a simple angle (or streamwise hole) arrangement. These comparisons are made as spanwise hole spacing, normalized streamwise location, and blowing ratio are held constant. In addition, adiabatic film effectiveness variations are related to surveys over flow cross sections of mean streamwise velocity and injectant distributions.

Experimental Apparatus and Procedures

Wind Tunnel and Coordinate System. The open-circuit, subsonic wind tunnel is the same one used in the experiments of Ligrani et al. (1994a, b) and Ligrani and Ramsey (1997).

Contributed by the Heat Transfer Committee for publication in the JOURNAL OF TURBOMACHINERY. Manuscript received by the Heat Transfer Committee October 1, 1996. Associate Technical Editor: M. G. Dunn.

For the present investigation, the free-stream velocity is constant at 10 m/s and the free-stream turbulence intensity is approximately 0.13 percent based on the same velocity. The boundary layer is tripped using a 2-mm-high spanwise uniform strip of tape near the nozzle exit 1.072 m upstream of the constant heat flux transfer surface.

With the present coordinate system, Z is the spanwise coordinate measured from the test section spanwise centerline, X is measured from the upstream edge of the boundary layer trip, and Y is measured normal to the test surface. x is measured from the downstream edge of the injection holes and generally presented as x/d, as shown in Fig. 1. The total boundary layer thickness just downstream of the injection holes ($x/d = 2.75$) is 0.973 cm giving a thickness to hole diameter ratio of 1.05 (measured with no film cooling). The ratios of momentum thickness to hole diameter and displacement thickness to hole diameter at this location are then 0.140 and 0.230, respectively. At the upstream edges of the injection holes, these three parameters are estimated to be 1.02, 0.136, and 0.224, respectively.

Injection System. The injection system is described by Ramsey (1992) and by Ligrani et al. (1994a). The system provides the capability to produce heated injectant at blowing ratios from 0.5 to 4.0. With this system and test plate heating, the nondimensional injection temperature parameter Θ is maintained at values ranging from 0.0 to 3.0, which includes values within the range of gas turbine component operation. The ratio of injectant to free-stream density ρ_c/ρ_∞ is from 0.94 to 1.00. Each injection tube is about 7.6 cm long, giving a length-to-diameter ratio of about 8. The data produced with these film cooling, boundary layer, and free-stream flow characteristics are valuable because they provide a base set for CFD code calibration.

Stanton Number Measurements. The heat transfer surface is also described by Ramsey (1992) and by Ligrani et al. (1994a). It provides a constant heat flux over its area. Surface temperatures are measured using 126 thermocouples after their outputs are corrected for contact resistance and conduction through a sheet of foil located next to the air stream. An Electrofilm Corp. etched foil heater rated at 120 volts and 1500 watts powers the test surface. With this arrangement, an unheated starting length exists when the heat transfer surface is at elevated temperature, and the direction of heat transfer is from the wall to the gas. To determine the heat loss by conduction, an energy balance is performed. Radiation losses from the top of the test surface are analytically estimated. Corrections to account for streamwise and spanwise conduction along the test surface are employed using procedures developed and described by Wigle (1991). Rows of thermocouples are located x/d of 6.81, 17.62, 33.83, 55.46, 77.08, and 98.70. Corresponding X are $1.22m$, $1.222m$, $1.372m$, $1.572m$, $1.772m$, and $1.972m$, respectively.

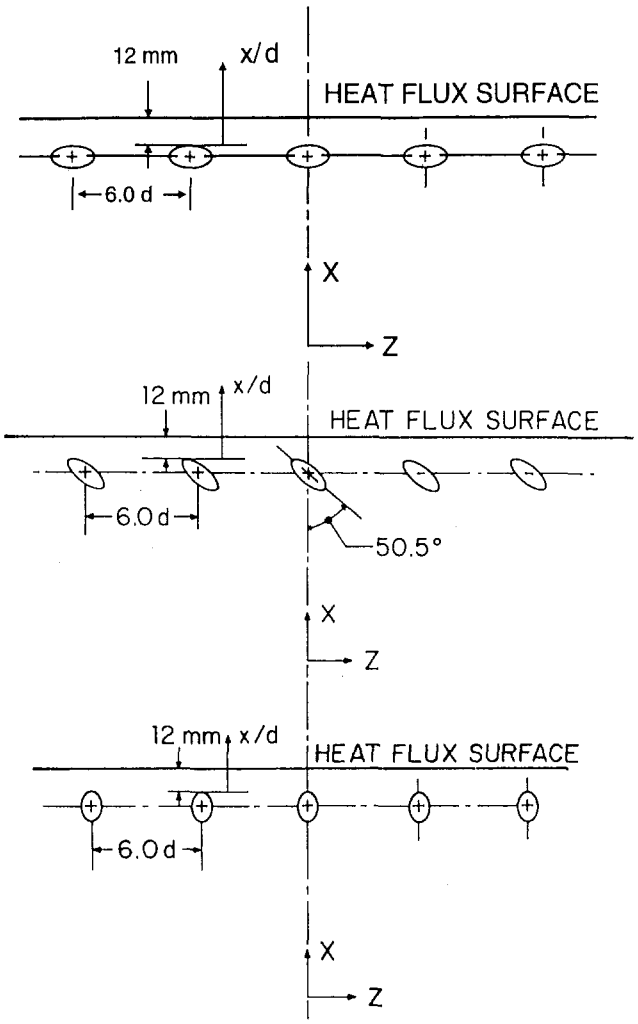

Fig. 1 Test surface geometry for: (*a*) configuration 4 (spanwise/normal plane) holes, (*b*) configuration 3 (compound angle) holes, and (*c*) configuration 2 (simple angle) holes

Mean Temperature Measurements. Copper-constantan thermocouples are used to measure temperatures along the surface of the test plate, the free-stream temperature, as well as temperature distributions correlated to injection distributions. For the distributions, a thermocouple is traversed over 10.2 cm by 20.3 cm spanwise/normal planes using the automated two-dimensional traversing system, which may be placed at different

Nomenclature

C_p = specific heat
d = injection hole diameter
h_0 = heat transfer coefficient with no film injection
h_f = iso-energetic heat transfer coefficient with film injection for $T_{r,c} = T_{r,\infty}$
m = blowing ratio = $\rho_c U_c/\rho_\infty U_\infty$
St_0 = baseline Stanton number, no film injection = $h_0/\rho_\infty U_\infty C_p$
St_f = iso-energetic Stanton number with film injection = $h_f/\rho_\infty U_\infty C_p$
T = temperature
U = mean (time-averaged) streamwise velocity
X, x = streamwise distance
Y = distance normal to the surface
Z = spanwise distance from test surface centerline
α = injection hole angle of orientation
η = adiabatic film cooling effectiveness = $(T_{aw} - T_{r,\infty})/(T_{r,c} - T_{r,\infty})$
θ = injection hole angle of inclination
Θ = nondimensional injection temperature parameter = $(T_{r,c} - T_{r,\infty})/(T_w - T_{r,\infty})$
ρ = density

Subscripts

$_{aw}$ = adiabatic wall
$_c$ = injectant at exits of injection holes
$_0$ = stagnation condition or baseline data
$_r$ = recovery condition
$_\infty$ = free-stream

Superscripts

$\overline{\ }$ = spanwise average

streamwise locations. For each survey, 800 probe locations spaced 0.51 cm apart in each direction are employed at locations as close as 2.0 mm from the test surface. The contours in Figs. 3, 5, and 6 produced by these surveys are more closely spaced than 0.51 cm because the DeltaGraph plotting routine employed places user-specified contour lines at interpolated locations between data points.

The recovery coolant temperature $T_{r,c}$ is given for the exit planes of the film holes. This is accomplished by measuring the plenum total temperature and ambient temperature. $T_{r,c}$ is then deduced using a correlation that accounts for these temperatures and the blowing ratio. The correlation was developed from calibration tests conducted using thermocouple probes placed to simultaneously measure: (*i*) the coolant temperature at the centerline of the exit plane of a single hole, (*ii*) the ambient temperature, and (*iii*) the plenum total temperature (Ramsey, 1992).

Voltages from thermocouples are digitally sampled and read using a Hewlett-Packard 3497A Data Acquisition Control Unit with a 3498A Extender. These units are controlled by a Hewlett-Packard Series 9000 Model 310 computer.

Adiabatic Film Cooling Effectiveness and Iso-energetic Stanton Number Ratio Measurements. Adiabatic film cooling effectiveness values and iso-energetic Stanton number ratios are determined using linear superposition theory applied to Stanton number ratios measured at different injection temperatures. Additional details of this approach are described by Ligrani et al. (1994a), including a test to check the procedure using a direct η measurement with a near-adiabatic condition on the test plate. η differences from the two techniques were always less than experimental uncertainties, ranging from 7 to 15 percent (Ligrani et al., 1994a).

Baseline Data Checks. Repeated measurements of spanwise-averaged Stanton numbers show good agreement (maximum deviation is 4 percent) with the appropriate correlation for turbulent heat transfer to a flat plate with unheated starting length and constant heat flux boundary condition. Ramsey (1992) provides additional details.

Experimental Uncertainties. Uncertainty estimates are based upon 95 percent confidence levels, and determined following procedures described by Kline and McClintock (1953) and Moffat (1982). Typical nominal values of free-stream recovery temperature and wall temperature are 18.0°C and 40.0°C, with respective uncertainties of 0.13°C and 0.21°C. The free-stream density, free-stream velocity, and specific heat uncertainties are, respectively, 0.009 kg/m^3 (1.23 kg/m^3), 0.15 m/s (10.0 m/s), and 1 J/kgK (1006 J/kgK), where typical nominal values are given in parentheses. For convective heat transfer, heat transfer coefficient, and heat transfer area, 10.5 W (270 W), 1.03 W/m^2 K (24.2 W/m^{2}K), and 0.0065 m^2 (0.558 m^2) are typical uncertainties. The uncertainties of St, St/St$_0$, m, and x/d are 0.000086 (0.00196), 0.058 (1.05), 0.025 (0.50), and 0.36 (41.9). Uncertainties of $\overline{\eta}$ and St$_f$/St$_0$ are dependent upon the linear superposition technique employed. The uncertainty of St$_f$/St$_0$ is the same as for St/St$_0$. For St$_f$/St$_0$ = 1.10, the uncertainty of this parameter amounts to 5.5 percent. The uncertainty of $\overline{\eta}$ varies between 0.02 and 0.04 effectiveness units where higher values in this range apply when $\overline{\eta}$ is less than about 0.15. At $\overline{\eta}$.= 0.30, this uncertainty corresponds to 6.7 percent of the best estimate of $\overline{\eta}$.

Injection Configurations

A total of four different film hole configurations are investigated in the overall test program (cf. Ligrani et al., 1994a, b). The experiments are designed so that all experimental parameters are maintained constant as the configurations are tested so that differences due to injection hole orientation are directly apparent. In the portion of the program reported in this paper, comparisons are made between the spanwise/normal plane holes (configuration 4) and streamwise/normal plane holes (simple angle configuration 2). Comparisons are also made between the spanwise/normal holes and another compound angle hole arrangement (configuration 3). In all cases, a single row of holes is used and spanwise hole spacing is maintained constant at 6*d*. Thus, the present series of tests are designed to compare the performances of three injection hole configurations, and to determine which orientation produces the highest effectiveness values.

Figure 1(*a*) shows a schematic of the film hole geometry for the spanwise/normal plane holes denoted configuration 4. Here, the hole arrangement along the test surface (*X*–*Z* plane) is seen in the negative *Y* direction. Holes are placed in a single row so that the centerline of the middle hole is located on the spanwise centerline (*Z* = 0.0 cm) of the test surface. Nominal hole diameter *d* is 0.925 cm. Geometries for configurations 3 and 2 are shown in Figs. 1(*b*) and 1(*c*), respectively. Nominal hole diameters for these two configurations are 0.945 cm and 0.925 cm, respectively. The reader is referred to Ligrani et al. (1994a, b) for additional data and discussion of the film cooling downstream of configurations 2 and 3.

The orientations of holes for configuration 4 as well as for configurations 2 and 3 (with which results are compared) are described in terms of the angle of orientation α and the angle of inclination θ. α is the angle between the *X*–*Y* (streamwise-normal) plane and the plane made by the hole axis and *Y* coordinate. The angle of inclination θ is the angle between the hole axis and the test surface or *X*–*Z* (streamwise-spanwise) plane. For configuration 4 holes, α = 90 deg, θ = 30 deg. For configuration 3 holes, α = 50.5 deg, θ = 24 deg. For configuration 2 holes, α = 0 deg, θ = 35 deg.

Local Adiabatic Effectiveness and Injectant Distributions

Effects of Blowing Ratio on Local Adiabatic Film Cooling Effectiveness and Injectant Distributions, Configuration 4. Results showing the effects of blowing ratio on local adiabatic film effectiveness and injectant distributions are presented in Figs. 2 and 3, respectively. Here, effectiveness results are determined from measurements at x/d = 6.8, whereas the injectant

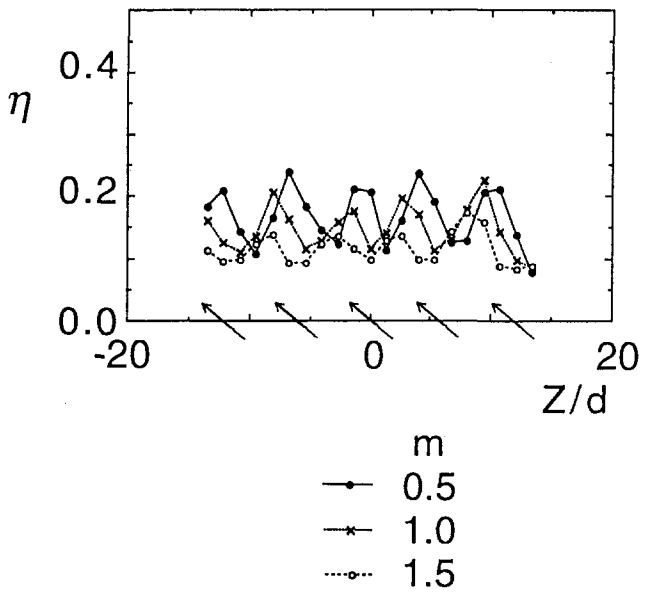

Fig. 2 Spanwise variations of adiabatic film cooling effectiveness downstream of configuration 4 holes at x/d = 6.8. Spanwise locations of holes are denoted by arrows along the abscissa.

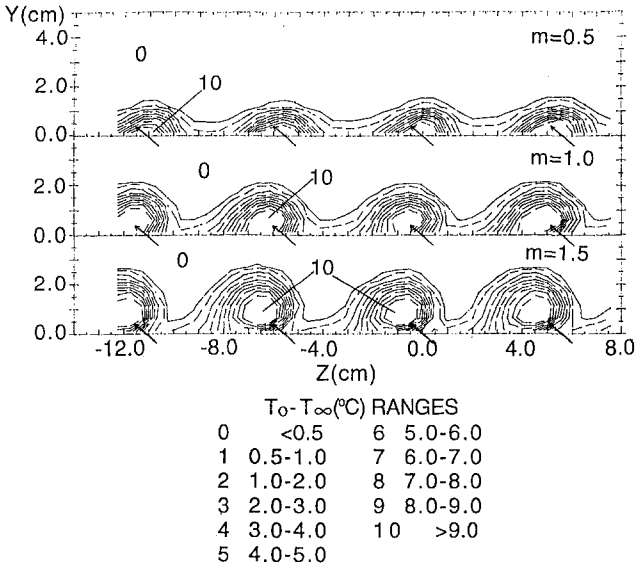

Fig. 3 Mean temperature fields showing distributions of film injectant downstream of configuration 4 holes at x/d = 7.4. Spanwise locations of holes are denoted by arrows along the abscissa.

surveys are given for $x/d = 7.4$. Data are presented for blowing ratios of 0.5, 1.0, and 1.5, which are equivalent to respective momentum flux ratios of about 0.25, 1.0, and 2.25. The injectant distributions are obtained using procedures described by Ligrani et al. (1994a, b) in which the injectant is heated without providing any heat to the test plate. With this approach, the temperature field is used to quantify injectant distributions in spanwise/normal planes.

The most important feature of the η distributions in Fig. 2 are the spanwise variations, which are significant for all three blowing ratios. When compared to other streamwise locations (Ramsey, 1992), the spanwise variations of η are more pronounced at smaller x/d of 6.8 and 17.6. This is because of accumulations of injectant such as the ones shown for x/d = 7.4 in Fig. 3, and because injectant accumulations at x/d of 43.8 and 85.6 are more diffuse and dissipated (Ramsey, 1992). The highest local η maxima in Fig. 2 exist at the lowest blowing ratio because jet lift-off is more pronounced as m increases. These local maxima shift to smaller Z/d as m increases because of injectant momentum, which causes injectant to become more aligned with hole axes and to move in the negative spanwise direction as it is advected downstream. The only exception occurs for $Z/d > 10$, where all three distributions decrease because they are measured at locations slightly away from the spanwise edge of the injectant. At $Z/d < 10$, the spanwise periodicity of the η distributions decreases with blowing ratio such that higher η values correspond to locations where more injectant is present near the test surface, and lower values correspond to locations where the injectant coverage is sparser. Such injectant variations are, of course, largely affected by injectant lift-off.

Additional explanation of the trends seen in Fig. 2 is obtained from Fig. 3. For each m, injectant distributions in this figure are also periodic and repeatable in the spanwise direction such that different concentrations show similar qualitative and quantitative characteristics. For m = 0.5, injectant accumulations are most significant just downstream of the centerlines of the injection holes ($Z = -11.1$ cm, -5.6 cm, 0.0 cm, 5.6 cm). For m = 1.0 and 1.5, injectant accumulations at x/d = 7.4 are most significant just to the left of the centerlines of the injection holes (i.e., at smaller Z). The results for m = 0.5 are thus different from the ones at the two higher blowing ratios because injectant is advected away from the injection holes a smaller distance in the spanwise direction. This spanwise shift with streamwise convection is consistent with the results in Fig. 2.

As the blowing ratio increases from 0.5 to 1.0 and 1.5, Fig. 3 also shows the oval-shaped injectant concentrations to be located farther and farther away from the immediate vicinity of the test surface. Such lift-off behavior is consistent with results in Fig. 2 since local η maxima decrease in magnitude as the blowing ratio increases thus decreasing average and local protection.

Comparison of Local Adiabatic Film Cooling Effectiveness Distributions and Injectant Distributions From Configurations 2, 3, and 4. Local adiabatic effectiveness distributions for x/d = 6.7–6.8 from configurations 2, 3, and 4 are presented and compared in Fig. 4 for m of 0.5, 1.0, and 1.5. Surveys of injectant distributions from configurations 2, 3, and 4 at x/d = 7.4–9.9 are compared in Figs. 5 and 6 for m of 0.5 and 1.5, respectively.

For all three blowing ratios, Fig. 4 shows η values for compound angle configuration 3 that are higher with greater variations across the span than the ones for configuration 4. η values for configuration 4 are then higher with significantly greater spanwise variations than the ones for simple angle configuration 2. These differences in magnitude and spanwise periodicity become larger as the blowing ratio increases to 1.5. η local maxima

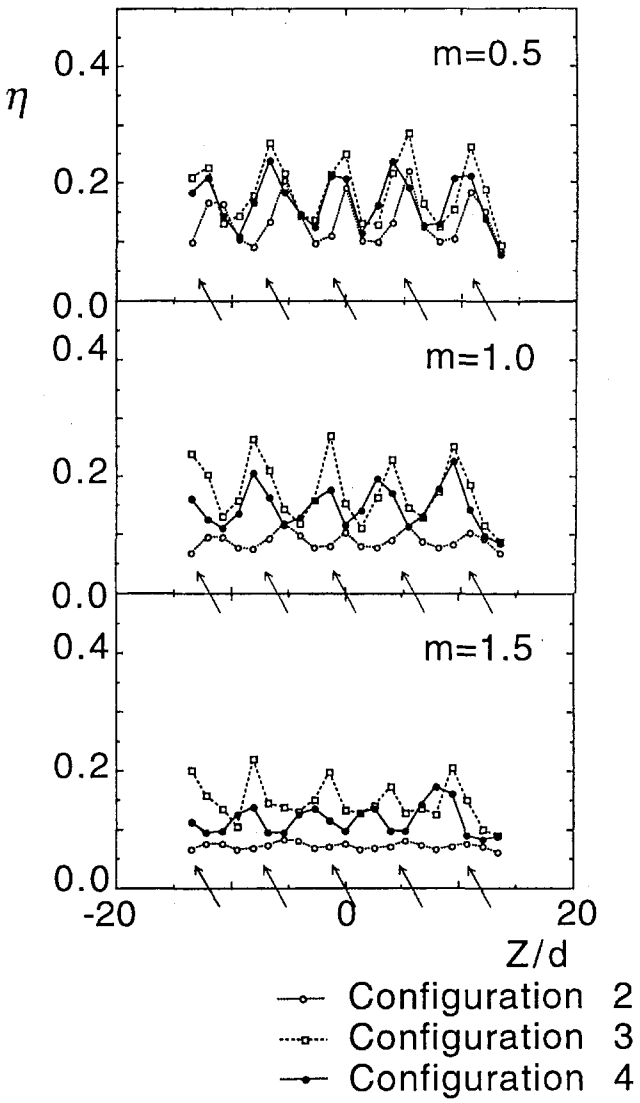

Fig. 4 Comparison of spanwise variations of adiabatic film cooling effectiveness downstream of configurations 2, 3, and 4 at x/d = 6.7–6.8. Spanwise locations of holes are denoted by arrows along the abscissa.

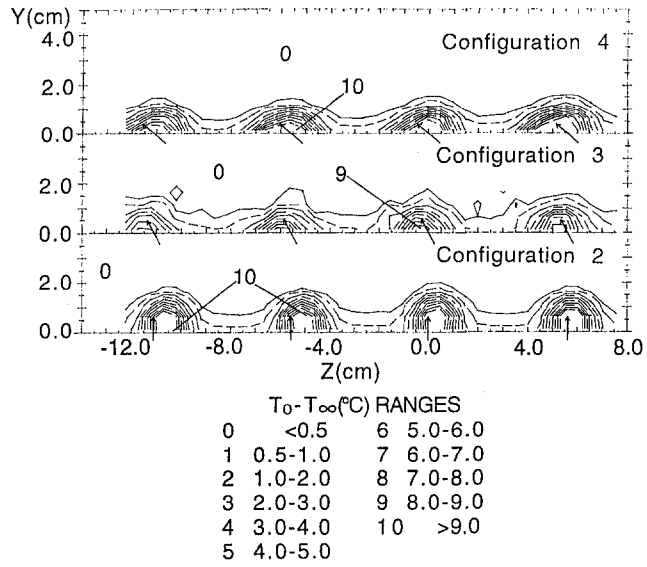

Fig. 5 Comparison of mean temperature fields showing distributions of film injectant downstream of configuration 2 at x/d = 9.4, configuration 3 at x/d = 9.9, and configuration 4 at x/d = 7.4 for m = 0.5. Spanwise locations of holes are denoted by arrows along the abscissa.

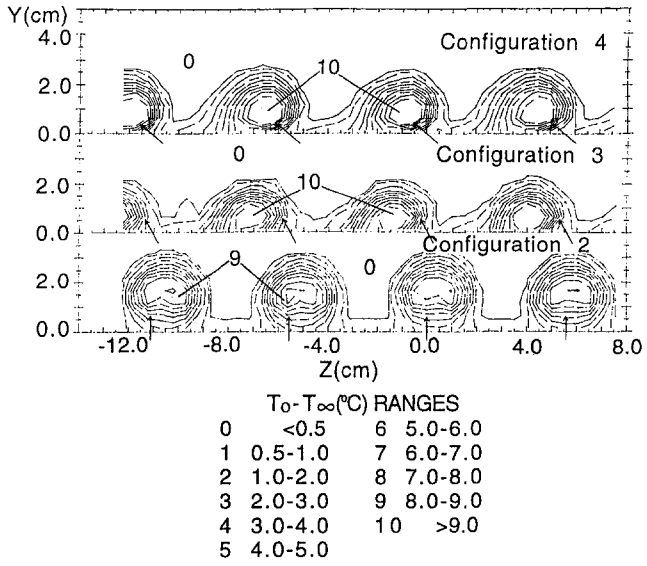

Fig. 6 Comparison of mean temperature fields showing distributions of film injectant downstream of configuration 2 at x/d = 9.4, configuration 3 at x/d = 9.9, and configuration 4 at x/d = 7.4 for m = 1.5. Spanwise locations of holes are denoted by arrows along the abscissa.

are highest at the lowest blowing ratio 0.5 as more injectant is present near the test surface. As the blowing ratio increases, momentum flux ratio also increases, which generally causes injectant to lift off of the wall at spanwise intervals resulting in local η decreases and overall lower η across the test section span. Examination of Fig. 4 indicates this effect to be most severe for configuration 2, followed by configuration 4 and then configuration 3. In particular, the m = 1.5 effectiveness distribution for configuration 2 is spanwise uniform compared to distributions from configurations 3 and 4, which still produce spanwise varying local injectant concentrations near the surface, and repeated η local maxima at different Z/d. More of the injectant from configurations 3 and 4 remains in close proximity to the wall downstream of individual compound angle holes. Consequently, the wall is exposed to a wider range of temperatures (and overall temperature levels, which give improved protection) across the span of the test surface. For simple angle holes, Fig. 6 for m = 1.5 shows that the largest concentrations of injectant barely touch the surface, which results in a nearly constant distribution of η with Z/d.

Also evident from Fig. 4 is the fact that amplitudes of η local maxima generally decrease with blowing ratio. The largest change for configurations 3 and 4 occur as m increases from 1.0 to 1.5 (momentum flux ratio increases from 1.0 to 2.25), and for configuration 2, as blowing ratio increases from 0.5 to 1.0 (momentum flux ratio increases from 0.25 to 1.0) This provides evidence of significantly different lift-off dependence on momentum flux ratio. Lift-off is most likely with configuration 2 (streamwise/normal plane holes), followed by configuration 4 (spanwise/normal plane holes) and then configuration 3 (compound angle holes).

The η distributions in Fig. 4 for configurations 3 and 4 should be ignored for $Z/d > 10$ because these locations lie away from the regions of injectant coverage along the test surface.

Injectant distributions from configurations 2, 3, and 4 are compared in Figs. 5 and 6 for the same spanwise hole spacing ($6.0d$), approximate streamwise location (x/d = 7.4–9.9), and blowing ratio (m = 0.5 and 1.5, respectively). Individual accumulations in Fig. 5 from the three configurations for m = 0.5 are different in shape but show significant quantitative and qualitative *similarities*. In all three cases, injectant concentrations are located at the wall at spanwise periodic intervals, which correspond to adiabatic effectiveness local maxima in the top portion of Fig. 4. There, slightly higher η peaks downstream of configuration 3 coincide with slightly greater concentrations of configuration 3 injectant near the wall in Fig. 5.

Figure 6 shows that the injectant distributions from configurations 2, 3, and 4 at x/d = 7.4–9.9 become significantly different in shape and location when the blowing ratio reaches 1.5. Different lift-off characteristics are evident that coincide well with the m = 1.5 variations of effectiveness with Z/d in the bottom portion of Fig. 4. Spanwise velocity components at the exits of the configurations 3 and 4 holes initially cause the emerging injectant to be advected in the spanwise direction and then swept along the test surface by boundary layer and mainstream flows just downstream. In many cases, this sweeping action then keeps injectant concentrations closer to the test surface. Local η maxima such as the ones in Fig. 4 then vary accordingly.

Spanwise-Averaged Adiabatic Film Cooling Effectiveness Values and Stanton Number Ratios

Effects of Hole Orientation (Compound Angle Configuration 4 and Simple Angle Configuration 2) With Constant Spanwise Hole Spacing. Referring first to configuration 4 data in Fig. 7, $\bar{\eta}$ generally decreases with x/d for each blowing ratio as injectant is diffused and advected downstream. For $x/d < 10$, $\bar{\eta}$ values decrease with blowing ratio as less injectant is in close proximity to the test surface (also see Figs. 2 and 3). This effect becomes particularly severe as the blowing ratio increases from 1.0 to 1.5 because the injectant momentum lifts the most protective accumulations away from the surface. As this happens, free-stream and boundary layer fluids accumulate between the film and the surface. The net results are diminished insulating characteristics and diminished thermal protection from the film.

Figure 7 also shows that the highest $\bar{\eta}$ from configuration 4 at all $x/d > 30$ occur at m = 1.0. Minimal lift-off is believed to occur at m = 0.5 and at m = 1.0 (Figs. 2 and 3). Consequently, $\bar{\eta}$ values for these two blowing ratios depend mostly on the amounts of film issued from the holes (rather than skewing, coalescence, or lift-off). This results in higher $\bar{\eta}$ at the higher blowing ratio, particularly at the downstream end of the test section. $\bar{\eta}$ are lower at m = 1.5 at all x/d because of lift-off.

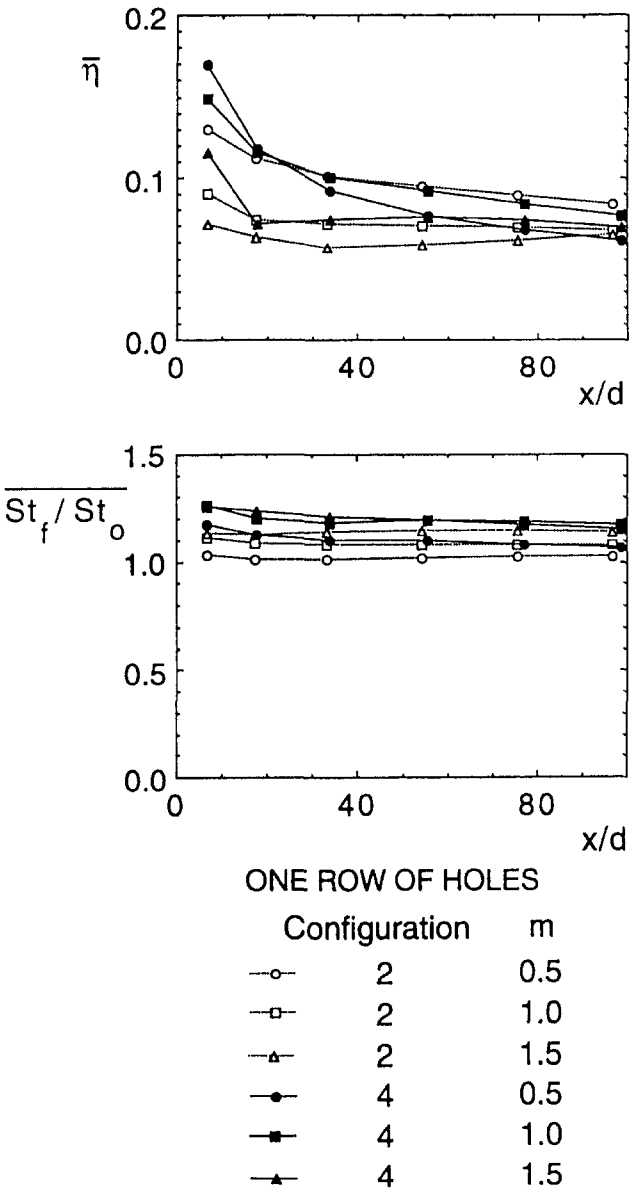

Fig. 7 Spanwise-averaged adiabatic film cooling effectiveness and iso-energetic Stanton number ratio versus normalized streamwise distance downstream of configuration 4 holes. Results are compared to ones measured downstream of simple angle configuration 2 holes.

The $\overline{\eta}$ data measured downstream of the configuration 2 simple angle holes in Fig. 7 show trends with some similarities and some differences compared to the ones from the configuration 4 holes. Like the configuration 4 results, the ones from configuration 2 generally decrease with x/d for each blowing ratio. In contrast to data from configuration 4, $\overline{\eta}$ from configuration 2 decrease with blowing ratio at individual x/d for all m and x/d tested.

From additional comparisons of effectiveness values from configurations 2 and 4 in Fig. 7, it is evident that the simple angle data lie below the spanwise ejected data for $x/d < 80$ except when $m = 0.5$. Thus, at m of 1.0 and 1.5, configuration 4 provides significantly improved protection for the same spanwise hole spacing, x/d, and blowing ratio m. The differences for $m = 1.0$ and 1.5 result mostly because the injectant from configuration 4 is less likely to lift off of the test surface than the injectant from the simple angle holes. The lateral component of momentum of the injectant from the compound angle holes causes the injectant to spread out much more in the lateral direction as it is advected downstream, which keeps it in closer proximity to the surface. Some influence is also exerted by the ratio of hole diameter to the *gap* between the holes. For $m = 0.5$, simple angle $\overline{\eta}$ data in Fig. 7 are higher for $x/d > 25$ because injectant is concentrated in close proximity to the surface, a result illustrated by Fig. 5. At $x/d > 80$, $\overline{\eta}$ values from configuration 4 generally cover about the same range as the simple angle data for all three m. This is evident from examination of data at individual blowing ratios. It is believed to occur because roughly equivalent amounts of injectant from each of the two configurations are present near the wall at the downstream portion of the test surface.

Spanwise-averaged iso-energetic Stanton number ratios in Fig. 7 for configurations 2 and 4 show several interesting trends. First, little $\overline{St_f/St_0}$ variation with x/d is evident for each value of m. Second, $\overline{St_f/St_0}$ values generally increase with m for each x/d. Exceptions occur with configuration 4 as m increases from 1.0 to 1.5 since these data have similar magnitudes. Configuration 4 data are also somewhat higher than the simple angle data, especially when the two sets of results are compared at the same blowing ratio.

Effects of Hole Orientation (Compound Angle Configurations 3 and 4) With Constant Spanwise Hole Spacing. The configuration 3 $\overline{\eta}$ data in Fig. 8 generally decrease with x/d for each blowing ratio. For each x/d less than 10, $\overline{\eta}$ values decrease with blowing ratio as increasing amounts of injectant are located farther from the test surface (Ligrani et al., 1994b). Spanwise-averaged configuration 3 effectiveness data for $m = 1.0$ are in close proximity to the $m = 0.5$ data at $x/d = 6.8$ and 17.6 because of minimal lift-off at both blowing ratios. This is evident from Fig. 4 where spanwise variations of η at $x/d = 6.8$ from these two blowing ratios are quite similar (also see Ligrani et al., 1994b). At larger x/d from 33.8 to 98.7, $\overline{\eta}$ distributions for configuration 3 in Fig. 8 are affected by spanwise convection and injectant diffusion, which cause it to spread laterally as it is advected downstream. Spanwise-averaged effectiveness from Schmidt et al. (1996) for a similar (but not matching) hole geometry at $m = 0.6$ and $x/d = 6$–15 show similar trends and slightly lower magnitudes compared to the configuration 3 $m = 0.5$ results. At $m = 1.25$, their results have magnitudes similar to ones for $m = 1.5$ in Fig. 8, but a different trend since they increase somewhat as x/d changes from 6 to 15.

The spanwise-averaged effectiveness values for configurations 3 and 4 in Fig. 8 generally cover about the same range of values. Results from the two configurations for $m = 1.5$ in particular are qualitatively similar. However, at blowing ratios of 0.5 and 1.0, configurations 3 and 4 show important differences as x/d increases from 17.6 to 33.8 since configuration 3 shows a larger decrease with x/d. Some convection of configuration 3 injectant away from the surface is responsible. However, significant lift-off is not occurring because configuration 3 results such as the ones in Fig. 6 for $m = 1.5$ indicate that the most important injectant accumulations remain in close proximity to the surface.

Spanwise-averaged iso-energetic Stanton number ratios in Fig. 8 for configurations 3 and 4 are consistent with results presented in Fig. 7. The most interesting feature is that configuration 4 values are higher than those produced by configuration 3 when compared at the same m and x/d.

Summary and Conclusions

Experimental results are presented that describe the development and structure of flow downstream of a single row of film-cooling holes oriented in spanwise/normal planes (denoted configuration 4). Holes are spaced 6d apart in the spanwise direction, and inclined at 30 deg with respect to the test surface.

A comparison of spanwise-averaged adiabatic effectiveness values measured downstream of injection hole configurations 2

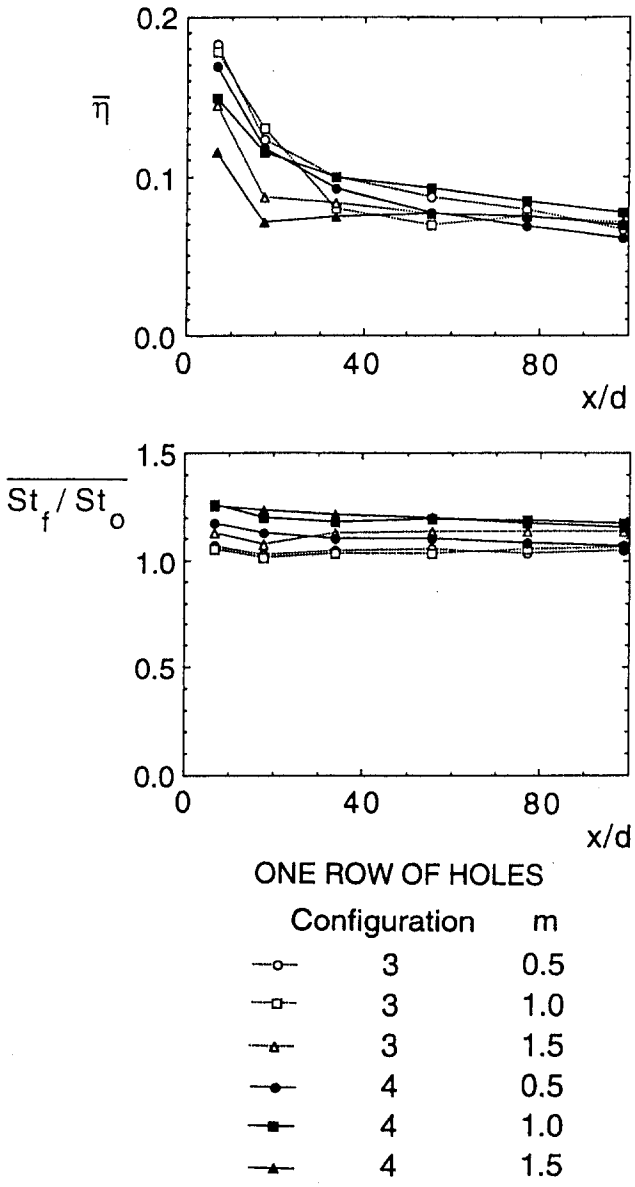

Fig. 8 Spanwise-averaged adiabatic film cooling effectiveness and iso-energetic Stanton number ratio versus normalized streamwise distance downstream of configuration 4 holes. Results are compared to ones measured downstream of compound angle configuration 3 holes.

and 4 shows that configuration 4 provides significantly improved protection compared to simple angle configuration 2 for the same spanwise hole spacing, x/d, and m when $m = 1.0$ and $m = 1.5$ for $x/d < 80$. These differences result mostly because the injectant from configuration 4 is less likely to lift off of the test surface than the injectant from the simple angle holes. Local adiabatic effectiveness values downstream of the configuration 4 holes, especially for $x/d = 6.7 - 6.8$, show significantly greater spanwise variations, and thus, significantly more local protection at locations immediately downstream of the holes than configuration 2. The simple angle $\bar{\eta}$ data for $m = 0.5$ are higher than configuration 4 data for $x/d > 25$ because more injectant is concentrated in close proximity to the surface.

Although small differences are evident at different m and x/d, spanwise-averaged effectiveness values from compound angle configuration 3 and from configuration 4 generally cover about the same range of values when compared at the same m and x/d.

Spanwise-averaged iso-energetic Stanton number ratios range between 1.07 and 1.26. Data measured downstream of compound angle configuration 4 are significantly higher than values measured downstream of configurations 2, and 3 (when compared at the same blowing ratio) for all three blowing ratios investigated.

Acknowledgments

This study was supported by: (1) the Naval Sea Systems Command, Job Order Numbers N622711-RGPLG and N622712-RTBPL (Dr. Dan Groghan and Dr. Sam Shepard were program monitors), and (2) the Aero-Propulsion Laboratory of Wright Patterson Air Force Base, MIPR Numbers FY 1455-89-N0670 and FY 1455-92-N0641 (Dr. Bill Troha was program monitor). A number of helpful discussions on this work with Mr. Dave Keucher are also acknowledged.

References

Gauntner, J. W., 1977, "Effects of Film Injection Angle on Turbine Vane Cooling," NASA TP-1095, NASA Technical Paper 1095.

Goldstein, R. J., Eckert, E. R. G., Eriksen, V. L., and Ramsey, J. W., 1970, "Film Cooling Following Injection Through Inclined Circular Tubes," *Israel Journal of Technology,* Vol. 8, pp. 145–154.

Honami, S., and Fukagawa, M., 1987, "A Study on Film Cooling Behavior of a Cooling Jet Over a Concave Surface," Paper No. 87-Tokyo IGTC-72; *Proc. 1987 Tokyo International Gas Turbine Congress,* Vol. 3, pp. 209–216.

Honami, S., Shizawa, T., and Uchiyama, A., 1994, "Behavior of the Laterally Injected Jet in Film Cooling: Measurements of Surface Temperature and Velocity/Temperature Field Within the Jet," ASME JOURNAL OF TURBOMACHINERY, Vol. 116, pp. 106–112.

Kim, H. K., Moffat, R. J., and Kays, W. M., 1978, "Heat Transfer to a Full-Coverage, Film-Cooled Surface With Compound-Angle (30° and 45°) Hole Injection," Report HMT-28, Thermosciences Division, Department of Mechanical Engineering, Stanford University, Stanford, CA.

Kline, S. J., and McClintock, F. A., 1953, "Describing Uncertainties in Single-Sample Experiments," *Mechanical Engineering,* Jan., pp. 3–8.

Ligrani, P. M., Wigle, J. M., Ciriello, S., and Jackson, S. W., 1994a, "Film-Cooling From Holes With Compound Angle Orientations: Part 1—Results Downstream of Two Staggered Rows of Holes With 3*d* Spanwise Spacing," ASME *Journal of Heat Transfer,* Vol. 116, pp. 341–352.

Ligrani, P. M., Wigle, J. M., and Jackson, S. W., 1994b, "Film-Cooling From Holes With Compound Angle Orientations: Part 2—Results Downstream of a Single Row of Holes With 6*d* Spanwise Spacing," ASME *Journal of Heat Transfer,* Vol. 116, pp. 353–362.

Ligrani, P. M., and Ramsey, A. E., 1997, "Film Cooling From Spanwise-Oriented Holes in Two Staggered Rows," ASME JOURNAL OF TURBOMACHINERY, Vol. 119, pp. 562–567.

Mayle, R. E., and Camarata, F. J., 1975, "Multihole Cooling Film Effectiveness and Heat Transfer," ASME *Journal of Heat Transfer,* Vol. 97, pp. 534–538.

Mehendale, A. B., and Han, J. C., 1992, "Influence of High Mainstream Turbulence on Leading Edge Film Cooling Heat Transfer," ASME JOURNAL OF TURBOMACHINERY, Vol. 114, pp. 707–715.

Moffat, R. J., 1982, "Contributions to the Theory of Single-Sample Uncertainty Analysis," ASME *Journal of Fluids Engineering,* Vol. 104, pp. 250–260.

Ramsey, A. E., 1992, "A Study of Film Cooling Downstream of One and Two Rows of Holes Oriented in Spanwise/Normal Planes," M. S. Thesis, Department of Mechanical Engineering, Naval Postgraduate School, Monterey, CA.

Sathyamurthy, P., and Patankar, S. V., 1990, "Prediction of Film Cooling With Lateral Injection," ASME HTD-Vol. 138, *Heat Transfer in Turbulent Flows,* pp. 61–70.

Schmidt, D. L., Sen, B., Bogard, D. G., 1996, "Film Cooling With Compound Angle Holes: Adiabatic Effectiveness," ASME JOURNAL OF TURBOMACHINERY, Vol. 118, pp. 807–813.

Sen B., Schmidt D. L., and Bogard D. G., 1996, "Film Cooling With Compound Angle Holes: Heat Transfer," ASME JOURNAL OF TURBOMACHINERY, Vol. 118, pp. 800–806.

Subramanian, C. S., Ligrani, P. M., Green, J. G., Doner, W. D., and Kaisuwan, P., 1992, "Development and Structure of a Film-Cooling Jet in a Turbulent Boundary Layer With Heat Transfer," *Rotating Machinery Transport Phenomena. Proc. Third International Symposium on Transport Phenomena and Dynamics of Rotating Machinery (ISROMAC-3),* J. H. Kim and W.-J. Yang, eds., Hemisphere Publishing Corp., pp. 53–68.

Wigle, J. M., 1991, "Heat Transfer, Adiabatic Effectiveness and Injectant Distributions Downstream of Single and Double Rows of Film-Cooling Holes With Compound Angles," M.S. Thesis, Department of Mechanical Engineering, Naval Postgraduate School, Monterey, CA.

A Systematic Computational Methodology Applied to a Three-Dimensional Film-Cooling Flowfield

D. K. Walters

J. H. Leylek

Department of Mechanical Engineering,
Clemson University,
Clemson, SC 29632

Numerical results are presented for a three-dimensional discrete-jet in crossflow problem typical of a realistic film-cooling application in gas turbines. Key aspects of the study include: (1) application of a systematic computational methodology that stresses accurate computational model of the physical problem, including simultaneous, fully elliptic solution of the crossflow, film-hole, and plenum regions; high-quality three-dimensional unstructured grid generation techniques, which have yet to be documented for this class of problems; the use of a high-order discretization scheme to reduce numerical errors significantly; and effective turbulence modeling; (2) a three-way comparison of results to both code validation quality experimental data and a previously documented structured grid simulation; and (3) identification of sources of discrepancy between predicted and measured results, as well as recommendations to alleviate these discrepancies. Solutions were obtained with a multiblock, unstructured/adaptive grid, fully explicit, time-marching, Reynolds-averaged Navier–Stokes code with multigrid, local time stepping, and residual smoothing type acceleration techniques. The computational methodology was applied to the validation test case of a row of discrete jets on a flat plate with a streamwise injection angle of 35 deg, and two film-hole length-to-diameter ratios of 3.5 and 1.75. The density ratio for all cases was 2.0, blowing ratio was varied from 0.5 to 2.0, and free-stream turbulence intensity was 2 percent. The results demonstrate that the prescribed computational methodology yields consistently more accurate solutions for this class of problems than previous attempts published in the open literature. Sources of disagreement between measured and computed results have been identified, and recommendations made for future prediction of film-cooling problems.

1 Introduction

Film cooling is commonly used in the gas turbine industry to prevent hot-section components from failing at elevated temperatures. Increasingly, designers are trying to extract greater cooling performance from less coolant air, particularly in next-generation high-efficiency gas turbines. To make significant advances in cooling technology requires a fundamental understanding of the physical mechanisms involved in film-cooling flowfields. At the same time, designers need a truly predictive design tool that allows relatively quick turnaround times without the "build 'em and bust 'em" approach that is currently used. Computational fluid dynamics presents the designer with the potential for an effective, fast, and accurate method of achieving these goals.

Most computational work for film-cooling problems has focused on the interaction of a three-dimensional discrete jet with a crossflow. It is exactly this problem that is at the heart of film-cooling physics. Unfortunately, the majority of past attempts to simulate this class of problems have suffered in one or more critical areas, resulting in solutions that have been inaccurate and, more importantly, inconsistent. This paper presents the results from a series of simulations based on a systematic approach to the four critical issues of a computational simulation. These are: (1) proper computational modeling of flow physics; (2) exact geometry and high-quality grid generation; (3) higher-order discretization scheme; and (4) effective turbulence modeling. By addressing each of the first three issues in a systematic manner, the present simulations allow a true judgment to be made regarding turbulence model performance for film-cooling problems. It is shown that adherence to the prescribed methodology results in a more consistently accurate computational procedure than any documented in the open literature to date.

2 Literature Review

The interaction of jets-in-crossflow has been heavily researched. The following review examines the more relevant studies that have been documented for three-dimensional jets, both experimental and computational.

2.1 Experimental Studies. Bergeles et al. (1976, 1977) documented early investigations of a single discrete jet injected into a crossflow, both normally (1976) and at a 30 deg streamwise injection angle (1977). The authors documented the variation in jet lift-off and penetration as blowing ratio increased along with the entrainment of the mainstream fluid into the separation region beneath the jet. They also identified the nonuniformity of the jet exit profile, suggesting the influence of the crossflow on the flow within the film-hole.

Andreopoulos and Rodi (1984) documented an extensive experimental study of an isolated normal jet-in-crossflow, showing the counterrotating vortex structure within the jet as the jet interacted with the crossflow and the presence of a "blockage" over the upstream portion of the coolant jet exit plane. They noted that the amount of blockage varied with blowing ratio,

Contributed by the International Gas Turbine Institute and presented at the 41st International Gas Turbine and Aeroengine Congress and Exhibition, Birmingham, United Kingdom, June 10–13, 1996. Manuscript received at ASME Headquarters February 1996. Paper No. 96-GT-351. Associate Technical Editor: J. N. Shinn.

suggesting an influence by the crossflow on the flow within the film hole. The authors concluded that eddy-viscosity turbulence models should be capable of accurately prescribing two of the three Reynolds stress quantities, the exception being the term influencing the lateral spreading of the coolant jet.

Pietrzyk et al. (1988, 1990) and Sinha et al. (1991) made significant advances in the experimental modeling of film-cooling flowfields. They studied the hydrodynamic and thermal characteristics of a row of discrete jets inclined at 35 deg to the crossflow with a short film-hole length-to-diameter (L/D) ratio. Detailed mean flow and turbulence quantities were presented throughout the flowfield, as well as surface measurements of adiabatic film effectiveness. The authors hypothesized the existence of a separation region within the film-hole itself as they attempted to explain the shape of the velocity profiles and high turbulence intensities measured at the exit plane of the film-hole. The results suggested that the presence of the supply plenum and the length of the film hole were important factors in determining the flowfield characteristics. They also found a direct correlation between the peaks in the mean velocity gradients and the peaks in turbulence shear stresses along the jet centerline, concluding that an eddy-viscosity turbulence model would be adequate in this region.

2.2 Computational Studies. Bergeles et al. (1978) supplemented their experimental study with a numerical treatment for normal and 30 deg inclined round jets. They used a "partially parabolic" scheme in which pressure information was allowed to propagate upstream and all other flow variables were treated using a fully parabolic space-marching procedure. Initially, the authors believed that the near-field character of the jet was insensitive to the jet exit profile. Based on this assumption, they imposed a uniform jet exit profile as a boundary condition on the crossflow. The simulation used an extremely coarse grid (5415 cells) in combination with a low-order discretization scheme. Turbulence quantities were obtained using a primitive anisotropic mixing length turbulence model. The results indicated that a fully elliptic solution procedure was needed to capture the near-field character of the jet accurately, especially in those cases where a separation region appeared downstream of the film hole. The authors also found that their assumption of insensitivity to jet exit profile was valid only for cases with blowing ratio less than 0.2. At more realistic blowing ratios, they suggested that the computational domain be extended into the film hole. Finally, the simulations demonstrated the anisotropic nature of the turbulent stresses, and the authors suggested the use of an algebraic Reynolds stress model in favor of the more conventional eddy-viscosity turbulence models.

Demuren (1982) performed a series of simulations for a row of discrete jets issuing normally into a crossflow, concentrating on the effects of grid refinement and discretization scheme on the overall solution. The results showed that for any grid level, the QUICK scheme (Leonard, 1979) introduced less numerical viscosity and gave superior solutions to the lower-order hybrid scheme (Patankar, 1980). However, the simulation domain used the typical practice of modeling only the crossflow region, introducing the jet as a uniform total pressure boundary condition with the exit plane geometry approximated as a right-angled polygon of equal area. The author noted the sensitivity of the solution to the jet exit boundary conditions, but ascribed deviations between predicted and measured data to the isotropic nature of the $k-\epsilon$ turbulence model.

Leylek and Zerkle (1994) were the first to perform a jet-in-crossflow simulation using a geometry typical of that found in film-cooling applications. The primary objective of their study was to develop a proper computational model of the gas turbine film-cooling flowfield. Their simulations were based on the experimental work of Pietrzyk et al. (1988, 1990) and Sinha et al. (1991) described above. The computational domain included not only the crossflow, but also the film-hole and supply plenum regions, with short film-hole length-to-diameter ratios of 3.5 and 1.75. Solving these regions simultaneously, the authors noted the strong three-way coupling between the plenum, film-hole, and crossflow regions. They identified a very complex flow structure within the film hole, which caused the jet exit conditions to change dramatically as blowing ratio varied. Unfortunately, the single-block structured grid procedure presented serious difficulties in maintaining a refined, high-quality grid in the jet exit region. The simulation also used a lower-order discretization scheme (hybrid), which resulted in increased numerical errors.

One of the earliest unstructured/adaptive simulations for this class of problems was documented by Weigand and Harasgama (1994). The study used the unstructured/adaptive code developed by Dawes (1991) on an entire turbine blade with multiple jet injection and rotation effects. Due to the large domain, the solution used an extremely coarse grid relative to the jet size, and gridding limitations forced the authors to model the injection holes along blade-to-blade grid lines. The study did not attempt to document the details of the jet–crossflow interaction, so unfortunately the performance of the unstructured/adaptive procedure could not be evaluated in this regard.

Recently, Garg and Gaugler (1997) demonstrated the importance of the jet exit plane conditions on downstream results. The authors performed simulations for three different blade configurations using $\frac{1}{7}$th power-law and "tuned" polynomial jet exit profiles for velocity and temperature distribution. The results showed that downstream heat transfer coefficient levels may differ by as much as 60 percent depending on the exit profile used, highlighting the critical influence of the jet exit conditions on downstream results.

2.3 Summary. The papers cited above show that the interaction between jet and crossflow is not confined to the crossflow region alone. Each study describes the profile variations at the jet exit plane as the operating conditions change. They also show that as the geometry of the experimental model more closely matches the small L/D geometries used in gas turbine film-cooling applications, the variation in exit profiles is even more significant. Particularly, for cases that use realistic L/D ratios, the flowfield exhibits a three-way coupling behavior between the crossflow, film-hole, and plenum regions. Despite this well-documented, complex behavior, computational simulations continue to apply boundary conditions at either the jet exit plane or the film-hole inlet. In addition, most documented computational treatments suffer from inadequate geometry and grid generation procedures, which do not allow a high-quality, refined grid to be maintained in the critical regions of the flow-

Nomenclature

D = film-hole diameter
DR = density ratio = ϱ_j/ϱ_∞
L/D = film-hole length-to-diameter ratio
M = blowing (or mass flux) ratio = $\varrho_j v_j/\varrho_\infty u_\infty$
T_j = coolant jet temperature
T_w = wall temperature
T_∞ = mainstream temperature
TKE = turbulence kinetic energy
u_∞ = mainstream velocity
v_j = jet exit velocity
x = streamwise coordinate
y^+ = nondimensional distance from wall
z = lateral coordinate
η = adiabatic effectiveness = $(T_\infty - T_{aw})/(T_\infty - T_j)$
$\overline{\eta}$ = laterally averaged adiabatic effectiveness
ϱ_j = coolant density
ϱ_∞ = mainstream density

field. Many simulations also suffer from the use of lower-order discretization schemes, which overwhelm the physical diffusive effects with artificial viscosity. As a result of these deficiencies, no reliable conclusions can be made about turbulence model performance for this class of problems. Nonetheless, turbulence models are typically blamed for most, if not all, of the discrepancies between predicted and measured results.

3 Computational Methodology

3.1 Simulation Hierarchy. Two companion papers documented by Butkiewicz et al. (1995) and Walters et al. (1995) identified the four issues critical to the success of a computational prediction and prescribed a simulation hierarchy based on these issues. They are: (1) computational model of the physical problem; (2) accurate geometry representation and high-quality grid generation; (3) higher-order discretization scheme; and (4) effective turbulence modeling. Using a two-dimensional test case, the authors showed that the practice of applying boundary conditions in complex regions of the flowfield results in significant errors in the solution. These observations are consistent with those recently reported by Garg and Gaugler (1997). For jet-in-crossflow problems, this is particularly true at the jet exit plane or, in the case of realistic (short) L/D ratios, at the film-hole *inlet* plane. Although this fact was demonstrated in Leylek and Zerkle (1994), recent computational studies have continued to apply improper boundary conditions in these highly complex regions. The current methodology dictates the application of boundary conditions in the supply plenum, allowing the flow conditions at the film-hole inlet and exit planes to develop realistically.

The results of Butkiewicz et al. (1995) and Walters et al. (1995) demonstrate the need for both grid quality and grid refinement levels—in the form of grid-independent solutions—to be addressed in any accurate simulation. It is also critical that the computational geometry reflect exactly the physical geometry of the problem being addressed. The current methodology depends on accurate geometry and grid generation using unstructured/adaptive gridding techniques, which are discussed in more detail below.

It has been well established that for equivalent grids, higher-order discretization schemes will introduce less numerical diffusion and yield more accurate results than lower-order schemes. It is also well known that lower-order schemes require finer grid densities to achieve grid independent solutions. Each of these was shown to be true for a two-dimensional jet-in-crossflow in Walters et al. (1995). However, it was also found that even for equivalent grid-independent solutions, the first-order discretization scheme did not resolve the finer details of the flowfield as well as the second-order scheme. In addition, the second-order scheme computed more accurate surface flux results when used in combination with wall functions. For these reasons the current three-dimensional methodology prescribes a second-order discretization scheme for all simulations.

Turbulence modeling presents the final difficulty in obtaining accurate computational results. Typically, this issue represents a trade-off between computational intensity and accuracy. The majority of past simulations have used either algebraic models, such as the Baldwin–Lomax model, or two-equation models with wall functions such as the high-Reynolds-number $k-\epsilon$ model. Unfortunately, erroneous conclusions have been drawn regarding turbulence model performance based on an ineffective treatment of the previous three issues. One of the strengths of the current methodology is that accurate treatment of the computational model, geometry/grid generation, and discretization scheme allows a true judgment to be made about the performance of the combination of turbulence model and near wall treatment. For example, Butkiewicz et al. (1995) and Walters et al. (1995) found that for two-dimensional normal jets, the reattachment length is overpredicted slightly using a standard $k-\epsilon$ turbulence model with wall function when the current methodology is followed. This is contrary to results that are typically reported in the open literature, in which the $k-\epsilon$ model is usually blamed for *under*predicting the reattachment length by 10 to 20 percent.

3.2 Unstructured/Adaptive Gridding Procedure. The complex geometries associated with film-cooling applications have created difficulties in accurate geometry and grid generation in past simulations. This has led to such practices as approximating round jets as square or as equivalent area stair-step regions, or of limiting simulations to unrealistic geometries, such as discrete normal jet cases. The use of structured gridding procedures has also limited the degree to which both high grid quality (orthogonality, low aspect ratio, and low stretching ratio) and grid refinement could be maintained. Unstructured gridding techniques provide an effective means of accurately representing a given flow geometry while maintaining both refinement and grid quality (in terms of cell skewness) in high gradient regions of the flowfield. Walters et al. (1995) documented these techniques for two-dimensional situations. For complex three-dimensional geometries, it is possible that unstructured gridding techniques may offer the only method of effectively reducing grid-based errors in the solution.

The current methodology also takes advantage of the solution-based adaption features of the unstructured/adaptive procedure. This feature allows grid independence to be established more quickly and with less effort than is typically required with structured grid methods, as well as ensuring that cell concentration levels are maximized in those regions of the flowfield with the highest gradients. Care must be taken, however, to ensure that grid quality is maintained in any final mesh, and this issue is addressed in section 5.2.

4 Present Contributions

This paper documents the results of fully elliptic Reynolds-averaged Navier–Stokes computations for the case of a row of three-dimensional round jets with streamwise injection on a flat surface. The study was primarily motivated by the desire to obtain truly predictive capability for film-cooling problems using currently available technology. Key aspects of the simulation include:

- Application of the systematic computational methodology discussed in Section 2. For the first time in the open literature, a computational film-cooling simulation is truly limited by the performance of the turbulence model and near wall treatment.
- The use of state-of-the-art solid modeling for geometry and unstructured/adaptive grid generation techniques that have yet to be documented for this class of problems.
- Three-way comparison between experimental data and a previously documented structured grid simulation of an identical test case.
- Identification of probable sources of discrepancy between predicted and measured results, including computational *and* experimental errors, as well as recommendations for treating these discrepancies in future work.

5 Test Case: Three-Dimensional Streamwise Injected Jet

The three-dimensional validation test case is based on the experimental work of Pietzryk et al. (1988, 1990) and Sinha et al. (1991). The authors documented flowfield and adiabatic effectiveness measurements for a single row of holes on a flat surface, with a 35 deg streamwise injection angle and a film-hole pitch-to-diameter ratio of 3. The experimental setup is

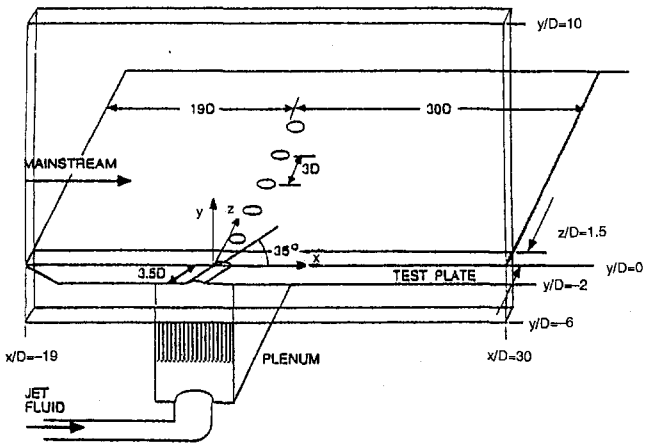

Fig. 1 Schematic of experimental test section and overall computational domain highlights the use of a supply plenum to model realistic *L/D* ratios

shown in Fig. 1. The film-hole diameter was 12.7 mm. The row of holes was located 19 diameters ($19D$) downstream of the flat plate leading edge, with measurements obtained from $1D$ upstream of the film holes to $30D$ downstream. The oncoming boundary layer was suctioned at the leading edge of the test surface, allowing a new boundary layer to develop upstream of the film holes. This boundary layer was experimentally determined to be fully turbulent from the leading edge onward.

The coolant fluid was injected from a supply plenum located beneath the test section, as shown in Fig. 1. Density ratio was controlled by varying the temperature of the coolant while maintaining the crossflow temperature at 302 K. The authors documented that coolant mass flow rates were equal for each of the film holes on a given test section.

Two series of measurements were performed. The first, documented in Pietzryk et al. (1988, 1990), used a length-to-diameter ratio of 3.5, with detailed measurements obtained for velocity and turbulence quantities throughout the flowfield. Density ratios of 1.0 and 2.0 were examined, with blowing ratios from 0.25 to 1.0. The second series, described in Sinha et al. (1991), used $L/D = 1.75$ and documented the downstream adiabatic effectiveness results, both along the centerline and at varying lateral locations. The density ratios examined ranged from 1.2 to 2.0, and blowing ratios ranged from 0.25 to 1.0. One important observation made at the time of the experiments involved a skewing of the coolant jets downstream of the film hole (Crawford, 1992, 1995). This fact was found to be significant when comparing predicted and measured results, and is discussed in more detail in section 7.1.3.

6 Details of Numerical Simulation

6.1 Approach. The computational model for this case matched the experimental test case, and was identical to the model used by Leylek and Zerkle (1994) for their structured grid simulation of a row of holes on a flat surface. The computational domain included the region of influence for a single film hole within the row, as shown in Fig. 1. The assumption of flow symmetry allowed a $\frac{1}{2}$ pitch extent in the lateral direction to be used to model the row of film holes. The key aspect of the model was the application of the coolant boundary condition within the supply plenum, instead of in the highly complex film-hole inlet or exit regions. The computational extent in the y direction was $10D$, which was far enough from the near-field region that a symmetry condition could be applied without significantly affecting the flowfield created by the jet-in-crossflow interaction. Velocity at the crossflow inlet was a uniform 20 m/s, with inlet temperature of 302 K. The plenum inlet velocity was varied so that the proper blowing ratio was maintained. For all computational cases, coolant inlet temperature was 153 K, corresponding to a density ratio of approximately 2.0. At both the crossflow and plenum inlet, turbulence intensity was 2 percent, and the length scale was taken as $\frac{1}{10}$th of the inlet extent in the y direction (crossflow) or x direction (plenum). All walls were adiabatic.

The simulation was performed using the RAMPANT software package from Fluent, Inc. Extensive in-house validation has been performed for the code including laminar flow over a cylinder, turbulent flow over a flat plate, and the two-dimensional jet-in-crossflow simulations documented in Walters et al. (1995) and Hyams et al. (1996). The solver uses the fully elliptic, explicit, time-marching procedure documented in Jameson et al. (1981), on a multiblock unstructured/adaptive mesh to solve the Reynolds-averaged form of the Navier–Stokes equations. The extension of the time-marching procedure to incompressible flowfields is accomplished through the use of artificial compressibility. The simulation used local time stepping, implicit residual smoothing, and multigrid techniques to accelerate convergence to the steady state. Note that the simulation was not time accurate, but only used the time stepping scheme to achieve a final steady-state solution. The current study did not attempt to determine the effects of unsteadiness on the problem, but instead assumed a steady flowfield. Discretization of the governing equations was performed using the second-order accurate linear reconstruction approach with the flux-difference splitting scheme of Roe (1986). Details of the solution procedure and discretization scheme are available in the RAMPANT User's Guide (1993).

Turbulence modeling for the problem used the standard $k-\epsilon$ model of Launder and Spalding (1974). Near-wall quantities were calculated using the generalized wall functions available in RAMPANT. The combination of standard $k-\epsilon$ with wall functions represents what is currently the standard approach to this class of problems. By minimizing sources of error due to computational modeling, grid generation and discretization scheme, the performance of the standard $k-\epsilon$ model with wall functions can accurately be determined in the present simulation. Neither the turbulence models nor the wall functions were adjusted in any way to provide better agreement with experimental data.

Computational simulations were carried out on the South Carolina Intel Paragon machine with 64 parallel central processing units. Convergence was determined based on solution steadiness as well as overall mass and energy imbalances of less than 0.01 percent. All residual levels were reduced approximately three orders of magnitude depending on the initialization. Convergence of a typical 200,000 cell case was achieved after approximately 2000 iterations on 24 processors, with a wall-clock run time of approximately one full day.

6.2 Three-Dimensional Geometry and Grid Generation. This section details the procedure by which the high-quality three-dimensional unstructured mesh used in all of the present simulations was generated. The final grid was produced in an iterative manner using two computational tools: (1) I-DEAS Solid Modeling and Finite Element Analysis software from Structural Dynamics Research Corporation; and (2) T-Grid mesh generator available in the RAMPANT software package from Fluent, Inc.

Initially, the solid modeling capability available in I-DEAS was used to obtain an accurate representation of the flow geometry, including the cylindrical film-hole and the "elliptic breakout" into the crossflow and plenum regions. The I-DEAS two-dimensional mesh generation feature was then used to generate a high-quality triangular surface mesh for the model. The surface mesh maintained the highest levels of cell concentration in the critical regions, including downstream of the jet exit and within the film-hole. The surface mesh also used a uniform

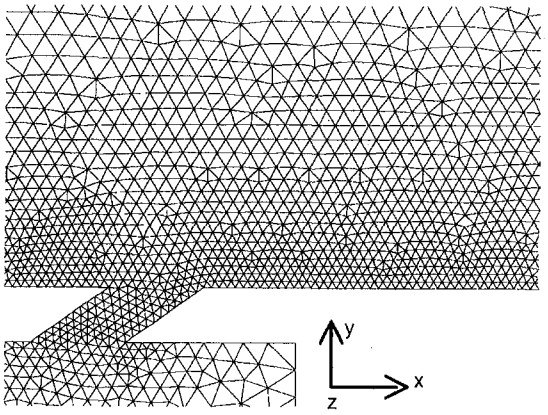

Fig. 2 Close-up of the initial grid on the centerline plane in the jet exit region shows the level of refinement in this critical region

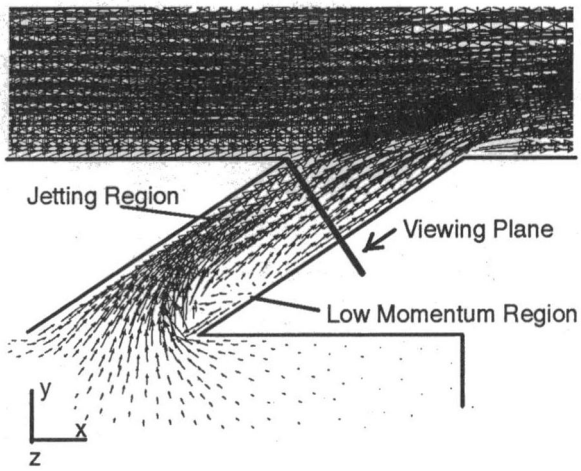

Fig. 3 Velocity vectors along the centerline plane in the film-hole region shows separation and jetting of the coolant jet

layer of imbedded nodes within the mesh to maintain a constant cell layer along the bottom walls in order to control y^+ levels. Since wall functions were used to calculate near-wall quantities, it was critical that cell y^+ levels remain above 12, in order for the wall function results to be meaningful. The cells along the downstream bottom surface were initially sized to a height of 2 mm, which corresponded to an estimated y^+ of 30 along the surface. The final, converged solution in all cases maintained average y^+ levels along the downstream bottom surface of approximately 25. Figure 2 shows the surface mesh in the vicinity of the jet exit. The figure highlights the accurate representation of the film-hole/crossflow geometry, as well as the fine mesh in the critical jet exit region. The surface mesh was imported to the T-Grid mesh generator and the initial internal mesh of tetrahedrons was created using a Delauney triangulation method. A typical initial, or background, mesh contained approximately 125,000 cells.

For each geometry—$L/D = 3.5$ and $L/D = 1.75$—solutions were obtained on the initial mesh for all of the blowing ratio cases. The solution-based adaption feature in RAMPANT was used to determine the refinement level required for a grid-independent solution in each case. The grid was adapted based on gradients of pressure, velocity, temperature, turbulence kinetic energy, and turbulence dissipation rate. Grid-independent results were typically obtained after two solution based refinement operations, with meshes containing approximately 200,000 cells. Unlike single-block structured grid approaches, the unstructured/adaptive approach allows all of the cells to be placed in the active flow regions. Also, the cells are concentrated in those regions of the flow with the highest gradients. As a result, the grid level of approximately 200,000 is actually comparable to a single block structured grid with several times that number of cells.

7 Results and Discussion

7.1 Hydrodynamic Results. The present study was primarily concerned with computational prediction of adiabatic effectiveness downstream of a discrete jet-in-crossflow. Since the thermal field of a jet-in-crossflow interaction is dictated by the hydrodynamics, field results were also obtained and compared to experimental data. Results were obtained for L/D = 3.5, density ratio of 2.0, and blowing ratios of 0.5, 1.0, and 2.0. The computed near-field velocity vectors along the centerline plane for the case of $DR = 2.0$ and $M = 0.5$ are shown in Fig. 3. The figure highlights the existence of a low-momentum region along the downstream wall and a corresponding high momentum or jetting region along the upstream wall within the film hole. Figure 4 shows an orthogonal view of the velocity vectors in a cross-sectional plane within the film hole, at the location shown in Fig. 3, exhibiting a counterrotating flow structure near the jet exit plane. Figures 3 and 4 indicate the three-dimensional swirling flow pattern within the film hole itself, a consequence of flow turning and three-dimensional separation due to the sharp-edged, inclined inlet along the downstream portion of the film hole. Note that these results are from the case of lowest blowing ratio ($M = 0.5$) and $L/D = 3.5$. As either blowing ratio increases, or film-hole length is reduced, the flow within the film hole is expected to exhibit stronger secondary motion. This is apparent in Fig. 4(*b*), which shows the flow at the same film-hole cross section for $L/D = 1.75$. This complex flow was first documented computationally by Leylek and Zerkle (1994), and highlights the importance of the computational model used in any jet-in-crossflow simulation. The results suggest that any accurate three-dimensional film cooling treatment must include the flow in the crossflow, film-hole, and plenum regions.

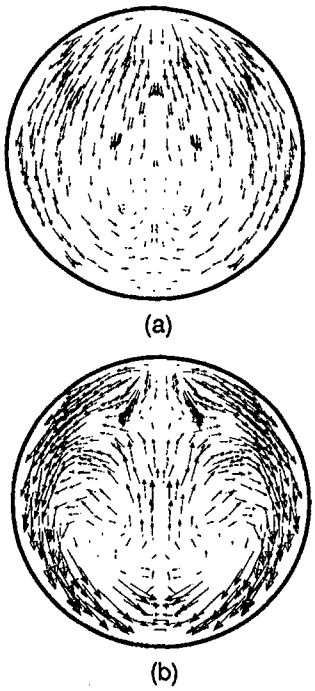

Fig. 4 Velocity vectors in a cross-sectional plane within the film hole for L/D = 3.5 (*a*) and L/D = 1.75 (*b*) show complex, counterrotating flowfield

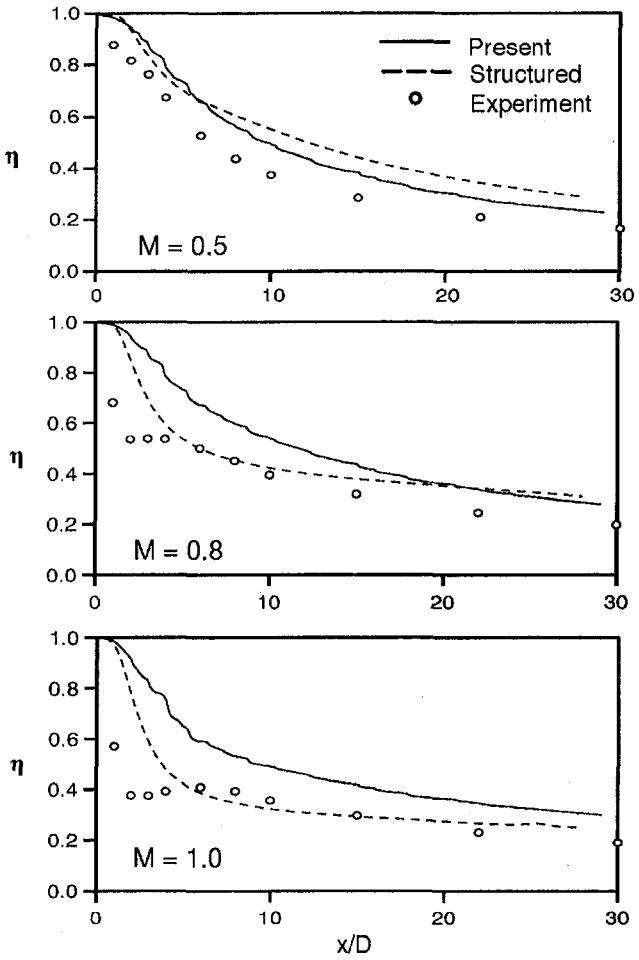

Fig. 5 Centerline adiabatic effectiveness highlights more consistent results obtained with the present computational methodology

7.2 Adiabatic Effectiveness Results. Adiabatic effectiveness results were obtained for the test case of $L/D = 1.75$, $DR = 2.0$, and M = 0.5, 0.8, and 1.0. Results were compared to experimental data documented in Sinha et al. (1991), in order to evaluate the performance of the computational methodology described above. Three comparisons are presented: centerline effectiveness versus downstream distance; laterally averaged effectiveness versus downstream distance; and lateral variation of effectiveness at various downstream locations. All of the results in this section are presented "as is." The following section (7.3) addresses possible sources of discrepancy between computational predictions and experimental measurements. When these sources are identified and corrected for, the results show improved agreement.

Figure 5 shows the adiabatic effectiveness along the jet centerline for M = 0.5, 0.8, and 1.0 respectively. Each plot contains a three-way comparison between the present unstructured/adaptive grid simulation, the structured grid results of Leylek and Zerkle (1994), and the experimental data. For all three blowing ratios, the present results show higher effectiveness along the centerline than the experimental data. This is especially true immediately downstream of the jet exit for M = 0.8 and M = 1.0. In these cases, the experiments found that the coolant jet lifts off and reattaches downstream, resulting in a sharp dip in the centerline effectiveness. Neither the present simulations nor the structured grid simulations were able to capture this detail of the flowfield, for reasons discussed in the following section. The structured grid results seem to indicate better overall agreement with the M = 0.8 and M = 1.0 data due to the sudden decrease in effectiveness immediately downstream of the jet. However, this sudden decrease is not due to the physical mechanism of jet lift-off and reattachment, but is instead likely due to increased numerical diffusion resulting from a combination of low-order discretization scheme and a coarse, poor quality grid in this region, which is known to have influenced the structured grid results. In the region downstream of jet reattachment, the current simulation is able consistently to match the decay rate of the effectiveness, although in each case the actual levels are higher for the computation. For all cases, the structured grid results show a flatter downstream effectiveness curve than either the present computations or the experiments. This indicates that the present simulations more accurately predict the decay *rate* of the centerline effectiveness downstream than the previous, structured grid results. Since the present results show consistent trends relative to the experimental data downstream of the jet lift-off, they are judged to be more consistent than the structured grid results.

Figure 6 shows laterally averaged values of adiabatic effectiveness plotted versus downstream distance for all three blowing ratios. For M = 0.5, both the present computational results and the structured grid results show reasonably good agreement with the experiments, in general underpredicting laterally averaged effectiveness by no more than 20 percent. As blowing ratio is increased to 0.8 and 1.0, it is apparent that significant discrepancies occur immediately downstream of the jet. This is of course due to the jet lift-off and reattachment mentioned above. Downstream of the jet reattachment, however, the agreement between current predictions and experimental results is remarkably good, particularly for the case of M = 1.0. The

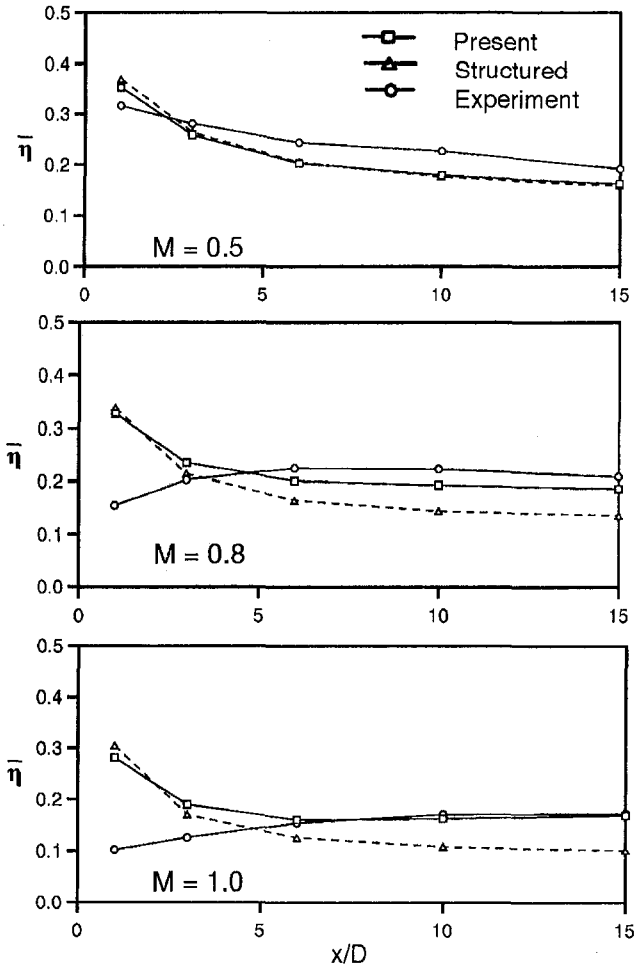

Fig. 6 Laterally averaged adiabatic effectiveness shows good agreement with experiments, particularly at higher blowing ratios

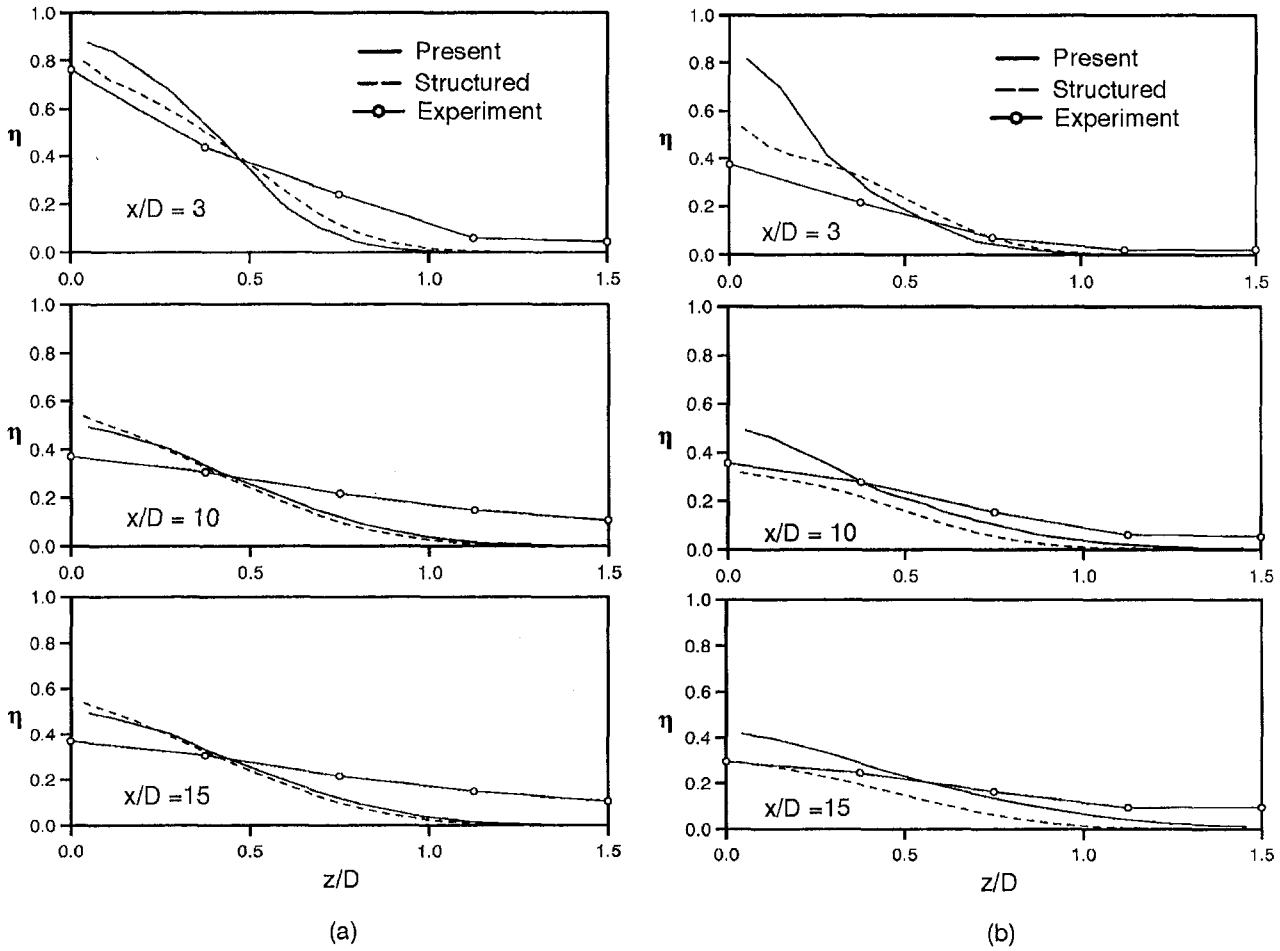

Fig. 7 Lateral variation of adiabatic effectiveness at downstream locations of 3*D*, 5*D*, and 15*D* for M = 0.5 (*a*) and M = 1.0 (*b*) shows underprediction of effectiveness spreading rate relative to experimental data

present results show marked improvement over the comparable structured grid results and suggest that, except for regions of lift-off that are not captured computationally, the present method does an accurate job of representing the laterally averaged effectiveness.

A key aspect of any predictive method for this class of problems is the ability to simulate accurately the lateral variation of adiabatic effectiveness downstream of the film hole. Representative plots of this lateral variation are shown in Fig. 7 for the bracketing cases of M = 0.5 and M = 1.0. Adiabatic effectiveness is plotted in the lateral (z) direction at three different downstream locations. For all cases, both the present results and the structured grid results underpredict the lateral spread rate of the effectiveness. However, it can be seen in the figure that the present results show an increase in the spreading rate over the structured grid results as the jet moves downstream. The structured grid results do indicate a sudden widening of the effectiveness band immediately downstream of the jet exit, but as mentioned above, this is likely due to numerical, and not physical, diffusion mechanisms. The figures suggest that the present methodology is more capable of representing the lateral variation than that used in Leylek and Zerkle (1994), but still underpredicts the spreading rate of the adiabatic effectiveness downstream when compared to the measurements.

7.3 Discussion of Results. Two of the cases examined, M = 0.8 and M = 1.0, were shown experimentally to exhibit jet lift-off and reattachment downstream of the film hole. This behavior was not found computationally for any of the blowing ratios. The inability of the current simulation to capture this behavior represents a serious limitation. It is believed that the near-wall grid was too coarse to resolve this detailed feature of the flowfield accurately. The use of wall functions to obtain near-wall turbulence quantities places a restriction on the minimal cell size adjacent to a wall. For the present cases the cell sizing at the wall was 2 mm, for reasons explained in section 5.2. This cell size is rather large relative to the expected height of jet lift-off. A "proof-of-concept" simulation was performed in which the grid was refined in the near-wall region immediately downstream of the jet so that y^+ was well below the minimum levels required by the wall functions. For this case the jet lift-off and reattachment was indeed predicted. However, these results cannot be regarded as physically meaningful, since the near wall quantities could not accurately be represented with the wall functions that were implemented. The results do indicate that near-wall treatments that allow an extremely fine mesh to be used in this region will perform better than wall functions, at least at the jet exit itself. Future improvements to the simulation of this class of problems will need to include the use of two-layer or low-Re turbulence models instead of wall functions.

The results also showed discrepancies farther downstream regarding both centerline and lateral variation of adiabatic effectiveness. It is believed that the computational methodology has eliminated any sources of numerical error due to either modeling, grid, or discretization scheme in this region of the flowfield. The only sources of numerical error are likely to come from the turbulence modeling and near-wall treatment. It is known that the turbulence in jet–crossflow interactions is strongly ani-

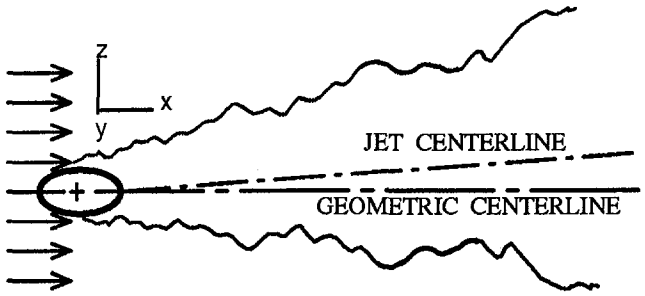

Fig. 8 Graphic depiction of jet skewness present in experimental test case. Skewness angle is exaggerated for clarity.

sotropic, while the standard $k-\epsilon$ turbulence model is inherently isotropic. Past simulations documented in the open literature have in fact placed the blame for poor performance exclusively on the $k-\epsilon$ model. Before assessing the turbulence model performance, however, it is helpful to identify possible sources of discrepancy arising from the experimental data itself.

One likely source of discrepancy is due to a slight skewness in the jet trajectory observed at the time of the experiments (Crawford, 1992, 1995). This skewness had the effect of misaligning the geometric centerline and the actual jet centerline, as shown in Fig. 8. Experimental results for centerline effectiveness were presented based on measurements along the geometric centerline. Experimental results for lateral variation of adiabatic effectiveness were obtained using an average of both sides of the geometric centerline. In order to demonstrate the sensitivity of the results to tiny amounts of skewness, the computational results were corrected consistent with the experimental technique, using a nominal skew angle of 1.5 deg. Corrected centerline effectiveness is shown in Fig. 9 for M = 0.5 and M = 1.0. As expected, the corrected, "off-centerline" values are lower than the uncorrected values, and closer to the experimental results. Figure 10 shows the corrected lateral variation of adiabatic effectiveness for M = 0.5 and M = 1.0 at a downstream location of $x/d = 15$. The corrected curves are flatter, and show significantly better agreement with the experimental data. Both of these figures suggest that the jet "skewness" in the experiments

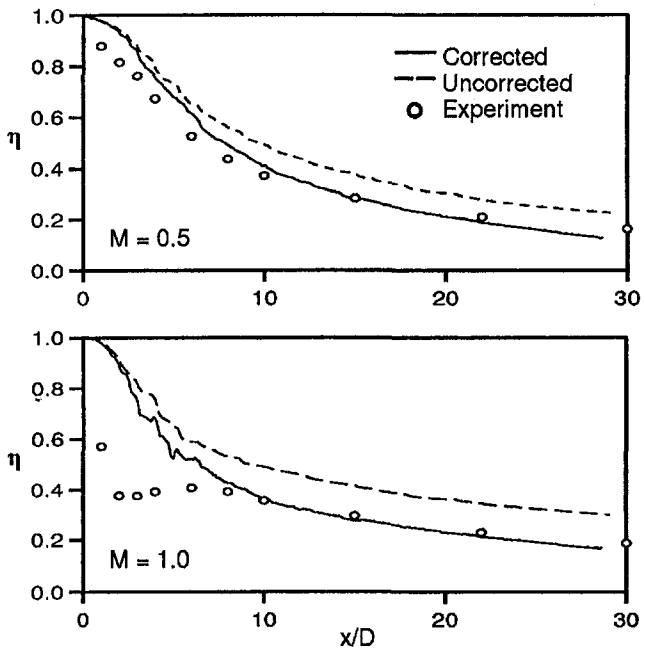

Fig. 9 Centerline adiabatic effectiveness adjusted to account for experimental jet skewness shows improved agreement with measured data

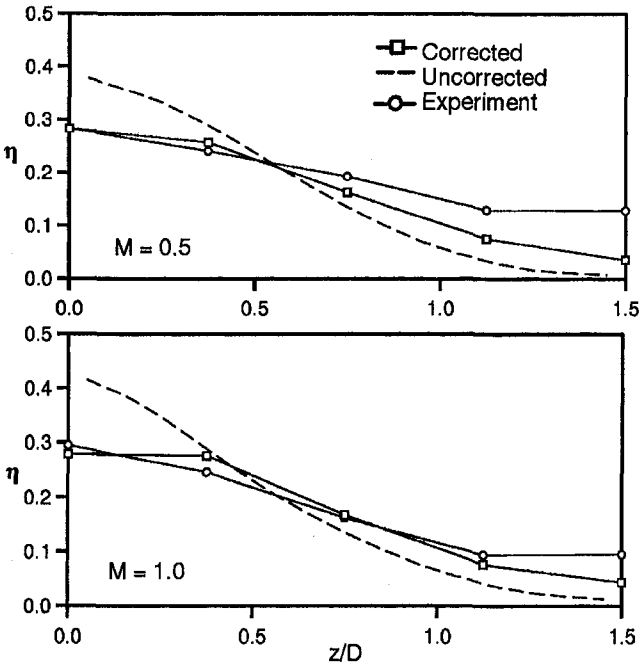

Fig. 10 Lateral variation of adiabatic effectiveness at $x/D = 15$ shows better agreement with experimental data when adjusted to account for jet skewness

may introduce some discrepancy in the results. It should be noted that the skewness angle of 1.5 deg is based on a rough estimate made from observations of the experiments, and should not be considered as an exact correction. However, the adjusted results do indicate that the current simulations may in fact do a better job of predicting both centerline and lateral variation of adiabatic effectiveness than what is suggested in Figs. 5–7. It is worth noting that the predicted result that most closely matches the experimental data in the downstream region is laterally averaged effectiveness. This is also the result that is least likely to be influenced by a slightly skewed jet trajectory.

The authors believe that turbulence anisotropy is still a serious issue to be resolved in the simulation of film-cooling problems, especially regarding lateral spreading of the coolant jet. However, it is also clear that more code validation quality data are needed to establish the true limitations of the existing turbulence models.

8 Conclusions

A systematic computational methodology has been applied to a three-dimensional jet-in-crossflow problem typical of a realistic film-cooling application. The methodology reduces errors by addressing each of the four critical issues in a computational simulation: computational model of the physical problem, geometry and grid generation, discretization scheme, and turbulence models. Results were compared to high quality experimental data and a previously documented structured grid simulation in order to highlight the present methodology. The following specific conclusions are drawn from the study:

- The present methodology resulted in more consistent agreement with experimental data than the previous structured grid simulation documented in Leylek and Zerkle (1994). This is due to a minimization of numerical errors by a high-quality, unstructured/adaptive grid generation procedure in combination with a second-order discretization scheme.
- Downstream of the film hole, computational results tended to show higher centerline effectiveness values and

less lateral spreading of the effectiveness than the experimental results. This may be due in some part to a skewed exit condition in the experiments. Corrected computational values indicate that the data presented represents a "worst case" scenario, and in fact may do a better job of predicting downstream effectiveness levels when experimental errors are accounted for.

- The computational methodology presented has brought this class of problems to the limits of the technology that is currently readily available. The study highlights the areas of turbulence modeling and near-wall treatment that need to be improved. In particular, the use of low-Re or two-layer models that do not restrict the near-wall cell sizing and allow accurate capture of jet lift-off and reattachment at elevated blowing ratios. Also, it is likely that turbulence models that accurately represent anisotropic turbulence will be needed finally to resolve downstream characteristics, particularly the lateral spreading of the coolant jet.

Acknowledgments

This paper was prepared with the support of the U.S. Department of Energy, Morgantown Energy Technology Center, Cooperative Agreement No. DE-FC21-92MC29061. The authors would like to thank Mr. Dewitt Latimer, Mr. Gary Berger, and Mr. Richard Baldwin of the Engineering Computer Operations at Clemson University for their assistance in all computer related matters. Also, Dr. Pat Fay provided first-rate support for the Intel Paragon supercomputer. Finally, we are deeply indebted to Dr. Rick Lounsbury at Fluent, Inc. for his invaluable support with RAMPANT.

References

Andreopoulos, J., and Rodi, W., 1984, "Experimental Investigation of Jets in a Crossflow," *Journal of Fluid Mechanics,* Vol. 138, pp. 92–127.

Bergeles, G., Gosman, A. D., and Launder, B. E., 1976, "The Near-Field Character of a Jet Discharged Normal to a Main Stream," ASME *Journal of Heat Transfer*, Vol. 107, pp. 373–378.

Bergeles, G., Gosman, A. D., and Launder, B. E., 1977, "The Near-Field Character of a Jet Discharged Through a Wall at 30° to a Mainstream," *AIAA Journal,* Vol. 14, pp. 499–504.

Bergeles, G., Gosman, A. D., and Launder, B. E., 1978, "The Turbulent Jet in a Cross Stream at Low Injection Rates: A Three-Dimensional Numerical Treatment," *Numerical Heat Transfer,* Vol. 1, pp. 217–242.

Butkiewicz, J. J., Walters, D. K., McGovern, K. T., and Leylek, J. H., 1995, "A Systematic Computational Methodology Applied to a Jet-in-Crossflow; Part 1: Structured Grid Approach," presented at the ASME Winter Annual Meeting, San Francisco, CA, Nov. 12–17.

Crawford, M. E., 1992, 1995, personal communications.

Dawes, W. N., 1991, "The Development of a Solution-Adaptive Three-Dimensional Navier–Stokes Solver for Turbomachinery," presented at AIAA/ASME/SAE/ASEE 27th Joint Propulsion Conference, Sacramento, CA.

Demuren, A. O., 1982, "Numerical Calculations of Steady Three-Dimensional Turbulent Jets in Cross Flow," Rep. SFB 80/T/129. Sonderforschungsbereich 80, University of Karlsruhe, Germany.

Garg, V. K., and Gaugler, R. E., 1997, "Effect of Velocity and Temperature Distribution at the Hole Exit on Film Cooling of Turbine Blades," ASME JOURNAL OF TURBOMACHINERY, Vol. 119, pp. 343–351.

Hyams, D. G., McGovern, K. T., and Leylek, J. H., 1996, "Effects of Geometry on Slot-Jet Film Cooling Performance," ASME Paper No. 96-GT-187.

Jameson, A., Schmidt, W., and Turkel, E., 1981, "Numerical Solution of the Euler Equations by Finite Volume Methods Using Runge–Kutta Time Stepping Schemes," Technical Report AIAA-81-1259, AIAA 14th Fluid and Plasma Dynamics Conference, Palo Alto, CA.

Launder, B. E., and Spalding, D. B., 1974, "The Numerical Computation of Turbulent Flows," *Computer Methods in Applied Mechanics and Engineering,* Vol. 3, pp. 269–289.

Leonard, B. P., 1979, "A Stable and Accurate Convection Modeling Procedure Based on Quadratic Upstream Interpolation," *Computer Methods in Applied Mechanics and Engineering,* Vol. 19, pp. 59–98.

Leylek, J. H., and Zerkle, R. D., 1994, "Discrete-Jet Film Cooling: A Comparison of Computational Results With Experiments," ASME JOURNAL OF TURBOMACHINERY, Vol. 113, pp. 358–368.

Patankar, S. V., 1980, *Numerical Heat Transfer and Fluid Flow,* Hemisphere Publishing Corporation, New York.

Pietrzyk, J. R., Bogard, D. G., and Crawford, M. E., 1988, "Hydrodynamic Measurements of Jets in Crossflow for Gas Turbine Film Cooling Applications," ASME Paper No. 88-GT-194.

Pietrzyk, J. R., Bogard, D. G., and Crawford, M. E., 1990, "Effects of Density Ratio on the Hydrodynamics of Film Cooling," ASME JOURNAL OF TURBOMACHINERY, Vol. 112, pp. 437–443.

RAMPANT User's Guide, 1993, Fluent Incorporated, Lebanon, NH.

Roe, P. L., 1986, "Characteristic Based Schemes for the Euler Equations," *Annual Review of Fluid Mechanics,* Vol. 18, pp. 337–365.

Sinha, A. K., Bogard, D. G., and Crawford, M. E., 1991, "Film Cooling Effectiveness Downstream of a Single Row of Holes With Variable Density Ratio," ASME JOURNAL OF TURBOMACHINERY, Vol. 113, pp. 442–449.

Walters, D. K., McGovern, K. T., Butkiewicz, J. J., and Leylek, J. H., 1995, "A Systematic Computational Methodology Applied to a Jet-in-Crossflow; Part 2: Unstructured/Adaptive Grid Approach," presented at the ASME Winter Annual Meeting, San Francisco, CA, Nov. 12–17.

Weigand, B., and Harasgama, S. P., 1994, "Computations of a Film Cooled Turbine Rotor Blade With a Non-uniform Inlet Temperature Distribution Using a Three-Dimensional Viscous Procedure," ASME Paper No. 94-GT-15.

Aerodynamic Aspects of Endwall Film-Cooling

S. Friedrichs

H. P. Hodson

W. N. Dawes

Whittle Laboratory,
University of Cambridge,
Cambridge, United Kingdom

This paper describes an investigation of the aerodynamic aspects of endwall film-cooling, in which the flow field downstream of a large-scale low-speed linear turbine cascade has been measured. The integrated losses and locations of secondary flow features with and without endwall film-cooling have been determined for variations of both the coolant supply pressure and injection location. Together with previous measurements of adiabatic film-cooling effectiveness and surface-flow visualization, these results reveal the nature of the interactions between the ejected coolant and the flow in the blade passage. Measured hole massflows and a constant static pressure mixing analysis, together with the measured losses, allow the decomposition of the losses into three distinct entropy generation mechanisms: loss generation within the hole, loss generation due to the mixing of the coolant with the mainstream, and change in secondary loss generation in the blade passage. Results show that the loss generation within the coolant holes is substantial and that ejection into regions of low static pressure increases the loss per unit coolant massflow. Ejection upstream of the three-dimensional separation lines on the endwall changes secondary flow and reduces its associated losses. The results show that it is necessary to take the three-dimensional nature of the endwall flow into account in the design of endwall film-cooling configurations.

Introduction

An increase in the cycle efficiency of gas turbines can be achieved through higher turbine entry temperatures. In turn, this requires the development of materials and efficient cooling methods. One cooling method that has gained increasing importance is endwall film-cooling, where coolant air is discharged through discrete holes in the inner and outer endwalls (platforms) of a turbine blade passage. After leaving the holes, the coolant forms a protective layer between the hot mainstream gas and the surface that is to be protected.

The external flow near the endwall, which interacts with the ejected coolant, is three dimensional due to the presence of secondary flow. A general overview of secondary flow in turbine blade passages is given by Sieverding (1984). Harrison (1989) and Friedrichs et al. (1996) describe the secondary flow structures in the turbine cascade used in this investigation.

The first work published on endwall film-cooling seems to be by Blair (1974). He found that both heat transfer and film-cooling on the endwall are influenced by secondary flow. A similar observation was made by Takeishi et al. (1990). Their leading edge horseshoe vortex, for example, increased heat transfer and decreased film-cooling effectiveness near the leading edge on the endwall. Granser and Schulenberg (1990) also observed the influence of secondary flow. They ejected coolant from a slot in the endwall upstream of the leading edge and measured higher levels of film-cooling effectiveness near the suction side of the blade than near the pressure side. As an application of a new measurement technique, Friedrichs et al. (1996) measured the distribution of film-cooling effectiveness on a cooled endwall and found interactions between the ejected coolant and the secondary flow. The secondary flow had a strong influence on coolant trajectories and coolant ejection delayed the three-dimensional separation of the inlet boundary layer on the endwall.

Bourguignon (1985) observed that coolant ejection tends to turn the endwall streamlines toward the inviscid streamlines. In Bourguignon's investigation, endwall film-cooling was effective for up to ten hole diameters downstream of ejection. Both Bourguignon (1985) and Bario et al. (1990) found that ejecting the coolant at an angle to the flow has little effect on the jet trajectory, except in the vicinity of the holes. Despite the interactions present in endwall film-cooling, the investigations of Harasgama and Burton (1992), Jabbari et al. (1996), and Friedrichs et al. (1996) show that high mean levels of cooling can be achieved with endwall film-cooling.

Goldman and McLallin (1977) and Sieverding and Wilputte (1981) performed aerodynamic measurements and found a significant effect of endwall film-cooling on the loss and angle distributions downstream of the blade passage, illustrating that endwall coolant ejection influences the passage flow field. After initially increasing, the overturning near the endwall and the depth of the loss core associated with the passage vortex were found to be reduced with increasing coolant supply pressures. Goldman and McLallin (1977) evaluated loss per percent coolant massflow and found it to increase almost linearly with increasing coolant supply pressures.

Bario et al. (1990) also found an effect of endwall coolant ejection on the flow in the blade passage, indicating that coolant ejection may reduce secondary flow. Biesinger (1993) reduced secondary flow in a linear cascade by ejecting air from a slot in the endwall upstream of the leading edge plane. He concluded that a net benefit could be achieved if the ejected air was used for cooling purposes.

This paper is a continuation of the work presented by Friedrichs et al. (1996) and looks at the aerodynamic impact of endwall film-cooling on the flow downstream of the blade passage. Together with measurements of film-cooling effectiveness and surface-flow visualization on the endwall, these results reveal the interactions between the ejected coolant and the flow in the blade passage and allow the aerodynamic losses to be compared to the achieved levels of film-cooling effectiveness.

Turbine Cascade and Cooling Configuration

The endwall film-cooling investigation presented here and by Friedrichs et al. (1996) was performed on a large-scale, low-speed, linear turbine cascade. The cascade consists of four

Contributed by the International Gas Turbine Institute and presented at the 41st International Gas Turbine and Aeroengine Congress and Exhibition, Birmingham, United Kingdom, June 10–13, 1996. Manuscript received at ASME Headquarters February 1996. Paper No. 96-GT-208. Associate Technical Editor: J. N. Shinn.

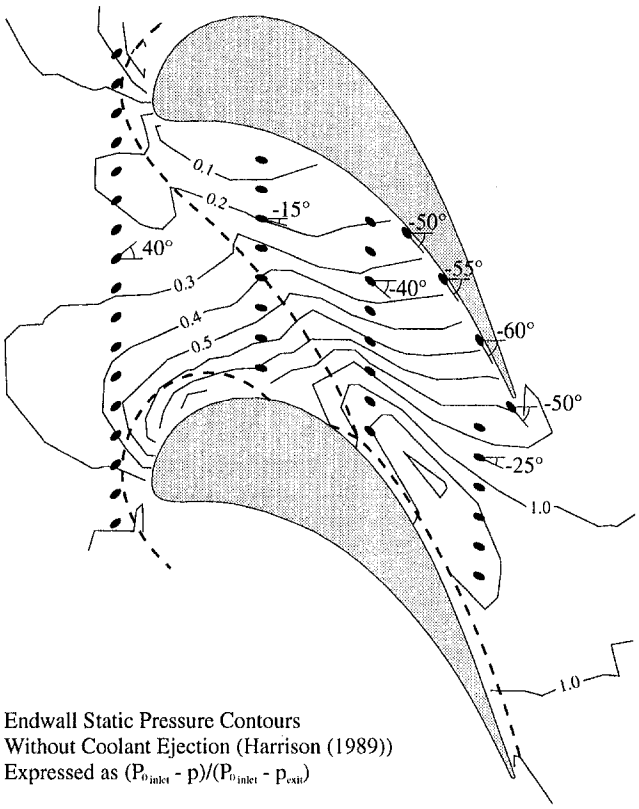

Endwall Static Pressure Contours
Without Coolant Ejection (Harrison (1989))
Expressed as $(P_{0_{inlet}} - p)/(P_{0_{inlet}} - p_{exit})$

Fig. 1 Cascade endwall with film-cooling holes, static pressure contours and lift-off lines without film-cooling

blades with a true chord of 278 mm, a span of 300 mm, and a pitch of 230 mm. The flow enters the cascade at an angle of 40 deg and is turned through 105 deg. With the low aspect ratio and high turning angle, the blades produce strong secondary flows. These are stronger than the ones found in high-pressure nozzle guide vanes with a typical turning angle of 70 to 75 deg, and therefore allow a more detailed observation of the basic interactions between endwall coolant ejection and the passage flow field. Details of the basic cascade without coolant ejection can be found in Harrison (1989).

Coolant air is ejected from a common plenum chamber through 43 holes in one endwall of a single passage. Figure 1 shows the cooling configuration that consists of four single rows of holes and four individual holes, all having a diameter of 4 mm and ejecting at an angle of 30 deg to the surface. The thickness of the endwall is 12 mm, giving a length-to-diameter ratio of 6, typical of endwall film-cooling configurations. For testing individual rows of holes the unused holes were closed with adhesive tape, thus giving a smooth surface.

The rows of holes are located at four axial positions: upstream of the leading edge, at 30, 60, and 90 percent axial chord. Four single holes are located near the blade pressure surface. All of the holes, except for the row at 90 percent axial chord and the hole at the trailing edge, eject in approximately the inviscid streamline direction. This cooling configuration might be expected to provide cooling to most of the endwall surface in the absence of secondary flow effects. In practice, Friedrichs et al. (1996) showed that large uncooled areas remain.

Each of the cooling holes experiences a different exit static pressure as it ejects into the flow field near the endwall. The undisturbed endwall static pressure field as measured by Harrison (1989) is shown in Fig. 1. Coolant ejection will locally affect the pressure field in the vicinity of the holes due to the blockage presented by the jet. Due to its interaction with the passage flow field, coolant ejection will also influence the overall passage pressure field. As an approximation, the undisturbed pressure field is used to define the local hole exit static pressures.

Test Conditions

Air is supplied to the common plenum chamber at approximately the same temperature as the free stream, resulting in a unity coolant-to-free-stream density ratio. Experiments were performed at several different coolant supply pressures. The coolant supply pressure can be characterized by defining an inlet blowing ratio M_{inlet}. This is the blowing ratio that an idealized loss free coolant hole would have when ejecting to inlet conditions. It is defined as:

$$M_{inlet} = \sqrt{\frac{P_{0_{plenum}} - p_{inlet}}{P_{0_{inlet}} - p_{inlet}}} \quad (1)$$

This characterization of the coolant supply pressure is convenient, as it is simply derived from measured pressure differences. Comparisons with other configurations and operating conditions should, however, be performed on the basis of momentum ratios.

For the investigation of all of the coolant holes blowing simultaneously, M_{inlet} was varied between 0.8 and 2.4. The lower limit of 0.8 is fixed by the hole at 30 percent axial chord closest to the blade pressure surface. Below an inlet blowing ratio of 0.8, this hole ingests mainstream air. Investigations for the individual rows of holes were performed at two values of the inlet blowing ratio, $M_{inlet} = 1.0$ and $M_{inlet} = 2.0$.

Local blowing ratios M can be calculated from the total measured coolant massflow and the uncooled hole-exit static pressures, assuming a uniform discharge coefficient for all of the coolant holes. The measurements presented by Friedrichs et al. (1996) were performed at an inlet blowing ratio of 1.0. This is a special case, as the coolant plenum pressure is equal to the inlet stagnation pressure. In this special case, all coolant holes operate with a local blowing ratio $M \approx 0.67$, a value equal to the discharge coefficient at $M_{inlet} = 1.0$. For all other values of M_{inlet} the local hole blowing ratios M will vary. Shown in Fig. 2, for example, are the local blowing ratios determined for $M_{inlet} = 2.0$. The local blowing ratios can be seen to vary with the endwall static pressure between $M = 0.92$ near the rear of the blade suction surface and $M = 2.30$ near the front of blade pressure surface.

Nomenclature

c_p = specific heat capacity at constant pressure
$M = \rho_{coolant} \cdot V_{coolant} / \rho_\infty \cdot V_\infty$ = coolant blowing ratio
$\dot{m}$ = massflow
p = static pressure
P_0 = stagnation pressure
T_0 = stagnation temperature
V = velocity
Y = stagnation pressure loss coefficient
ρ = density

Subscripts

coolant = coolant jet
exit = cascade exit
inflow = mixing control volume inflow
inlet = cascade inlet
mixed = mixed-out
outflow = mixing control volume outflow
plenum = coolant plenum
ref = inlet reference
∞ = local free stream

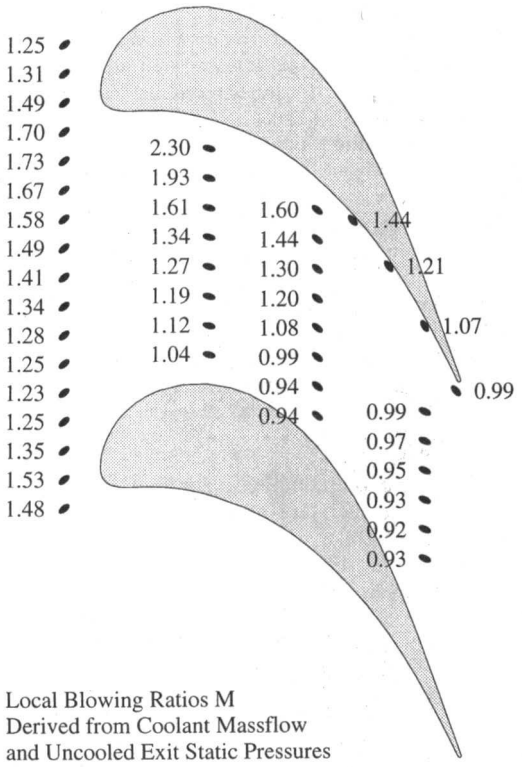

Fig. 2 Local hole blowing ratios M for $M_{inlet} = 2.0$

For $M_{inlet} = 1.0$, the total coolant massflow into the passage under investigation was equivalent to 1.64 percent of the passage massflow, if both endwalls had been cooled. The percentages for the other investigated inlet blowing ratios are shown in Fig. 3.

The results presented in this paper were produced with the cascade operating at a Reynolds number of 8.6×10^5 based on exit velocity and true chord. Harrison (1989) measured the inlet boundary layer at a point half an axial chord upstream of the leading edge and found it to have a thickness of 18 mm, a displacement thickness of 2.6 mm, a momentum thickness of 1.9 mm, and a shape factor of 1.36. The inlet turbulence level of the free stream was 0.5 percent.

Aerodynamic Measurements

The flow field downstream of the cascade was measured in an axial plane located at 23 percent axial chord downstream of the trailing edges. Measurements were performed with and without coolant ejection for individual rows of holes and all

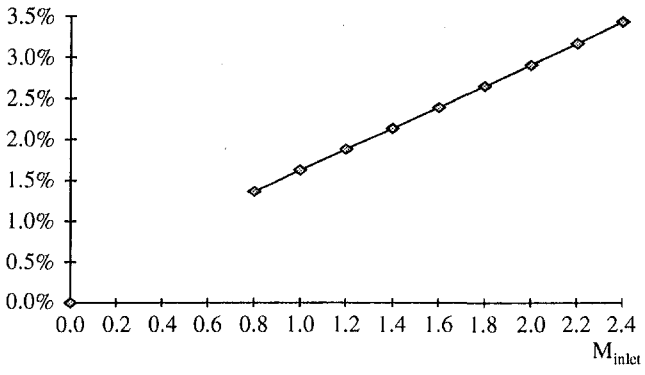

Fig. 3 Coolant massflow as percentage of the massflow in the cooled half of the passage, for all coolant holes blowing

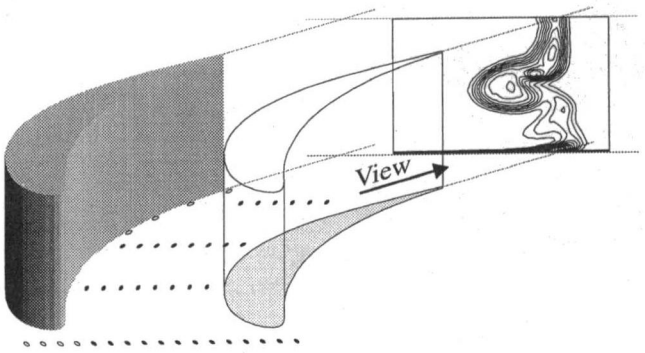

Fig. 4 Traversing plane in relation to the cooled passage

holes blowing simultaneously. A five-hole probe with a diameter of 3.29 mm was traversed over one pitch at 45 pitchwise positions and over half the span at 43 spanwise positions. To determine loss, these five-hole probe data were complemented by 14 spanwise traverses in the endwall boundary layer using a pitot probe with a diameter of 0.8 mm.

The traversing plane, as indicated in Fig. 4, is shifted relative to the wake centerlines to capture the entire wake and loss core downstream of a blade. All the ejected coolant, with two exceptions, passes through this traversing plane. The exceptions are the coolant from four holes upstream of the leading edge, and the coolant ejected from the four single holes in the blade pressure surface and endwall corner. The coolant ejected from these holes does not affect the results presented here and is disregarded in the following determination of loss coefficients.

The measured, nonuniform flow field in the traverse plane was mixed-out to uniform conditions by performing a constant area mixing calculation. The mixed-out stagnation and static pressures were used together with a reference inlet stagnation pressure to determine loss. The loss coefficient Y is defined as

$$Y = \frac{P_{0_{ref}} - P_{0_{mixed}}}{P_{0_{ref}} - p_{mixed}} \tag{2}$$

Three definitions of the reference inlet stagnation pressure have been used. The loss coefficient Y represents the overall cascade loss if the reference inlet stagnation pressure is determined by mass averaging the cascade inlet and the coolant plenum stagnation pressures. This overall cascade loss coefficient includes the loss generation within the coolant holes along with the loss generation within the blade passage. This is similar to the way that coolant conditions were taken account of by Goldman and McLallin (1977), Wilfert and Fottner (1996), and Biesinger (1993).

The second definition of the reference inlet stagnation pressure is to take the mass average of the cascade inlet and the coolant hole exit stagnation pressures. The resulting loss coefficient then represents the cascade loss excluding the loss generation within the coolant holes. The hole exit stagnation pressures are calculated using the method described in the next section.

The third definition of the reference inlet stagnation pressure is that it is equal to the cascade inlet stagnation pressure. This is the definition used in cascade tests without coolant ejection. With coolant ejection, the resulting coefficient Y does not represent loss, but a dimensionless mixed-out exit stagnation pressure.

Loss Decomposition

Three entropy generation mechanisms lead to the measured changes in loss. Entropy is generated within the coolant hole, as the coolant mixes with the mainstream and in the blade passage where the flow is changed due to the coolant ejection.

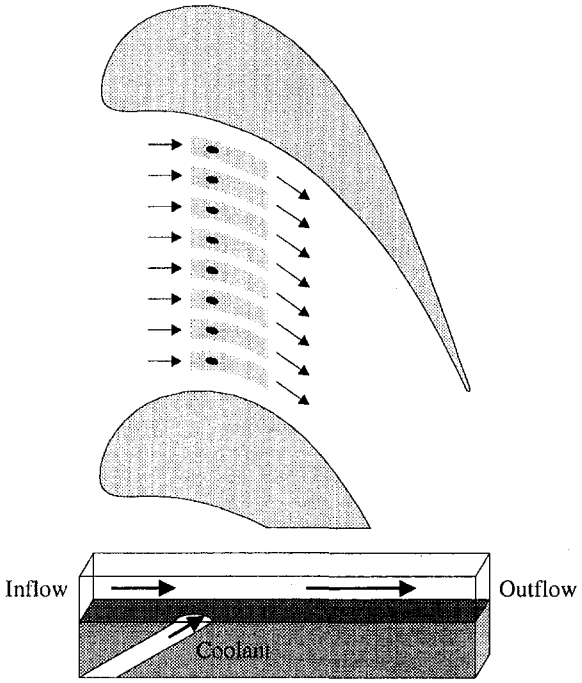

Fig. 5 Schematic of the mixing control volumes

The flow within the coolant hole is three dimensional, as can be seen in the computational predictions of Leylek and Zerkle (1994). A separation at the hole inlet is the cause of a pair of counterrotating vortices and a region of increased velocity opposite of the separation bubble. The blockage created by the jet as it enters the mainstream creates a local variation of pressure at the hole exit. Depending on the blowing ratio, either the "jetting effect" or the pressure increase on the upstream side of the hole can dominate, giving a nonuniform coolant flow at hole exit.

The entropy generation in this separated, nonuniform, swirling flow within the coolant hole can be approximated by measuring the massflow through the coolant hole and calculating an exit stagnation pressure that is consistent with the measured massflow, the coolant hole exit area, and the conservation of mass and energy. The reduction in stagnation pressure between hole inlet and exit is used to calculate the loss generated within the coolant hole. Uncertainties in this calculation arise from the assumption of one-dimensional flow, measurement uncertainties, and from the assumption that the exit static pressures with coolant ejection are very similar to the exit static pressures measured without coolant ejection.

After leaving the hole, the coolant mixes with the mainstream. An approximation of the entropy generated during this mixing process can be obtained by assuming that the mixing takes place within a short distance downstream of the hole, thus justifying a constant static pressure mixing calculation.

The mixing calculation is similar in character to the one-dimensional analytical model proposed by Hartsel (1972). For this mixing calculation, the blade passage is divided into several mixing control volumes in the vicinity of the coolant holes. For the row of holes shown in Fig. 5, for example, eight mixing control volumes were used to mix in the coolant from each of the eight holes, with the remaining flow being the "unaffected" mainstream. The flow upstream and downstream of these control volumes is assumed to be isentropic. The mixing control volumes have a width of two and a height of six hole diameters at inlet. The exact dimensions are not important as it was found that varying the streamtube height between two and ten hole diameters had a negligible effect on the result.

In the mixing calculation the equations for the conservation of mass (Eq. (5)), momentum (Eq. (6)), and energy (Eq. (7)) are applied to each of the mixing control volumes. The static pressure is taken to be constant during the mixing process, using the hole exit static pressure measured without coolant ejection.

$$\dot{m}_{\text{inflow}} + \dot{m}_{\text{coolant}} = \dot{m}_{\text{outflow}} \tag{5}$$

$$(\dot{m} \cdot \vec{V})_{\text{inflow}} + (\dot{m} \cdot \vec{V})_{\text{coolant}} = (\dot{m} \cdot \vec{V})_{\text{outflow}} \tag{6}$$

$$(\dot{m} \cdot c_p \cdot T_0)_{\text{inflow}} + (\dot{m} \cdot c_p \cdot T_0)_{\text{coolant}} = (\dot{m} \cdot c_p \cdot T_0)_{\text{outflow}} \tag{7}$$

The outflow values of stagnation pressure and temperature from each of the mixing control volumes are mass averaged to determine the overall stagnation values and the overall loss.

Uncertainties in this calculation arise from measurement uncertainties, from the assumption of one-dimensional flow in the mixing streamtubes, from using the exit static pressures measured without coolant ejection, from the assumption of constant ejection angles to the free stream within a row of holes, and from the assumption of constant static pressure mixing. The real mixing process is not immediate. Denton and Cumpsty (1987) have shown that entropy generation from mixing in accelerating and decelerating flows differs significantly. Nonetheless, most of the mixing will have been completed a short distance downstream of the hole, and so will have taken place at approximately constant static pressure.

The third mechanism that leads to the measured change in loss is the change of entropy generation in the blade passage due to the ejection of coolant. It can be approximated by comparing the measured losses with the sum of the predicted hole and mixing losses. The difference can be attributed to the change in loss production in the blade passage. Uncertainties arise from experimental errors and from errors due to the approximations made in the calculations.

In real engine endwall film-cooling there are additional entropy generation mechanisms not simulated in the cascade experiment. These may include shocks within the coolant holes and at hole exit, and entropy generation due to heat transfer.

Discussion of Results

All Holes Blowing Simultaneously. Figure 6 shows contours of stagnation pressure loss and secondary flow lines for all the holes blowing simultaneously, with and without coolant ejection. The results show the impact of endwall coolant ejection on secondary flow. With increasing blowing, the main passage vortex is confined closer to the endwall. The core of the passage vortex is located at 22 percent span without coolant ejection, at 21 percent span for $M_{\text{inlet}} = 1.0$, and at 11 percent span for $M_{\text{inlet}} = 2.0$.

After its separation off the endwall, the inlet boundary layer and its associated loss are entrained in the passage vortex. In the traversing plane, the passage vortex therefore shows up as a concentrated region of loss for the case without coolant ejection. Figure 6 shows that at $M_{\text{inlet}} = 2.0$ this concentrated region of loss is almost eliminated, as coolant with a high stagnation pressure is ejected into the endwall boundary layer. This agrees with the results of Goldman and McLallin (1977) and Sieverding and Wilputte (1981), who also found a reduction in the depth of the main loss cores at high coolant supply pressures.

Figure 7 shows the integrated loss in the traversing plane and the mixed-out overall cascade loss as variations of inlet blowing ratio. The difference between the two losses is the mixing loss generated when the nonuniform flow in the traversing plane is mixed-out to uniform conditions far downstream. Figure 7 shows that the mixing loss is reduced with increasing inlet blowing ratio. Below $M_{\text{inlet}} \approx 1.4$, the mixing loss with endwall coolant ejection is larger than the mixing loss in the uncooled case. Above $M_{\text{inlet}} \approx 1.4$, it is smaller than in the uncooled case,

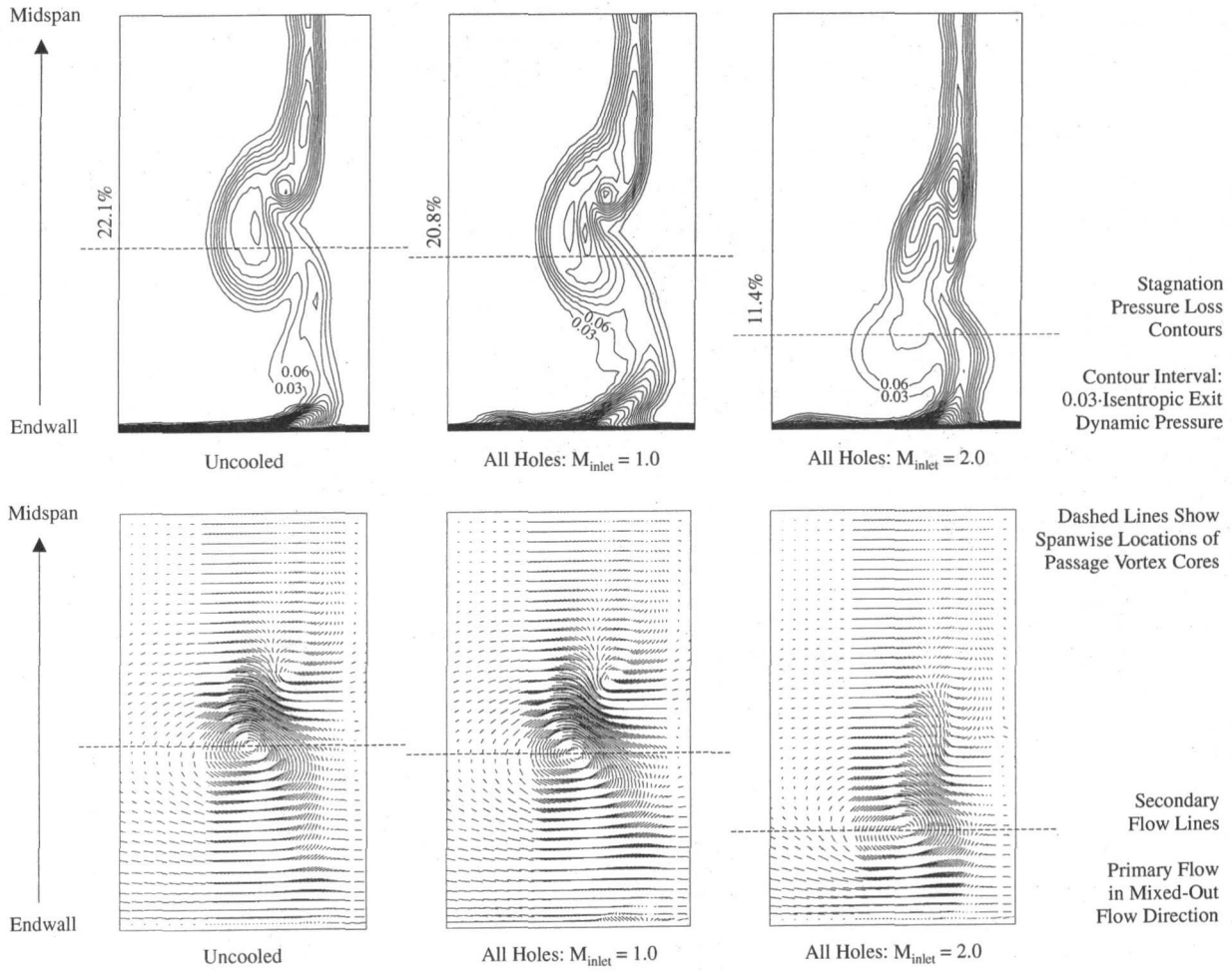

Fig. 6 All cooling holes: contours of stagnation pressure loss and secondary flow lines

indicating fewer nonuniformities to mix out. This can be due to either enhanced mixing upstream of the traversing plane or due to reduced secondary flow. Gregory-Smith and Cleak (1992) also observed reduced mixing losses in an investigation of the effect of high inlet turbulence on secondary flow in a cascade. They concluded that the reduction in mixing losses was probably due to a reduced inlet boundary layer thickness producing a smaller vortex closer to the endwall rather than the turbulence causing a more rapid dissipation of the secondary flows. The same is probably true for the effect observed here. Below $M_{inlet} \approx 1.4$, the local momentum ratios of the coolant jets upstream of the leading edge are below 1.0. This results in the coolant being ejected into the inlet boundary layer with a stagnation pressure lower than the free stream, thus increasing the inlet vorticity and producing stronger secondary flows. Above $M_{inlet} \approx 1.4$, the coolant stagnation pressure is higher than in the free stream. This probably re-energizes the inlet boundary layer and reduces the inlet vorticity, thus reducing secondary flows and subsequent mixing losses downstream.

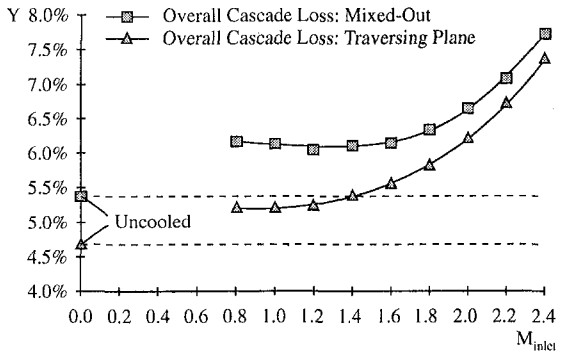

Fig. 7 Traversing plane and mixed-out losses for all holes blowing

The results shown in Fig. 7 display an increase in overall cascade loss due to endwall coolant ejection, with the increase of the mixed-out loss being almost constant over a part of the range of inlet blowing ratios. This characteristic is desirable for the turbine designer, as it results in a similar performance over a range of operating conditions.

Figure 8 shows the mixed-out loss coefficients based on the three reference inlet stagnation pressures described above, for all the coolant holes blowing simultaneously. The cascade loss excluding the hole losses does not differ greatly from the loss without coolant ejection. The difference between the two is due to the loss generation during the mixing of the coolant with the mainstream and the loss reduction due to the change in loss generation in the blade passage. These two loss changing mechanisms seem to be of the same order, with the loss generation dominating below $M_{inlet} \approx 1.4$ and the loss reduction dominating between $M_{inlet} \approx 1.4$ and $M_{inlet} \approx 2.4$.

The variation of the dimensionless mixed-out exit stagnation pressure in Fig. 8 shows that above $M_{inlet} \approx 1.6$ the following blade row can experience a flow with an average stagnation pressure that is higher than in the uncooled case, thus changing the matching point of the blade row.

Figure 9 shows the increase in mixed-out loss divided by the coolant massflow, which is expressed as a percentage of the

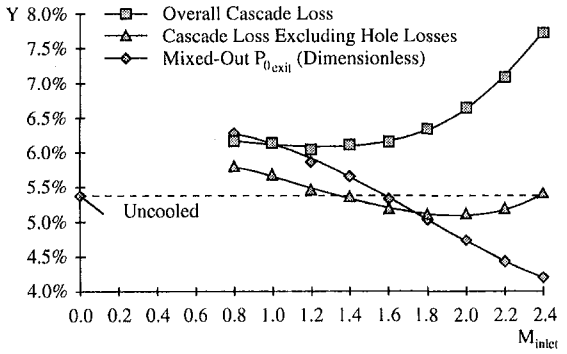

Fig. 8 Mixed-out losses for all holes blowing simultaneously

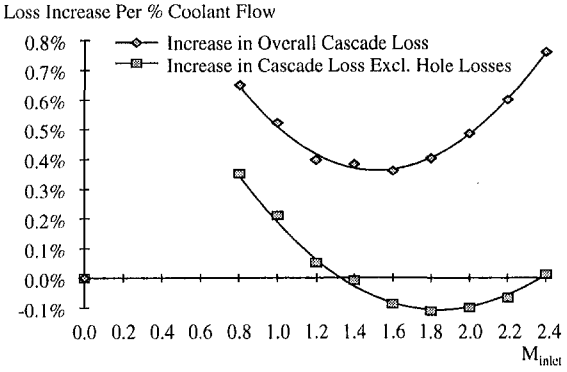

Fig. 9 Increase in loss, per percent coolant, for all cooling holes blowing simultaneously

massflow in the cooled half of the blade passage. As the slopes of the curves in Fig. 8 already indicate, Fig. 9 shows that there are optimum values of M_{inlet}. The loss increase per unit coolant massflow in the blade passage (excluding the hole losses) is at a minimum at $M_{inlet} \approx 1.8$. For this condition, the average ratio of the streamwise component of the coolant velocity to the local free-stream velocity is 1.01. This average has been calculated from the local hole blowing ratios and the coolant ejection angles relative to the surface and the free stream, assuming constant ejection angles within a row of holes. It can be concluded that the loss increase in the blade passage, per unit coolant massflow, is at a minimum when the streamwise velocity components of the coolant and the mainstream are equal. When the losses generated within the coolant holes are included, the minimum shifts to a value of $M_{inlet} \approx 1.6$. This is probably due to the loss generation within the coolant holes increasing disproportionally with coolant massflow.

Goldman and McLallin (1977) also evaluated the loss per percent coolant massflow for their endwall film-cooling configuration. Their results show an increase with increasing coolant supply pressures without a minimum. This is probably because they only had a few holes upstream of where one would expect the lift-off lines on the endwall. As a result, the possible loss reduction due to the change in loss generation in the blade passage must have been much smaller than in the current investigation.

Individual Rows of Holes. Aerodynamic measurements were also performed for individual rows of holes. Figure 10 shows the resulting contours of stagnation pressure loss for $M_{inlet} = 2.0$. The contours for $M_{inlet} = 1.0$ are not shown, as they display the same trends with much smaller variations. For $M_{inlet} = 2.0$, the spanwise locations of the passage vortex cores were at 18 percent span for both the ejection from the row of holes at the leading edge and from the row of holes at 30 percent axial chord, at 21 percent span for the row at 60 percent axial chord, and at 22 percent for the row at 90 percent axial chord. Comparing Fig. 10 with the contour for the unblown case shown in Fig. 6, it can be seen that ejection from the row of holes at the leading edge and at 30 percent axial chord changes the secondary flow by confining the passage vortex close to the endwall and by reducing the depth of the associated loss core. Ejection from the row of holes at 60 percent axial chord does not have a visible effect and ejection from the row at 90 percent axial chord only seems to thicken the exit boundary layer.

The mixed-out losses for the individual rows of holes, divided by the coolant mass flow expressed as a percentage of the mass flow in the cooled half of the blade passage, are shown in Fig. 11. As was to be expected, the loss per unit coolant mass flow increases with ejection toward the rear of the blade passage as the exit static pressure decreases.

Table 1 shows the comparison between the sum of the measured losses for the individual rows of holes and the losses measured for all the holes blowing simultaneously. The comparison shows that the individual losses cannot be added linearly, probably due to the effect of coolant ejection on the change of loss generation in the blade passage.

Loss Decomposition. The losses generated within the coolant holes and from the mixing of the coolant with the mainstream have been calculated for the individual rows of holes. They have been divided by the coolant mass flow, expressed as a percentage of the massflow in the cooled half of the blade passage, and are shown together with the measured losses in Fig. 12. The difference between the sum of the predicted losses and the measured losses is a measure of the change in loss generation in the blade passage.

The calculated loss components in Fig. 12 illustrate that most of the loss is generated within the coolant holes. For injection in approximately the free-stream direction (holes at the leading edge, 30 percent axial chord, and 60 percent axial chord), the loss generated within the coolant holes is approximately double the loss generated during the mixing of the coolant with the mainstream. For injection at an angle of approximately 35 deg to the mainstream (holes at 90 percent axial chord) the mixing loss increases to the amount of loss generated within the coolant holes.

The sums of the hole and mixing losses compare well with the measured losses for the rows of holes at 60 and 90 percent axial chord. For the rows of holes at the leading edge and at 30 percent axial chord, the measured losses are lower than the sum of the hole and mixing losses, indicating a reduction of the losses generated in the blade passage.

Surface-flow visualization by Friedrichs et al. (1996) has shown the three-dimensional separation of the inlet boundary layer on the endwall to be delayed by ejection upstream of the lift-off lines, thus changing the secondary flow on the endwall. Figure 10 has shown that only ejection upstream of the lift-off lines changes the secondary flow downstream of the blade passage by changing the spanwise position of the passage vortex and the depth of the loss core associated with the inlet boundary layer. Together with the reduction in secondary losses shown in Fig. 12, these results support the conclusion that only ejection from holes located upstream of the lift-off lines can significantly change secondary flow and reduce its associated losses.

Comparing the sum of the predicted hole and mixing losses in Fig. 12 with the measured loss increase for all the holes blowing simultaneously gives a loss reduction of 1.0 percent for $M_{inlet} = 2.0$. This reduction will be the result of several mechanisms. First, the delay of the three-dimensional separation of the inlet boundary layer on the endwall results in a reduced wetted area for the new, thin endwall boundary layer. This will probably reduce the loss generated in the endwall boundary layer, as the extremely thin new boundary layer is expected to generate high losses per unit surface area. Harrison (1989)

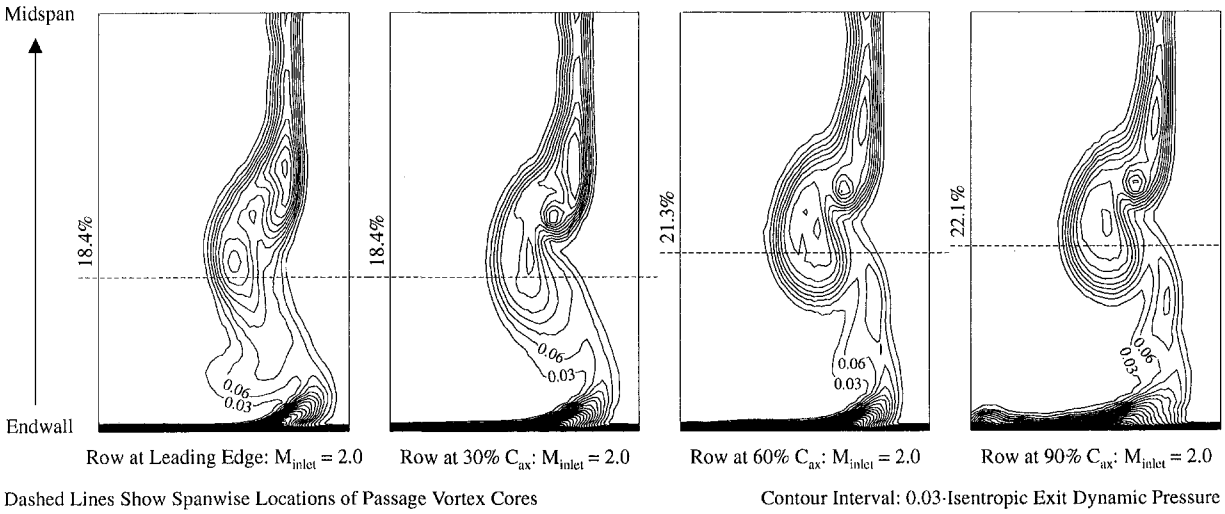

Fig. 10 Contours of stagnation pressure loss for individual rows of cooling holes

predicted the loss generated in the entire endwall boundary layer of the investigated cascade to be approximately 1.0 percent. So although it will probably reduce loss, this mechanism will only reduce it by a fraction of the predicted 1.0 percent.

Second, ejection of high stagnation pressure coolant into the inlet boundary layer will reduce the inlet vorticity, thus producing a smaller passage vortex closer to the endwall. The inlet loss, which Harrison (1989) determined to be 0.6 percent for this cascade, will be reduced. The loss generated by the inlet boundary layer as it mixes-out within and downstream of the blade passage will also be reduced. Figure 7 shows that for M_{inlet} = 2.0 the mixing loss between the traversing plane and a fully mixed-out condition far downstream is reduced by about 0.3 percent, probably due to the effect of a reduced inlet vorticity.

A further loss reduction mechanism is due to a reduced spanwise extent of the secondary flow region. Secondary flow interferes with the blade suction surface boundary layers and can result in losses due to flow separations and premature transition. A reduced spanwise extent of these interferences can result in associated loss reductions.

Loss reduction may also be possible downstream of the lift-off lines as a result of the thickening of the new, thin endwall boundary layer due to the ejection of coolant. This effect is visible in Fig. 10 as a result of the ejection of coolant from the row of holes at 90 percent axial chord. A thicker boundary layer will reduce local entropy generation. On the other hand, the ejection of high-turbulence coolant may promote transition in previously laminar regions and thus increase entropy generation. The observed reduction in secondary losses is the result of a combination of all of these mechanisms.

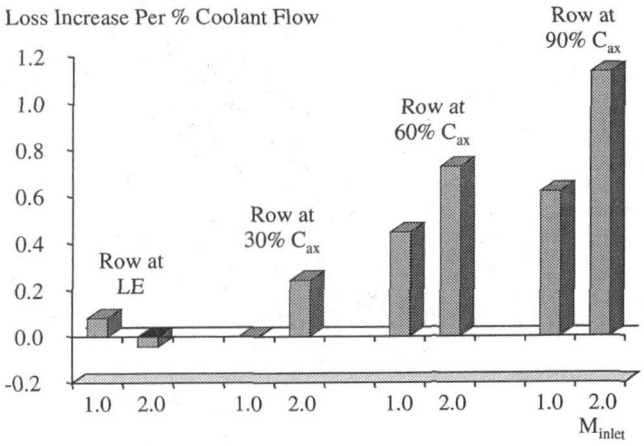

Fig. 11 Increase in overall cascade loss, per percent coolant mass flow, for individual rows of holes at two inlet blowing ratios

Table 1 Comparison of the loss increases due to all holes blowing simultaneously and all holes blowing as individual rows of holes

Overall Cascade Loss Increase	M_{inlet} = 1.0	M_{inlet} = 2.0
Σ of Individual Rows of Holes	0.59%	1.53%
All Holes Simultaneously	0.76%	1.27%

Conclusions

Endwall film-cooling increases losses. The increase is almost constant over a range of coolant supply pressures. Viewed as an increase per percent coolant massflow, an optimum coolant supply pressure is reached when the streamwise velocity components of the coolant and free stream are similar.

Losses generated within the coolant holes contribute significantly to the overall loss increases and can be up to double the losses generated during the mixing of the coolant with the mainstream. Excluding these hole losses, the change in overall cascade loss due to endwall film-cooling is small, and can be both positive and negative depending on the coolant supply pressure.

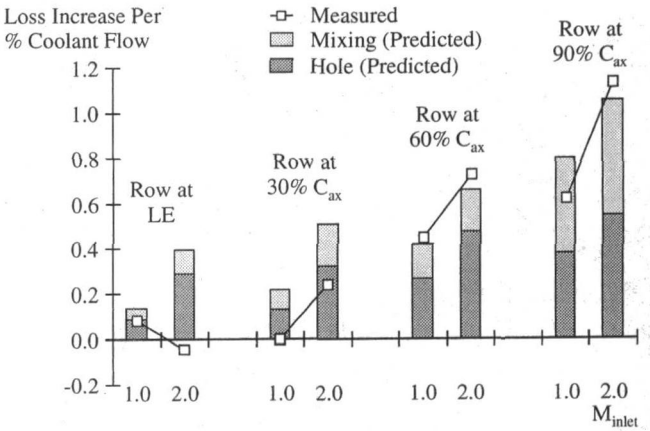

Fig. 12 Comparison of measured and calculated losses, per percent coolant mass flow, for individual rows of holes

Testing rows of holes individually has shown that the loss increases cannot be added linearly. Ejection into regions of low static pressure was shown to increase the loss per unit coolant massflow.

Ejection from the holes located upstream of the lift-off lines can significantly change the secondary flow and reduce its associated losses. The spanwise extent of the secondary flow effects and the depth of the associated loss cores are reduced, thus improving the flow into the following blade row. The reduction of the associated losses is the result of a combination of several mechanisms that are not yet fully understood.

The results presented in this paper and by Friedrichs et al. (1996) have shown that it is necessary to take the three-dimensional nature of the endwall flow into account in the design of endwall film-cooling configurations. The interaction of the ejected coolant with the secondary flow in the blade passage not only influences the distribution of the coolant and hence the cooling effectiveness, but also influences the generation of aerodynamic loss. Ejection locations have to be viewed with respect to the three-dimensional separation lines on the endwall, taking account of the fact that these can be changed due to upstream endwall coolant ejection.

Acknowledgments

The authors are grateful for the support provided by Rolls-Royce plc, the Engineering & Physical Sciences Research Council (EPSRC), and the Frankfurt Main Flughafen Stiftung (Frankfurt Main Airport Foundation). They would also like to thank Prof. Denton for the use of the cascade and the technical staff of the Whittle Laboratory for their assistance.

References

Bario, F., Leboeuf, F., Onvani, A., and Seddini, A., 1990, "Aerodynamics of Cooling Jets Introduced in the Secondary Flow of a Low-Speed Turbine Cascade," ASME JOURNAL OF TURBOMACHINERY, Vol. 112, pp. 539–546.

Biesinger, T. E., 1993, "Secondary Flow Reduction Techniques in Linear Turbine Cascades," PhD Thesis, University of Durham; see also Biesinger, T. E., and Gregory-Smith, D. G., 1993, "Reduction in Secondary Flows and Losses in a Turbine Cascade by Upstream Boundary Layer Blowing," ASME Paper No. 93-GT-114.

Blair, M. F., 1974, "An Experimental Study of Heat Transfer and Film Cooling on Large-Scale Turbine Endwalls," ASME *Journal of Heat Transfer,* Vol. 96, pp. 524–529.

Bourguignon, A. E., 1985, "Etudes des Transferts Thermiques sur les Plates-Formes de Distributeur de Turbine avec et sans Film de Refroidissement," AGARD-CP-390, *Heat Transfer and Cooling in Gas Turbines.*

Denton, J. D., and Cumpsty, N. A., 1987, "Loss Mechanisms in Turbomachines," IMechE Paper No. C260/87.

Friedrichs, S., Hodson, H. P., and Dawes, W. N., 1996, "Distribution of Film-Cooling Effectiveness on a Turbine Endwall Measured Using the Ammonia and Diazo Technique," ASME JOURNAL OF TURBOMACHINERY, Vol. 118, pp. 613–621.

Goldman, L. J., and McLallin, K. L., 1977, "Effect of Endwall Cooling on Secondary Flows in Turbine Stator Vanes," AGARD-CPP-214.

Granser, D., and Schulenberg, T., 1990, "Prediction and Measurement of Film Cooling Effectiveness for a First-Stage Turbine Vane Shroud," ASME Paper No. 90-GT-95.

Gregory-Smith, D. G., and Cleak, J. G. E., 1992, "Secondary Flow Measurements in a Turbine Cascade With High Inlet Turbulence," ASME JOURNAL OF TURBOMACHINERY, Vol. 114, pp. 173–183.

Harasgama, S. P., and Burton, C. D., 1992, "Film Cooling Research on the Endwall of a Turbine Nozzle Guide Vane in a Short Duration Annular Cascade: Part 1—Experimental Technique and Results," ASME JOURNAL OF TURBOMACHINERY, Vol. 114, pp. 734–741.

Harrison, S., 1989, "The Influence of Blade Stacking on Turbine Losses," Ph.D. Thesis, University of Cambridge; see also Harrison, S., 1990, "Secondary Loss Generation in a Linear Cascade of High-Turning Turbine Blades," ASME JOURNAL OF TURBOMACHINERY, Vol. 112, pp. 618–624.

Hartsel, J. E., 1972, "Prediction of Effects of Mass-Transfer Cooling on the Blade-Row Efficiency of Turbine Airfoils," AIAA Paper No. 72-11.

Jabbari, M. Y., Marston, K. C., Eckert, E. R. G., and Goldstein, R. J., 1996, "Film Cooling of the Gas Turbine Endwall by Discrete-Hole Injection," ASME JOURNAL OF TURBOMACHINERY, Vol. 118, pp. 278–284.

Leylek, J. H., and Zerkle, R. D., 1994, "Discrete-Jet Film Cooling: A Comparison of Computational Results With Experiments," ASME JOURNAL OF TURBOMACHINERY, Vol. 116, pp. 358–368.

Sieverding, C. H., 1984, "Recent Progress in the Understanding of Basic Aspects of Secondary Flows in Turbine Blade Passages," ASME *Journal of Engineering for Gas Turbines and Power,* Vol. 107, pp. 248–257.

Sieverding, C. H., and Wilputte, P., 1981, "Influence of Mach Number and Endwall Cooling on Secondary Flows in a Straight Nozzle Cascade," ASME *Journal of Engineering for Power,* Vol. 103, No. 2.

Takeishi, K., Matsuura, M., Aoki, S., and Sato, T., 1990, "An Experimental Study of Heat Transfer and Film Cooling on Low Aspect Ratio Turbine Nozzles," ASME JOURNAL OF TURBOMACHINERY, Vol. 112, pp. 488–496.

Wilfert, G., and Fottner, L., 1996, "The Aerodynamic Mixing Effect of Discrete Cooling Jets With Mainstream Flow on a Highly Loaded Turbine Blade," ASME JOURNAL OF TURBOMACHINERY, Vol. 118, pp. 468–478.

Numerical Simulation of Turbine Blade Boundary Layer and Heat Transfer and Assessment of Turbulence Models

J. Luo[1]
Graduate Student.
Mem. ASME

B. Lakshminarayana
Evan Pugh Professor and Director.
Fellow ASME

Center for Gas Turbine and Power,
The Pennsylvania State University,
University Park, PA 16802

The boundary layer development and convective heat transfer on transonic turbine nozzle vanes are investigated using a compressible Navier–Stokes code with three low-Reynolds-number $k-\epsilon$ models. The mean-flow and turbulence transport equations are integrated by a four-stage Runge–Kutta scheme. Numerical predictions are compared with the experimental data acquired at Allison Engine Company. An assessment of the performance of various turbulence models is carried out. The two modes of transition, bypass transition and separation-induced transition, are studied comparatively. Effects of blade surface pressure gradients, free-stream turbulence level, and Reynolds number on the blade boundary layer development, particularly transition onset, are examined. Predictions from a parabolic boundary layer code are included for comparison with those from the elliptic Navier–Stokes code. The present study indicates that the turbine external heat transfer, under real engine conditions, can be predicted well by the Navier–Stokes procedure with the low-Reynolds-number $k-\epsilon$ models employed.

Introduction

An improved understanding of and predictive capability for turbine viscous flowfield and heat transfer is crucial for achieving higher turbine inlet temperatures and for minimizing various aerodynamic losses. The turbine flow and thermal fields are dominated by complex flow phenomena including laminar, transitional, and turbulent flows; stagnation flow; large pressure gradients and free-stream turbulence; three-dimensional vortical flows; and unsteady separated flow at the trailing edge. Simoneau and Simon (1993) reviewed the progress in predicting heat transfer in the turbine gas path in three major areas: transition (for midspan flows), three-dimensional endwall flows, and film-cooling. A comprehensive review of transition in gas turbines was presented by Mayle (1991), in which three modes of transition: natural transition, bypass transition, and separation-induced transition were discussed. For transition at high free-stream turbulence levels, such as is typically found in turbines, the linear stability mechanism (i.e., the two-dimensional Tollmien–Schlichting instability wave) is bypassed such that the turbulence spots are directly produced, which leads to the so-called bypass transition. The third transition mode is caused by the separation of laminar boundary layer, which may occur in flows subjected to adverse pressure gradients.

Schmidt and Patankar (1992) presented a detailed analysis of the mechanism by which low-Reynolds-number (LRN) $k-\epsilon$ models simulate the transition process. Savill (1993) coordinated a comprehensive comparison of several test cases of flat-plate boundary layers undergoing bypass transition with various LRN turbulence models. A number of researchers have applied LRN $k-\epsilon$ models to calculate convective heat transfer to turbine blading, e.g., Hylton et al. (1983), and Schmidt and Patanker (1992). These computations are performed with boundary-layer codes, which are efficient and can provide high resolution of the viscous layer. However, the boundary layer solutions are sensitive to the starting profile and conditions specified at the edge of the boundary layer. The prediction of transition by a boundary layer code (with LRN $k-\epsilon$ models) is particularly sensitive to the initial profile of ϵ, which is not well defined and not available from experimental measurements, thus increasing the uncertainty about the prediction accuracy (Savill, 1993). For separated flows or three-dimensional endwall flows, Navier–Stokes procedures must be used. There have been some attempts using Navier–Stokes procedures with LRN $k-\epsilon$ models to compute turbine heat transfer, e.g., Hah (1989), Ameri and Arnone (1994), and Luo and Lakshminarayana (1995). However, mixed success has been achieved; there is no consistency in the quality of predictions for various test cases used.

The objective of this paper is to develop a numerical procedure for computation of coupled turbine aerodynamics and heat transfer, and to assess the accuracy and suitability of various turbulence models for predicting transition and heat transfer. Two modes of transition, the bypass transition and the separation-induced transition, are studied comparatively. Numerical predictions are compared with the experimental data obtained by Hylton et al. (1983) at Allison Engine Company. A two-dimensional boundary layer code, TEXSTAN (Crawford, 1985), was employed to predict heat transfer for comparison with the Navier–Stokes solutions.

Turbulence Models and Numerical Techniques

The compressible Navier–Stokes equations in conservative form are utilized, with the effective stress tensor τ_{ij} and the effective heat flux vector q_i given by

$$\tau_{ij} = \tau_{lij} - \rho\overline{u_i u_j} = (\mu_l + \mu_t)[(\partial U_i/\partial x_j + \partial U_j/\partial x_i) - \tfrac{2}{3}\delta_{ij}\partial U_k/\partial x_k] - \tfrac{2}{3}\delta_{ij}\rho k \quad (1)$$

$$q_i = -C_p\left(\frac{\mu_l}{\mathrm{Pr}_l} + \frac{\mu_t}{\mathrm{Pr}_t}\right)\frac{\partial T}{\partial x_i} \quad (2)$$

where μ_t is the turbulent eddy viscosity, which is computed using the $k-\epsilon$ model; $\mathrm{Pr}_l = 0.9$.

[1] Current address: Solar Turbines Inc., CA.

Contributed by the Heat Transfer Committee for publication in the JOURNAL OF TURBOMACHINERY. Manuscript received by the Heat Transfer Committee October 1, 1996. Associate Technical Editor: M. G. Dunn.

Table 1 Low-Reynolds-number functions used in CH, LB, and FLB models

Model	f_μ	f_1	f_2
CH	$1-\exp(-0.0115y^+)$	1.0	$1-0.22\exp(-\mathrm{Re}_t^2/36)$
LB	$[1-\exp(-0.0165\mathrm{Re}_y)]^2(1+20.5/\mathrm{Re}_t)$	$1+(0.06/f_\mu)^3$	$1-\exp(-\mathrm{Re}_t^2)$
FLB	$0.4f_w/\sqrt{\mathrm{Re}_t}+(1-0.4f_w/\sqrt{\mathrm{Re}_t})[1-\exp(-\mathrm{Re}_y/42.63)]^3$	1.0	$(1-0.22\exp(-\mathrm{Re}_t^2/36))f_w^2$

Low-Reynolds-Number $k-\epsilon$ Model. In the low-Reynolds-number $k-\epsilon$ model, the eddy viscosity is obtained from the Prandtl–Kolmogorov relation:

$$\mu_t = C_\mu f_\mu \rho \frac{k^2}{\epsilon} \tag{3}$$

where $C_\mu = 0.09$ and f_μ is a near-wall damping function given in Table 1. The low-Reynolds-number $k-\epsilon$ equations can be written as

$$\frac{\partial(\rho k)}{\partial t} + \frac{\partial(\rho U_i k)}{\partial x_i} = \frac{\partial}{\partial x_j}\left[\left(\mu + \frac{\mu_t}{\sigma_k}\right)\frac{\partial k}{\partial x_j}\right] + \rho P_k - \rho(\epsilon + D) \tag{4}$$

$$\frac{\partial(\rho \epsilon)}{\partial t} + \frac{\partial(\rho U_i \epsilon)}{\partial x_i} = \frac{\partial}{\partial x_j}\left[\left(\mu + \frac{\mu_t}{\sigma_\epsilon}\right)\frac{\partial \epsilon}{\partial x_j}\right] + \rho\frac{\epsilon}{k}[C_{\epsilon 1} f_1 P_k - C_{\epsilon 2} f_2 \epsilon] + \rho E \tag{5}$$

where D, E, f_1 and f_2 are near-wall terms.

Three representative LRN $k-\epsilon$ models are evaluated: Chien's (1982) version (denoted CH), Lam–Bremhorst's (1981) version (denoted LB); and a recent model from Fan, Lakshminarayana, and Barnett (1993, denoted as FLB). Chien's $k-\epsilon$ model is popular in Navier–Stokes solvers due to its good numerical stability, which can be attributed to its near-wall asymptotic consistency, as shown by Patel et al. (1985) and the algebraic form of its near-wall terms. However, the important low-Reynolds-number function f_μ in this model depends only on y^+, which makes it inaccurate for separated flows. The LB model does not contain y^+ in the low-Reynolds number functions, but it is not asymptotically consistent in the near-wall region (Patel et al., 1985). Fan et al. (1993) developed an improved LRN $k-\epsilon$ model with near-wall asymptotic consistency. This model has been shown to capture wake-induced transition on compressor blades quite accurately (Fan and Lakshminarayana, 1996).

Table 1 gives the near-wall functions in the three models described above, where the near-wall function in the FLB model is given by

$$f_w = 1 - \exp\left\{-\frac{\sqrt{\mathrm{Re}_y}}{2.30} + \left(\frac{\sqrt{\mathrm{Re}_y}}{2.30} - \frac{\mathrm{Re}_y}{8.89}\right) \times \left[1 - \exp\left(-\frac{\mathrm{Re}_y}{20}\right)\right]^3\right\} \tag{6}$$

Numerical Procedure

Navier–Stokes Code. The Navier–Stokes code (hereafter referred to as RK2D, Kunz and Lakshminarayana, 1992) uses a standard four-stage Runge–Kutta scheme. Fourth-order artificial dissipation is included to damp high wave number errors and second-order artificial dissipation is added to improve the shock capturing. Second-order artificial dissipation is also added to the k and ϵ equations to prevent odd–even decoupling since the convection terms in Eqs. (4) and (5) are discretized with second-order accurate central differences. Multiplied by the square of the normalized local velocity, $(U/U_\infty)^2$, the smoothing in both mean-flow and turbulence equations was reduced

Nomenclature

ARC = distance along airfoil surface from stagnation point to trailing edge
C_f = skin friction coefficient (nondimensionalized by local free-stream dynamic head)
C_p, C_v = specific heat at constant pressure and volume
C_μ, C_1, C_2, $C_{\epsilon 1}$, $C_{\epsilon 2}$ = turbulence modeling parameters
D, E = near-wall terms in $k-\epsilon$ equation
f_1, f_2, f_μ, f_w = near-wall damping functions
h = shape factor = δ^*/θ
H = heat transfer coefficient = $q_w/(T_{o1} - T_w)$, W/m^{2}K
k = turbulent kinetic energy = $\overline{u_i u_i}/2$
K = acceleration factor = $(\nu/U_e^2)dU_e/dS$
L = turbulence length scale
M = Mach number
P = pressure
P_k = production rate of turbulent kinetic energy = $-\overline{u_i u_j}(\partial U_i/\partial x_j)$
Pr_l, Pr_t = laminar and turbulent Prandtl numbers
PS = pressure surface
q_i = Cartesian components of heat flux vector (Eq. (2))
Re = Reynolds number
Re_y, Re_t = turbulent Reynolds numbers ($\mathrm{Re}_y = (\sqrt{k}y/\nu)$, $\mathrm{Re}_t = (k^2/\nu\epsilon)$)
Re_θ = momentum thickness Reynolds number
S = coordinate along blade surface (positive for SS and negative for PS)
SS = suction surface
T = temperature
Tu_∞ = free-stream turbulence intensity
u_τ = friction velocity
U_i = mean velocity component
U^+ = U/u_τ
u_i = fluctuating velocity component
$\overline{u_i u_j}$ = Reynolds stress
x = coordinate along axial chord
y = coordinate in tangential direction (pitchwise)/normal distance to the wall
y^+ = wall distance variable = yu_τ/ν
δ_{ij} = Kronecker delta
δ, δ^* = boundary layer and displacement thicknesses
ϵ = dissipation rate of turbulent kinetic energy
θ = boundary layer momentum thickness
μ_l, μ_t = molecular, turbulent viscosity
ν = kinematic viscosity
ρ = density
σ_k, σ_ϵ = Prandtl numbers in k and ϵ equations
τ_{ij} = Cartesian components of stress tensor (Eq. (1))

Subscripts

e = boundary layer edge
is = isentropic
1, 2 = cascade inlet, exit condition
l, t = laminar, turbulent
o = stagnation condition
w = wall
∞ = inlet free stream

Table 2 Computed cases

Cases	P_{o1}(Bar)	T_{o1} (k)	$Re_{is,2}$ (10^6)	$M_{is,2}$	Tu_∞(%)	T_w (k)
Mark15	2.643	772	1.6	0.90	8.3	540
Mark63	2.765	771	2.0	0.90	8.3	547
Mark58	3.907	719	2.5	0.91	8.3	597
C3X148	2.448	802	1.5	0.91	6.5	586
C3X158	2.435	808	1.5	0.90	8.3	590
C3X113	3.232	781	2.0	0.89	8.3	578
C3X156	4.007	781	2.5	0.89	8.3	656

to zero near the wall to avoid contamination of the solution by artificial dissipation.

An H-grid was used in the RK2D. The use of a combination of algebraic and elliptic methods (Basson et al., 1993) makes it possible to generate a smooth grid while maintaining strict control over grid spacing and orthogonality near the blade surface. The grid orthogonality inside blade boundary layers is highly desirable for implementation of low-Reynolds-number turbulence models.

At the inlet, the total pressure, total temperature, and flow angle are specified. The left-running Riemann invariants are extrapolated from the interior of computation domain. The back pressure is specified at the outlet for subsonic (axial) outlet flow.

For all three $k-\epsilon$ models, k is zero at the wall. The ϵ in the CH model is the isotropic component of the dissipation rate, and thus should be zero at the wall. For the LB and FLB models, the normal gradient of ϵ is set to zero at the wall as suggested by Patel et al. (1985) and Fan et al. (1993). Constant values of k and ϵ are imposed at the inlet based on specified free-stream turbulence intensity and length scale:

$$Tu_\infty = \frac{\sqrt{\frac{2}{3}k_\infty}}{U_\infty} \tag{7}$$

$$\epsilon_\infty = k_\infty^{1.5}/L_\infty \tag{8}$$

where the value of Tu_∞ is available from experimental data. Following Hah (1989), the free-stream turbulence length scale L_∞ is assumed to be 1 percent of the pitch since the exact value of L_∞ is not reported by Hylton et al. (1983). At the cascade exit, values for k, ϵ and mean flow variables are extrapolated along j = constant grid lines.

The Navier–Stokes code with the three LRN $k-\epsilon$ turbulence models was validated by computing a flat-plate turbulent boundary layer. The predictions of mean-velocity profile ($u^+ \sim y^+$) in the near-wall region with the three models were in good agreement with the standard linear-log law. The predicted turbulence quantities show good agreement with the experimental data (Patel et al., 1985).

Boundary Layer Code—TEXSTAN. The TEXSTAN code (Crawford, 1985) is an extension of the well-known boundary layer code STAN5. A variety of LRN two-equation turbulence models are available from this code.

Computation of Turbine Cascade Aerodynamics and Heat Transfer

Test Cases and Numerical Details. The Mark II and C3X turbine guide vane cascades studied by Hylton et al. (1983) and Nealy et al. (1984) were selected as the primary test cases in the present work. The two cascades have close chord length (around 14 cm) and turning angle (around 71 deg). The test conditions are given in Table 2 for these two cascades.

As shown in Table 2, the test conditions ($Re_{is,2}$, $M_{is,2}$ and Tu_∞) are close to actual engine operations. The total and wall temperatures (T_{o1} and T_w) are not representative of real engines, but the ratio $T_w/T_{o1} \approx 0.7$ is similar to those encountered in modern jet engines.

In the present computations, a 151×99 H-grid is employed. The predictions with a finer grid (171×121), were found to be very close to those obtained from the 151×99 grid. About 25 to 35 orthogonal grid points are distributed inside the boundary layers. The first grid point away from the wall is located at $y^+ \approx 1$ in converged solutions. Both the original blade profiles and the blade profiles modified with cusped trailing edges have been used in the computations. It is found that the addition of a cusped trailing edge greatly reduces the residue level in the trailing edge region and required values of artificial dissipations, without influencing the upstream boundary layer development. The modified blade profiles with cusped trailing edges for both Mark II and C3X airfoils are used in the heat transfer computations presented below.

Convergence criteria are taken as three decades drop of the residuals for rms density and turbulent kinetic energy. The difference between the mass flow rate at the inlet and at the exit is typically less than 0.1 percent of the inlet mass flow rate. The computations of all these cases, by all three models, have been carried out with identical grids, boundary conditions, artificial dissipation rates and convergence criteria for accurate comparison and assessment. The converged solution from the CH model is used to initialize the computations with LB model and FLB model, respectively. It normally takes less than half an hour of CPU on the CRAY-YMP to obtain a convergent solution.

Blade Surface Pressure Distribution. It is known that the transition of turbine boundary layers is greatly affected by the free-stream turbulence level and the surface pressure gradient. Increased free-stream turbulence promotes early transition, while large flow acceleration tends to delay transition. The Reynolds number and the Mach number (e.g., the shock wave location) also influence the boundary layer transition.

As shown in Fig. 1(a), the predicted surface pressure distributions are in excellent agreement with the data for both cascades. The pressure distributions are similar on the pressure surfaces of these two airfoils. However, there is significant difference in the suction surface pressure distributions. A very strong adverse pressure gradient is clearly seen in the region from about 26 to 34 percent suction surface arc length (i.e., ARC) on the Mark II airfoil, while the pressure distribution on the C3X airfoil suction surface exhibits only mild adverse gradient.

The predicted value of acceleration factor K ($K = (\nu/U_e^2)dU_e/dS$) is very helpful in an understanding of the boundary layer development, including transition and re-laminarization on the blade. Figure 1(b) shows the acceleration factors along both surfaces for Mark II and C3X airfoils at $Re_{is,2} \approx 1.5 \times 10^6$. For values of K larger than 3.0×10^{-6} (relaminarization criterion), transition is suppressed for low free-stream turbulence, and the turbulent boundary layer begins to relaminarize. Over about half the length of the pressure surface, K is much larger than 3.0×10^{-6} for the Mark II airfoil. In contrast, K is larger than the criterion only in a small region close to the leading edge on the C3X pressure surface. On the suction surface, Mark II airfoil exhibits a sharp spike of negative acceleration at about 30 percent surface arc length. This spike corresponds to the large adverse pressure gradient observed in that region (Fig. 1(a)). The C3X airfoil's acceleration factor on the suction surface is seen to be close to zero except the region near the leading edge (Fig. 1(b)).

Boundary Layer Development and Heat Transfer for Mark II and C3X. The predictions of heat transfer rate (normalized by H_{ref}, H_{ref} = 1135 W/K/m^2) for Mark15 (Table 2) by both the Navier–Stokes and the boundary-layer methods are presented in Fig. 2(a). The LB $k-\epsilon$ model used in the bound-

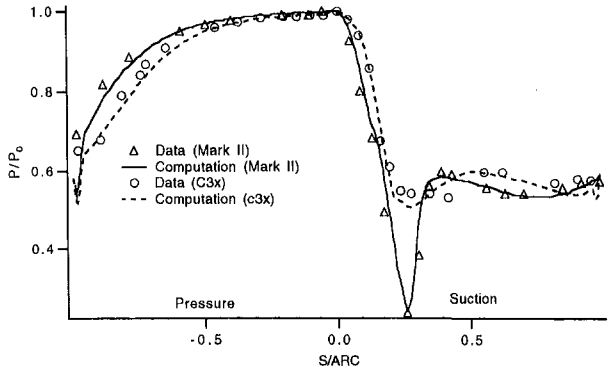

Fig. 1(*a*) Surface static pressure distribution (for cases with $M_{is2} = 0.90$, Mark15 and C3X158)

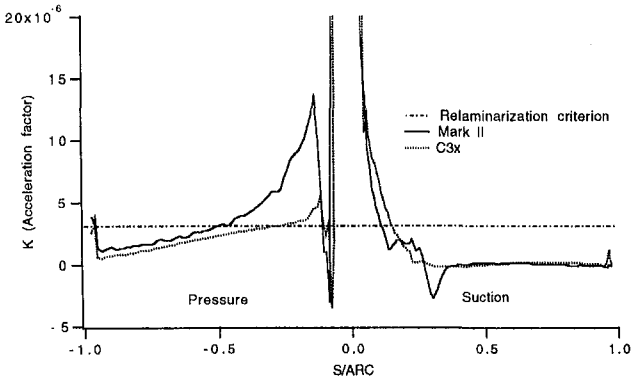

Fig. 1(*b*) Acceleration factors for above cases (Mark15 and C3X158)

ary-layer code is the same as that in the Navier–Stokes code. The boundary layer prediction on the pressure side is in good agreement with the measurement. The Navier–Stokes predictions also agree with the data well, the prediction by the CH $k-\epsilon$ model being the best. The LB $k-\epsilon$ model (in the Navier–Stokes code) predicts a slightly early transition, which results in an overprediction of the heat transfer to the rear of the surface. The heat transfer over a large region near the midchord is underpredicted by the FLB $k-\epsilon$ model because this model predicts a delayed transition. Some difference is observed between the Navier–Stokes prediction and the boundary layer prediction using the same LB $k-\epsilon$ model. This difference can be attributed to the difference in grid resolution, free-stream turbulence level as well as the discretization scheme in these two codes.

On the suction side, the parabolic boundary layer computation is terminated around $S/\text{ARC} = 26$ percent due to separation, as shown in Fig. 2, while the elliptic Navier–Stokes computations with all the models have captured the sharp increase in heat transfer due to separation-induced transition, with the prediction by the FLB $k-\epsilon$ model being the best. The transition onset location is observed to be coincident with the starting location of strong adverse pressure gradient on the suction surface (i.e., around 26 percent arc length, see Figs. 1(*a*) and 1(*b*)). The prediction by the CH $k-\epsilon$ model exhibits an overshoot after the transition, which is due to the poor performance of this model near the reattachment point. The major deficiency of the CH $k-\epsilon$ model lies in its use of y^+ in the near wall damping function f_μ. The wall shear stress is reduced to zero at the separation point, which makes the inner variable y^+ become zero for any value of y. Thus the damping of eddy viscosity is applied even to the outer region of the flow, which is clearly incorrect.

The calculated skin friction coefficients (nondimensionalized by local free-stream dynamic head) are plotted in Fig. 2(*b*). Though experimental data are not available for the C_f, the agreement between the heat transfer computation and data provides confidence in the accuracy of the C_f prediction through the Reynolds analogy. Indeed, the transition location indicated by the variation in skin friction is consistent with that derived from

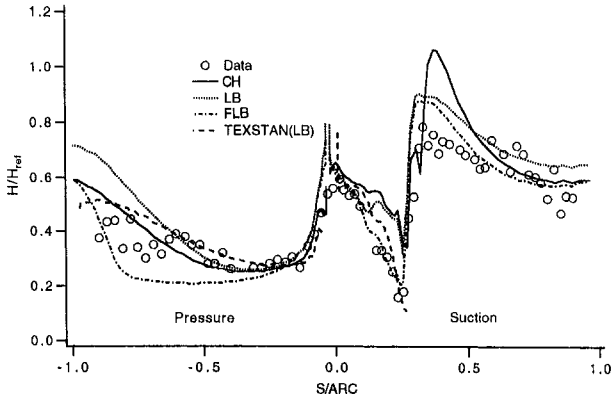

Fig. 2(*a*) Heat transfer prediction for case Mark15 ($M_{is2} = 0.90$, $\text{Re}_{is2} = 1.6 \times 10^6$, $Tu_\infty = 8.3$ percent)

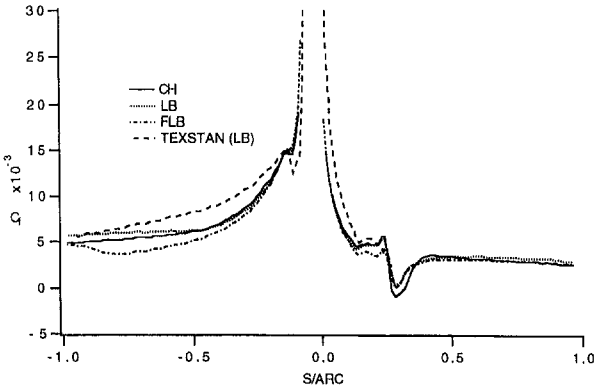

Fig. 2(*b*) Skin friction (C_f) prediction for case Mark15

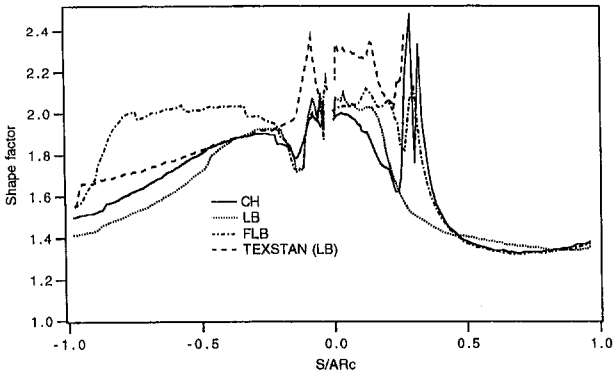

Fig. 2(*c*) Boundary layer shape factors (h) for case Mark15

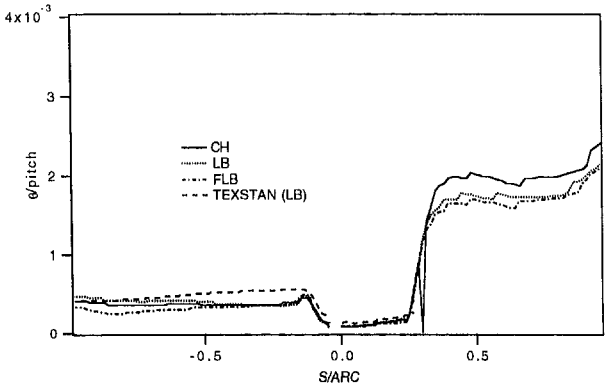

Fig. 2(*d*) Boundary layer momentum thicknesses for case Mark15

the heat transfer distribution. From the C_f distribution on the suction side, it is clear that the CH $k-\epsilon$ model predicts the largest separation bubble among the three models. On the pressure side, the relative magnitudes of C_f computed by different models are also consistent with those observed in the prediction of heat transfer.

As can be seen from Fig. 2(c), the shape factor variation computed by both the elliptic and parabolic methods follows the heat transfer distribution. The shape factor predicted by the FLB $k-\epsilon$ model starts to decrease from 2.0 (corresponding to laminar boundary layers) at about 75 percent pressure surface arc length, which is exactly the location where the heat transfer rate begins to increase (Fig. 2(a)). Among all the models in the Navier–Stokes code, the LB $k-\epsilon$ model predicts the lowest shape factor (about 1.4, corresponding to turbulent boundary layers) and thus the highest heat transfer rate near the pressure surface trailing edge. On the suction side, the shape factors computed by the three models drop to around 1.35 near the trailing edge.

In Fig. 2(d), the boundary layer momentum-thicknesses (θ) predicted by all the models at the rear of the pressure surface are about 0.0004 pitch, which is much lower than the predicted θ (about 0.002 pitch) at the rear of the suction surface. Also, the pressure surface boundary layer thickness appears to grow very slowly and even decreases in some region, primarily due to the flow acceleration along the entire surface. Mee et al. (1992) made similar observations from a detailed boundary layer measurement of a transonic turbine cascade. The thin boundary layer on the pressure surface made it necessary to employ large number of grid points for proper near-wall flow resolution.

The boundary layer properties and heat transfer for the case C3X158 predicted by all three models are presented in Figs. 3(a), 3(b), 3(c), and 3(d). On the pressure surface, all three models have captured transition with the prediction from the LB $k-\epsilon$ model being the closest to the data. Once again, the FLB $k-\epsilon$ model yields a delayed transition and thus underpredicts the heat transfer over a large area on the surface. The C3X airfoil exhibits a smooth transition on the suction surface since the acceleration factor is close to zero except the leading edge region (as seen in Fig. 1(b)). The transition onset predicted by the CH $k-\epsilon$ model is too close to the leading edge, and the transition process appears to have been smeared out. The tendency of the CH model in predicting a premature transition has been observed by other researchers (Simoneau and Simon, 1993). The LB $k-\epsilon$ model predicts a more distinct transition process, but the transition onset is predicted to be earlier than the data. The transition location predicted by the FLB $k-\epsilon$ model is in best agreement with the data.

As expected, the variation of boundary layer integral parameters (see Figs. 3(b) and 3(c)) predicted by different models are consistent with the heat transfer predictions from the same model. As seen in Fig. 3(c), the computed Re_θ near the trailing edge reaches only around 750, which is far below a value of 2000 usually considered as the lower limit for fully turbulent boundary layers. Thus, from the predicted heat transfer, shape factor, and Re_θ, it may be concluded that the boundary layer remains transitional along the entire pressure surface. On the suction surface, the predicted Re_θ is around 2200 near the trailing edge. The streamwise evolution of suction surface boundary layer velocity profile ($u^+ \sim y^+$) predicted by the LB $k-\epsilon$ model is shown in Fig. 3(d). The prediction provides a clear simulation of the transition process in which the velocity profile in outer layer changes from the type of a laminar boundary layer to that of a fully turbulent boundary layer (log-law). Thus, the computed heat transfer, shape factor, Re_θ and $u^+ \sim y^+$ (Figs. 3(a), 3(b), 3(c), and 3(d)) all indicate that the suction surface boundary layer has become fully turbulent near the trailing edge.

From Figs. 2 and 3, it maybe concluded that the $k-\epsilon$ model of Lam–Bremhorst (1981) provides the best prediction of tran-

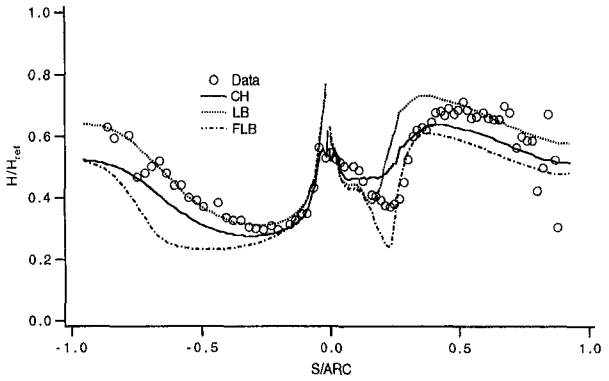

Fig. 3(a) Heat transfer distribution along blade surfaces for case C3X158 (M_{is2} = 0.90, Re_{is2} = 1.5 × 10^6, Tu_∞ = 8.3 percent)

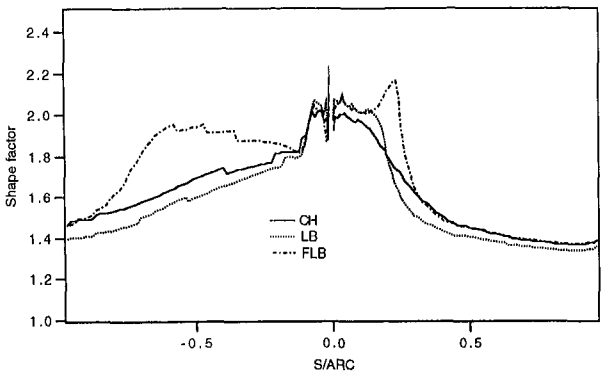

Fig. 3(b) Predicted boundary layer shape factors along blade surfaces for case C3X158

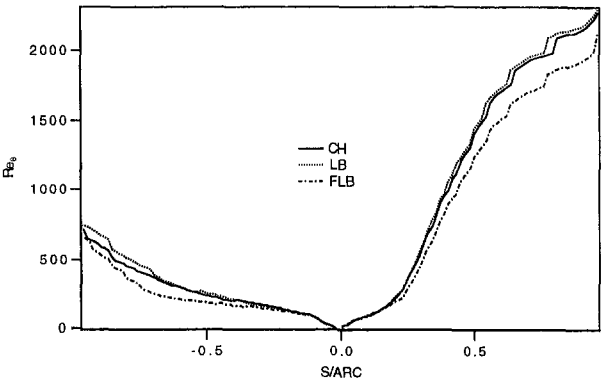

Fig. 3(c) Predicted momentum-thickness Reynolds number for case C3X158

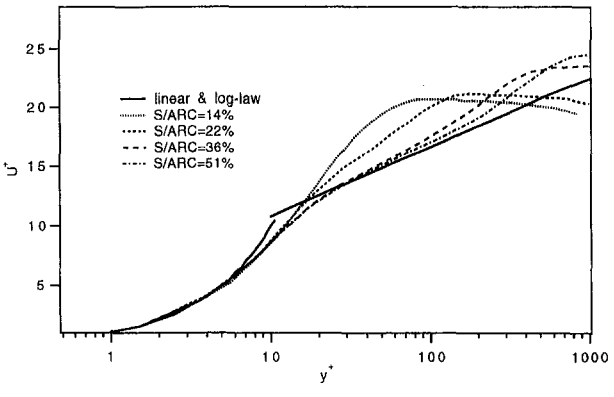

Fig. 3(d) Predicted velocity profile (by Lam–Bremhorst model) along suction surface (case C3X158)

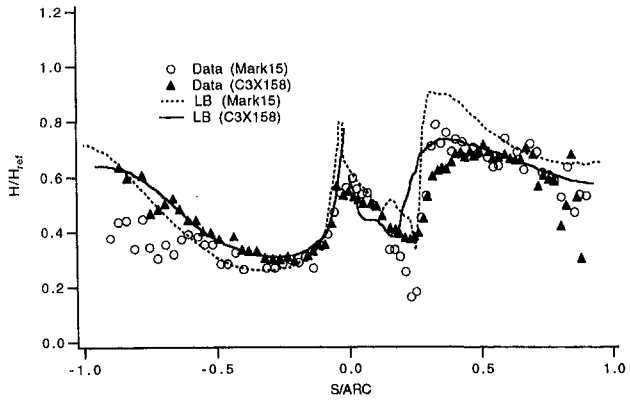

Fig. 4(*a*) Effects of pressure gradient on heat transfer distribution (Mark15 and C3X158)

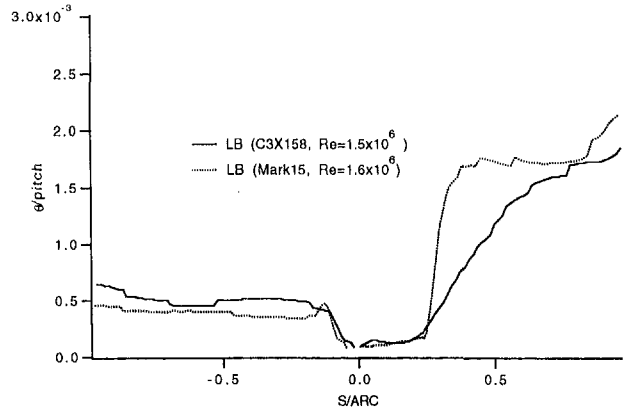

Fig. 4(*b*) Effect of pressure gradient on momentum thickness variation (Mark15 and C3X158)

sitions on these two airfoils among the three $k-\epsilon$ models evaluated. Sieger et al. (1993) reached a similar conclusion after a detailed evaluation of various LRN $k-\epsilon$ models for predicting bypass transition, using a boundary layer code.

Pressure Gradient Effect. Since the major difference between the Mark II and the C3X airfoils lies in the suction surface pressure distribution, a comparison of heat transfer rates on this two airfoils is made in Fig. 4(*a*). The test conditions (Re, Mach number, Tu_∞) are the same for the two cases. On the pressure surface, the C3X airfoil exhibits an earlier transition than the Mark II airfoil, which is due to the fact that the acceleration factor of the C3X airfoil is lower than that of the Mark II airfoil along the entire pressure surface (Fig. 1(*b*)). On the suction surface, the increase in local heat transfer caused by the separation-induced transition (on Mark II) is much sharper than that caused by the nominal bypass transition (on C3X). Similar behavior in the variation of the momentum thickness can be seen in Fig. 4(*b*).

Reynolds Number Effect. The effect of Reynolds number on the airfoil heat transfer distribution is shown in Figs. 5 and 6 for the Mark II and C3X airfoils, respectively. The predictions by the LB $k-\epsilon$ model generally capture the increase in heat transfer rate with increasing Reynolds numbers for both airfoils. As discussed in Hylton et al. (1983) and Nealy et al. (1984), in the case of Mark II airfoil, the Reynolds number effect (at a fixed M_{is2}) appears to be largely reflected in a shift in the heat transfer level rather than in heat transfer distribution, since the transition apparently occurs at a fixed location (i.e., around 26 percent arc length, Fig. 5). The transition predicted by the LB $k-\epsilon$ model is independent of Reynolds number. This is in good agreement with the measurement. For the C3X airfoil,

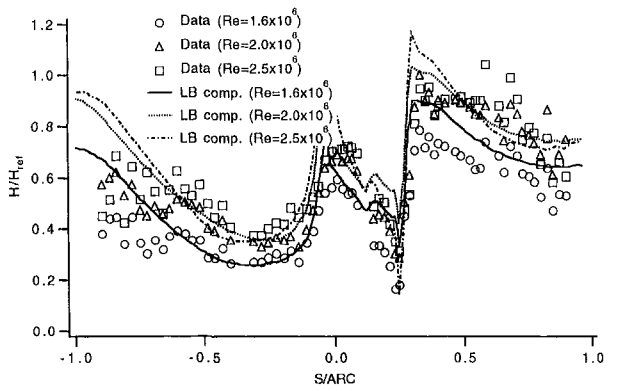

Fig. 5 Effects of Reynolds number on Mark II heat transfer distribution (computation with Lam–Bremhorst $k-\epsilon$ model)

however, the Reynolds number effect on the heat transfer distribution is reflected in both the transition onset location and the general level of heat transfer (see Fig. 6). The higher the Reynolds number, the earlier is the transition and thus the higher the heat transfer rate. The LB $k-\epsilon$ model captures this trend quite well, especially on the pressure surface.

Free-Stream Turbulence Intensity Effect. In the experiments carried out by Hylton et al. (1983), the free-stream turbulence intensity Tu_∞ was varied from 6.5 to 8.3 percent for the C3X airfoil. Figure 7 shows the effect of free-stream turbulence intensity on the heat transfer level. The computed results (by

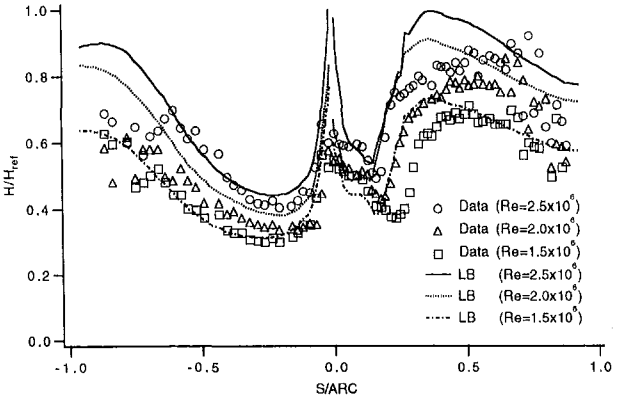

Fig. 6 Effect of Reynolds number on C3X heat transfer distribution (computation with Lam–Bremhorst $k-\epsilon$ model)

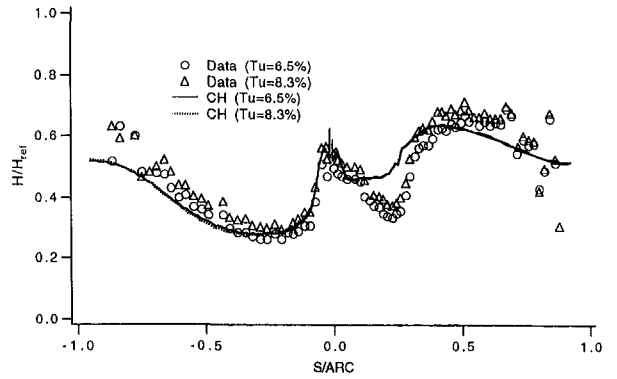

Fig. 7 Free-stream turbulence intensity effect on heat transfer distribution along blade surfaces for case C3X148 and C3X158 (M_{is2} = 0.90, Re_{is2} = 1.5*10^6, Tu_∞ = 6.5 percent for C3X148 and Tu_∞ = 8.3 percent for C3X158)

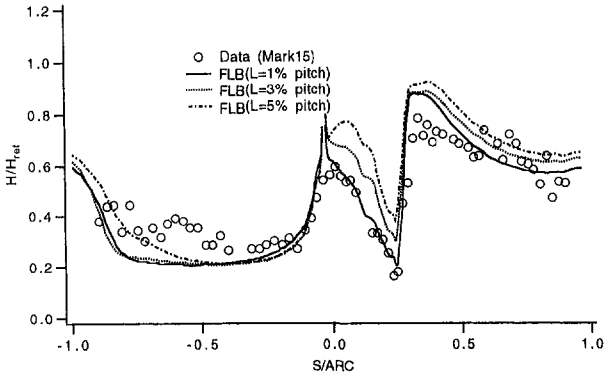

Fig. 8 Length scale effect on heat transfer distribution for case Mark15 (computation with Fan–Lakshminarayana–Barnett $k-\epsilon$ model)

the CH $k-\epsilon$ model) are almost identical for the two cases (C3X148 and C3X158). The predictions from the other two models (not shown) indicate similar features. The experimental data indicates a slightly higher level of heat transfer on both surfaces under higher free-stream turbulence intensity (i.e., case C3X158).

Free-Stream Turbulence Length Scale Effect. As stated earlier, the free-stream turbulence length scale L_∞ was specified as 1 percent of the pitch at the computational inlet (about 0.8 axial chord upstream of the leading edge), since no data are available for this parameter. The effect of this length scale on the airfoil heat transfer distribution is examined in Figs. 8 and 9 for the Mark II and C3X airfoils, respectively. Increasing the free-stream length scale is equivalent to increasing the free-stream turbulence intensity, since larger length scale means lower decay rate of free-stream turbulence (Eq. (8)) and hence higher turbulence level at the blade leading edge. Indeed, the predicted heat transfer rate increases with the specified value of L_∞, as seen in Fig. 8, Figs. 9(a) and 9(b). Predictions from different models exhibit quite similar trends.

However, it should be noted that the predicted heat transfer on the suction surface is much more sensitive to the variation in L_∞ than that on the pressure surface. This is essentially due to the isotropic character of the present $k-\epsilon$ models, which provide a poor representation of normal stress components even in a flat plate boundary layer. It is known that isotropic models are not accurate for stagnation flow, where the production of turbulence is dominated by normal stress components. As shown by Taulbee et al. (1989), the turbulence level along the stagnation streamline is overpredicted considerably by the $k-\epsilon$ model, but is predicted accurately with the Reynolds stress model. This can be understood by a comparison of the production terms P_k. For two-dimensional incompressible flows, P_k arising from an isotropic eddy-viscosity model and a Reynolds stress model are given by

$$P_k = 2\nu_t\left(\frac{\partial U}{\partial x}\right)^2 + 2\nu_t\left(\frac{\partial V}{\partial y}\right)^2 + \nu_t\left(\frac{\partial U}{\partial y} + \frac{\partial V}{\partial x}\right)^2 \quad (9)$$

$$P_k = -\overline{uu}\frac{\partial U}{\partial x} - \overline{vv}\frac{\partial V}{\partial y} - \overline{uv}\left(\frac{\partial U}{\partial y} + \frac{\partial V}{\partial x}\right) \quad (10)$$

The large velocity gradient (i.e., $\partial U/\partial x$) during the deceleration of the flow toward the stagnation point makes the first two terms ($\partial V/\partial y = -\partial U/\partial x$ due to continuity equation) to be dominant in P_k. Since $\overline{uu}$ does not differ greatly from $\overline{vv}$, the first two terms in Eq. (10) (i.e., $(-\overline{uu} + \overline{vv})\partial U/\partial x$) can still yield a nominal level of turbulent energy production in the stagnation region. However, Eq. (9) will inevitably provide a very high level of turbulence production due to the existance of the square of large strains multiplied by a large eddy viscosity. The inaccurately amplified turbulent kinetic energy in the leading edge region is convected downstream, along both surfaces. The velocity gradient (and P_k in Eq. (9)) downstream of the leading edge on the suction side is much higher than that on the pressure side, thus the free-stream turbulence level near the suction surface as computed by the $k-\epsilon$ models is significantly higher than that near the pressure surface, resulting in significant overpredictions of heat transfer on the suction surface near the leading edge (Figs. 8 and 9). For an accurate prediction of free-stream turbulence in the stagnation region, it is thus necessary to employ anisotropic models, such as the low-Reynolds-number Reynolds stress models.

Concluding Remarks

The numerical simulations discussed in this paper indicate that the turbine blade heat transfer, under conditions close to real engine operating conditions (high free-stream turbulence, high Re, and favorable-to-adverse pressure gradient), can be predicted with engineering accuracy by the three low-Reynolds-number $k-\epsilon$ models developed by Chien (1982), Lam–Bremhorst (1981), and Fan et al. (1993), respectively. The Navier–Stokes predictions with various low-Reynolds-number $k-\epsilon$ models capture the location of separation-induced transition very well. Both the data and computations indicate that the separation-induced transition results in much sharper increase in the local heat transfer rate than the nominal bypass transition. The effects of Reynolds number have been captured well by all the models. It has also been shown that the Navier–Stokes procedure provides accurate predictions of both heat transfer and boundary layer aerodynamic parameters.

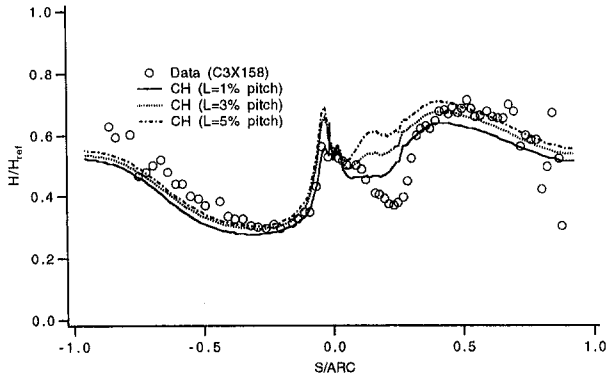

Fig. 9(a) Length scale effect on heat transfer distribution for case C3X158 (computation with Chien $k-\epsilon$ model)

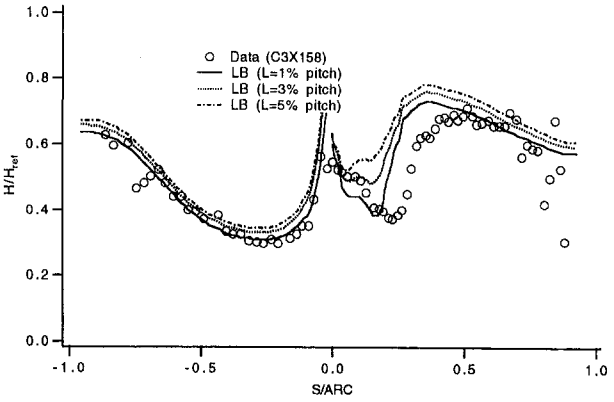

Fig. 9(b) Length scale effect on heat transfer distribution for case C3X158 (computation with Lam–Bremhorst $k-\epsilon$ model)

The Lam–Bremhorst $k-\epsilon$ model provides relatively better predictions of the transition and the heat transfer than the other two models for the cases studied. While performing well in fully turbulent boundary layers, Chien's $k-\epsilon$ model tends to predict a premature transition and smear out the transition process. This model is also not accurate for separated flows. The Fan–Lakshminarayana–Barnett $k-\epsilon$ model provides the best prediction of separation-induced transition, but tends to predict delayed transitions for accelerating boundary layers on the pressure surface.

Detailed experiments should be performed to examine the variation of free-stream turbulence through the passage, particularly near the stagnation point and accelerating region on the suction surface. To improve the predictions of convective heat transfer near the stagnation point, low-Reynolds-number anisotropic turbulence models such as a low-Reynolds-number Reynolds stress model should be used.

Acknowledgments

This work was supported by the U.S. National Aeronautics and Space Administration through contract NAS 8-38867 monitored by Lisa Griffin of Marshall Space Flight Center (MSFC). The authors wish to acknowledge NASA for providing supercomputer resources at the NASA Ames research center. The National Science Foundation grant (NSF Grant INT 90-15984) enabled interaction with the turbulence group at Ecole centrale de Lyon (France).

References

Ameri, A. A., and Arnone, A., 1994, "Prediction of Turbine Blade Passage Heat Transfer Using a Zonal and a Two-Equation Turbulence Model," ASME Paper No. 94-GT-122.

Basson, A. H., Kunz, R. F., and Lakshminarayana, B., 1993, "Grid Generation for Three-Dimensional Turbomachinery Geometries Including Tip Clearance," AIAA *Journal of Propulsion and Power,* Vol. 9, p. 59.

Chien, K. Y., 1982, "Prediction of Channel and Boundary-Layer Flows With a Low-Reynolds-Number Turbulence Model," *AIAA Journal,* Vol. 20, No. 1.

Crawford, M., 1985, TEXSTAN program, Dept. of Mech. Engr., Univ. of Texas at Austin.

Fan, S., Lakshminarayana, B., and Barnett, M., 1993, "Low-Reynolds-Number $k-\epsilon$ Model for Unsteady Turbulent Boundary-Layer Flows," *AIAA Journal,* Vol. 32, No. 10, pp. 1777–1784.

Fan, S., and Lakshminarayana, B., 1996, "Computation and Simulation of Wake-Generated Unsteady Pressure and Boundary-Layers in Cascades: Parts 1 & 2," ASME JOURNAL OF TURBOMACHINERY, Vol. 118, pp. 96–122.

Hah, C., 1989, "Numerical Study of Three-Dimensional Flow and Heat Transfer Near the Endwall of a Turbine Blade Row," AIAA Paper No. 89-1689.

Hylton, L. D., Mihelc, M. S., Turner, E. R., Nealy, D. A., and York, R. E., 1983, "Analytical and Experimental Evaluation of the Heat Transfer Distribution Over the Surface of Turbine Vanes," NASA CR-168015, May.

Kunz, R., and Lakshminarayana, B., 1992, "Explicit Navier–Stokes Computation of Cascade Flows Using the $k-\epsilon$ Model," *AIAA Journal,* Vol. 30, No. 1.

Lam, C., and Bremhorst, K., 1981, "Modified Form of the $k-\epsilon$ Model for Predicting Wall Turbulence," ASME *Journal of Fluids Engineering,* Vol. 103, p. 456.

Luo, J., and Lakshminarayana, B., 1995, "Navier–Stokes Analysis of Turbine Flowfield and Heat Transfer," *J. of Propulsion and Power,* Vol. 11, pp. 221–229.

Mayle, R. E., 1991, "The Role of Laminar-Turbulent Transition in Gas-Turbine Engines," ASME JOURNAL OF TURBOMACHINERY, Vol. 113, pp. 509–537.

Mee, D. J., Baines, N. C., and Oldfield, M. L. G., 1992, "Detailed Boundary Layer Measurements on a Transonic Turbine Cascade," ASME JOURNAL OF TURBOMACHINERY, Vol. 114, pp. 163–172.

Nealy, D. A., Mihelc, M. S., Hylton, L. D., and Gladden, H. J., 1984, "Measurements of Heat Transfer Distribution Over the Surfaces of Highly Loaded Turbine Nozzle Guide Vanes," ASME *Journal of Engineering for Gas Turbines and Power,* Vol. 106, pp. 149–158.

Patel, V. C., Rodi, W., and Scheuerer, G., 1985, "Turbulence Models for Near-Wall and Low-Reynolds-Number Flows," *AIAA Journal,* Vol. 23, No. 9, pp. 1308–1319.

Savill, A. M., 1993, "Some Recent Progress in the Turbulence Modeling of By-Pass Transition," *Near-Wall Turbulent Flows,* R. M. C. So et al., eds., Elsevier Science Publishers.

Schmidt, R., and Patankar, S., 1992, "Simulating Boundary Layer Transition With Low-Reynolds-Number $k-\epsilon$ Turbulence Models," ASME JOURNAL OF TURBOMACHINERY, Vol. 114, pp. 10–17.

Sieger, K., Schulz, A., Crawford, M. E., and Wittig, S., 1993, "An Evaluation of Low-Reynolds-Number $k-\epsilon$ Turbulence Models for Predicting Transition Under the Influence of Free-Stream Turbulence and Pressure Gradient," *Engr. Turbulence Modelling and Experiments,* W. Rodi and F. Martelli, eds., Elsevier Science Publishers.

Simoneau, R. J., and Simon, F. F., 1993, "Progress Towards Understanding and Predicting Heat Transfer in the Turbine Gas Path," *Inter. J. of Heat & Fluid Flow,* Vol. 14, pp. 106–128.

Taulbee, D. B., Tran, L. T., and Dunn, M. G., 1989, "Stagnation Point and Surface Heat Transfer for a Turbine Stage: Prediction and Comparison With Data," ASME JOURNAL OF TURBOMACHINERY, Vol. 111, pp. 28–35.

J. P. Gostelow
University of Leicester,
Leicester, United Kingdom

G. J. Walker

W. J. Solomon

University of Tasmania,
Hobart, Tasmania, Australia

G. Hong

N. Melwani

University of Technology, Sydney,
Sydney, Australia

Investigation of the Calmed Region Behind a Turbulent Spot

Measurements are presented of the calmed region behind triggered wave packets and turbulent spots under a controlled diffusion adverse pressure gradient in a wind tunnel. Similar measurements are also presented from the stator blades of an axial flow compressor, where turbulent spots are induced by the passing of rotor wakes. The purpose is to gain an appreciation of turbulent spot behavior under a strong adverse pressure gradient as a foundation for the more accurate modeling of spots and their environment in predictions of transitional boundary layer flows. Under an adverse pressure gradient the calmed region behind the spot is extensive; its interaction with the surrounding boundary layer is complex and is dependent on whether the surrounding natural boundary layer is laminar or turbulent. Some insights are gleaned concerning the behavior of the calmed region, which will subsequently be used in attempts to model the calmed region. Although these fundamental investigations of the calmed region have been extensive, much remains to be understood.

Introduction

Results presented in 1995 highlighted the nature of the time-resolved flow over representative compressor and turbine blade surfaces (Halstead et al., 1997; Solomon and Walker, 1995a). Many designers and researchers had previously ignored laminar–turbulent transition phenomena or treated them as essentially two-dimensional time-independent events. This approach was carried through into the computational modeling of turbomachinery flows.

Emphasis in computational fluid dynamics has hitherto been placed on modeling three-dimensional flows. This is a demanding exercise for turbomachines; it has focused attention on numerical and gridding issues. Because of these issues, and limitations on computing power, the resolution afforded near blade surfaces has usually been inadequate. Turbulence modeling has rarely taken account of the laminar boundary layer, its stability and separation limitations and the attendant transition phenomena. It has been quite common to assume that the boundary layer is turbulent from the leading edge.

Although the importance of transition in flows over turbine blades had been known for some time, the problem of unsteady transition on axial compressor blades had received comparatively little attention. The recent work on axial compressors at General Electric and the University of Tasmania, referred to above, showed significant unsteady wake-induced transition effects on compressor blades. It was established that wake-induced transition phenomena can delay separation on compressor blades. The effects of calming in increasing transition length and resisting laminar separation are at least as strong as on turbine blades. These results from rotating machines have shown quite clearly that the neglect of laminar and transitional flows is not sustainable. A more accurate modeling for most operating conditions would treat the flow over most surfaces as both unsteady and transitional.

Measurements in a Compressor Stage. Figure 1 gives the measured intermittency variation over the suction surface at 1 deg incidence on the C4 stator blading of the University of Tasmania research compressor. The Reynolds number is 117,000 based on stator inlet velocity and chord. Distance along the blade surface is plotted as a function of time and the effects of wake impingement from upstream rotor blades and the subsequent interaction with the developing boundary layer on the stator are illustrated. The shading changes from white to black as intermittency changes from zero (laminar) to unity (turbulent).

The dark wedges commencing around 30 percent chord at intervals of $t^* = 1$ correspond to transitional and turbulent flow wedges (or strips) induced by passing free-stream disturbances from the wakes of upstream rotor blades. These are interspersed with laminar or transitional flow regions extending back to around 90 percent chord. The turbulent strip, which should have been initiated around $t^* = 2$, is missing because the corresponding rotor blade was deliberately removed to investigate the influence of changing wake frequency on the unsteady flow behavior. This follows the procedure of Halstead et al. (1997), except that their flow interpretation was based on contour plots of ensemble-averaged rms output from surface film gages.

The probability of relaxing nonturbulent flow, designated κ, was given by a simple detector applied to identify regions of relaxing flow immediately following the passage of turbulent spots in wake-disturbed flow. The flow is identified as relaxing while, following a change in intermittency from unity to zero, $d\tau/dt$ is negative. Isoprobability contours for this flow regime are superimposed on the shaded plot of turbulence intermittency. This quantitative information on relaxing flow provides an important new perspective on the wake-induced transition process.

The contours at the rear of relaxing flow zones, which follow wake-induced transitional/turbulent strips, are nearly parallel, with a slope corresponding to a velocity of $0.2U$. The extent of the relaxing flow region grows almost linearly with s^*. The increase in maximum κ with s^* parallels the increase of maximum γ within the wake-induced strip for $0.3 < s^* < 0.5$. This provides strong confirmation for the initially transitional nature of these wake-induced strips, which are a collection of isolated and merging spots as described by Halstead et al. (1997).

The present observations have broad similarities with those of Halstead et al., but there are also some significant differences in detail. In the absence of the wake-induced transitional strip, which would originate near $t^* = 2$, the onset of turbulent flow following the passage of this strip is seen to move forward to around 50 percent chord when the next wake-induced transi-

Contributed by the International Gas Turbine Institute and presented at the 41st International Gas Turbine and Aeroengine Congress and Exhibition, Birmingham, United Kingdom, June 10–13, 1996. Manuscript received at ASME Headquarters February 1996. Paper No. 96-GT-489. Associate Technical Editor: J. N. Shinn.

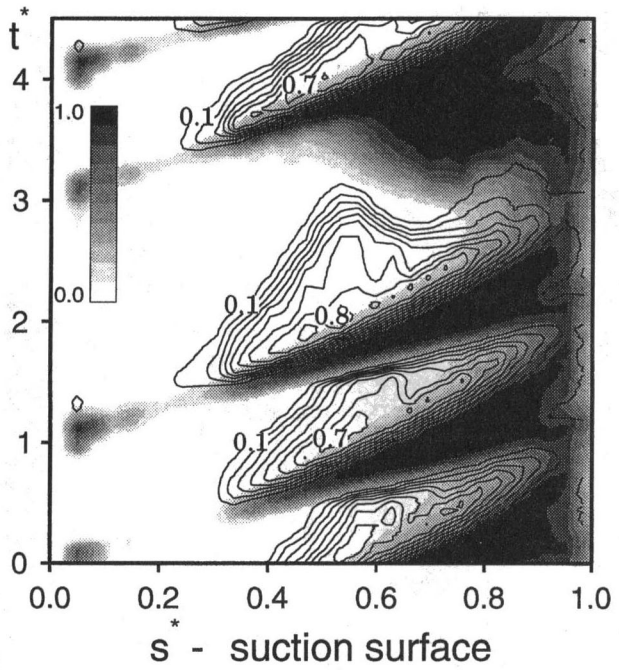

Fig. 1 $s^* \sim t^*$ plane distributions of flow state on compressor stator suction surface. Shading indicates the probability, γ, of turbulent flow (intermittency) and contours indicate probability, κ, of relaxing nonturbulent flow. One upstream rotor blade removed to vary wake spacing.

tional strip arrives. (The mechanism of interwake transition may be bypass, separated flow, or natural depending on the conditions.) This clearly demonstrates the influence of the relaxing flow in delaying transition onset in the region between the wakes. It appears that the interwake turbulent flow onset would asymptote to a fixed streamwise location given a sufficiently long time interval between passing rotor wakes (possibly around $s^* = 0.4$ where laminar separation is predicted by steady flow boundary layer calculations).

In the tests of Halstead et al., the interwake turbulent onset position had fully stabilized within two rotor blade passing periods. In the stabilized regime the interwake transition appeared to occur via a midchord separation bubble. The calming influence of the preceding wake-induced transitional strip was not as clear, as the boundary of the interwake transitional flow region initially exhibited a positive slope ($ds^*/dt^* > 0$) in the time–space plots of rms surface gage output.

The apparent decrease in intermittency and increase in probability of relaxing flow close to the stator trailing edge is believed to be associated with turbulent separation. There is evidence of oscillation in separation location as the boundary layer thickness fluctuates with time. The turbulent separation is most advanced at the center of the wake-induced turbulent strip where the boundary layer is thickest.

The University of Tasmania work has corroborated the more extensive program at General Electric. Solomon and Walker (1995b) have particularly emphasized the importance of the calmed region behind well-developed transitional strips. This has the important effect of greatly extending the length of transitional flow by delaying transition from other modes. It delays the onset of laminar separation because of the periodic energizing of wall-layer fluid by the wake-induced turbulent spots.

Figure 1 demonstrates the engineering significance of relaxation (or calming) effects on the blades of axial turbomachines. Provided the wake passing frequency is sufficiently high, the altered boundary layer velocity profile behind the wake-induced transitional strip maintains laminar flow over the majority of the blade chord while preventing intermittent laminar separation. Full optimization of axial turbomachine blade design obviously requires a detailed understanding of these phenomena and an ability to incorporate them into design calculations.

Investigations on the Calmed Region. The few models that have hitherto enjoyed any success in predicting the transition region, whether in conjunction with integral boundary layer codes or two-equation models, have been intermittency based and have taken no account of the calmed region. It is clearly desirable to move to a further stage of refinement in which consideration is given to the influence of the calmed region. Modeling the calmed region is an ambitious undertaking and in this paper no such attempt is made. Rather, some of the available evidence is assembled that then might become a platform for a subsequent modeling effort.

As a basic feature of turbulent spots and transitional flows, the calmed region is deserving of study in its own right. A number of the researchers who have investigated triggered turbulent spots have also provided information on the behavior of the calmed region. In investigations on triggered spots under zero pressure gradient Wygnanski et al. (1976) found that the velocity profile immediately after the passage of a spot was significantly fuller than the Blasius velocity profile. Zilberman et al. (1977) introduced a triggered spot into a turbulent boundary layer and found that it was smaller in extent than a spot evolving in a laminar layer and that it had no stabilizing effect on the layer.

In 1987 Gutmark and Blackwelder investigated the interaction between two triggered spots separated by varying time intervals. This situation was analogous to the incident wake-passing situation of a turbomachinery blade. They found that if the streamwise separation between spots was below a certain threshold, an interaction would occur that could reduce the leading edge celerity of the following spot. This retardation of the following spot was dependent on the calmed region. It could be hypothesized from that paper that the calmed region, with its associated time delays, was crucial in determining whether

Nomenclature

E = hot-film anemometer output voltage
T = rotor blade passing period
$U(x)$ = free-stream velocity
s = streamwise distance
s^* = normalized distance along suction surface = s/s_{max}
t = time
t^* = normalized time = t/T
u = local velocity
x, y, z = streamwise, normal, and spanwise coordinates
β = Hartree parameter
γ = probability of turbulent flow (intermittency)
δ = boundary layer absolute thickness ($u/U = 0.99$)
δ' = boundary layer disturbance level thickness (Eq. (1))
δ^* = boundary layer displacement thickness
θ = boundary layer momentum thickness
κ = probability of relaxing non-turbulent flow
τ = quasi shear stress = $((E^2 - E_0^2)/E_0^2)^3$
Ω = spanwise vorticity term (du/dy)

Subscripts

c = beginning of calmed region
max = maximum value
nat = natural boundary layer
0 = at zero flow

the response of a blade to a periodic stimulation (such as wake passing) was unsteady or only quasi-steady. Such information would have implications for aeroelasticity and acoustics as well as aerodynamics.

Krane and Pauley (1994), working with a different configuration, which gave a weaker interaction than the Gutmark and Blackwelder work, reached a different conclusion. Their measurements supported the view that only if the trailing spot was formed inside the calmed region would its celerity be influenced by the presence of the leading spot.

Seifert and Wygnanski (1995) investigated a spot under an adverse pressure gradient and concluded that the normalized length of the calmed region was much greater for an adverse pressure gradient spot than for a zero pressure gradient spot. Katz et al. (1990) had previously concluded that for a zero pressure gradient the normalized length of the calmed region was twice as great as that under a favorable pressure gradient. Seifert and Wygnanski suggested that the extent of the calmed region scaled with the span of the spot rather than its length. van Hest et al. (1994) have also presented measurements on an adverse pressure gradient triggered spot, which include information on the extent of the calmed region.

Cumpsty et al. (1995) presented sets of measurements from C4 compressor rotor blading and a controlled diffusion blade. These showed that because of its higher skin friction, the calmed region is able to suppress a separation bubble. They pointed out that the observed transition behavior was at variance with most current modeling approaches and that turbomachinery flows with strong pressure gradients and wake-induced transition were not properly understood.

A program of work has been undertaken, on a flat plate under adverse pressure gradients, at the University of Technology, Sydney. An extensive data set was obtained on a triggered spot under a controlled diffusion pressure distribution. This was, in part, reported by Gostelow et al. (1996). Care was taken to incorporate measurements throughout the calmed region. The undisturbed boundary layer on the flat plate was itself the subject of a laminar-to-turbulent transition so that it was possible to study the interaction of a triggered wave packet, which evolved into a turbulent spot, with a transitioning boundary layer, which will be described as the "natural" layer. The implications for calmed region behavior of the data set is the principal subject of the work described below.

Measurements of a Triggered Spot

The wind tunnel and data acquisition techniques were described by Gostelow et al. (1996), which work also describes the main data set. The pressure distribution was of the controlled diffusion type, giving strong adverse pressure gradients. The spot was triggered by a low amplitude air jet of 0.4 ms duration at $x = 207$ mm. Phase-averaged velocity traces of triggered spots and wave packets were formed from single hot-wire readings over 128 realizations. Disturbance levels were established as the rms velocity variation over a cohort of 30 raw velocity traces. The ensemble of averaged velocity traces was intercepted at each time interval; profiles of velocity perturbation and rms disturbance level were plotted throughout the spot and its surrounding region and integral properties were derived.

A good overview of the physical processes is given by a parameter, δ', suggested by Blackwelder (1993). This is defined as:

$$\delta' \equiv \int_0^\infty (u'(y)/U)dy \qquad (1)$$

where

$$u' = \sqrt{(u(t) - \bar{u})^2}.$$

At any instant of time the integrated rms disturbance level is

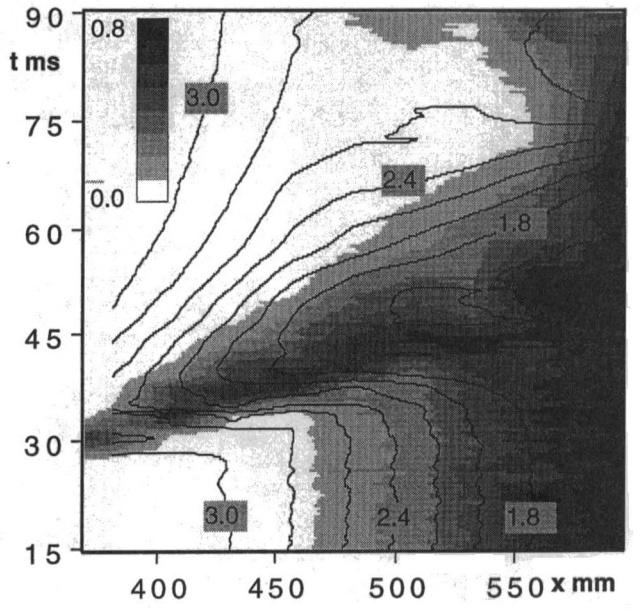

Fig. 2 $x \sim t$ plane distributions of flow state for adverse pressure gradient triggered spot in wind tunnel. Shading indicates rms disturbance level and contours indicate shape factor, H.

normalized by the temporally averaged displacement thickness, δ^*, of the incoming boundary layer.

Figure 2 gives an $x \sim t$ diagram for the centerline behavior of the triggered spot resulting from the application of the Blackwelder procedure. The shading, which represents levels of δ'/δ^*, shows clearly the progress of the spot and how, at a sufficient distance downstream, the unperturbed boundary layer ahead of the spot undergoes its own natural transition. In this region, however, the boundary layer after the spot has passed is not transitional but becalmed. The calmed region is seen to be extensive, both in time duration after the spot's passage, and in distance downstream of the natural transition. For much of the region, and a significant duration after the passage of the spot, the boundary layer becomes laminar and undisturbed in character but its velocity profile does not revert instantly to the laminar shape.

A mapping of the character of the velocity profiles in the calmed region is obtained by integrating the instantaneous phase-averaged velocity profiles over the height of the spot. Contours of shape factor, H, are superimposed on Fig. 2. These show that the transition of the unperturbed boundary layer, prior to the arrival of the triggered spot, is quite conventional with H falling from values above 3.0 (actual maximum 3.23) to values below 1.8 (minimum value 1.56). The triggered spot is characterized by a relatively rapid decrease in H to the fully turbulent value. Within the spot H temporarily attains the values below 1.6 normally associated with a turbulent boundary layer. After the spot has passed, instead of an immediate return to laminar levels of shape factor, levels that would be more typical of turbulent flow prevail for an extended duration. H gradually relaxes from around 1.8 to the unperturbed values. The region exhibits a gradual and lengthy "recovery trail," in the words of Schubauer and Klebanoff (1955).

The Blackwelder procedure highlights the nature of the calmed region. Inspection of raw data traces indicated that the smaller length scales, prevalent within the spot itself or in the turbulent layer, were almost entirely absent in this region.

An advantage of wind tunnel measurements is that parameters based on integration over the boundary layer thickness may be used. For the compressor it was convenient to use parameters based on surface film gage measurements. Figures 1 and 2 demonstrate that the $x \sim t$ diagram obtained from wind tunnel

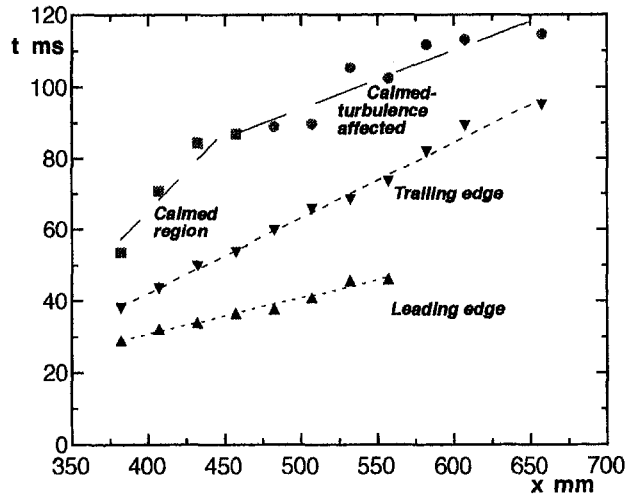

Fig. 3 Arrival times for spot leading and trailing edges and the end of the calmed region

measurements is quite similar to the $s^* \sim t^*$ diagram from the compressor blade. In particular the spot leading and trailing edge celerities are similar as is the behavior of the calmed region. Both diagrams also provide information on the "natural" state to which the boundary layer would revert, given sufficient time. Much fundamental research has been performed on triggered spots, and although the analogy may not be perfect, the behavior of the triggered spot is close enough to the events on the compressor blade to provide a good model.

Figure 3 presents the arrival times of spot leading and trailing edges and of the end of the calmed region. As described by Gostelow et al. (1996) determination of the leading edge celerity was relatively unambiguous and a criterion of 2 percent velocity perturbation gave a propagation velocity of $0.872U$. The trailing edge celerity of the turbulent region of the spot was more difficult to determine and the most robust criterion was found to be the rearward extent of the 4 percent rms disturbance level contour. A linear fit on the $x \sim t$ diagram gave a trailing edge propagation velocity of $0.413U$. (This compares with the value of $0.431U$ reported by Gostelow et al. (1996) for a subset of the present data; the small difference reflects measurements of Fig. 3, which extend further downstream than the previous data set.)

The trailing edge of the calmed region was followed over an extensive streamwise distance of 275 mm. Its behavior is a function of the state of the natural surrounding boundary layer. In these experiments, because the natural boundary layer undergoes transition, the calmed region essentially consists of two regions that are rather different in character. From the initial development of the wave packet to that station for which the turbulence in the natural boundary layer is first detected (x = 457 mm), it can be assumed that the calmed region is unaffected by boundary layer turbulence generated in the natural transition process. In the early region, where the natural boundary layer is laminar, consideration of the velocity perturbation from the natural layer is the obvious basis for quantifying the extent of the calmed region. The criterion selected was that the velocity perturbation from the laminar layer should have been reduced to below 4 percent at all heights above the surface. A straight line fit to the $x \sim t$ plane data gave a propagation velocity for the trailing edge of the calmed region, for x values of 457 mm and lower, of $0.194U$. For larger values of x, as the natural boundary layer becomes transitional and then turbulent, the calmed region interacts with the surrounding turbulence. The turbulent fluid propagates at a higher velocity and gradually reduces the length of the calmed region. For this reason the trailing edge of the calmed region in a transitional or turbulent natural layer propagates at a higher velocity than in a laminar flow. Because of the nonlinear interactions, the data are scattered, but a straight line fit gives a propagation velocity of $0.539U$. For triggered spots under a zero pressure gradient, the trailing edge of the turbulent region of the spot propagates with a higher celerity than the Tollmien–Schlichting (TS) waves. A possible explanation of the calmed region was that that region was inaccessible to the TS waves. For this adverse pressure gradient spot there is no such celerity difference and that explanation is therefore not applicable.

Examples of Calmed Region Behavior. Since the behavior described above is quite complex, it is worthwhile to provide examples of the types of influences that the calmed region exerts, and to which it is subjected. The first example is of a wave packet developing into a spot in a laminar layer. The second is of a spot in a turbulent layer.

In the first example Fig. 4 presents representative single raw traces of velocity ratio, u/U, for three streamwise locations at 50 mm intervals, taken at a height of 0.3 mm above the surface for a flow with a free-stream velocity slightly lower than that of the main data set. In trace (a) a quiescent laminar layer hosts a conventional triggered wave packet. In this adverse pressure gradient the wave packet is strongly amplified. At the second station, (b), the natural boundary layer develops strong TS periodicity. Again the amplification due to the adverse pressure gradient results in relatively pure periodic behavior of high amplitude. The wave packet, meanwhile, becomes further amplified and develops harmonic content. As demonstrated by Gostelow and Hong (1995), this harmonic behavior is confined to the wall region. By the third station, (c), the natural boundary layer becomes further amplified and also develops similar harmonic content. The triggered wave packet develops further harmonics, which, by wavelet analysis (Gostelow and Hong), are determined to extend to at least 1 kHz; it can reasonably be described as a turbulent spot. This spot has a substantial calmed region, which is exercising two principal effects:

(i) The calmed region acts to reduce the amplitude of fluctuations in the natural boundary layer. In this case the fluctuations in the calmed region have only about one half of the fluctuation amplitude of the natural boundary layer.

(ii) Perhaps as a result of this amplitude reduction the development of harmonics in the calmed region is also suppressed.

The calmed region has the effect of delaying the breakdown to turbulence; it is aptly named. It plays the important stabilizing role of reducing oscillation amplitudes and delaying harmonic development. The results also demonstrate that the transition processes undergone by the natural boundary layer replicate those of the triggered spot. This is strong evidence that the triggered spot does indeed constitute a valid model for the development of transition in a boundary layer.

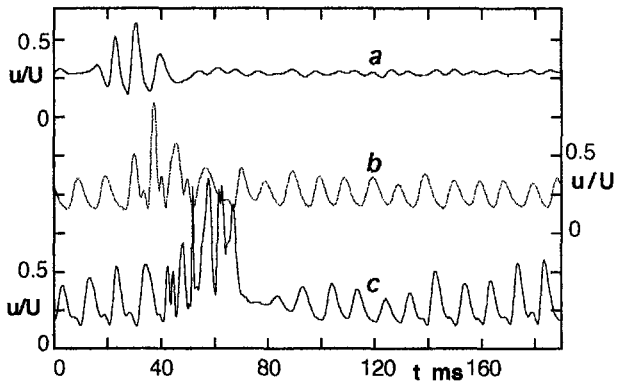

Fig. 4 Velocity traces for locations (*a*), (*b*), and (*c*) at 50 mm intervals showing effect of calmed region in suppressing harmonic development

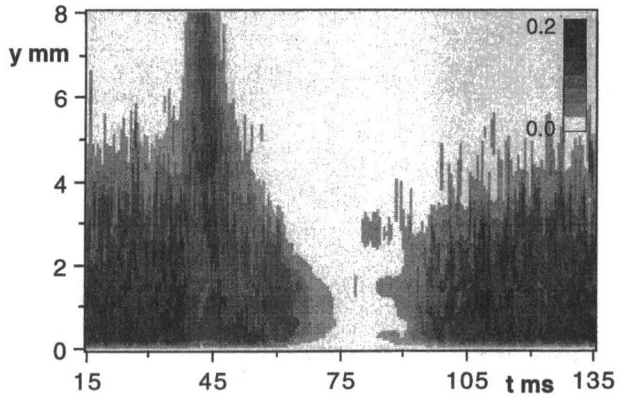

Fig. 5 $y \sim t$ plane variation of rms disturbance level on spot centerline at x = 532 mm

Figure 5 gives a $y \sim t$ plane view of rms disturbance level on the spot centerline at a streamwise location, x, of 532 mm. The natural boundary layer is clearly seen with turbulence extending to about 5 mm from the surface. The spot is still not completely absorbed into the natural boundary layer. It protrudes beyond 8 mm from the surface. Paradoxically the triggered spot has a lower disturbance level than the natural boundary layer. This may be because the triggered spot is composed of older turbulence while the natural boundary layer has not yet completed its transition process (rms disturbance levels tend to reach a maximum toward the end of the transition region). The triggered spot still has its characteristic shape, sweeping down to reach its maximum time extent near the wall. The calmed region follows the spot. It continues to exist for a considerable distance downstream despite the encroaching turbulent layer, although the $x \sim t$ diagram suggests that the turbulence will gradually eliminate the calmed region. The spot is gradually submerged into the natural boundary layer and the only evidence of its separate existence is the cell of calmed fluid. The spot has gone but the calmed region lingers on.

Velocity Distributions. To examine the evolution of the boundary layer profile along the centerline of the triggered spot, and the ensuing calmed region, phase-averaged velocity profiles are plotted in Fig. 6. The station chosen corresponds to x = 457 mm; this is the farthest downstream location for which the natural boundary layer is laminar and for which the calmed region is therefore not contaminated by turbulence. The velocity profiles are plotted at intervals of 1 ms. Only the first two are from the natural laminar layer. These exhibit the low wall shear stress and slightly inflectional profile characteristic of a laminar layer under a moderately strong adverse pressure gradient. The next 16 traces constitute the main body of the spot and are clearly turbulent in character, with higher wall shear. The calmed region then starts with a relatively full profile, which gradually relaxes back to the laminar state of the natural layer. Although presentation of the traces in this form gives a reasonable overview of the development of the velocity profile, it does not allow firm conclusions on the boundary layer state to be drawn.

To do this a more selective approach to the phase-averaged velocity profiles is taken in Fig. 7. The data are drawn from the same set as Fig. 6. Velocity profiles are presented for the natural laminar layer (labeled 457), at the very beginning of the calmed region (labeled 457C), and at an instant 10 ms later. Laminar profiles calculated by Hartree (1937) for β values of −0198. (limiting adverse value), −0.14, 0, and 0.6 are superimposed for reference purposes.

For this strong adverse pressure gradient the natural laminar profile coincides with the profile for β = −0.14 over most of its height. In the calmed region under the adverse pressure

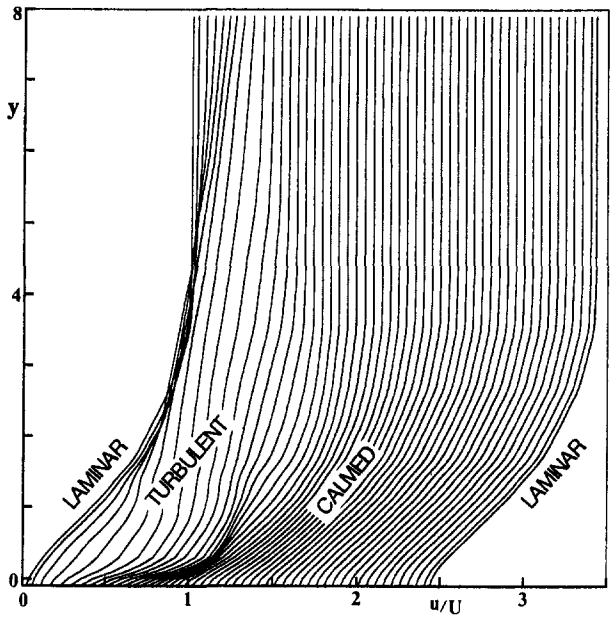

Fig. 6 Boundary layer profiles through spot and calmed region at x = 457 mm

gradient, the velocity profile tends to be fuller than in the natural laminar layer. This effect was also demonstrated by Seifert and Wygnanski (1995). The profile immediately at the beginning of the calmed region is laminar in character. It agrees well with a calculated profile for β = 0.6, corresponding to a favorable pressure gradient. The wall shear stress is nevertheless considerably lower than that of a turbulent layer. After a time of 10 ms, about a third of the way through the calmed region, the boundary layer has relaxed to have a Blasius-like profile. For the remainder of the calmed region, the profile continues its relaxation trail back to the natural laminar profile. Figure 7 is representative of the velocity profiles observed at different streamwise locations in the calmed region while that region is not significantly contaminated by turbulence.

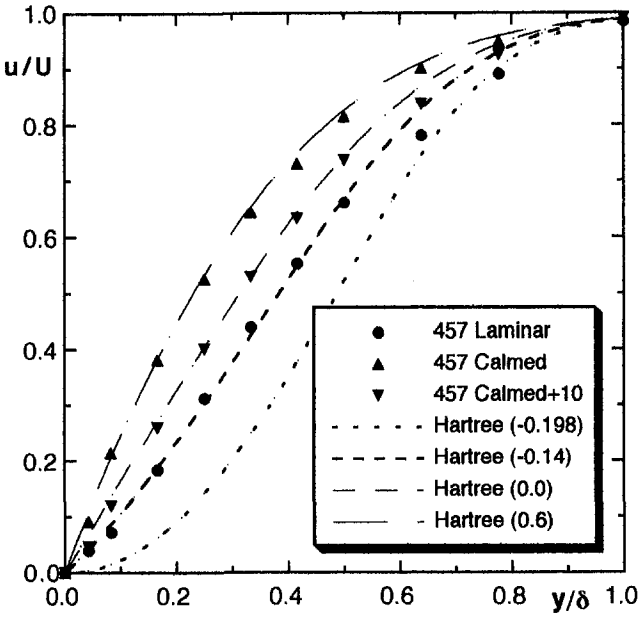

Fig. 7 Velocity profiles in natural boundary layer and calmed region compared with Hartree velocity profiles for a range of pressure gradients

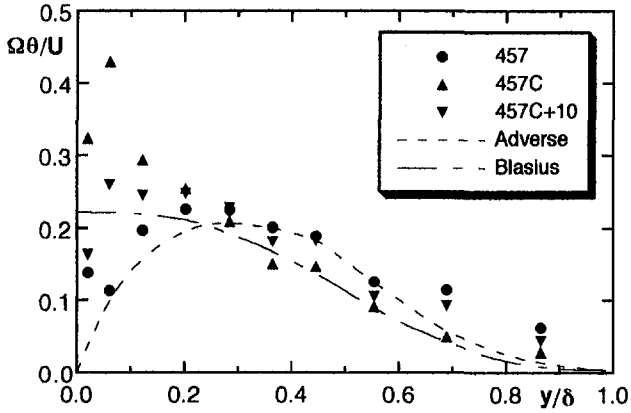

Fig. 8 Vorticity profiles in natural boundary layer and calmed region with predictions of Oliver for zero and limiting adverse pressure gradients

Vorticity Distributions. Boundary layer velocity profiles are not a particularly sensitive indicator of the magnitude of pressure gradient effects and the attendant physics. The associated vorticity distributions, obtained by differentiating the streamwise velocity profile in a normal direction, give greater discrimination. Within the spirit of the boundary layer approximation the spanwise vorticity, Ω, is represented by du/dy, and a dimensionless term, $\Omega\theta/U$, is plotted against y/δ, as suggested by Oliver (1965). As can be seen from that work the dimensionless peak vorticity for decelerating laminar flow is approximately constant with x at around 0.2.

Figure 8 presents vorticity profiles corresponding to the velocity profiles presented in Fig. 7. The predictions are for zero and limiting adverse pressure gradients, as given by Oliver. The comparisons show that the measured vorticity distribution of the natural boundary layer is quite close to that of the predicted vorticity profile for a limiting adverse pressure gradient, the vorticity tending to zero as the wall is approached. The vorticity at the beginning of the calmed region, on the other hand, is higher near the wall than levels associated with a Blasius boundary layer. By one third of the way through the calmed region (457C + 10) the vorticity profile is quite Blasius-like.

Figure 9 presents streamwise development of the vorticity profile at the beginning of the calmed region with the distribution from the natural boundary layer as a reference. These plots are of the same type as Fig. 8, but y is normalized by θ instead of δ. The normalizing values of θ and δ are those of the natural boundary layer ahead of the spot. The legends signify streamwise locations between x values of 407 mm and 557 mm. In order to compare the calmed region shear stress distributions with those of the turbulent region of the spot, distributions from the most turbulent instant of time at each station are presented in Fig. 10. It should be noted that the vorticity scales are different in Figs. 8, 9, and 10.

Because the vorticity profiles are obtained by differencing the measured phase-averaged velocity profiles, significant scatter might be expected. These profiles should therefore be taken as indicators of levels and trends.

While it is still laminar, the natural boundary layer has a peak normalized value of around 0.2 near the wall. This level increases as the boundary layer undergoes transition.

At x = 407 the "spot" is really still a wave packet and the wall shear is low, although the calmed region has already developed and its vorticity distribution is already quite Blasius-like. Under an adverse pressure gradient a wave packet can have a calmed region too, and this might be an important clue concerning the nature of the calmed region. Essentially it has much to do with the stability of the velocity profile as influenced by the wave packet or spot and not much to do with turbulence in the flow. Along with the evidence of Fig. 4, this tells us that

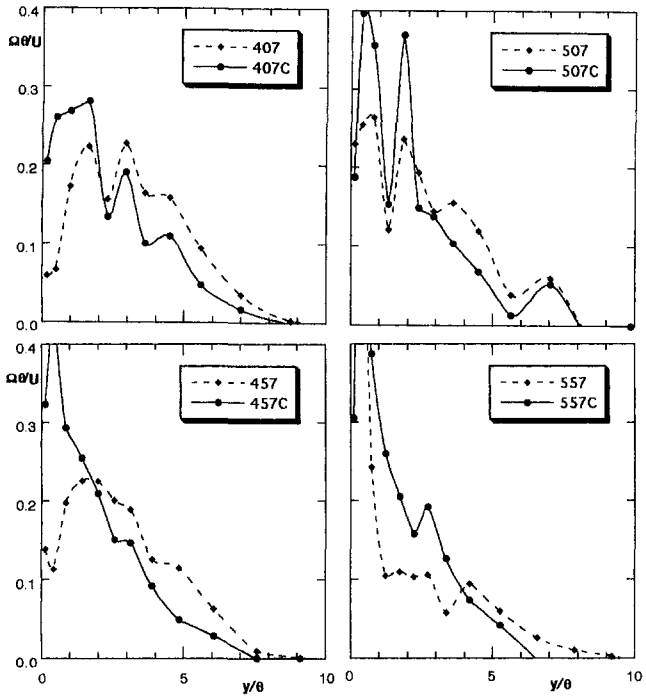

Fig. 9 Vorticity profile development in the natural boundary layer and the calmed region

the calmed region works because its relatively stable velocity profile reduces the amplitude of oscillations and in doing so delays the development of harmonics. This still does not explain why the calmed region has such a stable profile, but it does indicate that it is not simply associated with the delay in the recovery from a turbulent profile to a laminar profile. It might also be noted that the reduced level of H from calming will affect the onset of both natural and forced transition.

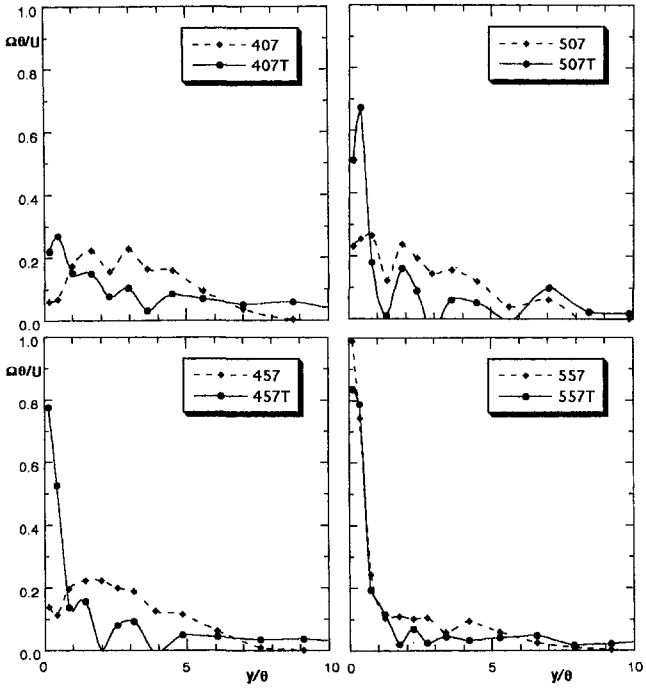

Fig. 10 Vorticity profile development in the natural boundary layer and the turbulent region

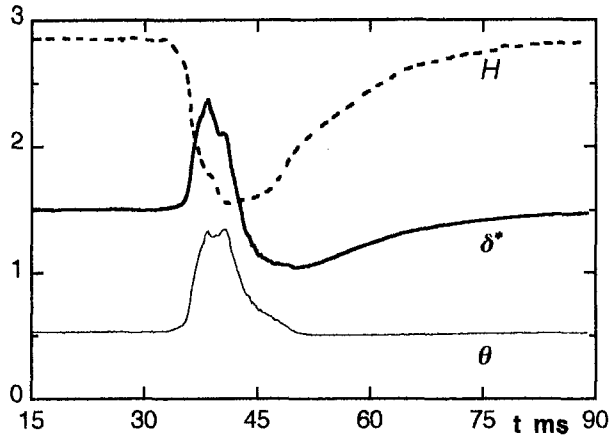

Fig. 11 Variation of integral parameters through spot and calmed region at x = 457 mm

At subsequent stations, as the spot develops and its wall shear rises, so the calmed region also develops and its wall shear also rises, although typically only to about half of the level of the turbulent region. The discrepancies between the calmed region and the natural layer are highest in the early stages where the natural layer is laminar. As the natural layer becomes turbulent, the calmed region gradually acquires a similar vorticity profile, as does the turbulent region of the spot itself. Eventually the natural layer, the triggered spot and the calmed region become indistinguishable but it takes a long streamwise distance for the calmed region to be obliterated, even in an adverse pressure gradient. As shown in Fig. 5, and in Fig. 4 of Gostelow et al. (1995), the turbulence of the natural layer gradually contaminates the calmed region.

Unlike the case of a spot under zero pressure gradient, for an adverse pressure gradient there is no forbidden zone the encroaching turbulence cannot penetrate—merely a region of greater stability, which is quite persistent. TS waves originating upstream of the triggered spot breakdown position are also able to penetrate this region behind the spot in the strongly decelerating flow situation (where the TS wave celerity is of the same order as that of the spot trailing edge). The fact that these waves do not produce new turbulent spots indicates that they must be damped, and that this is the primary reason for the persistence of laminar flow. In the adverse pressure gradient situation the rear of the calmed region is never isolated from unstable flow and this applies whether this is an isolated spot or a strip.

Boundary Layer Thickness in Calmed Region. As an example of the variation of the integral properties along the centerline of the spot and the calmed region, these are plotted in Fig. 11 for the x = 457 location used for Figs. 6–8. Variations of H, δ^*, and θ with time, between 15 ms and 90 ms, are given. The considerable drop in H to turbulent values within the spot is predictable; the gradual rise represents well the relaxation process associated with the calmed region. The low values of H at the beginning of the calmed region are associated with the full and stable velocity profile previously noted. At the beginning of the calmed region, the value of δ^* drops well below that of the natural boundary layer, to which it gradually relaxes. The value of θ does not here drop significantly below the natural value, although this is not universally the case.

It has often been claimed that in the calmed region the boundary layer is thin. Particular emphasis is placed on this aspect by Katz et al. (1990) and Cumpsty et al. (1995). The boundary layer thickness is perhaps best characterized by comparing integral parameters at the beginning of the calmed region with those of the undisturbed natural boundary layer. Katz et al. did this and found, for a favorable pressure gradient spot, a $\delta_c^*/\delta_{nat}^*$ value of 0.8; the equivalent value for a zero pressure gradient spot was 0.57. The corresponding values of θ_c/θ_{nat} were 0.92 for a favorable pressure gradient spot and 0.5 for a zero pressure gradient spot. At the x = 457 location the values for this adverse pressure gradient spot were 0.69 for $\delta_c^*/\delta_{nat}^*$ and 0.95 for θ_c/θ_{nat}. These values are not particularly consistent with the data of Katz et al. The reason for this seems to be that the boundary layer thickness at the beginning of the calmed region is sensitive to the stage of development of the spot, especially as it relates to the surrounding natural boundary layer.

The ratios of integral parameters are plotted in Fig. 12 as a function of streamwise location. They are not constant and are particularly affected by the transition of the natural boundary layer. Although H is not plotted, levels indicate the robustness of the calmed region. While that of the natural layer is falling from 3.18 to 1.62, the value of H_c only drops from 2.85 to 2.62 on moving downstream through the transition region.

Overall it can be said that, on a displacement thickness basis, the calmed region is thinner than the natural boundary layer. As the spot develops, the calmed region becomes significantly thinner; this trend reverses somewhat when the natural boundary layer itself undergoes transition.

Conclusions

Similarities are indicated between space ~ time plots for the condition of developing boundary layers on axial turbomachine blades (caused by wake interaction) and the equivalent plots for triggered wave packets and turbulent spots on a flat plate in a wind tunnel. Although this latter case is still not fully understood, it has been studied extensively, and the available data are considered to be a valuable resource for modeling studies.

Wind tunnel measurements are presented of the calmed region behind a triggered turbulent spot under a strong adverse pressure gradient at different streamwise locations.

Phase-averaged velocity and rms disturbance level profiles are plotted. The trailing edge of the calmed region propagates at different rates depending on whether the natural boundary layer is laminar or turbulent.

Raw data traces (and associated wavelet analyses) from the former case have shown that the calmed region, which may be present even behind a wave packet, acts by reducing the amplitude of dangerous instabilities and by delaying the associated harmonic development. Distributions of rms disturbance level from the latter case have shown that the turbulence of the surrounding natural boundary layer eventually contaminates the calmed region and leads to its destruction, although this process may be quite protracted.

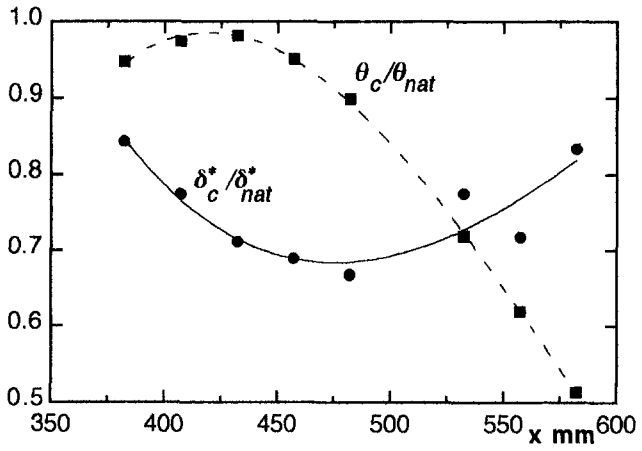

Fig. 12 Streamwise variations of normalized displacement and momentum thicknesses at beginning of calmed region

The calmed region exhibits a significantly more stable velocity profile than the natural boundary layer. The boundary layer in the calmed region is thinner than the natural boundary layer, but its thickness is quite sensitive to the state of the natural layer. The calmed region behind a turbulent spot is extensive and exhibits a complex interaction with the encroaching natural turbulent layer.

Acknowledgments

The authors acknowledge the financial support of the Australian Research Council and Rolls-Royce plc. Discussions with Professor N. A. Cumpsty were most helpful.

References

Blackwelder, R. F., 1993, private communication.

Cumpsty, N. A., Dong, Y., and Li, Y. S., 1995, "Compressor Blade Boundary Layers in the Presence of Wakes," ASME Paper No. 95-GT-443.

Gostelow, J. P., Melwani, N., Solomon, W. J., and Walker, G. J., 1995, "Effects of a Self-Similar Adverse Pressure Distribution on Turbulent Spot Development," AIAA Paper No. 95-2254.

Gostelow, J. P., and Hong, G., 1995, "Representation of Boundary Layer Transition and Turbulent Spots in Temporal and Frequency Domains," *Proc. 7th ISFV, Seattle; Flow Visualization VII,* Begell House, New York, pp. 218–223.

Gostelow, J. P., Melwani, N., and Walker, G. J., 1996, "Effects of Streamwise Pressure Gradient on Turbulent Spot Development," ASME JOURNAL OF TURBOMACHINERY, Vol. 118, pp. 737–743.

Gutmark, E., and Blackwelder, R. F., 1987, "On the Structure of a Turbulent Spot in a Heated Laminar Boundary Layer," *Experiments in Fluids,* Vol. 5, pp. 217–229.

Halstead, D. E., Wisler, D. C., Okiishi, T. H., Walker, G. J., Hodson, H. P., and Shin, H-W., 1997, "Boundary Layer Development in Axial Compressors and Turbines: Parts 1–4," ASME JOURNAL OF TURBOMACHINERY, Vol. 119, pp. 114–127; 426–444; 225–237; 128–139.

Hartree, D. R., 1937, "On an Equation Occurring in Falkner and Skan's Approximate Treatment of the Equations of the Boundary Layer," *Proc. Cambridge Phil. Soc.,* Vol. 33, pp. 223–239.

Katz, Y., Seifert, A., and Wygnanski, I., 1990, "On the Evolution of the Turbulent Spot in a Laminar Boundary Layer With a Favourable Pressure Gradient," *J. Fluid Mech.,* Vol. 221, pp. 1–22.

Krane, M. H., and Pauley, W. R., 1994, "The Effects of Weak Interaction and Reynolds Number on Boundary Layer Scalars With Tandem Turbulent Spots," ASME *Journal of Fluids Engineering,* Vol. 116, pp. 653–656.

Oliver, A. R., 1965, "Velocity Distribution in a Laminar Boundary Layer," *Aeronautical Research Laboratories (Australia) Mech. Eng.,* Note 268.

Schubauer, G. B., and Klebanoff, P. S., 1955, "Contributions on the Mechanics of Boundary-Layer Transition," NACA Rep. 1289.

Seifert, A., and Wygnanski, I., 1995, "On Turbulent Spots in a Laminar Boundary Layer Subjected to a Self-Similar Adverse Pressure Gradient," *J. Fluid Mech.,* Vol. 296, pp. 185–209.

Solomon, W. J., Walker, G. J., and Gostelow, J. P., 1996, "Transition Length Prediction for Flows With Rapidly Changing Pressure Gradients," ASME JOURNAL OF TURBOMACHINERY, Vol. 118, pp. 744–751.

Solomon, W. J., and Walker, G. J., 1995a, "Observations of Wake-Induced Transition on an Axial Compressor Blade," ASME Paper No. 95-GT-381.

Solomon, W. J., and Walker, G. J., 1995b, "Incidence Effects on Wake-Induced Transition on an Axial Compressor Blade," *Proc. 12th ISABE,* Melbourne.

van Hest, B. F. A., Passchier, D. M., and van Ingen, J. L., 1994, "The Development of a Turbulent Spot in an Adverse Pressure Gradient Boundary Layer," *Proc. IUTAM Symposium,* Sendai.

Wygnanski, I., Sokolov, M., and Friedman, D., 1976, "On a Turbulent Spot in a Laminar Boundary Layer," *J. Fluid Mech.,* Vol. 78, pp. 785–819.

Zilberman, M., Wygnanski, I., and Kaplan, R. E., 1977, "Transitional Boundary Layer Spot in a Fully Turbulent Environment," *Physics of Fluids,* Vol. 20, No. 10, pp. 258–271.

The Effect of Vortex Shedding on the Unsteady Pressure Distribution Around the Trailing Edge of a Turbine Blade

G. Cicatelli

C. H. Sieverding

von Karman Institute,
Ch. de Waterloo, 72,
Rhode St. Genèse, Belgium

The wakes behind turbine blade trailing edges are characterized by large-scale periodic vortex patterns known as the von Karman vortex street. The failure of steady-state Navier–Stokes calculations in modeling wake flows appears to be mainly due to ignoring this type of flow instabilities. In an effort to contribute to a better understanding of the time-varying wake flow characteristics behind turbine blades, VKI has performed large-scale turbine cascade tests to obtain very detailed information about the steady and unsteady pressure distribution around the trailing edge of a nozzle guide vane. Tests are run at an outlet Mach number of $M_{2,is}$, $= 0.4$ *and a Reynolds number of* $Re_C = 2 \times 10^6$. *The key to the high spatial resolution of the pressure distribution around the trailing edge is a rotatable trailing edge with an embedded miniature pressure transducer underneath the surface and a pressure slot opening of about 1.5 deg of the trailing edge circle. Signal processing allowed differentiation between random and periodic pressure fluctuations. Ultrashort schlieren pictures help in understanding the physics behind the pressure distribution.*

1 Introduction

The steady-state approach for solving turbomachinery flow problems, which has prevailed for many decades of turbomachinery research, is progressively being abandoned in favor of the study of the true unsteady character of the flow through the bladings. The recent rapid increase of experimental and numerical research projects devoted to the wake–blade interaction phenomena in stages clearly demonstrates this new viewpoint. The intensity of the periodic phenomenon, which is related to the blade passing frequency, directly depends on the pressure gradient field generated by the wake at the inlet to the downstream blade row and thereby on the mixing process of the wake.

To date, the mixing process of the wake behind a turbine (or compressor) blade is still viewed as a steady-state process, although it is well known that the separation of the boundary layers at the trailing edge is a highly unsteady phenomenon, which leads to the formation of large coherent structures, known as the von Karman vortex street. For turbine blades the vortex shedding frequency is typically between 5 and 50 kHz.

Steady-state Navier–Stokes calculations using conventional mixing length and two-equations models fail to predict correctly the wake evolution behind turbomachinery blading for two reasons: (*a*) They ignore the strong time-varying character of the wake flow and (*b*) they are unable to deal with the highly nonisotropic character of turbulent separated flows and wake flows. Unsteady Navier–Stokes solvers, improved turbulence models like nonlinear two-equation and Reynolds stress models and Large-Eddy Simulation techniques are presently being investigated regarding their suitability for the calculation of the wake mixing process.

The technical literature concerning the investigation of unsteady turbine wake characteristics is rather scarce; see Cicatelli and Sieverding [1]. To date the most comprehensive studies are those by Lawaczeck and Heinemann [2] on the effect of boundary layer state on vortex shedding from flat plates and turbine cascades, on vortex shedding frequency measurements for a wide variety of cascades by Sieverding and Heinemann [3], and on the observation of different types of vortex streets behind turbine blades by Carscallen and Gostelow [4]. None of these studies reported any detailed quantitative measurements on the time-varying trailing edge flow and wake flow characteristics. The reason for this is the relatively small trailing edge size of most cascade blades, which does not allow for a sufficient spatial resolution for detailed investigations in the most important region, i.e., the near-wake flow region. Clearly only large-scale models can provide sufficient spatial resolution for detailed flow field measurements.

Large-scale models have already been used by Han and Cox [5] for smoke visualizations of the von Karman vortex street in the wake of a low-speed nozzle guide vane and by Mee [6] for detailed measurements of boundary layer characteristics and pressure distribution in the trailing region. Our present knowledge on the mechanism of vortex formation, turbulence production, and dissipation, however, is entirely based on research of the flow over large-scale bluff bodies [e.g., 7–9]. But these results cannot be transferred directly to turbine blades because of the different flow conditions for flows separating from bluff bodies and from turbine blades: blade circulation and different boundary layers states on pressure and suction side before separation for turbine blades, symmetric flow conditions for bluff bodies.

The investigations reported in this paper are part of a BRITE EURAM project. The aim of the project is twofold: (*a*) to improve our understanding of physics of unsteady turbine blade wakes and (*b*) to provide high-quality experimental data for the validation of Navier–Stokes codes. The turbine blade selected for this study is a large-scale nozzle guide vane with thick trailing edge. The main scope of this paper is the presentation of detailed measurements of the trailing edge pressure distribution, steady and unsteady. Ultrashort schlieren pictures contribute to the interpretation of these data.

2 Tunnel and Cascade Model

The tests described in this paper were performed in the VKI high-speed cold flow open circuit blow down cascade tunnel.

Contributed by the International Gas Turbine Institute and presented at the 41st International Gas Turbine and Aeroengine Congress and Exhibition, Birmingham, United Kingdom, June 10–13, 1996. Manuscript received at ASME Headquarters February 1996. Paper No. 96-GT-359. Associate Technical Editor: J. N. Shinn.

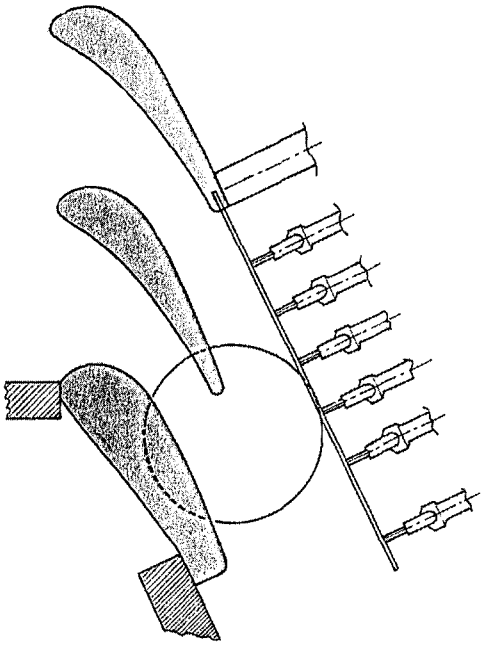

Fig. 1 Blade model and cascade test section

The overall blade dimensions were determined by the need for the highest possible spatial resolution for the trailing edge pressure, requiring a maximum trailing edge thickness, and the maximum dimensions of the test section, i.e., 400 mm height and 200 mm width. The compromise resulted in a three-bladed cascade with blades of 280 mm chord length, 200 mm blade height, and 15 mm trailing edge thickness, Fig. 1. The blade was designed front loaded with an overall low suction side turning in the overhang section and in particular a straight rear suction side from halfway down the throat. These design features met the following requirements:

- (a) to ensure a turbulent state of the suction side boundary layer at the trailing edge.
- (b) to ease the use of tailboards (easier with a weakly curved rear suction side than with a highly curved rear suction side).
- (c) to ease the implementation of an optical window in the rear suction side of the lower blade of the cascade for PIV measurements in a later phase of the project.

The fine tuning of the blade shape was accomplished using a semi-inverse blade design method by Leonard and van den Braembussche [10]. The most important geometric dimensions of the cascade are summarized below:

chord length, C = 280 mm
pitch to chord ratio, g/C = 0.696
blade height, h = 200 mm
aspect ratio, h/C = 0.7
trailing edge to chord ratio, D/C = 0.0531
trailing edge wedge angle, ϵ = 7.5 deg
stagger angle, γ = −49°83
gaging angle, α_2^* (arcsin o/g) = 19.1 deg

The blade coordinates are given in the appendix.

2 Blade Instrumentation

A first blade (Blade A) was equipped with 31 wall pressure tappings along the suction side and 22 tappings along the pressure side at midspan to determine the blade velocity distribution. Regarding the trailing edge, the placement of individual pressure tappings around the trailing edge would not have provided the required dense spatial distribution in this region. Therefore, the blade trailing edge is designed with a rotatable cylinder of 20 mm height placed at midspan (Fig. 2(a)). This cylinder is equipped with a single Kulite pressure sensor, and an ordinary pneumatic pressure tapping implemented side by side.

The need of a high-frequency response ideally requires the transducer to be surface mounted. The relative large diameter of the Kulite transducer (type XCS-062 5PSI) poses a severe limitation to the spatial resolution. A 1.62-mm-dia surface-mounted transducer on a 15-mm-dia circular trailing edge covers an angular sector of 12.4 deg.

To reduce the opening angle, the transducer is mounted under the trailing edge surface and connected to the external environment via a small rectangular window of 1.0 mm length and 0.2 mm width, reducing the sensing area to an angular sector of 1.53 deg only. Notice that the area of this window is equal to the total area of the opening in a typical "B" screen frequently mounted by the manufacturer on these transducers. The total distance between the trailing edge surface and the transducer chip is 0.5 mm: a depth of the rectangular slot of 0.3 mm and a retreat of the pressure chip from the head of the Kulite probe of 0.2 mm (Fig. 2(b)). The opening of the pneumatic pressure tapping is the same as for the Kulite, i.e., 1 × 0.2 mm. The rotatable cylinder is rigidly connected to a manual device enabling the rotation of the cylinder. The angular position is controlled with a circular protractor. With a gap of ~0.01 mm between the rotatable cylinder and the blade and a thickness of the blade lips of ~0.02 mm, the angular position of the lips with respect to the tangential points of the ideal blade surfaces to the trailing edge circle are 5 and 4.5 deg for the suction side and pressure side, respectively, (Fig. 2(a)).

A second blade (Blade B) was instrumented with six Kulite transducers placed at and slightly upstream of the trailing edge, Fig. 2(c). The manufacturing of this second blade was suggested by the need to verify the possible influence of the rearward-facing step between the blade lip and the rotatable cylinder on blade A and to obtain information on the effects of the vortex shedding on the flow upstream of the trailing edge. Each Kulite transducer is coupled with a pressure tap following the same

Nomenclature

C = turbine blade mechanical chord
C_{ax} = axial chord
C_{Pb} = base pressure coefficient
D = turbine blade trailing edge thickness
g = pitch
h = blade height
$M_{2,is}$ = isentropic outlet Mach number
o = throat opening
P_b = base pressure
P_{01} = inlet total pressure
P_{S2} = outlet static pressure
Re_C = Reynolds number based on chord length
S = curvilinear abscissa
T_{01} = inlet total temperature
Tu = inlet turbulence level
u = boundary layer velocity
u_e = boundary layer external velocity
W_{max} = blade velocity peak
W_2 = blade outlet velocity
X = axial direction
α_2^* = gaging angle = arcsin o/g
α = probe angle
γ = stagger angle
δ = boundary layer thickness
δ^* = boundary layer displacement thickness
ϵ = wedge angle
θ = boundary layer momentum thickness
ρ = air density
ω = total pressure loss coefficient

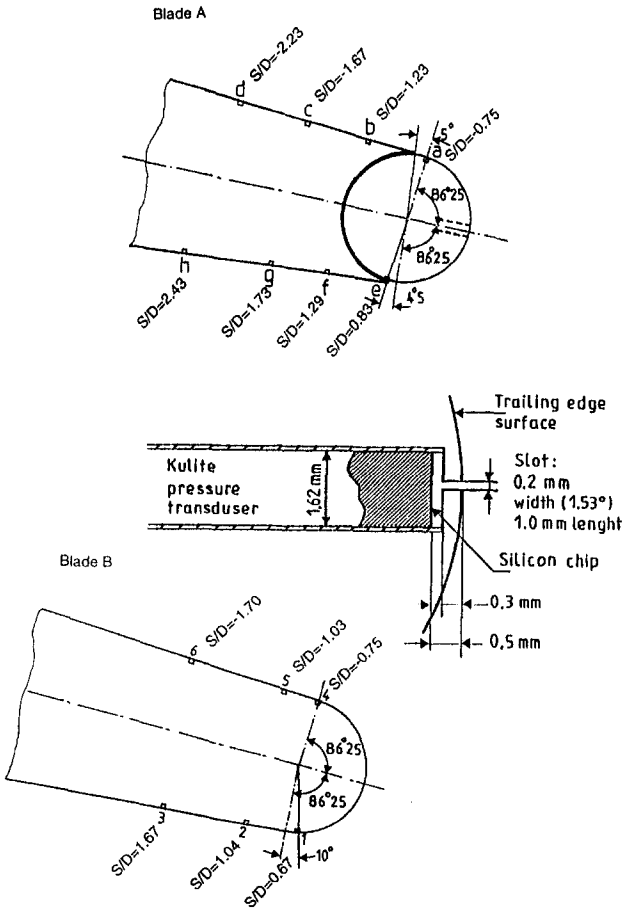

Fig. 2 Blade instrumentation

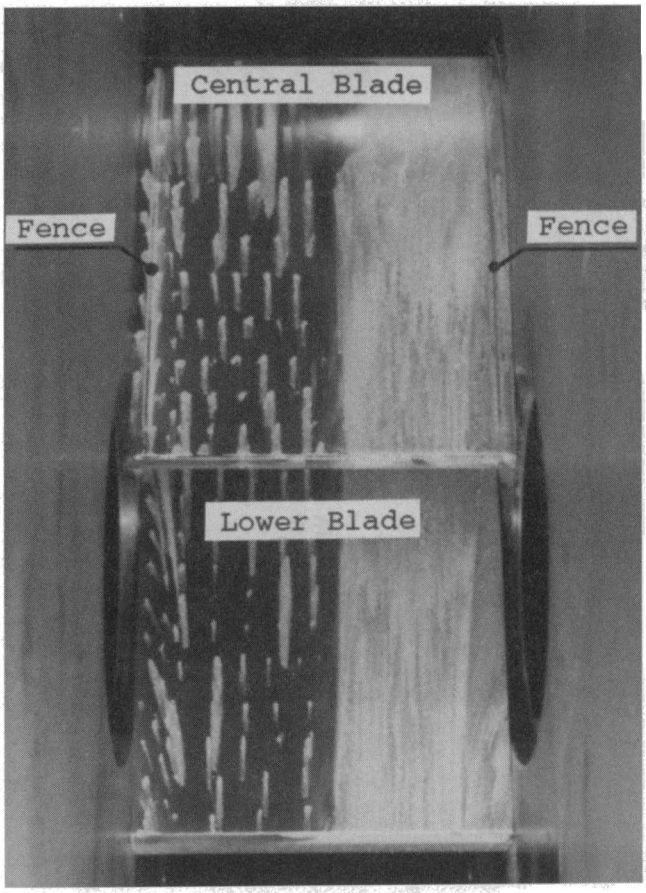

Fig. 4 Oil flow visualization

criteria used for blade A. The exact positions are indicated in Fig. 2(*c*). The Kulite transducer No. 1 is placed on the pressure side of the trailing edge surface, 10 deg from the tangent point, while No. 4 is placed on the suction side exactly on the tangent point. The transducers 2, 3, 5, 6 are located on the pressure side and suction side, respectively, at 1.5 and 5 percent of the mechanical chord from the tangent points.

The frame of reference in which all data will be represented is illustrated on Fig. 3. The origin of the reference system is fixed on the center of the trailing edge. All the data are presented in curvilinear abscissa nondimensionalized by the trailing edge diameter.

3 Flow Conditions

3.1 Overall Conditions. The overall flow conditions for the tests are summarized below:

total pressure upstream P_{01} = 1178 mbar

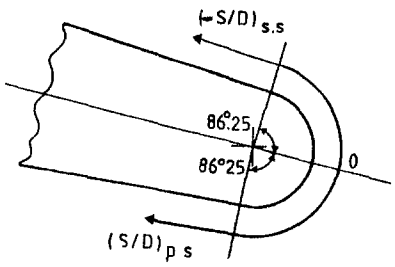

Fig. 3 Trailing edge reference system

total temperature upstream T_{01} = 287 K
isentropic outlet Mach number $M_{2,is}$ = 0.4
Reynolds number Re_C = 2×10^6
degree of turbulence Tu = 1.15 percent

3.2 Two Dimensionality. In view of the relatively small aspect ratio, it appeared opportune to attempt to reduce secondary flow effects through the use of boundary layer fences. Following Kawai and Adachi [11], the optimum endwall distance of the fences from the side wall is equal to $\frac{2}{3}$ of the inlet boundary layer on the side wall. The maximum height of the fence is equal to the blade surface boundary layer thickness close to the trailing edge. Based on inlet endwall boundary layer measurements and blade boundary layer calculations, the fences were placed at 5 mm from the endwall (blade height 200 mm) with a maximum height of 5 mm at the trailing edge.

The effectiveness of the fences was verified by blade surface oil flow visualizations and downstream total pressure probe traverses. Figure 4 shows, for the oil flow visualization, the result of the comparison between the lower blade not fenced and the central blade where boundary layer fences were installed. With boundary layer fences two-dimensional conditions exist over approximately 75 percent of the blade height.

3.3 Periodicity. The use of a flexible tailboard extending from the upper blade allowed to set up a nearly uniform downstream static pressure distribution over both pitches of the cascade, Fig. 5.

3.4 Blade Velocity Distribution. The surface pressure distribution is measured using the static pressure tappings on the suction and pressure side of the central blade. The associated midspan isentropic Mach number distribution is presented in Fig. 6.

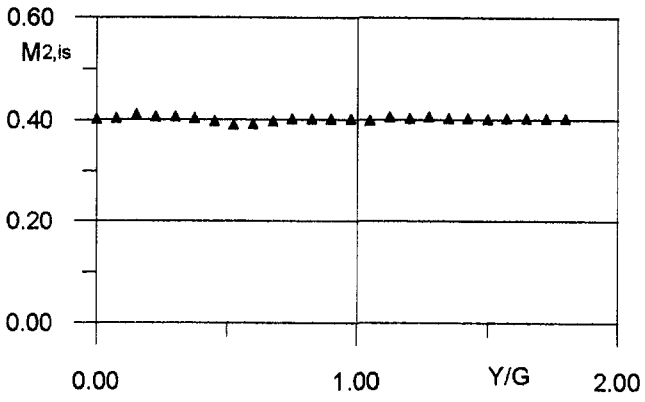

Fig. 5 Outlet Mach number distribution

The blade velocity is typical for a front-loaded blade. The suction side velocity peaks at around $X/C_{ax} \cong 0.6$ with a ratio of $W_{max}/W_2 = 1.25$. This peak is followed by a smooth deceleration and a plateau on the rear suction side before the start of the trailing edge acceleration. On the pressure side the flow constantly accelerates up to the trailing edge.

3.5 Boundary Layer Characteristics. Sieverding and Heinemann [3] clearly demonstrated that the state of the boundary layer at the trailing edge influences the vortex shedding frequency in the wake. Furthermore, the shape of the vortex shedding frequency spectrum depends on the state of the boundary layer on both blade sides. If the boundary layers are laminar or turbulent on both sides, the vortex shedding frequency spectrum is very narrow. In case of mixed laminar/turbulent boundary layers, the dominant frequency spectrum tends to broaden. A transitional boundary layer on one or both sides results in a very large vortex shedding frequency spectrum, with possibly the appearance of two maxima. The expected data processing implying conditional phase averaging of the base pressure signal, however, requires the identification of a clear peak in the shedding frequency spectrum. The suction side boundary layer is expected to be turbulent at the trailing edge while the pressure side boundary layer is either laminar or transitional. Preliminary tests have led to the decision to trip the boundary layer on the pressure side to have fully developed turbulent boundary layers on both pressure and suction side. A 0.4-mm-dia trip wire was installed along the span at a station $X/C_{ax} = 0.61$.

Boundary layer profiles were measured with a flattened pitot probe at a distance equal to one trailing edge diameter upstream of the trailing edge circle. The flattened probe had a thickness of 0.25 mm. The uncertainty in the probe position is ±0.05 mm. The characteristics of the compressible boundary layer were determined with the following relationships:

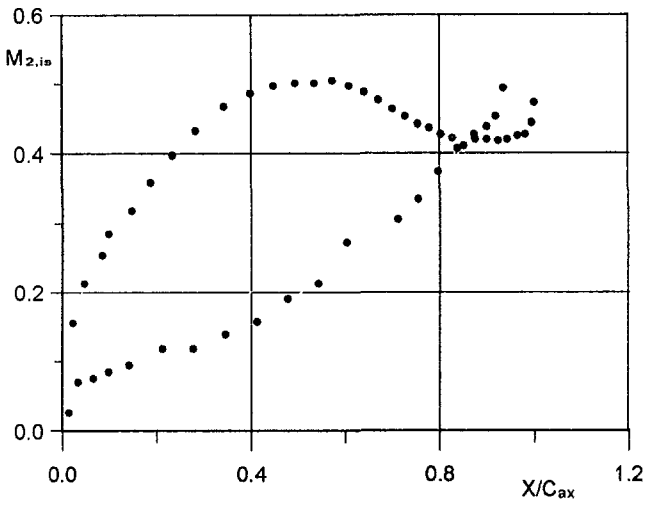

Fig. 6 Blade velocity distribution

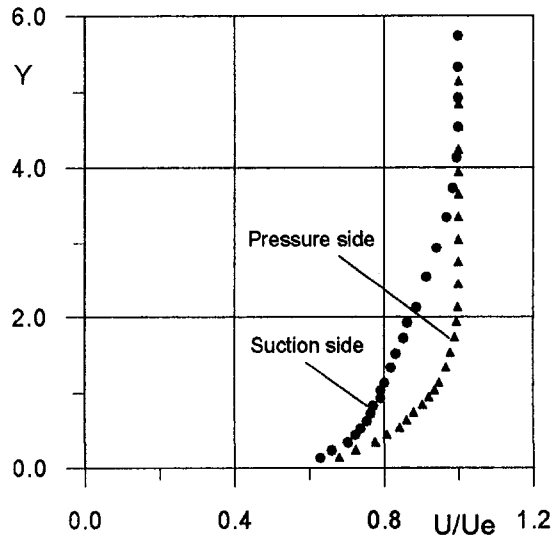

Fig. 7 Boundary layer velocity profiles

$$\delta^* = \int_0^\delta \left(1 - \frac{\rho u}{\rho_e u_e}\right) \cdot dy \tag{2}$$

$$\vartheta = \int_0^\delta \frac{\rho u}{\rho_e u_e} \cdot \left(1 - \frac{u}{u_e}\right) \cdot dy \tag{3}$$

$$H = \frac{\delta^*}{\vartheta} \tag{4}$$

The correction for the displacement effects for pitot tubes in shear flows is of the same order as the uncertainty for the probe position and therefore has been neglected. Corrections for the wall interference have been applied. A second-order formula was used:

$$\frac{\Delta u}{u} = \frac{(y/l - 1.9)^2}{1.4^2} \cdot 0.016 \quad \text{for} \quad y/l < 1.9 \tag{5}$$

where l is the thickness of the probe head (in this case K = 0.25 mm). The boundary layer velocity profiles are presented in Fig. 7.

The boundary layer characteristics are summarized below:

	Pressure side	Suction side
δ/D	0.01336	0.2772
δ^*/D	0.0167	0.0405
θ/D	0.0102	0.0288
H	1.64	1.41

The boundary layers are clearly turbulent on both pressure and suction sides with the particular characteristic that on the suction side the thickness is approximately double that on the pressure side.

4 Trailing Edge Pressure Measurements

4.1 Experimental Procedure. The data acquisition was realized with a BE490 acquisition card installed on 486 DX4 100 MHz PCI bus personal computer. The system has a maximum sampling frequency of 1 MHz with 12 bits resolution. The board provides access to 8 different channels. The sampling

frequency was set to 25 kHz and 4096 samples were acquired. Two channels were dedicated to the acquisition of the trailing edge pressure signal: one for the Kulite pressure transducer and one for the pneumatic static pressure tappings mounted in parallel with the Kulite transducer. In order to guarantee that all the tests were effectively performed at the same outlet flow conditions, for each individual test, the inlet total pressure P_{01} and outlet static pressure P_{S2} were also acquired to determine the outlet Mach number on line.

4.2 Data Processing Strategy: Signal Splitting. In order to analyze the unsteady base pressure, the signal provided by the fast-response pressure transducers can be regarded as a combination of a time-averaged component $\bar{P}$ and a fluctuating component $\tilde{P}$:

$$P = \bar{P} + \tilde{P} \tag{6}$$

As regards the time-averaged pressure $\bar{P}$, its value can be derived from either the pressure signal of the Kulite transducer or the corresponding pneumatic wall pressure measurements. With a careful adjustment of the zero shift before each blow down of the tunnel, the time-averaged value of the Kulite transducer signal differed from the pneumatic wall pressure measurements by less than 2 percent. However, the continuous adjustement turned out to be quite a tedious task, in particular when recording several transducers simultaneously. It was therefore decided to use the $\bar{P}$ value of the pneumatic wall pressure measurements and use the Kulite signal for the pressure fluctuations only.

A quantitative evaluation of the term $\tilde{P}$ in Eq. (6) can be obtained from the root mean square of the fluctuating signal and nondimensionalized by the dynamic downstream pressure $P_{01} - P_{S2}$:

$$\text{rms} = \frac{\sqrt{\tilde{P}^2}}{P_{01} - P_{s2}} \tag{7}$$

A further analysis of the term $\tilde{P}$ can be performed starting from the assumption that the term $\tilde{P}$ is the result of two different contributions: a random contribution P' due to the small-scale turbulent structures, and a more organized component, essentially periodic, P_{pha}, whose origin can be found in the presence of the organized vortical activity in the wake, mainly the von Karman vortex street:

$$\tilde{P} = P' + P_{pha} \tag{8}$$

It is not possible to extract directly from the row signal the amplitude of the pressure fluctuation P_{pha}. Then, in order to appreciate the presence of this contribution, a frequency analysis is essential. A Fast Fourier Transform was applied to the fluctuating part of the pressure signal only, because it was immediately evident that the energy content of the fluctuating part of the signal is much lower than the energy content of the entire signal and this fact could mask the appreciation of the frequency peak in view of a further signal processing.

Once the vortex shedding frequency is identified, it is possible to extract the contribution of the organized vortical activity P_{pha} from the global fluctuating component $\tilde{P}$. For this purpose an ensemble phase-averaging technique has been used. The processing is based on the identification of the dominant period T of the signal obtained thanks to the FFT. Then the entire fluctuating signal $\tilde{P}$ is subdivided into pieces of one-period time length T, and eventually a phase averaging of all these small signals is done. This means that every period length signal is further subdivided into a fixed number of intervals, phase averaged over the N cycles of the entire signal. The process can be summarized with the relationship:

$$P_{pha_i} = \frac{1}{N} \sum_j P_{pha_{ij}} \tag{9}$$

where N is the number of cycles.

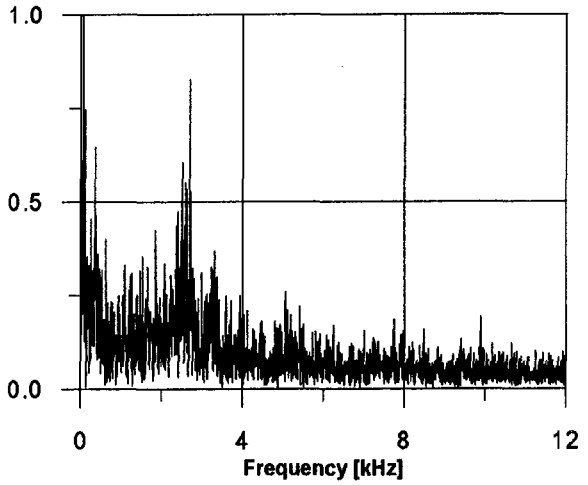

Fig. 8 Vortex shedding frequency spectrum

4.3 Vortex-Shedding Frequency. A typical result of the vortex shedding frequency spectrum is shown in Fig. 8. This frequency spectrum was measured by a Kulite transducer positioned on the trailing edge circle at $\alpha = 72$ deg ($\alpha = 0$ corresponds to the trailing edge center) near the point of the highest fluctuations, as will be shown later. The dominant frequency peak was found at 2.65 kHz. The frequency is usually expressed by the Strouhal number

$$\text{S} = \frac{f \cdot D}{u} \tag{10}$$

In cascades, the reference velocity "u" is typically taken equal to the downstream velocity. Using this definition the Strouhal number is S = 0.27. Comparing the Strouhal numbers from a large number of tests, the authors noticed variation in the Strouhal number of up to 4 percent, although most tests did not vary by more than 2–3 percent. These variations are in line with the observation that the dominant frequency does not appear as a single peak in the frequency spectrum but rather as a dominant frequency band width. The Strouhal number of 0.27 is somewhat high for a blade with turbulent boundary layers on both sides of the trailing edge, which appears to be normally in the range S = 0.2–0.4 [1]. However, tests at the University of Genova on the same blade with very similar flow conditions showed the same Strouhal number [13].

4.4 Error Analysis. The uncertainty related to both instruments mainly depends on the transducer characteristics, the calibration curve, and the acquisition card characteristics. The acquisition card gives an uncertainty of ±2.44 mV that corresponds to a card resolution of one digit. For the calibration of both transducers, a digital calibrator with an uncertainty of ±0.5 mbar and a voltmeter with an uncertainty estimated around ±5 mV were used. To compute the measurement uncertainty, the following relationship can be used:

$$\delta P = \sqrt{(\delta P_0)^2 + \left(\frac{\partial P}{\partial \alpha} \cdot \delta \alpha\right)^2 + \left(\frac{\partial P}{\partial V} \cdot \delta V\right)^2} \tag{11}$$

where δP_0 represents the uncertainty related to the zero balance, the second term represents the uncertainty related to the calibration, and the last one that related to the acquisition card. For the Validyne transducer used for the pneumatic pressure measurements (steady-state measurements) an uncertainty of ±2 percent of the reference pressure value was found. For the Kulite transducer, the first term is equal to zero because we used only the fluctuating part of the signal. The pressure uncertainty is

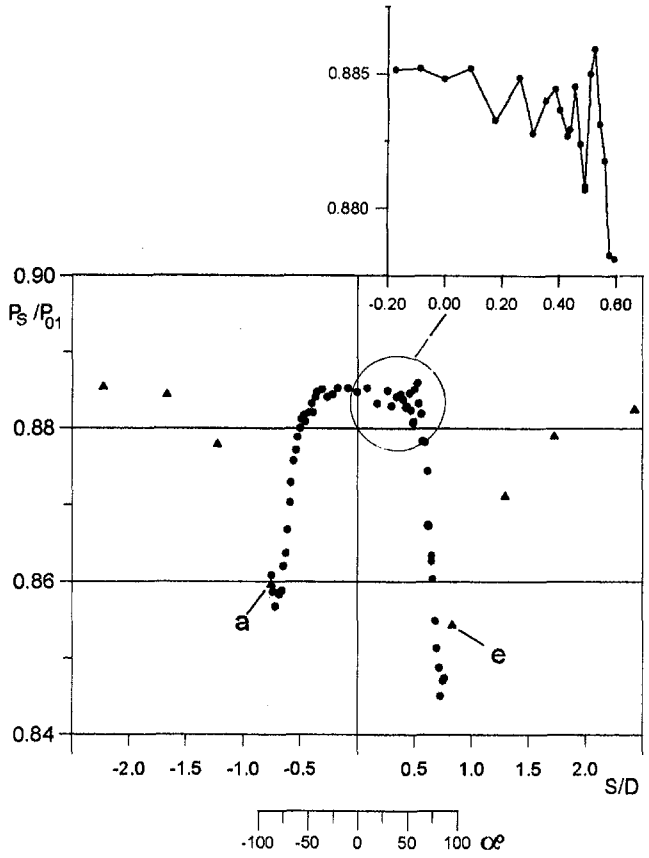

Fig. 9 Time-averaged base pressure distribution

±0.17 percent of the reference pressure value. Finally the error on the angular positioning of the rotatable cylinder is ±1 deg.

4.5 Steady-State Trailing Edge Pressure Distribution. Figure 9 shows the time-averaged base pressure distribution around the trailing edge, nondimensionalized by the inlet total pressure. The frame of reference is the one proposed in Fig. 3. The points represented with circles are obtained with the rotatable cylinder, while the triangles are obtained from the pressure taps installed on blade A and indicated on Fig. 2(*b*) with *a*–*d* and *e*–*h*. Note that the data designated by *a* and *e* are positioned aside the rotatable cylinder at 70 mm from midspan.

From Fig. 8 it results that the flow approaching the trailing edge experiences a strong over expansion compared to the surrounding flow field. Moreover the pressure curve shows a remarkable asymmetry for the pressure side and suction side expansion. The corresponding isentropic peak Mach numbers together with their exact positions are:

	S/D	α	P_b/P_{01}	Mach
S.S	−0.72	82°5	0.857	0.473
P.S.	0.73	83°6	0.845	0.496

Such high overexpansions could never be reached with a steady-state flow separation. The peak Mach number exceeds the downstream Mach number by 18.7 and 24 percent, respectively. The higher expansion on the pressure side is probably related to the much thinner boundary layer on the pressure side and to the blade circulation, which strengthens the pressure side vortex shedding, as suggested by Han and Cox [5]. The pressure distribution shows a pressure plateau at a value of $P_b/P_{01} \approx 0.885$ extending between the points $S/D = -0.325$ and $S/D = 0.5$. These points correspond to an angle of −37 deg 5 min for the suction side and 57 deg 3 min on the pressure side, covering globally an angle sector of 94 deg 5 min. The pressure coefficient describing the pressure in this region, in general referred to as base pressure coefficient, amounts to:

$$C_{Pb} = \frac{P_b - P_{S2}}{P_{01} - P_{S2}} = -0.095 \qquad (12)$$

This value is in good agreement with the base pressure coefficient derived from the correlation by Sieverding et al. [12]. It is interesting to notice that on the pressure side of the base pressure region, around $S/D = 0.5$, the graph shows a significant dispersion of the pressure data which is not observed on the suction side. The enlargment of the region shows, however, instead of a random scatter, an ordered fluctuating pressure distribution, which is maximum in the transition from the base pressure plateau to the rapid pressure drop and is gradually damped out toward the center of the plateau pressure. An explanation for this phenomenon cannot be given at present.

4.6 Unsteady Trailing Edge Pressure Distribution. Figure 10 shows the root mean square of the fluctuating signal around the trailing edge and upstream of it. The reference system is again the one shown on Fig. 3. The points represented by circles stand for the pressure signal acquired with the instrumentation of blade A, while the triangles represent the pressure fluctuations acquired with the instrumentation of blade B. The data scatter is in general of the order of ±0.5 percent (absolute) with, however, some higher values near the pressure side flow separation point.

The curve presents a small flat region around the center of the trailing edge with a value of the rms approximately equal to 4.8 percent of the downstream dynamic head. The fluctuations increase toward the pressure side and suction side flow separation points. The maximum values and their positions are:

	S/D	α	RMS/*Q*
S.S.	−0.6	68°75	7.8%
P.S.	0.775	88°8	8.0%

The two peaks are almost comparable for the values of the rms, but the abscissae at which they are located are quite different. Moreover, one would expect that these locations correspond to the pressure minima in the time-averaged pressure distribution (Fig. 8). While this is approximately true for the pressure

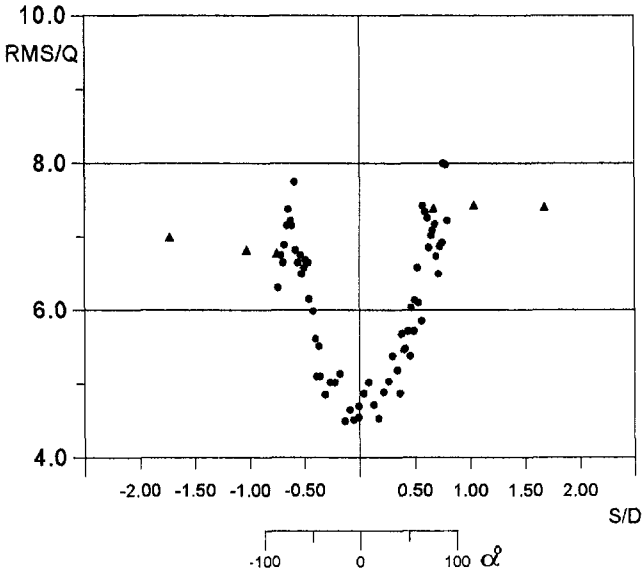

Fig. 10 The rms of the fluctuating pressure signal around the trailing edge

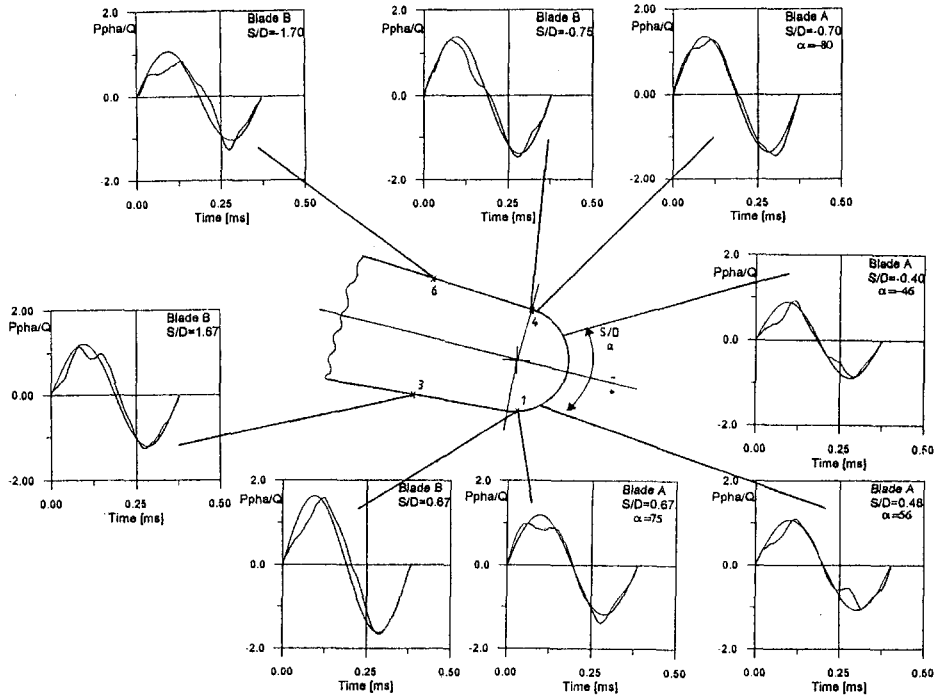

Fig. 11 Time-varying pressure oscillations

side, on the suction side the peak of the rms appears to be at a location closer to the center of the trailing edge. Of course the highest periodic fluctuations are expected to occur at the flow separation points, but this is not necessarily so for the location of the random fluctuations and the rms values presented here contain both contributions. It is further interesting to note that these fluctuations are also felt at the same distance upstream of the trailing edge: 7.4 and 6.85 percent for the pressure side and suction side, respectively. The difference may be due to the difference in the boundary layer transition on both sides: natural transition on the suction side and forced transition on the pressure side.

4.7 Time-Varying Pressure Oscillations. The periodic character of the pressure oscillation at the trailing edge is clearly shown in Fig. 11, which reports the phase-averaged pressure signals nondimensionalized by the downstream dynamic pressure for several locations. Where possible, a comparison between the results coming from blades A and B is proposed. The figures show also the comparison with a simple sinusoidal signal having the same period and amplitude as the corresponding experimental signal. The signals have been averaged over 400 cycles. The quality of the phase-averaged signals depends on the sharpness of the dominant frequency band of the periodic pressure oscillations. The "best" frequency spectra are those of the transducers positioned near the boundary layer separation points. Each graph indicates the maximum pressure difference over one cycle. Overall the pressure variations appear to be slightly higher on the pressure side. The highest variations occur in the region of the boundary layer separation points. The comparison of the data from blades A and B at these locations is fairly good: on the pressure side 3.28 percent for blade A and 2.78 percent for blade B, on the suction side 2.78 percent for blade A and 2.72 percent for blade B. Considering that the pressure variations at $S/D = \pm 2.5$ are still 2.4 and 2.16 percent for pressure and suction sides, respectively, it appears that the induced trailing edge vortex pressure variations seem to propagate relatively far upstream. As regards the trailing edge base region, the lack of a dominant vortex shedding frequency did not allow to extract a time-varying pressure signal.

5 Flow Visualization

5.1 Optical Setup. In order to clarify the results coming from the previous tests, it was decided to perform a series of flow visualizations over one vortex shedding cycle. The schlieren technique adopted is a combination of a relatively simple optical arrangement with a high degree of resolution.

The need to avoid blurred images due to the high-frequency vortex shedding requires a specific light source able to provide a very short duration spark. The presented tests were carried out using a Nanolite high-speed system manufactured by Impulsphysik, emitting a light spark of 20 nanosecond duration. The optical arrangement is shown on Fig. 12. The light emitted by the flash lamp is collimated by the lens L and directed toward the test section. The light is then deviated by the flat mirror M1 to the parabolic mirror M2. An image of the source light is formed in the focal point of mirror M2, where a knife edge has been placed. The image is then captured on a Polaroid camera, as shown in Fig. 11.

5.2 Vortex Shedding. The schlieren pictures shown in Fig. 13 document the formation and the evolution of the vortex street behind the blade trailing edge. The upper blade surface is the blade suction side. Due to the low downstream Mach number, $M_{2,is} = 0.4$, the density variations are very weak and hence the vortex

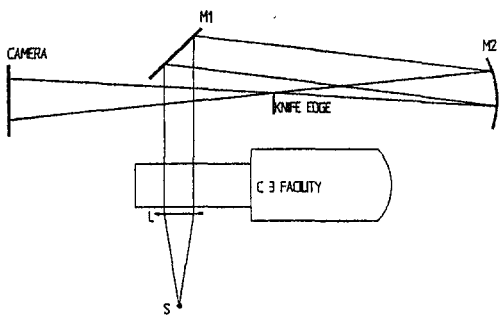

Fig. 12 Setup of schlieren system

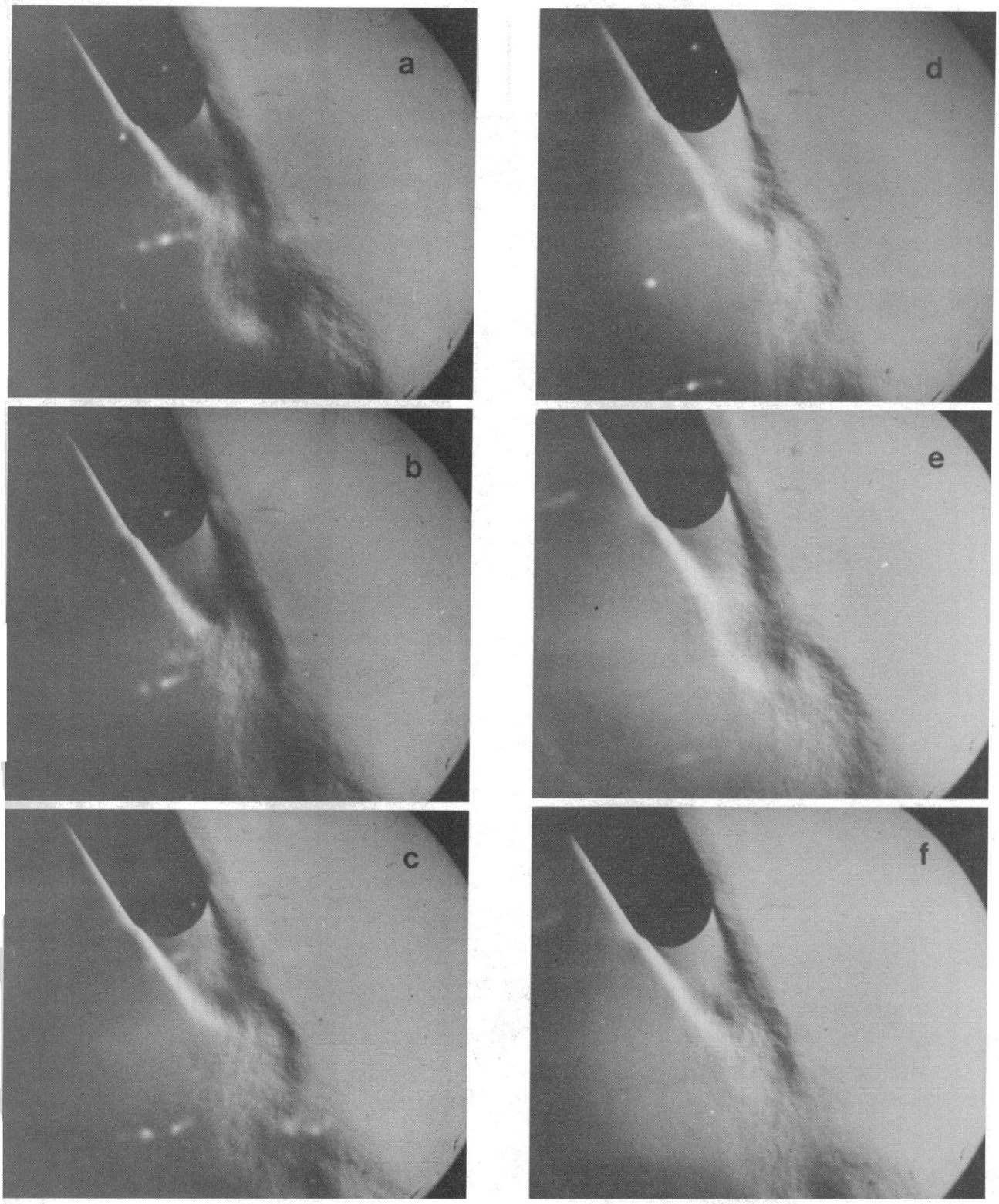

Fig. 13 Vortex shedding cycle schlieren pictures

patterns in the wake are not as well defined as at high Mach number. Nevertheless, the quality of the flow visualizations is rather satisfactory considering that not only the vortex formation but also the blade surface boundary layers could be clearly visualized. The measurements of the suction side boundary layer thickness from the schlieren photographs of 4–5 mm are in close agreement with the measured boundary layer profile thickness of $\delta = 4.1$ mm in Fig. 6. Before discussing the schlieren photographs, it may be useful to refer to the description of Gerrard [14] concerning the vortex formation behind cylinders. The model proposed by this author is illustrated in Fig. 14.

The growing vortex (A) is fed by the circulation existing in the upstream shear layer until the vortex is strong enough to entrain fluid from the opposite shear layer bearing vorticity of opposite circulation. When the quantity of entrained fluid is sufficient to cut off the supply of circulation to the growing

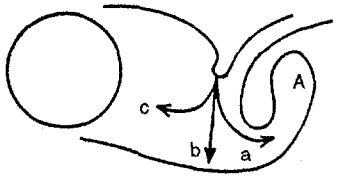

Fig. 14 Vortex formation mechanism

vortex—the opposite vorticities of the fluid in both shear layers cancel each other—then the vortex is shed off. In picture 13(a), the pressure side vortex is just forming. Its center appears about 0.8× trailing edge diameter downstream of the blade. The growing vortex approaches the suction side shear layer (13(b)) and entrains fluid from it (13(c)), as indicated by the curvature of the suction side shear layer to the wake center. This appears to be also the start of a weak suction side vortex. The entrainment of fluid from the opposite shear layer continues until the pressure side vortex is shed off (13(e)) and the formation of a new vortex starts. Contrary to the pressure side vortex, the evolution of the suction side vortex is much less clear, which suggests a significant difference in the strength of the pressure side and suction side vortices. This result is supported by smoke visualization of Han and Cox [5] behind a turbine guide vane, which shows a strong dominance of the pressure side vortex in the wake. The effect of blade circulation appears to be the most appropriate explanation.

Following Gerrard [14] and Berger [15], there is another characteristic parameter that plays a significant role for the vortex shedding: the shear layer thickness referred to by the authors as "diffusion length," which plays a key role in determining the shedding frequency. The thicker the shear layer, the longer it takes for the circulation to be carried across the wake in a sufficient concentration to determine the beginning of the shedding. In the present case the "diffusion length" is quite different for both shear layers and hence the transverse transport of fluid will be different for the formation of the suction side and pressure side vortex. This could possibly lead to an unstable vortex shedding with a result of a loss in sharpness of the vortex shedding frequency spectrum as observed in the present tests, Fig. 8. Finally, the stronger pressure side vortex would explain the higher expansion around the trailing edge as shown in Fig. 9.

6 Conclusions

The design of a turbine blade with a rotatable trailing edge cylinder instrumented with a fast responce pressure transducer and a pneumatic wall pressure tapping allowed to measure the steady and unsteady trailing edge pressure distribution with an unusually high spatial resolution. This device allows one to determine very accurately the overexpansion at the trailing edge, which in the present case exceeded the downstream Mach number by 24 and 19 percent for the pressure and suction sides, respectively.

The unsteady pressure measurements showed rms values for the fluctuating pressure of maximum 8 percent of the downstream dynamic head near the flow separation points and 4.8 percent in the base region. The decomposition of the fluctuating pressure signal into a random and a periodic component showed for the latter a maximum pressure variation of 3 percent of the dynamic downstream pressure over one cycle. Both the pressure distribution around the trailing edge and the schlieren photographs of the vortical wake patterns point out the dominance of the pressure side vortex shedding related to the influence of the blade circulation.

Acknowledgments

This research was carried out under contract for the CEC as part of the BRITE EURAM AER2-92-0048 project "Time Varying Wake Flow Characteristics Behind Flat Plates and Turbine Cascades." The authors wish to acknowledge this support as well as that of MTU and SNECMA.

References

1 Cicatelli, G., and Sieverding, C. H., "A Review of the Research on Unsteady Turbine Blade Wake Characteristics," presented at the AGARD PEP 85TH Symposium on Loss Mechanisms and Unsteady Flows in Turbomachines, Derby, United Kingdom, May 8–12, 1995.

2 Lawaczeck, O., and Heinemann, J., "von Karman Vortex Street in the Wake of Subsonic and Transonic Cascades," *AGARD Conference Proceedings No. 177 on Unsteady Phenomena in Turbomachinery,* AGARD CP-177.

3 Sieverding, C. H., and Heinemann, H., "The Influence on Boundary Layer State on Vortex Shedding From Flat Plates and Turbine Cascades," ASME JOURNAL OF TURBOMACHINERY, Vol. 112, 1990, pp. 181–187.

4 Carscallen, W. E., and Gostelow, J. P., "Observation of Vortex Shedding in the Wake From Transonic Turbine Nozzle Vanes," presented at the Fifth International Symposium on Transport Phenomena and Dynamics of Rotating Machinery (ISROMAC-5), Kaanapali, HI, May 8–10, 1994.

5 Han, L. S., and Cox, W. R., "A Visual Study of Turbine Blade Pressure Side Boundary Layer," ASME *Journal of Engineering for Power,* Vol. 105, 1983, pp. 47–52.

6 Mee, D. J., "Large Chord Turbine Cascade Testing at Engine Mach and Reynolds Number," *Exp. in Fluids,* Vol. 136, 1983, pp. 321–374.

7 Cantwell, B., and Coles, D., "An Experimental Study of Entrainment and Transport in the Turbulent Near Wake of a Circular Cylinder," *J. of Fluid Mech.,* Vol. 136, 1983, pp. 321–374.

8 Hussain, A. K. M. F., and Hayakawa, M., "Eduction of Large-Scale Organized Structures in a Turbulent Plane Wake," *J. of Fluid Mech.,* Vol. 180, 1983, pp. 193–229.

9 Kiya, M., and Matsumura, M., "Incoherent Turbulence Structure in the Near Wake of a Normal Plate," *J. of Fluid Mech.,* Vol. 190, 1988, pp. 343–356.

10 Leonard, O., and Van den Braembussche, R. A., "Design Method for Subsonic and Transonic Cascade With Prescribed Mach Number Distribution," ASME JOURNAL OF TURBOMACHINERY, Vol. 114, 1992, pp. 553–561.

11 Kawai, T., and Adachi, T., "Effects of Boundary Layer Fences on Secondary Flow and Losses in a Turbine Cascade," presented at the Int. Gas Turbine Congress, Tokyo, 1987.

12 Sieverding, C. H., Stanislas, M., and Snoeck, J., "The Base Pressure Problem in Transonic Turbine Cascades," ASME *Journal of Engineering for Power,* Vol. 102, July 1980.

13 Zunino, P., private communication.

14 Gerrard, J. H., "The Mechanism of the Formation Region of Vortices Behind Bluff Bodies," *J. of Fluid Mech.,* Vol. 25, Part 2, 1999, pp. 401–413.

15 Berger, E., *Jahr. Wis. Ges. L. & R.,* Berlin.

APPENDIX

Xax	Y	Xax	Y	Xax	Y
0.00	0.00	40.61	21.38	83.83	0.02
0.20	1.75	42.37	21.27	85.07	-1.22
0.75	3.44	44.13	21.10	86.31	-2.48
1.53	5.01	45.87	20.87	87.52	-3.75
2.54	6.47	47.61	20.58	88.72	-5.04
3.67	7.81	49.33	20.23	89.89	-6.35
4.93	9.04	51.05	19.82	91.05	-7.68
6.24	10.22	52.75	19.36	92.19	-9.01
7.60	11.33	54.43	18.85	93.33	-10.36
9.00	12.40	56.10	18.29	94.44	-11.73
10.45	13.40	57.75	17.67	95.54	-13.10
11.93	14.34	59.39	17.00	96.62	-14.49
13.46	15.22	60.99	16.29	97.69	-15.89
15.02	16.03	62.58	15.54	98.75	-17.29
16.62	16.78	64.15	14.73	99.79	-18.71
18.24	17.47	65.70	13.89	100.82	-20.14
19.88	18.11	67.23	13.01	101.83	-21.58
21.54	18.69	68.73	12.10	102.84	-23.03
23.22	19.21	70.21	11.15	103.83	-24.48
24.92	19.68	71.67	10.16	104.81	-25.94
26.63	20.10	73.11	9.14	105.77	-27.41
28.35	20.47	74.52	8.09	106.73	-28.89
30.08	20.77	75.91	7.02	107.67	-30.38
31.83	21.03	77.28	5.91	108.61	-31.87
33.58	21.22	78.63	4.77	109.54	-33.36
35.33	21.34	79.96	3.62	110.46	-34.87
37.09	21.41	81.27	2.45	111.36	-36.37
38.86	21.43	82.56	1.25	112.26	-37.89
113.14	-39.41	149.20	-115.75	181.19	-193.94
114.02	-40.94	149.88	-117.38	181.87	-195.57
114.89	-42.47	150.55	-119.00	182.54	-197.19
115.75	-44.00	151.23	-120.63	183.22	-198.82
116.61	-45.54	151.90	-122.25	183.71	-200.06
117.45	-47.09	152.57	-123.88	183.93	-200.77
118.29	-48.63	153.24	-125.51	184.07	-201.50
119.13	-50.18	153.91	-127.13	184.14	-202.24
119.95	-51.74	154.58	-128.76	184.14	-202.86
120.77	-53.29	155.25	-130.39	184.08	-203.60
121.58	-54.86	155.92	-132.02	183.94	-204.33
122.38	-56.42	156.58	-133.65	183.72	-205.04
123.18	-57.99	157.25	-135.28	183.44	-205.73
123.97	-59.56	157.91	-136.91	183.09	-206.39
124.76	-61.14	158.58	-138.54	182.68	-207.01
125.54	-62.72	159.24	-140.17	182.21	-207.58
126.31	-64.30	159.91	-141.80	181.68	-208.10
127.09	-65.88	160.57	-143.43	0.00	-0.89
127.85	-67.46	161.23	-145.06	0.23	-2.63
128.61	-69.05	161.89	-146.69	0.72	-4.34
129.37	-70.64	162.56	-148.32	1.43	-5.94
130.12	-72.23	163.22	-149.95	2.36	-7.45
130.86	-73.83	163.88	-151.58	3.46	-8.82
131.61	-75.42	164.54	-153.21	4.70	-10.06
132.34	-77.02	165.21	-154.84	6.00	-11.26
133.08	-78.68	165.87	-156.47	7.34	-12.40
133.81	-80.22	166.53	-158.10	8.69	-13.52
134.53	-81.83	167.20	-159.73	10.07	-14.62
135.26	-83.43	167.86	-161.36	11.45	-15.71
135.98	-85.04	168.52	-162.99	12.84	-16.78
136.70	-86.64	169.19	-164.62	14.25	-17.84
137.41	-88.25	169.85	-166.25	15.67	-18.88
138.12	-89.86	170.52	-167.88	17.10	-19.91
138.83	-91.47	171.18	-169.51	18.54	-20.93

Xax	Y	Xax	Y	Xax	Y
139.54	-93.08	171.85	-171.14	19.97	-21.94
140.24	-94.70	172.51	-172.77	21.42	-22.95
140.94	-96.31	173.18	-174.40	22.86	-23.96
141.64	-97.93	173.85	-176.03	24.30	-24.97
142.34	-99.54	174.51	-177.66	25.74	-25.97
143.03	-101.16	175.18	-179.29	27.18	-26.99
143.72	-102.78	175.85	-180.92	28.62	-28.01
144.42	-104.40	176.52	-182.54	30.05	-29.03
145.10	-106.02	177.18	-184.17	31.48	-30.05
145.79	-107.64	177.85	-185.80	32.91	-31.09
146.48	-109.26	178.52	-187.43	34.33	-32.13
147.16	-110.88	179.18	-189.06	35.74	-33.18
147.84	-112.50	179.85	-190.69	37.15	-34.24
148.52	-114.13	180.52	-192.32	38.54	-35.30
39.93	-36.38	99.51	-96.06	147.00	-165.76
41.32	-37.47	100.63	-97.42	147.87	-167.29
42.69	-38.57	101.74	-98.78	148.74	-168.82
44.06	-39.68	102.85	-100.14	149.61	-170.35
45.42	-40.79	103.96	-101.51	150.48	-171.88
46.78	-41.92	105.07	-102.88	151.35	-173.41
48.13	-43.05	106.17	-104.26	152.22	-174.94
49.47	-44.19	107.26	-105.63	153.10	-176.47
50.80	-45.34	108.35	-107.02	153.97	-177.99
52.13	-46.49	109.44	-108.40	154.85	-179.52
53.45	-47.66	110.52	-109.79	155.73	-181.04
54.76	-48.83	111.60	-111.18	156.61	-182.57
56.07	-50.01	112.67	-112.58	157.49	-184.09
57.37	-51.19	113.74	-113.98	158.37	-185.62
58.67	-52.38	114.80	-115.38	159.25	-187.14
59.95	-53.58	115.85	-116.79	160.13	-188.66
61.24	-54.79	116.90	-118.21	161.01	-190.19
62.51	-56.00	117.94	-119.62	161.89	-191.71
63.79	-57.21	118.98	-121.05	162.77	-193.24
65.05	-58.44	120.01	-122.47	163.64	-194.77
66.31	-59.67	121.03	-123.91	164.52	-196.29
67.57	-60.90	122.04	-125.35	165.40	-197.82
68.81	-62.14	123.05	-126.79	166.27	-199.34
70.06	-63.39	124.05	-128.24	167.15	-200.87
71.29	-64.64	125.05	-129.69	168.03	-202.39
72.53	-65.90	126.04	-131.14	168.92	-203.92
73.75	-67.16	127.01	-132.61	169.80	-205.44
74.97	-68.43	127.99	-134.07	170.38	-206.48
76.19	-69.70	128.95	-135.55	170.81	-207.09
77.40	-70.98	129.91	-137.02	171.29	-207.66
78.61	-72.26	130.86	-138.50	171.82	-208.17
79.81	-73.54	131.80	-139.99	172.40	-208.63
81.01	-74.84	132.74	-141.48	173.03	-209.03
82.20	-76.13	133.67	-142.97	173.69	-209.37
83.38	-77.43	134.60	-144.47	174.39	-209.63
84.56	-78.74	135.52	-145.97	175.10	-209.83
85.74	-80.05	136.43	-147.48	175.84	-209.96
86.91	-81.36	137.33	-148.99	176.58	-210.01
88.08	-82.68	138.23	-150.50	177.32	-209.98
89.24	-84.00	139.12	-152.02	178.06	-209.88
90.40	-85.32	140.01	-153.54	178.78	-209.71
91.55	-86.65	140.89	-155.06	179.48	-209.47
92.70	-87.99	141.77	-156.59	180.16	-209.16
93.85	-89.32	142.65	-158.11	180.80	-208.78
94.99	-90.66	143.52	-159.64	181.40	-208.34
96.12	-92.01	144.40	-161.17		
97.26	-93.36	145.26	-162.70		
98.38	-94.71	146.13	-164.23		

The blade coordinates reported here represent only 30 percent of the entire set. The complete set of coordinates can be down-loaded from the FTP site at the von Karman Institute at the following address: ftp.vki.ac.be/pub/exchange/turbo/asme96/vkiwake.dat.

Application of a Multi-Block CFD Code to Investigate the Impact of Geometry Modeling on Centrifugal Compressor Flow Field Predictions

M. D. Hathaway
Vehicle Technology Center,
Cleveland, OH 44135

J. R. Wood
NASA Lewis Research Center,
Cleveland, OH 44135

CFD codes capable of utilizing multi-block grids provide the capability to analyze the complete geometry of centrifugal compressors including, among others, multiple splitter rows, tip clearance, blunt trailing edges, fillets, and slots between moving and stationary surfaces. Attendant with this increased capability is potentially increased grid setup time and more computational overhead—CPU time and memory requirements—with the resultant increase in "wall clock" time to obtain a solution. If the increase in "difficulty" of obtaining a solution significantly improves the solution from that obtained by modeling the features of the tip clearance flow or the typical bluntness of a centrifugal compressor's trailing edge, then the additional burden is worthwhile. However, if the additional information obtained is of marginal use, then modeling of certain features of the geometry may provide reasonable solutions for designers to make comparative choices when pursuing a new design. In this spirit a sequence of grids were generated to study the relative importance of modeling versus detailed gridding of the tip gap and blunt trailing edge regions of the NASA large low-speed centrifugal compressor for which there is considerable detailed internal laser anemometry data available for comparison. The results indicate: (1) There is no significant difference in predicted tip clearance mass flow rate whether the tip gap is gridded or modeled. (2) Gridding rather than modeling the trailing edge results in better predictions of some flow details downstream of the impeller, but otherwise appears to offer no great benefits. (3) The pitchwise variation of absolute flow angle decreases rapidly up to 8 percent impeller radius ratio and much more slowly thereafter. Although some improvements in prediction of flow field details are realized as a result of analyzing the actual geometry there is no clear consensus that any of the grids investigated produced superior results in every case when compared to the measurements. However, if a multi-block code is available, it should be used, as it has the propensity for enabling better predictions than a single block code, which requires modeling of certain geometry features. If a single block code must be used, some guidance is offered for modeling those geometry features that cannot be directly gridded.

Introduction

The complexity of realistic turbomachinery fluid dynamic problems routinely challenges the ability of computational fluid dynamic analysis codes to obtain reasonable flow field predictions. As such, good engineering approximations are often required to model those aspects of the problem that either defy direct analysis, unnecessarily complicate the problem, or adversely affect convergence. Often, modeling is required to simplify analyses sufficiently such that CFD predictions can be obtained in reasonable time frames so as to be useful as a design tool. One relatively simple means of decreasing analysis time is to reduce the total number of grid points used to discretize the flow field. Thus, in areas of the flow field where the details of the flow may not be required, such as within the clearance gap of turbomachinery blades, modeling may be used to reduce the total number of grid points. Although this type of modeling is often routine practice, to our knowledge no investigations of the impact of such modeling on the flow field predictions has been reported in the literature.

CFD codes capable of utilizing multi-block grids provide the capability to define accurately the complete geometry of centrifugal compressors including, among others, multiple splitter rows, tip clearance gaps, blunt trailing edges, fillets, and slots between moving and stationary surfaces. Attendant with this increased capability is potentially increased grid setup time and more computational overhead—CPU time and memory requirements—with the resultant increase in "wall clock" time to obtain a solution. If the increase in "difficulty" of obtaining a solution significantly improves the solution from that obtained by modeling the features of the tip clearance flow or the typical bluntness of a centrifugal compressor's trailing edge, then the additional burden is worthwhile. However, if the additional information obtained is of marginal use, then modeling of certain features of the geometry may provide reasonable solutions for designers to make comparative choices when pursuing a new design. In this spirit a sequence of grids were generated for the NASA Low Speed Centrifugal Compressor (LSCC) for which there is considerable detailed internal laser anemometry data available for comparison.

Contributed by the International Gas Turbine Institute and presented at the 41st International Gas Turbine and Aeroengine Congress and Exhibition, Birmingham, United Kingdom, June 10–13, 1996. Manuscript received at ASME Headquarters February 1996. Paper No. 96-GT-372. Associate Technical Editor: J. N. Shinn.

The CFD code, ADPAC, was chosen for this study. ADPAC is a general purpose time marching three-dimensional Euler/Navier–Stokes aerodynamic analysis code capable of predicting steady and unsteady compressible transonic flows about ducted and unducted propulsion systems employing multiple blade rows.

For this investigation, several grids were generated to determine the relative importance of grid topology on the final solution. Four analyses were obtained: two solutions for conventional single block grids with the tip modeled and two different trailing edge models, a multiple-block solution wherein the blade tip is modeled and a rather coarse trailing edge block is used, and a multiple-block solution wherein detailed grids for the main channel, tip, and trailing edge blocks were used. The resulting solutions were then compared to assess the relative importance of the various modeling schemes on the final solution obtained, as well as the benefits and costs relative to CPU time and memory requirements of single versus multi-block analyses. The laser anemometer results are included for comparison to provide a degree of reality for assessing the absolute measure of a solution's worth.

Test Compressor and Measurement Technique

The test compressor is a backswept impeller that has 20 full blades with a backsweep of 55 deg from radial. The compressor was tested at a mass flow rate of 30 kg/s (66 lbm/sec) at a corrected shaft speed of 1862 rpm. The inlet diameter is 870 mm and the inlet blade height is 218 mm. The exit diameter is 1524 mm and the exit blade height is 141 mm. The tip clearance between the impeller blade and the shroud is 2.54 mm and is constant from inlet to exit. This tip clearance is 1.8 percent of blade height at the impeller exit and 1.2 percent at the inlet. The blade surfaces are composed of straight-line elements from hub to tip. A vaneless diffuser was used for the laser anemometer investigation. This allows an axisymmetric boundary condition to be used in the numerical simulations. A complete description of the facility can be found in Wood et al. (1983) and Hathaway et al. (1992). Hathaway et al. (1993) and Chriss et al. (1996) give a detailed presentation of the laser data, which is summarized below.

The measurement results consist of standard five-hole pneumatic probe surveys and torque measurements for performance characteristics, and detailed laser anemometer surveys of the impeller flow field. A two-component laser fringe anemometer operating in on-axis backscatter mode was used in the experiment. In order to obtain all three velocity components, two sets of measurements were obtained, each at a different orientation to the flow. The resulting four measured velocity components were then combined with a least-squares fit in order to obtain the three components of velocity.

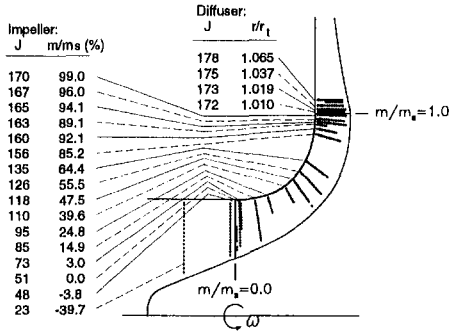

Fig. 1 Laser anemometer survey station locations

The laser anemometer surveys are shown in Fig. 1, and the streamwise indices of the body-fitted grid at which the laser surveys were acquired are noted together with the percent meridional shroud distance of survey planes within the impeller and radius ratio of survey planes within the vaneless diffuser. The streamwise indices corresponding to the leading and trailing edges are 51 and 171, respectively.

All the data are ensemble-averaged across the 20 blade channels to yield a single "representative" blade passage. This passage is divided into 1000 equal arc lengths or window "bins." For presentation purposes these bins are usually averaged down to 200 measurement locations across the blade passage.

An estimate of the uncertainty in the calculated results was made from the least-squares fit calculations. Throughout most of the impeller passage the uncertainty is estimated to be ± 1.5 m/s, which is about 2 percent of the throughflow velocity, although the uncertainties can approach 15 percent in the throughflow wake near the impeller exit.

Further details of the philosophy and the method used to obtain and average the data can be found from Strazisar et al. (1989). Complete documentation of the aero and laser data acquisition and reduction procedures, including documentation of all data acquired during the low speed centrifugal compressor program, can be found from Hathaway et al. (1995).

CFD Analysis Approach

The computational results for the LSCC flow field were obtained using the Advanced Ducted Propfan Analysis Code (ADPAC) developed by Allison Engine Company under NASA contract (Hall and Delaney, 1992; Hall et al., 1994). ADPAC is a general purpose time-marching three-dimensional Euler/Navier–Stokes aerodynamic/heat transfer analysis tool for predicting steady and unsteady compressible transonic flows within modern turbomachinery propulsion systems employing multiple

Nomenclature

ccf = cumulative mass flow through tip clearance gap, kg/s
cf = clearance mass flow per unit meridional chord, kg/s
$\hat{g}_m$ = unit vector in local meridional grid direction
J = streamwise measurement grid index
mf = inlet mass flow, kg/s
m/m_s = nondimensional shroud meridional distance
P_t = total pressure, N/m^2
PS = pressure surface/side
r/r_t = radius nondimensionalized by exit tip radius
SS = suction surface/side
T_t = total temperature, K
U_t = impeller speed at trailing edge, m/s
V_m = meridional velocity component = $\sqrt{V_z^2 + V_r^2}$, m/s
V_r = radial velocity component, m/s
V_{tf} = throughflow velocity component = $\vec{V}_m \cdot \hat{g}_m$, m/s
V_z = axial velocity component, m/s
V_θ = tangential velocity component, m/s
y^+ = nondimensional distance from wall
β = absolute flow angle, deg, $\beta = \tan^{-1}[V_\theta/V_m]$
ω = rotational speed, rad/s

Subscripts

1 = impeller inlet station
2 = impeller exit station, $r/r_t = 1.065$
cfd = ADPAC prediction
exp = measurements

Superscripts

— = mass averaged

blade rows. ADPAC is based on a flexible multiple-block grid discretization scheme permitting coupled two-dimensional/three-dimensional mesh block solutions with application to a wide variety of geometries. Aerodynamic calculations are based on a four-stage Runge–Kutta time-marching finite-volume cell-centered technique with added numerical dissipation. Steady flow predictions are accelerated by a multigrid procedure. ADPAC is capable of either serial execution or parallel execution on multiple workstations or other CPU's.

Numerical Technique. The numerical solution procedure is based on an integral representation of the strong conservation law form of the Navier–Stokes equations expressed in a cylindrical coordinate system. The discrete numerical solution is developed from the integral governing equations by employing a finite-volume cell-centered solution procedure. This procedure closely follows the basic scheme described by Jameson et al. (1981). The numerical technique is second-order accurate in space using central differences for flux evaluations. The discretized system of equations has unstable properties and can exhibit odd-even decoupling. To suppress these instabilities, artificial dissipation terms made up of second and fourth-order difference operators are added to the equations. The time stepping scheme used to fully discretize the system of equations is a four-stage Runge–Kutta integration. Local time stepping for each cell and residual averaging is used to accelerate the convergence of steady flow analyses. Turbulent stresses are simulated using the model of Baldwin and Lomax (1978). For all calculations presented herein, wall functions were used whenever ADPAC determined the near-wall mesh spacing was greater than a y^+ of 10.0.

In multi-block grid systems such as is employed by ADPAC, the domain of interest is subdivided into one or more structured arrays of hexahedral cells. Each array of cells is referred to as a "block," and the overall scheme is referred to as a multiple blocked mesh solver as a result of the ability to manage more than one block. A multiple blocked grid system has advantages over a single block grid as it is not often possible to generate a single structured grid to encompass the domain of interest without sacrificing grid quality. Unstructured grid codes, of course, provide another alternative. Multiple block grid systems differ from single block grid systems only in that the numerical solution is generated from multiple computational domains (blocks). ADPAC utilizes the multiple blocked grid concept to the full extent by permitting an arbitrary number of structured grid blocks with user specifiable communication paths between blocks. The inter-block communication paths are implemented as a series of boundary conditions on each block, which, in some cases, communicate flow information from one block to another.

All solid surfaces must satisfy flow tangency for inviscid flow and, in addition, no slip for viscous flows. In both cases, no convective flux through the boundary (an impermeable surface) is permitted. These conditions are satisfied by using a phantom cell located outside of the computational domain for each cell that touches a solid boundary. The phantom cell velocity components are thus constructed to ensure that the cell face average values used in the convective flux calculation are identically zero. The phantom cell pressure is simply extrapolated based on the boundary layer flow concept that the normal pressure gradient is zero at the wall.

Inflow and exit boundary conditions are applied numerically using characteristic theory. For subsonic normal inflow, the upstream running Reimann invariant is extrapolated to the inlet and the flow variables at the boundary are determined using the equation of state along with the specified total pressure, total temperature, and radial and circumferential flow angles. Outflow boundaries require a specification of the exit static pressure at either the top or bottom of the exit plane. The remaining pressures along the outflow boundary are calculated using simple radial equilibrium, which for the LSCC, results in a constant static pressure since the exit boundary is at a constant radius. In this case the downstream running invariant is used to update the phantom cells at the exit boundary.

Artificial damping is applied at the block boundaries by prescribing zero dissipation flux along block boundaries to maintain the global conservative nature of the solution for each mesh block. Fourth-order dissipation fluxes at near-boundary cells are computed using a modified one-sided difference scheme. Implicit residual smoothing is applied at the block boundary by imposing a zero residual gradient condition at the boundary. For the multiple-block scheme, the solution is performed on a single block at a time. Therefore, special boundary conditions are required along block boundaries to provide for transport of information between blocks. For all meshes presented herein the neighboring mesh blocks have coincident mesh points along the interface separating the blocks. Therefore, a simple direct specification of the phantom cell based on the near-boundary cell data from the neighboring block is employed. In other words, each phantom cell in the block of interest has a direct correspondence with a near-boundary cell in the neighboring mesh block, and the block coupling is achieved numerically by simply assigning the value of the corresponding cell in the neighboring block to the phantom cell in the block of interest. This procedure essentially duplicates the interior point solution scheme for the near-boundary cells, and uniformly enforces the conservation principles implied by the governing equations.

Computational Grids. As previously mentioned, the purpose of this investigation was to assess the impact of detailed gridding versus modeling of the tip gap and trailing edge on the computational predictions, as well as the benefits and costs in terms of CPU time and memory requirements. As such, several grids were generated using computer codes developed by Wood (1994) to determine the relative importance of grid topology on the final solution. Four analyses were obtained: two solutions for conventional single block grids with the tip modeled and two different trailing edge models, a multiple-block solution wherein the blade tip is modeled and a rather coarse trailing edge block is used, and a finer mesh multiple-block solution wherein detailed grids for the main channel, tip, and trailing edge blocks were used. Table 1 provides a comparison of the various grids analyzed and Figs. 2 and 3 illustrate the differences in the gridding for modeling versus blocking the tip gap and trailing edge of the LSCC. The mesh sizes quoted in Table 1 are the number of streamwise, spanwise, and pitchwise nodes, respectively. Sheared H-grids were used for all cases

Table 1 Comparison of modeling differences and mesh sizes of various mesh configurations analyzed

		MESH CONFIGURATIONS STUDIED			
	Block Structure	Single Block		Multiple Block	
	Case	S	M	C	F
	Tip Model	Yes	Yes	Simulated	Mesh Block
	T.E. Model	Tapered to mean camber line	Suction side tapered to pressure surface	Mesh Block	Mesh Block
Mesh Size	Main Block	129×61×41	129×61×41	129×61×41	155×71×51
	Tip Block	N/A	N/A	75×5×9	101×11×21
	T.E. Block	N/A	N/A	29×61×13	29×71×21
	Total Nodes	322,629	322,629	349,001	628,936
	Ratio	1.000	1.000	1.082	1.949

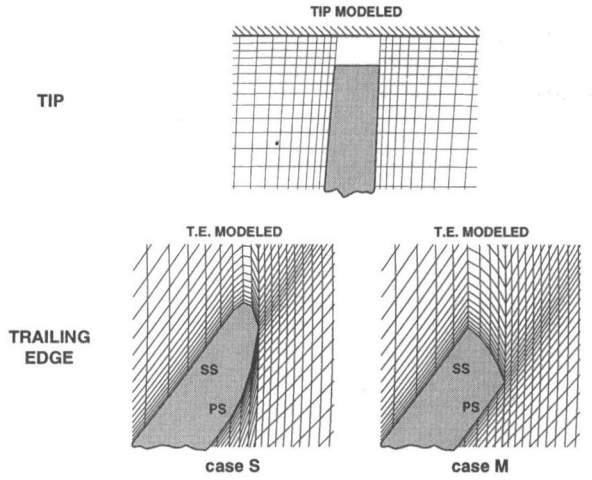

Fig. 2 Single block meshes

presented herein with the exception of the leading edge tip gap region, which used a modified C-grid. Inspection of the LSCC blade tips indicated that the tips are slightly rounded at each corner. We therefore assumed that there would be no vena-contracta in the tip gap flow as would exist for sharp-edged tips, and that a discharge coefficient of 1.0 is appropriate for the tip gap flow (Chriss et al., 1996). Therefore, the full physical gap height was used for all computations. However, each model incorporates a square edge tip rather than the "true" rounded tip corners.

The single block case *S* models the trailing edge by quadratic curves blending the suction and pressure surfaces to the trailing edge at the mean camber line point. The single block case *M* uses a quadratic curve to blend the suction surface to the trailing edge with no modification of the pressure surface. For both cases *S* and *M* the trailing edge modifications occur over the last 1.5 percent of meridional chord from the trailing edge (78 percent of the midspan trailing edge thickness).

The trailing edge model of case *M* was guided by the observed differences in flow turning near the trailing edge as shown in Fig. 4. Figure 4 shows that the flow near the trailing edge of the single block case *S* is underturned relative to the multi-block cases *C* and *F*. This underturning is being driven by the pressure surface curvature, which results in the pressure surface flow driving the flow toward the suction side and thus underturning the flow relative to that predicted by the multi-block cases, which accurately model the trailing edge geometry.

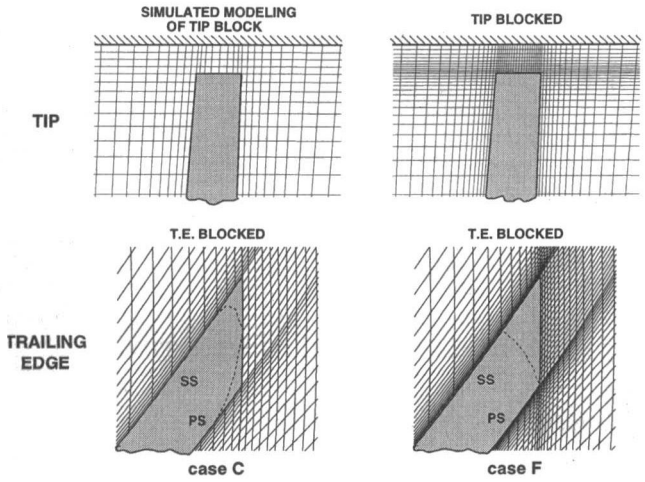

Fig. 3 Multi-block meshes

As a result, the trailing edge modeling of case *M* was accomplished by following the suggestion of Adamczyk (1995), which he has employed in the past in order to alleviate the tendency of compressor trailing edges to underturn as a result of inadequate modeling of the trailing edge details. By cutting back the suction surface, the tendency of the suction surface flow to be "pushed back" by the pressure surface flow is reduced.

Both cases *S* and *M* model the blade clearance gap by a squared-off tip at the physical blade tip wherein the pressure and suction surface grids are separated by the physical blade thickness and their respective boundary conditions across the clearance gap are forced to be reflective (i.e., the phantom cells along the suction surface boundary are substituted with the flow variables from the adjacent pressure surface boundary and vice versa). The supposition behind this approach is that the details of the flow through the clearance gap are not necessary so long as the correct amount of flow is allowed to pass through the clearance gap. Previous analysis of the LSCC impeller reported in the literature tend to support this supposition (Chriss et al., 1996).

Cases *C* and *F* feature a trailing edge block that grids the true blade trailing edge geometry, which is truncated at the impeller exit radius. Grid block matching requirements in the clearance gap at the trailing edge dictated that we add a grid block over the blade tip when the trailing edge block was added. In an attempt to separate the differences in the predictions resulting from the tip and trailing edge blocks, the blade tip and

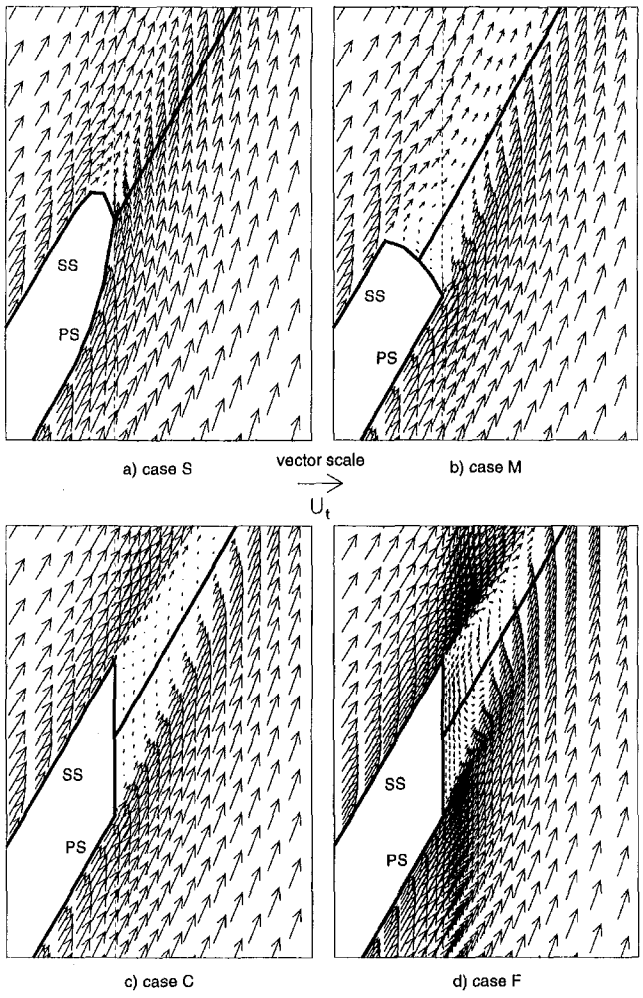

Fig. 4 Comparison of predicted relative velocity vectors showing effect of trailing edge modeling on flow turning at midspan

casing surface boundaries of the tip block are treated as inviscid boundaries for the coarse multiple block case C. The clearance flow treatment for case C is therefore quite similar to that for cases S and M and differences between these three cases should be due mainly to trailing edge treatment variations. The finer mesh multi-block case F allows the blade tip and casing boundaries of the clearance gap mesh block to be viscous so as to allow the CFD code to predict "blockage" through the clearance gap. Case F also features a sizable increase in grid density in the tip mesh block and moderate increases in grid density in the main and trailing edge blocks.

The mesh for both single block cases and the coarse multiple block case are identical with the following exceptions: The suction side tapering for case M results in slight local changes in the mesh relative to the case S mesh, which are commensurate with the different trailing edge modeling. The coarse block case C includes a tip block, which fits within the modeled tip gap of case S and a trailing edge block, which results in pitchwise redistribution of the main block mesh downstream of the trailing edge relative to case S. To insure good definition of the blade leading edge, a C grid was used for the tip block, which has coincident sides at the blade mean camber line. The fine block mesh, case F, in addition to providing increased meshing, redistributes the spanwise mesh to insure that the main block mesh smoothly transitions to the spanwise spacing of the tip block mesh near the blade tip. As a result, the fine mesh case is actually slightly coarser away from the hub and casing (roughly from 10 to 85 percent span) than in the coarse mesh case. This decreased spanwise grid density away from the blade end walls is partly responsible for some of the observed differences between fine and coarse mesh predictions, as will be discussed later. The maximum spanwise mesh spacing for case F is 9 percent of span at 65 percent span relative to 5.5 percent of span at 55 percent span for all other cases. It would be desirable to achieve the same spanwise spacing, but satisfying that condition as well as the others imposed would have increased the grid size by 25 percent to 788,000 points.

Boundary Conditions and Convergence. For all cases studied, the same inlet boundary conditions were imposed based on five-hole probe survey data, and the exit back pressure was adjusted to achieve the desired mass flow rate. For the comparisons to detailed flow field measurements presented herein, all predictions were converged to the tested mass flow rate, 30 kg/s. Convergence was determined when the maximum residuals were reduced by at least three orders of magnitude and the inlet and exit mass flow, pressure ratio, efficiency, and number of separated points were all converged and stable for at least twice the number of iterations required for these parameters to stabilize after a given perturbation in back pressure.

Results and Discussion

Since our focus is to illuminate differences in the CFD solutions obtained by modeling certain geometric features (rather than constructing a computational grid that faithfully reproduces those features) we have assumed the baseline for our comparisons to be the solutions from grid case C. Since the measured laser data provide a degree of reality for assessing the absolute measure of a solution's worth, we have also included it for comparison. As will be seen in the following discussion, in comparisons of the solutions to the measured data, there is no clear consensus that any of the grid cases studied provides predictions that are clearly superior to those of the other grid cases. Although one metric may indicate better agreement with the data for one grid case, another metric may indicate better agreement with a different grid case. In our opinion, the relative differences between the various cases studied herein would translate to the same relative degree of differences if we had used a different turbulence model, grid topology, increased grid density, etc.

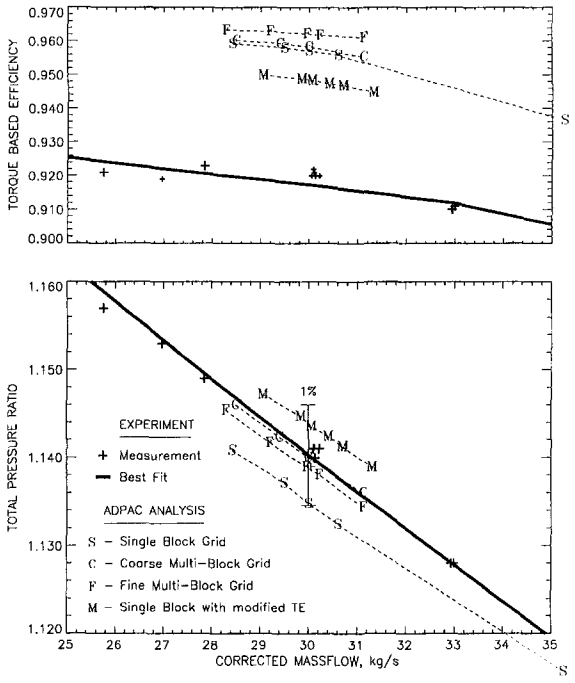

Fig. 5 Comparison of predicted and measured performance maps for the large low-speed centrifugal impeller

In comparing the results of the various analyses, their ability to predict the compressor overall performance is considered first. Second, the axisymmetric averaged exit profiles are compared to determine differences resulting from the detailed gridding versus modeling, which might impact the design of the impeller or downstream diffuser. Next, a comparison of blade-to-blade flow field features such as the blade wake, characteristic throughflow wake (formed by the accumulation of low-momentum fluid, which migrates to the blade tip and is entrained in the tip clearance vortex), and other secondary flow features at the exit of the impeller is provided to indicate potential improvements in impeller designs to minimize loss production. Finally, the relative costs in terms of CPU time and resources required are assessed to determine whether the additional costs incurred are worth the benefits gained.

Comparisons between cases S and M, which model the physical geometry, show the impact of modifications to the trailing edge taper (modeling), which are made over the last 1.5 percent of meridional chord from the trailing edge. Comparisons of case C to cases S and M show the impact of using a multi-block code to define correctly the blunt trailing edge geometry of the LSCC impeller and also grid the tip gap. Case F shows the impact of increased mesh density in some areas (e.g., case F has over six times as many grid nodes as case C in the tip gap region) and a viscous treatment of the flow through the tip clearance gap.

Overall Performance. Figures 5–7 give a good indication of the differences produced by the four grids from a one-dimensional perspective. The predicted performance characteristics for the tested operating conditions are compared in Fig. 5 and show considerable variation in efficiency and overall pressure ratio. The two single block solutions, cases S and M, predict pressure ratios that differ by ± 0.5 percent from the multi-block predictions from grid C, which agrees quite well with the experimental pressure ratio data. The single block grid M overpredicts pressure ratio by an almost equal amount that S underpredicts. The finer multiblock grid F differs very little from C and agrees no better with the data even though the number of grid points is nearly doubled. For all cases, the slopes of the predicted

overall pressure ratio and efficiency characteristics are in good agreement with the measurements. However, the predicted efficiencies are 3–5 points higher than measured. Grids S, C, and F predict, essentially, the same efficiency curve although they produced slightly different overall pressure ratios. (Note: The uncertainties in the measured torque based efficiency, and adiabatic efficiency based on probe surveys, are 0.5 points and 2 points, respectively.)

The observed differences in predicted pressure ratio of the various cases was investigated further by calculating the predicted meridional distribution of energy-averaged pressure rise and mass-averaged temperature rise (work input) relative to that based on measured values at the impeller exit, as shown in Fig. 6. Up to about 95 percent meridional chord all cases predict essentially the same pressure rise (within 0.5 percent up to 70 percent meridional chord, and within 1.4 percent up to 95 percent meridional chord). At about 85--90 percent meridional chord the four cases begin to diverge. Figure 6(b) shows that the reduction in overall pressure rise of case S is predominantly due to under prediction of the overall work input. The increased overall pressure rise of case M resulted from additional work input as a direct result of the different trailing edge modeling. The local turning of the flow around the trailing edge is evident in Fig. 4 where the underturning of grid S and the slight overturning of grid M near the suction surface is consistent with the pressure rise difference. A comparable plot of the efficiency (not shown) indicated that the predicted efficiencies using grids S, M, and F are virtually identical at 98 percent chord, whereas grid C is about 0.3 points lower (97.4 to 97.1 percent). However, from 98 percent chord to 106 percent chord, the efficiency for cases S, M, C, and F decrease by 1.5, 2.3, 1.1, and 0.9 points, respectively. The entropy rise up to 96 percent chord for grids S, M, and F is about 10 percent lower than for grid C. However, from 96 percent chord to 102 percent chord (which includes the taper region of the blade trailing edge for the single block grids and the dump loss for the blocked grids) the entropy rise for cases S, M, and F are 1.7, 2.8 and 1.0 times as great as for case C. Obviously, the trailing edge treatment has considerable impact upon entropy production as well as work input.

Although the tip clearance gap is handled quite differently for the single block grids and the multi-block grids, the only discernible difference in the solutions for S, M, and C at 98 percent chord is 0.3 points in efficiency for the C grid below the other two. The local and cumulative clearance flows for the four cases are shown in Fig. 7. Grids C and F yield the same overall clearance flow (8.4 percent of the inlet flow), which is about 1 percent of inlet flow higher than that obtained with the

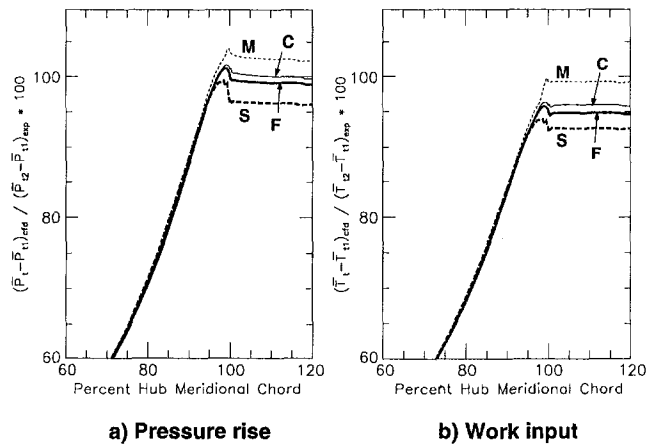

Fig. 6 Comparison of meridional distributions of mass averaged pressure rise and work input through the impeller normalized by their respective measured values

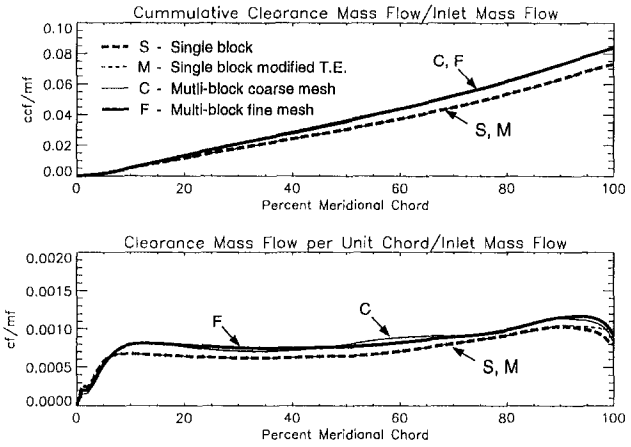

Fig. 7 Comparison of predicted meridional distributions of clearance mass flow

single block grids that model the tip gap. Grids C and F also give virtually identical distributions of clearance flow even though there are 6.5 times as many grid nodes in the gap for grid F as for grid C. As noted above, at 98 percent chord, the efficiency for grid C is 0.3 points lower than grids S and M, which can be attributed to the difference in the clearance mass flow rate. Analysis of the flow in the vicinity of the tip clearance gap indicated that the modeling of the gap employed in the single block cases, S and M, resulted in less pressure difference across the blade tip than in the blocked cases, C and F. This resulted in the lower mass flow rate through the tip clearance gap for the single block grids. In order to put these differences in predicted tip clearance mass flow rate into perspective, consider a modern impeller at about 4.5:1 pressure ratio and inlet mass flow rate of 4.5 kg/s running with an axial tip clearance gap at the impeller exit of 0.254 mm (0.010 in.), which is a reasonable value for this size machine. Since clearance flow varies directly with gap height, the difference in the clearance flow rates predicted herein (about 1 percent) would translate to an uncertainty in the running clearance of 0.0025 mm (0.001 in.) for the aforementioned impeller. Dynamic clearance measurements made by Skoch (1995) on a 4.5 kg/s impeller indicated a 23 percent change in axial tip clearance when the mass flow rate changed by 10 percent from the design value at a constant rotational speed. Consequently, the uncertainty in accurately determining the tip clearance gap that directly influences the tip clearance mass flow rate is much larger than the differences noted between the different grid cases investigated herein. Therefore, from the standpoint of predicting the "absolute value" of the impeller performance the differences are insignificant. From the standpoint of predicting the "relative differences" all grids should predict the same trends.

With the observed differences in predicted tip clearance mass flow distributions shown in Fig. 7 in mind, the differences in the predicted distributions of pressure rise and work input shown in Fig. 6 are further explored. Although not discernible from Fig. 6, between 60–85 percent meridional chord the predicted pressure rise and work input of cases F and C decrease by about 1 percent relative to cases S and M. Since the only common difference between the single and multi-block cases is the predicted differences in tip clearance mass flow distributions (see Fig. 7), the changes in predicted pressure rise and work input that occur between 60–85 percent meridional chord are probably tied to the differences in predicted tip clearance mass flows. Most of the observed differences in the various predictions are tied to the differences in the trailing edge modeling, which are made over the last 1.5 percent of meridional chord from the trailing edge. Cases S and M, which produce the largest changes in predicted pressure rise and work input, differ only in their

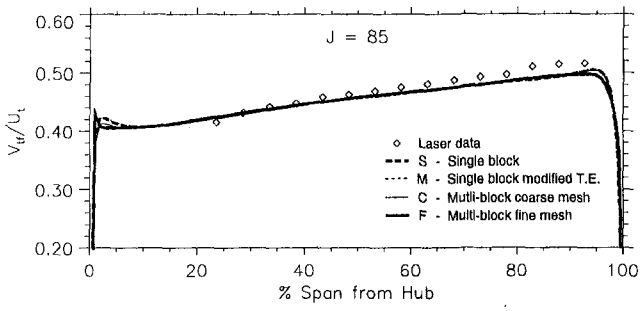

a) Through-flow velocity normalized by exit tip speed

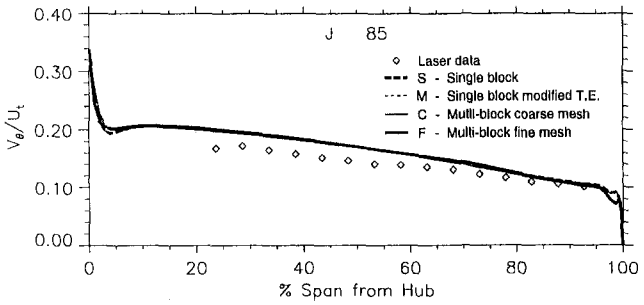

b) Absolute tangential velocity normalized by exit tip speed

Fig. 8 Spanwise velocity distributions at station 85 (15 percent m/m_s)

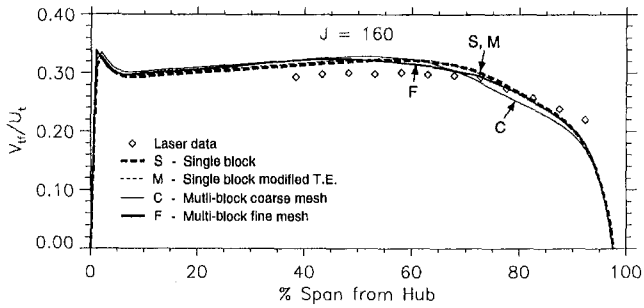

a) Through-flow velocity normalized by exit tip speed

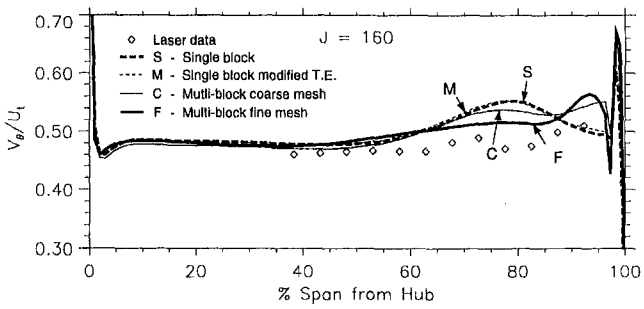

b) Absolute tangential velocity normalized by exit tip speed

Fig. 9 Spanwise velocity distributions at station 160 (89 percent m/m_s)

trailing edge modeling, see Fig. 6. Therefore, the differences in tip modeling or gridding of the tip, at least from this one-dimensional perspective, appear to play a small role in contributing to the observed differences in predicted overall pressure rise and work input.

Axisymmetric Averaged Flow Field. Aside from the ability to predict overall performance, it is important to be able to predict accurately the spanwise distribution of relevant flow quantities, or at the very least their relative shape and trends, in order for the predictions to provide guidance in the design of the compressor blades. Figures 8–11 show comparisons of the predicted and measured spanwise distributions of throughflow and absolute tangential velocities normalized by impeller exit tip speed at several meridional chord locations. The axisymmetric average velocities are calculated as pitchwise velocity weighted averages (density is assumed constant). As will be shown in the following discussion, up to about 90 percent meridional chord the variations in the solutions from the various grids are small, and are predominantly due to the differences in tip clearance mass flow. Downstream of 90 percent meridional chord the impact of the different trailing edge models or gridding becomes apparent. Again, the comparisons focus on differences between the single block cases and the multi-block case *C*.

The results in Fig. 8, at about 15 percent meridional chord, illustrate that all predictions, although different than the measured distribution, agree favorably with each other (cases *S*, *M*, *C* are generally within ±0.3 percent). At 89 percent meridional chord, Fig. 9, where the predicted one-dimensional pressure rise (see Fig. 6) starts to show marked differences between the four cases, the effect of differences in the clearance flow and trailing edge model or gridding are becoming apparent. The difference between the single block cases and case *C* is predominantly confined to the outer 40 percent of span, within the influence of the throughflow wake. From 0 to 90 percent span case *C* is within ±3 percent of cases *S* and *M*, which are essentially identical. Additional comparisons of contour plots of throughflow and absolute tangential velocity at 89 percent chord (not shown) show little differences between the four predictions in spite of the 1 percent increases in tip clearance mass flow for the multi-block predictions relative to the single block predictions. Differences within the throughflow wake region are evident, but the zone of influence of the throughflow wake is essentially unchanged. The major differences between the multi-block case *C* and the single block cases at 89 percent chord are tied to their different clearance mass flow rates. An integration of entropy production from 0–40 percent span and

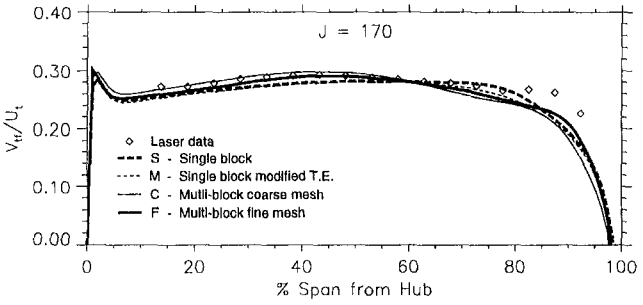

a) Through-flow velocity normalized by exit tip speed

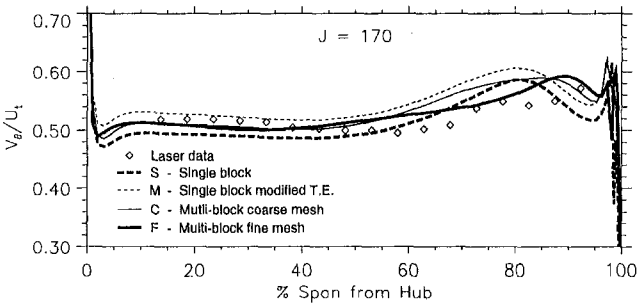

b) Absolute tangential velocity normalized by exit tip speed

Fig. 10 Spanwise velocity distributions at station 170 (99 percent m/m_s)

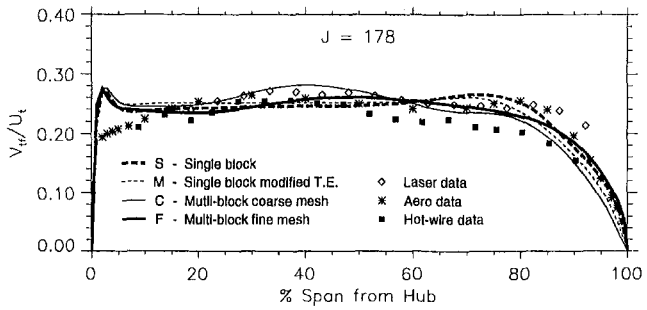

a) Through-flow velocity normalized by exit tip speed

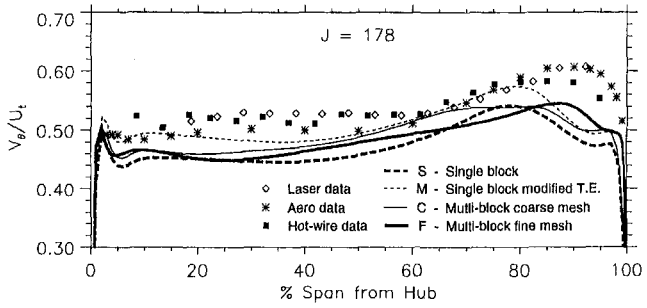

b) Absolute tangential velocity normalized by exit tip speed

Fig. 11 Spanwise velocity distributions at station 178 (109 percent m/m_s, 1.065 r/r_t)

from 40–100 percent span was done to assess the relative effects of the tip clearance flow. The cut off at 40 percent span was determined from inspection of the throughflow velocity contours at 89 percent chord, which indicated that the throughflow velocity wake was confined to the outer 60 percent of span. For the lower 40 percent span there was no difference between cases *S*, *M*, and *C*. This provides confirmation that the tip clearance flow is responsible for the small decrement in efficiency for case *C* versus cases *S* and *M*.

At 99 percent meridional chord, Fig. 10, the relative differences in overall work input previously mentioned are supported by the observed differences in absolute tangential velocity profiles. These differences are a direct result of the differences in trailing edge geometry since at 89 percent chord (see Fig. 9) the tangential velocity distributions for *S* and *M* are identical. These rather large differences in predicted work input occur even though modifications to the trailing edge geometry are made over only the last 1.5 percent of meridional chord from the trailing edge.

Downstream of the impeller trailing edge at 109 percent meridional chord (1.065 radius ratio), Fig. 11, the difference between the various predictions is slightly more pronounced than at 99 percent chord. Although there is no clear consensus that one grid case provides better predictions than another, the next section, which describes blade-to-blade results, indicates that case *C* does the best job of capturing certain blade-to-blade flow features that agree with the measurements as a result of gridding the trailing edge region. This may explain why the coarse multi-block solution, case *C*, which uses essentially the same grid as the single block cases, except for the additional tip clearance gap and trailing edge blocks, comes closest to predicting the general character of the spanwise distribution of throughflow velocity at 1.065 radius ratio. The fine multi-block solution, case *F*, does no better than the single block solutions in predicting the spanwise distribution of throughflow velocity in spite of having almost twice the mesh. The best agreement with the measured spanwise distribution of tangential velocity is provided by the single-block predictions of case *M*. However, for this station it appears that the finer resolution of case *F* in the outer span region may be enabling a better prediction of the increase in tangential velocity near the casing. The reduced overall tangential velocity we attribute to lack of adequate grid resolution in the middle part of the channel. The spanwise distribution of tangential velocity at 1.065 radius ratio has been independently confirmed by pneumatic probe survey data (aero data), laser data, and hot-wire data (data are within ±4 percent of each other), and is very consistent with the comparison of one-dimensional work input shown in Fig. 6(*b*).

Although there appears to be no consensus as to which case affords the best predictions, the multi-block codes that better define the geometry appear to show improvements in predicting certain flow features. The single block solutions do as good a job as the multi-block solutions for comparative analysis of designs. However, as indicated by the fine multi-block solution, case *F*, the improvements in predictive capability afforded by multi-blocking can be offset by insufficient gridding in regions of flow gradients. The fine multi-block solution mesh is coarser than the other cases from 10–85 percent span, which is where the measurements are indicating some spanwise character in the throughflow velocity distribution. However, the hump in throughflow velocity evident in the data at around 80–85 percent span is somewhat better predicted by the fine multi-block solution, case *F*, which is exactly where the fine multi-block mesh density begins to increase. Case *F* has 16 percent more points total in the spanwise direction compared to the other cases, but 25 percent fewer mesh points in the spanwise direction from 10–85 percent span and 40 percent fewer from 55–85 percent span. Not surprisingly, the mesh distribution is as important as accurate modeling of the flow.

Blade-to-Blade Flow. The last area to consider is the details of the predicted blade-to-blade flow variations in the region where a designer might locate a diffuser. For example, the blade-to-blade details might be used to identify regions of accumulated low-momentum fluid, which could greatly alter the intended flow pattern and affect the diffuser performance. The ability to predict the blade-to-blade flow features implies better prediction of the fundamental flow physics and would suggest more confidence in the predictions of the spanwise and overall performance parameters.

Figure 12 compares contour plots of the measured and predicted distributions of throughflow velocity at 1.065 radius ratio. The multi-block cases show better qualitative agreement with the laser measurements, whereas the single block cases are quite different in character. The predictions of the magnitude of the velocities near the blade wake and within and bounding the throughflow velocity wake show good comparison to measurements for the multi-block cases, particularly the coarse multi-block case, relative to the single block cases. The better agreement with measurements of the throughflow wakes predicted by the multi-block cases is in part due to the differences in predicted tip clearance mass flows relative to the single block cases (Fig. 7). Case *C* also resolves more details of the blade wake than the other cases. Further analysis of the solutions shows that the predominant difference of case *C* relative to the single block cases is the development of what appear to be two counterrotating vortices in the "near streamwise direction" that form aft of the trailing edge and severely distort the wake fluid. These counterrotating vortices appear to be generated as a result of strong secondary flows, which feed flow into the wake above and below about 40 percent span. This persists downstream and appears to give rise to the region of high throughflow velocity along the suction side of the wake at about 40 percent span, as depicted in the contour plots of Fig. 12 for both the case *C* predictions and the laser measurements. This may also explain why case *C* shows a slight increase in throughflow velocity, relative to the other cases, near about 40 percent span in Fig. 11(*a*). Comparison of plots of the secondary velocity vectors (not shown) from the case *C* predictions with the laser measure-

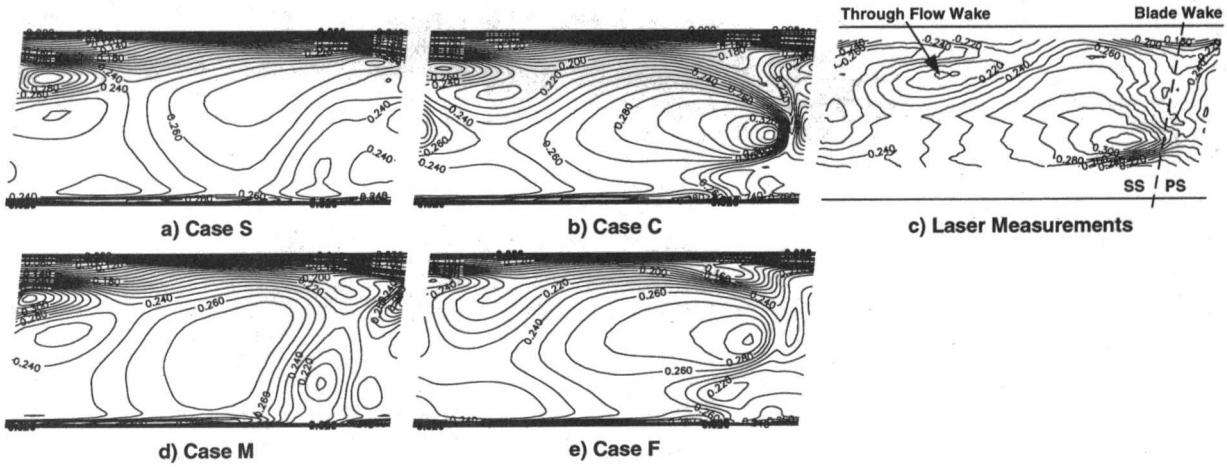

Fig. 12 Comparison of predicted and measured distributions of throughflow velocity at station 178 (r/r_t = 1.065) normalized by exit tip speed, 153 m/s

ments acquired at 1.02 radius ratio (station J = 173) show good qualitative agreement. The laser measurements tend to confirm the predictions of case C since they also show flow moving into the wake in the same areas as those seen in the prediction. Again, due to inadequate spanwise mesh distribution, the fine multi-block solution, case F, does not do as good a job in predicting the flow character as the coarse multi-block solution. It would have been better to place the increased grid points in the passage rather than in the tip gap (given that case F has over six times more grid points as case C within the tip clearance gap yet does no better than C in predicting the tip clearance flow). The two vortices meet near 50 percent span where the spanwise spacing for C is 5.7 percent of span (versus 7.6 percent for F). For C the edges of the vortices at midspan are not well defined (i.e., there are only a few cells defining the interface of the two vortices). This would indicate that this spanwise spacing is marginal in terms of capturing spanwise flow details such as these. At this time, however, that conclusion is problematic and requires more exploration.

The extent to which the various cases predict the decay of absolute flow angle fluctuations indicates their potential for use in analysis of the unsteady impeller/diffuser interactions. Thus, the pitchwise variations in absolute flow angle fluctuations are shown in Fig. 13 and the magnitude of these fluctuations are tabulated in table 2 for 1.037 and 1.065 radius ratio at 40 and 90 percent span from the hub. Forty percent span is about the location where C yields a high value of throughflow velocity in Fig. 12 and 90 percent span is in the throughflow wake. For 90 percent span and 1.037 radius ratio C and F predict a double peak indicative of the blade wake and the throughflow wake, whereas S and M predict only one peak. The agreement of C and F at this location compared to the laser data is quite good. At 40 percent span and 1.037 radius ratio C produces a very strong wake angle fluctuation that is twice as large as the measured values (see Table 2). Case F does not produce this large swing, but in this region the spanwise grid spacing for F is much coarser than it is for C and, thus, could contribute to some smearing of the flow. At 90 percent span and 1.065 radius ratio, F is the only one of the four cases to produce the double peak measured and may be indicative of the greater pitchwise mesh density of F in this region. A plot of all spanwise locations (not shown) indicated that by a radius ratio of 1.08, the flow angle fluctuations for all solutions are below 15 deg, and by 1.2 radius ratio the flow angle fluctuations are less than 12 deg. If one looks at all percent span locations there is not a clear choice as to which grid yields the best results and further work needs to be done to determine what factor is most important in predicting the correct magnitude of the flow angle variation.

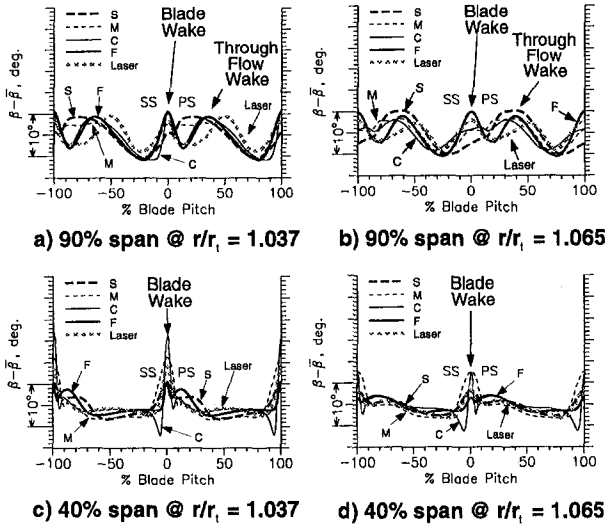

Fig. 13 Pitchwise distribution of absolute flow angle variation, $\beta - \bar{\beta}$, in the vaneless diffuser

Table 2 Magnitude of absolute flow angle fluctuations in the vaneless diffuser, in deg

% Span from Hub	Case	r/r_t	
		1.037	1.065
40	S	9	6
	M	15	11
	C	24	14
	F	8	4
	Laser	12	7
90	S	10	11
	M	9	9
	C	12	8
	F	12	11
	Laser	7	8

Table 3 Comparison of computer resources in terms of CPU time and memory requirements

CASE	NUMBER OF PROCESSORS	RELATIVE MEMORY PER PROCESSOR	RELATIVE CPU TIME PER ITERATION
S	3	1.000	1.000
M	3	1.000	1.002
C	4	0.909	1.083
	3	1.114	1.164
F	6	0.980	1.408
	3	1.993	2.052

Relative "Costs" of Analyses. Table 3 provides a comparison of the relative "costs," in terms of CPU time and memory requirements, of running the various cases. The basis for comparison is the single block solution, case *S*. The benchmark results provided in Table 3 were obtained using the NASA LACE cluster, a network of IBM RS/6000 Model 590 computers. As previously mentioned, all cases, whether single or multi-block were run as multi-block jobs in order to take advantage of ADPAC's parallel execution capability, which parallelizes a job according to its multiple block structure. The single block cases were each run using three equally loaded processors (in terms of number of mesh nodes per processor). The multi-block cases were run two ways: (1) with the minimum number of equally loaded processors required for each to be loaded similar to the single block cases, and (2) with three equally loaded processors as in the single block cases. The rationale behind the comparisons were to both try to assess the relative CPU time as a result of increased number of grid nodes (and not due to any differences that might occur as a result of one processor being more heavily loaded than another), and to assess the relative CPU time due to increased processor loading as a result of additional grid nodes required for the multi-block cases. Although not measured, there was an additional perceived penalty for the multiple-block cases, which seemed to require more iterations to achieve convergence, roughly proportional to the increased time per iteration for the comparatively loaded processors (i.e., case *F* using six processors required roughly 40 percent more iterations as case *S* to converge from a given perturbation in back pressure).

Summary of Results

The focus of the paper is to identify areas of interest in a design mode where a designer could use a single block grid for a Navier–Stokes solver with some modeling of the true geometry versus a more complicated multi-block grid that better models the actual geometry of the turbomachine under consideration. Our intent was to focus on one-dimensional overall parameters, pitchwise-averaged spanwise variations, and the complete flowfield, which would indicate the level of interest the designer had in the details of the machine being analyzed. Of the four solutions presented it is not possible to conclude that one particular grid always gives better results since, depending upon the flow feature of interest, some agree with the data better for some features and others agree better with the data for other features. However, we can state that if one is interested in prediction of overall performance numbers, whether the tip gap is modeled (cases *S* and *M*) or gridded (cases *C* and *F*), the results are the same within an acceptable level of accuracy (± 0.5 percent in pressure ratio and ± 1 point in efficiency). This same statement is also true for the spanwise distributions and the details of the flow. The different predicted tip clearance flow between the modeled cases (*S* and *M*) and the gridded cases (*C* and *F*)—1 percent of inlet flow—does not alter the results to any significant degree.

Modeling of the trailing edge, however, produces significant differences between both the single block cases (*S* and *M*) and the multi-block cases (*C* and *F*) for the overall work input and pressure ratio. Whether one models the trailing edge as a tapering of both sides of the blade to the mean camber line (*S*) or as a taper of the suction surface to the pressure surface (*M*) results in about a 7 percent difference in work input with the *M* solution being less than 1 percent below the experimental value of work input. A comparable difference exists in pressure rise with *M* being 2 percent higher than the measured value. Both multi-block solutions underpredict the work input by about 5 percent of the measured value and predict the pressure rise correctly for case *C* and 1 percent low for case *F*. The differences in work input begin at about 90 percent chord (recall the modification of the trailing edge began at 98.5 percent chord so there is considerable upstream influence of the trailing edge) and persists downstream. Case *C* resolves more flow details of the throughflow velocity at a radius ratio of 1.065 than the others in part because of two counterrotating vortices that form aft of the trailing edge and severely distort the wake fluid. In terms of predicted wake decay, there is little difference in how the wake decays. All solutions predict most of the wake decay occurs before the 6.5 percent radius ratio and that setting a diffuser beyond that radius ratio would not decrease flow angle swings into the diffuser by a significant amount. Near the trailing edge the magnitude of the angle swing is greatly dependent upon the modeling of the trailing edge, but by 8 percent radius ratio all the cases predict angle swings less than 15 deg (this considers all percent span locations) and not much reduction occurs beyond that radius ratio.

Conclusions

Although none of the grids investigated produced superior results in every case when compared to the measurements, in general, we can say that grid *C*, which added coarse gridding to the tip gap region and a blocked grid downstream of the trailing edge, yielded the best results. However, the results from *F* indicate that increased grid density away from the hub and tip may improve the results from *C*. In summary we conclude the following:

1 Increasing grid density in the tip gap by a factor of 6.5 resulted in no difference in predicted tip clearance overall flow nor in the chordwise distribution of the clearance flow. A fairly coarse grid as used in *C* seems perfectly adequate. Also, the modeling used in the single block grids gives results that are quite good, especially if one is doing comparative studies. For analysis cases the difference in tip clearance mass flow rate between the modeled and gridded cases is well within the uncertainty of the actual tip clearance gap height.

2 Blocking the trailing edge with a grid so the trailing edge geometry is properly modeled reduces uncertainties in how to taper the blade to zero thickness if using a single block code but appears to offer no great benefit for the present case, although some details of the flow downstream of the impeller are better predicted. However, we caution that more cases need to be investigated before we would offer this as a more general conclusion.

3 Since the trailing edge treatment used for a single block code can significantly affect the results, we would recommend using a multi-block code. If a multi-block code is not available, we recommend using the blade trailing edge taper for grid *S* since it produces the same type of pressure and temperature rise behavior near the trailing edge as produced with *C*. However, we would suggest a more gradual taper than used in *S* to reduce any spurious entropy rise due to high grid shear. It may also be better to make a more symmetric taper around the mean

camber line based upon normal thickness taper rather than tangential thickness taper as done for S. This may inhibit the tendency of the flow to turn rapidly around the pressure surface with the resultant underturning of the flow.

4 For this case, in order to capture the spanwise details measured with the laser downstream of the trailing edge, it appears that a grid spacing of 5.7 percent span at midspan is marginal and should be reduced in order to resolve the local gradients.

5 The choice of grids for the trailing edge yields considerable differences in the swings in the pitchwise absolute flow angle near the trailing edge. However, all four grids predict swings less than 15 deg by an 8 percent radius ratio and none predicts much decrease beyond that radius.

Acknowledgments

The authors are grateful to Dr. Ed Hall, and Nathan Heidegger at Allison Engine Co. and Dr. Chris Miller at NASA's Lewis Research Center for their helpful suggestions and assistance regarding the ADPAC analyses. The authors are also grateful for the suggestions of Dr. Ali Ameri of the University of Kansas Center for Research Inc., Resident Research Associate, NASA Lewis Research Center.

References

Adamczyk, J. J., 1995, private communication.

Baldwin, B. S., and Lomax, H., 1978, "Thin-Layer Approximation and Algebraic Model for Separated Turbulent Flows," AIAA Paper No. 78-257.

Chriss, R. M., Hathaway, M. D., and Wood, J. R., 1996, "Experimental and Computational Results From the NASA Lewis Low-Speed Centrifugal Impeller at Design and Part Flow Conditions," ASME JOURNAL OF TURBOMACHINERY, Vol. 118, pp. 55–65.

Hall, E. J., and Delaney, R. A., 1992, "Investigation of Advanced Counterrotation Blade Configuration Concepts for High Speed Turboprop Systems: Task V—Counterrotation Ducted Propfan Analysis, Final Report," NASA CR 187126, NASA Contract NAS3-25270.

Hall, E. J., Topp, D. A., Heidegger, N. J., and Delaney, R. A., 1994, "Investigation of Advanced Counterrotation Blade Configuration Concepts for High Speed Turboprop Systems: Task VIII—Cooling Flow/Heat Transfer Analysis, Final Report," NASA CR 195360, NASA Contract NAS3-25270.

Hathaway, M. D., Wood, J. R., and Wasserbauer, C. A., 1992, "NASA Low Speed Centrifugal Compressor for 3-D Viscous Code Assessment and Fundamental Flow Physics Research," ASME JOURNAL OF TURBOMACHINERY, Vol. 114, pp. 295–303.

Hathaway, M. D., Chriss, R. M., Wood, J. R., and Strazisar, A. J., 1993, "Experimental and Computational Investigation of the NASA Low-Speed Centrifugal Compressor Flow Field," ASME JOURNAL OF TURBOMACHINERY, Vol. 115, pp. 527–542.

Hathaway, M. D., Chriss, R. M., Wood, J. R., and Strazisar, A. J., 1995, "Laser Anemometer Measurements of the Three-Dimensional Rotor Flow Field in the NASA Low-Speed Centrifugal Compressor," NASA TP-3527.

Jameson, A., Schmidt, W., and Turkel, E., 1981, "Numerical Solutions of the Euler Equations by Finite Volume Methods Using Runge-Kutta Time-Stepping Schemes," AIAA Paper No. 81-1259.

Skoch, G. J., 1995, private communication.

Strazisar, A. J., Wood, J. R., Hathaway, M. D., and Suder, K. L., 1989, "Laser Anemometer Measurements in a Transonic Axial-Flow Fan Rotor," NASA TP-2879.

Wood, J. R., Adam, P. W., and Buggele, A. E., 1983, "NASA Low-Speed Centrifugal Compressor for Fundamental Research," NASA TM 83398.

Wood, J. R., 1994, private communication.

Variable Geometry Pipe Diffusers

J. W. Salvage
Senior Staff Engineer,
United Technologies, Carrier,
Syracuse, NY 13221

Theoretical analyses and experimental results are reported for two unique variable geometry techniques used with pipe diffusers to enhance off-design performance. One technique mechanically closes the diffuser throat in an unusual manner. The other allows flow recirculation to close the throat artificially while attempting to improve diffuser inlet flow characteristics. Results clearly show that surge margin may be significantly improved by either method and that flow recirculation may offer improved efficiency.

Introduction

As a matter of course, modern turbomachinery incorporates variable geometry since "range" and "performance" are such important, often mutually exclusive, objectives. The basic behavior of a compressor incorporating "variability" is illustrated in Fig. 1, taken from Cumpsty (1989) after the work of Casey and Marty (1986). (Two lines have been added to the original figure, as described below.) Here, a centrifugal compressor is depicted as having variable speed drive, variable inlet guide vanes (IGVs), and variable diffuser vanes, each being used independently to control the head (or pressure rise) of the compressor. The figure illustrates the characteristic behavior of the surge line for each device.

Two unique variable diffuser techniques will be considered for application to constant-speed compressors that already employ variable IGVs, thereby using a combination of two methods illustrated in Fig. 1. The particular application is a centrifugal compressor employed in large chillers, typically used for air conditioning buildings.

The operating line for such compressors is very demanding. For example, the Air-Conditioning & Refrigeration Institute (ARI) will certify a chiller system's rating if a manufacturer can prove by test that the system will perform as claimed for various system conditions that make up the "ARI line." (See ARI Standard 550 for details.) The ARI line may be represented by a line extending from the design point down to 50 percent of design head at 10 percent of design flow. This approximation is shown in Fig. 1. Variable speed may not be sufficient in this case, requiring the compressor to have some type of variable geometry.

For operation in the Asia-Pacific region, for example, ambient conditions are more constant throughout the year, implying higher head must be maintained. This load demand is approximated by a line from design point down to 85 percent of design head at 10 percent of design flow. This (APO) line is also shown in Fig. 1, illustrating that even the variable diffuser surge line may not be sufficient for this application.

Theoretical and experimental results will be presented for devices that enhance a compressor's surge line. However, the investigation's principal objective was to define means to improve compressor performance on the ARI line.

Description of the Compressor

The compressor used for this investigation is comprised of a set of seven uncambered IGVs, a backswept impeller (Table 1) and a pipe diffuser (Table 2) that discharges into a constant-cross-sectional-area collector. Design operating conditions for the compressor are given in Table 3.

The design incorporates a pipe diffuser because of its high performance and wide operating range. Pipe diffuser characteristics are described by Kenny (1968, 1979) and Reeves (1977), for example. A partial cross section of the pipe diffuser is shown in Fig. 2. The section is taken normal to the impeller axis of rotation, illustrating several pipe centerlines. The diffuser geometry consists of (1) a short, constant-area throat section, (2) a length of 4 deg divergence, followed by (3) a longer section of 8 deg divergence.

The simple, effective, circular cross section of the pipe diffuser makes varying its geometry difficult. Unlike two- or even three-dimensional vane- or channel-type diffusers, it is virtually impossible to adjust the pipes' leading edges for varying flow conditions. Adjusting the direction of flow seems more appropriate, if this were possible.

The cross section of one variable geometry pipe diffuser concept, designated the split ring diffuser, is shown in Fig. 3. The pipe diffuser is divided into two concentric rings, one of which is rotated with respect to the other. The radius dividing the diffuser's two parts was made as small as possible. However, about 10 percent of the local area is left open, regardless of the relative position of the rings, to prevent overheating resulting from stagnating the impeller flow. The dividing radius equals $1.223 R_{tip}$.

The split ring diffuser is obviously little more than a throttling device. However, it was imagined that throttling the impeller exit flow, in conjunction with controlling the impeller inlet flow by IGVs, might allow significant performance improvement. Other throttling devices, such as a throttle ring positioned between the impeller and diffuser, as proposed by Bandukwalla (1983), were considered but dismissed because of the resulting asymmetric downstream flow field.

The second concept allowing pipe diffuser "variability" is depicted within the compressor cross section of Fig. 4. It is designated the recirculation diffuser because a portion of the gas from the collector re-enters the impeller exit flow stream. Table 4 provides the design geometry. The recirculating flow may be metered by the shut-off ring. The flow passes inward through deswirl vanes, a swirl chamber situated above the impeller, and a vaned channel before mixing with the impeller exit flow field and then entering the pipe diffuser. Flow into the pipe diffuser is kept as invariant as possible despite changes to the impeller flow caused by manipulation of the IGVs. The recirculating flow tends to fill the diffuser passage even as impeller flow is reduced. Obviously, application of the concept is not limited to pipe diffusers.

Theoretical Approach

Both variable diffuser concepts were evaluated theoretically before they were built and tested to anticipate their performance on the ARI line. The base compressor was modeled by a one-dimensional throughflow analysis normally used for centrifugal compressor preliminary design. The method is similar to that

Contributed by the International Gas Turbine Institute and presented at the 41st International Gas Turbine and Aeroengine Congress and Exhibition, Birmingham, United Kingdom, June 10–13, 1996. Manuscript received at ASME Headquarters February 1996. Paper No. 96-GT-202. Associate Technical Editor: J. N. Shinn.

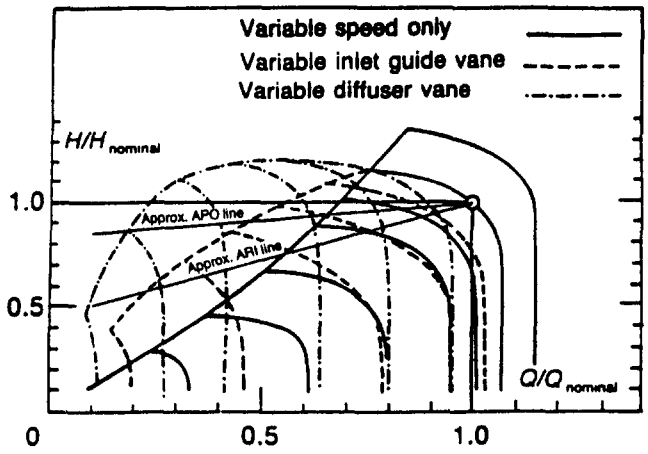

Fig. 1 Compressor head rise versus flow as separately influenced by variable speed, variable inlet guide vanes, and variable diffuser vanes

Table 1 Impeller geometry

Blade tip radius	4.600 in. (116.8 mm)
Inlet hub radius/blade tip radius	0.30435
Inlet hub-to-shroud radius ratio	0.446
Inlet shroud blade angle	57.6°
Number of blades/splitters	11/11
Exit blade angle	53.6°
Exit blade height/tip radius	0.1325
Average exit blade thickness/blade height	0.167
Running clearance/blade height	0.025

Note: Angles are measured with respect to meridional direction.

Table 2 Pipe diffuser geometry

Number of pipes	16
Tangent radius	4.600 in. (116.8 mm)
Throat diameter	0.620 in. (15.7 mm)
Throat length/throat diameter	0.226
Initial divergence angle	4°
Initial divergence length/throat diameter	1.8065
Second divergence angle	8°
Discharge radius/tangent radius	2.0109
Overall area ratio	4.38

Table 3 Compressor design conditions

Working fluid	R134a
Inlet flow coefficient, $Q_0/(a_0 D_2^2)$	0.088
Polytropic head coefficient, $\Delta H_p/a_0^2$	0.975
Wheel Mach number, U_{tip}/a_0	1.34
Impeller wheel speed	16,131 rpm
Inlet volume flow rate, Q_0	1495 CFM (0.706m^3/s)
Overall pressure ratio	2.7

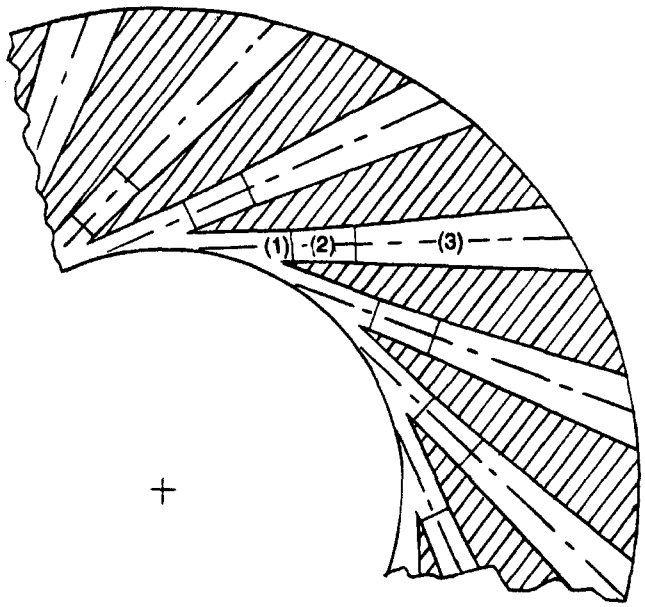

Fig. 2 A typical pipe diffuser cross section shown normal to the axis of impeller rotation

of Aungier (1995). (See all references by Aungier cited in that paper.)

The unique diffuser geometries required flow model modifications. Simple calculations revising flow parameters were inserted at discrete stations within the flow field. Any diffuser–impeller interaction was neglected. The impeller exit flow field was considered a discrete station after the impeller trailing edge, after taking wake mixing loss into account. This is notable since Fig. 4 clearly shows recirculating flow re-entering partially below the impeller tip.

Nomenclature

A = area
a = sonic velocity
D = diameter
d_h = hydraulic diameter
F = flow rate
F_h = fraction of the maximum deswirl vane height open as allowed by the shut-off ring
f = friction factor
H = head rise
h = height
L = length
M = Mach number
Q_0 = compressor inlet volume flow rate based on stagnation specific volume
P_0 = total pressure
R = radius
t = vane thickness
U = impeller tangential velocity
V = velocity
Z = axial position, or number of vanes
α = angle of slope with respect to axial direction
β = flow angle with respect to meridional direction
θ = polar angle
κ = ratio of specific heats (assumed constant, 1.035)
ω = total pressure loss coefficient

Subscripts

avg = average
CAV = cavity
CH = channel
des = design
DV = deswirl vane
in = inlet
out = outlet
p = polytropic
tip = impeller blade exit
0 = collector, or total conditions
1 = deswirl vane leading edge before expansion into vane passage
2 = impeller exit, or deswirl vane passage entrance
3 = deswirl vane passage exit
6 = channel vane passage entrance
7 = channel vane passage exit

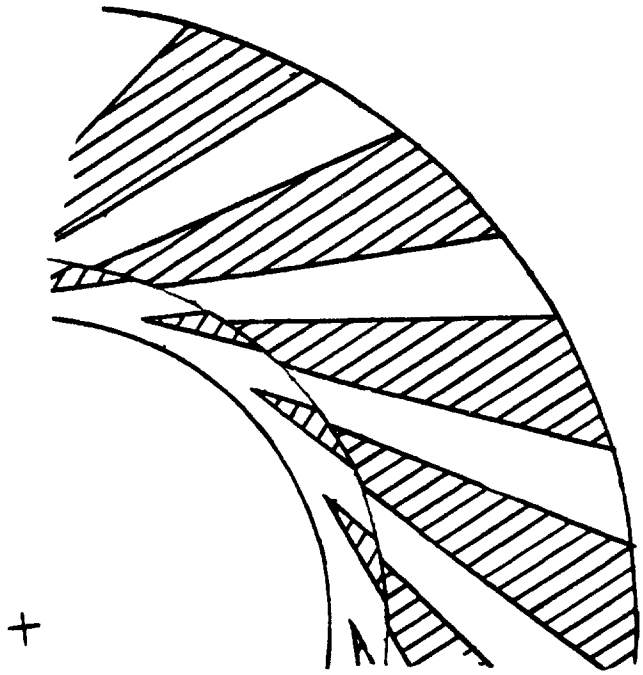

Fig. 3 A cross section of the split ring diffuser

Model and Calculation Results

The Split Ring Diffuser. When one ring is rotated with respect to the other (Fig. 3), the pipe diffuser flow encounters an area contraction, then an area expansion. The total pressure loss coefficient for each area change is given by the following expression:

$$\omega = (A_{in}/A_{out} - 1.)^2 \qquad (1)$$

Equation (1) is derived from steady, incompressible forms of the one-dimensional continuity and momentum equations assuming the base pressure equals the inlet station static pressure. The inlet station dynamic head is used to normalize pressure differences. For the split ring diffuser analysis, losses are applied after determining properties at the (original) diffuser throat.

Analysis details are not shown here because application of additional losses, without any modification of work done by the impeller, led to inferior theoretical performance at all ARI-line conditions when compared to base compressor results. The configuration was later tested only because it is so simple to construct. Furthermore, since other throttling-type devices have shown enhanced range, this geometry was considered likely to do so.

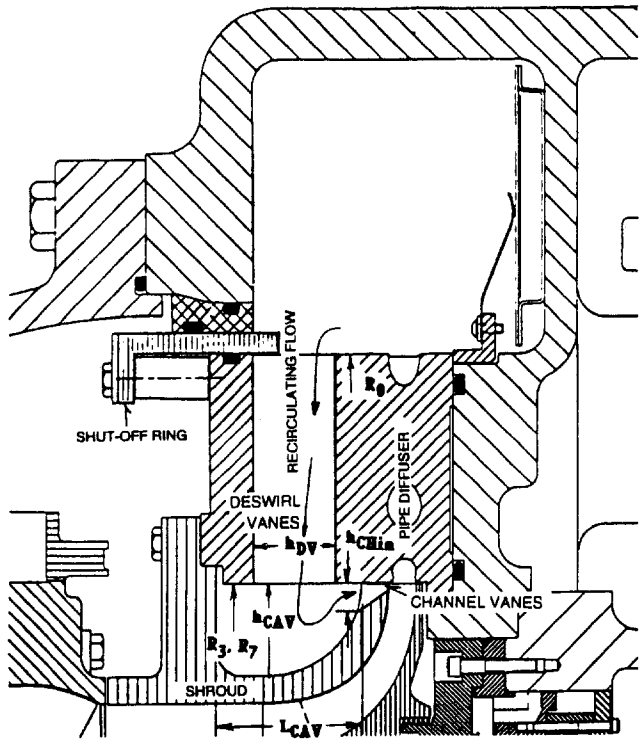

Fig. 4 A compressor flow path cross section showing recirculation diffuser geometry

Table 4 Recirculation flow geometry

Collector lower radius, deswirl vane inlet radius	9.250 in. (235.0mm)
Deswirl vane leading edge angle *	71.12 °
Deswirl vane height	1.500 in. (38.1mm)
Number of deswirl vanes	12
Deswirl vane thickness	0.2 in.
Deswirl vane passage length-to-hydraulic-diameter ratio	7.74
Deswirl vane outlet radius	4.600 in. (116.8mm)
Deswirl vane trailing edge angle *	54.0°
Axial length of the cavity	2.779 in. (70.6mm)
Cavity cross-sectional area	2.710 in^2 (1750mm^2)
Radial height of cavity	0.975 in. (24.8)
Channel vane leading edge angle *	60.15°
Channel vane axial length	0.468 in. (11.9mm)
Radial height at the channel inlet	0.668 in. (17.0)
Number of channel vanes	24
Channel vane thickness	0.100 in. (2.5mm)
Channel hub slope angle **	45.0°
Channel vane passage length-to-hydraulic-diameter ratio	2.552
Mean radius at channel outlet	4.600 in. (116.8mm)
Channel vane trailing edge angle *	70.0°
Radial height at channel outlet	0.200 in. (5.1mm)

* Measured with respect to meridional direction
** Measured with respect to axial direction

The Recirculation Diffuser. Ten discrete stations are modeled for the recirculation diffuser. Two fundamental loss processes are considered, sudden area expansion/contraction, Eq. (1), and friction.

When the flow process is frictional, the outlet total pressure is given by the following equation from Shapiro (1958):

$$P_{0out} = P_{0in}\,[1. - 0.5\,\kappa M^2\,(4f)\,(L/d_h)]$$

The specific heat ratio, κ, is held constant to a value near that expected (1.035) as a time-saving approximation to the real gas behavior. Similarly, 4f is assumed equal to 0.020. The Mach number, M, is an arithmetic average of inlet and outlet values. Iteration is required for outlet station conditions because the average Mach number is involved.

With these relations substituting for a rigorous solution of the meridional momentum equation, (1) either tangential momentum is conserved, or flow is assumed perfectly guided by a vane, (2) total enthalpy is assumed constant, (3) the continuity equation is solved at every station, and (4) the equation of state employs the real gas properties of Refrigerant 134a (except as noted for κ above).

Choking is checked at every station except those after an expansion process. The channel vane exit station will most

likely limit flow because it has the smallest physical area. Wherever choking occurs during the calculation procedure, the limiting flow rate is found by setting velocity equal to the local acoustic velocity. Calculations are restarted from the collector with the reduced recirculating flow rate.

When flow is choked and the recirculating flow's static pressure at the impeller exit station is greater than the impeller exit static pressure, loss is too small for the recirculation process. Physically, the driving pressure for the process (i.e., the collector total pressure) must be decreased. This may occur naturally as the overall iteration continues; i.e., as combined effects of impeller flow and recirculating flow are included in loss evaluation for the diffusion system. However, to continue the calculation process, the recirculating flow total pressure at the impeller exit station is artificially reduced by the difference between the two calculated impeller exit static pressures. Flow angle is temporarily maintained at the value found for the choked condition, simplifying determination of the full velocity's magnitude. Velocity is re-evaluated by solving continuity and the equation of state.

The ten stations and the flow processes connecting them are now described briefly.

0 *The collector.* Collector conditions "drive" the recirculation process. However, these conditions result directly from (*a*) the combined impeller exit flow and any recirculating flow, and (*b*) the flow process through the vaneless space, pipe diffuser, and collector. The diffusion system's total enthalpy is constant. Collector total pressure is initially guessed, but known thereafter from previous iteration steps. The recirculation mass flow rate is guessed and varied until the recirculated flow stream's static pressure matches the impeller exit flow stream static pressure. Between collector and shut-off ring, the continuity equation is solved assuming isentropic flow into the area blocked by the shut-off ring.

1 *Deswirl vane leading edge after contraction due to vane thickness but before expansion into the vane passage.*

2 *Deswirl vane leading edge after expansion into the vane passage.*

3 *Deswirl vane trailing edge before expansion into the swirl cavity.* The flow process through the deswirl vane passage is modeled as entirely frictional.

4 *Cavity entrance after expansion from the deswirl vane trailing edge.*

5 *Cavity exit before channel vane leading edge.* The cavity flow process is modeled as entirely frictional, taking into account increased flowpath length due to swirling flow there. The cavity flow angle is assumed constant, equal to the flow angle after expansion from the deswirl vane.

6 *Channel vane leading edge after contraction due to vane thickness.*

7 *Channel vane exit before expansion into the impeller exit flow field.* The channel flow process is modeled as entirely frictional.

8 *Recirculated flow at impeller exit after expansion from channel but before mixing with impeller discharge flow.* This station's calculated static pressure is compared to the impeller exit static pressure. If the two values are not equal, the recirculated flow rate is adjusted; and calculations are repeated. However, if flow is choked anywhere within the flow field such that recirculating flow is maximum, the procedure is modified slightly, as discussed above.

9 *Vaneless space inlet after mixing the recirculated flow with the impeller exit flow.* The tangential velocity components for the two streams are combined by mass flow weighting. The continuity and energy equations, as well as the equation of state, are then satisfied for the total flow, determining the meridional velocity as well as other combined flow stream properties. Calculations continue through to the collector where the total pressure driving the recirculating flow is reevaluated. Calculations are complete when the collector total pressure is determined that yields a match of impeller exit static pressures as described for station 8.

Investigation of Geometric Parameters Affecting the Recirculation Flow Process

Certain geometric parameters were fixed by the test compressor's geometry; e.g., the basic radii R_0, R_3, and R_7. However, h_{DV}, L_{CAV}, h_{CAV} (hence, A_{CAV}), and L_{CH} were limited by mechanical considerations. Similarly, h_{CHin} was confined to a maximum value when the analysis indicated an advantage for a converging channel.

Values of Z_{DV}, t_{DV}, Z_{CH}, t_{CH} and α_{CHhub} were chosen within ranges leading to easily manufacturable parts.

The deswirl vane trailing edge angle, β_3, was chosen early in the investigation in order to procure the part. The value of β_3 was that angle that would occur in an inward flowing vaneless space having losses estimated for the frictional process at 50 percent of compressor design flow rate. Vanes were used to guide the velocity for conditions other than design flow rate.

The deswirl vane camber line was derived as follows. First, the meanline angle was maintained constant for the inner 10 percent of the vane's radial length. Next, the radial distribution of vane angle was calculated assuming

$$R \cos \beta = \text{const}$$

Results are given in Table 5. The vanes have constant cross section and a constant thickness of 0.2 in. (5.1 mm).

The channel vane trailing edge angle, β_7, is one of the principal variables in the analysis. Although the final design value of the channel vane leading edge angle, β_6, was varied to limit losses, β_6 was set equal to β_7 for most of the parametric studies described below. The channel vane meanline is defined by linear variation of angle along the hub contour (a 45 deg cone). The meanline polar angle was maintained constant while radially defining the vane. Results are given in Table 6.

Other principal variables included the fraction of deswirl vane height open to flow, F_h, and the channel height, h_{CH}. Channel height was held constant from inlet to outlet for most of the analysis. However, a convergent channel proved superior. Independent variables include the mass flow rate and IGV setting angle.

The "figure of merit" was head rise (or pressure ratio) achieved by the geometry. Efficiency might seem a more natural

Table 5 Definition of deswirl vane meanline

R cos β = const for R > 5.092			
Radius		θ	β
[in.]	[mm]	[°]	[°]
4.630	117.7	0.0	54.00
5.092	129.3	7.51	54.00
5.554	141.1	14.81	57.39
6.016	152.8	22.37	60.16
6.478	164.5	30.13	62.48
6.940	176.3	38.04	64.45
7.402	188.0	46.08	66.15
7.864	199.7	54.21	67.63
8.326	211.5	62.425	68.93
8.788	223.2	70.71	70.09
9.250	235.0	79.05	71.12

Table 6 Definition of channel vane meanline

β varies linearly along a 45° cone from 70° at Z = 0.0 to 60° at Z = 0.475 in. (12.1 mm)					
Axial Length		Radius		θ	β
[in.]	[mm]	[in.]	[mm]	[°]	[°]
0.0000	0.000	4.6100	117.09	0.0	70.0
0.0475	1.207	4.5625	115.89	2.246	69.0
0.0950	2.413	4.5150	114.68	4.399	68.0
0.1425	3.620	4.4675	113.47	6.469	67.0
0.1900	4.826	4.4200	112.27	8.462	66.0
0.2375	6.033	4.3725	111.06	10.383	65.0
0.2850	7.239	4.3250	109.86	12.240	64.0
0.3325	8.446	4.2775	108.64	14.035	63.0
0.3800	9.652	4.2300	107.44	15.773	62.0
0.4275	10.858	4.1825	106.24	17.459	61.0
0.4750	12.065	4.1350	105.03	19.095	60.0

choice. However, impeller work is assumed independent of changes in the recirculation flow field. Then, because the impeller is rotating at constant speed, an increase in head is equivalent to an efficiency increase for the same flow rate and IGV setting.

Figure 5 shows the influence of shut-off ring position (portrayed as varying values of F_h) for a geometry where the channel vane height is relatively large ($h_{CH} = 0.1304 R_{tip}$). The IGV setting is held constant. Curves are shown for different compressor inlet flow rates, F/F_{des}. Head changes as the shut-off ring is opened (i.e., F_h increases) increasing flow recirculation. Note that (a) performance improves with recirculation (i.e., increased head above its value at $F_h = 0$ for a given compressor flow rate) only for a limited range of F_h, and (b) there is more head difference between the various stage flow rate curves as F_h increases. The latter means the compressor head-flow characteristic becomes steeper for the IGV setting, implying a more stable compressor characteristic.

The influence of channel vane height is shown in Fig. 6 where the head achieved at a particular compressor inlet flow rate, $0.327 F_{des}$, is plotted versus recirculation flow rate. Channel height is a principal geometric variable controlling performance.

For the h_{CH}/R_{tip} equal to 0.0217 and 0.0435, calculations were carried to $F_h = 1.0$, showing that performance is maximum when the shut-off ring is fully open for small channel heights. For larger channel heights, performance is maximum at considerably smaller shut-off ring openings.

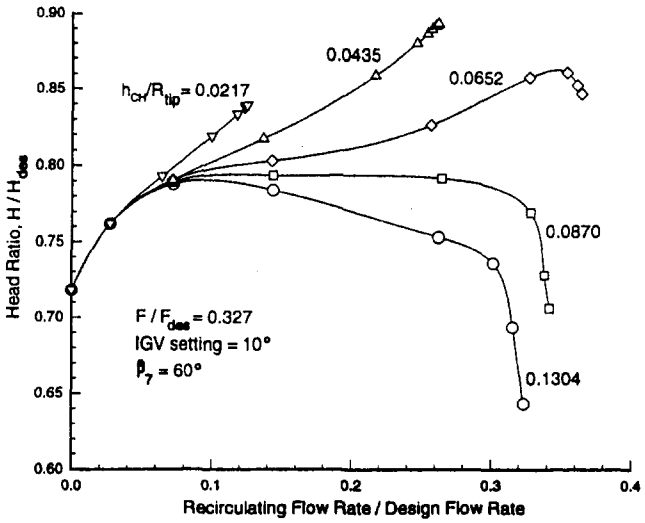

Fig. 6 Theoretical variation of head with recirculating flow rate as a function of channel vane height

These results suggest there may be an optimum channel vane height. Maximum performance at any given channel vane height (and, indeed, the optimum vane height) corresponded to the flow condition for which the calculated diffuser incidence loss was minimum. Calculation details indicated that performance deteriorates rapidly with mismatch of the mixed impeller-recirculation flow direction and the diffuser leading edge direction.

Figure 7 shows head rise achieved for $F_h = 1.0$ versus channel height as a function of compressor inlet flow rate. For IGVs set to 10 deg and a flow ratio of 0.386 (where the vane line was anticipated to cross the ARI line), the optimum h_{CH} is about $0.042 R_{tip}$.

Influence of the channel vane trailing edge angle, β_7, is illustrated in Fig. 8. For h_{CH}/R_{tip} of about 0.05 or less, optimum performance exists at about 65 deg. However, the maximum value of head rise increases as β_7 increases. Hence, performance is better when the trailing edge vane angle is properly coordinated with the channel exit vane height. Obviously, the recirculating flow's exit velocity vector is the controlling parameter.

Influence of channel streamline slope is shown in Fig. 9. As streamline slope increases, channel height must be increased to attain maximum performance.

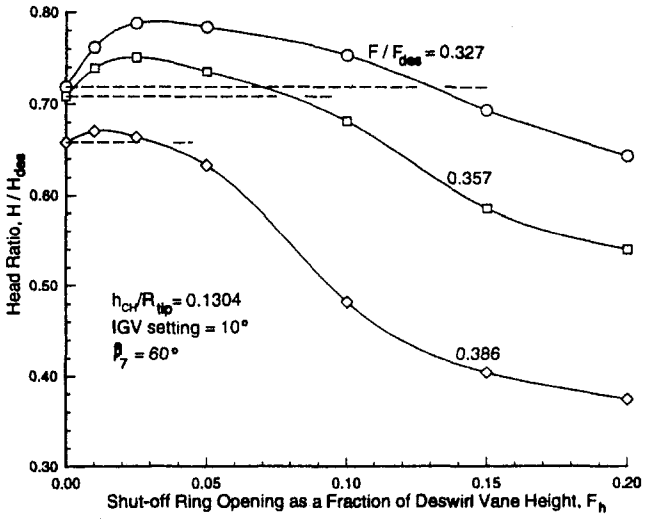

Fig. 5 Theoretical variation of head with shut-off ring position as a function of impeller flow rate

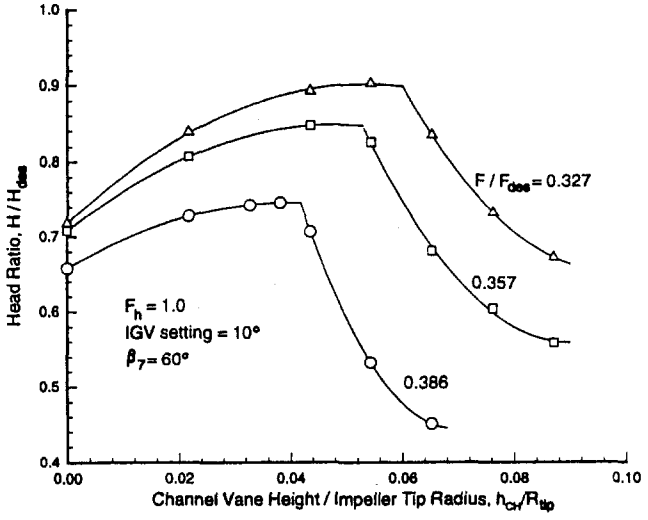

Fig. 7 Theoretical variation of head with channel vane height as a function of impeller flow rate

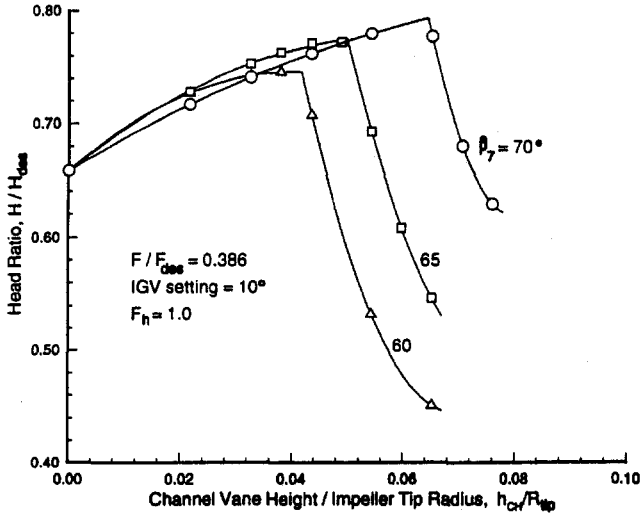

Fig. 8 Theoretical variation of head with channel vane height as a function of channel vane exit angle

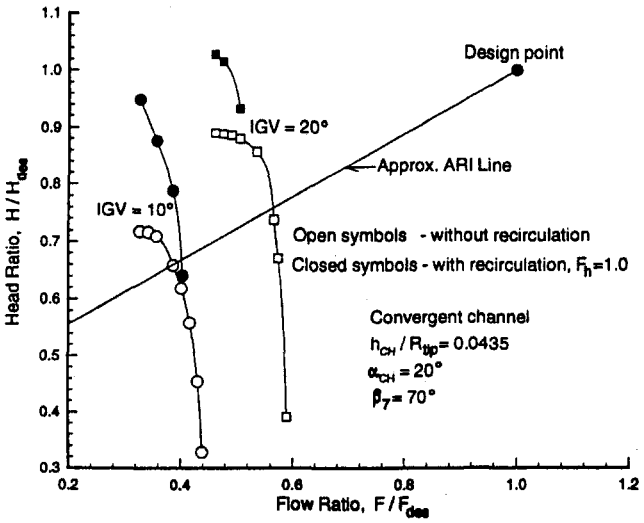

Fig. 10 Theoretical results for compressor head versus impeller throughflow rate with and without recirculation

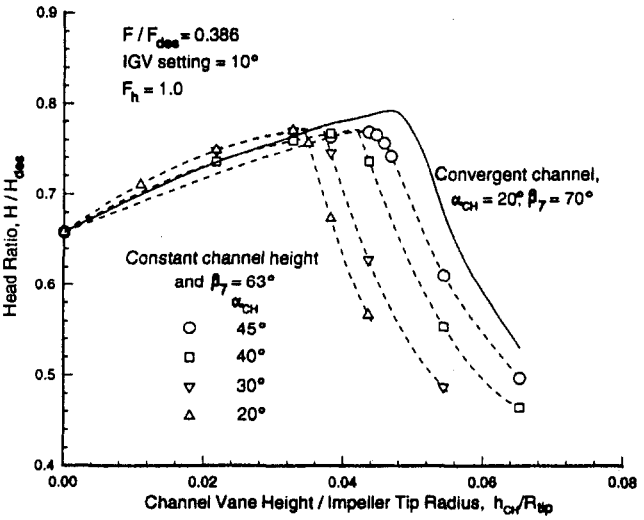

Fig. 9 Theoretical variation of head with channel vane height as a function of channel flow path slope

Figure 9 includes the variation of head with channel height for final design values of channel vane trailing edge angle and channel mean streamline slope. Note that a convergent channel flowpath was also introduced to lower loss due to friction.

Finally, predicted performance of the recirculation concept is shown in Fig. 10. The configuration is designed to begin showing improved performance on the ARI line at an IGV setting of 10 deg. The performance increase was expected to be on the order of 7.5 percent.

Test Description

Compressor configurations were tested on a complete refrigeration system. The system is composed of an evaporator, compressor, condenser, and flask subcooler. The compressor is driven by a constant-speed hermetic motor.

Measured pressures include evaporator and cooler pressures, both assumed saturated (hence, head rise is measured from vessel to vessel and includes piping losses as well as normal compressor loss sources) and subcooler leaving-refrigerant pressure. Measured temperatures include subcooler entering-refrigerant-liquid and leaving-refrigerant-vapor temperatures, subcooler leaving-water temperature, compressor suction temperature (an average of four readings), compressor discharge temperature (an average of two readings) and evaporator and condenser water flow inlet and outlet temperatures. Evaporator and condenser water flow rates are measured. Power-rate meter readings are recorded as well as the current and voltage drawn by the motor.

Compressor flow is deduced from the system's thermodynamic properties. Refrigerant charge is specially adjusted to achieve 2° to 4° temperature rise from evaporator to compressor suction to avoid liquid entering the compressor. Compressor shaft horsepower is deduced from power meter readings less the calculated electrical loss and mechanical loss estimates. Its value is compared with the gas horsepower deduced from compressor thermodynamic measurements. "Power balances" within 5 percent are considered acceptable. Energy (heat) exchanged in the evaporator plus energy consumed by the motor are compared to energy exchanged within the condenser. "Energy balances" within 2 percent are considered acceptable.

Accuracy of compressor-related measurements is considered to be ±1 percent for flow, ±0.5 percent for head rise and efficiency.

Test results described below are from "proof-of-concept" prototype investigations. Hence, diffuser geometry is not really variable. The "variable" diffusers are manually set in discrete positions, requiring partial disassembly to alter the setting. On the other hand, the IGVs are externally actuatable.

Test Results

Only two split ring diffuser settings were tested, fully open (i.e., collateral pipe centerlines) and 4 deg rotation from fully open. Results for head versus flow are shown in Fig. 11. The fully open diffuser surged at a significantly higher flow than the baseline configuration. Although the baseline data were taken for a similar, but not identical system, another explanation for the surge difference is that a small leakage path (less than 0.005 in., or 0.13 mm, radial clearance) existed between diffuser pipes. (Leakage outside of the diffuser flowpath was eliminated by "O" rings fore and aft of the pipes.) Further testing is required to assure the lost stall margin can be regained at the full open IGV setting when individual pipes are adequately sealed.

On the other hand, the surge line is significantly improved when the ring is positioned at 4 deg. (Note that the highest-head point taken for the IGV's set at 5 deg was not near surge. The machine had been running stably at 3.2 percent of design capacity when other system problems occurred.)

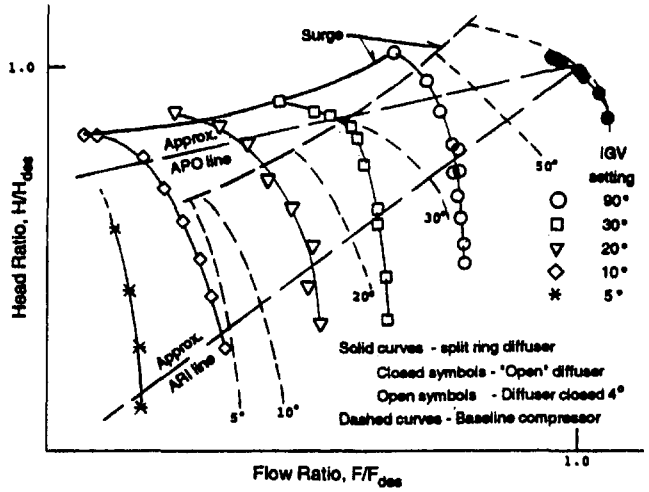

Fig. 11 Test results for the split-ring diffuser

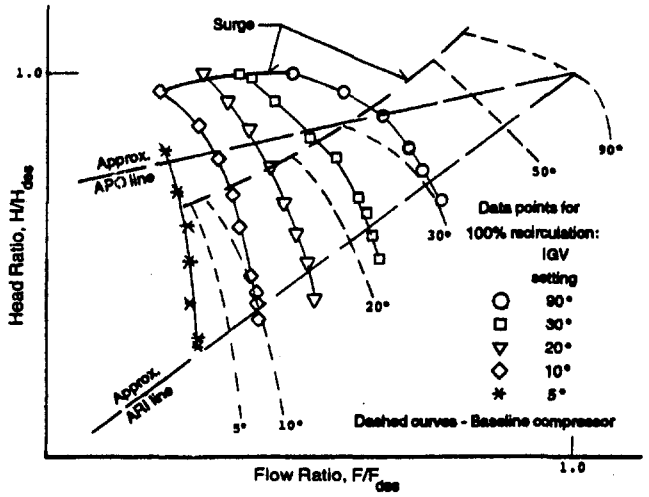

Fig. 12 Test results for the recirculation diffuser

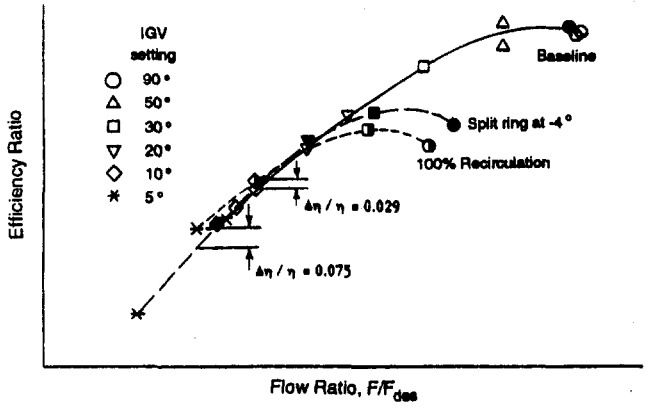

Fig. 13 Comparison of efficiencies along the ARI line

Head versus flow for the recirculation diffuser is shown in Fig. 12. Again, significant surge line improvement is noted.

Figure 13 shows efficiency along the ARI line plotted versus flow for the base compressor and the two "variable" geometry diffusers. The recirculation diffuser leads to improved performance for IGV settings of about 15 deg or less. Performance improvement at the 10 deg IGV setting is only about 3 percent,

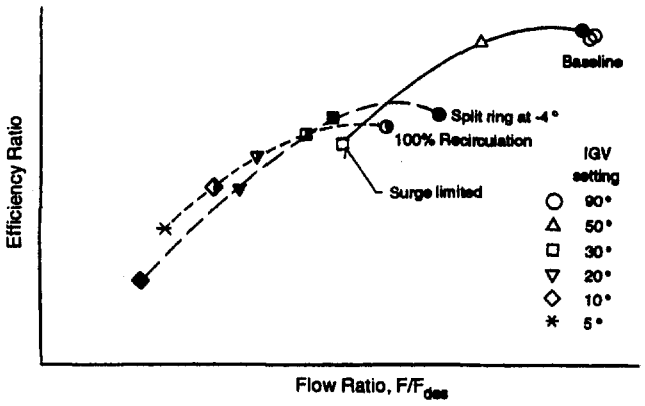

Fig. 14 Comparison of efficiencies along the APO line

compared to the theoretical estimate of 7.5 percent. Performance does improve by about 7.5 percent for the 5 deg IGV setting, however. The split ring diffuser appears to perform no worse than the baseline compressor at certain IGV settings, yet the configuration has superior surge margin as Fig. 11 has shown.

This is further emphasized in Fig. 14 where efficiency along the APO line is plotted versus flow. The baseline compressor is limited by surge for this operating line whereas both the split ring and recirculation diffusers permit operation to significantly lower flows. Again the recirculation diffuser is found to outperform the split ring concept.

In the present configuration, the shut-off ring had a 0.010 in. (0.25 mm) gap at the pipe diffuser outer radius when otherwise fully closed. This is about 0.7 percent of the flow area available when the shut-off ring is fully open. This gap was widened in increments to see if smaller deswirl vane heights were feasible and to discern the surge line's character as a function of recirculation flow rate. Results are shown in Fig. 15 for the fully open IGV setting. Note that head-versus-flow curves are indistinguishable for area openings greater than about 10 percent. However, surge appears to be discontinuous, suddenly showing more range for recirculation areas between 10 and 50 percent. This phenomenon is currently unexplained.

Input head (i.e., compressor work) is plotted versus flow in Fig. 16 for the same test series as in Fig. 15. The data are taken for the same IGV setting; therefore, the input head should be described by a unique curve. On the other hand, recirculated flow is discharged below the impeller blade tip (Fig. 4). Hence, the impeller should do more work with recirculation than the baseline case which has no recirculation. Results in Fig. 16 show that additional work is measurable, but small, and apparently confined to high flow rates.

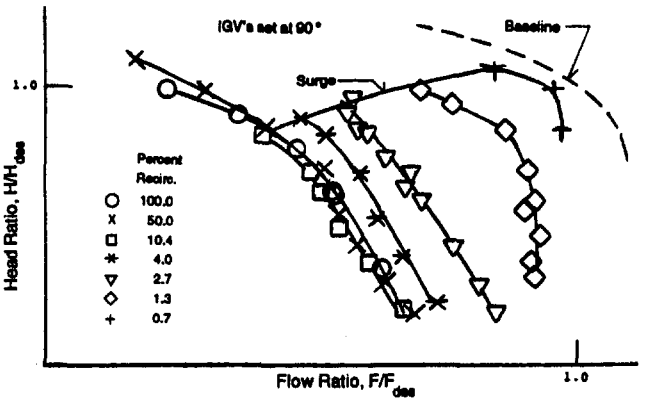

Fig. 15 Experimental variation of head versus flow for varying shut-off ring openings at a constant IGV setting

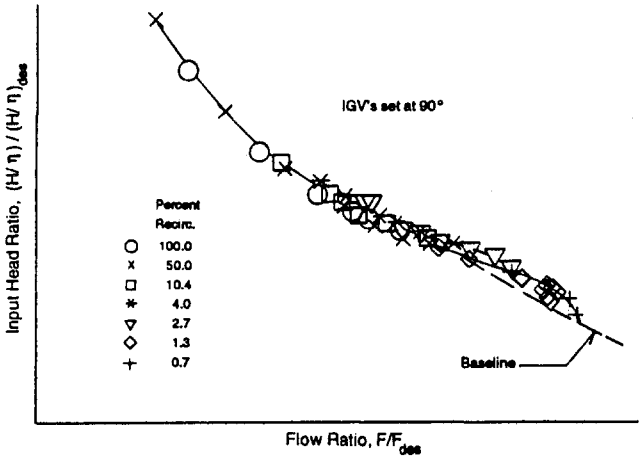

Fig. 16 Experimental variation of compressor input head (or work) versus flow for varying shut-off ring openings at a constant IGV setting

Conclusions

The test results, limited to discrete geometric settings for both the split ring diffuser and the recirculation diffuser, demonstrated significant increases in surge margin. Such devices would benefit compressor applications requiring nearly constant head down to conditions approaching shut-off. Of course, mechanical implementation and device control challenges remain.

The combination of variable IGVs and the split ring diffuser led to performance on the ARI line that was no worse than when variable IGVs were used alone. A simple loss model developed to describe this geometry had suggested performance should be worse, but impeller-diffuser interaction (or any change to this interaction) was ignored in the analysis.

Theoretical analysis developed for recirculation diffuser design indicated performance improvement was possible on the ARI line. This was later confirmed by tests. Analysis showed that performance is improved by control of the diffuser inlet velocity vector, confirming that flow incidence is a large off-design influence.

The recirculation diffuser can be used for other vane- or channel-type diffusers. The particular configuration considered here should be modified to move the improved performance to higher flows (higher IGV settings).

Certainly, the prototype test results have shown the need to minimize effects of even small leakage paths.

Acknowledgments

The author is grateful to Carrier Corporation for permission to publish this paper and, particularly, to Dr. Joost Brasz for his encouragement.

References

Aungier, R. H., 1995, "Mean Streamline Aerodynamic Performance Analysis of Centrifugal Compressors," ASME JOURNAL OF TURBOMACHINERY, Vol. 117, pp. 360–366.

Bandukwalla, P., 1983, United States Patent No. 4,378,194.

Casey, M. V., and Marty, F., 1986, "Centrifugal Compressors—Performance at Design and Off Design," *Proc. Institute of Refrigeration,* Vol. 00, pp. 000–000.

Cumpsty, N. A., 1989, *Compressor Aerodynamics,* Longman Scientific & Technical, Harlow, Essex, England.

Kenny, D. F., 1968, "A Novel Low Cost Diffuser for High Performance Centrifugal Compressors," ASME Paper No. 68-GT-38.

Kenny, D. F., 1979, "A Novel Correlation of Centrifugal Compressor Performance for Off-Design Prediction," AIAA/SAE/ASME 15th Joint Propulsion Conference, Paper No. 79-1159.

Reeves, G. B., 1977, "Design and Performance of Selected Pipe-Type Diffusers," ASME Paper No. 77-GT-104.

Shapiro, A. H., 1958, *The Dynamics and Thermodynamics of Compressible Fluid Flow,* Parts I and II from Vol. I, The Ronald Press Company, New York.

Flow Visualization and Leakage Measurements of Stepped Labyrinth Seals: Part 1—Annular Groove

D. L. Rhode

J. W. Johnson

Mechanical Engineering Department,
Texas A & M University,
College Station, TX 77843

D. H. Broussard

Texaco USA,
P. O. Box 1404,
Houston, TX 77002

An improved understanding of a new category of stepped labyrinth seals, which feature a new "annular groove," was obtained. A water leakage and flow visualization test facility of very large scale (relative to a typical seal) was utilized. Flow visualization experiments using a new method and digital facilities for capturing and editing digital images from an 8 mm video were conducted. The presence of an annular groove machined into the stator land increases the leakage resistance by up to 26 percent for the cases considered here. Tracer particles show the degree of throughflow path penetration into the annular groove (i.e., serpentining), which gives the largest and the smallest leakage resistance improvement over that of the corresponding conventional stepped seal.

Introduction

Physically the labyrinth seal consists of a rotating surface, referred to as the rotor, and a stationary surface, referred to as the stator. These surfaces are separated by a very small radial gap, known as the clearance. Shown in Fig. 1 is a stepped labyrinth seal with the fairly new annular groove of dimensions 13.94 cm (5.49 in.) by 15.24 cm (6.0 in.).

The performance of all seal types has become an important topic of late due to the continuously increasing demand for more efficient turbomachines. Advances in turbomachine designs have yielded machines that operate at higher and higher operating temperatures and differential pressures. Leakage through seals in many applications results in parasitic losses and a decrease in overall efficiency. Higher operating pressures result in increased labyrinth seal leakage due to the larger pressure gradient across the sealing element.

The primary objective of the current work is an improved understanding of a stepped labyrinth seal containing the new annular groove design feature. A second objective is to demonstrate the translation of 8 mm flow visualization videos into digital format for improved expediency and clarity.

Previous Work

Stocker (1975) and Stocker et al. (1977) used flow visualization to eliminate advanced labyrinth seal design candidates that would likely be ineffective. Seals that appeared to have promising attributes were kept and continued in the next phase of the evaluation. In Phase 1, seals were tested in a two-dimensional planar water tunnel, enlarged ten times. Air bubbles were injected into the flow, and the seal specimens were judged based on bubble concentration density, recirculation zone velocity, and measured leakage rates. Stocker's final labyrinth seal designs showed improvements in leakage loss of 10 to 25 percent, however they appear to be very expensive to manufacture.

Rhode et al. (1993) conducted a series of experiments in which leakage resistance data and flow visualization recordings were made on stepped labyrinth seals in a two-dimensional, planar test rig using water. The rig was sufficiently large to allow close observations of the flow details. The data revealed that, for certain geometries, there exists a step height s at which increasing s has little effect on leakage resistance. For example, the authors found that for large clearances, the leakage resistance is increasingly sensitive to rotor axial position, and that a sudden change in the throughflow jet trajectory accompanied sudden changes in leakage resistance.

Waschka et al. (1990) investigated the effect of shaft rotation speed on leakage and heat transfer rates in labyrinth seals. The data reveal that, at significant Reynolds numbers (approximately 5000 to 10,000), the effect of shaft rotation speed is negligible. Other testing has shown a 5 percent decrease in leakage at high tooth tip speeds. The limiting Reynolds number after which shaft speed has little effect is apparently dependent on clearance, and the larger clearances correspond to higher Reynolds numbers. However, since most applications in which labyrinth seals are utilized run at Reynolds numbers well into the turbulent regime, it could be said that shaft rotation speed has little effect for most realistic clearances.

Experimental Facilities

A variable reluctance pressure transducer was used to measure the pressure drop across the seal specimen and also across the orifice flow meter. The test section is rectangular in shape, as shown in Fig. 2, and measures 0.914 m × 2.438 m × 0.914 m (3 ft × 8 ft × 3 ft). The very large size of the test section allows labyrinth seal specimens that are, for example, a 100 times enlargement of a true-size seal with a 0.0305 cm (0.012 in.) clearance. This large scale was chosen so that flow visualization movies could be made that show small flow details. As mentioned previously, shaft rotation has little effect on leakage at significant Reynolds numbers, hence this model was designed to provide two-dimensional planar flow as opposed to the two-dimensional axisymmetric flow found in actual labyrinth seals. Figure 2 shows the "radial" direction and the radial push rods that extend through the test section wall. Notice that in this test rig, the rotor is defined as the part of the labyrinth seal with teeth, and the stator is either a flat or stepped wall.

Flow Visualization Equipment. Silver glitter (commonly used in children's artwork) has been particularly desirable for recording pathlines. In such cases, these tracer particles were

Contributed by the International Gas Turbine Institute and presented at the 41st International Gas Turbine and Aeroengine Congress and Exhibition, Birmingham, United Kingdom, June 10–13, 1996. Manuscript received at ASME Headquarters February 1996. Paper No. 96-GT-136. Associate Technical Editor: J. N. Shinn.

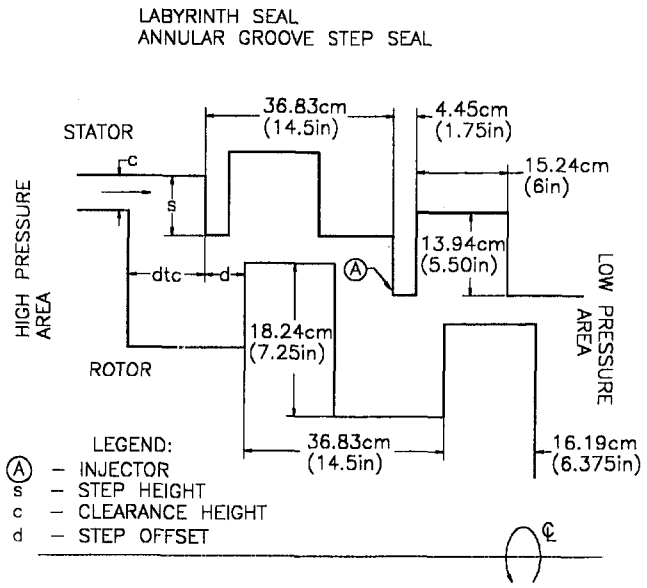

Fig. 1 New annular groove category of stepped seals showing the dye injector location

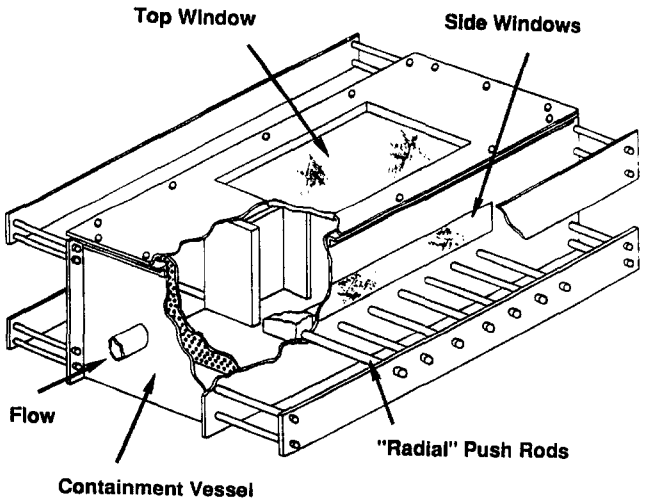

Fig. 2 Cut-away view of the test section

illuminated by halogen lamps. Imaging the flow visualization experiments was accomplished using an 8 mm camcorder. The RCA Pro845 camcorder had a 12X zoom lens and was capable of operating in several different modes, depending on lighting conditions, with shutter speeds between 60 and 10,000 frames per second. A personal computer was equipped with a video capture board. When capturing digital video, data through-put and the storage capacity of the computer are of the utmost importance. For this reason, a 90 MHz Intel® Pentium™ based personal computer with 32 MB of RAM, a 2.05 GB Fast SCSI-2 hard disk drive, an Intel® Smart Video Recorder PRO™ digital video capture board, and a 128-bit video card with 4 MB VRAM was chosen. The 8 mm recording of the experiment was captured as a full motion video with at least 20 frames per second. The captured digital video was then played back with the full capability of analyzing each frame individually.

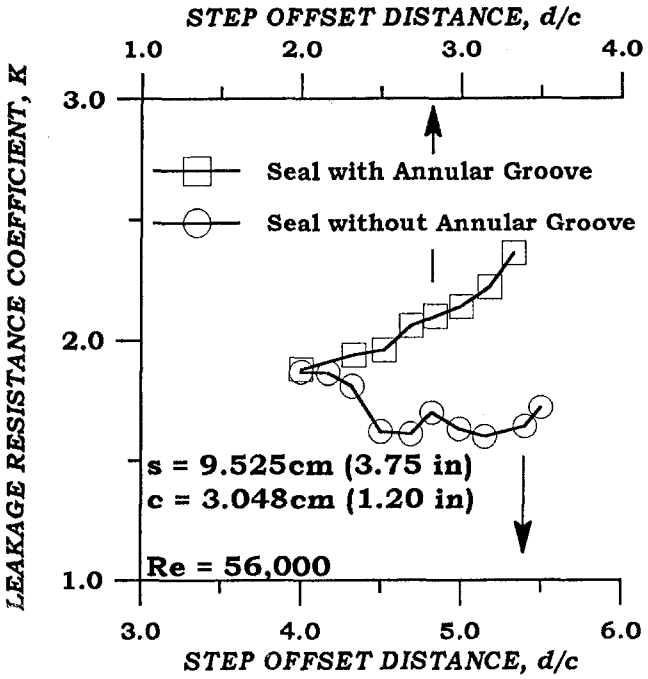

Fig. 3 Comparison of measured leakage resistance showing the effect of the presence of the annular groove for c = 3.05 cm (1.2 in.) and s = 9.53 cm (3.75 in.)

Measurement Uncertainty. Using the Kline-McClintock (1953) method of uncertainty analysis, the flow rate uncertainty for a fixed geometry was calculated as 0.86 percent. For the leakage resistance coefficient the uncertainty was calculated as 3.4 percent at normal operating conditions.

Discussion

The new "annular groove" design feature is shown in Fig. 1 as the groove of axial width 15.24 cm (6.0 in.) in the "stator" (upper) surface. The annular groove provides additional curvature of the throughflow, and thus was expected to give generally improved performance.

Seal geometries have been evaluated at leakage Reynolds numbers in the turbulent range. The conversion by the action of turbulent Reynolds stresses of mean kinetic energy into thermal energy within a labyrinth seal are conveniently expressed as the minor loss coefficient K. This coefficient is typically used to express losses in pipe bends, etc. Seals with low leakage, for a given pressure drop, have a high leakage resistance coefficient.

Large Clearance and Large Step Case. For the case of c = 3.048 cm (1.2 in.) and s = 9.525 cm (3.75 in.), observe in Fig. 3 that, at rather small values of the step offset axial distance

Nomenclature

c = tooth radial clearance
d = step offset axial distance
K = nondimensional leakage resistance coefficient = $((P_{in} - P_{ex})/\rho V_c^2/2)$
P_{ex} = bulk pressure of fluid at test section exit
P_{in} = bulk pressure of fluid at test section inlet
Re = Reynolds number based on clearance = $(\rho 2 c V_c/\mu)$
s = stator step height
V_c = bulk velocity at seal clearance
μ = absolute laminar viscosity of working fluid
ρ = density of working fluid

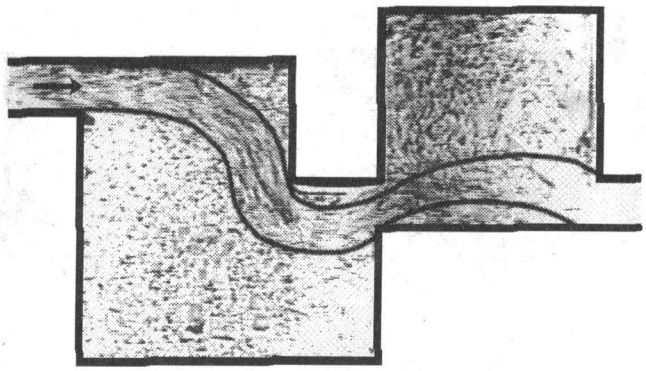

Fig. 4 Digital image of the throughflow jet for c = 3.05 cm (1.2 in.), s = 9.53 cm (3.75 in.) and d/c = 1.83

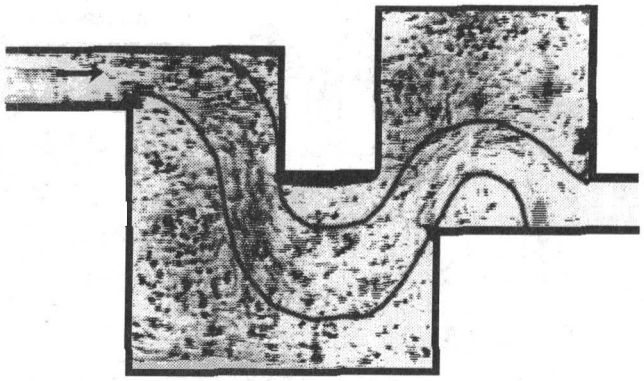

Fig. 5 Digital image of the throughflow jet for c = 3.05 cm (1.2 in.), s = 9.53 cm (3.75 in.) and d/c = 3.42

d, the presence of the annular groove provides no improvement in leakage resistance coefficient. However, there is an increasing improvement over the nongrooved seal with increasing d/c. Further, the increasingly upward slope of the curve for the annular groove configuration shows substantial gains at large values of d/c. Larger d/c values correspond to smaller distance-to-contact (dtc) values (Fig. 1). A smaller dtc means that a fluid particle undergoes a more dramatic deflection, which causes greater penetration into the rotor cavity. Thus, different dtc values produce different degrees of throughflow serpentining, which is expected to affect the turbulence generation, Reynolds stresses, etc. For the d/c values at which data were taken, the leading edge of the tooth was generally in axial alignment with the upstream portion of the annular groove. For gas and steam turbines, many specific annular-groove seal configurations are expected to be most applicable for: (a) large-diameter seals (i.e., large clearance seals that require less scale-down from the present model) and (b) seals axially located not too far from a thrust bearing. That is, these situations are not generally expected to require a very large dtc seal. In addition to reducing leakage, such seals may have application for the goal of reducing seal lengths. Depending on the situation, numerous dimensions would probably need to be adjusted to obtain good seal performance while preventing the rotor teeth from contacting the stator step.

Digital flow visualization images of the throughflow path at d/c = 1.83, using glitter tracer particles, for the c and s values of Fig. 3 are shown in Fig. 4. The curved dark lines were sketched, using the software package Photoshop, to show the approximate edges of the throughflow jet. The dark lines are approximate visual interpretations by two of the authors, after viewing the computer monitor images, which are considerably more clear and detailed than the printed version shown here. The flow images shown herein are not exactly to scale because of parallax distortion from the camcorder. Note from the Fig. 4 that there is very little penetration of the throughflow into either the rotor cavity or the annular groove. If there is concern that the step fence of thickness t = 4.45 cm (1.75 in.) may suffer mechanical damage, it can be strengthened by replacing the vertical, upstream surface of the annular groove with a sloping surface. Note that the teeth used here are rather short and thick. Without the presence of the annular groove, teeth that are thick at the tips have often given a lower leakage resistance coefficient because of the strikingly different flow pattern.

Increased penetration into the rotor cavity is attributed to the large d/c (small dtc) values, which result in greater penetration into the annular groove. The Fig. 5 image is that of a high resistance configuration (at d/c = 3.42), exhibiting a resistance value about 26 percent higher than that of Fig. 4. Apparently, the increased serpentining of the throughflow in Fig. 5 is responsible for the increased resistance.

As expected, a range of throughflow paths was observed for each flow condition due to fluid dynamic oscillations inherent in the flow field. These oscillations are purely the result of the fluid flow itself, i.e., the seal specimen and test facility were structurally very rigid. Perhaps this oscillation results from the feedback mechanism as explained by Rockwell and Naudascher (1978). The mechanism is the emanation of fluctuations, from the tip of a tooth toward the upstream tooth. This emanation is believed to be caused by the impacting of the throughflow jet turbulent eddies on the downstream tooth tip. The fluctuations amplify unstable vortices in the throughflow shear layers. As mentioned earlier, for an enhanced understanding of these fluid dynamic oscillations, diluted fluorescein dye was injected through a tube installed flush with the surface where labeled "A" in Fig. 1. The flow angle of the dye was measured from hundreds of digital images captured with an Intel video capture card.

Large Clearance and Small Step Case. Figure 6 shows the degree of improvement of an annular groove configuration with a small step height of 7.62 cm (3.0 in.). In this case the

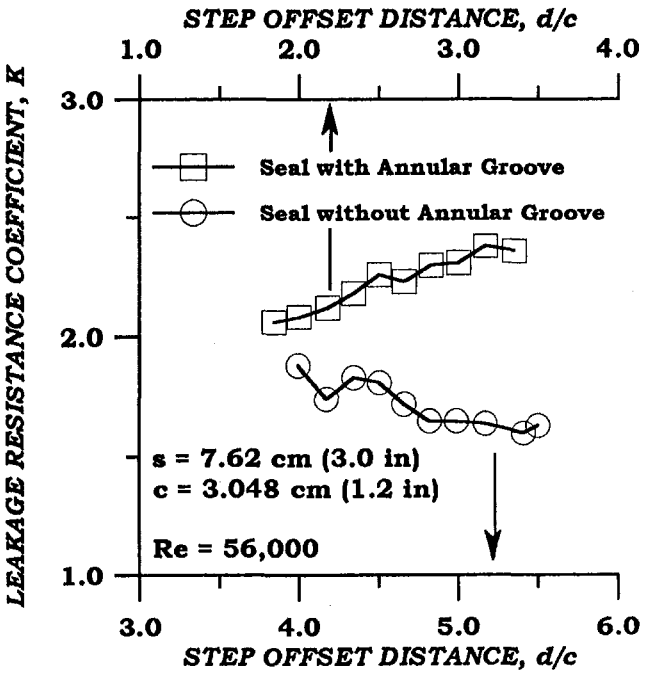

Fig. 6 Comparison of measured leakage resistance showing the effect of the presence of the annular groove for c = 3.05 cm (1.2 in.), s = 7.62 cm (3.0 in.)

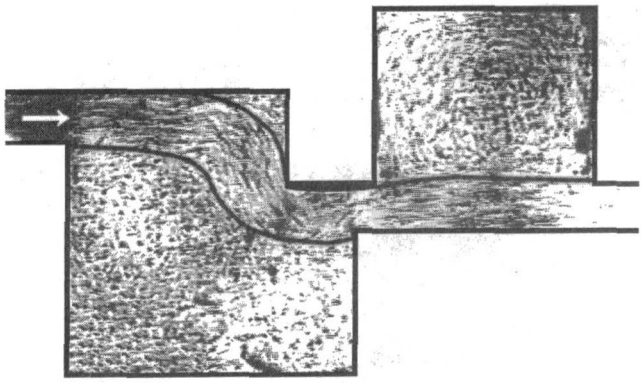

Fig. 7 Digital image of the throughflow jet for c = 3.05 cm (1.2 in.), s = 7.62 cm (3.0 in.) and d/c = 1.83

resistance of the standard stepped configuration continuously decreases, whereas that of the annular groove continuously increases with increasing d/c.

Figure 7 shows the approximate throughflow path for the groove configuration of Fig. 6 at d/c = 1.83. The various digital images obtained for this case show the throughflow to be deflected by the step slightly more abruptly than for the larger step case in Fig. 4. Further, reduced rotor cavity penetration is found in Fig. 7. There is only slight upward momentum generated as the throughflow approaches the annular groove in Fig. 7, and thus negligible penetration into the annular groove results.

As was found for the larger step height case of Fig. 5, the throughflow path exhibiting the highest leakage resistance has more serpentining than do the cases of smaller d/c. This is shown in Fig. 8 for the d/c = 3.42 case. Further, the same serpentine throughflow path was found at the d/c value of highest resistance for both the larger and the smaller step heights.

Small Clearance and Large Step Case. The improvement of the annular groove at a smaller tooth clearance of 2.032 cm (0.8 in.) and the larger step height is seen in Fig. 9. Observe that both curves show nearly zero slope. Further, the resistance improvement of the annular groove is much smaller than for the previous cases. Note that one should not compare the resistance values of two seal specimens, at a given Reynolds number, which have different clearances. Specifically, the bulk velocity and the radial clearance in the tooth-clearance gap vary inversely and linearly for the two specimens. Thus the smaller clearance specimen gives the lower value for the leakage resistance coefficient, even though it has the higher pressure drop. This results from the fact that the resistance coefficient has the clearance-velocity squared in the denominator, such that the

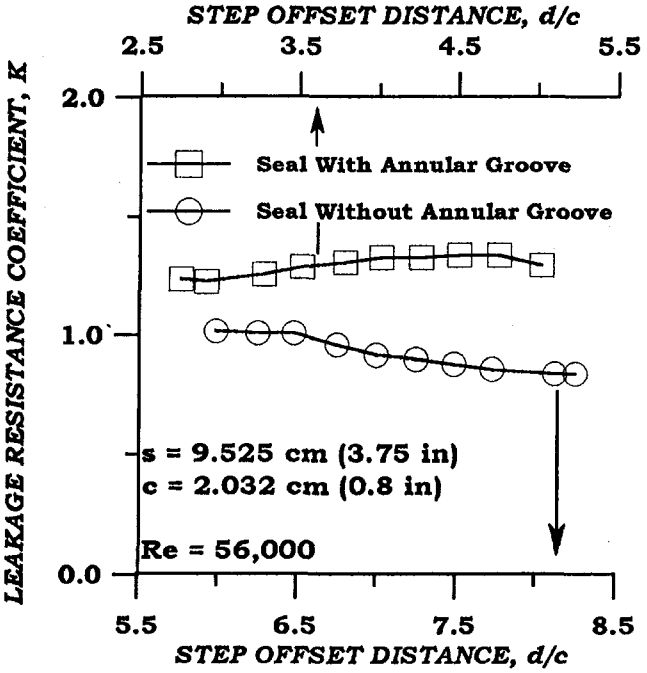

Fig. 9 Comparison of measured leakage resistance showing the effect of the presence of the annular groove for c = 2.03 cm (0.8 in.), s = 9.53 cm (3.75 in.)

higher value of V^2 for the smaller clearance specimen overcomes the higher pressure drop, resulting in a lower resistance coefficient. Therefore, even though the smaller clearance specimen exhibits the lower resistance coefficient at a given Reynolds number, it gives lower leakage for a given pressure drop.

Figure 10 shows the throughflow path for c = 2.03 cm (0.8 in.) and s = 9.53 cm (3.75 in.) with d/c = 2.75, which is the same d value as for Figs. 4 and 7. The smaller clearance effectively makes the step a more effective flow deflector. The throughflow effect is shown in Fig. 10, where a dramatic increase in serpentining occurs over that of Fig. 4, particularly within the annular groove. The finding that, for small clearance and large step height, resistance does not increase significantly with d/c is attributed to the increased penetration into the annular groove. It is speculated that excessive penetration allows excessive reduction of throughflow jet velocity via turbulent diffusion. The velocity reduction results in decreased Reynolds stresses, which are the primary resistance mechanism.

Conclusions

Comparison of leakage resistance measurements with digital flow visualization images provides new insight concerning the

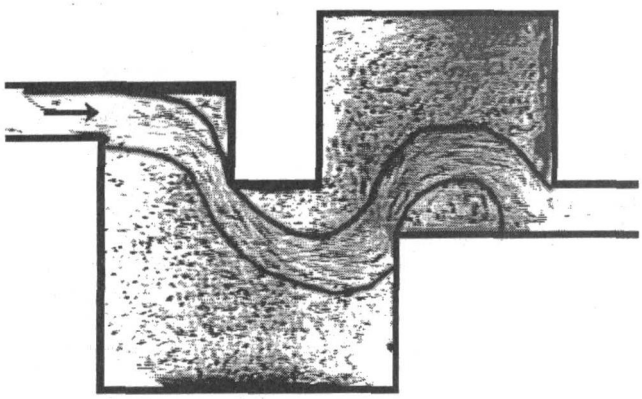

Fig. 8 Digital image of the throughflow jet for c = 3.05 cm (1.2 in.), s = 7.62 cm (3.0 in.) and d/c = 3.42

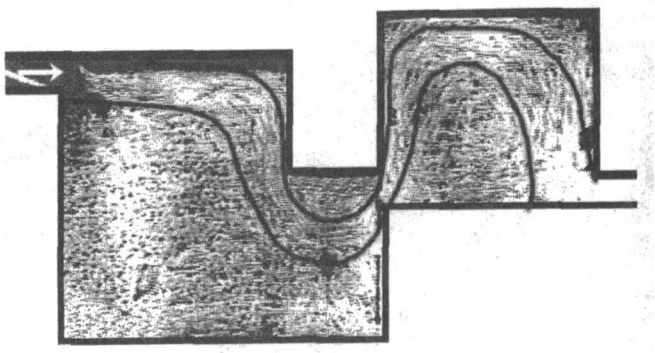

Fig. 10 Digital image of the throughflow jet for c = 2.03 cm (0.8 in.), s = 9.53 cm (3.75 in.) and d/c = 2.75

relationship between throughflow jet penetration into the annular groove, as well as into the rotor cavity, and leakage resistance. Specific findings for the cases examined here are:

1 The presence of the annular groove increases the leakage resistance by up to 26 percent for the cases presented here. However, small clearance with larger step height cases, for example, for which flow visualization images are not available, have shown a 90 percent increase of resistance due to the presence of the annular groove.

2 The step offset axial distance d has a significant effect for both of the large clearance cases presented.

3 The small clearance case shown here gives only slight improvement, as well as only slight variation, with the step offset distance.

4 The configuration and resulting throughflow path for which the annular groove gives a large improvement is found in Figs. 5 and 8, whereas that giving a small improvement is found in Figs. 4, 7, and 10.

Acknowledgments

The authors are grateful for the financial support from the NASA Center for Space Power and from the Texas Advanced Technology Program. Also, the authors are indebted to L. Chavez, who spent countless hours reading the flow angles as well as performing numerous other tasks.

References

Kline, S. J., and McClintock, F. A., 1953, "Describing Uncertainties in Single-Sample Experiments," *Mechanical Engineering,* Vol. 75, Jan., pp. 3–9.

Rhode, D. L., Broussard, D. H., and Veldonda, S. B., 1993, "Labyrinth Seal Leakage Resistance and Visualization Experiments in a Novel, Variable-Configuration Facility," *STLE Tribology Transactions,* Vol. 36, pp. 213–218.

Rhode, D. L., 1993, "Labyrinth Seal," U.S. Patent No. 5,244,216.

Rockwell, D., and Naudascher, X. X., 1978, "Review—Self-Sustaining Oscillations of Flow Past Cavities," ASME *Journal of Fluids Engineering,* Vol. 100, pp. 152–165.

Stocker, H. L., 1975, "Advanced Labyrinth Seal Design Performance for High Pressure Ratio Gas Turbines," ASME Paper No. 75-WA/GT-22.

Stocker, H. L., Cox, D. M., and Holle, G. F., 1977, "Aerodynamic Performance of Conventional and Advanced Design Labyrinth Seals With Solid-Smooth, Abradable, and Honeycomb Lands," NASA CR-135307, Detroit Diesel Allison, Indianapolis, IN.

Waschka, W., Wittig, S., and Kim, S., 1992, "Influence of High Rotational Speeds on the Heat Transfer and Discharge Coefficients in Labyrinth Seals," ASME JOURNAL OF TURBOMACHINERY, Vol. 114, pp. 462–468.

D. L. Rhode
Mechanical Engineering Department,
Texas A & M University,
College Station, TX 77843

J. S. Younger
Solar Turbines, Inc.,
215 Center Park Blvd.,
DeSoto, TX 75115

M. D. Wernig
Schlumberger Anadrill,
200 Gillingham Lane, #125,
Sugar Land, TX 77478

Flow Visualization and Leakage Measurements of Stepped Labyrinth Seals: Part 2—Sloping Surfaces

An experimental investigation was conducted to determine the geometry–leakage relationship for advanced, stepped labyrinth seals. A unique, variable-geometry water test facility was constructed and used to acquire leakage resistance measurements for two-dimensional, planar models. Flow visualization techniques were also used to assist in identifying and understanding the turbulence generating flow patterns. It was found that contoured surfaces and restrictor tooth leading-edge shapes of proper dimensions can be incorporated into the cavity geometry to reduce seal leakage. Specifically, the combination of a sloping surface and a curved surface on the rotor within the labyrinth cavity gave significant improvement.

Introduction

The advantages of labyrinth seals are primarily their simplicity and reliability, as well as their applicability to severe operating conditions. For example, Zimmerman et al. (1994) explain the advantages over other sealing alternatives for high temperatures and high circumferential speeds. Sneck (1974) indicates that labyrinth seals are popular because they are relatively damage resistant and thus continue to provide effective leakage resistance over long periods of time.

The following section outlines significant earlier work relevant to the present objective. The next section describes the objectives, followed by a section discussing the results from the flow visualization and leakage test facility. Then, the conclusions and acknowledgements are found in the final sections.

Previous Work

By the 1970s, the focus of experimental labyrinth seal research began to shift from trying to gain a better understanding of the labyrinth flow field to searching for ways to optimize labyrinth seal performance. An example of such an effort can be seen in the stepped labyrinth experiments of Hughes and Ralph (1970) who attempted to identify an optimum step height for various seal geometries. Utilizing a two-dimensional air test apparatus, they concluded that the optimum seal step height depended upon seal clearance.

Stocker et al. (1977) developed a true-scale, "two-flat-plates" type of air test facility in which the effects of seal land (stator wall) surface roughness, rub grooves, and honeycomb cell size on seal leakage resistance were examined for numerous intricate geometries. In addition, Stocker (1975) confirmed that leakage could be minimized by increasing turbulence within seal cavities. He also used flow visualization techniques to observe and photograph labyrinth flow fields.

Wittig et al. (1983) considered the dependence of the flow coefficient on particular scaling effects. They found that the effects of Reynolds number as well as of small geometric details must be taken into account. The authors suggest that certain discrepancies could be due to a scale dependence of the turbulence structure within the seal.

Morrison et al. (1983) investigated the effects upon leakage resistance of shaft rotation rate, seal tooth number and spacing, as well as pressure ratio. A three-dimensional, rotating, water test apparatus was used. It was found that: (*a*) a leakage resistance dependence upon turbulence exists and (*b*) leakage resistance is essentially independent of the number of cavities for a seal with more than eight cavities.

Rhode et al. (1993) developed the presently used test section, and investigated the leakage effects of adjusting tooth radial clearance, step height, and axial position of the rotor. The results suggested that in certain cases, the presence of annular grooves can result in a substantial improvement in leakage resistance. It was confirmed that turbulence generation contributes to improved leakage resistance. More importantly, the complicated coupling that exists between geometry and leakage resistance was identified for a particular seal configuration.

Objective

The overall objective of this investigation is to obtain an enhanced understanding of the geometry–leakage relationship for a stepped labyrinth seal with advanced geometric features. Specifically, design insight is sought concerning which component is best for the upstream portion as well as the downstream portion of the rotor surface. It is also of interest to identify the flow field features that appear for the more leakage resistant configurations.

Flow Visualization and Leakage Facility

The large-scale, variable-geometry, flow visualization test facility is a component of a closed-loop water system with a 2.84 m^3 (750 gallon) outdoor reservoir. The labyrinth seal test section, shown in Fig. 2 of Part 1 (Rhode et al., 1997) comprises a 0.914 m × 0.914 m × 2.438 m (3 ft × 3 ft × 8 ft) welded Hastelloy-X containment vessel. The seal model represents a very large-scale specimen with a tooth radial clearance of 3.05 cm (1.2 in.). This constitutes, for example, a 100× enlargement of a geometrically similar seal, which has a radial clearance of 0.0305 cm (0.012 in.). Very small and localized recirculation zones, which are not visible with the smaller specimen sizes previously used, become visible at this large model size. This allows videocassette recording and hand sketching from the television monitor. In order to allow attachment of a wide variety of acrylic, bolt-on building block modules to construct a

Contributed by the International Gas Turbine Institute and presented at the 41st International Gas Turbine and Aeroengine Congress and Exhibition, Birmingham, United Kingdom, June 10–13, 1996. Manuscript received at ASME Headquarters February 1996. Paper No. 96-GT-137. Associate Technical Editor: J. N. Shinn.

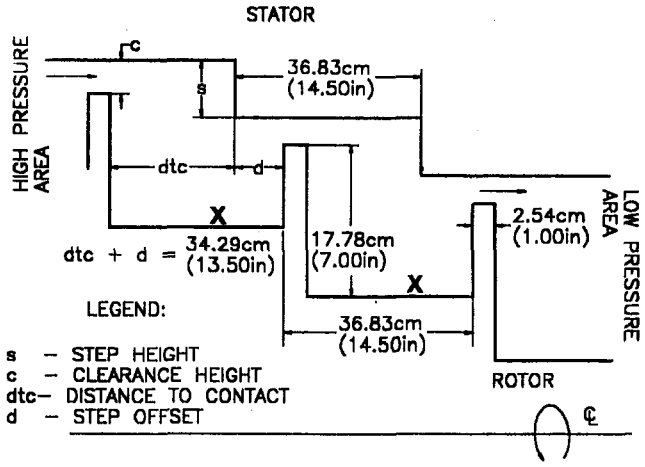

Fig. 1 Basic seal structure to which components A–S were attached in the flow visualization and leakage test facility

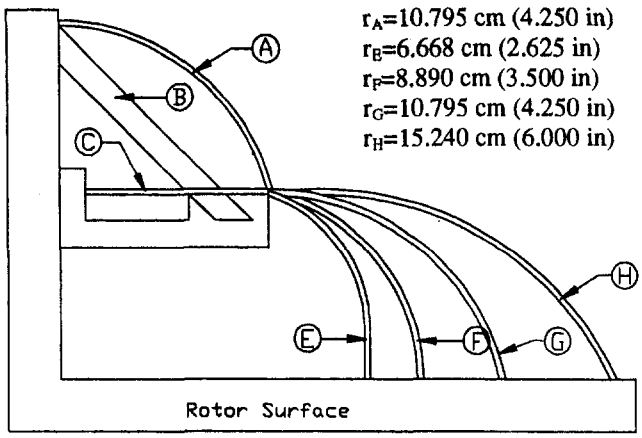

Fig. 2 Interchangeable acrylic components of Region I

desired seal geometry, the rotor and stator surfaces were designed using the common "two-flat-plates" approach. Many investigators have adopted this approach. Yamada (1961), Waschka et al. (1992), and others have shown that rotation effects are negligible at significant (i.e., typical) Reynolds numbers. The rotor and stator basic surfaces are generally composed of three acrylic pieces to which the various modules may be attached. Further, each seal element may be adjusted in the "radial" and/or "axial" directions via a pair of push-rods. The pair of push-rods extend from the point of attachment (to each element), through the vessel vertical walls, where they are connected to an adjustable screw mechanism.

Several observation windows, incorporated into the containment vessel, allow flow visualization via a sheet of light, which passes through a cross section of the seal model. The flow was illuminated using a series of 150 W halogen flood lamps. Fine pieces of metallic glitter were used as tracer particles. Glitter tracer particles are quite effective in following the flow within this facility because: (*a*) The largest dimension of a glitter particle is only about 5 percent of the seal clearance and (*b*) it is the time-averaged trajectories rather than the particle velocity fluctuations that are of interest. The flow path characteristics for a particular geometry were recorded using hand sketches, and in some cases a videocassette recorder.

In an effort to study only geometric effects on leakage resistance properties, seal geometries have been evaluated at a series of similar flow Reynolds numbers in the turbulent range. The mechanical energy losses converted into thermal energy within a labyrinth seal are conveniently expressed as the leakage resistance (minor loss) coefficient K, which is typically used to express losses in pipe bends, etc. Minor losses are primarily due to flow separation (Fox and McDonald, 1985). Seals with low leakage have a high leakage resistance coefficient.

Uncertainty Analysis. Estimations regarding experimental data validity have been made using the Kline–McClintock method of uncertainty analysis (Fox and McDonald, 1985; Kline and McClintock, 1953). The Kline–McClintock analysis gave an uncertainty of ±6.3 percent for the leakage measurement and subsequent Reynolds number calculation. Further, a Kline–McClintock analysis gave an uncertainty in leakage resistance coefficient of ±3.4 percent, under normal operating conditions.

Evaluation of Labyrinth Seal Geometries. As mentioned previously, each of a series of interchangeable, acrylic components was added in a building block fashion to the basic seal structure (Fig. 1) to construct different seal geometries. The rotor areas on the left-hand and the right-hand side of the "X" shown in Fig. 1 are referred to as Regions I and II, respectively. The upstream and downstream portions of Region I have interchangeable components A–C and E–G available, respectively, as shown in Fig. 2. Considering the upstream cavity of the basic seal structure shown in Fig. 1, for example, the location of components A, B, and C (upstream portion of Region I) corresponds to the area immediately downstream of the first tooth shown in Fig. 1. Further, the location of components O–S, which are shown in Fig. 3 for Region II, corresponds to the area immediately upstream of the second tooth of Fig. 1. Components O–S have a surface inclined at 45 deg. Each configuration is named according to the components included in its construction. For example, seal configuration AGMQ would include components A and G in Region I and components M and Q in Region II.

The components shown in Figs. 2 and 3 are approximations of the actual surfaces considered in order to facilitate model construction. Some of the configurations shown here will increase the manufacturing cost and possibly tool wear.

Comparison of Geometry Components in Region I. Figure 4 shows the effect of the Reynolds number on leakage resistance, comparing components A, B, and C in the presence of components G, M, and Q. Similar to the Reynolds number trend seen in a plot of pipe flow friction factor, the leakage resistance values decrease as fluid inertia forces increase with increasing Reynolds number. At Reynolds numbers above 4×10^4, it is observed that component A gives the highest leakage resistance, although component B values are very close. At low

Nomenclature

c = tooth clearance
d = step offset axial distance
K = nondimensional leakage resistance coefficient = $(P_{in} - P_{ex}/\frac{1}{2}\rho V_c^2)$
P_{ex} = bulk pressure of fluid at test section exit
P_{in} = bulk pressure of fluid at test section inlet
Re = Reynolds number based on clearance = $(\rho 2 c V_c/\mu)$
ρ = density of working fluid
s = stator wall step size
V_c = bulk velocity at seal clearance
μ = absolute laminar viscosity of working fluid

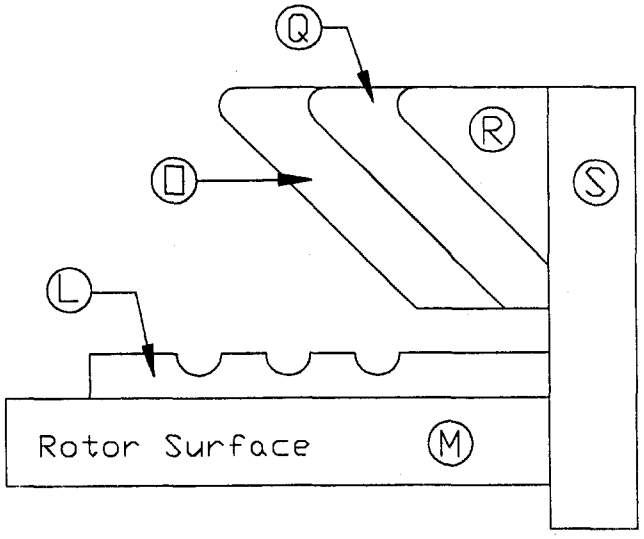

Fig. 3 Interchangeable acrylic components of Region II

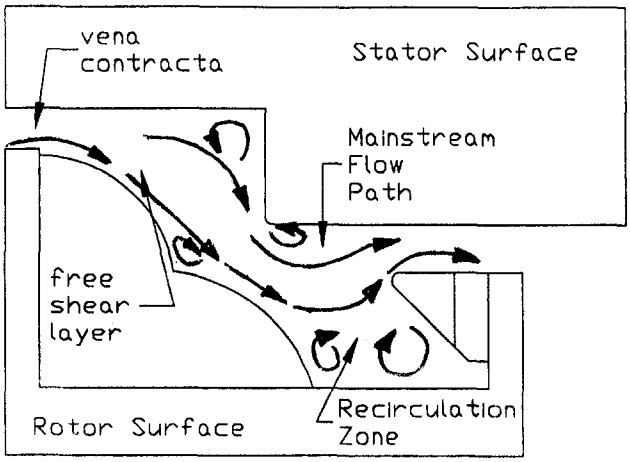

(A) Re = 3 X 10⁴

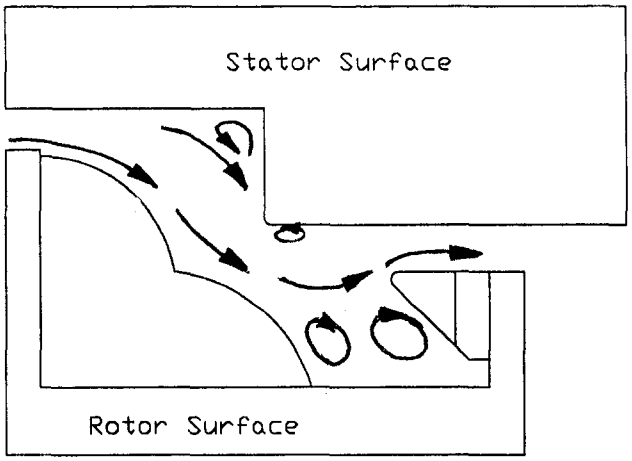

(B) Re = 5 X 10⁴

Fig. 5 Flow visualization sketch showing the throughflow path bending and recirculation zones of configuration AGMQ (c = 1.2 in., s = 3.5 in., d/c = 3.167)

Reynolds numbers, component B is by far the best. The reason that combination BG is preferred for low Re appears to be related to the development of the vena contracta and the free shear layer as labeled in Fig. 5(a). The Region II component also affects these.

Possible explanations for the improvement in leakage resistance, afforded by including component A or B in the upstream portion of Region I, can be found when flow visualization techniques described in Part 1 are examined. Figures 5(a) and 5(b) are flow visualization sketches of the visually time-averaged flow through seal configuration AGMQ at Reynolds numbers of 3×10^4 and 5×10^4, respectively. These sketches were made from video recordings of the fluid flow and were taken through the window in the test section lid shown in Rhode et al. (1997). Flow characteristics shown in Fig. 5(a) are: (a) the vena contracta, (b) the free shear layer, and (c) the recirculation zones. The most intense turbulence was found in the vena contracta, which is shown in Fig. 5(a). Here it is labeled just downstream of a tooth, but it is also seen near the cavity discharge in the clearance region. Note that a high velocity and very thin recirculation zone is found adjacent to the vena contracta in the upstream portion of Region I. In contrast, configuration CGMQ (not shown) exhibits a much larger, low-velocity recirculation zone adjacent to the vena contracta in the upstream portion of Region I, without intense shear stresses. Further, Fig. 5(b) reveals almost no vena contracta in Region I at a Reynolds number of 5×10^4.

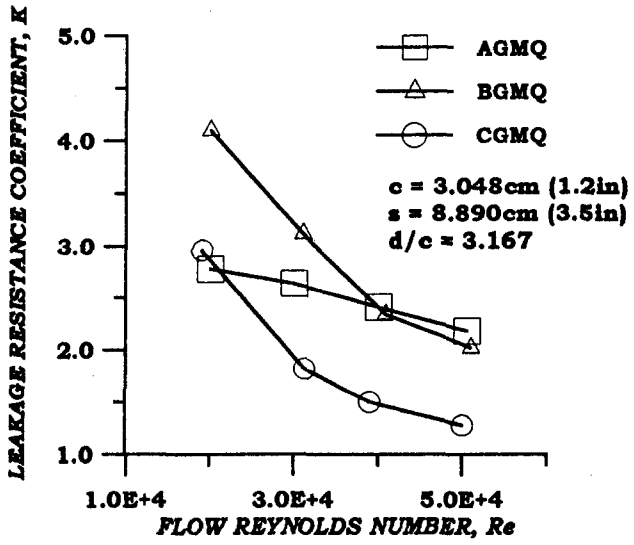

Fig. 4 Measured effect of Reynolds number on leakage resistance comparing components A, B, and C

The downstream portion of Region I has available components E–G, which have increasing radii, respectively. As shown in Fig. 2, r_E = 6.668 cm (2.625 in.), r_F = 8.890 cm (3.5 in.), r_G = 10.795 cm (4.25 in.). While maintaining components M and Q, the resistances of E, F, and G are compared in the presence of A and B in Figs. 6 and 7, respectively. Figure 6 shows that the use of component G produces the highest resistance for Reynolds numbers above 2.2×10^4. Although there is no appreciable difference in resistance between components E and F above Reynolds numbers near 3×10^4, at lower Reynolds numbers component E is preferred.

Figure 7 shows that component G gives the highest resistance at all Reynolds numbers for the case where component B is installed into the upstream portion of Region I. Observe that component G provides a considerable improvement for this configuration, even at Reynolds numbers near 1×10^4 (by extrapolation). The leakage resistance values associated with

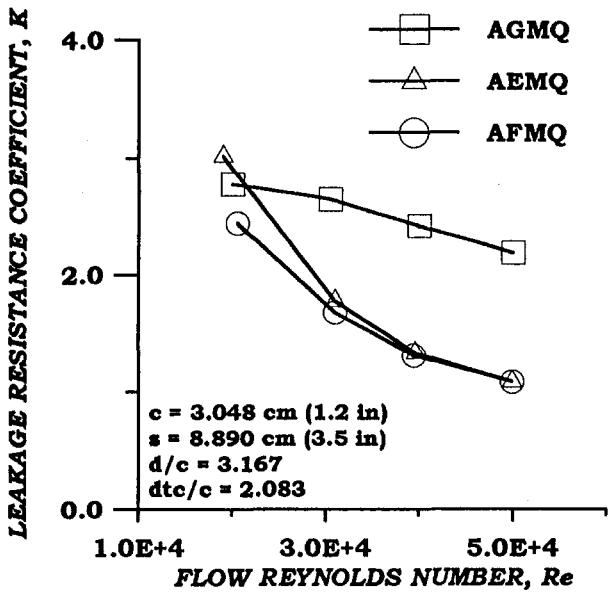

Fig. 6 Measured effect of Reynolds number on leakage resistance comparing components E, F, and G with component A in place

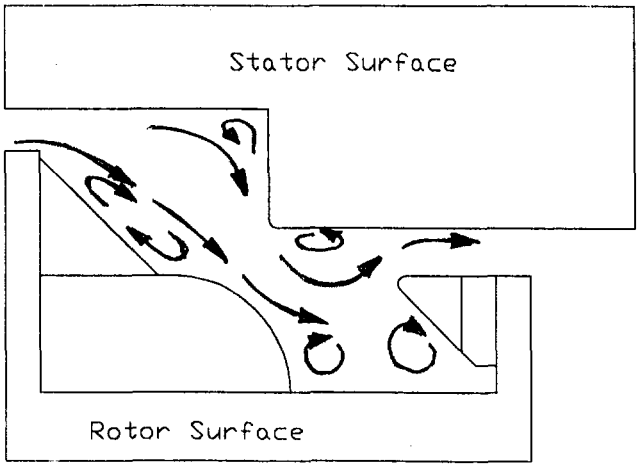

Fig. 8 Flow visualization sketch showing throughflow path bending and recirculation zones of configuration BFMQ at Re = 30,000 (c = 1.2 in., s = 3.5 in., d/c = 3.167)

component G are nearly 30 percent greater than those of component E, and almost twice that of component F. Figure 7 also shows that component E gives higher resistance values than component F for the entire range of Reynolds number. Thus the improvement of component G is more pronounced with component B, rather than A, present in the upstream portion of Region I. Further, Figs. 6 and 7 show that, as the radius of a component such as E–G increases, a local minimum resistance occurs in the presence of component A, as well as component B, at a radius of curvature between r_E = 6.668 cm (2.625 in) and r_G = 10.795 cm (4.25 in). Specifically, the middle value of the radius of curvature (i.e., component F) gives the lowest K value for almost the entire range of Reynolds numbers.

Figure 8 gives a sketch of the visually time-averaged flow field at Re = 3×10^4 for configuration BFMQ, which is exemplary of the local minimum mentioned above. Note that for this case (although not obvious as sketched), the mainstream penetrates deeper into the rotor groove (lower right-hand portion of cavity) than for configuration AGMQ at the same Reynolds number [see Fig. 5(*a*)]. The penetration is probably due to the fact that component F in Fig. 8 has a smaller radius of curvature than does component G in Fig. 5(*a*), resulting in a wider rotor groove in Fig. 8, which allows more mainstream penetration. Increased penetration contributes to a longer path for the mainstream flow, resulting in an increased area (as well as time interval) over which turbulence may be generated and dissipated. In addition, observe that the recirculation zone at the junction of components B and F, for configuration BFMQ, is much larger in Fig. 8 than that at the corresponding junction for configuration AGMQ in Fig. 5(*a*). A direct effect of this could not be easily ascertained from the visualization recordings.

Comparison of Geometry Components in Region II. Figure 9 is a comparison of the resistance for leading-edge extensions giving different shapes for the downstream tooth in Region II as shown in Fig. 3. Component O gives a 12.7 cm (5 in.) tooth tip thickness, component Q a 10.16 cm (4 in.) thickness, and component R a 7.62 cm (3 in.) thickness. Component S is

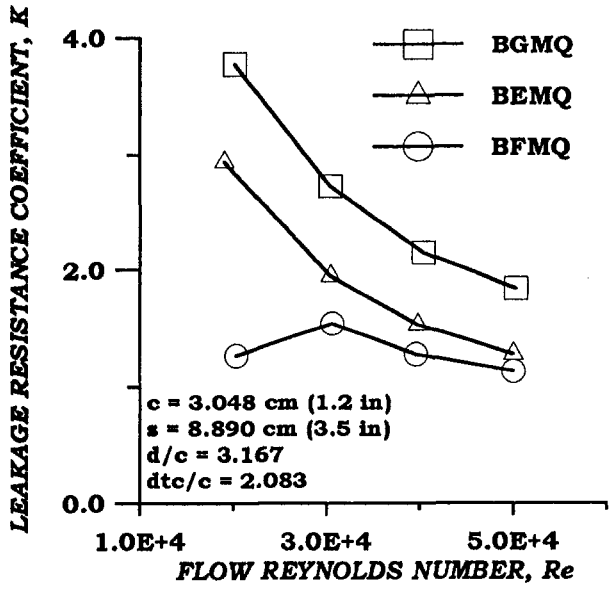

Fig. 7 Measured effect of Reynolds number on leakage resistance comparing components E, F, and G with component B in place

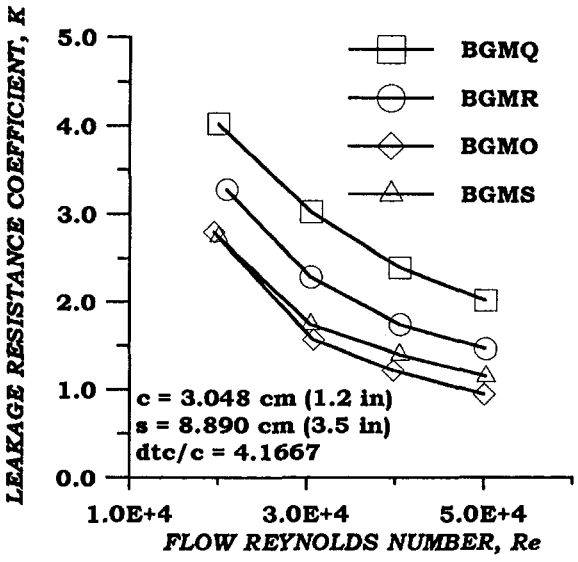

Fig. 9 Measured effect of Reynolds number on leakage resistance comparing effects of leading-edge extension components O–S

the restrictor tooth without a leading edge extension. Observe that the largest leakage resistance values are associated with the 7.62 cm (3 in.) leading-edge extension (component Q) across the entire range of Reynolds numbers. These values display close to a 25 percent improvement over those of component R, which produced the next largest leakage resistance. Components O and S, exhibiting approximately the same value across the range of Reynolds numbers, generated the least resistance with values more than 30 percent less than component Q. No results are available for the effect of component P.

Although no specific flow visualization studies of components O–S are available, leading-edge extensions play a role in determining the amount of rotor groove penetration. Shorter extensions will increase the width of the rotor groove and tend to increase the throughflow path length. Shorter extensions also reduce the tooth tip width.

Conclusions

To obtain an enhanced understanding of the geometry–leakage relationship for the stepped seals considered, the influence of geometry components has been investigated. A very unique test facility was used, which allows flow visualization as well as leakage resistance measurement using a variable-geometry, extremely large-scale model. Two-dimensional, planar models (using the "two-flat-plates" approach) of different advanced seal geometries were studied using a fixed tooth clearance and step height. Comparison of leakage resistance measurements and visualization video recordings gave greater insight into the turbulence generating flow field characteristics. The performance of the specific configurations shown here is not a lot different from that of the annular groove case found in Rhode et al. (1997). For the specific cases and conditions considered here, the primary findings were:

1 Components B and G used in the upstream and downstream portions, respectively, of Region I are generally the best combination. Further, the combination of components B and F are particularly poor for this region.
2 The leakage resistance is not particularly sensitive to the axial location of components E–G in the downstream portion of Region I.
3 Component Q is the best choice for the tooth shape in Region II.
4 The vena contracta recirculation zone produces an intense turbulence shear region, which exerts a significant effect on seal performance.

Acknowledgments

The authors gratefully acknowledge the financial support from the NASA Center for Space Power and from the Texas Advanced Technology Program. Further, the considerable assistance of L. Chavez and B. Evans is appreciated.

References

Fox, R. W., and McDonald, A. T., 1985, *Introduction to Fluid Mechanics,* 3rd ed., Wiley, New York, pp. 359–395.

Hughes, A. F., and Ralph, N., 1970, "The Leakage of Air Through Stepped Labyrinth Seals," thesis submitted to the Department of Mechanical Engineering, University of Bristol, Bristol, England.

Kline, S. J., and McClintock, F. A., 1953, "Describing Uncertainties in Single-Sample Experiments," *Mechanical Engineering,* Vol. 75, Jan., pp. 3–9.

Morrison, G. L., Rhode, D. L., Cogan, K. C., and Chi, D., 1983, "Labyrinth Seals for Incompressible Flow," Final Report for NASA contract No. NAS8-34536.

Rhode, D. L., Broussard, D. H., and Veldanda, S. B., 1993, "Labyrinth Seal Leakage Resistance and Visualization Experiments in a Novel, Variable-Configuration Facility," *STLE Tribology Transactions,* Vol. 36, No. 2, pp. 213–218.

Rhode, D. L., Johnson, J. W., and Broussard, D. H., 1997, "Flow Visualization and Leakage Measurements of Stepped Labyrinth Seals: Part I—Annular Groove," ASME JOURNAL OF TURBOMACHINERY, Vol. 119, pp. 839–843.

Sneck, H. J., 1974, "Labyrinth Seal Literature Survey," *Journal of Lubrication Technology,* Vol. 96, pp. 579–582.

Stocker, H. L., 1975, "Advanced Labyrinth Seal Design Performance for High Pressure Ratio Gas Turbines," ASME Paper No. 75-WA/GT-22.

Stocker, H. L., Cox, D. M., and Holle, G. F., 1977, "Aerodynamic Performance of Conventional and Advanced Design Labyrinth Seals With Solid-Smooth, Abradable, and Honeycomb Lands," Detroit Diesel Allison, Indianapolis, IN, NASA CR-135307.

Waschka, W., Wittig, S., and Kim, S., 1992, "Influence of High Rotational Speeds on the Heat Transfer and Discharge Coefficients in Labyrinth Seals," ASME JOURNAL OF TURBOMACHINERY, Vol. 114, pp. 462–468.

Wittig, S. L. K., Dörr, L., and Kim, S., 1983, "Scaling Effects on Leakage Losses in Labyrinth Seals," ASME *Journal of Engineering for Power,* Vol. 105, pp. 305–309.

Yamada, Y., 1961, "On the Pressure Loss of Flow Between Rotating Co-axial Cylinders With Rectangular Grooves," *Bulletin of JSME,* Vol. 5, No. 20, pp. 642–650.

Zimmerman, H., Kammerer, A., and Wolf, K. H., 1994, "Performance of Worn Labyrinth Seals," ASME Paper No. 94-GT-131.